D 2017

U.PORTO

FEUP **FACULDADE DE ENGENHARIA**
UNIVERSIDADE DO PORTO

SEISMIC BEHAVIOR OF PRECAST PIERS ON HIGH SPEED RAILWAY BRIDGES

ANDRÉ MANUEL BESSA MONTEIRO

A thesis submitted to the Faculty of Engineering of the University of Porto, in accordance with the requirements of the degree of Doctor in Civil Engineering

Porto, 2017

Supervisor: António José Coelho Dias Arêde

Co-Supervisor: Nelson Saraiva Vila Pouca

ACKNOWLEDGEMENTS

ABSTRACT

The context of bridge engineering and, in particular, High Speed Railway Line (HSRL) bridges, has always been one of the most demanding frameworks for structural engineers. In that regard, it is common for technological breakthroughs to be achieved as a result of solving the numerous challenges that high-end structures create, acting as a driving force for constant updates of the common engineering practices. Precast solutions are a prime example of that, regarding economic objectives and strict deadlines, as they strive for optimization of geometrical layouts, reinforcement designs and material compositions, in order to achieve a competitive synergy between design and construction while reducing costs and overall building times.

Precast systems for the construction of bridge decks have undoubtedly become a widespread solution, however full-scale applications for bridge piers have not been considered as much, particularly in the HSRL framework. As far as it is possible to assess, important operational constraints influencing the cost-effectiveness of precast solutions relative to the more common monolithic alternatives, and also critical performance requirements such as those presented by seismic loading, leading to weaker or unreliable designs, are some of the main reasons preventing a larger prevalence of precast for bridge piers.

It is within that context that the current work aimed to provide further insight, by studying a precast bridge pier solution in comparison with monolithic alternatives. In that regard, a double column bridge pier layout is presented, based on a previous design of the foreseen Portuguese venture into HSRL. The pier structure is constituted by two large columns and a short span beam to couple the column heads for displacement compatibility, resulting in a high stiffness bent frame capable of addressing the strict HSRL deformation limits, which is studied in a three stage experimental campaign (for monolithic specimens, precast specimens and single column foundation specimens) under cyclic loading and reduced scale (1:4) conditions.

The experimental data is further used to calibrate refined numerical modelling strategies for evaluation of different and not tested pier conditions, using a 2D FEM based methodology. In addition, it is also used to calibrate global bridge modelling tools within a concentrated plasticity approach, for the comparative assessment of the seismic performance of different bridges designed for monolithic and precast piers, subjected to a variety of increasing intensity ground motions under incremental dynamic analysis procedures.

SUMÁRIO

No âmbito da engenharia de estruturas, o contexto das pontes e, em particular, das pontes inseridas em Linhas de Alta Velocidade (LAV) ferroviária, é reconhecidamente um dos campos de aplicação mais exigentes. Nesse contexto, os desafios criados pelas estruturas mais complexas constituem oportunidades regulares para a utilização de sistemas e processos na vanguarda da tecnologia, servindo como elemento dinamizador para uma atualização constante das práticas mais comuns. As soluções prefabricadas assumem-se como exemplos típicos do referido, no contexto dos objetivos económicos e logísticos a cumprir pelas estruturas, uma vez que permitem a otimização de geometrias, armaduras de reforço e composições materiais, de forma a fomentar sinergias competitivas entre o dimensionamento e a construção, ao reduzir custos e tempos de construção.

Ainda assim, sendo já vasta a experiência de aplicação de sistemas prefabricados em tabuleiros de pontes, o mesmo não se pode dizer para uma utilização em larga escala aplicada aos respetivos pilares, particularmente no que diz respeito a estruturas de LAV. Nesse sentido, sabe-se que não só existem condicionalismos operacionais importantes, capazes de influenciar o rácio custo-benefício das soluções prefabricadas relativamente a soluções monolíticas alternativas, como também questões de exigência estrutural, como por exemplo o carregamento sísmico, que facilmente conduzem a soluções fracas ou pouco fiáveis e, dessa forma, pouco desejadas.

Esse é o contexto do presente trabalho, que visa estudar uma solução prefabricada para pilares de pontes em comparação com soluções monolíticas, através de uma campanha experimental sob condições de carregamento cíclico e escala reduzida (1:4) organizada em três fases (modelos monolíticos, modelos prefabricados e modelos de fundação). A estrutura estudada foi baseada no projeto, entretanto cancelado, para implementação de LAV em Portugal, e é constituída por dois grandes fustes verticais e uma viga de vão curto para compatibilidade de deslocamentos, resultando em elevada rigidez transversal capaz de garantir o cumprimento dos rígidos limites de deformação aplicáveis a LAV.

A informação experimental é posteriormente utilizada para calibrar ferramentas refinadas de modelação numérica, para avaliação de condições de carregamento diferentes das testadas em ambiente laboratorial, através de uma metodologia 2D baseada no MEF. Por fim, realiza-se também o estudo comparativo da performance sísmica de diferentes pontes com sistemas monolíticos e prefabricados, quando sujeitas a carregamentos sísmicos de intensidade crescente e através de procedimentos de análise dinâmica incremental, utilizando modelos globais com plasticidade concentrada calibrada de acordo com a informação experimental.

TABLE OF CONTENTS

LIST OF FIGURES

LIST OF TABLES

LIST OF MAIN SYMBOLS

A_b Cross-section area of beams;

A_c Cross-section area of columns;

A_{sl} Longitudinal reinforcement;

A_{st} Transverse reinforcement;

α_{gR} Reference peak ground motion acceleration;

α_s Shear span-to-depth ratio;

C Stiffness coefficient;

ξ Critical damping ratio;

d^- Concrete compressive damage variable;

d^+ Concrete tensile damage variable;

d_y Yielding displacement;

Δd_i Displacement increment for post-yielding half-cycle i;

$\Delta \mu_i$ Ductility increment for post-yielding half-cycle i;

δ_j Normal joint displacement;

E Young Modulus;

E_{cm} Mean concrete Young Modulus;

ε_{11} Principal tensile strains on Plane stress analyses;

f_{cc} Concrete confined strength;

f_{cm} Mean concrete compressive strength;

f_{uc} Concrete unconfined strength;

F Lateral force;

F_p Peak lateral force;

ϕ Rebar diameter;

g_f, G_f Fracture energy;

γ_I Importance factor;

γ_j Tangential joint displacement;

h Cross-section height;

I Flexural moment of inertia;

J Torsional moment of inertia;

K Secant stiffness;

K_y Yielding stiffness;

K_n Normal joint stiffness;

K_s Shear joint stiffness;

L_h Plastic hinge length;

l_w Wall length;

M   Moment;

M_{Ed} Design moment;

M_S Surface wave magnitude;

N   Axial load;

ν   Axial load ratio;

θ   Slope angle of the compressive struts of shear in concrete;

P_{DL} Probability of exceedence of the damage limitation criterion;

P_{NCR} Probability of exceedence of the non collapse criterion;

$φ_c$ Curvature on columns;

$φ_b$ Curvature on beams;

$φ_{cy}$ Yielding curvature on columns;

$φ_{by}$ Yielding curvature on beams;

q Behavior factor;

R_v Vertical reaction at a column base load cell;

ρ   Longitudinal reinforcement ratio;

s Concrete-steel bond slip;

S_a Spectral acceleration;

S_v Spectral pseudo-velocity;

$σ_{22}$ Principal compression stresses on Plane stress analyses;

$σ_n$ Normal joint stress;

$σ_{n0}^+$ Tensile normal joint stress threshold;

$σ_{sl}$ Longitudinal reinforcement stress;

$σ_{sly}$ Longitudinal reinforcement yield strength;

$σ_{slu}$ Longitudinal reinforcement ultimate strength;

$σ_{st}$ Transverse reinforcement stress;

$σ_{sty}$ Transverse reinforcement yield strength;

$σ_{stu}$ Transverse reinforcement ultimate strength;

t_w Wall thickness;

T Vibration period;

T_1 Fundamental vibration period of a structure;

T_{DL} Return period of the seismic load for the damage limitation criterion;

T_{NCR} Return period of the design seismic load for the non collapse criterion;

$τ_b$ Concrete-steel bond stress;

$τ_s$ Tangential joint stress;

$μ$ Displacement ductility;

μ^{cum} Cumulative ductility;

V_{Ed} Design shear;

V_c Shear capacity component carried by concrete struts;

V_{sd} Shear capacity component carried by main reinforcement;

V_{st} Shear capacity component carried by transverse reinforcement;

V_{Rd} Design shear strength;

LIST OF ABBREVIATIONS

HSRL   High Speed Railway Lines;

RC   Reinforced Concrete;

FEUP   Faculty of Engineering of University of Porto;

LESE   Laboratory of Earthquake and Structural Engineering;

SIPAV   *Soluções Inovadoras Pré-Fabricadas para Vias Férreas de Alta Velocidade*;

MEBEP   *Mota Engil – Betões e Prefabricados*;

RAV   *Rede de Alta Velocidade*;

LUD   Lock-up Devices;

RTRI   Railway Technical Research Institute;

ULS   Ultimate Limit States;

SLS   Service Limit States;

SI   Spectral Intensity;

PGA   Peak Ground Acceleration;

EQ   Earthquake;

CIP   Cast-in-place;

PRESS   PREcast Seismic Structural System;

DFRCC   Ductile Fiber Reinforced Cement Composite;

STU   Shock Transmission Unit;

FBD   Force Based Design;

DBD   Displacement Based Design;

FEM   Finite Element Method;

WC   Wall-pier column segment;

WP   Wall-pier panel segment;

LVDT   Linear Displacement Voltage Transducers;

DWT   Draw Wire Transducers;

LC   Load Cell;

PL   Performance Level;

IM   Intensity Measure;

EDP   Engineering Demand Parameter;

DM   Damage Measure;

DV   Decision making Variables;

PBEE   Performance Based Earthquake Engineering;

IMK   Modified Ibarra-Medina-Krawinkler;

1
INTRODUCTION

1.1. BACKGROUND OVERVIEW

The permanent technological evolution supporting man's standing against the multiple challenges posed by history has truly been promoting globalization in our world. Individual social scopes are broadening, people are changing how they think regarding family, business and career management, and the economical background of the XXI century has been growing support on the concept of multinational companies and populations.

One of the main reasons behind that evolution has been the refinement of the international travelling and transportation routes, nowadays enabling the establishment of efficient connections that were, in the past, either too costly or time-consuming. On that context, the importance of Railway and, particularly, High Speed Railway Lines (HSRL) is duly noted, benefitting from high technological advances and an increase in territorial coverage which confirmed them as a clear alternative to more common means of transportation, presenting an adequate balance between costs and travel time while usually associated with significant levels of comfort. Unsurprisingly, it can be seen that more and more countries are improving their railway networks, with more than a dozen now promoting dedicated high speed lines.

From a technological perspective, railway lines are usually quite long, developing over hundreds of kilometers and presenting difficult morphological challenges that are often addressed with the construction of bridges and viaducts. In that regard, since the control of high initial investments is usually a common concern for the railway promoters, using optimized structural layouts and construction methods can strongly improve the economic viability of the whole project. Therefore, Reinforced Concrete (RC) precast techniques can prove to be a good

option, providing economic solutions and reduced construction time periods, while still guaranteeing adequate performance under safety and service conditions.

In the specific case of HSRL, there are multiple examples of structures built using full or partial precast solutions for bridge decks. One can observe cases with "*U-shaped*" beam elements (e.g. Spain), cases where the decks are supported by multiple prestressed beams (e.g. France), or even where full-span box girders are used (e.g. Italy, Taiwan), thus highlighting precast solutions applicable to a wide array of bridge layouts. On the other hand, precast elements are rarely considered for the construction of full railway bridge piers, particularly in HSRL. In fact, apart from a few cases in Belgium and Netherlands where the bridge substructure was designed using an unconventional layout where some precast elements were included, the generalized application of that technology for bridge piers still seems to be a non-reality, at least to the extent that was possible to investigate. There are a number of reasons that can help on explaining that circumstance but still, in the author's opinion, extending the general use of precast solutions to bridge piers, as well as to decks, could potentially lead to substantial economic advantages and increased production capacity of construction companies, provided the challenge is technically viable.

From a purely technical perspective, structural solutions for railway bridge and viaduct piers are designed for compliance against very strict performance criteria, particularly considering applications on high speed lines. Train nosing, traction and braking forces, horizontal deflection limits and, additionally, seismic loads are some of the more impactful aspects of railway bridge substructure design. Moreover, although the seismic performance of bridge piers is a well documented area involving numerous experimental and numerical works performed by scientific community members in the latest decades, the specific context of railway bridges and, particularly, those designed for high-speed trains is not yet as thoroughly addressed. Also, this fact is further enhanced when discussing the possibility of adopting precast applications, raising other concerns related with durability and on-site workability issues that are important for the design of precast RC structures.

In this framework, the present thesis aims at studying, discussing and providing relevant contribution to general knowledge on that area and, hopefully, to foster further discussion of the above mentioned subjects.

1.2. MOTIVATION AND OBJECTIVES

The main motivation for this work originated from a research project carried out at the *Faculty of Engineering of University of Porto* (FEUP) between 2009 and 2013, named SIPAV – *Soluções Inovadoras Pré-Fabricadas para Vias Férreas de Alta Velocidade* (Innovative Precast Solutions for High Speed Lines), where the author actively participated. The project aimed to study the application of precast techniques on the context of High Speed Railway Lines, and to evaluate the potential for technical innovation regarding new and/or existing improved design solutions. With that in mind, FEUP and the external construction contractor MAPREL/MEBEP (*Mota Engil – Betões e Prefabricados*, now a part of *Mota Engil – Engenharia e Construção*) joined efforts hoping to profit from the technical knowledge and analytical capabilities of the former, together with the practical insight of the latter concerning common practices and design misconceptions. This joint endeavor engaged two worlds that take significant benefit in learning from one another, since academic studies ultimately aim to provide practical solutions to the real world requirements. Therefore, the whole project was highly appealing to the author, as he firmly believes that the development of new skills and knowledge in this area is greatly enhanced by industry interest, and that its technological outlook should be a main driving force for related research objectives.

Part of the work presented in this thesis was initially developed for the SIPAV project, from which some guidelines were established. Considering the main area of expertise of MAPREL/MEBEP, only RC construction was addressed; in addition, fully precast pier elements were sought instead of partial precast applications. Furthermore, some decisions taken during the development of the research project, which affected the general outline of this thesis, were also influenced by political and economic objectives at that time, strongly supporting HSRL implementation in Portugal starting with the Poceirão-Caia line portion (whose construction was initiated but halted at mid-course). Nonetheless, owing to the complexity of the different thematic areas likely to influence the technical viability of a precast application for HSRL bridges, such as structural behavior (e.g. strength, ductility and durability), building process (e.g. joint connections execution, on-site element handling and accessibility) and also logistics (e.g. formwork reuse capability, precast tables setup, transportation, storage capacity), the approach followed in the present work narrowed the study mostly to the issues related with structural behavior and, particularly, those on the seismic performance framework.

Therefore, this thesis, as expressed by its title "*Seismic Behavior of Precast Piers on High Speed Railway Bridges*", addresses the main objective of promoting the study and possible use of precast solutions designed for railway bridge structures, particularly focusing on the piers, in

areas of moderate to high seismicity, where concerns regarding stable mechanisms of earthquake energy dissipation and ductile deformation capacity are of critical importance. In that context, the precast applications studied within this work aim to provide good seismic performance, accounting for the difficulty of ensuring ductile behavior with potentially large inelastic incursions, particularly in the precast joints. In order to assess different design options for precast systems and to identify their most significant strengths and weaknesses relative to equivalent monolithic construction, the elaboration of an experimental campaign capable of providing such information was also a significant objective of this work.

Finally, while the local demand and global response of specific precast system components can be adequately assessed from experimental testing, the influence of such findings on the performance of a real bridge is still one of the most important aspects to consider when full-scale application is desired. Therefore, the complementary link between those two issues (system/component analysis and full bridge behavior) constitutes the final objective of this work, intended to be addressed resorting to experimentally calibrated numerical applications, where the performance of the pier systems is tested on both a local and global perspective.

1.3. THESIS OUTLINE

The organization of the present document aims to reflect the strategy adopted to accomplish the proposed objectives. For that purpose, it should be acknowledged that while each chapter tackles fundamentally distinct parts of the work, a common guideline is still followed throughout, which can roughly be linked to the thought process for designing, analyzing and validating the structural solutions herein presented. Thus, the thesis is comprised of eight chapters, which are presented as follows:

- Chapter 1, of which this section is a part of, essentially aims at briefly describing the framework of the thesis, its general outline as well as its objectives;

- Chapter 2 presents the first stage of the work, mostly focusing on understanding the design challenges that HSRL piers are required to overcome. For that purpose, railway specific loading and design criteria are briefly discussed, particularly addressing aspects that impact the pier design. Furthermore, pier layouts commonly used in HSRL structures are also reviewed, aiming at the definition of a *"typical use"* profile by taking into account the geometric and structural characteristics of the bridges and viaducts they were designed for;

- Chapter 3 consists of a state-of-art review of the main precast solutions for RC columns, with special emphasis on bridge piers. Aspects related with the manufacturing process, transportation, handling and joint connections are also herein discussed. Additionally, some of the most recent design strategies for improving the seismic performance of bridge piers on high seismic demand situations are also discussed in order to evaluate their potential for application with precast systems;

- Chapter 4 aims to describe the studies performed to define the conceptual solution proposed for experimental testing. The RAV[1] Poceirão-Caia design proposal is presented as the basis for this work, taking into account its importance in the development on the SIPAV project. Also, the design and detailing strategy for the structural solution of the proposed pier concept is object of several analysis and discussions, including a numerical study made for a selection of viaducts from the previously mentioned Poceirão-Caia design project, where seismic response parameters are estimated for the test specimen design.

- Chapter 5 encloses all the activities related with the experimental campaign carried out within this work. Thus, the process of designing and testing the laboratory setup is thoroughly described, and experimental observations for all the tests are also presented. Moreover, the obtained results are discussed and compared for a variety of different response parameters, aiming at further characterizing differences between monolithic and precast models.

- Chapter 6 presents the first stage of numerical applications performed on this work, essentially aiming to use the experimental data for calibration of numerical models suitable for exploring and studying further non-tested scenarios. For that purpose, a refined FEM modeling strategy was prepared for simulation and validation against a selection of pier tests, which was then used to simulate similar applications with different constraints and geometric characteristics, aiming at representing the expected demand range defined for the pier systems.

- Chapter 7 describes the second stage of numerical applications, based on the global simulation of a set of idealized case study viaducts for seismic performance assessment regarding several damage measures. The experimental data was used to

---

[1] RAV stands for "*Rede de Alta Velocidade*" (in portuguese), which translates into "*High Speed Network*".

calibrate the behavior of piers on each structure, according to monolithic and precast results, and incremental dynamic analysis were performed for the calculation of fragility curves, which are the statistical representation of the probability of exceedence of a given damage or performance state;

- Chapter 8 concludes this thesis and, as such, describes the main conclusions extracted from multiple areas of the present document, as well as the future development proposals relevant to the addressed frameworks. Due to its preponderance on the work development, the relative performance of precast and monolithic systems is given particular attention;

2
PIERS FOR HSRL BRIDGES AND VIADUCTS

2.1. INTRODUCTION

The main objective established for the present work, integrated in the previously mentioned SIPAV research project, involves three thematically different areas addressing the following topics: railway bridge design, pier seismic performance and precast mechanisms. Moreover, while its focus is directed to the seismic performance of bridge piers, it is undeniable that each of those frameworks can present varied design challenges that need to be taken into account when discussing a precast application for HSRL structures.

In that regard, a global overview of existing railway bridges and viaducts enables the following conclusion: the use of precast elements in the construction of pier structures is limited, especially in the context of HSRL. Some cases can be observed where precast pieces were used as casting forms for the footing and deck connections, or where unconventional design options were adopted to allow industrialized construction procedures, but virtually no application could be identified where the main body of the pier structure was fully precast.

In a way, that circumstance highlights the innovative nature associated with the SIPAV project, considering that a precast construction is sought on the framework of structures that are usually built with *in situ* methods. More importantly, the knowledge of the common layout solutions used for those situations can help on guiding the design for precast, because similar demands can be expected assuming that the general behavior patterns of the structure can be maintained for the present application. Additionally, there are important railway bridge performance requirements for compliance with safety and service conditions that are not

considered for other structure types (namely motorway bridges), which have a relevant impact in structure design and, therefore, provide valuable insight for the current discussion.

With that in mind, this chapter essentially aims to review the most common railway bridge design options and associated performance criteria, by observing typical application cases which may help on understanding some of the main design challenges set for the present endeavor.

2.2.   COMMON RAILWAY BRIDGE LAYOUTS

In general, decisions regarding the construction of new bridges and viaducts address multiple thematically distinct areas. Concerns related to politics and economics (initial investment/maintenance costs, expropriations, economic potential of affected locations), environmental issues (existence of water courses, impact on biological activity) and, naturally, technical difficulties are some of the most relevant. In that regard, the applicable performance requirements are heavily dependent of the specific use that the structures are to be designed for, which, for bridges and viaducts, generally refers to motorway or railway purposes.

Moreover, while this often leads to concerns of similar nature, the different characteristics of the travelling stock of each type of traffic lead to distinct design challenges. For example, on railways the trains move through a rigorously defined path whose positioning is strictly set by the rail track, and the train operators solely control the longitudinal movement issues, such as speed and direction. Additionally, the physical dimension of trains is larger than road vehicles (AREMA (2003)). By contrast, on motorways there is more freedom of transverse movements associated with the steering capacity of vehicles, which also have generally higher ratios of power per mass unit.

As a consequence, railway bridge design is more rigorously defined by track related safety and operational issues than motorway structures, where structural performance is often the critical factor. For example, a common characteristic of some railway lines is the use of continuous welded rail (particularly on HSRL); in that context, the rail stress levels must be controlled, especially under traction and braking forces as well as thermal loading, to prevent the occurrence of instability phenomena such as rail buckling, which is illustrated in Figure 2.1.
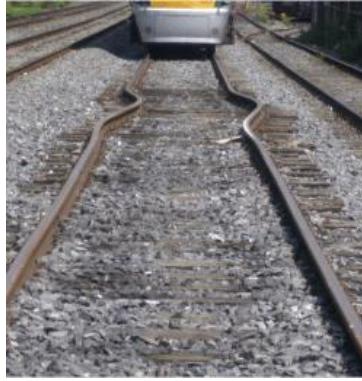
Figure 2.1 – Rail buckling (from http://www.railtemperature.com/)

The potential for the occurrence of track instability can force the use of rail expansion devices, in order to reduce the stresses produced due to longitudinal bridge movement, but that can be an undesired design decision since it may end up reducing overall track durability (Figueiredo *et al.* (2009)). Moreover, the increasing design speed for railway lines brought to light severe dynamic performance problems, related to deck accelerations capable of causing loss of wheel-rail contact or track side-resistance (Zacher and Baeßler (2005)), which also require rigorous structure stiffness and displacement control.

In this context, it is understandable that railway bridge design options require adequate structural layouts capable of providing generally low displacements. Concerning the longitudinal direction, simply supported deck spans or continuous decks are often some of the most common options. The former may ensure track stability without the need of track expansion devices, benefitting line durability and is also simpler to evaluate. However, it may also present a significant limitation to the structural stiffness contribution provided by the bridge deck for longitudinal movement, therefore increasing the need for strong piers capable of controlling horizontal deformations. It is usually observed in low rise bridges with short spans between 25m to 35m, where decks can provide sufficient stiffness to vertical deflections while horizontal movement is largely controlled by the columns.

By contrast, continuous span decks can ensure higher overall stiffness and generally perform better under dynamic loading. When used with rail expansion devices, the length of continuous structures can go up to 1200m (Manterola and Cutillas (2004)), otherwise a maximum value of 90m should be respected for concrete structures. This type of deck is frequently seen with longer spans and in high rise bridges, often designed to cross deep valleys. Therefore, the longer spans are often a considerable challenge for design, requiring the use of advanced construction technologies such as the balanced cantilever method.

Other options include design of an association of smaller multi-span continuous decks, where the length of each segment can be adjusted according to the needs of any particular project. That means this approach can avoid using rail expansion devices by having each deck part with less than 90m of length and separated by a structural joint or, alternatively, single span frames, as illustrated in Figure 2.2 - a). However, just like in the case of simply supported spans (and for the same reasons), it also means that each continuous deck segment should present sufficient longitudinal stiffness; when that is not possible, it is usual to provide a certain number of higher stiffness fixation zones, where the structure can mobilize horizontal reactions. Those zones can be simply constituted by columns that are designed for higher stiffness, or by using a different support bearing scheme (possibly including some type of rigid shear key device).
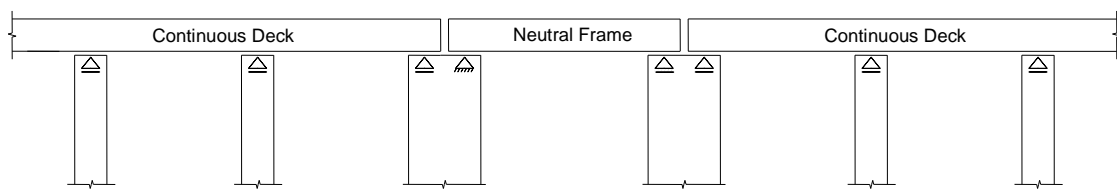
a) Single neutral frame in between continuous decks
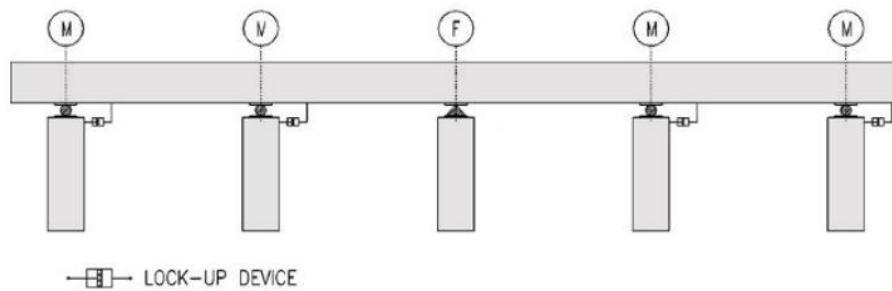
b) Continuous deck using LUDs (Marioni (2006))

Figure 2.2 – Different longitudinal static schemes for continuous span railway bridges

Additionally, the use of Lock-up Devices (LUD, as shown in Figure 2.2 – b)) is also a possibility that enables a good compromise between performance due to creep, shrinkage and thermal related movements, and dynamic loading. These devices are usually constituted by a hollow cylinder with two chambers, filled with a viscous silicon compound and separated by a movable piston (Figure 2.3). When the two anchor points of the device are displaced due to a slow-velocity action such as thermal load or creep/shrinkage effects, the piston slowly moves through the compound with very little friction, therefore generating low reactions, comparable to sliding bearing behavior. However, when high-speed loads are applied such as train traction, braking or earthquake loads, the compound is squeezed through the piston, generating high friction that blocks movement between the two anchor points, therefore enabling fixed support

behavior. This is the main difference between LUDs and regular Viscous Dampers, as the former provides considerably higher damping and stiffness.
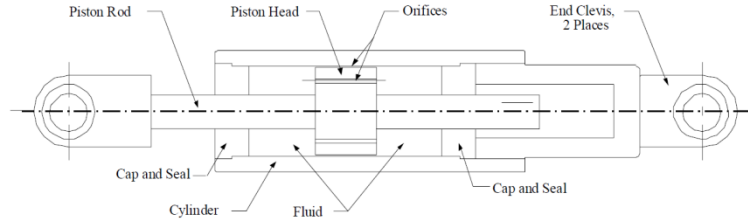
Figure 2.3 – Lock-up Device: Schematic view (Taylor, Taylor Devices Inc.)

2.3. RAILWAY BRIDGE SEISMIC DESIGN

2.3.1. GENERAL REMARKS

In order to understand some of the most common seismic design concerns associated with railway bridges and viaducts (particularly with the piers), a brief review of relevant performance requirements is presented. For applications in Portugal, the Eurocodes are usually considered, and their main railway specific recommendations can be found in Eurocode 0 (EC0 - EN1990-1, +A1:2005 (2002)) and Eurocode 1 (EC1 - EN1991-2 (2003)), whereas general seismic design guidelines are included in Eurocode 8 (EC8 - NP EN1998-1 (2010) and EN1998-2 (2005)). For further guidance on the subject, other relevant literature can also be consulted, such as the Japanese standard issued by the Railway Technical Research Institute (RTRI), for example (RTRI (2007a) and RTRI (2007b)), which provide additional insight onto the seismic performance problem.

The design principles considered for structure compliance regarding Ultimate Limit States (ULS) are generally related to structural safety and users' safety. The corresponding main concern is to prevent collapse, which is defined for loss of equilibrium of the structure or any part of the structure, loss of stability due to excessive deformations or member failure, and/or failure due to time-dependent effects (e.g. fatigue). Regular practice involves the combination of loads in such a way to obtain the most unfavorable effects for each structural element. Within the context of Eurocode 0 and Eurocode 8, applicable ULS combinations are represented by equation 2.1 for persistent action design and 2.2 for seismic action design.

$$E_d = \sum_{j \geq 1} \gamma_{G,j} \cdot G_{k,j} \; " + " \gamma_P \cdot P " + " \gamma_{Q,1} \cdot Q_{k,1} " + " \sum_{i>1} \gamma_{Q,i} \cdot \psi_{0,i} \cdot Q_{k,i} \qquad 2.1$$

$$E_d = \sum_{j \geq 1} G_{k,j} \; " + " P_k " + " A_{Ed} " + " \sum_{i>1} \psi_{2,i} \cdot Q_{k,i} " + " Q_2 \qquad 2.2$$

where:

- γ - Partial safety factors for actions;

- G - Permanent loads;

- P - Prestress loads;

- Q - Variable loads;

- Q_2 – Long duration load effects;

- A_{Ed} – Design seismic load;

- ψ – Combination coefficient;

Furthermore, Service Limit States (SLS) are also considered to ensure that, for example, deformation limits are compatible with normal structure use. Within that context, ULS design tends to lead to strength capacity checks, implying that the effects of the actions are inferior to structural capacity within a small margin of probability of exceedence for extreme occurrences (as represented in equation 2.3), while SLS design generally involves explicit or implicit control of structure displacements (and stress levels) under loading scenarios correspondent to higher probability of occurrence.

$$E_d \leq R_d \qquad\qquad 2.3$$

The condition of railway traffic, however, introduces a few performance requirements that challenge the previous notion by involving several checks of structure deformations that aim to provide safety to the circulation of trains. In that regard, those can effectively be considered as ULS and not SLS (Goicolea (2007)), for the purpose of rail traffic safety checks, despite them being introduced as such. Additionally, there are other requirements related with ensuring passenger comfort, which are also relevant for SLS design. The following list includes most of the applicable performance checks according to EC0/EC1, for which the associated limits tend to be stricter for higher design speed values:

Performance checks related with running safety of trains:
- Vertical accelerations of the deck;

- Vertical deflection of the deck;

- Twist of the deck measured along the centre line of each track;

- Rotation of the deck extremities about a transverse axis;

- Vertical displacement between deck end sections;

- Longitudinal displacement of the upper surface deck extremities;

- Transverse deck deflection;

- Horizontal rotation of the deck about a vertical axis;

- First natural frequency of lateral vibration of the spans;

- Unrestrained uplift at the bearings;

Performance requirements relative to traveling comfort of passengers:

- Vertical accelerations inside the coach;

Among all the previous, most of the listed criteria influence the design in order to provide control of not only the associated displacements, but also the rail stress levels, as previously discussed. Moreover, the criteria that influence pier design are essentially those that suggest a limitation of horizontal deformations, namely the relative longitudinal movement between upper surface deck extremities and the horizontal rotation of decks about a vertical axis, which can be linked to global transverse displacements of pier and deck. In this regard, the consideration of large train traction and braking forces, nosing forces and centrifugal forces on curved viaduct segments lead to some of the most relevant design challenges.

Within that context, it is understandable the increased stiffness of railway bridge and viaduct design layouts relative to equivalent motorway structures. However, increased structural stiffness can often induce larger seismic forces, involving a different major concern for bridges and viaducts, particularly on areas prone to strong earthquake activity. In that regard, according to the design philosophy of EC8, seismic performance must be assessed for two different intensity levels, corresponding to the following requirements:

- No collapse
  This demand level requires the structure to withstand the action of a design seismic load while retaining structural integrity and some residual capacity, even if local or global collapse occurs. The design seismic load is defined for a reference probability of exceedence P_{NCR} of 10% in 50 years, corresponding to a reference return period T_{NCR} of 475 years.

- Damage limitation
  The damage limitation requirement represents the need to account for earthquake events that happen more frequently than the design seismic action. For economic reasons, the structure is expected to remain fully functional, with little or no display

of structural damage requiring immediate attention and repair. The seismic event related to this criterion has a probability of exceedence P_{DL} of 10% in 10 years, corresponding to a reference return period T_{DL} of 95 years.

One of the most relevant aspects of seismic design with interest to pier applications is that the formation of flexural plastic hinges is allowed, as long as specific detailing rules are adopted for provision of sufficient ductile deformation capacity. In addition, bridge decks are expected to remain essentially elastic, with only local damage allowed in secondary components such as expansion joints. Within this context, it is possible to understand that this methodology incorporates a tradeoff between strength capacity and deformation capacity, since the piers can be designed for a reduced strength demand but involving the accommodation of displacements above than the elastic levels.

Therefore, it can casually be said that railway and seismic performance criteria are associated with nearly opposite perspectives concerning pier design: the former leads to increased stiffness while the latter accepts increased displacements. Finding the right balance between the two is not an easy task, and it is made harder by the fact that there is no distinction between running safety check limits proposed for regular railway travels and those that may be applicable to seismic events (constituting a much more severe and rare occurrence).

In fact, other sources show that usually larger values are considered for rail traffic safety during an earthquake event. The Japanese standards, for example, provide a more straightforward integration of these issues, as they include a clear distinction between ordinary railway travels and those under seismic loading conditions. Furthermore, a performance based approach is adopted, where different objectives are established for varying levels of structure response. For ordinary travel conditions, riding comfort (serviceability) and running safety (safety) are checked, while for seismic conditions running safety is the main concern. An additional restorability performance level is also introduced, associated with expectations of no or minimal need for repair. Restorability is checked for rail traffic operating under both ordinary and seismic conditions. The associated performance items are illustrated in Figure 2.4.

Structure Type	Performance Item	Verification Index	Computation of Response Values	Setting Limit Values and Verification
Single span girders, continuous girders	Running safety in ordinary conditions	Deflection of main girder	Girder deflection of concrete structures / Girder deflection of steel-composite structures	Verification of girder deflection
		Deflection of lateral girders	Differential displacement of track surfaces	Verification of differential displacement on track surfaces
		Displacement of vertical supports		
	Riding comfort	Deflection of main girder	Girder deflection of concrete structures / Girder deflection of steel-composite structures	Verification of girder deflection
		Deflection of lateral girders	Differential displacement of track surfaces	Verification of differential displacement on track surfaces
		Displacement of vertical supports		
	Restorability of track damage in ordinary conditions	Displacement of vertical supports	Differential displacement of track surfaces	Verification of differential displacement on track surfaces
Piers, abutments, rigid frame viaducts	Displacement associated with running safety in a seismic condition	Vibration displacement (SI)	Lateral vibration displacement of structures during an earthquake	Verification of lateral vibration displacement of a structure in a seismic condition
		Angular rotation of girder ends	Differential displacement of track surfaces during an earthquake	Verification of differential displacement of track surfaces in a seismic condition
		Alignment irregularity of girder ends		
	Displacement associated with track damage in a seismic condition	Angular rotation of girder ends	Differential displacement of track surfaces during an earthquake	Verification of differential displacement of track surfaces in a seismic condition
		Alignment irregularity of girder ends		

Figure 2.4 – Performance assessment strategy for railway bridge service, prescribed in the Japanese RTRI standard (RTRI (2007b))

According to the previous, the set of requirements for railway performance within seismic events' framework, are slightly less strict when compared to those applicable for ordinary operating conditions, which is a reasonable compromise. Likewise, according to Dutoit *et al.* (2004), it is a usual practice to associate the displacement verifications and serviceability requirements to a seismic event of reduced intensity, which is similar to how EC8 considers a damage limitation requirement comparatively to the no collapse requirement. However, eurocode's provisions do not account for different performance targets according to ordinary travel conditions or those under seismic loading, and single limit values are proposed for each criteria.

Within this context, the following sub-sections aim to briefly present the seismic action as considered for this work, in addition to the verification limits associated with the relevant performance requirements for pier design, according to the previous discussion.

2.3.2. RAILWAY PERFORMANCE REQUIREMENTS

2.3.2.1. Longitudinal deformations

The main concerns associated with large longitudinal deck displacements are related to the increased stresses accumulated in the rails due to thermal and variable loads which, according to EC1, require careful assessment and limitation to 72 MPa in compression and 90 MPa in tension. Therefore, the horizontal displacement δ_2 between deck parts (or relative to the abutments) due to traction or braking (Figure 2.5 – a)) is limited to:

- 5 mm for continuous welded rails without rail expansion devices or with a rail expansion device at one end of the deck;

- 30 mm for rail expansion devices at both ends of the deck;

- More than 30 mm only if both expansion devices and ballast movement gaps are considered;

As a reference, the values presented by Dutoit *et al.* (2004) on account of the design of HSRL in Mediterranean France and Asia for continuous welded rail structures, without rail expansion devices and under the moderate earthquake, were 20mm and 25mm, respectively. Additionally, the horizontal movement between deck parts (or relative to the abutments) due to vertical loading (Figure 2.5 – b)) is limited to:

- 8 mm when track-structure interaction is taken into account;

- 10 mm when track-structure interaction is ignored;

a) Limit due to traction and braking

b) Limit due to vertical loading
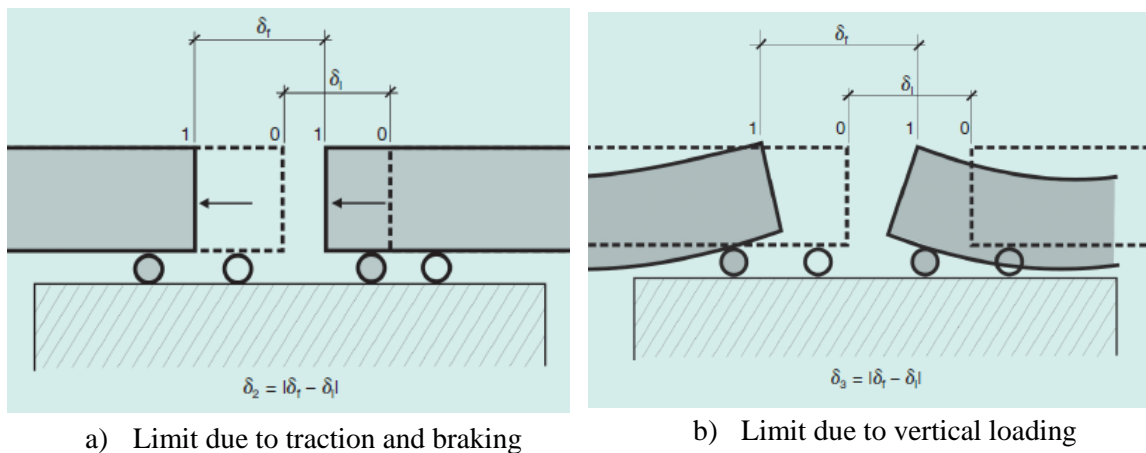
Figure 2.5 – Illustration of horizontal movement limit (DGF (2007))

The previously presented conditions are a significant challenge to the longitudinal stiffness of bridges and viaducts. Moreover, the limits are small enough so that the combined effect of at least pier bending, foundation rotation and displacement, as well as bearing displacements must

be taken into account in the global stiffness, in order to obtain realistic results. For that reason, track-structure interaction analyses are usually mandatory, because simplified procedures generally lead to results that are too conservative (Dutoit (2007)).

2.3.2.2. Transverse deformations

With respect to transverse deformations, lateral deflection is checked to ensure an appropriate track radius for rail traffic. The main performance checks imply the assessment of the maximum horizontal rotation between deck parts (or between the deck and the abutments), as well as the maximum change in curvature radius. EC0 suggests the following limits, presented in Table 2.1.

Table 2.1 - Limits for the maximum transverse deformation (EN1990-1, +A1:2005 (2002))

Speed range V (km/h)	Maximum horizontal rotation (radian)	Maximum change of radius of curvature (m)	
		Single deck	Multi-deck bridge
$V \leq 120$	α_1	r_1	r_4
$120 < V \leq 200$	α_2	r_2	r_5
$V > 200$	α_3	r_3	r_6

NOTE 1 The change of the radius of curvature may be determined using:

$$r = \frac{L^2}{8\delta_h} \tag{A2.7}$$

NOTE 2 The transverse deformation includes the deformation of the bridge deck and the substructure (including piers, piles and foundations).

NOTE 3 The values for the set of α_i and r_i may be defined in the National Annex. The recommended values are:
$\alpha_1 = 0,0035$; $\alpha_2 = 0,0020$; $\alpha_3 = 0,0015$;
$r_1 = 1700$; $r_2 = 6000$; $r_3 = 14000$;
$r_4 = 3500$; $r_5 = 9500$; $r_6 = 17500$

δ_h – transverse deflection of the deck;
L – deck span length;

The values from the previous figure highlight a critical dependence of railway line design speeds, as the performance limits for its highest values are more than two times as severe as for speeds lower than 120 km/h. Therefore, the maximum horizontal rotation would be limited to 0.0015 rad for bridges and viaducts designed for train speeds greater than 200 km/h.

In this regard, the limits considered by Dutoit *et al.* (2004) for performance under the moderate intensity earthquake for the design of the French Mediterranean and Asian HSRL structures were slightly larger, 0.0030 rad for the former, and up to 0.0017 rad for the latter.

Additionally, the Japanese lateral deflection and corresponding angular rotation limits, for running safety under seismic conditions, vary according to the type of track deformation experienced (parallel shift or folding). For design speeds greater than 360 km/h, the minimum angular rotation limit considered is 0.002 rad, according to Table 2.2, which is still larger than the EC0 value. For the restorability performance level, even larger values of 0.006 rad or 0.008 rad are considered, for slab track or ballast track, respectively. Nonetheless, it should be noted that these values are associated with the Japanese JIS 50N and JIS 60 specifications, and not the UIC54 or UIC60 rail types that are usually observed in European HSRL.

Table 2.2 – Seismic condition displacement limits on the Japanese RTRI Standard (RTRI (2007b))

Direction	Maximum Speed (km/h)	Angular rotation θ ($\cdot 1/1000$)			Alignment Irregularity (mm)
		Parallel shift		Folding	
		L_b=10m	L_b=30m		
Lateral	130	7.0		8.0	14
	160	6.0		6.0	12
	210	5.5	3.5	4.0	10
	260	5.0	3.0	3.5	8
	300	4.5	2.5	3.0	7
	360	4.0	2.0	2.0	6

a) Running safety performance level

Displacement Direction	Track Type	Angular Rotation ($\theta/1000$)		Alignment irregularity δ (mm)	
		Folding/Parallel shift			
		50N Rail	60kg Rail	50N Rail	60kg Rail
Vertical direction	Slab track	5.0	3.5	4.5	3.5
	Ballast track	7.5	6.5	3.5	4.0
Lateral direction	Slab track	6.0	6.0	2.0	2.0
	Ballast track	8.0	8.0	2.0	2.0

b) Restorability performance level

In addition, maximum lateral vibration displacements are also checked for the seismic condition, resorting to the Spectral Intensity (SI) calculated from the pseudo-velocity of an equivalent period structure at the track level. The corresponding verification is made by comparison against values of Figure 2.6, where the design SI (in mm) should, for the associated structural period range, stand below the threshold represented by the blue line.
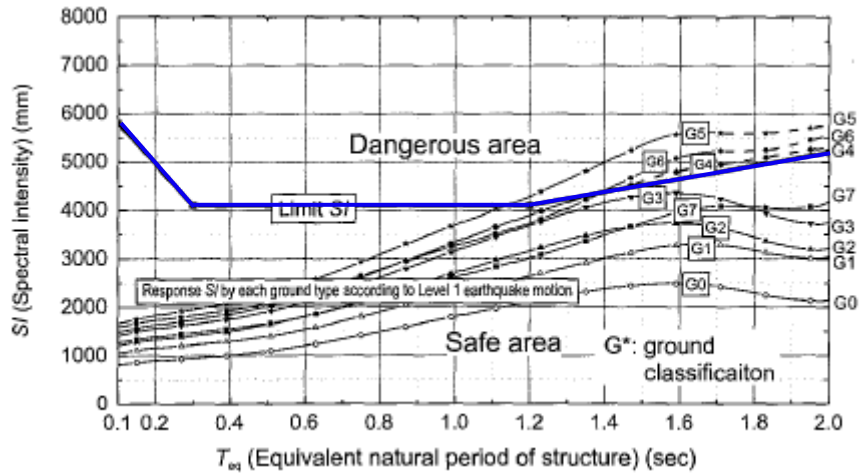
Equivalent natural period of structure T_{eq} (sec)		
shorter than 0.3	0.3~1.2	longer than 1.2
$-8,500T_{eq}+6,650$	4,100	$1,375T_{eq}+2,450$

Figure 2.6 – Lateral vibration displacement limits (adapted from RTRI (2007b))

2.3.3. SEISMIC LOAD

In addition to the horizontal train loads, seismic loading is widely acknowledged as a critical factor in bridge pier design. Regarding applications in Portugal, the Eurocode requirements of no collapse and damage limitation are associated with the definition of two seismic intensity levels, identified by reference peak ground acceleration values (PGA) α_{gR} of earthquake (EQ) events reflecting the local seismicity of the construction site under analysis. Furthermore, EC8 suggests the consideration of two different sets of EQ characteristics for each reference PGA, in order to reflect the influence of distinct seismic events regarding for example magnitude and distance to epicenter:

- Type 1 EQ: High and moderate seismicity regions ($M_s > 5.5$);
- Type 2 EQ: Low seismicity regions ($M_s \leq 5.5$) and near-field earthquakes;

Structures are also classified according to the importance factor γ_I, enabling the characterization of seismic intensity levels that are different than the reference values, reflecting the different evaluation of the importance of specific bridges, regarding consequences for human life in case of failure, or *"for maintaining communications, especially in the immediate post-earthquake period, and on the economic consequences of collapse"*. Three importance classes are established for bridges, according to Table 2.3, which can be related to the consequence classes defined in EN1990 (2002).

Table 2.3 – Seismic Importance factors

Importance class	Importance factor γ_I
I	0.85
II	1.00
III	1.30

The reference seismic PGA for either type of EQ and return period T_{NCR} of 475 years can be determined from the national zoning maps, which are a representation of the local seismic hazard assumed to be constant within each zone, found in each country's National Annex. Figure 2.7 illustrates the seismic zoning maps for mainland Portugal, whereas the corresponding reference PGA values can be obtained from Table 2.4. Those values can be adjusted for the return period T_{NCR} of 95 years correspondent to the damage limitation requirement by using the recommended reduction factors ν of 0.40 and 0.55 for Type 1 and Type 2 EQ, respectively.
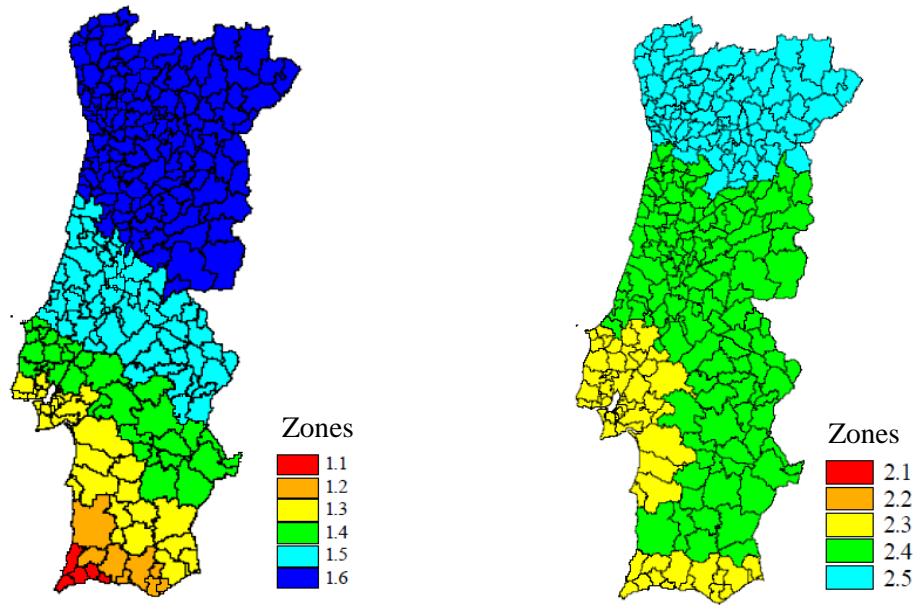
Figure 2.7 – Seismic zoning map for Portugal (adapted from NP EN1998-1 (2010))

Table 2.4 – Reference PGA values for Portugal (NP EN1998-1 (2010))

Type 1 EQ		Type 2 EQ	
Seismic Zone	a_{gR} (m/s^2)	Seismic Zone	a_{gR} (m/s^2)
1.1	2.50	2.1	2.50
1.2	2.00	2.2	2.00
1.3	1.50	2.3	1.70
1.4	1.00	2.4	1.10
1.5	0.60	2.5	0.80
1.6	0.35	-	-

Characterization of multi components for the seismic action according to different loading directions should be provided in order to mobilize the capacity of structures that account for significant differences between the longitudinal, transverse and vertical performances. However, bridge pier design is usually not critically influenced by vertical seismic loading, which is why, according to EC8, the effects of the vertical component should only be taken into account in zones of high seismicity, when the piers are *"subjected to high bending stresses due to vertical permanent actions of the deck, or when the bridge is located within 5 km of an active seismotectonic fault"*. The EQ motions relative to both horizontal loading directions are described by the elastic ground motion acceleration response spectra illustrated in Figure 2.8, notwithstanding the fact that different spectra may actually be obtained according to distinct combinations of site dependent parameters (such as soil type).

a) Type 1 EQ

b) Type 2 EQ
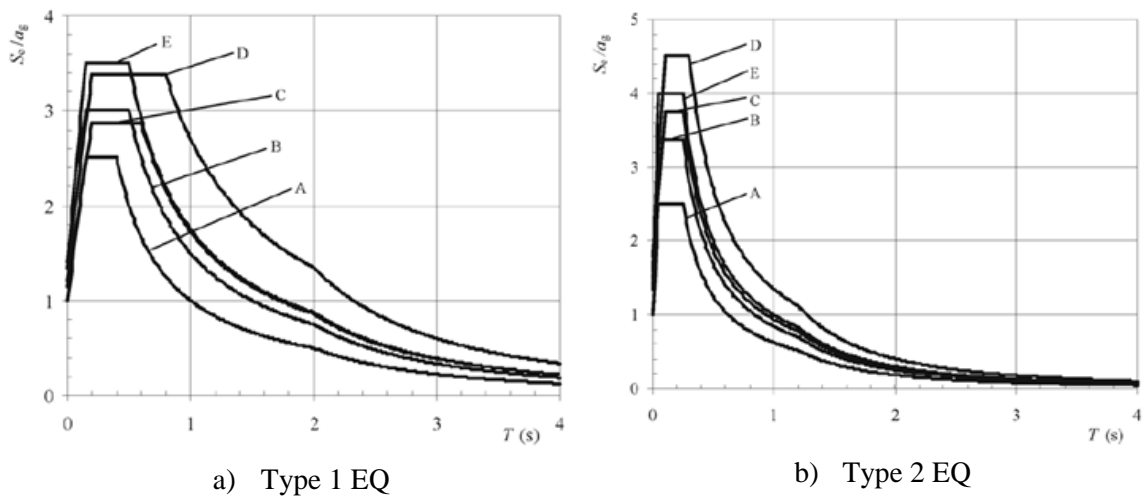
Figure 2.8 – EC8 elastic acceleration response spectra (NP EN1998-1 (2010))

2.4.   PIER TYPES ON RAILWAY BRIDGES

2.4.1. OVERVIEW

A detailed characterization of different pier types for a bridge substructure is presented in the form of a flow chart in Figure 2.9.
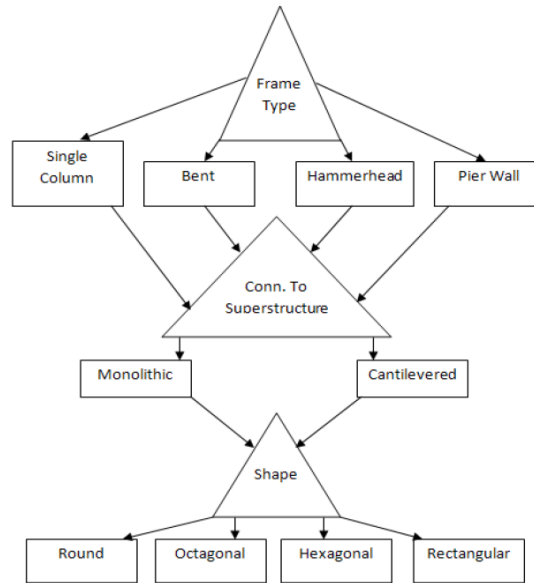
Figure 2.9 – Flow chart for pier types in bridge structures (Carmichael and Desrosiers (2008))

An attentive review of many concrete railway bridge structures, however, shows that, although piers can be found within a wide variety of shapes and forms, most of the actual layouts can be included in one of three distinct categories:

- Single column;

- Wall-pier;

- Multiple column pier (with or without transverse connection, e.g. bent-type columns);

The main distinction between single columns and wall-piers (which may be solid or hollow) reports to the cross-section dimensions of the elements and their respective thickness (t_w) to length (l_w) ratios (Figure 2.10). This is a key issue for substructure design, because usually single columns are expected to perform as mainly flexural elements, while wall-piers develop important shear deformations that must be taken into account in the design.
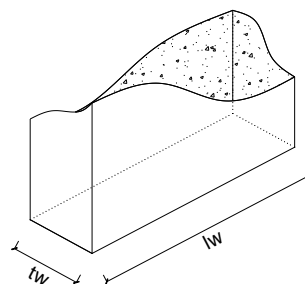
Figure 2.10 – Representation of a wall cross-section geometry

According to Eurocode 2 (NP EN1992-1-1 (2010)), the following should be considered for wall segments:

"...reinforced concrete walls with a length-to-thickness ratio of 4 or more..."

The latter is a broad characterization of walls as structural elements, and is not specific to wall-piers. Caltrans (Caltrans (2000)) bridge design manual indicates some design principles applicable to wall-piers with a clear height to length ratio higher than 2.0, while on the other hand, both the ACI 318-14 (ACI 318 (2014)) and the International building code (International Building Code (2009)) define a wall-pier as *"a wall segment with a horizontal length-to-thickness ratio of at least 2.5, but not exceeding 6, whose clear height is at least two times its horizontal length."*. This last definition is clearer and in line with the geometrical dispositions of actual bridge wall-piers. As such, this work adopts the ACI318 and IBC definition and the $\frac{l_w}{t_w}$ ratio of 2.50 for distinction between columns and wall-piers.

Multiple column pier layouts are simpler to describe, involving the use of more than one vertical element to support the same bridge alignment with or without a transverse connection. For all purposes, Caltrans bridge design manual relates the concept to that of bridge bents, stating that *"Bents are a bridge support system consisting of one or more columns supporting a single cap"* and is a suitable definition for the current purpose.

Considering the impact that several design speed performance criteria applicable to railway structures have on pier stiffness, as previously discussed, it can be worthwhile to examine the common layouts used within the framework of HSRL, aiming to understand some of its merits and shortcomings. With that in mind, the following section presents a brief review of common geometrical characteristics of viaduct structures associated with each of the three previous pier layout categories, particularly total length, main span and pier height.

2.4.2. SINGLE COLUMNS

The use of single columns for supporting railway bridge decks is a very common practice. Typical cross-sections are solid (shorter structures) or hollow (taller structures) in nature, with a square, rectangular, circular or octagonal geometry, and their main advantage is granting similar stiffness on both the main horizontal loading directions (longitudinal and transverse). This is because most single columns (with no monolithic connection) perform like a vertical cantilever, with considerably larger restrictions of rotation at the footings than at the deck connections.

On another note, the transverse dimension of bridge decks is often quite larger than the piers, posing a challenge regarding the implementation of support bearings on top of the shorter

cross-section of the pier heads. For that reason, bridges with single column substructure systems commonly adopt a flared form or even a distinguishable pier cap (e.g. a hammerhead column for caps with larger dimensions). In fact, that helps to accommodate the rotations resulting from deck loads, and to increase the available surface for positioning the support bearings, although at the expense of potentially increased bending moments on the columns due to eccentric positions of vertical reactions. This particular aspect is observed in many cases over different countries, as shown in Figure 2.11 which illustrates a few located in Spain, Taiwan, France and Japan.

a) *Jalon* Viaduct – Spain
(from http://en.structurae.de/)

b) *C270* Viaduct – Taiwan
(from http://www.lusas.com/)

c) *Avignon* Viaduct – France
(from http://www.rff.fr/)
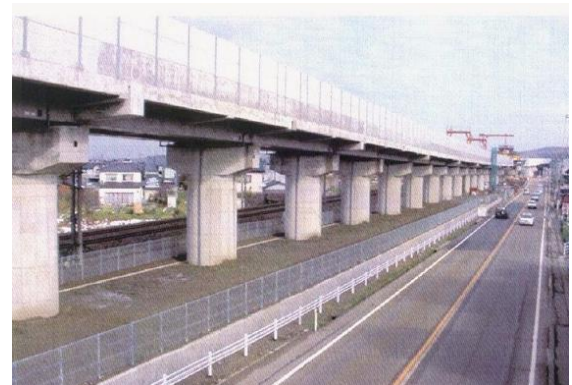
d) *Ishikawa* Viaduct – Japan
(from http://www.nishimatsu.co.jp/)

Figure 2.11 – Single column flare/cap on HSRL viaducts

The use of single column piers tends to be more prevalent in high rise structures, or those with longer spans (typically beyond 30m to 35m), since these key parameters are generally related and influenced by one another regarding design options. In the interest of economic structures, the overall height of the deck should dictate the main span length, with longer spans being adopted for taller bridges, in order to minimize the number of pier alignments. That is because regular on site construction of tall columns often requires the use of special and costly technologies, such as climbing formwork, when compared with regular solutions. On the other

hand, deck height directly impacts the stiffness contribution that can be expected from single columns for longitudinal and transverse movements, but the main advantages of multi column or wall pier alternatives also lose effectiveness in that regard. In this case, the use of hollow-sections for single columns can be valuable, as they provide a higher ratio of stiffness per mass unit and, generally, a cheaper structure.

On tall bridges of short length, the use of a continuous deck and the influence of the abutments can be sufficient to control the deformation levels, while longer bridges need to explore more creative solutions to ensure small displacements under service loads. Some bridges in Germany incorporate inverted *"V-shape"* alignments designed to address this problem (see Figure 2.12 a) and b)) because the longitudinal stiffness provided by these elements is considerably higher. Another layout that incorporates a similar idea (although with multi column piers) can also be found in the *Gänsebach* Viaduct (Figure 2.12 c)), where sets of shorter *"V-shape"* piers along both the longitudinal and transverse directions grants additional horizontal stiffness to the bridge. All these cases relate to long viaduct structures, with lengths around 1000m.

a) *Fulda* Viaduct – Germany
(from http://en.structurae.de/)

b) *Pfieffe* Viaduct – Germany
(from http://en.structurae.de/)

c) *Gänsebach* Viaduct – Germany
(from http://cms.asce.org/)

Figure 2.12 – Special solutions for horizontal stiffness

On bridges with irregular height development, it can be beneficial to combine adequate structural solutions for short and tall zones. The design strategy of the *Vérnegues* Viaduct, from the French Mediterranean HSRL, which is presented in Figure 2.13, is a clear example of that. As it is possible to observe, the bent-type frame solution adopted in the lower rise zones (a)) is gradually replaced by a single column layout on taller zones (b)).

<table>
<tr><td>a)   Lower rise zone</td><td>b)   Taller zone</td></tr>
</table>

Figure 2.13 – Pier layout variation in the HSRL *Vernégues* Viaduct in France
(from http://en.structurae.de/)

The number of railway tracks of the HSRL lines is another important detail for design decisions regarding bridge pier layouts. In fact, most lines consider ongoing train traffic on both ways, therefore it is common to see two track bridges with decks around 8 to 14 meters wide. Single track structures are also a possibility, mainly when considering the construction of two sideway bridges (one for each traffic direction), although that is not very commonly observed. With that in mind and considering that the transverse dimension of single columns is generally considerably smaller than the upper deck surface width, the possibility for strong torsion moments can be an issue of concern. Therefore, it is not surprising that single columns are typically used to support box girder decks, which are more suitable to provide a good performance under such loading conditions, as well as optimal configurations to use with advanced construction methods for spans longer than around 40 meters.

There are also multiple examples of single column supported bridges with composite decks using strong steel girders and concrete slabs. The most common configuration is a plate girder deck that uses two or more main steel girders, and transverse bracing with steel trusses or precast concrete elements. As long as the transverse bracing is designed to account for force transfer between the main girders, the behavior of this type of deck can also be similar to that of a reinforced concrete (RC) box girder, while benefitting from a generally lighter structure. It is a structural solution very common in France, and Figure 2.14 illustrates some of those cases. Just

like in RC box girders, the bottom width of the plate girder deck is larger than the single columns, requiring the use of a pier cap to accommodate its support.

a) Orgon Viaduct – France

(from http://en.structurae.de/)

b) Tech Viaduct – France

(from http://www.ioa.fr/)

Figure 2.14 – Composite deck bridges

Single column piers were also observed supporting steel truss decks. This is a structure type that is especially suited for cases where ground conditions advise a reduction in structure weight, according to Millanes Mato (2004)). A typical construction is the *"Warren truss"*, which was very common in the first Tokkaido Shinkansen Viaducts as illustrated in Figure 2.15 - a) (Konishi (2012)), where the track is located on the bottom of the truss. On the other hand, Figure 2.15 b) is an example of a half-lenticular design, where the track is located on top of the supporting steel truss.

a) *Tokkaido Shinkansen* Viaduct - Japan

(from Konishi (2012))

b) *Viaduc de L'Arc* - France

(from http://en.structurae.de/)

Figure 2.15 – Composite deck bridges

Overall, the use of single columns in HSRL viaducts is common and associated with several different structure designs. However, one of the defining traits of a single column seems to be the use of a flare or pier cap, as most structures support two-track lines and there is the need to

provide support over the wider deck sizes. Single columns are also more prevalent in high rise bridges and viaducts, that usually also correspond to longer span structures.

2.4.3. WALL-PIERS

As mentioned before, wall-piers are pier structures that have a transverse-to-longitudinal dimension ratio higher than 2.5. Usually, the longitudinal thickness is between 1.0 to 2.0 meters, while the transverse length can be as high as the supported deck widths. Due to this, wall-piers have high lateral stiffness and are heavily influenced by shear, especially on low-rise structures, which is a very common occurrence for wall-pier supported viaducts (deck heights between 10m to 25m), as illustrated in Figure 2.16.

a) *Innerste* Viaduct - Germany
(from http://en.structurae.de/)

b) *Padulicella* Viaduct – Italy
(from Calçada *et al.* (2008))

Figure 2.16 – Wall-piers' examples on low-rise viaducts

The higher width that wall-piers provide is a clear advantage of this type of structure, in contrast to single columns, since their transverse length is well suited to accommodate support bearings for wide box girder and multiple girder deck solutions. Some cases were identified, however, where a longitudinal enlargement (see Figure 2.16 – b)) is considered, especially with simply supported decks, because of the increased number of bearing devices needed for supporting two different spans.

In that regard, the close relation between the transverse dimension of the decks and the wall-pier bearing length (which are typically similar) is a common characteristic of the observed bridges and viaducts. On multiple girder bridges, the bearing width corresponds to the full transverse dimension of the deck, as seen, for example, in the *"TGV East-Europe"* and *"TGV Eastern"* junction bridges, illustrated in Figure 2.17.
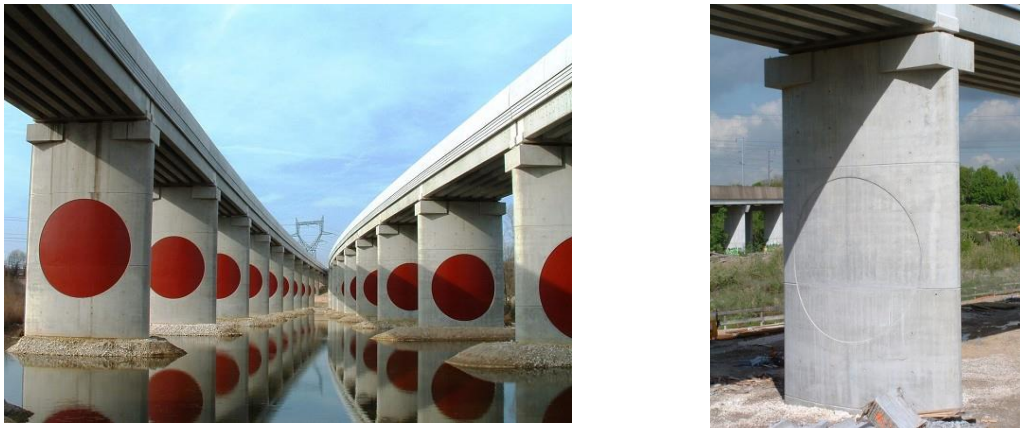
Figure 2.17 – TGV junction bridges – France (from http://en.structurae.de/)

In the previous example, each deck was built with seven precast concrete beams (PRAD system, Vavel (2004)) tightly fit within the deck width, which is nearly the same as the wall-pier length. Support is provided by four bearing devices placed along that same length, beneath stiff beams that are cast on site on the transverse direction of the deck. This is a widely acknowledged and common design strategy, and can be observed on multiple structures (even regardless of HSRL application). Another example with a different girder deck can be observed in Figure 2.18, where the bearing devices were placed directly beneath the main girders.

Figure 2.18 – *Auxonne* Viaduct – France (from http://en.structurae.de/)

The wall-pier layout is also observed to support other deck types, such as RC box girders and composite plate girders. In these cases, a reduced number of bearing supports is typically considered. Figure 2.19 illustrates some examples on French TGV HSRL viaducts where the decks were built with steel girders including two clear support bearing zones.

| a) *Mosel* Viaduct | b) *Mondragon-Vénéjan* Viaduct | c) *Ardre* Viaduct |

Figure 2.19 – Wall-piers in composite steel girder viaducts (from
http://en.structurae.de/)

Additionally, although most wall-piers are associated with low-rise structures, some cases can also be observed in tall bridges and viaducts, which are typically related to box/plate girder decks and longer spans. Moreover, the length-to-thickness ratio of these taller wall-piers is usually small, often around the lower limits of 2.5 to 3.0, as evidenced in Figure 2.20.

To summarize, several characteristics of viaducts constructed using wall-pier layouts were observed, namely regarding span length, deck type and deck height. For example, the deck of the TGV junction bridges (French East-Europe HSRL) is constituted by several multiple girder short spans of 20m-30m. On the other hand, the *Meuse* Viaduct, on the same railway line, is a composite plate girder deck with a main span of around 50m, while the deck height of both structures is around 10m. A logical conclusion is that the wall-pier layout is a very adaptable design, although low-rise bridges are typically where the structural advantages of a wall-pier seem to prevail.

a) *Baüerbach* Viaduct – Germany
(from http://en.structurae.de/)

b) *Glems* Viaduct – Germany
(from http://en.structurae.de/)

c) *O Eixo* Viaduct – Spain
(from http://horsost.blogs.upv.es/)

d) *Saubach* Viaduct – Germany
(from http://www.vde8.de/)

e) *Arroyo Espinazo* Viaduct – Spain
(from http://www.ideam.es/)

f) *Ricardell* Viaduct – Spain
(from http://www.tucrail.be/)

Figure 2.20 – Box girder railway bridges supported by single column piers with similar width.

2.4.4. MULTIPLE COLUMN PIERS

One can identify mainly two types of multiple column layouts used for supporting railway bridges and viaducts: those that focus on taking advantage of a frame-like behavior resorting to some type of transverse connection for force transfer and displacement compatibility purposes, and those that mostly focus on the behavior of each column as an individual unit. In that regard, the former is the most commonly found one, typically considering the so-called bent-type columns.

As far as it was possible to observe, multiple column piers are generally found in structures whose characteristics are, in general, quite similar to those described before for wall-piers and,

particularly, in low-rise viaducts (around 10m to 20m high). In particular, bent-type piers seem well-suited to accommodate the large support widths of multiple girder decks, as the cap beam can be designed to the required bearing length. Just like in wall-pier structures, this usually leads to the use of several support bearings, placed beneath the main girders, which are well served by the extra space provided by the former. This can be observed, for example, in the viaducts from French and Turkish HSRL that are illustrated in Figure 2.21, showing a strong and wide cap beam, where a minimum of seven bearing devices for deck support is considered.

a) *Thérouanne* Viaduct – France (from http://en.structurae.de/)

b) *Vandiéres* Viaduct - France (from http://en.structurae.de/)

c) *Viaduct 4* – Turkey (from Millanes Mato and Ortega Cornejo (2007))

Figure 2.21 – Bent-type columns with multiple girder bridges

When used with other deck layouts, such as steel plate girders or RC box girders, where the transverse bearing length is shorter, the maximum effective length for the cap beams is also reduced. In this case, it was possible to observe cases where the pier design included a tall cap beam, in order to provide large stiffness under horizontal load (expecting significant shear demand), and cases where the cap beam was mostly adopted for a displacement compatibility function, focusing on providing strong column stiffness instead. An example of the former is the *Crould* Viaduct, from the French TGV North HSRL, where the cap beam is constituted by a tall element with short span, and is illustrated in Figure 2.22 - a). By contrast, Figure 2.22 – b) illustrates a part of the chinese *Danyang Kunshan* Grand Bridge, where the transverse beam is considerably more slender in relation to the corresponding vertical columns. Both of these structures are associated with RC box girder decks, as observed, highlighting different approaches to pier design.

a) *Crould* Viaduct – France   b) *Danyang Kunshan* Bridge – China

(from http://en.structurae.de/)   (from Zhao, E. - https://www.flickr.com)

Figure 2.22 – RC box girder decks supported by multiple column frames

Another case of a similar strategy to that observed in Figure 2.22 – b), where horizontal transverse stiffness is almost exclusively dependent on the strong columns' behavior and a small transverse beam is included for displacement compatibility purposes, is the *Anguera* viaduct, in the Spanish HSRL (Sobrino and Murcia (2007)), where a steel tubular element is used instead of a reinforced concrete beam, but with similar design purposes.

a) Viaduct overview   b) Pier alignment cross-section
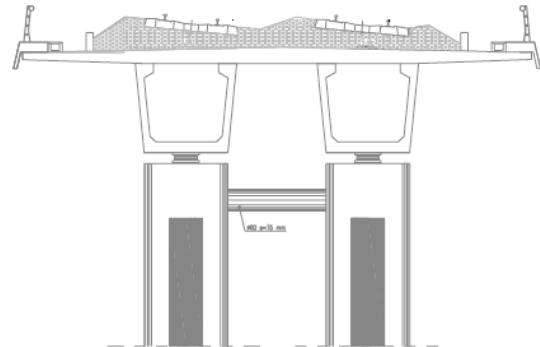
(from http://www.pedelta.es/)   (from Sobrino and Murcia (2007))

Figure 2.23 – *Anguera* Viaduct - Spain

Extreme cases of the strong column design strategy correspond to those where no cap beam is considered, which are not as common, as previously mentioned. Figure 2.24 shows one such example, the Viaduct over the *Guadalete* River, where columns have a skewed shape with larger cross-sections near the footing and thinner cross-sections at the deck level.

Figure 2.24 – Viaduct over the *Guadalete* River– Spain (from Cutillas (2007))

The two previously presented viaducts both involve twin box girder decks, where the position of each column is generally determined by the geometrical layout of the two girders, for optimal support and avoidance of eccentric loading. On that regard, a different design for a twin box girder deck is observed in the *Stöbnitz* Viaduct (Figure 2.25). In this case, the structure is designed as a monolithic *Vierendeel* girder, with horizontal load transfer between the superstructure, a concrete slab, concrete supports and pile caps, according to Schlaich (2012).
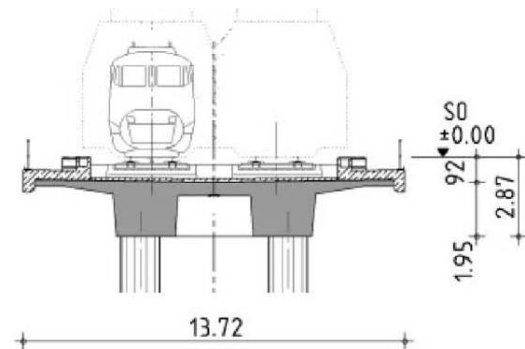
a) Viaduct overview	b) Pier alignment cross-section
(from http://en.structurae.de/)	(from Schlaich (2012))

Figure 2.25 – *Stöbnitz* Viaduct - Germany

Within the context of frame solutions for HSRL bridges, the classic Japanese rigid frame should also be mentioned. It is a structural solution used since the first *Shinkansen* lines, consisting of a series of monolithic frames with a rigid set of columns and stiffening beams, and a slab serving as railway track support. As stated by Koyama (1997), that was considered the most economic substructure layout also capable of exhibiting good seismic performance. The overall bridge and viaduct behavior with this substructure layout depends on the arrangement of the rigid frame units. The characteristics of each unit can vary, but they are usually less than 60m long and less than 20m tall. The longitudinal distribution of the vertical elements is often around 10m, while for frames higher than 15m, stiffening cross beams are used, as illustrated in Figure 2.26 (Tamai (2014)).

d = 5 to 15m; Standard is 10m

5 < h < 20m; Cross beams are desirable for h > 15m

a) Interval of columns

b) Frame height
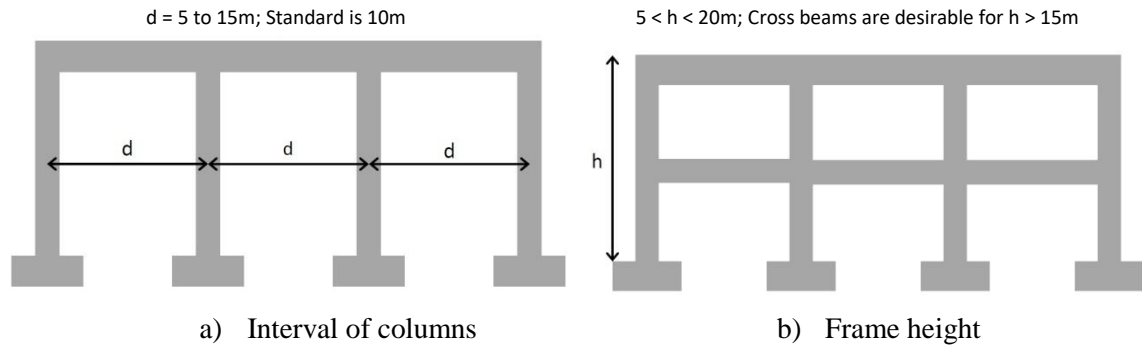
Figure 2.26 – Japanese *Shinkansen* rigid frame characteristics (adapted from Tamai (2014))

Additionally, the longitudinal interaction between the rigid frame units can be designed in different ways. The three main ones are, as indicated by Tamai (2014), the butt type connection, the girder connection and the integral frame behavior, shown in Figure 2.27.

Butt type

Connecting girder type

Integral type

Figure 2.27 – Japanese *Shinkansen* frame unit connections (adapted from Tamai (2014))

This structural layout gives the *Shinkansen* structures a different visual aspect than most of other HSRL bridges and viaducts, as the main span is generally quite smaller and the rigid frames make the substructure seem more visually condensed than single columns, wall-piers or bent-frames, as Figure 2.28 aims to illustrate.

a) *Shinkansen* Viaduct - Japan
(from Tamai (2014))

b) *Grenette* Viaduct – France
(from http://en.structurae.de/)

c) *Loire* Viaduct – France
(from http://en.structurae.de/)

d) *Piacenza* Viaduct – Italy
(from http://en.structurae.de/)

Figure 2.28 – Visual overview of different HSRL viaducts.

The tallest multiple column substructures were found in the French TGV *Rhine-Rhone* HSRL, illustrated in Figure 2.29, where in some zones the piers are above 30m high. The pier design from the *Lizaine* Viaduct (Figure 2.29 – a)) corresponds to a monolithic frame structure with a large cap beam, in comparison to the thinner vertical elements. It is interesting to note, however, that the cross sections of the vertical elements are wider in the longitudinal direction and, therefore, provide higher stiffness for longitudinal loading. As for the *Linotte* Viaduct (Figure 2.29 – b)), the layout provides high transverse stiffness mostly through the inclined columns, and their connection node cannot be interpreted as a classic cap beam.

a) *Lizaine* Viaduct

b) *Linotte* Viaduct

Figure 2.29 – Piers in the TGV *Rhine-Rhone* HSRL

(from http://www.lgvrhinrhone.com/)

Despite the cases like the previous ones, it is possible to observe that the vast majority of multiple column substructures are used in low-rise viaducts (up to 20m). As previously discussed, there is not an absolute reason in favor of such application; nonetheless it seems to benefit more from the structural advantages of multiple column and, particularly, bent piers. Additionally, it can also be observed that these structures are typically quite long, frequently spanning over a few hundreds of meters, while the main span length is mostly determined by the type of the deck considered for each case.

2.5. FINAL REMARKS

According to the objectives established for the present chapter, its content focused on analyzing design options for HSRL bridges and, in particular, of bridge piers. Within that context, common layouts for HSRL bridges were reviewed, focusing on the structural aspects relevant to the simply supported or continuous deck types. Regarding the substructure design and, in particular, of the bridge piers, seismic and HSRL specific performance requirements were presented, from which the importance of structural collapse prevention, structural and track damage limitation, as well as the running safety of trains was emphasized. Finally, cross-section shape options for HSRL bridge pier design were also reviewed and discussed, according to the associated structure's defining characteristics, where three of the most common layout types were presented: single columns, wall-piers and multiple column piers.

3
PRECAST TECHNOLOGY FOR BRIDGE PIERS

3.1. ADVANTAGES AND DISADVANTAGES OF PRECAST

On the context of developing a precast solution for bridge piers, discussion eventually focuses on the merits and shortcomings of the precast technology itself. In that regard, it is widely acknowledged that precast solutions contribute on a large scale to the construction speed of a particular project. There are a few reasons one can mention to support that claim, but enabling the simultaneous off-site construction of multiple elements is among the main ones. In fact, when the core part of a structure is constituted by an assembly of precast elements, the building process can be managed through several tasks in parallel, benefitting from workload distribution between site labor and precast plant manufacture for considerable gains in overall time spent. That strategy is not as well suited for the traditional on site casting, known as the cast-in-place (CIP) procedure in the construction industry, because most structures require some type of sequential construction, where supporting elements (even if temporary) must generally be concluded before the construction of supported elements.

Considering the rapid construction benefits, precast solutions are naturally convenient for situations that present considerable time constraints, such as reinforcing and retrofitting operations on active bridges. In those cases, traffic hindrance is common and the responsibility of a contractor is to minimize the disturbance as well as avoid traffic congestion altogether, if possible. When CIP construction is used, considerable resources must be allocated to formwork execution, steel reinforcement preparation and concrete pouring of multiple elements, such as foundations, columns, abutments and deck. Furthermore, construction schedules must account for the concrete curing between operations (Freeby *et al.* (2003)), often leading to situations

where the workforce volume is defined by the manpower required to prepare the next operation before curing periods are over. On the other hand, a common procedure on precast structures is to cast the foundations on site, while columns and beams are built elsewhere and quickly placed once brought to the construction site. In that regard, the time spent on assembling precast elements on site is considerably smaller than the duration of the process related to equivalent CIP construction, while also requiring less resources' allocation, since formwork and steel reinforcement preparation tasks are moved off-site, encompassing accountable economic gains.

A related benefit is that the construction process with precast elements becomes more environmental healthy, because noise, air pollution, dust and debris are all reduced when most of the casting occurs in the precast plant. Moreover, precast elements benefit from the increased quality of factory construction, as well as higher quality materials and independence from weather conditions. Therefore, the correspondent designs can provide significant savings over the course of a particular project, also relating to the sustainability of the construction activity as a whole (Yee (2001), VanGeem (2006)). This is further reinforced by the flexibility related to defining the assembly method and its relevance in the design process. A common procedure for beams, for example, is to use a hybrid solution where the precast element corresponds to the beam body (web and bottom flange, possibly including prestress), acting as formwork for combining with *"in situ"* concrete topping (the collaborating slab) for equivalent global behavior and considerable material savings (Figure 3.1).
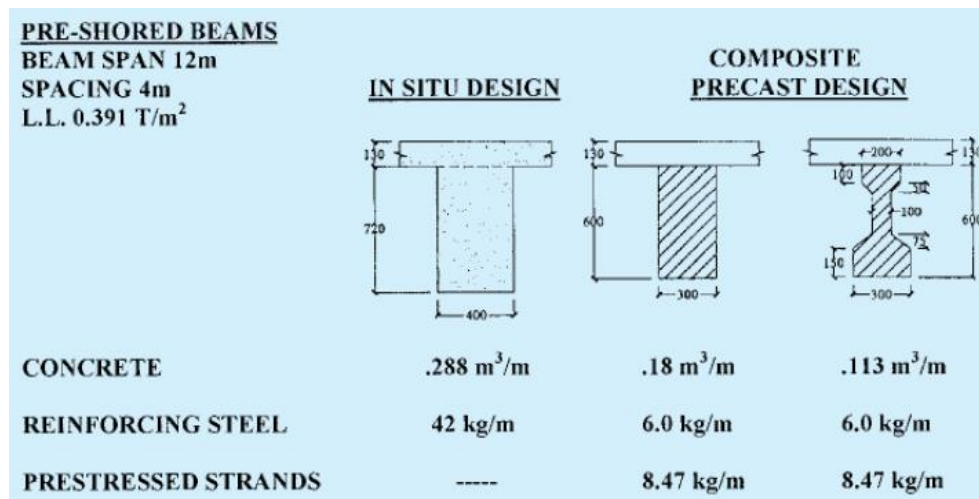
Figure 3.1 – Material savings using composite precast designs (Yee and Eng (2001))

Precast elements can also provide adequate technical solutions for situations where different constraints affect the application of a normal construction management strategy. For example, some bridges are built over long stretches of water, where work zones are limited and restricted to adjacent support platforms. Using precast elements reduces the site workload, since mostly assembly procedures are thus required. That situation can also occur on tall structures or

others where accessibility and work zone conditions are concerns, and consequently, by reducing the amount of time manpower required to operate in potentially dangerous conditions, the use of precast solutions also contributes to increased labour safety.

All the above describe the precast technology benefits in relation to design or construction related issues. Nonetheless, the importance of accounting for logistics and provision management difficulties is also paramount for achieving a good compromise between a technically adequate precast design and an economically viable solution. With that in mind, the production and application of precast elements in construction can be addressed in five main phases (Castilho and Lima (2012)), all raising specific concerns:

- Element fabrication;
- Transport and storage within factory environment;
- External transport from the manufacturing plant to the construction site;
- Placement of the elements in their final positions;
- Implementation of the connections to the local structure;

The development of adequate factory procedures to manufacture precast elements relies significantly on the capability to establish systematic labor circuits, imposing an industrialization mindset (Alinaitwe *et al.* (2006)). As a rule of thumb, the more repetitive the design for the precast elements is, the easier it is for production teams to achieve a certain operating rhythm, and also to train newcomer workers for. Moreover, the moulds used for casting are of high quality (steel moulds are frequently used), enabling first grade finishing, textures and accurate shape definition for better architectural appearance (Manrique *et al.* (2007)), and can be used several times before needing replacement. However, that potential can only be tapped into if a project requires several precast elements of similar characteristics, since casting beds and moulds can be used repetitively without significant time-consuming changes in between operations.

That also raises the issue of the production space in the precast plant, as well as transportation to storage areas. In fact, the weight of a precast unit is a common limitation for the design and relates directly to transportation concerns. In a factory environment, the lifting capacity can be relevant in determining whether the casting position is vertical or horizontal, because multiple cranes can easily be used to carry the heaviest elements by having spaced out lifting points. That is also a concern for external transportation to the construction site, since heavy trailers and trains have limited carrying capacity. For example, PCI (1997) points to practical limits of around 200 ton for truck shipping and 500 ton for rail shipping. Still, in the construction site, special lifting equipment and bracing may be necessary to move the precast

units, as well as to place them correctly before definitive connections are built. Additionally, temporary storage may be considered, if the construction site has suitable facilities.

Careful handling of the precast elements is also paramount to avoid unwanted damage before the structure is finished. PCI (1997) states that *"Precast concrete bridge products are designed to be furnished crack-free. However, cracks should not be considered a reason for rejection unless the product is structurally or aesthetically impaired beyond repair"*. In that regard, the main reasons for the appearance of cracks on concrete are widely known, but extra attention must also be dedicated to prevent accidental impacts, especially because handling precast specimens in between manufacture and installation generally involves some difficulty.

3.2. PRECAST CONNECTIONS

A precast system for bridge piers or building columns is generally characterized by two main aspects: the structural element itself and its components, as well as the connection mechanisms. In that regard, while the quality of the off-site manufactured pieces is undeniably higher than what is usually obtainable *"in situ"*, for the above discussed reasons, the global behavior of precast structures is dependent of the integrity achieved at the connection joints, since the intrinsic monolithism ensured by CIP construction is not easy to replicate within precast assemblies. Furthermore, inadequate joint detailing can lead to early structural damage, as they are the weakest points in the overall precast system, therefore raising also durability concerns.

There are four potential locations for precast pier connections, according to Marsh *et al.* (2011):

- *Pile-to-foundation*: typically the connection between pile caps and piles, which are regularly located below ground and also difficult to inspect and repair;
- *Foundation-to-element*: connection between the foundation system (the most common types of which are the spread footing, pile cap or drilled shaft) and the substructure element, which may or may not be accessible, and is a location prone to severe damage during seismic events;
- *Element-to-element*: element connections are established between segmental pieces or between a segment and a pier cap/cap beam. The connection itself can be performed with several different mechanisms, and be located on a variety of column points, but these are generally accessible to inspection and repair;
- *Element-to-superstructure*: structural layouts that require continuity between substructure and superstructure generally involve a connection between pier caps

or cap beams to a deck girder, typically a diaphragm. Depending on the specific detailing of the connection, severe seismic damage may occur;

Considering the scope of the present work, the following sections will mostly address connections related with the main pier elements.

3.2.1. FOUNDATION-TO-ELEMENT CONNECTIONS

This connection type is generally designed to enable the transfer of all weight loads, as well as lateral loads, while displaying overall behavior similar to monolithic construction and avoiding additional limitations. Footing connections for precast columns are usually performed as one of the following types:

- Pocket connection;
- Socket connection;
- Base plate connection;
- Cast-in-place footing with reinforcement continuity;
- Grouted sleeves connection;

3.2.1.1. Pocket connection

In general, pocket connections require an opening on the footing, with bigger size than the column cross section, upon which the latter is first introduced and then adequately held and braced. Afterwards, the gaps between the column and the footing are filled with concrete or grout. In order to have a large enough force transfer area between the socketed part of the column and the pocket hole, this connection can only be performed on fairly large footings (either CIP or precast). Figure 3.2 highlights the general configuration for a pocket connection. Similar solutions can also be adopted if pile shafts are needed instead of spread footings, as reported in Tran (2012) for seismic regions, as an example.

Figure 3.2 – Schematic pocket connection (*"fib Bulletin 43"* (2008))

Vertical design loads are defined for the column cross section and the adjacent bearing area of grout/concrete, while overturning moments are resisted by the lateral pair of reactions formed between opposing sides of the column, as shown in Figure 3.2. Additionally, shear stresses are developed at the interface between the column and the surrounding infill material, and rugged textures can be adopted in both the column and the pocket to increase the corresponding shear resistance. Moreover, according to *"fib Bulletin 43"* (2008), the depth of the pocket (d_c) should be calculated as follows in equations 3.1 and 3.2:

For $\frac{M}{N} < 0.15 \times h$, $d_c > 1.2 \times h$ $\hspace{5cm}$ 3.1

For $\frac{M}{N} < 2.00 \times h$, $d_c > 2.0 \times h$ $\hspace{5cm}$ 3.2

Where *h* represents the cross-section height and *M* and *N* relate to the overturning moment and vertical load, respectively.

Considering the previous, the difficulty of using this type of connection for structures with large moment demands is considerable (common occurrence on columns experiencing inelastic deformations during seismic events), typically resulting in inconvenient large sized foundations.

3.2.1.2. Socket connection

Socket connections are performed when the complete footing is cast around the vertical column instead of just the surrounding gap hole. Different authors studied the behavior of distinct variants (e.g. Marsh *et al.* (2010); Haraldsson *et al.* (2013)), but generally all involve previous column precasting and adequate placement on a pre-excavated site, according to Figure 3.3 - a). Afterwards, the footing is cast following the preparation of the reinforcement steel around the column.
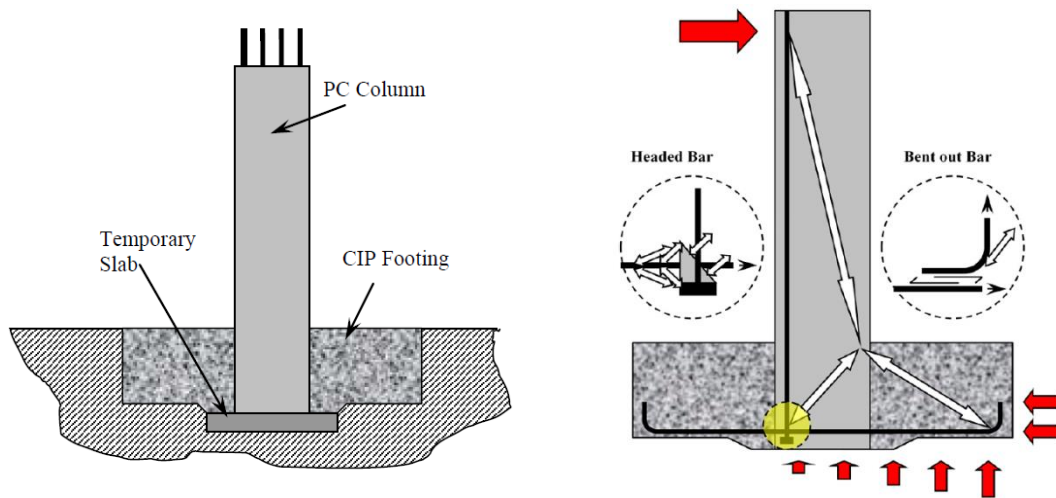
a) Schematic illustration (Marsh *et al.* (2010))   b) Lateral loading (Haraldsson *et al.* (2013))

Figure 3.3 – Socket connection

There are two noteworthy aspects regarding socket connections. First, the vertical load transfer from column to footing depends of the shear friction in the footing-column interface, often requiring the adoption of rugged textures on the precast element. Second, the fact that longitudinal rebars cannot be bent into the footing, therefore increasing the difficulty to develop adequate bond stresses on the tensile strained rebars and, consequently, to achieve the theoretical bending capacity of the column. As a result, the bending behavior of the socketed column can also rely on anchorage devices to mobilize the equilibrium of compressive forces between the footing and the column, as illustrated in Figure 3.3 – b). A common solution for those devices is to incorporate a steel or precast concrete plate at the column base, in order to facilitate the casting of the precast element, which also simplifies transportation and handling.

3.2.1.3. Base plate and shoe connections

There are also layouts that incorporate an end steel plate as a moment resisting element, which is an immediate solution for element stability during column placement and helps on reducing the required depth of the footings. The lack of reinforcement continuity usually requires welding of the rebars to enable adequate bond behavior, and both the steel plate thickness and dimensions should be determined in accordance with moment induced stresses and the position of the anchor bolts (see Figure 3.4).

Figure 3.4 – Column with base plate and welded rebars (*"fib Bulletin 43"* (2008))

Shoe connections can also be a particular case of steel plate connections, where openings are considered at the outer perimeter of the column to allow anchor bolting the vertical element to the footing without requiring additional space, as shown in Figure 3.5. The required devices are commercialized by several companies (e.g. http://www.peikko.ca/; http://www.pfeifer.de/), but generally their application is limited to moderately loaded columns, which is frequently not the case of bridge piers, particularly under seismic demands.

Figure 3.5 – Shoe column connection (http://www.peikko.ca/)

3.2.1.4.   CIP footing with reinforcement continuity

When footings are cast in place, a very common solution for establishing the foundation-to-element connection consists on extending the longitudinal rebars out of the precast element and into the designated space for the footing. Afterwards, complementing steel reinforcement is prepared and the footing is cast, encompassing a manufacture procedure similar to that of socketed columns. The main difference between them is that the present methodology ensures stronger moment capacity and less dependency on mobilizing contact surface shear forces.

The main difficulty associated with performing this connection tends to be the temporary placement of the precast unit before casting. Since the longitudinal rebars are extended out, temporary leveling pads can be used (Figure 3.6 – a)). Additionally, the foundations can be cast in two phases, considering adequate lap-splicing lengths for the second one (Figure 3.6 – b)). Nonetheless, the casting itself may be more complex due to the protruding nature of the column rebars, requiring specially adapted formwork and accessibility, in order to provide good concrete vibration. The potential for worker safety issues due to the danger of handling heavy elements with protruding reinforcement also comes to mind.

a) Temporary steel supporting pad   b) Preparation of the second casting phase
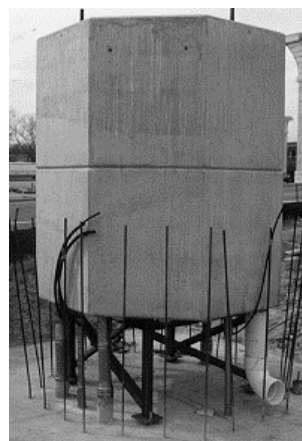
(Cruz Lesbros *et al.* (2003))   (Billington *et al.* (1999b))

Figure 3.6 – CIP footing connections

3.2.1.5.   Grouted sleeves connection

An important issue must be previously stated regarding grouted sleeves' connections: this is a common methodology in every type of joint connections, such as foundation-to-element, element-to-element, or element-to-superstructure. Therefore, although this section reports to the foundation-to-element joints, it is also generally applicable to other locations.

Grouted sleeve connections involve leaving duct openings on either the foundation or the vertical precast element (or both), in order to introduce continuity rebars during assembly procedures. The length of the ducts is related to the required bond lengths, as they are generally filled with grout, enveloping the rebars and enabling full bond mechanism. This procedure is simple to execute, doesn't require strenuous job site preparations and enables fairly rapid construction. Despite that, it can be susceptible to several shortcomings. For example, since the duct space is generally small, it can be challenging to ensure that the grout fully envelops the reinforcement bars. Larger duct diameters can be used to prevent this issue, but that can also be a detrimental solution. In fact, the inclusion of several sleeves can lead to steel congestion, as they occupy a large space in the cross-section (Stanton *et al.* (2006)), which is further aggravated if large diameter ducts are used. Furthermore, when specimens include protruding bars, careful positioning of the ducts must be ensured, in order to prevent gross misalignments and all the additional work and delays that would be required to overcome such problems.

According to Matsumoto *et al.* (2008), three different grout connection types can be performed: grouted pockets, grouted ducts and bolted connections, as shown in Figure 3.7 - a), b) and c), respectively. Bolted connections are difficult to perform in foundation-to-element joints due to inaccessibility for bolting, which is the reason why they're usually only considered

in the uppermost element-to-cap connections. Moreover, the main difference between grouted pocket and grouted duct connections is that the former is established for multiple rebars, while ducts are generally for individual bars.
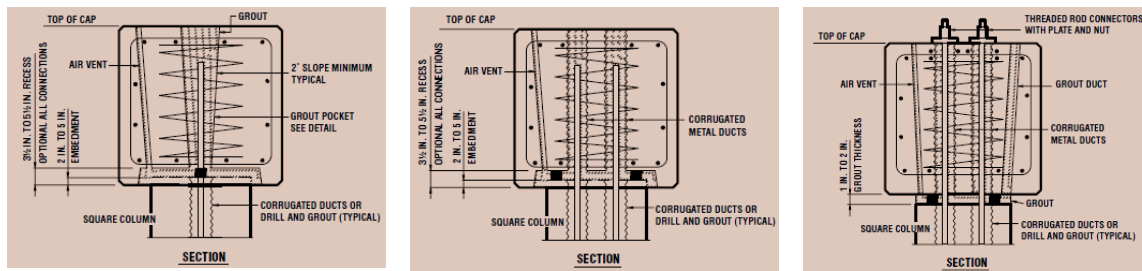
a) Grouted pocket   b) Grouted duct   c) Bolted connection

Figure 3.7 – Grouted connection types according to Matsumoto *et al.* (2008)

Alternatively, when available embedment lengths are short, mechanical couplers can also be considered. Haber *et al.* (2013) explored different solutions in the context of a precast footing including protruding bars, using conventional grout sleeves with either mechanical couplers or transition bars, as illustrated in Figure 3.8. It is also interesting to note the use of a concrete pedestal to facilitate the placement of the precast unit before establishing the grouted connection.
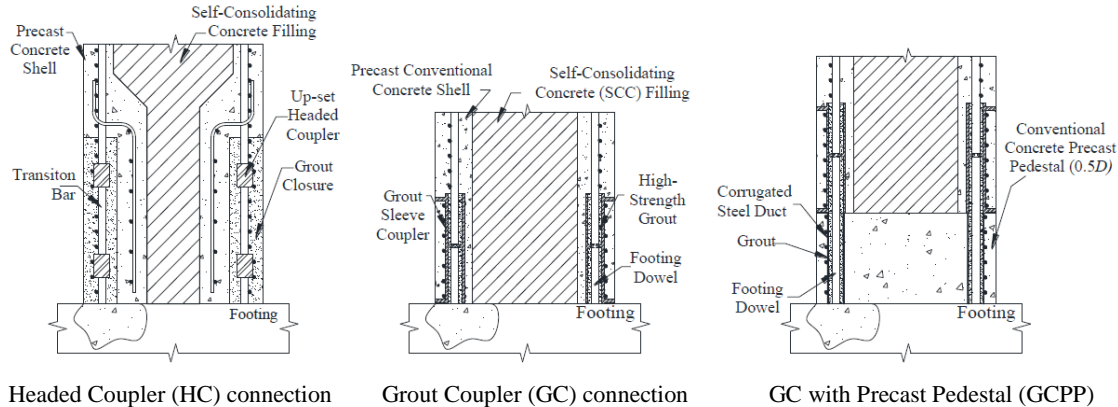
Headed Coupler (HC) connection   Grout Coupler (GC) connection   GC with Precast Pedestal (GCPP)

Figure 3.8 – Mechanical coupling connections (Haber *et al.* (2013))

For increased bond between the lap splices and the precast pieces, this type of connection is generally performed using corrugated sleeves, as illustrated in Figure 3.9. Therefore, careful handling and, if needed, temporary protection of precast units (including ducts) should be accounted for, because dirt, water and other construction residues can accumulate inside and impair the connection.

Figure 3.9 – Corrugated grout sleeves (Matsumoto *et al.* (2008))

As mentioned before, grouted sleeves can also be used in combination with a variety of other connection types. For example, Davis *et al.* (2012) presented a new layout for foundation-to-element and element-to-cap joints when vertical post-tension is used. In this variant, mild steel rebars are introduced through corrugated sleeves, while a socket connection is used for the reduced cross-section part of the column that includes the post-tension tendons, as illustrated in Figure 3.10.
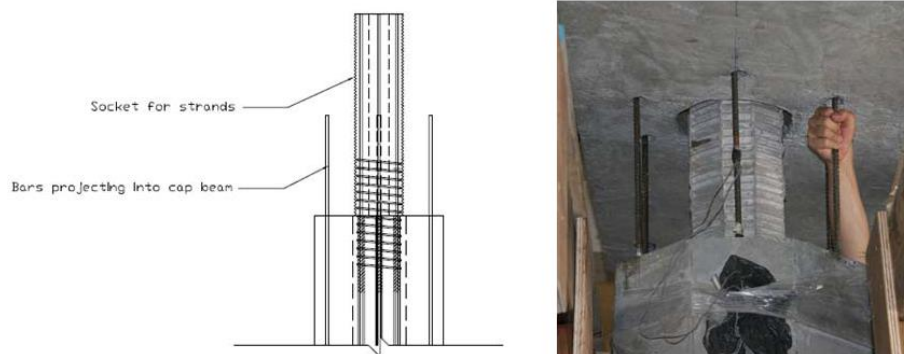
Figure 3.10 – Hybrid duct and socket connection for post-tensioned piers (Davis *et al.* (2012)).

3.2.2. ELEMENT-TO-ELEMENT CONNECTIONS

Precast element-to-element connections are found in segmental precast piers and can generally be included in one of two main categories: *loose-fit* joints and *match-cast* joints. The first type consists of unifying subsequent precast elements by lap splicing reinforcement bars through the joint and filling the space with grout, mortar or CIP concrete. It is a simple technique associated with low requirements for precast element manufacture, for which the productivity rate is only limited by the capacity of the precast plant. However, the difficulty of creating the connection tends to increase with the associated element dimensions, because careful suspension of the precast pieces in geometrically aligned positions is paramount to ensure optimal pier performance, thus generally leading to time-consuming operations. Additionally, it is also difficult to ensure an even distribution of the concrete/mortar, which

increases the risk of partially filled joints, stress concentrations, cracking and possible corrosion exposure of the reinforcement steel (Billington *et al.* (1999b)).

Match-cast joints avoid many of the inconvenients and difficulties associated with a *loose-fit* joint. This type of connection can be summarized as requiring precast element pieces to be cast against one another (or against pre-shaped formwork), ensuring a strong fit between them. Figure 3.11 presents an illustrative scheme of precast column *match-cast* elements proposed by Billington *et al.* (1999a), where the vertical casting of subsequent elements is performed on two levels, enabling the previously cast piece to serve as bottom formwork.
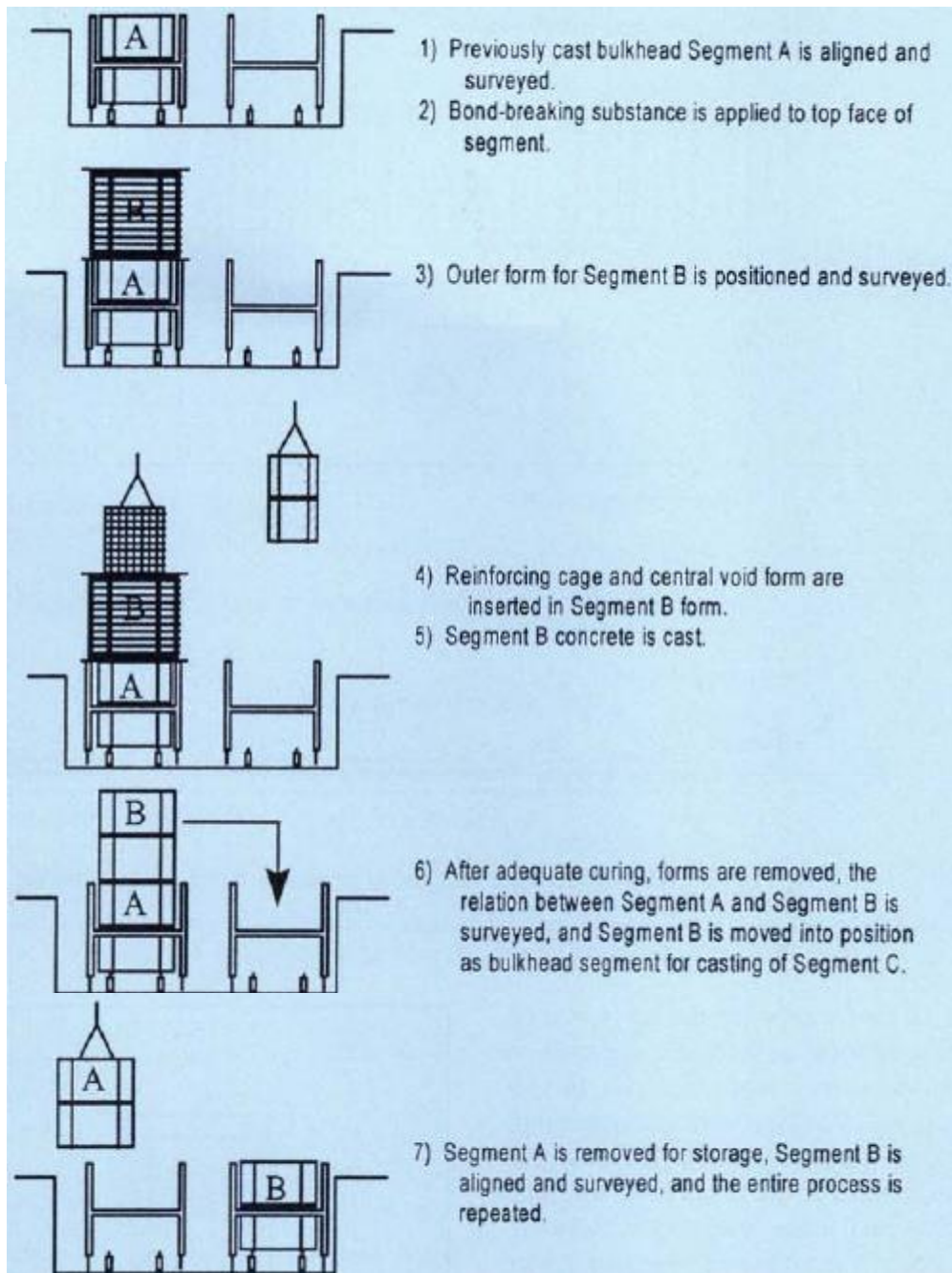
Figure 3.11 – *Match-cast* manufacture process by Billington *et al.* (1999a)

The joint surface created in the *match-cast* process can be either a dry joint or an epoxy or grout-filled joint. Dry joints are easier to perform, but lack protection against freezing or salt-waters. They usually also have some rough edges that are prone to crushing and, therefore, can potentially increase the fragility of the connection.

The structural integrity of *match-cast* products does not rely on the continuity of regular steel rebars. Instead, post-tension prestress steel is generally used to compress precast segments against one another, enabling adequate interaction on the fully assembled element. Moreover, while the shear friction induced by post-tension compressions can often be sufficient, shear keys can also be provided to further increase the shear capacity of the connection, as illustrated for segmental precast piers in Figure 3.12.

a) Segmental pier illustration (Billington *et al.* (2001))	b) Segmental pier element photo (Schokker *et al.* (1999))
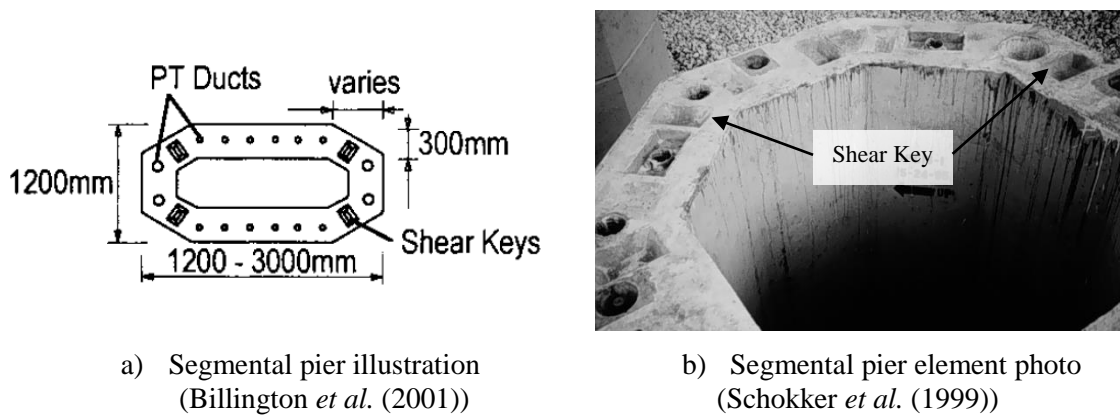
Figure 3.12 – *Match-cast* surface and shear keys

In conclusion, *loose-fit* and *match-cast* connections can be adopted depending on the situation, as they have a clear difference regarding advantages and disadvantages. It can be said that the former could be considered when the time and resources spent in performing the connections is not a project limiting constraint, and an increased precast piece productivity rate can translate into economic gains or faster construction. Such is the case where, for example, a large number of simultaneous work fronts are established, creating higher demand for precast elements that may not be easy to meet by adopting *match-cast* manufacture procedures. On the other hand, if pier erection time is a clear constraint, then *match-cast* products legitimately have the potential to be a better option.

3.3. BRIDGE PIER PRECAST SYSTEMS AND DESIGN

Over the years, precast systems for applications in bridge substructures have been gaining acceptance as a rapid construction focused alternative. Despite that, precast bridge piers are not as commonly observed as precast girders are for bridge decks. Several technologies and construction methods have been developed and improved, but CIP bridge piers are still

regularly accounted for as the most cost-effective alternative. On the scope of understanding the available technology to use in the precast application for the present work, this section aims to review some examples of design layouts studied for real applications of precast bridge piers, as well as relevant scientific developments related with performance assessment and possible improvement suggestions.

3.3.1. LAYOUTS FOR NON-SEISMIC ZONES

Billington *et al.* (1999a) presented one of the first fully integrated precast solutions for roadway bridge piers in non-seismic zones. In that regard, the corresponding development framework was established for compatibility with the most common superstructure configurations as well as existing precast plant equipment and infrastructures, leading to a limitation of the maximum element weight to the range between 700kN to 750kN.

The general layout defined a segmental construction comprising three basic precast elements: column segments, a template flared segment and an inverted T-cap element, illustrated in Figure 3.13 – a). The column segments were *match-cast* and the corresponding joints were epoxy-filled. Additionally, for adequate site geometry control, the connections of column segments to the foundations and the template element were expected to be cast-in-place with high strength concrete.

a) General assembly layout   b) Column segment sizes
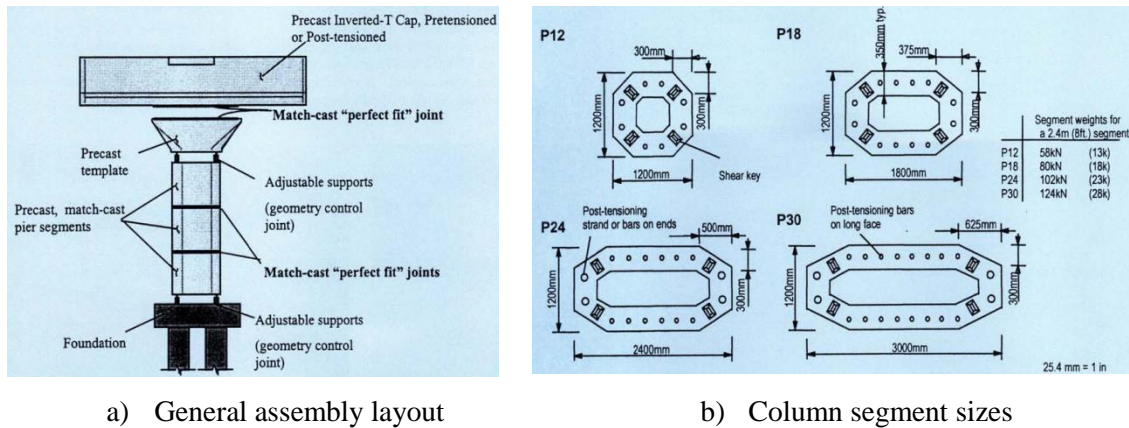
Figure 3.13 – Precast pier according to Billington *et al.* (1999a).

Four different segments were designed with heights between 0.60m and 2.40m, focused on a hollow cross-section configuration, where both post-tension strands and bars were included to help on achieving structural integrity, according to Figure 3.13 – b). The precast elements could then be combined to establish flexible technical solutions for supporting bridge superstructures, according to the specific needs of a given project (e.g. deck width, span length, pier height…), from single column layouts to multi-column frame bents as tall as 18m, as illustrated in Figure 3.14. This feature can relate well with standardization procedures, as the initial cost of preparing

the formwork for the four different sizes may translate into a reduced impact on overall project costs due to continuous use of the same layouts.
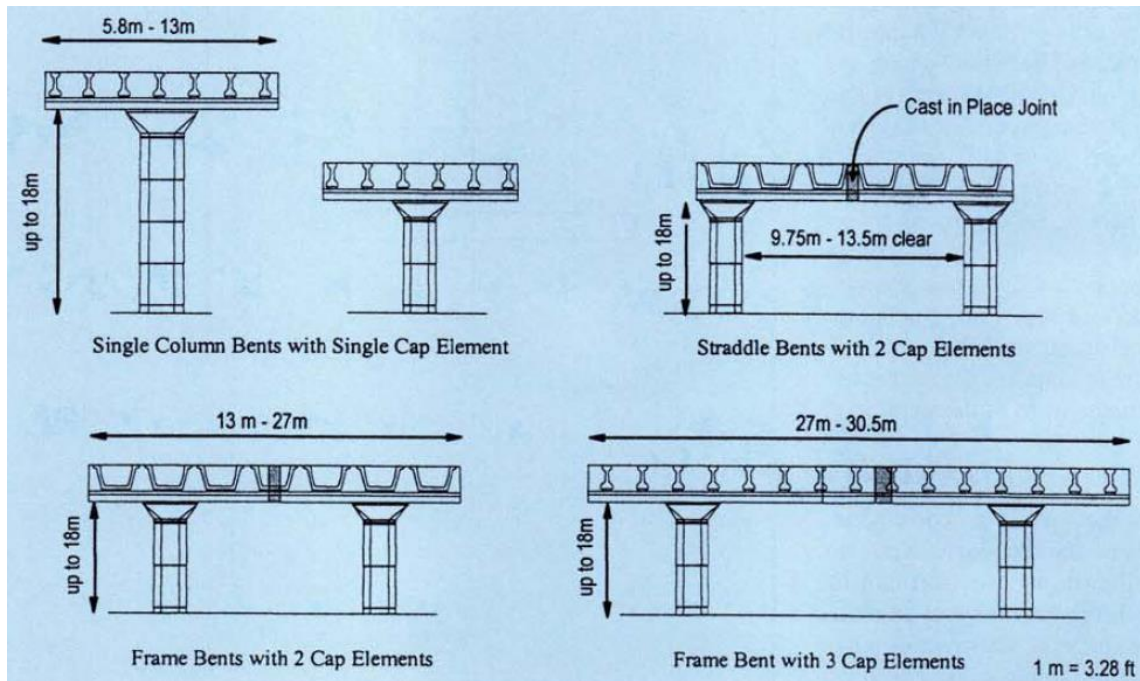
Figure 3.14 – Possible precast bent configurations (Billington *et al.* (1999a))

According to Billington *et al.* (1999a), the most critical design conditions report to service loads, where both maximum concrete stresses and zero tensile stress limit should be checked, due to existence of post-tensioning prestress. A minimum passive reinforcement ratio should also be considered, in order to control creep and shrinkage effects. However, the passive reinforcement was not continuous, and post-tension was the only mechanism expected to provide structural integrity. Therefore, although vertical prestress could contribute to a possible reduction of residual displacements and improvement of joint shear resistance, concerns were raised about the ductility and overall energy dissipation it provides, which has been a strong reason against the use of this type of solution in high seismicity areas.

Another fully precast segmental bridge pier system was presented by Cruz Lesbros *et al.* (2003), developed for the Ayuntamento 2000 bridge, located in a low-intensity EQ region in Mexico. That bridge is a six span structure with over 160m of length, which was built in four and a half months thanks to extensive use of precast, both in the superstructure and the substructure. Interestingly, the author himself indicates that the number of bridges built using fully integral precast systems amounts to less than 1 percent of all bridges in Mexico, which is a statement for the innovative nature of the endeavor. The bridge crosses a deep valley with a longitudinal slope of 7.5%, leading to pier heights from 12m to 42m, according to Figure 3.15.
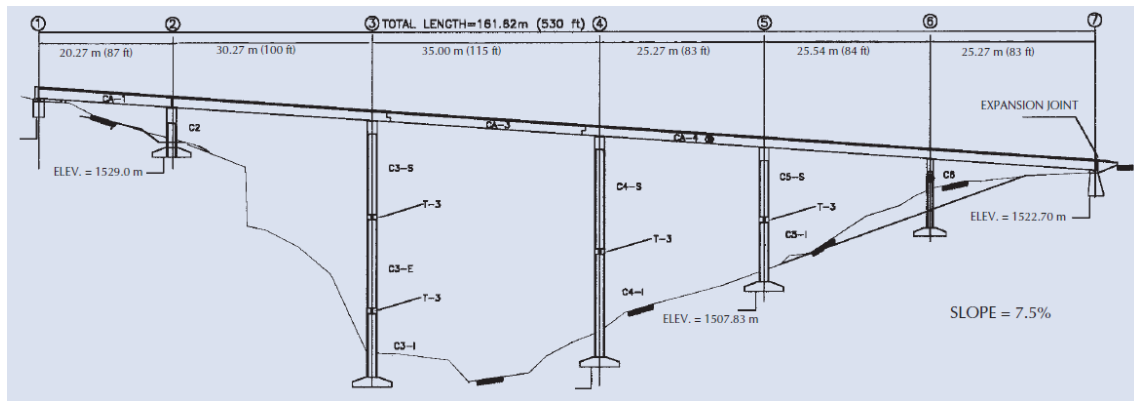
Figure 3.15 – Longitudinal view of the Ayuntamento 2000 bridge (Cruz Lesbros *et al.* (2003))

The substructure was constituted by two abutments and five bent-piers which, as evidenced in Figure 3.15, have considerably different heights. Additionally, hard accessibility to a deep valley limited the operational conditions of trucks and elevation equipment. In order to take that into account, the bent piers were designed as multi-column assemblies of up to three precast unit levels, corresponding to a maximum precast element size of 15m and maximum single element weight of around 60 ton, which required the use of hollow sections. Furthermore, for increased lateral stiffness and improved seismic behavior, piers included both an intermediate transverse beam and a cap beam, involving horizontal prestress to ensure adequate displacement compatibility.

The construction procedure of the Ayuntamento 2000 bridge piers was based on *loose-fit* CIP connections of the precast units. Therefore, it involved the use of a temporary supporting pad for the first vertical elements, in order to correctly establish full lap splicing between the precast elements and the CIP foundation, as shown before in Figure 3.6 – a). The column-to-column connection was performed with a similar procedure, where upper precast elements were placed on top of previously installed units, using corrugated sleeves for lap splicing bars (as no vertical prestress was used) and providing a void on the column cross section for posterior placement of the intermediate beams and to enable sufficient space for the CIP connection concrete pouring. This is illustrated in Figure 3.16 – b).

a) Protruding rebars on fixed element   b) Placement of subsequent elements

Figure 3.16 – Precast bent-pier assembly (Cruz Lesbros *et al.* (2003))

The construction of the Sorell Causeway Channel Bridge in Australia also evidenced the potential of precast solutions (Gibbens and Smith (2004)). The structure was meant to replace an old bridge that was in a high degree of deterioration due to sea water exposure and heavy chloride reactions, therefore enforcing the rapid construction requirements of the new bridge. Additionally, almost all the structure length developed over the sea, for 18 spans of around 25m. Using precast solutions enabled not only the reduction of construction times, but also the amount of supporting off-structure gear.

The precast system used in the new Sorell Causeway Channel Bridge involved a deck supported by twin piers, each erected from CIP pile caps. These pile caps were constructed by using precast formwork shells, according to Figure 3.17 - a). From there, *match-cast* pier sections were placed, prestressed and grouted, according to Figure 3.17 - b). This procedure enabled fast construction over sea by committing most of the heavy construction work to a land based precast plant, while also minimizing the accessibility requirement beside the sea structures.

a) Pile cap precast shells   b) Precast pier segments
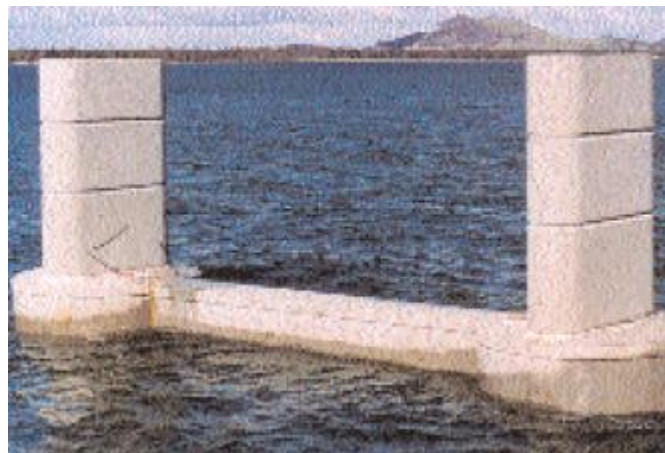
Figure 3.17 – Precast pier in the Sorell Causeway Channel Bridge (Gibbens and Smith (2004))

3.17

Despite the examples of the previously presented precast applications, the most common utility for precast solutions on bridge substructures is related to bent and pier caps. In this regard, it is usual to see vertical columns with protruding bars serving as guiding elements for the introduction of the precast cap beam, as illustrated in Figure 3.18.

a) Multi column bent cap beam

(Fouad *et al.* (2006))

b) Single column pier cap

(NCHRP (2003))

Figure 3.18 – Assembly of precast cap elements

To conclude this sub-section, there is a special case of precast usage that is worth mentioning. In fact, to the author's best knowledge, it is the only application of precast elements for substructure construction of high speed railway bridges that was identified. As described by Couchard and Detandt (2003), the José, Battice, Ruyff and Hervé viaducts were constructed using a concept based on inclined portal frames with sloping strut elements, illustrated in Figure 3.19 – a). Precast elements formed the inclined part of the rigid frames, which were then connected using prestress, according to Figure 3.19 – b). This configuration is capable of achieving high longitudinal stiffness through axial deformations of the inclined struts, while transverse stiffness of the frame is ensured by using adequately placed steel bracing along the sloping strut plane.

a) Inclined portal frame

b) Precast strut post-tensioning

Figure 3.19 – General substructure concept for the José, Battice, Ruyff and Hervé viaducts

(Couchard and Detandt (2003))

3.3.2. LAYOUTS FOR SEISMIC ZONES

The main difference of precast layout designs from non-seismic zones to seismic zones can be linked to the increased demand that the joints are subjected to during an earthquake event. For example, *match-cast* solutions as described by Billington *et al.* (1999b) tend to have high compressive stresses resulting from the vertical post-tensioning of their segments. When the seismic motion is further applied to the structure, causing the occurrence of horizontal displacements and joint deformations, it is resisted by additional forces provided by the prestress steel, holding the precast units together. Those additional forces are associated with exploring the full capacity of the prestress steel and, essentially, result in increased tensile stresses which can be associated with dangerous compression levels on the concrete, especially around the foundations. A potential shortcoming is that the overall ductility of the piers can be diminished, particularly if concrete crushing cannot be prevented, and the overall energy dissipation capacity of the prestressed layouts may also be an issue of concern. Furthermore, adequate detailing for providing a ductile pier response and the structural integrity of precast connections can easily lead to large congestion of reinforcement steel.

These issues have been some of the main technical reasons preventing a more generalized application of precast solutions for bridge piers, thus providing an open framework for research activity focused on improving knowledge over the seismic performance issues of precast piers, and also on developing solutions to address the associated shortcomings. For building applications, however, several authors have addressed this topic over the years (e.g. Yee (1991), Proença *et al.* (2002) or Pampanin (2003)), and the PRESS programme (PREcast Seismic Structural System, Priestley (1991)), in particular, enabled some of the most relevant technological advances. The general concept of the approach was based on setting the precast connections on the usual plastic hinge regions, in a lumped ductility design supported by prestress, aiming to reduce the usual CIP damage due to inelastic incursions.

Several results of that programme were also adapted for the context of bridges, where the use of unbonded prestress enabled designers to take advantage of the innate concentration of rotations on the precast joints, while disregarding the permanent effects of large inelastic deformations. One such work was that of Hewes and Priestley (2002), where a precast segmental bridge pier, which is illustrated in Figure 3.20, was studied to determine appropriate design detailing for good seismic performance. In that work, prestress was the only continuous reinforcement, providing structural integrity between the vertical segments of the structure.

3.19
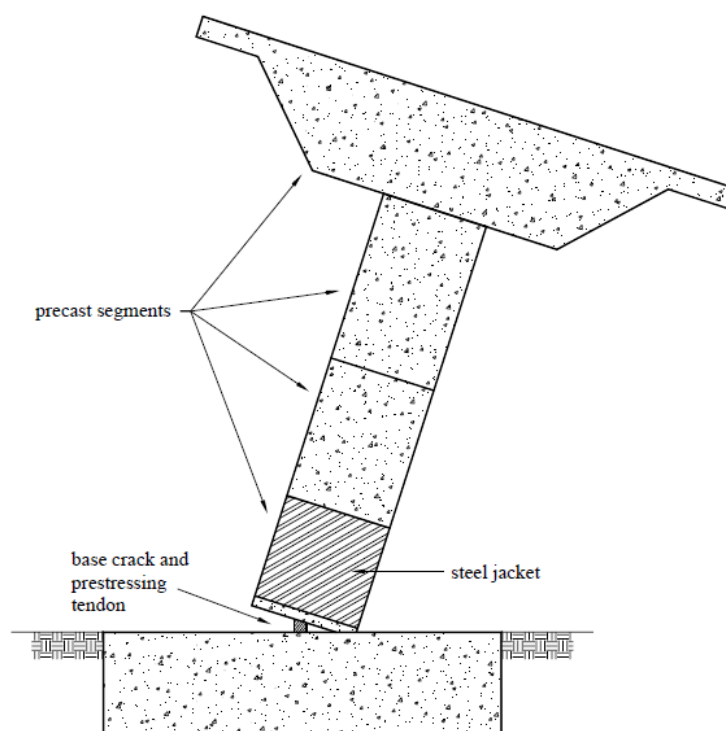
Figure 3.20 – Precast segmental bridge pier connected by unbonded post-tension (Hewes and Priestley (2002))

As shown in the previous illustration, the expected seismic behavior of this segmental pier involved, by design, a *"rocking joint"* mechanism, where the introduction of a steel jacket in the adjacent segment meant to provide increased concrete confinement to help on protecting against excessive base compression forces due to rotations. From a structural behavior perspective, this is a fundamentally different approach from usual CIP piers, where the designer normally selects and carefully details the specific zones (namely, the column bases) for intended flexural yielding of the longitudinal reinforcement and concentration of inelastic deformations. In this case, the plastic incursion of the materials is substantially lower, and large lateral displacements are associated with mostly rigid rotation of the pier segments around the compression toe, when dead-load induced moment strength is overcome. The post-tension contribution also acts as a self-centering element, since overturning moments produce increased elastic strains on the prestress steel that are naturally recovered after seismic motion. The overall solution was capable of achieving a low level of damage and strength deterioration (Figure 3.21 – a)), but it was found to lead to generally thin cyclic force-displacement loops (Figure 3.21 – b)), which can be associated with limited capacity of energy dissipation.

a) Precast segment damage
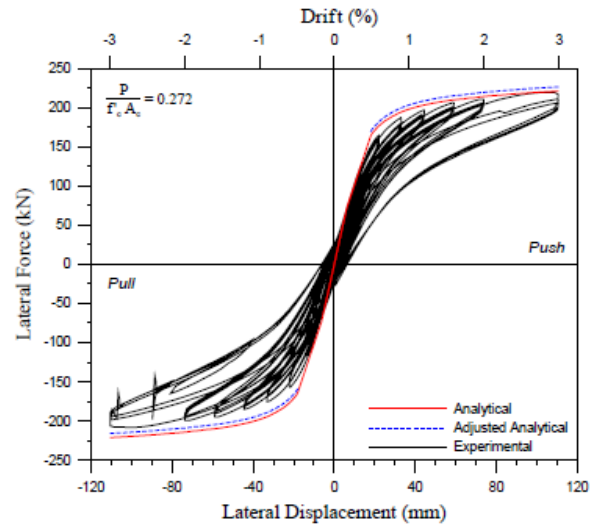
b) Force-displacement behavior

Figure 3.21 – Segmental precast pier seismic performance as reported by Hewes and Priestley (2002)

As rocking behavior was found not to be sufficiently dissipative, other authors such as Palermo *et al.* (2005), Palermo *et al.* (2007) or Ou *et al.* (2008) aimed to explore additional options. A very common approach was to design the precast connections for a hybrid, controlled rocking behavior. The general concept involved introducing conventional reinforcement or external dissipators across the *"rocking joints"* to increase the passive energy dissipation during rocking movements, as illustrated in Figure 3.22.
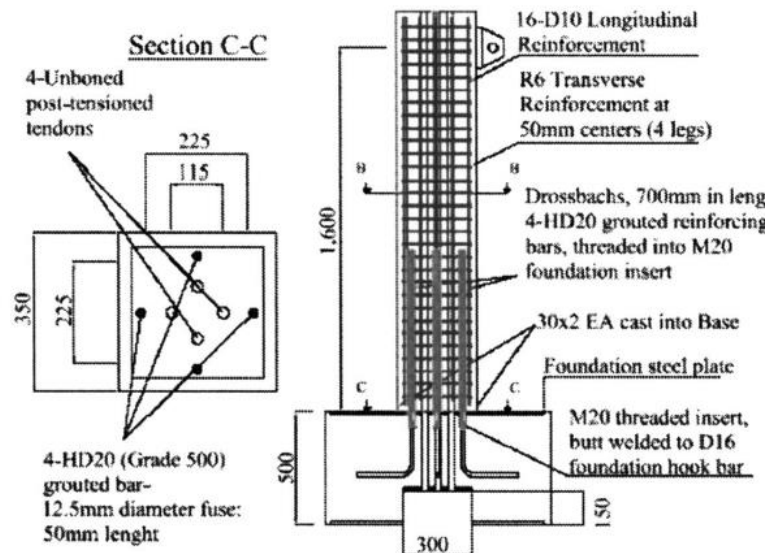
Figure 3.22 – Hybrid rocking mechanism as reported by Palermo *et al.* (2007).

The general seismic behavior of hybrid rocking solutions revealed considerably increased energy dissipation paired with low residual displacements, with the hysteresis loops forming a *"flag-shape"*, as evidenced in Figure 3.23. Furthermore, unbonding the passive reinforcement

by introducing the corresponding bars through corrugated ducts was also seen to improve the global performance of the pier by delaying bar fracture. However, according to Ou *et al.* (2010), despite the potential benefits of that approach, it might not be desirable due to increased labor work associated with unbonding those rebars and also because it weakens their protection against corrosion.

(e)
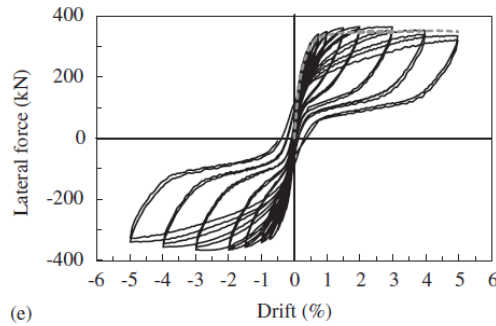
Figure 3.23 – *"Flag-shape"* hysteretic curves for hybrid rocking piers (Ou *et al.* (2010))

Wang *et al.* (2008) studied the adoption of high-strength steel bars crossing the precast joints as the main energy dissipating source, and different sizing of the plastic hinge segment, according to Figure 3.24. His work revealed that the increase in the height of the first precast segment enabled a more distributed cracking pattern to form in the plastic hinge region, in contrast with the regular pier segments where most of the deformation is concentrated in the joints.
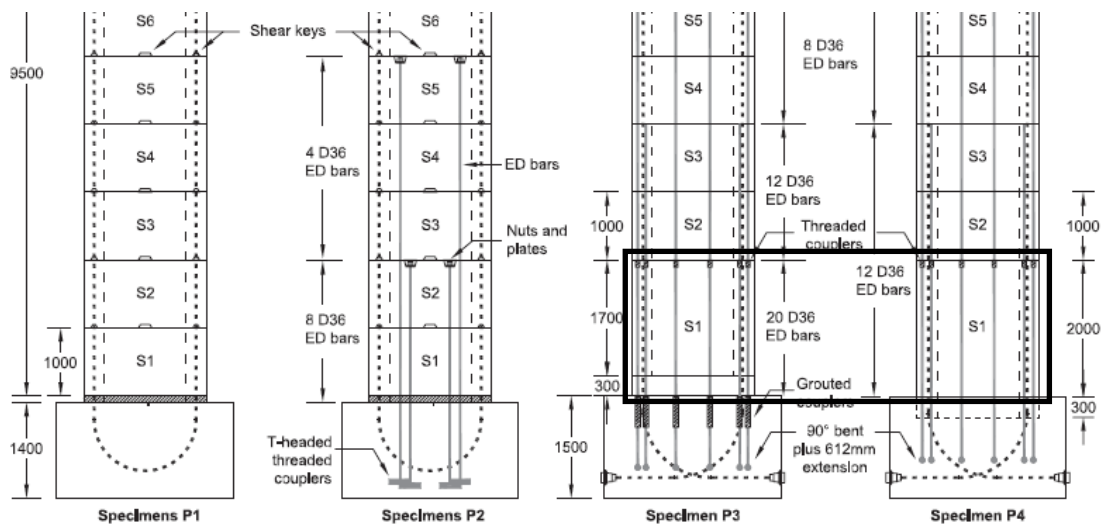
Figure 3.24 – Experimentally tested segmental pier variants by Wang *et al.* (2008).

Elgawady and Sha'lan (2011) studied the seismic performance of precast segmental bents, where the columns were fabricated within concrete-filled fiber tubes, and presented two additional and noteworthy details. One of the layouts included the isolation of the precast elements by introducing neoprene sheets in the foundation-to-element and element-to-cap

connections (Figure 3.25 - a)). The other included external energy dissipators located beside the previously referred connections (Figure 3.25 - b)). The overall results were satisfactory, but considerable differences were observed between the different proposals. In fact, using neoprene isolation drastically reduced the initial lateral stiffness of the bents, potentially leading to lower seismic forces but also to larger displacements. The use of external energy dissipators was successful in improving that aspect of the bent system seismic behavior, but, unfortunately, it was observed to lead to larger residual displacements and increased damage as well.

| a) Neoprene isolation | b) External energy dissipaters |
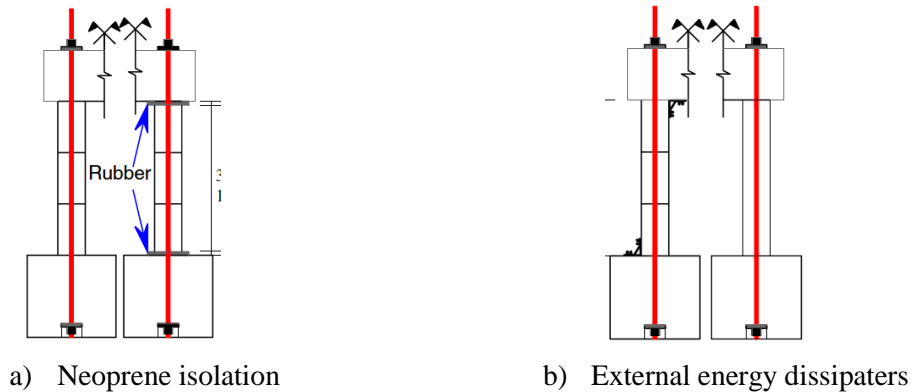
Figure 3.25 – Concrete-filled fiber tube segmental piers (Elgawady and Sha'lan (2011))

Billington and Yoon (2004) presented a Ductile Fiber Reinforced Cement Composite (DFRCC) with tensile strain hardening at the possible plastic hinge locations in order to increase the plastic deformation capacity of those sections and to reduce the potential for seismic damage as evidenced in Figure 3.26 - a). Furthermore, unlike the hybrid rocking solution, DFRCC piers did not include any reinforcement crossing the precast joints, carrying the load solely through the compressed region, the prestress tendons and the tensile cracked DFRCC region. Experimental evidence revealed that the fibers' composite enabled larger energy dissipation by providing an increased tension-stiffening effect, although its effect was mostly noticeable for earlier displacement cycles, as illustrated in Figure 3.26 - b).

| a) Segmental pier illustration | b) Energy dissipation per drift cycle |
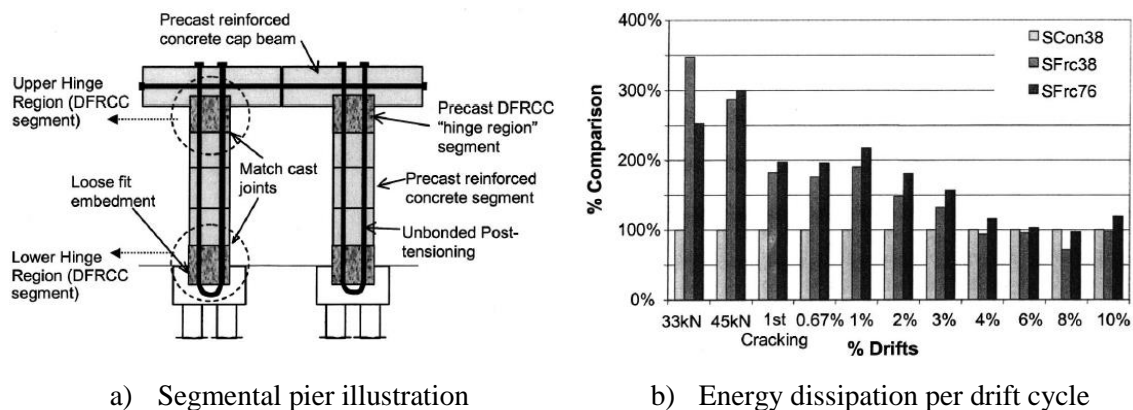
Figure 3.26 – Ductile Fiber Reinforced Cement Composite segmental pier (Billington and Yoon (2004))

Hoshikuma *et al.* (2009) presented the japanese experience on precast segmental hollow section piers. A particularly noteworthy layout was addressed, combining the concept of precast segmental construction with an internal steel shell, according to Figure 3.27, and was initially developed by Sumitomo Mitsui Co. Lda. (https://www.smcon.co.jp/en/). The assembly of this layout is enabled by accurate positioning of the internal shell, which is then connected by steel bolts and post-tension bars. In addition, the steel shells include shear key elements, in order to help on mobilizing the concrete segments during seismic events. As presented by the author, this configuration aims to carry the vertical dead and live loads mainly through the internal steel elements, while earthquake force resistance requires the contribution of the connection elements and the external concrete. In this case, considerable energy dissipation can occur in the precast joints with yielding of the steel bolts, which can also be easily replaced due to the improved accessibility provided by hollow-sections.
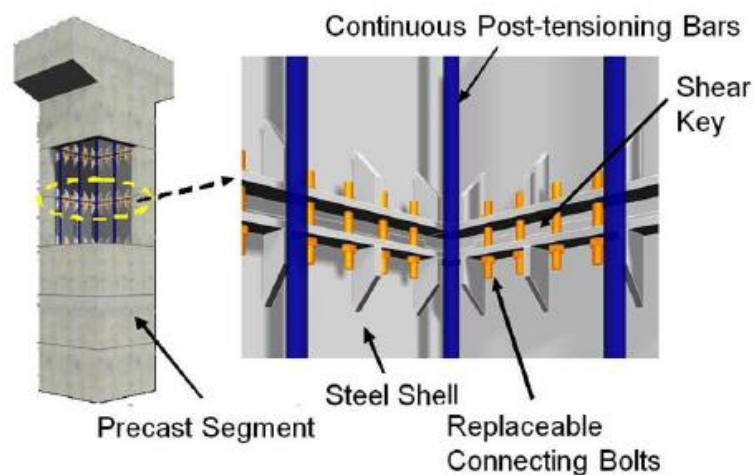
Figure 3.27 – Composite precast segmental pier layout by Sumitomo Mitsui Co. Lda
(Hoshikuma *et al.* (2009)).

One thing in common in all of the previously presented proposals is the focus on the enhancement of the seismic performance of mostly precast segmental piers, usually resorting to post-tension. That outcome may suggest that the use of post-tension for the rapid construction of bridge piers has been gaining acceptance for applications on seismic regions. Nonetheless, while the structural performance observed with these systems is often satisfactory, it can be argued that viable alternatives without prestress may be preferred, in favor of cheaper construction and less specialized operational requirements.

In that regard, adopting integral solutions with minimal element-to-element connections may be a preferred approach, considering that the alternative segmental systems were generally found to resort to the use of post-tension for ensuring structural integrity. Unfortunately, the amount of research activity focused on integral column precast layouts seems to be vastly

inferior. One such work was developed by Hieber *et al.* (2005), corresponding to the reinforced concrete alternative presented in that same publication, where a comparison against a hybrid system with unbonded post-tension is also included. According to the author, the design objective of the Reinforced concrete alternative was to *"emulate traditional reinforced, cast-in-place concrete columns"*. For that purpose, structural integrity was provided by the continuity of the longitudinal reinforcement, with protruding mild steel inserted through corrugated ducts. Furthermore, the column segments were designed on the basis of the same geometry, material properties and details of CIP equivalents. The seismic performance of this layout, which is illustrated in Figure 3.28 – a), was expected to enable the formation of column base plastic hinges (Figure 3.28 – b)), essentially relying on the same energy dissipation mechanisms of equivalent CIP systems. Experimental confirmation of that behavior was not available, unfortunately, as the study was essentially numerical.

a)   System illustration   b)   Expected seismic behavior
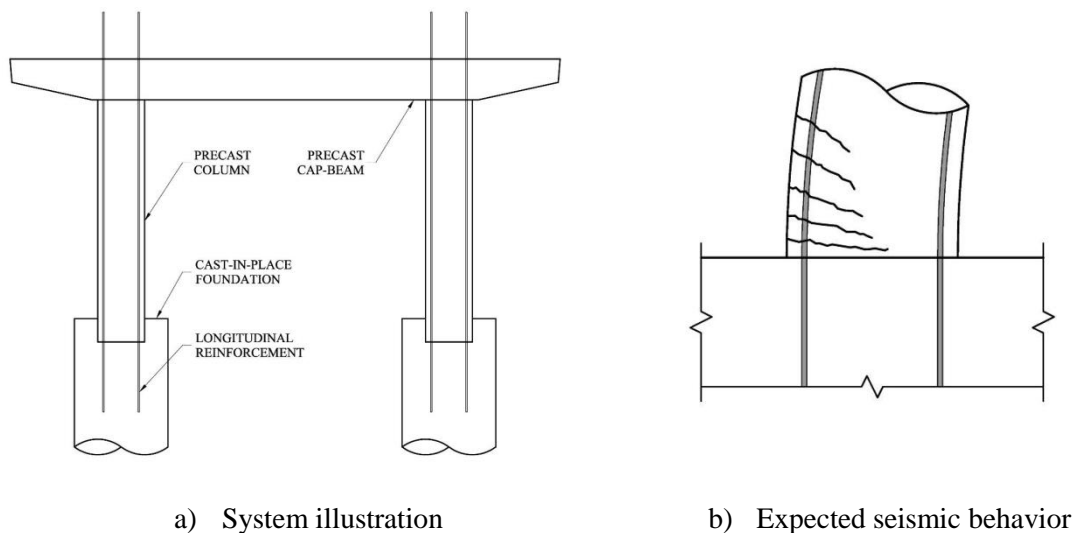
Figure 3.28 – CIP emulated Reinforced Concrete system by Hieber *et al.* (2005).

The biggest difference between this reinforced concrete system and the hybrid post-tension alternative was the displacement ductility, where the latter achieved around 50% higher values, according to Table 3.1. However, that mostly reflected a lower cracked stiffness of the non-prestressed system, since the overall maximum force and displacement capacity of both structures was found to be very similar. Different damage states representative of structural damage, such as concrete spalling or bar buckling, for example, were also found to occur for very similar demand levels. Overall, those results suggested that adopting integral precast solutions without prestress was a technically viable alternative.

Table 3.1 - Comparison between Reinforced Concrete and Hybrid systems (adapted from Hieber *et al.* (2005))

	Reinforced Concrete Frame	Hybrid Frame	Percent Difference
$\dfrac{K_{cracked}}{K_{uncracked}}$	0.276	0.369	34%
$\dfrac{\Delta_{max}}{\Delta_y}$	3.69	5.51	49%
F_{max}	429 kips	382 kips	11%

$K_{cracked}$ − Cracked stiffness; $K_{uncracked}$ − Uncracked stiffness;
Δ_{max} − Maximum displacement; Δ_y − Yielding displacement;
F_{max} − Peak force

Integral solutions were also addressed by Khaleghi (2005), essentially highlighting the advantages for slanted columns, where the assembly of segments is harder to perform than for vertical piers. Furthermore, an improvement is suggested by using a purposefully reduced size reinforcement layout in connection zones, according to Figure 3.29. This configuration can enable a reduction of the pier/bent cap reinforcement requirements due to a lower yielding moment on the connection section. The previous is a relevant feature of this proposal, since reducing rebar congestion may enable easier precast design and element manufacture. In addition, the reduced size of the reinforcement layout at the joint section also provides additional space for natural positioning of any required cap elements, which also represents a big advantage of this proposal.
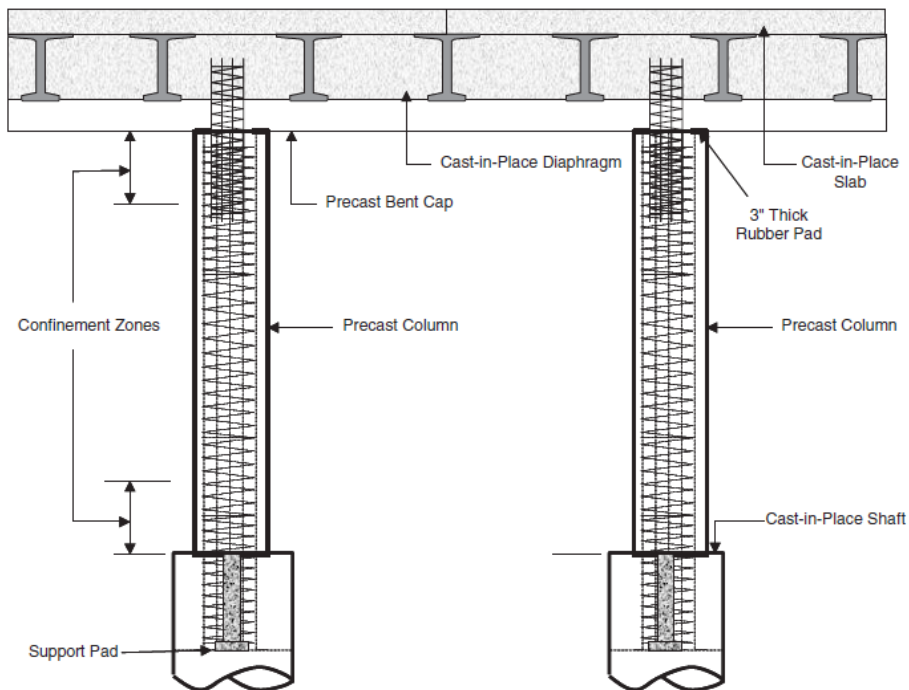
Figure 3.29 – Integral columns precast system proposed by Khaleghi (2005)

Alternatively, stable energy dissipation and a ductile behavior can still be achieved if no local reduction of the moment capacity of the bent structure is adopted. In that regard, Pang *et al.* (2010) studied the application of a reduced number of large diameter bars for establishment of element-to-cap connections, achieving comparable performance to CIP regarding hysteretic response and damage progression. Figure 3.30 illustrates the associated design, where $\phi 57$ rebars are introduced through 216mm diameter corrugated ducts.
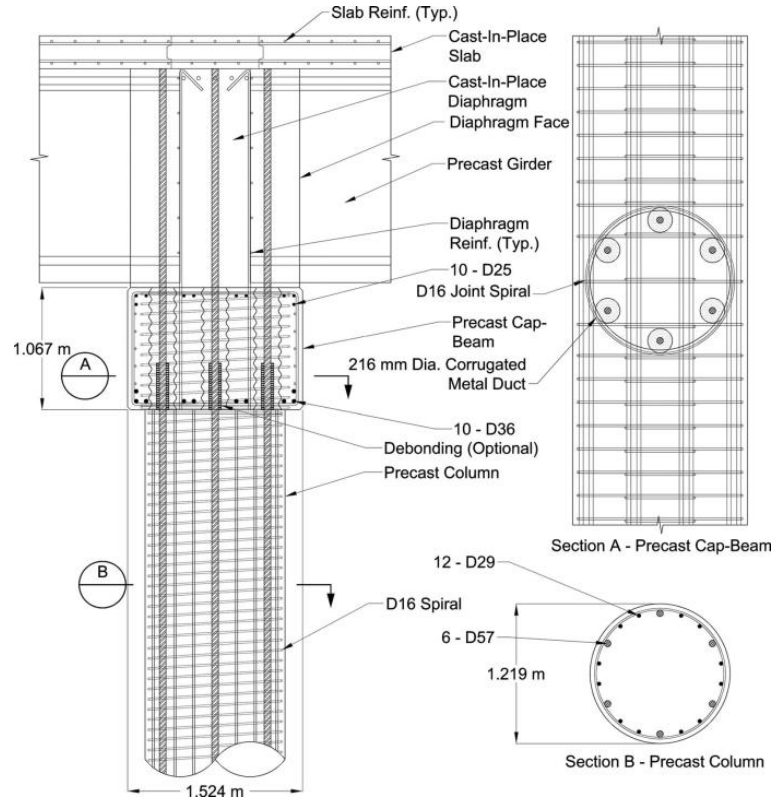
Figure 3.30 – Large diameter rebar connections for bridge piers by Pang *et al.* (2010).

3.4. FINAL REMARKS

In this chapter, the most relevant aspects of the precast technology to the current work were presented. Firstly, the main advantages and disadvantages of the precast technology were discussed, aiming to provide an overview of the most important decisions to be made when a large-scale precast application is considered, such as those related with construction schedules or transportation and site handling constraints. Afterwards, a state-of-the-art review of the most common precast connection types and pier systems was presented, taking into account that there are significant differences between precast layouts designed for seismic and non-seismic zones. Thus, the content of this chapter essentially provides detailed context of the precast technology, regarding the structural system that is addressed in the present work and, in particular, the decisions that influenced the conceptual design to be presented in the next chapter.

4

CONCEPTION AND SEISMIC DESIGN OF TEST SPECIMENS

4.1. REFERENCE PIER MODEL: THE RAV POCEIRÃO-CAIA CONCESSION PROJECT

The precast application studied in the current work was inspired in the Portuguese attempt at HSRL, embodied by the RAV Poceirão-Caia project (Altavia (2009)), whose construction was halted at an early beginning. Nonetheless, the project itself was presented as the first Portuguese venture onto the framework of high speed railways, aiming to provide fast quality traveling between Lisbon and Madrid, and contemplated double lane UIC compliant (http://www.uic.org/) ballasted tracks, designed for minimum and maximum speeds of 120 km/h and 350 km/h respectively. In addition, cargo transportation services were also considered, up to a maximum travel speed of 160 km/h. Figure 4.1 illustrates the layout for the full implementation of HSRL in Portugal and respective international connections with Spain, where the orange shaded part refers to the Poceirão-Caia segment.
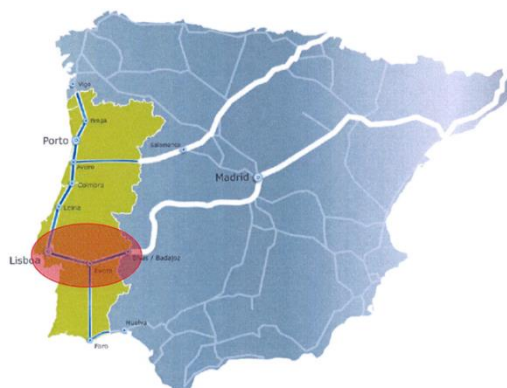
Figure 4.1 – Illustration of the Poceirão-Caia segment within the full Portugal and Spain HSRL expected layouts Altavia (2009)

A total of 164.7 km of new line was to be constructed, involving several new structures (around 6.3% of total length) from which 30 bridges and viaducts related to high speed railway traffic could be identified. In that regard, two main design trends could be observed:

- Shorter span structures (30-35 meters) which were associated with double box girder decks with 12.20m of width, using two precast *"U-shaped"* girders, CIP slabs and smaller bent piers (Figure 4.2– a)). A solid cross-section of around 3m^2 is used for the vertical columns, while the deck amounts to a total around 6.70 m^2;

- Longer span structures (40+ meters) that were designed with single box girders with 12.20m of width, usually resorting to advanced construction methods such as the launching gantry (Figure 4.2 – b)). Single column piers were adopted, including hollow shape cross-section of approximately 5.50 m^2, while the total deck cross-section was around 9.45 m^2;
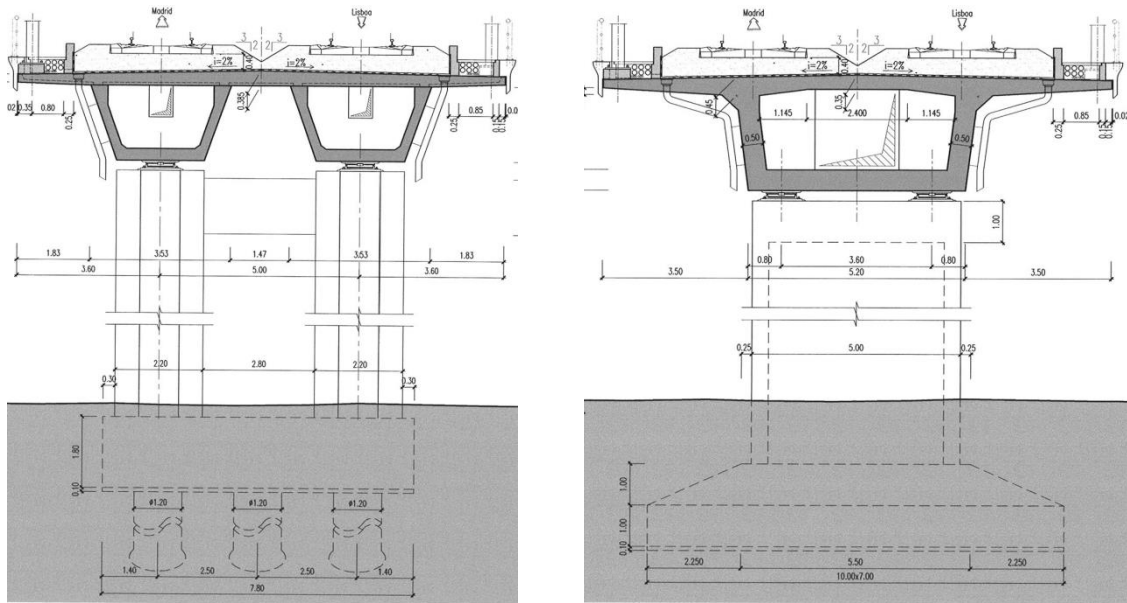
a) For shorter spans   b) For longer spans

Figure 4.2 – Pier layouts on the Poceirão-Caia project Altavia (2009)

On account of a possible large scale application of precast solutions for the construction of those bridge piers, it should be acknowledged that the endeavor may only be reasonable if it is technically viable while also striving for economic competitiveness. In that context, the design should aim to reflect optimal conditions regarding manufacture, transportation and assembly, where minimal costs, duration and operational difficulty are preferred. Furthermore, maximum efficiency is generally associated with addressing repeatable layouts, considering the least possible changes in materials and formwork. Therefore, it makes sense to try to identify an optimal scenario for which most of these cost-efficiency driven guidelines may apply.

For that purpose, all the bridges and viaducts of the Poceirão-Caia line were further evaluated, according to the overview presented in Table 4.1. It is possible to observe that the majority of viaducts have a main span smaller than 35 meters, supported by structural systems constituted by double column bents and double box girders. It should be noted that these characteristics are in line with the findings presented in Chapter 2, as single column piers tend to be used in longer span structures, while multi-column bents and walls are preferred for those with smaller spans. Furthermore, the majority of the 14 double column bent structures with main span of 30 meters represent medium to long viaducts, and around 70% of them with total length between 100m and 600m, as illustrated by Table 4.2.

Table 4.1 – Poceirão – Caia structures overview

Main Span (m)	Technical Solution		Number of Viaducts	% of Total
	Piers	Deck		
30	Double column bent	Double Box girder	14	46.67
35	Double column bent + Rectangular Hollow Pier	Double Box girder + Single Box girder	5	16.67
40	Rectangular Hollow Pier	Box girder	3	10.00
45	Rectangular Hollow Pier	Box girder	7	23.33
55	Rectangular Hollow Pier	Box girder	1	3.33
		Total:	**30**	

Table 4.2 – Structures with double column bent-type piers

Structure Length (m)	# of spans	# of structures	Pier height (m)		% of Total
			Minimum	Maximum	
< 100	< 4	3	4.83	6.43	21%
100 - 300	5 to 9	6	4.90	17.44	43%
300 - 600	10 to 18	4	6.04	19.00	29%
> 600	> 20	1	5.58	9.83	7%
				Total:	**100%**

As previously discussed, this is a common scenario on the HSRL framework, since the requirement for small horizontal radii and vertical slope structures is often fulfilled by constructing long viaducts, which is also favorable regarding precast applications by enabling large-scale production and increased efficiency, through replicable design and optimized assembly procedures. Improved scheduling and resource management due to a larger number of possible simultaneous work fronts may also come to mind. In light of these observations, the double column bent pier layout of Figure 4.2 – a) seems to provide a favorable background for the development of a precast solution, making it reasonable to consider partial application focused only on the HSRL viaducts with that structural layout.

Regarding horizontal loads, the double column bent pier system provides high stiffness against forces applied in the transverse direction. However, controlling the longitudinal direction performance requires selection of an appropriate force anchoring layout, considering the medium to long bridge lengths in question. The following design features were adopted on the Poceirão-Caia line structures depending on the total bridge length:

i. Shorter structures include some variation of fixed piers around the bridge midsection, as illustrated by the blue rectangle in Figure 4.3 – a);

ii. Longer structures concentrate the longitudinal stiffness in the pier alignments near one of the abutments, according to the blue rectangle in Figure 4.3 – b);

iii. The installation of a STU device for restraining longitudinal high speed movements in one of the abutments is expected, regardless of bridge length (highlighted by the red circle in Figure 4.3);
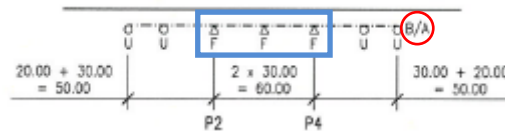
a) Short viaduct example (U – free connection; F – pinned connection)
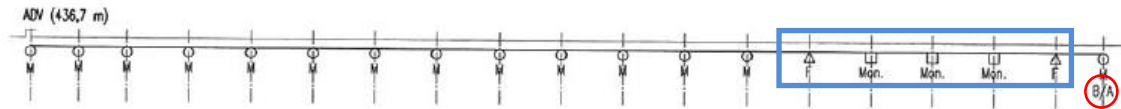
b) Long viaduct example (M – free connection; F – pinned connection; Mon. – monolithic connection)

Figure 4.3 – Longitudinal connection layouts on Poceirão-Caia HSRL structures

With this in mind, the pier alignments where provision of longitudinal stiffness was a concern were generally observed to be at most 30% of the total, and in some of the cases requiring monolithic connections. On the other hand, the main concern for the remaining majority of alignments is the transverse behavior, corresponding to the main advantage of the double column bent system. Therefore, it can be assumed that the longitudinal performance may be evaluated on a case-by-case basis, enabling focusing the precast application mostly on the transverse challenged piers with free longitudinal connections. In light of this, the main design guidelines for this work were the following:

i. Double column bent pier and double box girder deck as the main structural layout;

ii. Medium to long viaducts, between 100m and 600m of length;

iii. Pier height range limited to values between 5.00m and 20.00m;

iv. Focus on the transverse performance of the piers, enabled by free longitudinal connections;

4.2. PIER SEISMIC DESIGN

In order to design a precast system for this pier layout, including the core elements and their respective connections, it is necessary to have realistic expectations for the capacity demand on the fully assembled structures. A logical and straightforward approach to that problem is to study equivalent monolithic solutions from which a precast alternative can be derived. For that purpose, since mostly the transverse performance was assumed to be the main concern, seismic events represent one of the more relevant load cases. Within those premises, the design methodology described in the following sub-sections was established, essentially aiming to obtain realistic design parameters for the test models, used in the experimental campaign later presented in Chapter 5.

4.2.1. GENERAL CONSIDERATIONS AND DESIGN METHODOLOGY

Traditionally, structural design has always been related to the assessment of the applied loads relative to resisting capacity for a given limit state. For most purposes that approach is successful, since the loading characteristics can be determined independently from the elastic response of the structure and the comparison between capacity and demand is straightforward: collapse is avoided if the strength capacity available is greater than the applied loads. On the framework of seismic events, elastic loads are often too large, preventing a cost-effective design for strength capacity. As acknowledged by the community over the last decades, the most adequate approach is to expect the occurrence of structural damage, associated with inelastic deformations and ductile behavior, for which avoiding relevant strength losses becomes the main concern. Considering this context, there are two main trends associated with current seismic design methodologies:

- Force based methodologies (FBD);
- Displacement based methodologies (DBD);

Both of these are related to the concept of ductility, which is defined as the ratio between the maximum and effective yield values of a chosen deformation parameter such as displacement or rotation. FBD methodologies have associated an elastic force reduction factor, which governs the design strength while indirectly ensuring smaller deformations than the actual capacity through detailing. That approach is known to have some shortcomings, which are mostly related to evaluation of the structure stiffness and the fact that it is not completely independent from design strength, since both influence and are influenced by the initial period estimation and the force distribution between resisting elements.

Alternatively, DBD methodologies essentially aim to design structures to be capable of achieving a given limit state described by a maximum deformation parameter in line with the desired hysteretic energy dissipation mechanism. In order to do that, they forego the characterization of the effective period from the elastic properties of the system and instead rely on the concepts of equivalent hysteretic damping, or inelastic displacement spectra, to relate the evaluation of the effective period of the structure under design with the targeted deformation capacity. This approach has been acknowledged to lead to more consistent results and, provided that the characterization of the inelastic properties of the structural system is sufficiently accurate, the resulting design process is straightforward. A more detailed discussion on these subjects can be found in Priestley *et al.* (2007).

In this context, a common point of both the seismic design approaches addressed above is the reliance on the choice of a stable energy dissipating mechanism by selecting adequate locations for plastic hinges, as well as capacity design procedures for some specific elements and conditions. This methodology leads to some level of predictability of structural damage, and also helps designers on accommodating higher strains on critical zones by adopting a reinforcement layout capable of larger deformations. For example, building structures are normally designed to develop plastic hinges in beam ends and the base of the columns, while avoiding soft-storey mechanisms (Figure 4.4 – a)); single column bridge structures are designed mostly as a vertical cantilever, with a plastic hinge developing just above the footing (Figure 4.4 – b)); multi-column bents, however, are usually expected to display double bending behavior, with high stiffness cap beams (Figure 4.4 – c)). Of course, on all cases, plastic hinges are considered to be conditioned, by design and detailing, with sufficient ductile capacity to withstand expected rotation demands under seismic loading.

a) Portal frame building

b) Single Pier bridge

c) Multi-column bent bridge
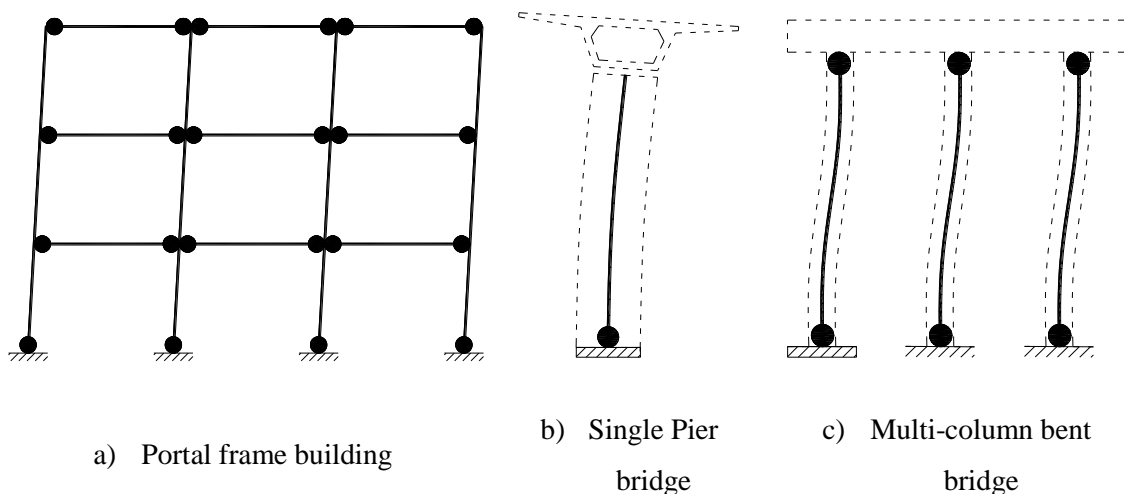
Figure 4.4 – Plastic hinge placement on different structural systems

In the FBD framework, the adoption of a global elastic force reduction factor can also be difficult to evaluate for some structures, since it relies on the misleading assumption of simultaneous formation of the plastic hinges on the main resisting elements. Furthermore, different structure types and materials are assumed to lead to different reduction factors, for which design codes usually provide reference and limit values. This strategy also requires the adoption of detailing rules which are assumed to provide the necessary ductility, but a direct relation between demand and capacity is not explored beyond that. However, for design purposes of regular structures where the simultaneous yielding assumption is acceptable, FBD still provides a straightforward procedure for reliably calculating design forces.

Regarding DBD, the ductility demand is generally also imposed by design codes, according to the applicable performance limit states, but unlike in FBD, it is directly associated with the response for each particular structure. Therefore, the yielding displacements associated with the adopted plastic hinge dissipating mechanism must be calculated, because they are a key component in the determination of the ductility capacity, and the difficulty of that assessment is directly related with the complexity of the structure. That assessment is relatively straightforward on regular structures such as buildings, since relations between cross-section, structure geometry and the target displacement profiles are generally easy to determine by analytical or numerical means. However, considering the geometry of the present bridge system and its bent pier (and, particularly, the presence of the coupling beam) increased difficulties and concerns are raised by the use of DBD.

4.2.2. IMPLICATIONS OF THE STRUCTURAL SYSTEM ON THE DESIGN STRATEGY

Figure 4.5 – a) presents illustrations of different height bent piers, roughly covering the minimum and maximum values observed in Table 4.2. According to those values, the respective width-to-height ratios vary between approximately 1.0 and 0.25, where the pier structure is composed of two columns with varying heights along the full bridge length, and a constant size coupling beam. In fact, the total span of the beam actually depends on the rail track conditioning, because the columns are vertically aligned with a centered position relative to each rail track, in order to eliminate eccentric moments from traffic loads and, for operating speeds greater than 300 km/h, track centre distances are recommended to be adopted between 4.50m to 5.00m (UIC (2010)).

a) Different pier heights

b) Element cross-section and properties
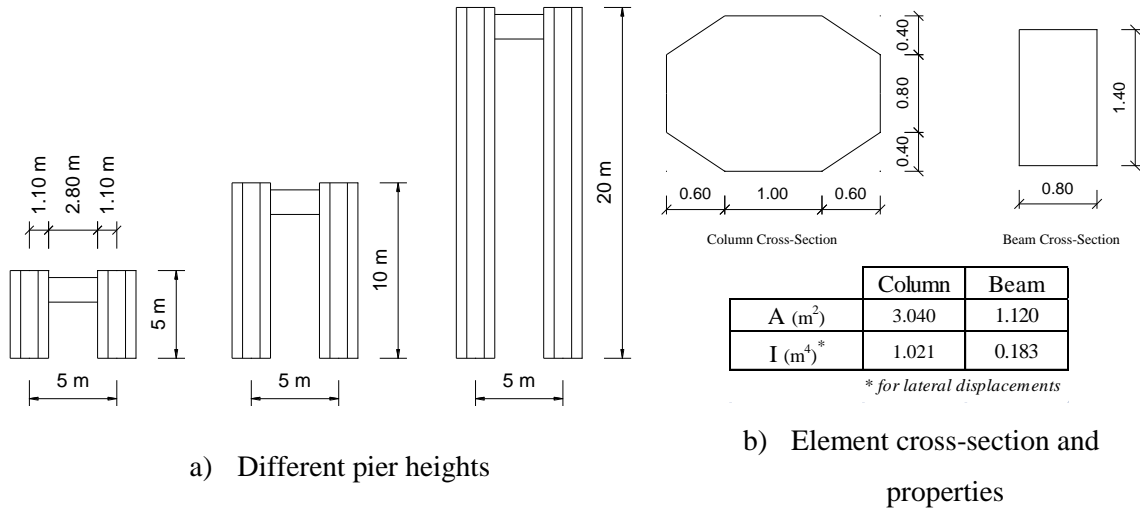
Figure 4.5 – Double Column Bent-pier geometry

Consequently, the stiffness ratios between the columns and beam are not constant, i.e., they change according to pier height. In that regard, a simplistic evaluation can be made, assuming no deformations take place in the beam-column nodes due to lateral displacement and considering fixed base restraint conditions. For that purpose, the column and bending stiffness ratios illustrated in Figure 4.6 can be represented by Equations 4.1 and 4.2, which are associated with linear elastic properties calculated for the gross cross-sections shown illustrated in Figure 4.5 – b).

$$C_c = \frac{4.085}{4.085 + 0.220 \times H} \quad 4.1$$

$$C_b = \frac{0.220 \times H}{4.085 + 0.220 \times H} \quad 4.2$$
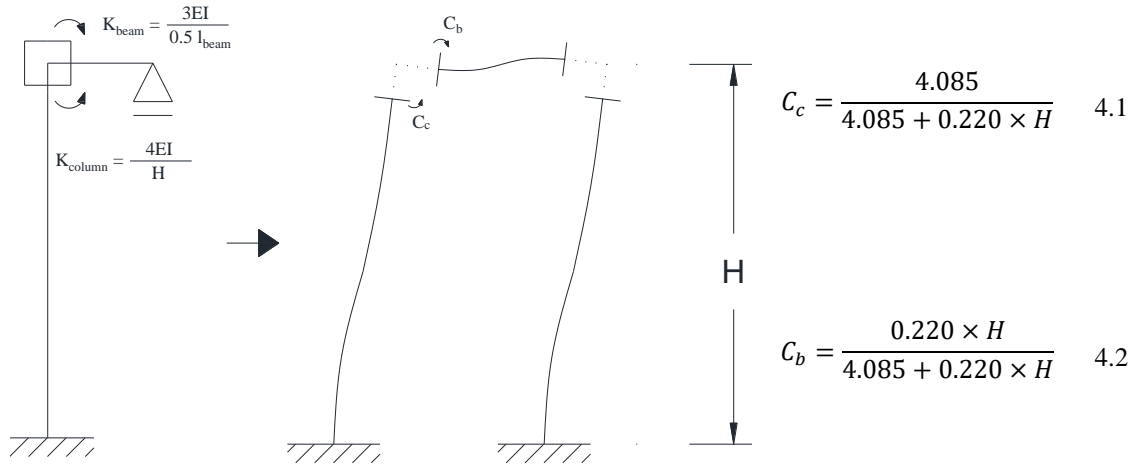
Figure 4.6 – Stiffness ratios for lateral displacements

Values of C_c and C_b for the pier height range (between 5.00m and 20.00m) were determined for the following three scenarios of element stiffness and plotted in Figure 4.7 – a):

1. 100% of elastic stiffness on both column and beam (C_c-*100C_100B* and C_b-*100C_100B*, respectively), corresponding to the reference structure;

2. 50% of the elastic column stiffness and 100% of the elastic beam stiffness (C_c-*50C_100B* and C_b-*50C_100B*);

    3. 100% of the elastic column stiffness and 50% of the elastic beam stiffness (C_c-*100C_50B* and C_b-*100C_50B*);

In the referred plot, the upper bound value of 1.00 can be related to fully rigid behavior of the respective element, while an intermediate value of 0.50 relates to equal stiffness between both. The overtake threshold is represented by the colored triangle shape within each Beam-Column result set. Concerning only the results of the reference system (*100C_100B*, represented by the blue lines), it can be observed that the beam element provides higher stiffness to the bent-pier structure for total heights greater than 15.50m (when the respective lines intersect each other), whereas the opposite occurs for shorter piers.

      When significant variations of the stiffness ratio between columns and beam are considered, the overtake threshold shifts accordingly, as illustrated in Figure 4.7 – a) by the additional plotlines (colored red and green). In addition, it can be argued that such change may be representative of the structural impact caused by the occurrence of cracking or localized damage (on the elements with the 50% reduced stiffness) during the structure's lifecycle. The red lines represent a situation where the contribution of the beam element to the total lateral stiffness is larger, while the opposite is represented by the green lines, illustrating an amplitude range of the overtake threshold between 7.00m in the case of the former (50C_100B), and a value greater than the maximum height for this study of 20.00m, in the case of the latter (100C_50B).

      In both cases, the red and green plots are closer representations of the upper (fully rigid cap beam behavior) and lower (non-existence of cap beam) bound scenarios under analysis, respectively, but, nonetheless, a more direct comparison can also be made. Aiming at doing that, the reference structure system (100C_100B) was assumed to provide the most accurate estimate of the expected stiffness for the present structure (K_{100C_100B}), enabling the evaluation of the absolute variation of stiffness between itself and equivalent structures having…:

- *Rigid*: …fully rigid cap beam behavior, corresponding to a double column bent structure whose total lateral stiffness can be evaluated by $K_{Rigid} = 24 \times \frac{EI}{H^3}$, according to the concepts on Figure 4.6;

- *No beam*: …no cap beam (or a null stiffness beam), corresponding to two single columns responding as vertical cantilevers, whose total lateral stiffness can be evaluated by $K_{nobeam} = 6 \times \frac{EI}{H^3}$, according to the concepts on Figure 4.6;

Furthermore, the stiffness relations $K_{nobeam} < K_{100C\text{-}100B}$ and $K_{100C\text{-}100B} < K_{rigid}$ are valid and, consequently, the absolute variation of stiffness was evaluated differently for the *Rigid* and *No beam* scenarios, according to equations 4.3 and 4.4, respectively, whose results are illustrated Figure 4.7 – b):

$$\Delta K_{Rigid} = \frac{K_{rigid}}{K_{100C-100B}} \qquad\qquad 4.3$$

$$\Delta K_{Nobeam} = 1 - \frac{K_{Nobeam}}{K_{100C-100B}} \qquad\qquad 4.4$$

The black line that marks the 1.00 value illustrates the reference structure 100C-100B, and its equivalent structural systems regarding total lateral stiffness. Likewise, values above and below that threshold represent structures whose lateral stiffness is, respectively, greater than or smaller than that of the reference case. Therefore, Figure 4.7 – b) shows that the difference between the present structure and the boundary cases under analysis, regarding the lateral stiffness, gradually decreases with total pier height. That also suggests that the only element whose behavior varies between the three analyzed structural systems - the coupling beam -, has negligible contribution to the lateral stiffness of very tall piers. Nonetheless, for the pier height range under analysis differences are still greater than 30%, indicating that the contribution of the coupling beam to the total lateral stiffness cannot be ignored, and that the resulting interactions between the columns and the beam should be carefully evaluated.

a) *Column* vs. *Beam* stiffness ratios   b) *Rigid* vs. *No beam* stiffness variation ratios
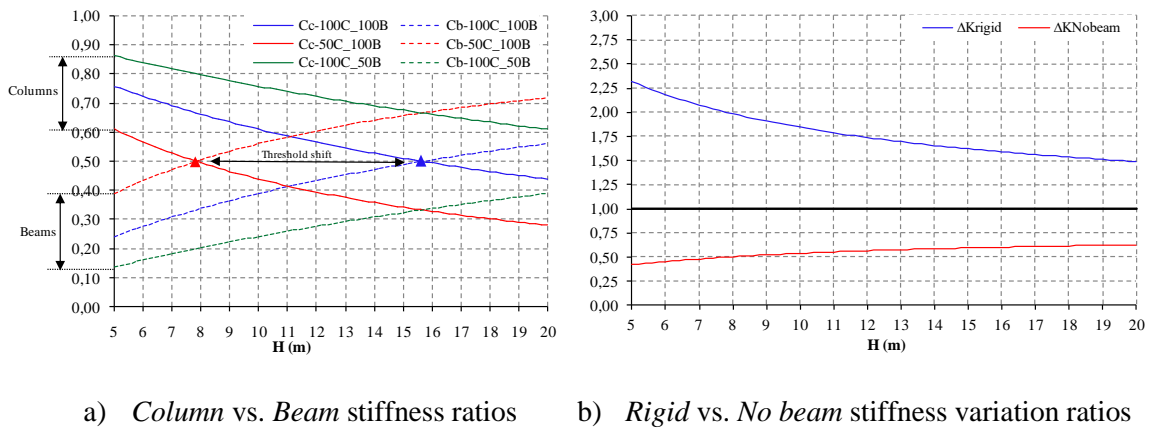
Figure 4.7 – Comparisons of structure stiffness relative element ratios and absolute variation for pier heights in the assumed range and different analysis scenarios

A simple exercise based on moment-curvature analyses can be performed to provide better understanding of the interaction between the columns and the beam. With that in mind, 2D fiber representations of the cross-sections illustrated in Figure 4.5 – b) were prepared and subjected to a monotonic increasing curvature load history in the Cast3m FEM software (http://www-cast3m.cea.fr/) to find the yielding curvature ranges for both the column and the beam. For that purpose, an existing procedure on the referred software was used (labeled MOCU), wherein the constitutive models adopted to simulate the stress-strain relationships of concrete and steel fibers were a variation of Hognestad's model (labeled BETON_UNI - Hognestad *et al.* (1951)) in representation of a class C30/37 concrete, and Menegotto-Pinto (labeled ACIER_UNI - Menegotto and Pinto (1973)) in representation of S500 reinforcing steel

4.10

(corresponding modeling parameters included in Annex A). In that regard, while the concrete constitutive model can be considered fairly outdated (since other, more powerful, alternatives can be found in the literature), it was still considered effective for the purpose of finding yielding curvatures on the scope of this exercise, enabling the straightforward use of the above referred procedure and avoiding resorting to more complex tools. For simplicity, a peripheral distribution of longitudinal rebars was assumed for the column, while both top and bottom rebar layers were considered in the beam. Two modeling assumptions were explored:

- Axial load ratio ν variation between 0.05, 0.10 and 0.20 for the column;
- Longitudinal reinforcement ratios ρ of 0.75%, 1.00% and 2.00% of the gross concrete area for both column and beam;

The obtained results were compiled on Figure 4.8, where the color of the lines refers to the axial load ratio (blue for 0.05, green for 0.10 and red for 0.20 on the columns, Figure 4.8 - a); blue only on the beam, Figure 4.8 - a)), while the line style refers to the reinforcement ratio (dash lines for 0.75%, dash-dot lines for 1.00% and solid line for 2.00%). As observed, the effective yielding curvatures for columns (φ_{cy}) are roughly between 0.0015rad/m and 0.0035rad/m and around 0.0025rad/m for the beam (φ_{by}).

a) Column cross-section   b) Beam cross-section
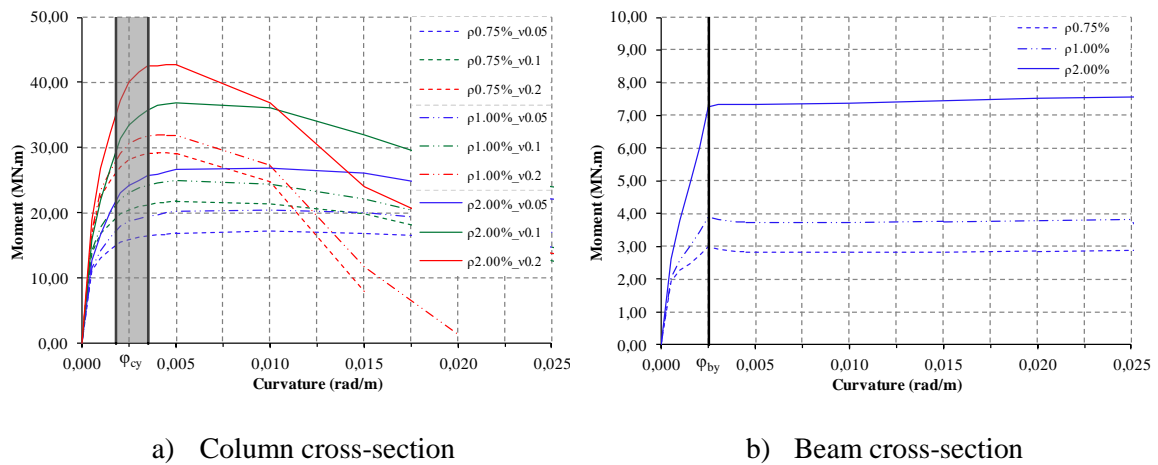
Figure 4.8 – Moment curvature analyses

Comparison of these results is better achieved by merging with the influence of the relative stiffness ratios presented in Figure 4.7 – a). Adopting a mean reference column yielding curvature φ_{cy} of 0.0025rad/m, and also assuming that yielding occurs first through inelastic incursion on the columns, enables determination of the expected beam curvature values associated with column driven yielding. The corresponding results, which are illustrated in Figure 4.9, are obtained by multiplying φ_{cy} by the ratio defined between the column and beam stiffness ratios, C_c and C_b, respectively (for the sake of simplicity, it was also assumed that no

deformations occur inside the beam-column node during lateral displacement induced rotations).

As it is possible to observe, the comparison of those values with the previously estimated yielding curvature of the beam (φ_{by}), shows that rotations of the beam-column node capable of inducing column yielding generally demand beam curvatures larger than the reference φ_{by} value. These results suggest that the likelihood of the occurrence of significant beam strains is relatively unavoidable for a large part of the pier systems within the assumed height range, even if the demand decreases for the tallest structures. Likewise, it is also clear that the assumption of cap beam rigid behavior, usually considered for multi-column bent pier design, cannot be enforced in this structural system.
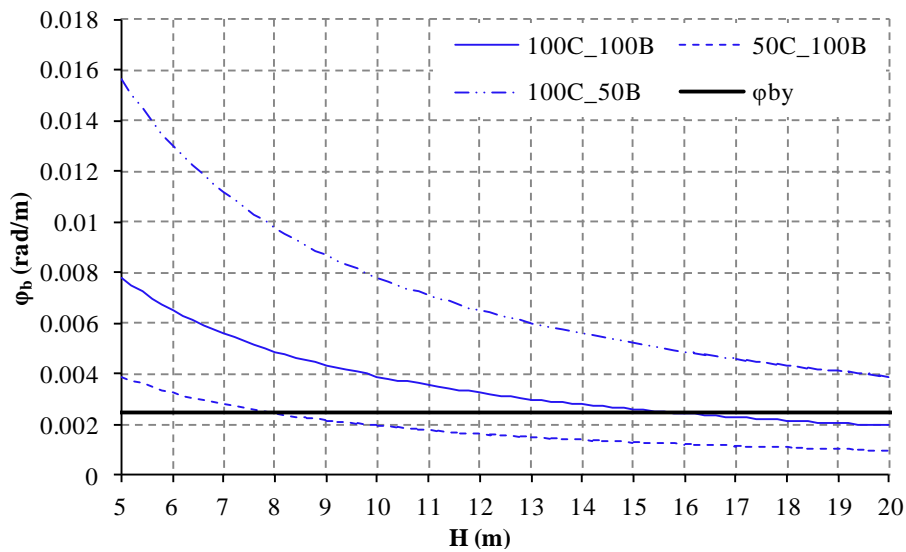
Figure 4.9 – Beam curvature φ_b demand variation (with column height) for node rotations associated with column yielding for different column-beam elastic stiffness ratios.

The implications of that on general design strategy can be significant, since the plastic hinge locations (Figure 4.4) and the preferred dissipating mechanisms should be defined accounting for the most critical parts of the structure. Within that context, and considering the beam free span with a fixed length of 2.80m and the section depth represented in Figure 4.5 - b), the shear span-to-depth ratio α_s is 1.0. If a plastic hinge length equal to the section depth is considered, according to EC8 recommendations, then the full length of the beam would be required for the formation of plastic hinges on opposing sides, which seems to be a conflicting scenario.

Similarly to the present bent pier, this problem can also be found in coupling beams of shear-wall systems (which are also characterized by high stiffness vertical elements), where shear span-to-depth ratios of 1.0 are more common. Assuming that this system can display

4.12

similar behavior, additional design guidelines can be provided by analogy with context related research. In that framework, beam deformations are usually characterized by the differential displacements between the respective ends (Figure 4.10 – a)), caused by the motions of the stiffer walls that they connect. The resulting system behavior can mainly relate to three different collapse mechanisms (Figure 4.10 – b)):

1. Beam failure in bending;
2. Beam failure in shear;
3. Wall concrete crushing near the base;

a) Differential movement between beam ends   b) Different collapse mechanisms
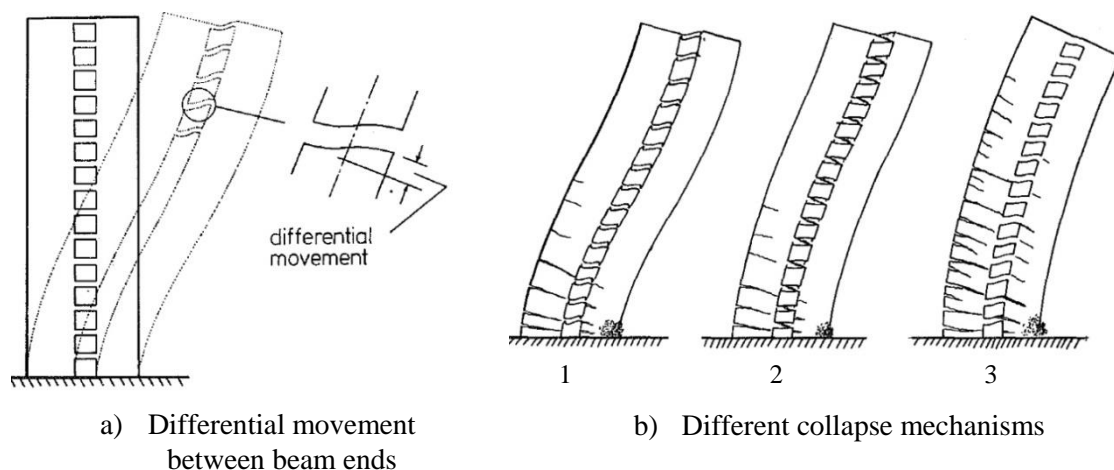
Figure 4.10 – Coupled shear wall systems (Kumar Subedi (1991a), Kumar Subedi (1991b))

The third mechanism implies quasi-monolithic deformation of the two wall sets, which can only be achieved through very rigid connections for displacement compatibility, with small differential movement. The other two are related with less extreme cases, where the differential movement is larger, causing large beam bending (1) and shear (2) demands. For the present bent pier system, an intermediate scenario could be the most accurate representation, but that should be carefully evaluated since the difference between mobilizing a mostly bending or a shear dominated beam response is very relevant to design. In fact, the latter may lead to dangerous strain concentrations at beam-wall interfaces, thus activating brittle failure modes such as sliding shear or diagonal splitting (Figure 4.11), which can prevent the development of other, more ductile, failure mechanisms.
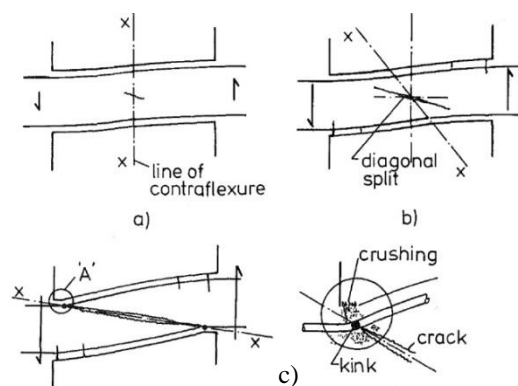
a) Start of the differential movement; b) Start of the diagonal cracking; c) Concrete crushing at beam ends;

Figure 4.11 – Beam shear dominated response. Diagonal splitting example (Kumar Subedi (1991a))

All these aspects will be addressed further ahead, but nonetheless they indicate potentially limiting factors to the behavior of the adopted bent pier, which may reflect on its inelastic capacity evaluation. Therefore, rigorous numerical assessment of its behavior should be required for the purpose of accuracy and reliability, and common empirical-based assumptions of force-displacement relationships that are often used for more simple structures could be considerably off target. Procedures such as pushover analyses, which are often used for this purpose, are also difficult to apply to this case since only the geometrical properties of the pier are known at this point (no reinforcement).

It is within this context that the simplicity of application of FBD methodologies can be appreciated, where the definition of a single elastic force reduction factor encloses several of these concerns. By doing so, it essentially enables disregarding the influence of many of these subjects on a pre-analysis stage, contributing to fasten the preliminary design process. While that may not always be a critical concern, this work was still subject to the timeframe defined for the research project it was associated with, which essentially meant that a faster start of the experimental campaign was desirable.

4.2.3. DESIGN STRATEGY

4.2.3.1. Introductory remarks

Based on the preliminary study and discussion addressed in the previous sub-section, it was assumed that it can support the use of FBD procedures for the purpose of this work and, in light of that decision, the Response Spectrum Method (prescribed in Eurocode 8 as the reference methodology) was selected for the design. It should also be noted that the same procedure was, in fact, used for the main seismic evaluation of the structures included in the original Poceirão-Caia project, as it is possible to observe in its main document. Within that framework, the definition of the elastic ground motion response spectra and the selection of an adequate elastic

force-reduction factor (or behavior factor *q* as stated in EC8) is paramount for performing the analyses.

4.2.3.2.   Seismic Action and Response Spectra

The general seismic design strategy for this work followed the main guidelines of EC8, as discussed earlier in Chapter 2. With that in mind, combining the original layout of the Poceirão-Caia presented in Figure 4.1 and the applicable seismic zoning maps shown in Figure 2.7 results in Figure 4.12, where the blue outline can be observed to cross seismic zones 1.3, 1.4 and 1.5 for Type 1 EQ, as well as 2.3 and 2.4 for Type 2 EQ. In addition, those zones were identified with soil profiles ranging from categories A through C as presented in Table 4.3.

a)   Type 1 EQ   b)   Type 2 EQ

Figure 4.12 – Seismic zoning of the Poceirão-Caia HSRL line

For full definition of the seismic load, an importance factor must also be established. In that regard, some argument could be made for an increased importance of viaducts included in a HSRL line, considering that their full length amounts to hundreds of kilometers and is generally associated with more expensive equipment/rolling stock than motorway structures, thus leading to a high economic value at risk during a seismic event, even if human losses are not accounted for. Despite that, the relevance of HSRL viaducts for post-earthquake communication in Portugal isn't as critical as, for example, in countries like France or Japan where it has widespread use. Furthermore, the risk of human fatalities can likely be mitigated, to a certain extent, by the systemic control over the traveling speed of trains that current monitoring systems can provide (Boqueho (2002)), which may help with reducing the probability of occurrence of seismic events capable of affecting structures where trains are still travelling close to top speeds (even if they cannot fully prevent them). Within that context, it was decided that importance class II was adequate for these analyses, leading to an importance factor $\gamma_I = 1.0$.

Table 4.3 – Poceirão-Caia Response Spectra Parameters

Seismic Zone	Soil Category	a_g (m/s^2)	Response Spectrum Parameters			
			S	T_B (s)	T_C (s)	T_D (s)
1.3	C	1.50	1.50	0.10	0.60	2.00
1.4	A	1.00	1.00	0.10	0.60	2.00
	B	1.00	1.30	0.10	0.60	2.00
1.5	A	0.50	1.00	0.10	0.60	2.00
	B	0.50	1.30	0.10	0.60	2.00
2.3	C	1.70	1.50	0.10	0.25	2.00
2.4	A	1.10	1.00	0.10	0.25	2.00
	B	1.10	1.30	0.10	0.25	2.00

The numerical analyses were performed for the highest seismic intensities of each type of earthquake; zone 1.3 for Type 1 and 2.3 for Type 2, which, combined with soil type C leads to the most unfavorable conditions, as highlighted in Table 4.3 by the shaded rows. These parameters result in the elastic ground motion response spectra illustrated in Figure 4.13.

a) Type 1 EQ

b) Type 2 EQ
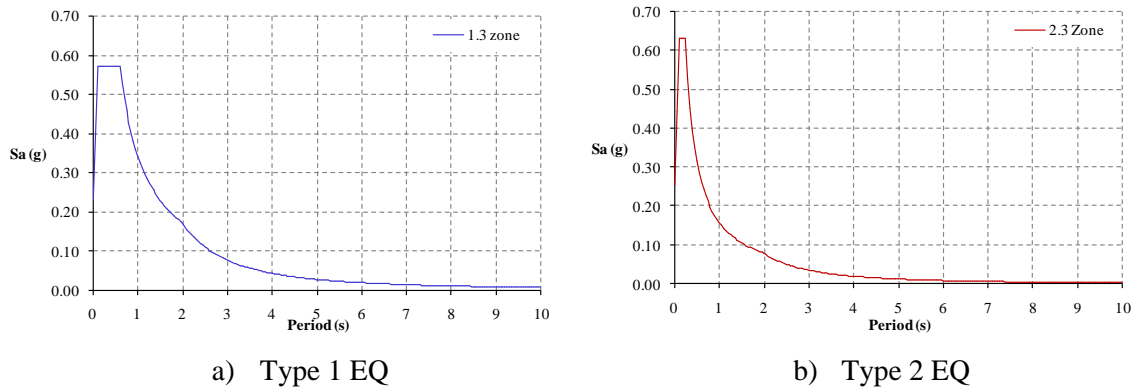
Figure 4.13 – Elastic ground motion response spectra for soil type C

4.2.3.3.   Behavior factor *q*

In the context of the Response Spectrum Method prescribed in EC8, behavior factors are globally defined for the whole structure, enabling the definition of reduced intensity design spectra relative to the elastic response spectra, reflecting the overall capacity for post-yielding deformations; the corresponding maximum values for *q* factor are those represented in the EC8 table reproduced in Figure 4.14. In that regard, for RC piers the values presented reproduce bending dominated failure, which can be adjusted according to the $\lambda(\alpha_s)$ parameter, to account for the influence of shear in shorter elements.

Type of Ductile Members	Seismic Behaviour	
	Limited Ductile	Ductile
Reinforced concrete piers:		
Vertical piers in bending	1,5	3,5 $\lambda(\alpha_s)$
Inclined struts in bending	1,2	2,1 $\lambda(\alpha_s)$
Steel Piers:		
Vertical piers in bending	1,5	3,5
Inclined struts in bending	1,2	2,0
Piers with normal bracing	1,5	2,5
Piers with eccentric bracing	-	3,5
Abutments rigidly connected to the deck:		
In general	1,5	1,5
Locked-in structures (see. **4.1.6(9), (10)**)	1,0	1,0
Arches	1,2	2,0

$^{*}\alpha_s = L_s/h$ is the shear span ratio of the pier, where L_s is the distance from the plastic hinge to the point of zero moment and h is the depth of the cross-section in the direction of flexure of the plastic hinge.

For $\alpha_s \geq 3$ $\lambda(\alpha_s) = 1,0$

$3 > \alpha_s \geq 1,0$ $\lambda(\alpha_s) = \sqrt{\dfrac{\alpha_s}{3}}$

Figure 4.14 – Maximum behavior factors for the Response Spectrum Method (EN1998-2 (2005))

Selection of q is determined from the structural elements designed to provide the main energy dissipation on the overall system, taking into account the desired plastic hinge layout. For usual bent pier structures, plastic hinges near the base should be mandatory, as well as around the beam-column nodes, according to Figure 4.4 – c), and energy dissipation in the beam should ideally be prevented with capacity design provisions and detailing. However, according to previous discussion, it is possible that such strategy is not viable for the present structure.

Within that context, the behavior factor values presented in Figure 4.14 may not able to reflect the expected level of ductility of the pier structure as they are related to straightforward interpretations of the non-linear behavior usually reproduced by bridge columns. Additionally, they don't account for the possibility of the coupling beam being a limiting factor on the overall ductile capacity. Therefore, two scenarios were considered for upper and lower bounds of the behavior factor:

1. Maximum behavior factor value assuming ductility limited by the column: $q_1 = 3.00$;

2. Minimum behavior factor value assuming ductility limited by the beam: $q_2 = 2.00$;

The previous q factor values were calculated assuming null moment point at mid element section. The first scenario corresponds to a mean column height (among all the pier alignments between both abutments of a full length viaduct) value of 10.00m subjected to lateral bending, leading to α_s of around 2.30. The second scenario was determined from the free span of the beam, which leads to α_s of 1.00. Considering the range between the previous values,

4.17

adoption of an intermediate behavior factor value of $q = 2.50$ was, instead, preferred. The corresponding design spectra based on the elastic response spectra represented in Figure 4.13 were, therefore, defined for the Type 1 EQ and Type 2 EQ and $q = 2.50$.

4.2.4. CASE STUDY VIADUCTS

Following the guidelines presented earlier, four viaducts were selected from the Poceirão-Caia line as study cases, aiming to represent as different structural responses as possible within the previously defined framework. A side view is presented for each of those structures in Figure 4.15.
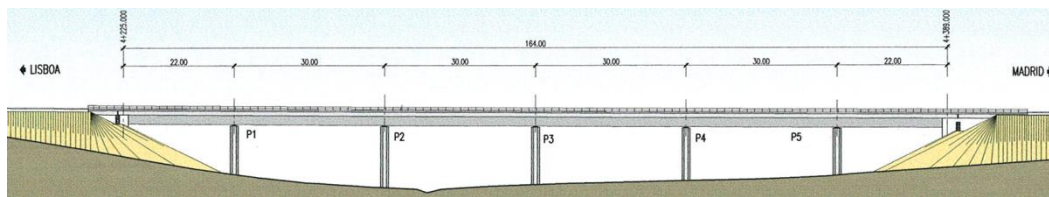
a)   Macheda Viaduct

Figure 4.15 – Case Study Viaducts
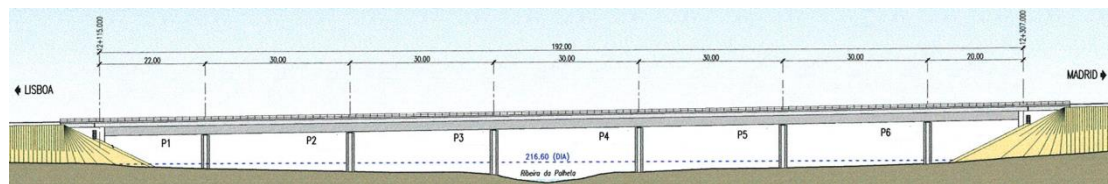
b)   Palheta Viaduct
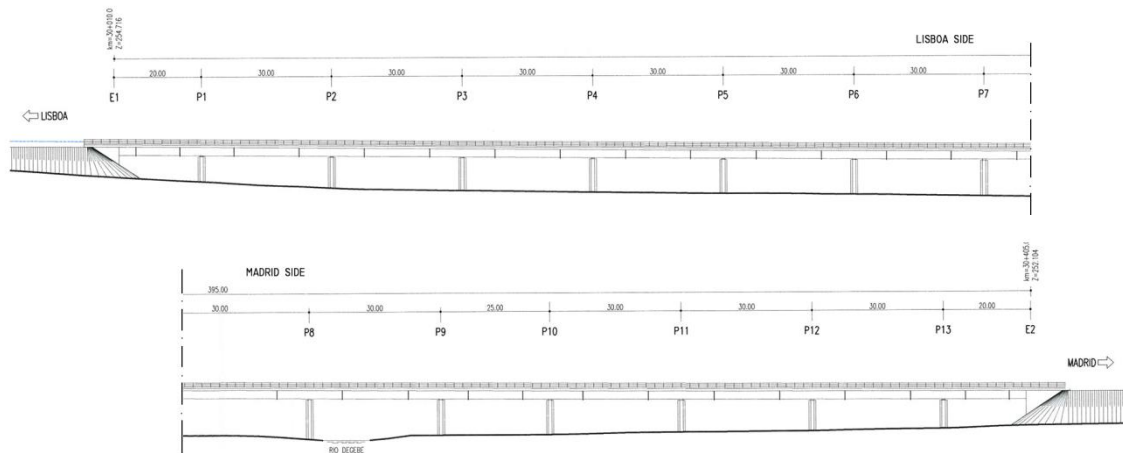
c)   Viaduct over Degebe River
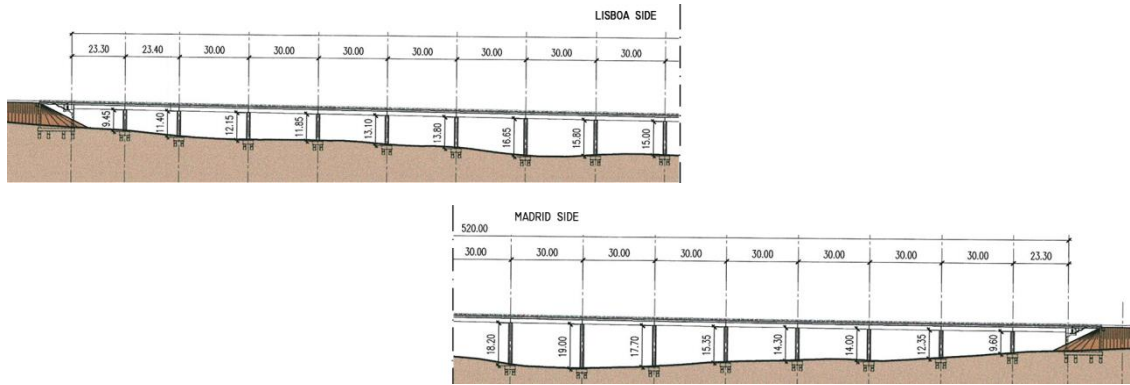
d) Viaduct over Ribeira da Laje

Figure 4.15 (cont.) – Case Study Viaducts

As it can be observed, all the viaducts exhibit a regular layout, with constant span (except near the abutments) and small pier height changes between alignments. For further detailed information, Table 4.4 includes a summary of the main general geometric characteristics of each of the selected viaducts.

Table 4.4 – Main characteristics of viaducts

Name	Length (m)	# of spans	Pier height (m)		
			Minimum	Maximum	Mean
1 - Macheda Viaduct	164	6	9.31	12.29	10.73
2 - Palheta Viaduct	192	7	8.48	9.38	8.64
3 - Viaduct over Degebe River	395	14	7.33	8.80	7.56
4 - Viaduct over Ribeira da Laje	520	18	9.45	19.00	14.14

Although transverse forces are transmitted to the piers throughout the bridge length, longitudinal forces are anchored at selected points, as previously discussed. Figure 4.16 illustrates a representation of the support types expected on each pier alignment, as relevant for bridge modeling and design, and for which the respective displacement constraints are further detailed on Table 4.5.
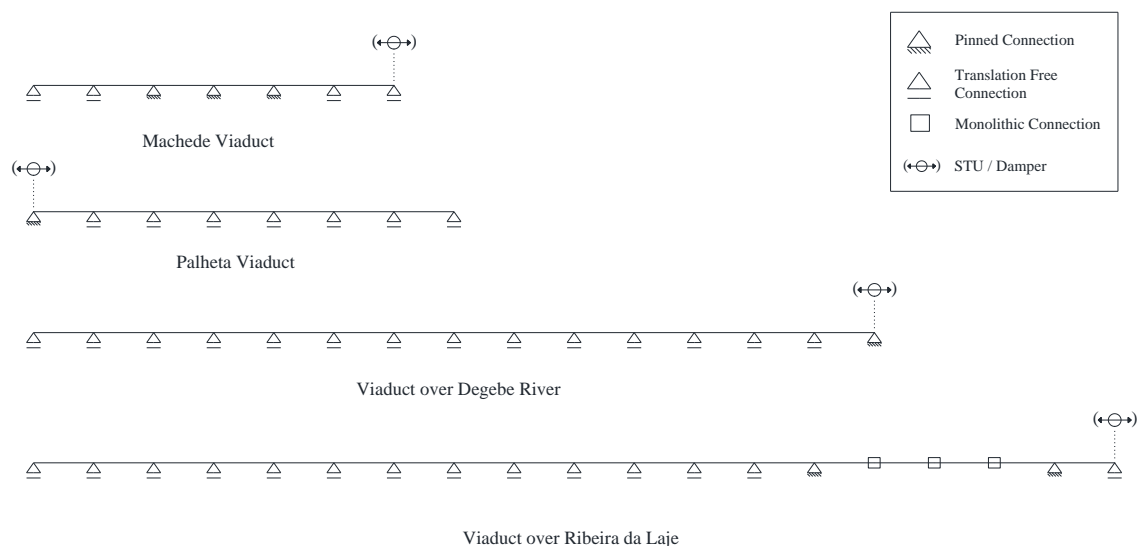
Figure 4.16 – Support layouts on the case study viaducts (illustrative scale).

Table 4.5 – Node Constraints between pier-head and deck nodes

Deck connection type	Constrained DOFs	
	Translation	Rotation
Pinned	ux, uy, uz	-
Free	ux, uz	-
Monolithic	ux, uy, uz	rx, ry, rz

ux - transverse direction
uy - longitudinal direction
uz - gravity direction

Furthermore, a summary of the expected dead-loads according to the non-structural elements indicated in the Poceirão-Caia project is presented in Table 4.6, whereas structural element dead-weight is considered using the typical RC unit weight of 25 kN/m^3.

Table 4.6 – HSRL Bridge dead-loads

Dead Loads	kN/m
Ballast	101.50
Waterproofing	8.70
Rails	5.60
Metallic guardrails and concrete cornices	10.00
Ballast sleeper-walls	7.50
Gutter walls and cover	6.30
Total	**139.6** ~ 140 kN/m

4.2.4.1. Numerical Models

The numerical models for pier design were developed in the SAP2000 structural software (http://www.csiamerica.com/products/sap2000) using a combination of bar elements and constraints for representation of both the piers and deck. Figure 4.17 – a) shows an example of

4.20

the numerical model for the Macheda Viaduct, wherein the element cross sections were defined from the gross geometry of the structure as available in the Poceirão-Caia project. Therefore, columns and beams follow the geometry illustrated in Figure 4.5 – b), while the deck follows Figure 4.2 – a); the materials prescribed in the original project were also respected, leading to the mechanical properties presented in Table 4.7. In addition, Figure 4.17 – b) presents a frontview of a pier alignment, edited for description purposes.

Table 4.7 – Element properties

	Column	Beam	Deck
A (m^2)	3.040	1.120	6.694
I (m^4) [*]	1.021	0.183	61.649
J (m^4) [**]	1.372	0.154	7.081
Concrete class	*C30/37*	*C30/37*	*C35/45* - Slab *C50/60* - Precast "U" beams

[*] flexural moment of inertia for lateral displacements
[**] torsional moment of inertia
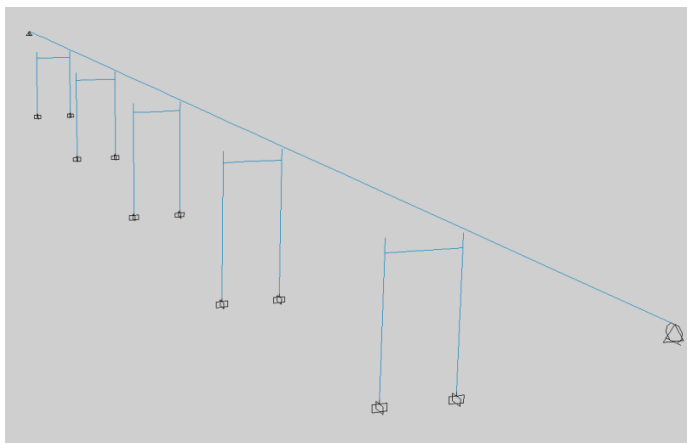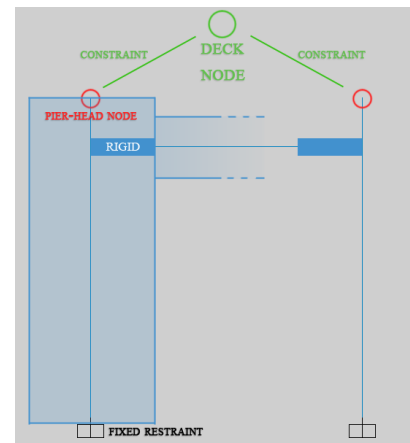
a)   General Overview   b)   Pier alignment frontview

Figure 4.17 – Macheda Viaduct model in SAP2000

In order to accurately simulate the stiffness provided by the pier system, rigid connections were introduced at the beam level, acting as joint offsets due to the large column cross-section. The pier head nodes (red circles) were also connected to the deck element (green circle), at the respective cross-section centroid, by associating the relevant DOFs using rigid body constraints defined according to the respective bearing connection, as indicated in Table 4.5. No soil-structure interaction was considered and fully fixed restraints were applied at the column bases.

Furthermore, following EC8 guidelines regarding member stiffness, the deck was modeled using uncracked gross cross-section properties with 30% of the computed torsion stiffness. Regarding the piers, however, EC8 points to the use of the effective secant-to-yielding stiffness (EI_{eff}) rather than the gross cross-section values (EI_g). It also suggests two methods for evaluating the effective stiffness from the relation between the yielding moment and section

curvature; however, both of these methods require having previous knowledge of the reinforcement ratios, which is one of the main objectives of this exercise. In order to address that shortcoming, designers usually resort to iterations using the reinforcement ratios for non-seismic loads, while taking into account the detailing rules and minimum ratios suggested by EC8. Alternatively, some relationships, based on empirical knowledge, can also be found in literature for predicting the effective stiffness using available information, such as pier geometry and axial load, as indicated by Fardis *et al.* (2012). A common, but conservative, value to adopt for the effective stiffness reduction is 50%. Another example is the proposal of Biskinis and Fardis (2010), resulting from the numerical fitting of vast experimental data from columns, and given by Equation 4.5:

$$\frac{EI_{eff}}{EI_g} = a \times \left(0.8 + \ln\frac{L_s}{h}\right) \times \left(1 + 0.048 \times \left(\frac{N}{A_c}\right)^*\right) \qquad 4.5$$

where:

a – 0.081 for circular and rectangular cross-sections; 0.09 for hollow rectangular piers;

L_s - Shear span;

h - Cross section height;

N - Axial load;

A_c - Column cross section area;

$*$ $\frac{N}{A_c}$ in MPa;

Considering a main span of 30m and a mean column height of 10m (with null moment assumed at mid-section), it is possible to calculate the overall axial load transmitted to a single column from the dead loads, and determine the relation between effective secant-to-yielding stiffness to the uncracked stiffness using equation 4.5:

$$N_{dl,column} = 0.50 \times (6.70 \times 25 + 140) \times 30 = 4613 \ kN$$

$$\frac{EI_{eff}}{EI_g} \approx 0.081 \ \times \left(0.8 + \ln\frac{5.0}{2.2}\right) \times \left(1 + 0.048 \times \frac{4613 \times 10^{-3}}{3.04}\right) = 0.141$$

This low result should not be as accurate for the present bent pier case as for regular rectangular columns, since cracking may develop differently on the columns and beam. In addition, equation 4.5 was developed for a different application context, and mostly reflects results based on bending-dominated column responses, disregarding the possible influence of shear in the development of the moment-curvature behavior, which could be relevant for the present structure, as previously discussed. In order to address that, a higher estimate of the

effective stiffness was assumed acceptable. For that purpose, a value of 30% of the uncracked stiffness was globally adopted for all the bent-pier elements.

4.2.4.2.   Analysis and Results

Aiming at using the Response Spectrum Method, a modal analysis was performed on all the models. The resulting first vibration modes for all the studied viaduct decks are shown in Figure 4.18, along with the associated period and Modal Participating Mass Ratio (MPMR).

T = 0.583s (MPMR= 81%)

a)   Macheda Viaduct

T = 0.452s (MPMR= 77%)

b)   Palheta Viaduct

T = 0.394s (MPMR= 50%)

c)   Viaduct over Degebe River

T = 0.998s (MPMR= 47%)

d)   Viaduct over Ribeira da Laje
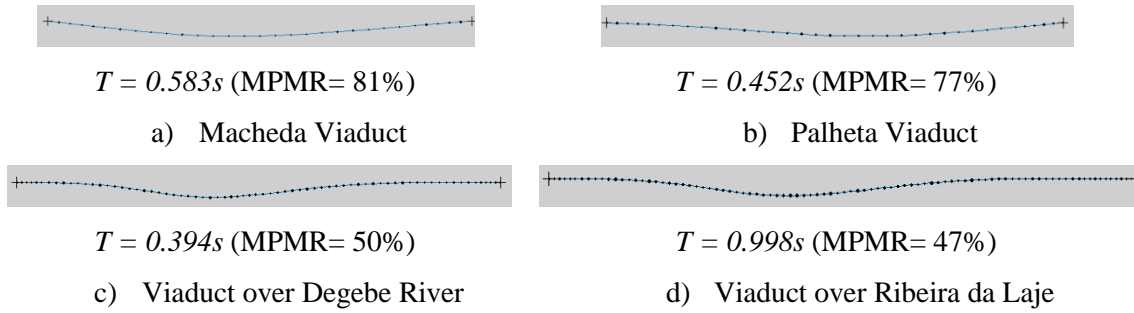
Figure 4.18 – First vibration mode shapes, period and MPMR values

It can be observed that, apart from the Viaduct over Ribeira da Laje, the fundamental period can be related to the higher intensity plateau of the design spectra for Type 1 EQ, and to the descending slope (between T_B and T_C) for Type 2 EQ. Within this context, an elastic spectral analysis was performed (accounting for the design spectra) in order to characterize the seismic demand and establish a design threshold for the test models. For that purpose, stiffness proportional viscous damping of 5% of the critical damping was also considered. Aiming for accuracy, the minimum number of modes in consideration for each structure was defined to guarantee a total Modal Participating Mass Ratio above 90%.

The obtained results are summarily presented in Figure 4.19, where the maximum base shear value on each viaduct (calculated from all the respective transverse horizontal reactions), is reported for both EQ types by the blue and red square markers. As observed, results for Type 2 EQ are always smaller than for Type 1 EQ, which could be expected considering that the first vibration mode period of the analyzed structures was generally within the highest intensity plateau for the latter, but on the descending slope in the case of the former. The overall maximum was found to be around 2800 kN on the Palheta Viaduct. The numerical value of the ratio (in percentage) between the maximum base shear on each structure and the base shear determined at the respective tallest pier alignment is also plotted for each viaduct and EQ type, representing a measure of the accuracy associated with just assuming peak demand at the tallest pier. In this regard, differences were found ranging between 14% and 29%.

Within this context, a design base shear of 3000kN was assumed to provide a realistic representation of the maximum seismic demand on the pier alignments for this type of structure, enabling further supported decisions regarding reinforcement and detailing layouts for the purpose of designing test models.
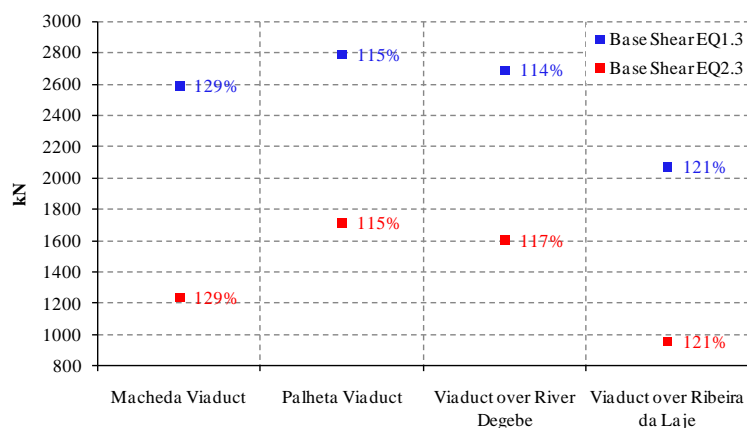
Figure 4.19 – Spectral Analysis Results: Maximum base shear values among all the piers for each viaduct

4.2.5. REINFORCEMENT AND DETAILING LAYOUTS

Energy dissipation mechanisms associated with seismic performance should, ideally, reflect the natural ability of the structure to produce inelastic deformations, in addition to the enhancements provided by design. Regarding the present structure, some discussion was already provided in the 4.2.1 sub-chapter, mainly presenting the influence of the beam in the overall deformation of the pier structure, and the impact it has on the usual bent-pier seismic design strategy, reliant on column head and base plastic hinges (Figure 4.4 – c)). The application of capacity design procedures, which are adopted to prevent significant energy dissipation on unintended different locations, is conceptually challenged if the structure is more likely to reach the yielding stage in the beam than in the columns.

Taking that into account, some level of damage and energy dissipation in the beam was assumed to be unavoidable, increasing the ductility capacity of that element in order for it not to be the limiting factor in the overall pier seismic performance. In addition, also according to the previous discussion, some resemblance can be observed between this problem and that of coupling beams of shear-walls, representing a framework that is better addressed in the relevant literature. Within that context, the demand for ductility in coupling beams of shear walls has been a common concern of several research works since the 1970s and, although some proposals enabled some improvements, the general outlook on providing effective ductility capacity is not straightforward.

The main shortcoming of coupling beams of shear walls is regarded to be the strong influence of the shear driven strains and distortions in the overall deformation of those beams, which are often responsible for the occurrence of considerable damage and even critical failure. In structural terms, the vertical walls are usually considered as providing fixed restraints to the beams. The latter's behavior depends of the dominant deformation mode: when bending is prevailing, double curvature occurs, leading to the alternate compressive and tensile strains associated with the maximum bending moments near the walls (Figure 4.20 – a)); when shear is dominant, the differential movement between beam ends tends to induce tensile strains appearing on both sides of the element due to element elongation, while compressive forces are transferred inside the element (Figure 4.20 – b)). The combined action of both bending and shear deformation mechanisms, however, is considerably more complex, as the compressions created by the double curvature in bending "conflict" with the tensile strains originated from shear, potentially invalidating analysis through classic beam bending theory. In light of this, correctly evaluating the relation between shear and bending deformations becomes critical for accurate behavior assessment.

a) Bending   b) Shear
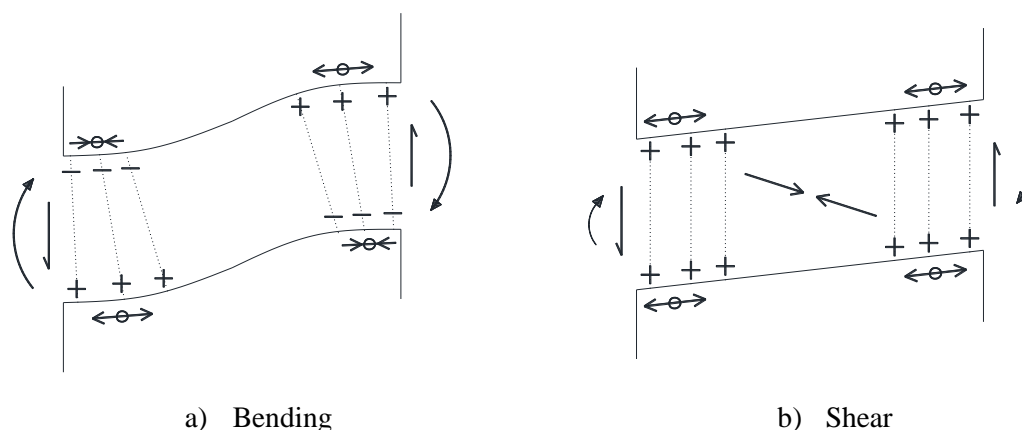
Figure 4.20 – Beam strains during differential movement

As noticed by Paulay (1971), that relation is directly influenced by the shear span-to-depth ratio α_s, since taller beams are observed to have a larger prevalence of shear strains and distortions, while slender beams are more likely to develop a deformation pattern similar to pure bending. Paulay and Binney (1974) developed further into this subject, by testing several conventionally reinforced beams, concluding that for elements with low α_s, even when the shear strength of the beam is large and capable of preventing diagonal splitting (Figure 4.11 – b)), the tensile strains that occur due to heavy shear distortions lead to the formation of large cracks at the interface between walls and beams (Figure 4.21), where aggregate interlock and rebar dowel effect become the main forms of force transfer. During cyclic loading, the overall ductility capacity of the beam is challenged by the continuous degradation of that section due to friction. This is particularly noteworthy because that phenomena was revealed to be relatively

independent of the transverse reinforcement ratio, since it relates to a very localized occurrence between the last stirrup and the wall interface.
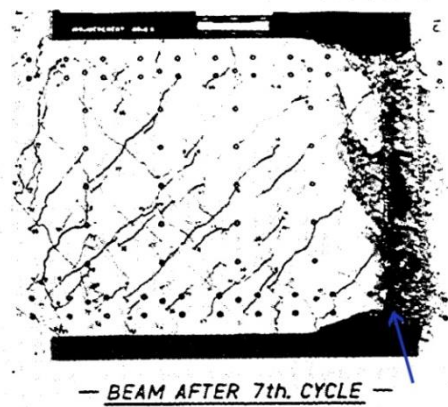
Figure 4.21 – Sliding shear failure at beam-wall interface (Paulay and Binney (1974))

Those conclusions were also pointed by Tassios *et al.* (1996) or Galano and Vignoli (2000), involving similar experimental tests, which showed that coupling beams exhibit low energy dissipation with strong "pinching", as evidenced in Figure 4.22.
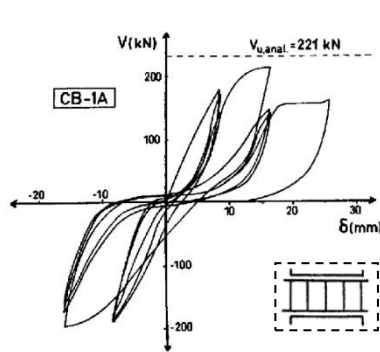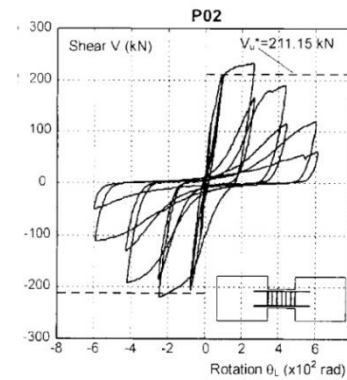
a) Adapted from Tassios *et al.* (1996)   b) Galano and Vignoli (2000)

Figure 4.22 – Cyclic loading results on conventionally reinforced coupling beams

In order to address this problem, Paulay and Binney (1974) proposed a layout that would be the basis for the reference recommendation of both EC8 and ACI318 guidelines, according to which rebars should be placed diagonally across the beam span, forming two vertically mirrored struts, as presented in Figure 4.23, following the basic idea that short coupling beams are likely to transfer shear forces through a single pair of strut and tie between the two walls.

a)   NP EN1998-1 (2010)

b)   ACI 318 (2014)
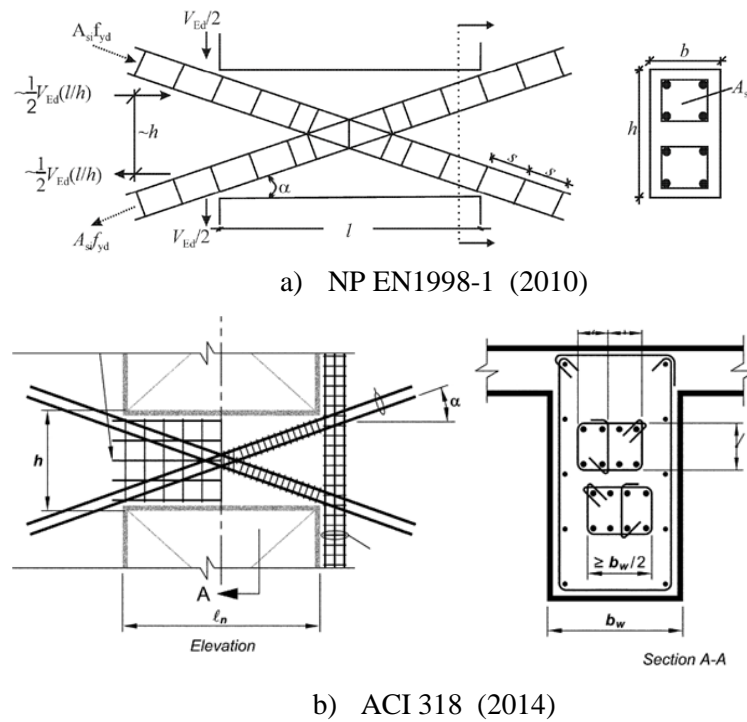
Figure 4.23 – Bi-diagonal Reinforcement Layouts

This system enables the diagonals to develop and carry the compressive or tensile stresses according to the direction of the differential movements, and it is common to observe cracks oriented along that geometry. The design capacity is determined from projecting the maximum axial force carried by each strut in the transverse and longitudinal directions. Failure is then expected due to rebar yielding, and concrete crushing may occur, leading to rebar buckling. For this reason, codes suggest the adoption of individual transverse confinement for both diagonal struts, in order to provide better control of the deformations occurring at the compressed sides, contributing to an improvement of the overall ductility capacity. This layout provided better results than conventional reinforcement, with larger energy dissipation and increased ductility, as illustrated in Figure 4.24.

a)   Adapted from Tassios *et al.* (1996)   b)   Paulay and Binney (1974)
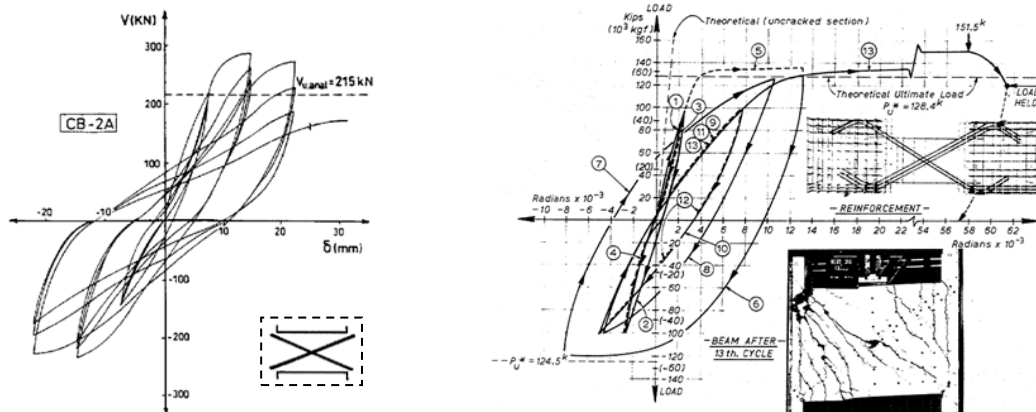
Figure 4.24 – Cyclic loading results on diagonally reinforced coupling beams

In the context of technical design for coupling beams and short columns, Tegos and Penelis (1988) presented a different layout, based on forming a rhombic truss with longitudinal rebars (Figure 4.25). This configuration provides a peculiar combination of inclined and horizontal reinforcement, increasing the flexibility for addressing both shear and bending demand, as observed by other authors as well (e.g. Galano and Vignoli (2000)). A variant of this solution was also tested by Tassios *et al.* (1996), where mainly the inclined parts of the rebars were brought closer to the interface between beam and walls, essentially aiming to prevent the occurrence of sliding shear. Other notable tested layouts include the adoption of horizontal reinforcement across all the beam height, or localized dowel rebars at the beam-wall interfaces.

a) Original proposal by Tegos and Penelis (1988)

b) Specimen tested by Galano and Vignoli (2000)
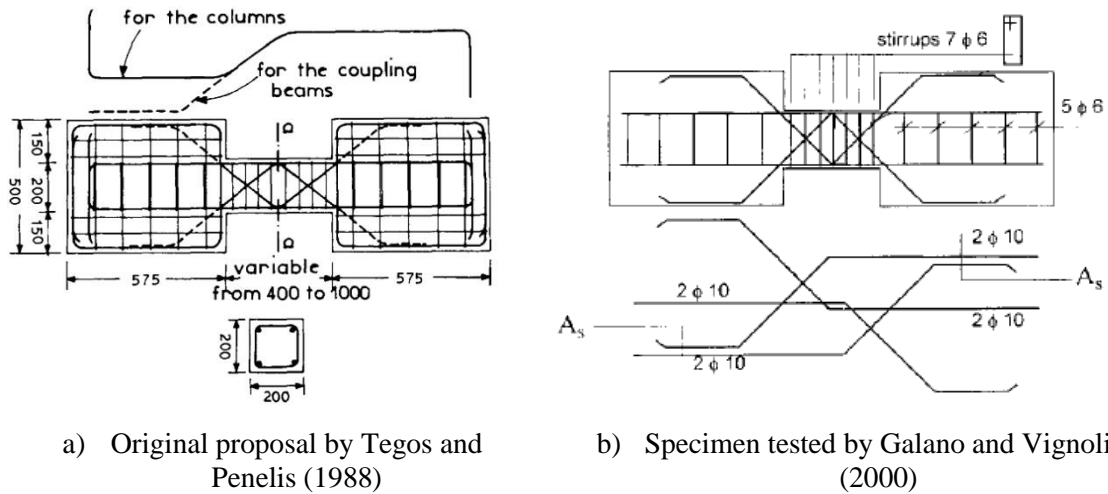
Figure 4.25 – Rhombic truss reinforcement layout

General consensus was achieved on the fact that the diagonal reinforcement layout provides the better performance for the shortest beams, and α_s values smaller than 0.75 are referred. In those cases, the slope of the diagonal struts is large enough, leading to high effectiveness of the axial load carrying capacity of the struts that is assumed by design. Simultaneously, conventional reinforcement is considered adequate for beams with shear span-to-depth ratios α_s larger than around $^4/_3$, since the cyclic degradation of the beam shear capacity can be observed to decrease considerably as the span increases. For intermediate values, the rhombic truss was pointed as one of the most favorable layouts, because it provides similar ductility and energy dissipation to diagonal rebar configurations and it is undeniably easier to detail and supplement than the other, more complex, design proposals.

A common problem of these layouts is that they usually result in high reinforcement ratios and large diameter bars (Figure 4.26), requiring careful evaluation of anchorage lengths and confinement detailing, in addition to reducing the inherent constructive workability and impacting productivity rates. Furthermore, casting concrete into a heavily reinforced cross-section can pose challenges regarding concrete quality and integrity, due to difficulties in

obtaining a good aggregate spread and vibration. Some authors proposed alternative solutions aiming at addressing this problem (Canbolat *et al.* (2005), Parra-Montesinos *et al.* (2010)), based on the use of fiber reinforced concrete to reduce the overall rebar ratios (therefore improving the constructability of the elements), for which positive results were obtained regarding overall ductility and energy dissipation. This particular technical solution was out of the present work scope, due to the industrial research partner interest, but it should still be retained as a viable option.

Figure 4.26 – Rebar density in coupling beams of shear walls (Parra-Montesinos *et al.* (2010))

Within this context, the pier design strategy for this work is presented in Figure 4.27. A column segment height of 15m was adopted (for reasons further on explained) and an equal distribution of the base shear between columns was considered. Column end-section moments, M_1 and M_2, are approximately equal (leading to null moment near the mid-height of the column) that are possible to determine from the global equilibrium and the design base shear V_{Ed}. As for the beam, either shear or moment can be assumed as the critical parameters for element design. In the calculations, an effective span l_{eff} of 4.20m was considered in the definition of the design forces for the beams, as defined by equation 4.6 adapted from EC2 (NP EN1992-1-1 (2010)),

$$l_{eff} = l_n + 2 \times a \qquad\qquad 4.6$$

where:

l_n – free span of the beam;

$a = \min\{0.5 \times t; 0.5 \times h\};$

with: t - column width; h - beam height;

| Global Layout: | Columns: | Beam: |
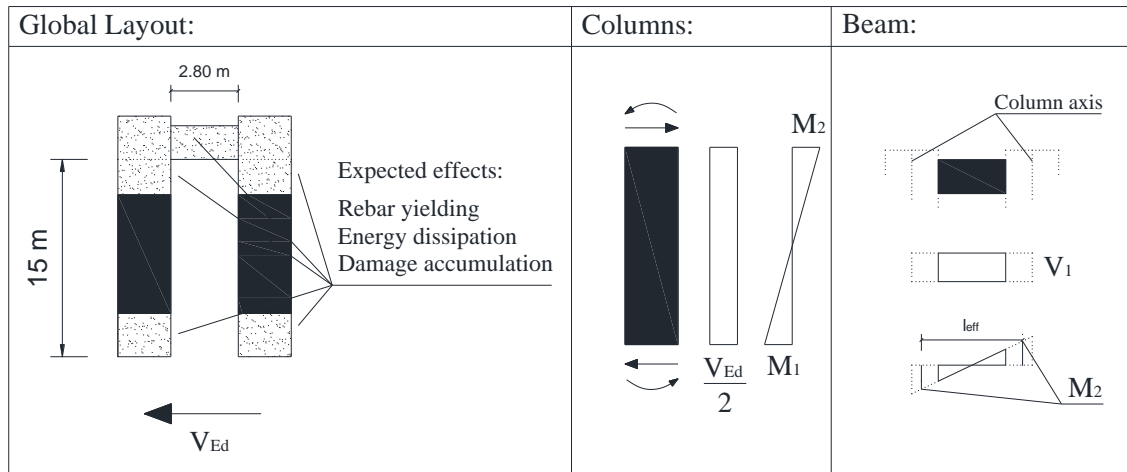
Figure 4.27 – Pier design strategy

An overview of all the relevant parameters is presented in Table 4.8. In this regard, it is worth mentioning that, taking the base shear demands previously obtained in section 4.2.4.2, the beam shear level determined with this strategy represents around 90% of the dead load transmitted from the deck to the columns, which can lead to almost achieving decompression during lateral displacements. Also, the strategy established to determine these reference parameters was meant only to provide a realistic seismic demand expectation for guidance of the test model design.

Table 4.8 – Reference design parameters for test models

	Columns	Beams
V_{Ed} (kN)	1500	4110
M_{Ed} (kN.m)	12210	8640

4.2.6. PRECAST CONCEPTION

Following the discussion of Chapter 3 and aiming to fulfill the interest and suggestions established by the industry partner, the following set of requirements was defined for the precast conception used in this work:

i). The precast solution should be adequate for road transportation from offsite precast plants to construction sites;

ii). Mostly reinforced concrete elements should be used. Composite and steel solutions were not desirable;

iii). The precast system should be aimed at fast construction, minimizing the amount of work required on site;

Concerning requirement i), according to Portuguese law (ANSR (2013)), vehicles should respect a certain set of geometrical dimensions in order to circulate freely in the national road system:

- Maximum width: 2.60m;
- Maximum height: 4.00m;
- Maximum length: 18.75m depending on the type of vehicle;

Respecting the previous statements is not absolutely required, since the Portuguese regulation allows individual permits to be issued for special cases, but it still indicates a range of dimensions that are associated with increased transportation easiness and reduced costs. Additionally, fast construction speed and minimal on site work requirements can strongly relate to reducing the amount of precast connections, since those are generally the bottleneck of the productivity rate, as previously discussed. Taking these guidelines into account mostly shows that, on one hand, large elements are preferred by leading to a reduced number of precast connections but, on the other hand, there is a limit to element size, for practical reasons.

That limit can also relate to precast units weight and the capacity for transportation and lifting tasks. In fact, for most purposes vehicles in Portugal are limited to a maximum of 44 ton, although that value is often surpassed through individual permits issued for special products such as precast bridge girders. For the sake of reference, LASO - Transportes, S.A. (which is a renowned and established service provider on the special cargo transportations Portuguese market) has several tractors available with up to 250 ton maximum capacity. If required, the weight of an individual precast unit can also be reduced by adopting smaller elements with segmental construction procedures and, considering the desired framework of reinforced concrete, maybe also adopting hollow cross-sections.

The influence of these operational constraints should be taken into account in addition to more technical aspects. The mechanisms adopted for force transfer and/or displacement compatibility between precast elements, such as rebar splicing, for example, come to mind as a defining trait for the viability of most precast structures. In light of that, the two following sub-sections aim to firstly discuss how the overall precast system is meant to function, focusing on evaluating the pros and cons of a variety of different alternatives and leading to a decision regarding the adoption of one of them. Afterwards, the details of precast connections are addressed, again presenting different alternatives for the purpose of experimental study.

4.2.6.1. System Layouts

Before deciding on committing to a precast system, varying options were considered, aiming to promote different layouts and functionalities. With that in mind, four systems were conceptualized, and their pros and cons were discussed in order to reach a decision.

System A:

This layout corresponds to a straightforward application of the industry staple procedure of resorting to descending precast cap beams onto a set of previously constructed columns (Figure 3.18). Associating the beam-column interface surfaces to suitable precast joint locations results in three different precast elements required per pier alignment: one beam (B) and two columns (C), as illustrated in Figure 4.28 – a). The concept for the connection mechanism is based on some form of rebar continuity from the columns onto the beam and the footings. Therefore, this system requires at least one foundation-to-element connection and one element-to-element connection per column; an idealized procedure for assembling the complete structure is illustrated in Figure 4.28 – b).

a) Element division: B – Beam; C – Columns;   b) Assembly procedure sequence: 1, 2, 3 and 4
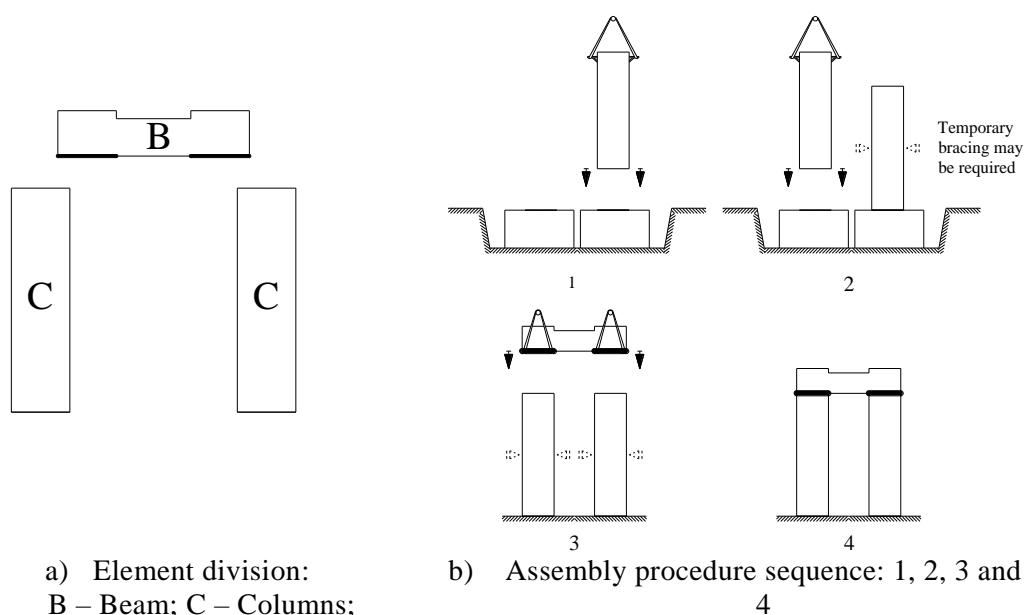
Figure 4.28 – Precast system: Option A

An important aspect of this proposal is the fact that both connections are placed on locations expected to develop high strains and, as previously discussed, possibly rebar yielding. That may present a challenge while accounting for anchorage forces for continuity rebars due to the high stresses expected in those sections, especially if large diameters are used, considering the limited space that is available. Taking into account that EC8 guidelines already lead to densely reinforced beam-column nodes, increasing the amount of detailing to accommodate the connection can create cumbersome design solutions, losing some of the appeal that a precast alternative could present. However, since high local demand is expected and the precast joints

are prone to strain concentrations, it makes sense to adopt a design option aiming at providing stability assuming that large deformations take place, instead of trying to prevent it from occurring. The solution considered in this work aimed to enforce early yielding at that section by reducing local moment capacity to about 50% (Figure 4.29 – a)) for the purpose of creating a stable rotating mechanism similar to a hybrid rocking motion. In theory, comparing the performance of equivalent monolithic and precast structures there would be expected larger beam strains on the monolithic case and larger column strains on the precast system due to joint opening, according to Figure 4.29 – b).

a) Moment demand and capacity along the column and across the joint
(A_{sl} – longitudinal reinforcement of the column)

b) Beam-column node rotation illustration (i) monolithic; ii) precast)
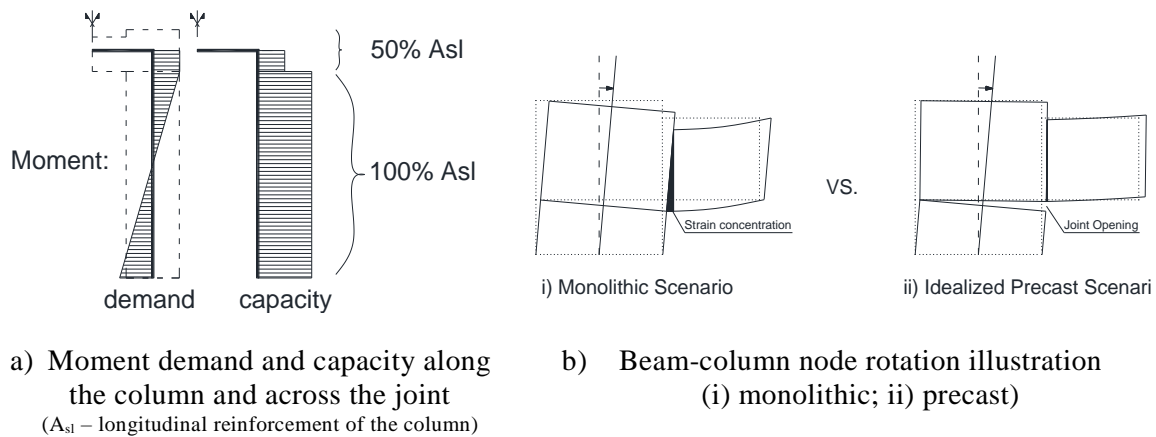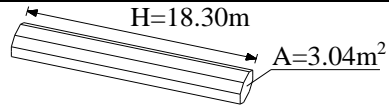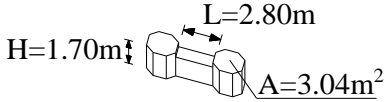
Figure 4.29 – Beam-column precast connection mechanism

This layout assumes simultaneous and precise descending placement of the beam on top of both columns, which presents a challenge which requires additional geometric clearance to account for slight positioning errors. Dimension accuracy on precast elements is achievable, but problems can arise to ensure precise verticality of the columns, for example. Moreover, the connection is likely to be made at considerable heights while holding a precast unit weighing several tons, thus adding to the operational complexity. On that topic, considering the pier height range set for this work (maximum possible height of 20.00m) and the geometrical properties defined earlier in Figure 4.5, the maximum weight per element can be calculated, and the respective results are presented in Table 4.9. Considering these values, horizontal casting is required for column segments, while vertical casting should be adequate for the beam element; both elements are suitable for easy formwork.

Table 4.9 – Precast element geometric characteristics

Element	Max. Dimensions (m^2, m)	Weight (ton)	Illustration
Columns (C)	3.04 x 18.30	141.77	H=18.30m A=3.04m^2
Beam (B)	2 x (3.04 x 1.70) + (1.40 x 1.10 x 2.80)	37.33	L=2.80m H=1.70m A=3.04m^2

This scenario indicates the possibility of using more conventional transportation for the beam elements, although the columns are too heavy for that. Furthermore, considering applications to long viaducts and fast construction purposes, the use of mobile or truck-mounted cranes is adequate, enabling the assembly of one pier alignment and fast relocation to the next one with minimal effort. It should also be taken into account that the capacity of the most common mobile cranes in the market is generally smaller than lattice/boom cranes, which are also less mobile due to the required extensive disassembly and reassembly procedures. For the sake of context, Liebherr (http://www.liebherr.com/) is one of the main manufacturers of construction machinery and their offer includes just one truck lattice/boom crane with 750 ton of capacity; moreover while they also present just two mobile cranes for that weight range, there are more than a dozen available cranes with capacity under 100 tons. Those values are a bit misleading, however, as the full capacity of a crane is set for a short working range and low heights, as enabled by the fully retracted boom. When considering lifting heights around 20m, working with an extended boom becomes inevitable, and the leverage effectiveness decreases considerably. Therefore, it takes a 350 ton capable crane such as the Liebherr LTM 1350 (illustrated in Figure 4.30) to be able to perform that operation.

m	14,9 m	20 m	25 m
3	350	155,7	
3,5	200,6	155,7	155,6
4	188,6	155,7	155,7	147,9
4,5	177,9	155,7	155,7	148,1
5	168,3	148,2	148,3	145,6
6	146,6	130,7	131,3	130,6

a) Load chart   b) Maximum lifting capacity (in ton)
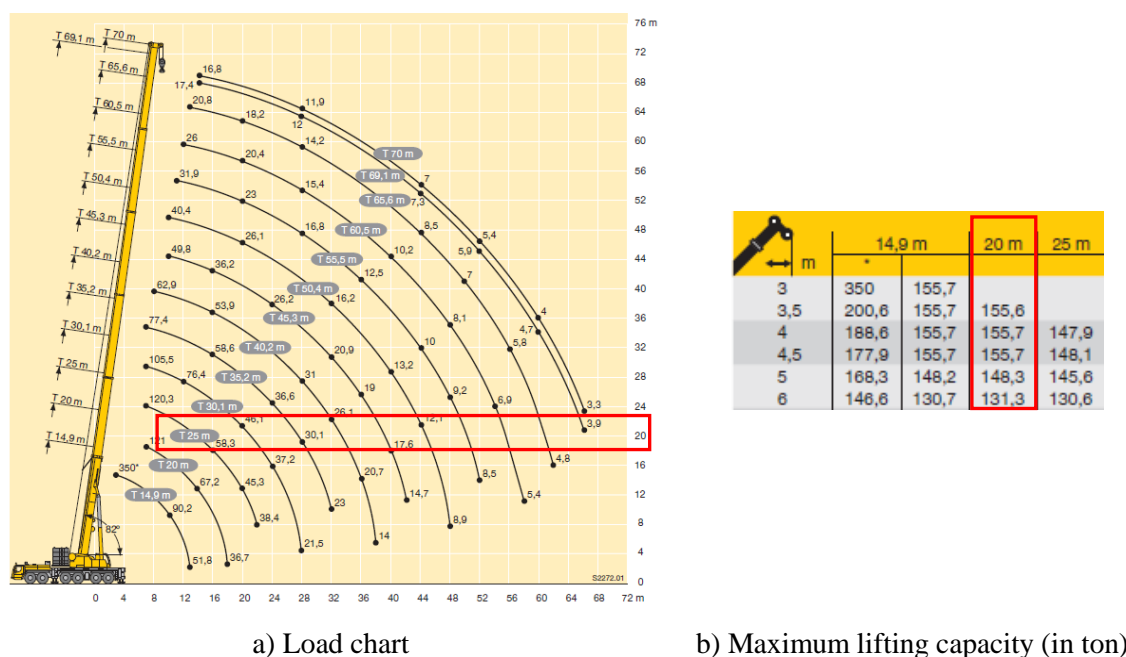
Figure 4.30 – Liebherr LTM 1350 lifting capacity calculation procedure
(http://www.liebherr.com/)

Reducing the precast unit weight down to a range that is manageable using less capable machinery would be desirable, as those are more common, require less operating constraints (such as counter-weight establishment) and are generally less expensive, but that does not prevent this from being a valid option even if it may not represent the most optimal one for every situation. Nonetheless, a strategy to address this shortcoming could involve the use of

hollow sections, in order to reduce each individual unit's weight. However, it was decided that the columns' inelastic behavior and potential plastic hinge zones should be associated with solid cross-sections rather than hollow shapes, in order not to excessively increase the concrete stresses and to further prevent local failure. Moreover, some of the precast connection mechanisms designed for testing make use of the internal cross-section area, as will be discussed on a later section.

Within this context, it is possible to perform a simple exercise to evaluate the gains from adopting a hollow configuration on the remaining segment lengths. In order to obtain a rough estimation of the plastic hinge length (L_h) on the columns, the general EC8 guidelines can be taken into account, leading to the consideration of $L_h = 2.20m$ (cross-section height along the bending direction). If a maximum axial load ratio is also assumed, including the axial load increase due to beam shear, it is possible to determine the minimum concrete area of the hollow segment. Considering an axial load ratio of 0.30, the solid part of the cross-section is approximately 1.00m², representing 0.16m thickness walls if constant thickness is considered. This design corresponds to a reduction of nearly two thirds of the original solid cross-section. Consequently, the weight reduction of the hollow columns designed according to Figure 4.31 – a), relative to equivalent solid columns, can be expressed as a function of the column height, as presented in Figure 4.31 – b).

$$A_c = \frac{8723}{0.3 \times 30 \times 10^6} = 0.96 \ m^2$$

a) Hollow segment definition   b) Weight reduction for varying height
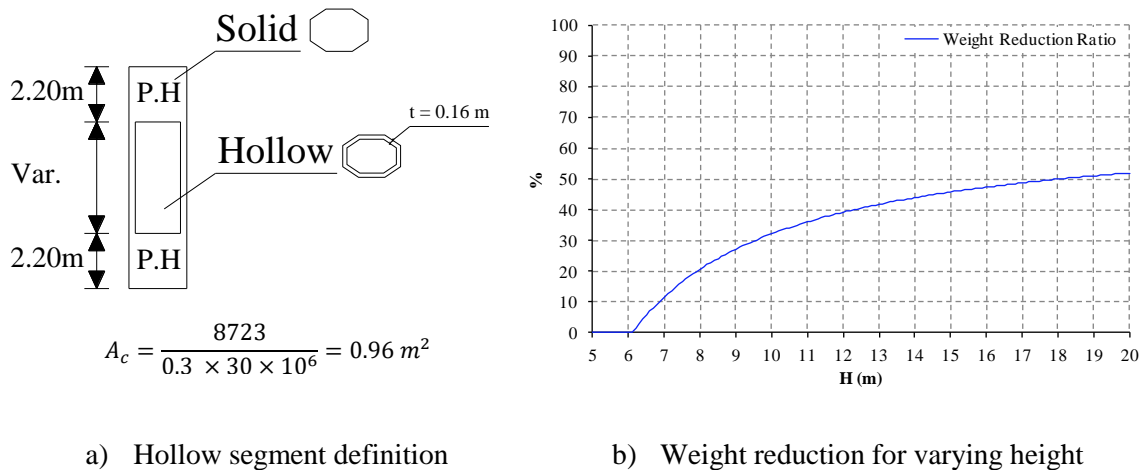
Figure 4.31 – Hollow sections for precast column elements

As observed, for the tallest piers (where the column segment length is 18.30m) the weight reduction for using a hollow section is around 50%, which is considerable. However, since most of the bridge piers for a given viaduct should be under the established maximum, analyzing a smaller size can be useful for understanding the implications of a hollow section on more common occurrences. Considering a column length of 15.00m, the full-weight of a hollow segment is around 60ton, while it is around 115ton using a solid cross-section. This also means

that the solid elements require around 200ton mobile cranes, while the hollow elements could be assembled using more readily available 90ton mobile cranes.

On the other hand, the adoption of hollow sections also makes the detailing more difficult and cumbersome, in addition to requiring the use of void forms that are not recoverable and that may complicate the preparation of the reinforcement cages for horizontal casting. Furthermore, the relative gain from using a hollow cross-section is not always as large as it may seem at a first glance. For example, considering application for the mean pier heights indicated in Table 4.4 would result in a relative weight reduction of 20% or less, for two of the viaducts. With that in mind, adopting a solid or hollow section should come down to a designer or contractor decision based on the characteristics of each particular project and the actual gains that could be achieved through it.

System B:

The concept for this system aimed at addressing two specific issues identified from system A. As presented in Figure 4.32, instead of placing the connections in the locations with the highest demand, the mid-height point was selected, as that is the vicinity of the expected null-moment point for transverse seismic loading, leading to simpler connections with lower stresses. Additionally, the bottom part of the columns (C) has significantly reduced height and straightforward geometry, and CIP procedures can now be considered for faster construction. The option of utilizing a precast element for that like in option A is still a viable possibility; whether it could lead to considerable gains or not depends on the actual column heights. In addition, the preparation of CIP columns can occur independently, as long as the contractor teams have sufficient workers and resources.

a) Element division:
BC – Beam with column segments;
C – Columns;

b) Assembly procedure sequence: 1, 2, 3 and 4
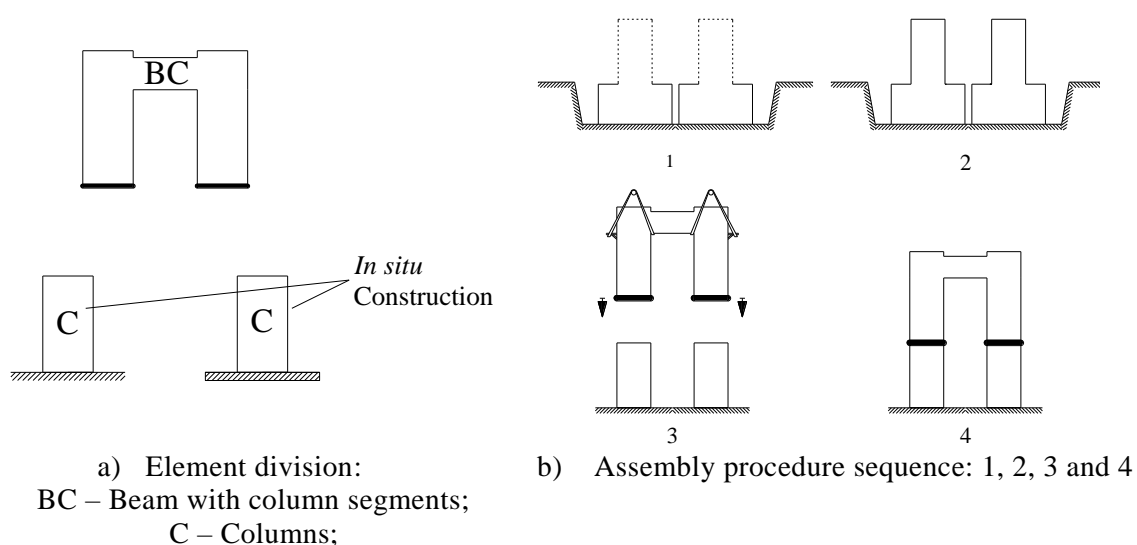
Figure 4.32 – Precast system: Option B

Therefore, this system includes only one precast unit (BC) required per pier alignment, but the increased length of the column parts results in two to three times the weight of the B unit from option A, depending on overall pier height. Some negative aspects can be associated with that:

- The two large masses on the columns can easily cause damage in the beams due to careless handling. Strong temporary bracing should be mandatory to prevent that until the connecting operation;

- Column verticality is much more susceptible to accurate geometry assessment, which may be harder to ensure since CIP column bases are adopted;

- The potential use of hollow sections is challenged by the need to execute the connections at mid pier height. The additional detailing required for that design can conflict with the existence of corrugated ducts or pocket holes, associated with either rebar continuity or the splicing reinforcement required for connection integrity and force transfers;

- Two cranes might be necessary for lifting the BC element in place for the connecting operation due to the large column masses. That seems undesirable due to the involved operating constraints, and guaranteeing the accessibility for two cranes might also be a challenge on certain situations;

- The existence of a visible precast joint at the mid-section of different piers might raise some concerns due to aesthetic reasons. Additional post-handling of the joint in order to minimize this may have an undesirable impact on the overall duration of those operations;

System C:

The concept for this system was aimed at finding an alternative layout to the double column bent pier that could perform as adequately and be more precast friendly. Also, taking into account the potential shortcomings related with the performance of the coupling beam identified earlier, the idea was to use a wall-pier structure for stronger shear capacity. The system involves a precast mechanism similar to that of the Sorell Causeway (Figure 3.17) pier-sections, constituted by match-cast pieces (W) on top of each other, according to the illustration of Figure 4.33. Flexible height (h_{el}) on the precast elements is taken into account, enabling the adoption of optimal sized segments for any given situation and preventing most of the size and weight related problems of the two previous layouts, although it requires multiple precast connections and assembly operations per pier. The geometry of each segment is easily suitable for both manufacture and in situ assembly, and vertical direction casting is possible, which is

desirable for better concrete spread and rebar wrapping but was hardly achievable in the other systems.

If no pier head enlargement is considered, the width of the wall-piers is relatively predetermined as a result of the support required for the twin box girder deck. Therefore it is safe to assume that a minimum of around 7.00m would be required, leading to considerably higher stiffness than provided by the current bent pier. A minimum wall thickness (t_w) of 1.00m was also assumed, in order to be able to accommodate four (2 per girder) pot-bearing devices with design shear strength of around 1900 kN each (an elastic horizontal shear force 2.5 times greater than the design base shear calculated in 4.2.5 was considered for those calculations, assuming that this wall-pier structure could be required to work under limited ductility scenarios). For reference, the TE10i Mageba Reston Pot bearing (http://www.mageba.ch/) fulfils the shear strength requirement ($V_{Rd} = 1950\ kN$) and has a diameter of 930mm.

a) Element division:
W – Wall-pier segment

b) Assembly procedure sequence: 1, 2, 3 and 4
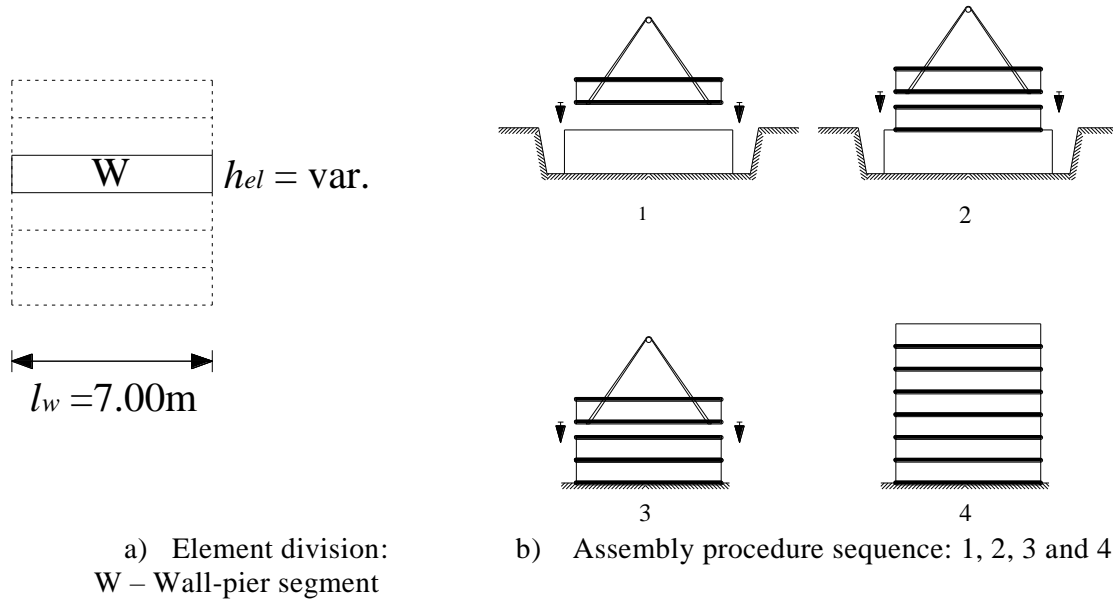
Figure 4.33 – Precast system: Option C

It is important to acknowledge that the structure change associated with this option can result in considerable differences regarding overall seismic behavior if it leads to a significant modification of structural periods. For the sake of context, three different lateral deformation scenarios are illustrated in Figure 4.34, where K_{pier} represents the lateral stiffness of the bent pier and K_{bend} and K_{shear} represent the bending and shear stiffness of the concept wall-pier, determined using equations 4.7 and 4.8, respectively.

$$K_{bend} = \frac{3EI}{h_w{}^3} \qquad 4.7$$

$$K_{shear} = \frac{5GA}{6h_w} \qquad 4.8$$
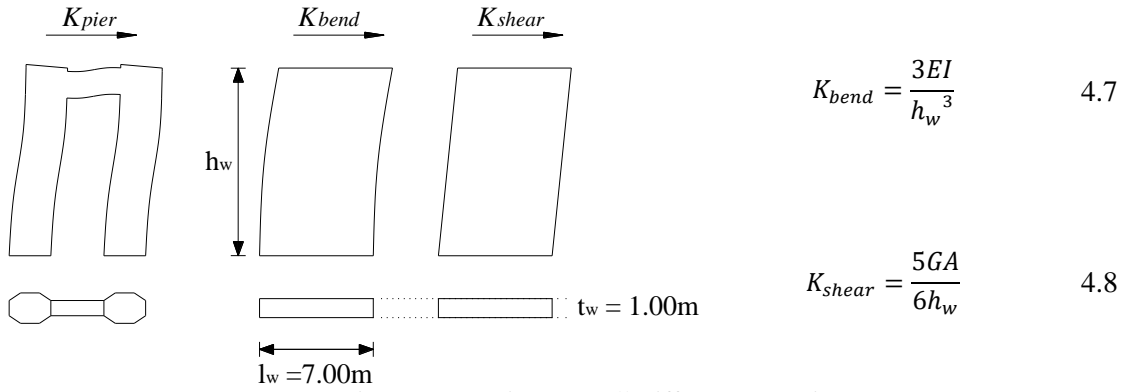
Figure 4.34 – Pier vs. Wall stiffness comparison

Those can be compared as a function of pier height, by calculating C_{bend} and C_{shear}, determined from dividing K_{pier} by K_{bend}, or by K_{shear}, respectively. According to section 4.2.1, rigid beam-column nodes were assumed in the calculations, as well as a Poisson ratio equal to 0.20. The results are plotted in Figure 4.35, where it is possible to observe that the stiffness of the double column structure is less than 20% of this wall pier for the height range under analysis. However, the difference between bending and shear stiffness is still noticeable, and illustrates the general seismic design guideline where a shear dominated response is expected for squat walls and bending dominated response is expected for slender walls.
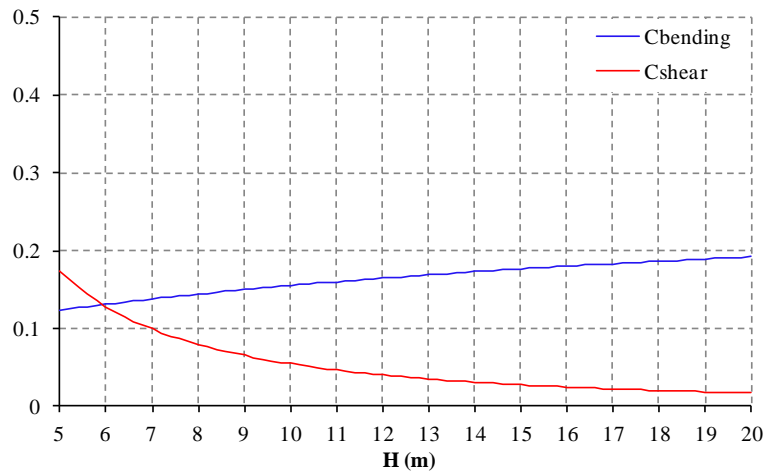
Figure 4.35 – Bent pier to Wall pier stiffness ratio

This raises an important question when considering the precast option C for application. According to Moehle *et al.* (2012), walls with very low aspect ratios ($h_w/l_w \leq 0.5$) tend to resist lateral forces through a diagonal strut mechanism in which concrete and distributed horizontal and vertical reinforcement resist shear. Conversely, slender walls ($h_w/l_w \geq 2.0$) typically behave like vertical cantilevers, while a combination of the two mechanisms tends to occur for intermediate geometric ratios. Considering the pier height range defined for this work and taking into account the same concept wall illustrated in Figure 4.34, values for the h_w/l_w ratio are between 0.70 and 2.85, meaning that the overall system design would have to address

4.39

both bending and shear critical failures, depending on the actual height of the pier under analysis, making it considerably less optimal for large-scale applications. This characteristic has particularly relevant impact in squat walls, as they exhibit limited deformation capacity under shear loading. Due to that, yielding in shear is often considered unacceptable, although the shear capacity of squat walls is often not a critical concern.

Within that context, two main challenges are associated with the precast system:

- Ensuring adequate shear stiffness for global element integrity and to enable the formation of diagonal compressive struts;
- Providing sufficient reinforcement to enable inelastic deformations at the critical sections, while accounting for anchorage of yielding forces along the plastic hinge length;

When designing for shear, adopting match-cast shear-keys to complement the friction forces along the joint length can be an adequate solution, granting interlock capability between subsequent precast segments in order to establish shear force transfer. A similar disposition to that of Figure 3.12 can be followed. However, providing adequate reinforcement for flexural yielding might be more difficult, because rebar continuity between precast units is not easily ensured with this system. Like in the Sorell Causeway, post-tension prestress is the most natural solution for that problem, but as previously discussed that may lead to excessive compressive stresses. Passive reinforcement could provide an interesting alternative, but the efficiency of a bond mechanism along several precast units would be quite a challenge.

System D:

The concept idea for layout D focused on providing another alternative system that was more capable of handling the flexural yielding requirements, while still providing the shear performance of a wall pier. In order to do that, this structure concentrates the bending capacity on the two wall column segments (WC) with continuous reinforcement, and provides shear capacity due to the interlocking forces developed through the indentations of the wall panel segments (WP). This can be related to the distribution of the coupling action (that is concentrated in the beam of the original bent column) along the whole column height, to emulate the behavior of coupled walls. An illustration of the different elements, as well as the proposed assembly procedure is presented in Figure 4.36.

a) Element division:
WC – Wall-pier column segment;
WP – Wall-pier panel segment;

b) Assembly procedure sequence: 1, 2, 3 and 4
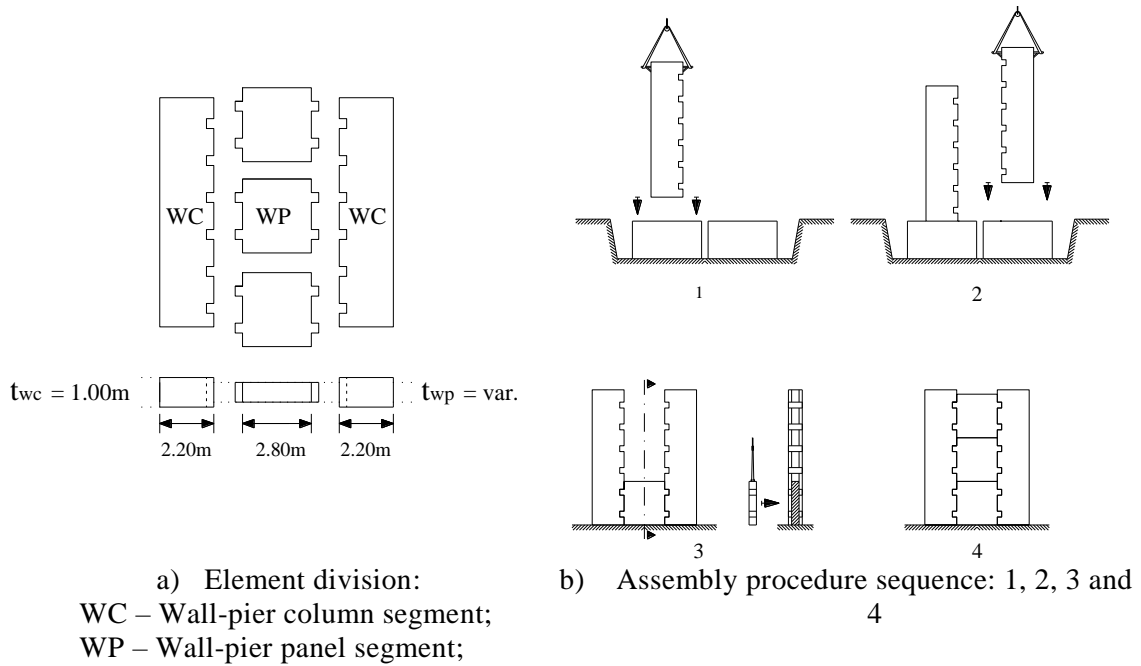
Figure 4.36 – Precast system: Option D

A complete definition of the indentation mechanism was not fully explored, as this was merely conceptual design. However, some guidelines can be introduced as there are basic requirements this structure is challenged by. Design of the WP elements essentially takes into account the shear transfer between indentations on opposing sides. The h_{wc} distance between two subsequent indentations is defined in order to ensure that a compression strut can form at an angle of around 30º, according to the illustration on Figure 4.37 – a). However, that value can easily be adjusted to accommodate varying pier heights, as long as it remains possible for compressions to develop at an effective angle. Additionally, the geometry of the indentations and the wall panel thickness t_{wp} are paramount to prevent concrete crushing. The t_{wc} thickness of the WC elements was defined as 1.00m due to the same reasons as briefly discussed regarding system C.

The core functionality of the WP element depends on the dominant deformation pattern expected for each particular structure. For that purpose, two scenarios can be considered, as illustrated in Figure 4.37 – b), although both may be relevant for intermediate situations:

- On taller piers, where bending is more relevant and longitudinal strains can be expected;
- On smaller piers, where shear is dominant and significant distortions occur;

In bending, tensile strains reduce the friction forces between segments, and only the mechanical interlock developed under indentation I1 is fully effective. In shear, that could be addressed by

the addition of shear keys along the horizontal joint, for improved force transfer between adjacent panel elements and to enable the formation of a second concrete strut under I2.

a) Shear transfer between columns   b) Compressive struts formation in bending and shear
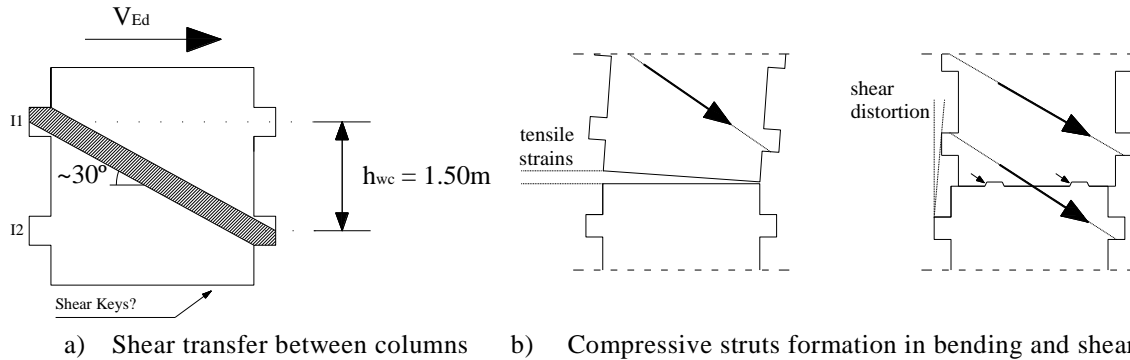
Figure 4.37 – WP element functionality

While this system could provide an easier solution to the problem of flexural yielding than system C, as well as to incorporate the influence of shear in the overall pier response more effectively than the coupling beam of systems A and B, it also has some unappealing characteristics from a precast perspective. One of the main shortcomings is the complex and dense detailing that should be required on the indentations. Both the protruding end on WP elements and the receiving pocket on the columns need strong reinforcement and confinement, in order to address the large compressions that are expected to develop there, which may also further decrease the potential for hollow section solutions. Furthermore, while a methodical assembly procedure can be established, it still represents several operations per pier, which can lead to considerable time consumption, especially if dry joints and connections are not accepted and grouting or local casting operations are also required. Even if that is not the case, some type of bearing should possibly be required for the contact interfaces between WP and WC elements, increasing the cost of the solution. Finally, while the other systems are roughly based on precast solutions that have been successfully applied on other occasions, and therefore can be envisioned within a reasonable level of previous industry experience, this system is a new and unproven design idea. Considering the scope of the research programme associated with this work, commitment to the full study of this layout was considered a big risk.

A general overview of the main characteristics of each system is presented in Table 4.10, where related pros and cons are summarized. In light of this discussion, it was considered that System A involved a set of characteristics making it the most suitable for this work and, therefore, it was adopted for designing the test specimens. One of the main reasons for that option is the ability to turn the potential weakness associated with precast joints located on high demand sections into a strong design feature, by selecting those locations for provision of stable energy dissipation. Furthermore, the main weaknesses of System A were also considered to be more easily addressed than some of the innate shortcomings of the remaining options.

4.42

Table 4.10 – Precast systems overview

Precast System	Main Characteristics	*Pros*	*Cons*
A	Two precast columns + precast coupling beam; Four precast joints per pier;	Common assembly procedure; Suitable for easy manufacture; Precast joints for stable energy dissipation;	Potentially heavy columns; Connection forces at critical sections; Solution sensitive to geometry;
B	Half CIP columns + Half precast coupled columns; Two precast joints per pier;	Connections at low strain sections; Single assembly operation per pier;	Difficult handling of the precast specimen; Solution very sensitive to geometry;
C	Wall pier constituted by horizontal segments; Pier height dependent precast joints;	Suitable for both easy manufacture and assembly; Strong shear capacity;	Difficult to provide reliable bending capacity; Several connection operations per pier;
D	Precast side columns + Shear panels; Four contact indentations per panel segment;	Wall model for high shear capacity; Continuous reinforcement on bending critical elements;	Complex and cumbersome design; Unproven success of the system;

4.3. TEST SPECIMENS

The framework for the experimental campaign, which will be further presented in Chapter 5, aimed to outline a three phase strategy:

- Phase 1: Analyzing different monolithic systems to develop an understanding of the actual interaction between the columns and the beam, and to evaluate the performance obtained from different sets of reinforcement layouts;
- Phase 2: Evaluating the performance of varied precast connections proposed for the element-to-element connection between the columns (C) and the beam (B), according to precast system A;
- Phase 3: Evaluating the performance of different precast connections proposed for the foundation-to-element connection, according to precast system A;

Taking into account a maximum height constraint of 4.00m on the *Laboratory of Earthquake and Seismic Engineering* (LESE), the test specimens had to be designed at a reduced scale. Considering the upper bound of the pier height range set for this work (around 20.00m) and a reduced scale of 1:4, it would result in specimens around 5.00m tall, which is still larger than intended. With that in mind, a decision was made to study only half structures, taking advantage of the curvature inflexion point where null moments are observed under lateral

loading. Furthermore, design of the test specimens for an intermediate pier height within the same range was considered appropriate. Therefore, the previously mentioned reference column length of 15.00m was adopted (total pier height of 16.70m), leading to more manageable test specimen heights around 2.30m on the 1:4 reduced scale.

Within that context, Phase 1 and 2 of this experimental campaign targeted the upper part of the bent pier frame and the element-to-element connections (A section), while Phase 3 was aimed at studying the bottom part and foundation-to-element connections (B section), as illustrated in Figure 4.38.
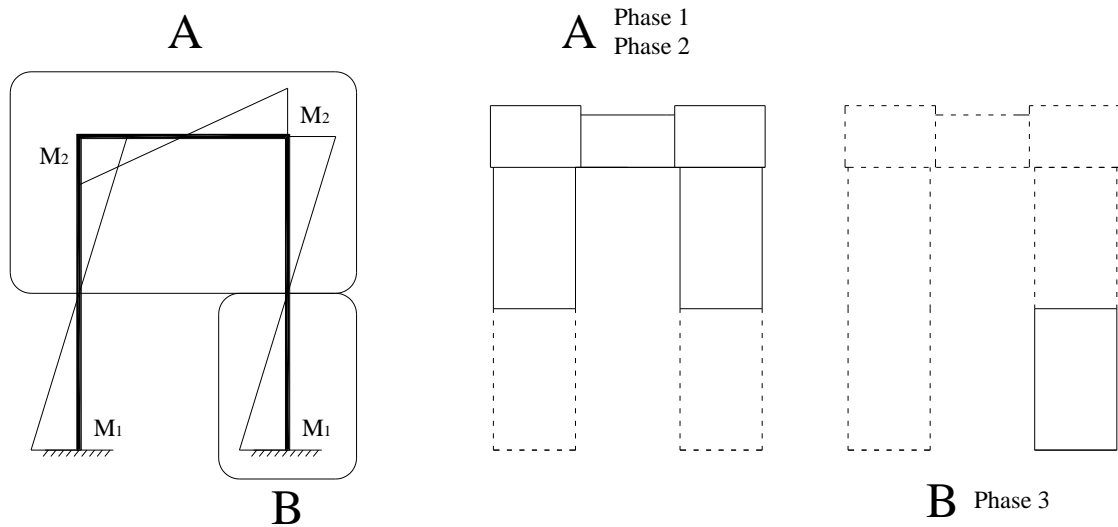
Figure 4.38 – Experimental phases in correspondence with elastic moments distribution

In light of the adopted reduced scale, both element geometry and the design parameters calculated earlier have to be reduced accordingly. Cauchy's similitude relationships have been used to determine the actual values for the test models (M) from those fit for a full scale prototype (P), as represented in Table 4.11.

Table 4.11 – Cauchy's similitude relationships for a 1:4 reduced scale

Length (m)	$L_P = (4) \times L_M$
Area (m²)	$A_P = (4)^2 \times A_M$
Force (kN)	$F_P = (4)^2 \times F_M$
Moment (kN.m)	$M_P = (4)^3 \times M_M$
Strain (m/m)	$\varepsilon_P = \varepsilon_M$
Stress (MPa)	$\sigma_P = \sigma_M$

Furthermore, the same materials considered for the response spectrum analyses were also adopted for test specimen design - C30/37 for concrete and A500 for steel rebars - although the actual capacity of those used to construct the test specimens was generally significantly higher than specified. In the relevant cases, the cement grout used for filling ducts and precast joints

4.44

was a proprietary product named Sika Grout (www.sika.pt), with compressive strength in the range $55 - 65\ MPa$ and tensile strength in the range $7.5 - 9.5\ MPa$. An overview of the general properties of the test specimens for the full experimental campaign, which are addressed in further detail in the following sections, is presented in Table 4.12.

Table 4.12 – General properties for the full experimental campaign

Specimen	Type [1]	Concrete properties [2]			Column						Beam					
		E	f_{cc}	f_{ct}	ρ_{sl}	σ_{sly}	σ_{slu}	ρ_{st}	σ_{sty}	σ_{stu}	ρ_{sl} [3]	σ_{sly}	σ_{slu}	ρ_{st} [4]	σ_{sty}	σ_{sty}
		GPa	MPa	MPa	%	MPa	MPa	%	MPa	MPa	%	MPa	MPa	%	MPa	MPa
Phase 1																
SP_M01	M	40	48	4,6	0,74	504	590	0,64	504	590	1,63	601	702	0,26	504	590
SP_M02	M	36	45	3,8	0,74	504	590	0,64	504	590	1,96	601	702	0,50	504	590
SP_M03	M	36	41	4,4	0,74	504	590	0,64	504	590	1,80	601	702	0,79	504	590
SP_M04	M	40	48	3,6	0,74	504	590	0,64	504	590	1,96	601	702	0,79	504	590
Phase 2																
SP_PC02A	P	36	37	3,0	0,74	504	590	0,64	504	590	1,96	601	702	0,50	504	590
SP_PC02B	P	37	45	3,4	0,74	504	590	0,64	504	590	1,96	601	702	0,50	504	590
SP_PC02C	P	36	49	3,1	0,74	504	590	0,64	504	590	1,96	601	702	0,50	504	590
SP_M02C	M	41	51	3,0	0,74	504	590	0,64	504	590	1,96	601	702	0,50	504	590
Phase 3																
SP_F01	M	40	47	2,8	0,74	504	590	0,64	504	590	*N/A*					
SP_F02	P	45	57	3,5	0,74	504	590	0,64	504	590						
SP_F03	P	37	47	3,7	0,74	504	590	0,64	504	590						

1 - P for Precast; M for Monolithic
2 - Values observed on the test date, or on the closest possible day
3 - Contribution of the diagonal bars calculated by taking into account the slope angle
4 - Not including the contribution of diagonal bars

4.3.1. PHASE 1 – MONOLITHIC SPECIMENS

The geometry outline for all the phase 1 and 2 specimens follows Figure 4.39, respecting the original double column design of Figure 4.2.
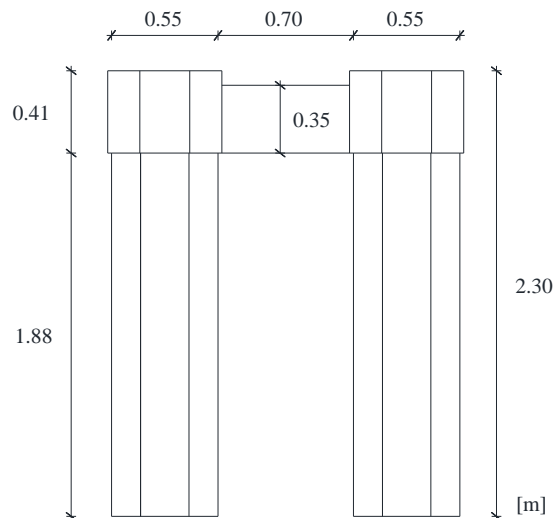
Figure 4.39 – 1:4 Reduced scale model geometry

In addition, a constant enlargement width of 0.02m was considered on the beam-column nodes, aiming to provide more space for reinforcement placement (since high densities are expected) and for connection detailing (further discussed on 0). Furthermore, the same column reinforcement was adopted in all the tests, designed accounting for both maximum and minimum axial load due to beam shear transfers (corresponding to axial load ratio range between approximately 0.00 and 0.10), and is illustrated in Figure 4.40.
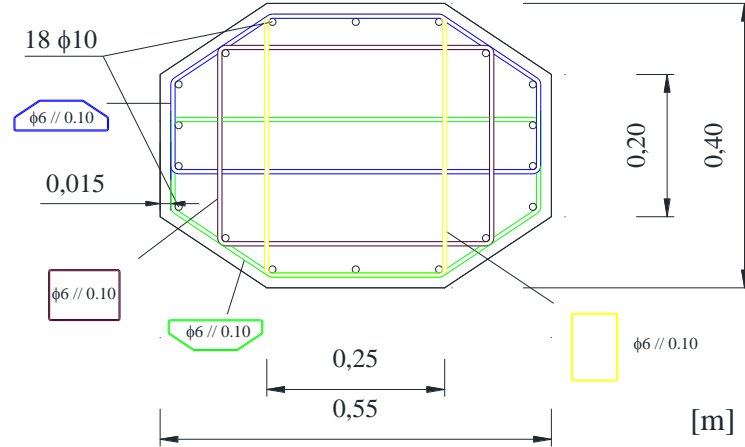
Figure 4.40 – General column reinforcement for all specimens.

According to the design strategy presented in Figure 4.27, some level of damage and energy dissipation was also expected in the coupling beam. Aiming to evaluate different reinforcement layouts to address that problem, four test specimens were designed, where only the beam reinforcement layouts were distinct. Those specimens were labeled according to the *SP_M#* tag, where *SP* stands for the SIPAV project, *M* relates to the monolithic aspect, and *#* is a number according to the following:

- *01*: EC8 bi-diagonal layout (Figure 4.23);
- *02*: Rhombic truss layout (Figure 4.25);
- *03*: Conventional layout, with horizontal main reinforcement and vertical stirrups;
- *04*: Rhombic truss layout with adjustment of the diagonal position;

4.3.1.1. Specimen SP_M01

This specimen was designed according to EC8 provisions for coupling beams of shear walls. In that regard, the design capacity of the beam is dependent of the vertical projection of the axial force developed in each diagonal, according to equation 4.9:

$$V_{Ed} \leq 2 \times A_{si} \times \sigma_{syd} \times \sin \alpha \qquad\qquad 4.9$$

Where:

A_{si} – Total reinforcement area of one diagonal;

σ_{syd} - Reinforcement yield strength;

α – Diagonal slope angle;

4.46

In addition, each diagonal must be detailed as if it were a column element, accounting for a minimum cross-section size equal to 50% of the beam width (leading to diagonal slope angles under 25º) and individual confining reinforcement. Additional horizontal and vertical reinforcement is also included for crack control and to ensure concrete integrity for large deformations, although it is not expected to contribute to the overall capacity. The result is presented in Figure 4.41, corresponding to a very dense layout that was a challenge to build, which is most evident on the beam-column nodes, as illustrated in Figure 4.41 – d). For further reference, due to an error of the formwork, the actual value of the beam-column node enlargement cap width on this specimen was 0.05m.
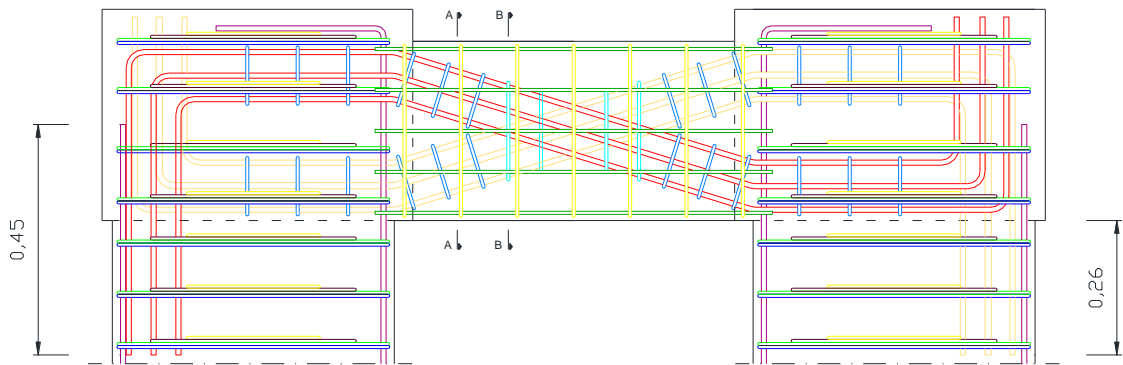
a) Beam detail drawings

b) Beam detail picture
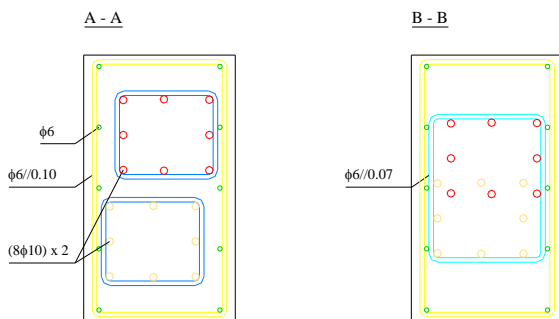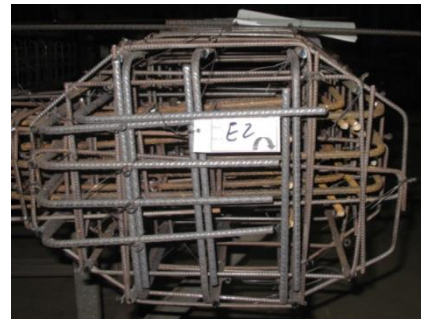
c) Beam cross sections   d) Beam-column node reinforcement

Figure 4.41 – Specimen SP_M01 reinforcement layout

4.3.1.2. Specimen SP_M02

This specimen was designed according to the model proposed by Tegos and Penelis (1988), where shear transfer is expected to occur through a complex interaction between different mechanisms. Design equation 4.10 can be used to calculate the shear strength of the beam, where V_{sd} is the shear component carried by the axial load of the main reinforcement (can be determined from equation 4.9 by using different diagonal slope values), V_{st} is the shear capacity associated with the design truss model, and V_c is related with a parallelogram of compressions carried through the concrete.

$$V_{Rd} = V_{sd} + V_{st} + V_c \qquad 4.10$$

As it stands, the diagonal bars carry most of the load, and the critical aspect for calculation of the transverse reinforcement is ensuring sufficient capacity to prevent failure at the mid-section of the beam, where diagonal rebar folding occurs. The resulting layout is presented in Figure 4.42, where a higher slope of nearly 40º for the diagonal parts of the main reinforcement is duly noted. The confining reinforcement used at the beam-column node was also adjusted from the previous specien, accounting for both easier assembly and reduction of reinforcement ratio, as presented in Figure 4.42 – d).
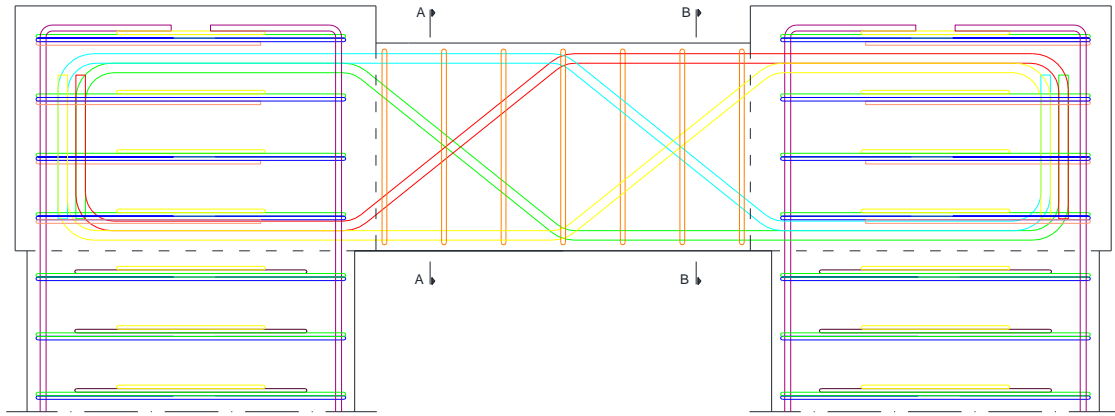
a)   Beam detail drawings

b)   Beam detail picture
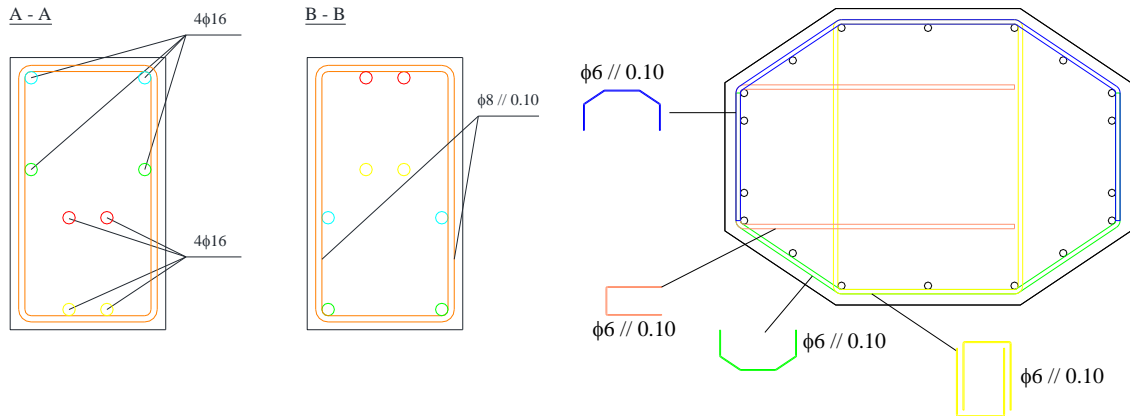
c)   Beam cross sections   d)   Beam-column node cross-section

Figure 4.42 – Specimen SP_M02 reinforcement layout

4.3.1.3.   Specimen SP_M03

SP_M03 corresponds to a standard beam design, using horizontal reinforcement on both sides of the beam, as well as strong transverse reinforcement in the form of vertical stirrups; the shear capacity of this beam is determined using the regular truss model of Eurocode 2, indicated in equation 4.11. The confining reinforcement on the beam-column node is the same of SP_M02.

$$V_{Rd} = \frac{A_{st}}{s} \times z \times \sigma_{syd} \times \cot\theta \qquad\qquad 4.11$$
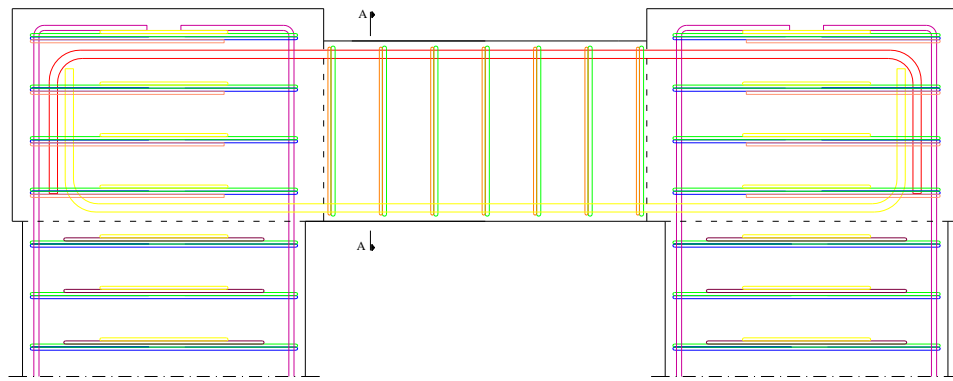
a)   Beam detail drawings

b)   Beam detail picture
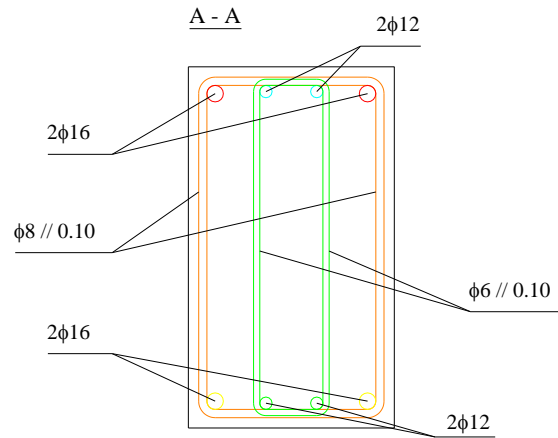
c)   Beam cross sections

Figure 4.43 – Specimen SP_M03 reinforcement layout

4.3.1.4.   Specimen SP_M04

This test specimen is a variant of SP_M02, where the relative position of the diagonal parts of the reinforcement was adjusted to be centered with the vertical interface between the beam and the adjacent nodes. The main objective behind such change was to seek an increase in the local capacity of that location, regarding the large shear transfers that occur therein, aiming to prevent heavy degradation of the interlock mechanism that leads to failure, by having the diagonals acting as dowel bars. However, this option has the consequence of creating a zone in

the mid-section of the beam where only horizontal bars exist, therefore locally reducing the shear capacity of the beam. In light of that, the transverse reinforcement had to be globally increased to the level of SP_M03, while the calculation model for the diagonals was the same of SP_M02 (equation 4.10).
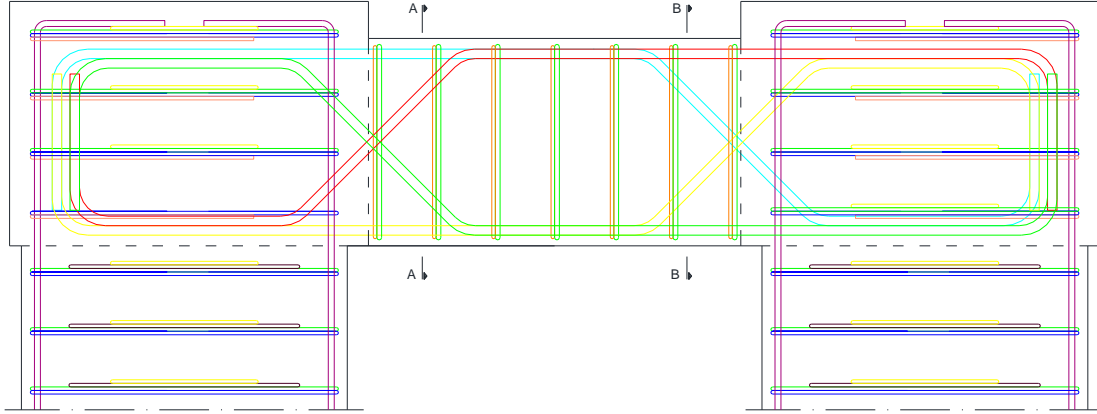
a) Beam detail drawings

b) Beam detail picture
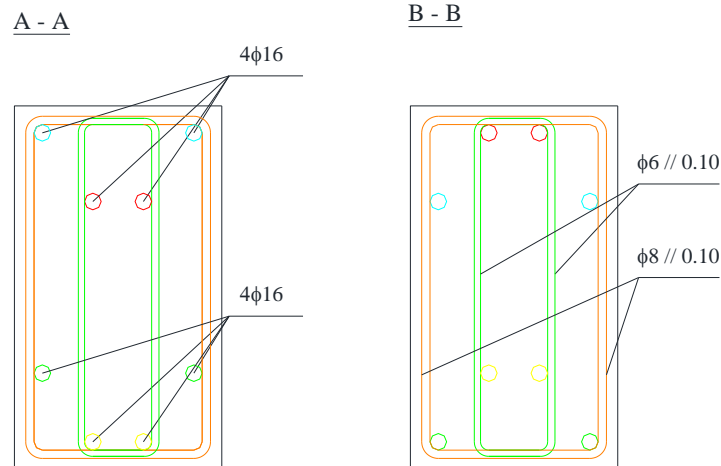
c) Beam cross sections

Figure 4.44 – Specimen SP_M04 reinforcement layout

4.3.2. PHASE 2 – PRECAST SPECIMENS

In phase 2 tests, all the specimens aimed to evaluate different connection mechanisms and detailing, therefore all the models used globally the same reinforcement layout. In particular, the column reinforcement illustrated in Figure 4.40 and the rhombic truss layout of SP_M02 (Figure 4.42) were adopted for that purpose; the only relevant modifications included therein were designed for the beam-column nodes and the inherent connection mechanisms.

Considering the previously described precast system A, the introduction of rebars through existing corrugated ducts in the precast beam for moment continuity was deemed the best option. In light of that, and taking into account that yielding is expected due to the joint location, some concerns can be raised regarding the efficiency of the connection for seismic loading. To expand on that, Figure 4.45 presents an illustrative representation of beam-column nodes subjected to negative moment. Under this load condition, the tensile forces developed through the longitudinal reinforcement balance the compressions that occur due to element bending, and moment continuity is achieved by ensuring adequate transfer of those forces between beam and column rebars. This can be provided through splicing, or by shear anchorage of the rebars on the surrounding concrete, especially when hooks are included, as illustrated in Figure 4.45 – a), although on most cases a minimum splicing or anchorage length is required. When considering a precast element, a vertical bar must be considered for ease of assembly, preventing the possibility for the mechanical anchorage of hooks. However, direct interaction between rugged indentations is hindered by the presence of the corrugated ducts, and interface friction forces develop to engage the rebar inside the duct, as illustrated in Figure 4.45 – b).

a) Monolithic node   b) Precast node
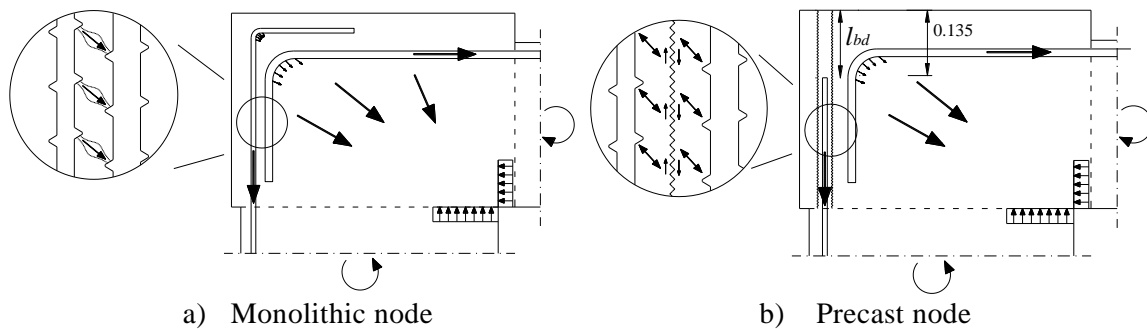
Figure 4.45 – Beam-column node rebar force transfers

The usual bond length (l_{bd}) code formulas do not directly consider the influence of that mechanism, and while high quality grouts can enable yielding development on short distances, the accuracy of l_{bd} calculations for these cases may be uncertain. The implications thereof for the current study case may be evaluated with a simple example, for discussion sake. Considering the application of Sika Grout, whose bond strength with deformed rebars is around 15 MPa, the resulting l_{bd} in tension would be around 10ϕ, depending on the actual conditions of

the application. If ϕ10 bars are used, the anchorage length would be 0.10m, which is dangerously close to the maximum available length between the top of the column and the bottom side of the hook.

Aiming to provide improved bond behavior to the connection, three different strategies were followed in this work, each related to an individual test. The respective specimens were labeled *SP_PC02#*, where *SP* stands for the SIPAV project, *PC* relates to the precast aspect, 02 characterizes the beam reinforcement layout based on SP_M02, and # is a letter according to the connection type tested in each:

- *A*: Protruding rebars from the column with post-connection bolting against a steel plate placed over the node;
- *B*: Splicing rebars inserted into the column, with post-connection bolting against a steel plate;
- *C*: Splicing "U-shaped" stirrups inserted from the top of the node into the column;

Furthermore, a fourth specimen was also designed, labeled SP_M02C. This last model is a monolithic replica of SP_PC02C, which was aimed at evaluating the effects of the precast technology itself, in comparison with the effects of the 50% continuity reinforcement reduction that was considered for every specimen of phase 2, using precast system A.

4.3.2.1.   Specimen SP_PC02A

This specimen accounts for columns produced with protruding rebars, as illustrated in Figure 4.46. Specifically, in this case, out of the total 18ϕ10 bars of the column, 8ϕ10 bars are extended onto the beam, and introduced through existing ducts during its descending placement. Subsequently, 10mm steel plates are put in place on the top of the node, and the joint sections are externally sealed, after which gravity-flow grouting is performed. The final step of the connection requires the rebars to be mechanically bolted against the steel plates for increased anchorage.

Descending beam into column   *Assembled structure*   *Beam cross-section*

Column top view

1 - φ10 rebars; 2 - M20 rods; A - φ30 ducts; B - φ50 ducts; C - Steel plates
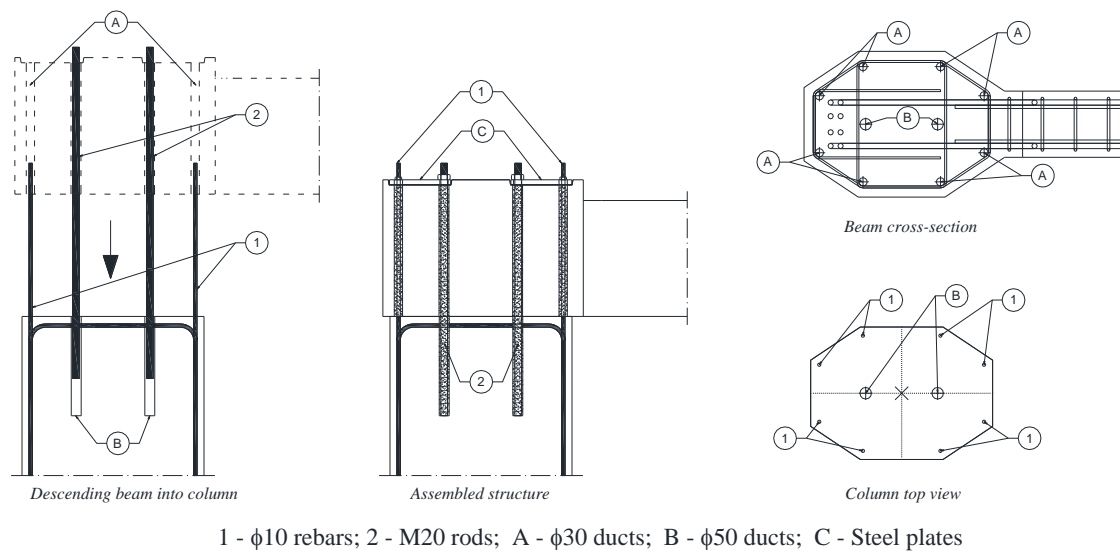
Figure 4.46 – Specimen SP_PC02A overview

Two M20 rods are also introduced into an inwards position in the columns, aimed at acting similarly to dowel bars or shear keys and to improve the shear capacity of the precast joints. The diameter for the ducts was defined as 2 to 3 times the diameter of the bars, in order to provide tolerance for misalignments and inaccurate geometry. Figure 4.47 briefly illustrates the sequence of operations required for full assembly of the system.

a) Descending placement of the beam   b) Sealing of the joint

c) Node with the steel plates   d) Grouted ducts with bolted connections
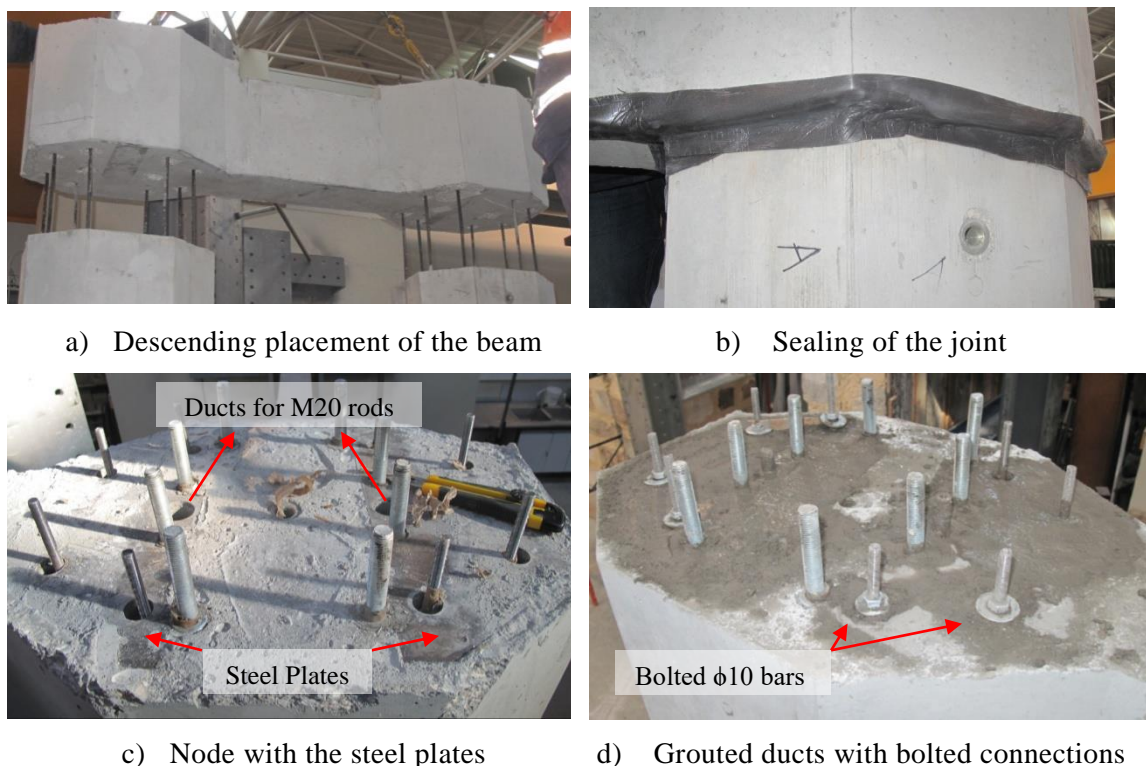
Figure 4.47 – Specimen SP_PC02A assembly operations

4.3.2.2.   Specimen SP_PC02B

Specimen SP_PC02B mainly aimed to test the efficiency of a connection that could be performed without the protruding rebars, as those tend to complicate manufacture, handling and assembly. For that purpose, 100% of the longitudinal reinforcement is cut at the joint section, and continuity is instead provided by lap splicing. Therefore, additional rebars are introduced downwards through the beam, into existing ducts extending 0.30m inside the column, placed at locations that result from a direct offset of the original rebars towards the centre of the cross-section, according to Figure 4.48. This strategy leads to a reduction of the maximum lever arm between rebars subjected to tensile and compressive forces at the joint section (0.435m compared to 0.50m of the original cross-section), which is to be compensated by the adoption of a larger rebar diameter of $\phi 12$, in order to avoid further moment capacity reductions.

Descending beam into column   *Assembled structure*   *Column top view*
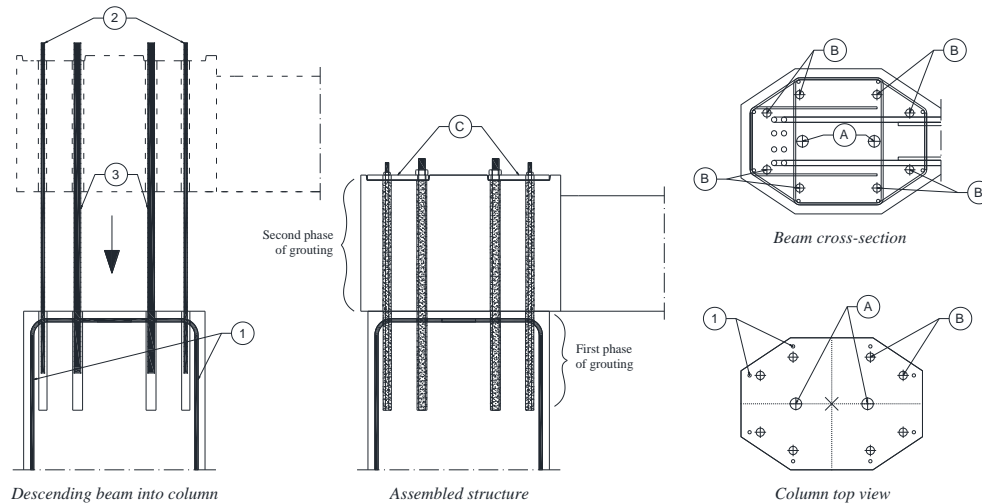
1 - $\phi 10$ Column rebars; 2 - $\phi 12$ Splice rebars; 3 - M20 rods; A - $\phi 30$ ducts; B - $\phi 50$ ducts; C - 15mm Steel plates;

Figure 4.48 – Specimen SP_PC02B overview

In this case, the gravity-flow grouting process is phased, occurring firstly on the duct sections that are located in the column, with the upper portion of the ducts grouted only when the first lower portion is hardened. That leaves the option of performing the beam descending operation before or after the first grouting phase. While it is believed that the former should be simpler to execute in a real full-scale application, the latter was adopted in this test specimen due to time constraints. An overview of different stages required for full assembly of this specimen is presented in Figure 4.49.

a) First phase grouting

b) Beam descent

c) Sealing of the joint

d) Second phase grouting
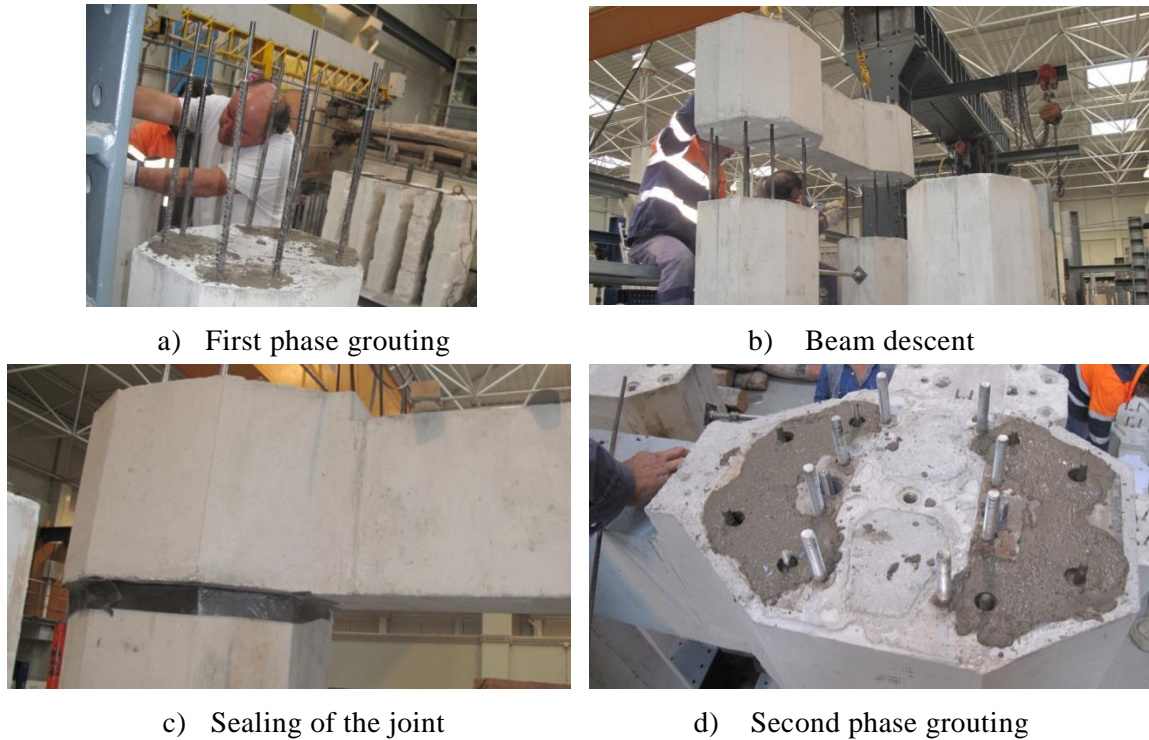
Figure 4.49 – Specimen SP_PC02B assembly operations

4.3.2.3. Specimen SP_PC02C

The precast connection of specimen SP_PC02C is based on the same concept tested in SP_PC02B, with 100% of column reinforcement interrupted at the joint section and continuity ensured by additional splicing rebars. Consequently, the same general layout of Figure 4.48 is also adopted for the current specimen, whereas the only difference is introduced in the anchorage system for the splicing rebars. As illustrated in Figure 4.50, SP_PC02C contemplates the use of "U-shaped" folded rebars (similar to open stirrups) that are introduced through existing ducts in the node and into the column. This layout enables more flexibility for design because, while rebar embedment length is limited in the beam, a larger depth is available in the columns for duct placement (although the same 0.30m length of SP_PC02B was also used in this case).

1 - φ10 Column rebars; 2 - φ12 "U-shaped" rebars; A - φ30 ducts; B - Canals for the stirrups;
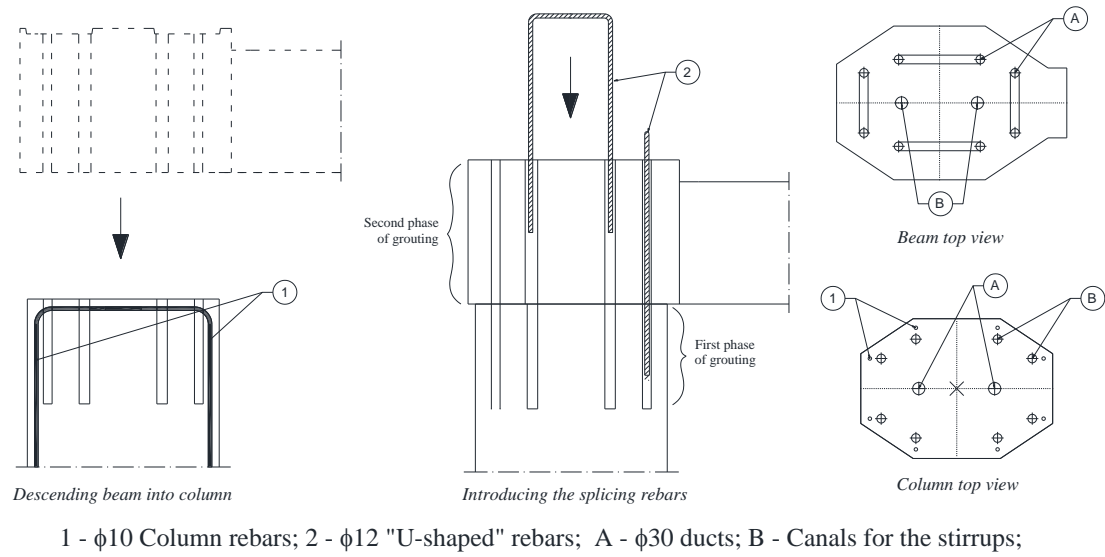
Figure 4.50 – Specimen SP_PC02C overview

The same grouting process used in SP_PC02B was also considered for SP_PC02C, with phased grouting, first in the column sections and later in the upper part of the node. However, in SP_PC02C, four canals were included on the top of the node, providing connection between vertical stirrup branches and enabling a horizontal surface. An overview of different stages required for full assembly of this specimen is presented in Figure 4.49.

a) Beam descent	b) Stirrup placement

c) Grouting	d) Fully assembled specimen
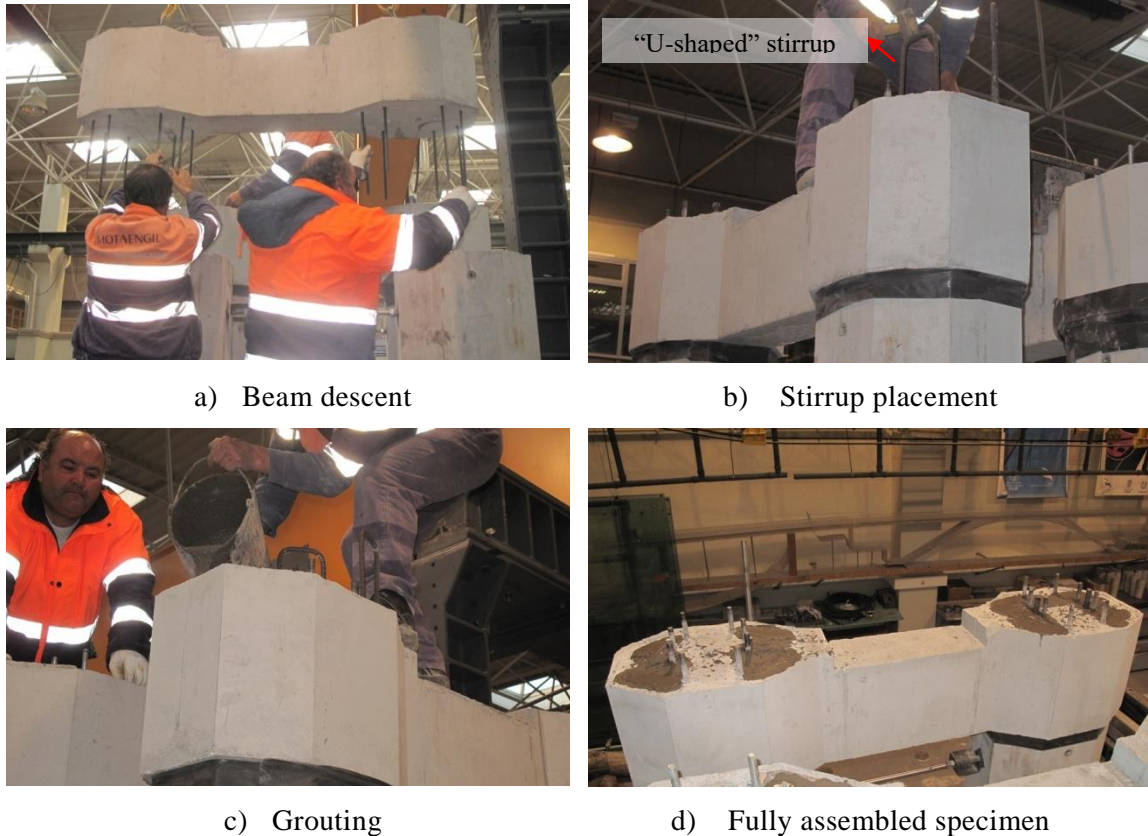
Figure 4.51 – Specimen SP_PC02C assembly operations

4.3.2.4. Specimen SP_M02C

As mentioned before, SP_M02C is a monolithic replica of the previous specimen SP_PC02C. With that in mind, it follows the original rhombic truss reinforcement layout of the SP_M02 specimen (Figure 4.42), while also including all the alterations introduced to perform the precast connection, namely the reduction of continuity reinforcement (Figure 4.48) and the "U-shaped" stirrups (Figure 4.50).

4.3.3. PHASE 3 – FOUNDATION-TO-ELEMENT CONNECTIONS

In phase 3, three different specimens were designed with the main objective of assessing the behavior of precast foundation-to-element connections. Therefore, the models were labeled *SP_F#*, where *SP* stands for the SIPAV project, *F* represents the focus on foundation-to-element connections, and # is a number according to the following:

- ▪ *01*: Fully monolithic specimen;
- ▪ *02*: Precast column with protruding rebars and CIP footing;
- ▪ *03*: Precast column with protruding rebars introduced in corrugated ducts in a precast or previously constructed CIP footing;

4.3.3.1. Specimen SP_F01

The first specimen of phase 3 tests is a monolithic system, including a column and the respective foundation, designed for providing a benchmark for the precast models. The reinforcement layout of the column is the same used for all the phase 1 and phase 2 specimens, consisting of 18ϕ10 bars placed around the outer perimeter of the cross-section, according to Figure 4.40. The column element is 1.85m tall and is placed on the top of a square footing with 1.30m width and 0.70m height, which was designed to perform as a rigid element while fixed to the lab floor through prestressed connections placed near its corners, (see Figure 4.52).

a) Side view   b) Footing top view
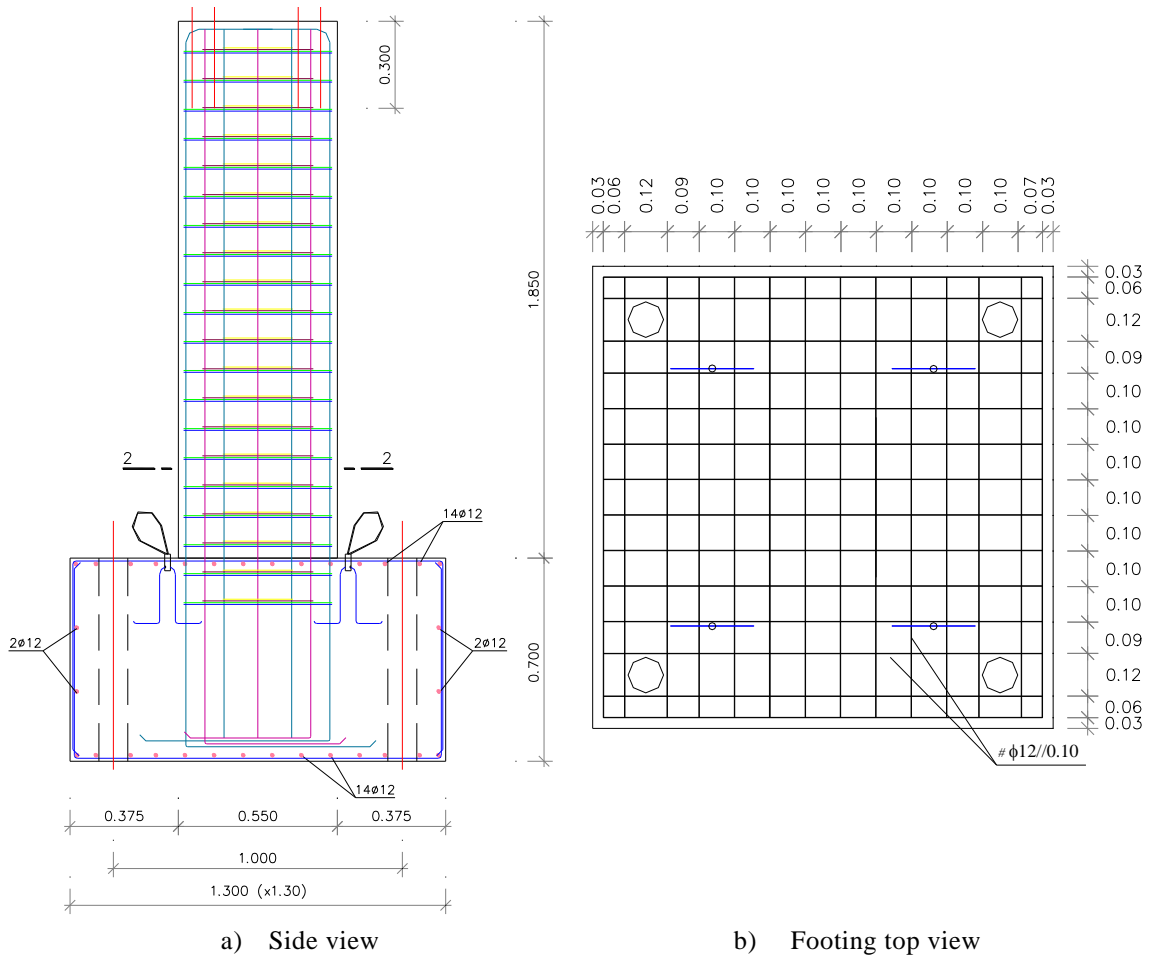
Figure 4.52 – Specimen SP_F01 overview

4.3.3.2.   Specimen SP_F02

Specimen SP_F02 incorporates a similar strategy to that presented earlier in Figure 3.6. Essentially, that involves precasting the column segment in a previous stage, accounting for the protruding reinforcement required to provide continuity between the footing and the element. Afterwards, the element is put in place, and both the reinforcement cage and formwork of the footing are prepared around it for posterior casting. This process is briefly illustrated in Figure 4.53. The reinforcement layouts for both the column and the footing are the same used in the monolithic specimen SP_F01.

Stage 1	Stage 2	Stage 3
Production of the precast segment	Preparation of the reinforcement cage and formwork for the footing	CIP production of the footing
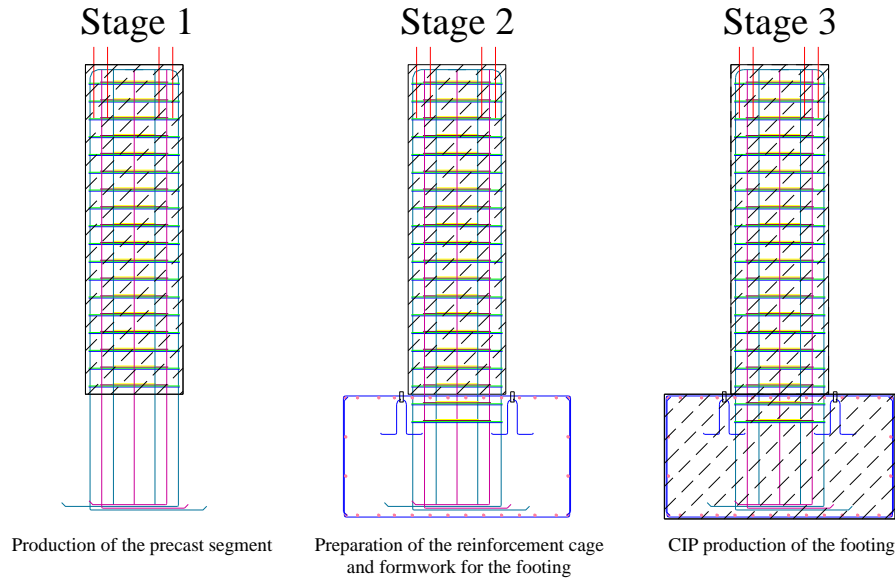
Figure 4.53 – Specimen SP_F02 construction process

4.3.3.1. Specimen SP_F03

The main design focus for SP_F03 aimed to enable independent preparation of the precast column and its respective footing, trying to further improve the appeal of a precast solution as a powerful tool for flexibility in construction management. For that purpose, the precast system is required to be fairly cheap and easy to assemble, avoiding complex connections, expensive gear and disproportionately time-consuming operations. Therefore, a solution using corrugated ducts was chosen for the present case, in light of the same strategy adopted at the beam-column precast joints for phase 2 tests. As illustrated in Figure 4.54 – a), the precast column is manufactured with 0.65m long protruding extensions, which are introduced through ϕ50 ducts extending 0.50m into the footing (Figure 4.54 – b) and c)).

This strategy involves leaving an empty band of 0.15m on the top of the footing (cross-section cut 1-1, Figure 4.54 – c)), which is meant for second stage casting after the associated transverse reinforcement is prepared. Furthermore, while the current column cross-section (2-2, see Figure 4.54 – a)) follows the original layout, this section is temporarily supported on top of a 0.15m width concrete core cube (previously cast from the same concrete mix used for the precast segment), to avoid resorting to more elaborate bracing solutions, according to Figure 4.54 – c). Normal or micro-concrete should be provided for the second stage casting of the empty band, although in the present work normal grout was used, and the concrete core cube used for temporary supporting of the precast column segment is not removed, remaining within the section as an integral part of the structure.

a) Precast column side view

b) Footing top view

c) 1-1 Cross-section cut

d) Footing side view
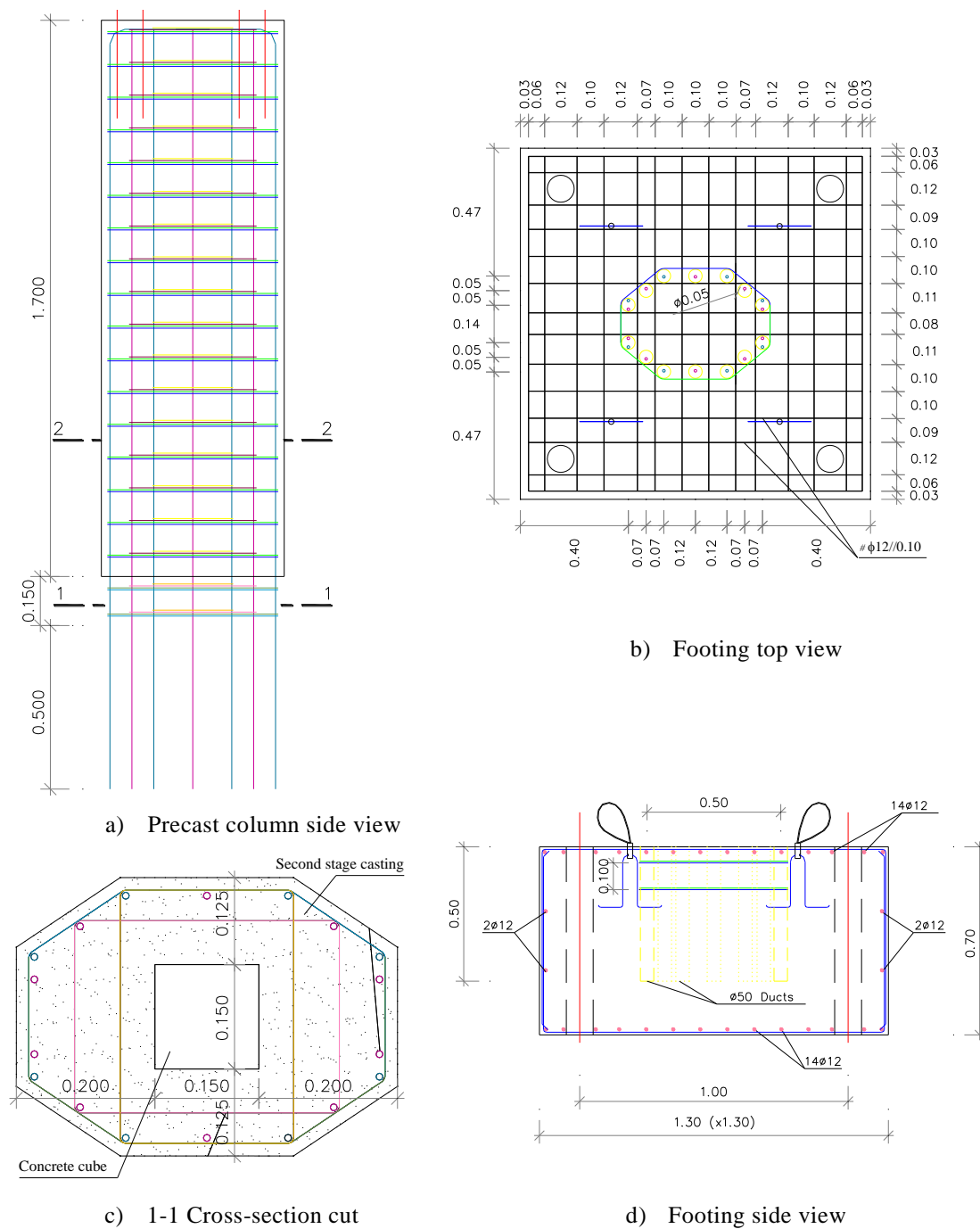
Figure 4.54 – SP_F03 overview

The complete assembly process of SP_F03 is the following, for which steps 3 to 6 are illustrated in Figure 4.55:

1. Manufacture of the precast column;
2. Construction of the footing with embedded corrugated ducts;
3. Placement of the column on the top of the footing by introducing the protruding

rebars through the relevant ducts. The system is temporarily supported by a 0.15m concrete cube;

4. Gravity-flow grout is used to fill the ducts, sealing the bottom part of the longitudinal reinforcement;

5. Preparation of the transverse reinforcement in the empty band;

6. Second stage casting of the bottom section of the column. The concrete core cube serving as temporary support of the precast segment is left within;
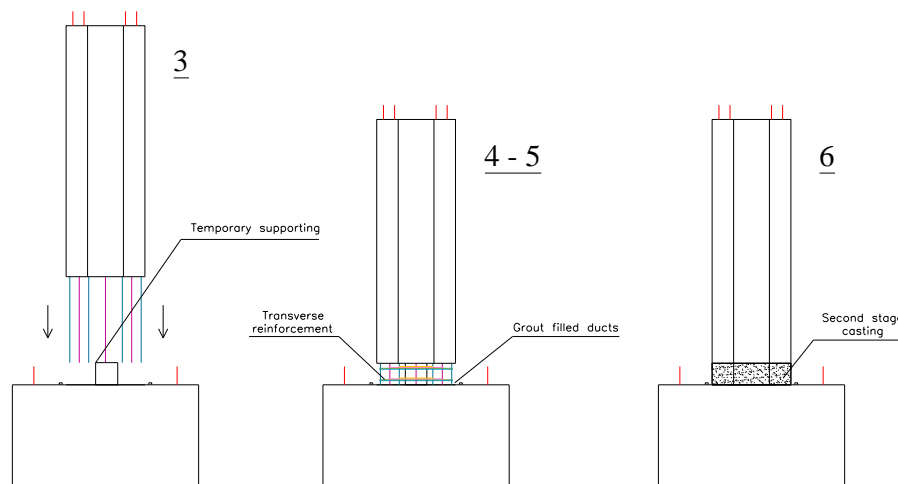
Figure 4.55 – SP_F03 assembly process

4.4. FINAL REMARKS

This chapter was aimed at describing the strategy and thought process associated with conceptual design of the test specimens. For that purpose, the HSRL Poceirão-Caia design proposal was presented as a core element of this study, from which it was possible to evaluate the structure layouts and design options that could benefit from large-scale application. In that regard, a decision was made to focus on medium to long viaducts, (100m to 600m) characterized by double box-girder decks, and supported by double-column piers between 5.00m and 20.00m tall, where the transverse performance was the main concern.

Within that context, the proposed double-column pier structure is defined by geometrical characteristics that may pose a challenge for adequate seismic design, due to low ductility capacity and proneness to shear-critical performance. This is mainly caused by the short span of the coupling beam which, as observed, has non-negligible impact on the stiffness relation between the columns and the beam and, therefore, also on the overall pier structure behavior for pier heights within the range relevant to this work. Nonetheless, the previously described chosen structural layout enabled the selection of a few case study viaducts for numerical

modeling, aiming to obtain reference data using the Response Spectrum Method to help with test specimen design.

In that regard, the outline of the experimental campaign and its test specimens were also presented, characterized by a three phase process and a total of 11 reduced scale (1:4) specimens tested under lateral cyclic loading conditions. The first phase involves the study of monolithic half-pier structures, resorting to different beam reinforcement layouts designed for provision of improved ductility under strong shear demand, using similar strategies to those developed for reinforcement of coupling beams on shear walls. Its main purpose is aimed at observing and analyzing the actual interaction between the columns and the beam, as well as evaluating the ductility capacity and failure characteristics of the current double column pier. Additionally, the first phase enables choosing one of the beam reinforcement layouts (according to the observed performance on the monolithic structures) to use in the design of phase two specimens.

Phase two is entirely focused on evaluating precast solutions for the double column pier, which is achieved by testing specimens designed with equivalent reinforcement and structural layouts, but using different precast mechanisms developed with attention to some of the main industry concerns. Finally, phase three is comprised of only three specimens, which were aimed at evaluating the performance of precast connections established at the footing-to-element interface.

5
EXPERIMENTAL CAMPAIGN

As previously discussed and highlighted in Table 4.12, the experimental campaign devised for this work involved three different stages, each related with different objectives. Therefore, the first section of this chapter will focus on presenting the main test setup details according to the clear distinction between bent pier and single column tests.

The later sections focus on presenting the main experimental observations, and on providing comparison between the performances of different systems according to generalized response parameters, which is also performed separately for testing stages 1 and 2 and testing stage 3.

5.1. TEST SETUP

Two test setups were developed at LESE to support this work, based on uniaxial cyclic loading of the test specimens according to the different circumstances associated with each testing stage. As previously mentioned, all the tests follow a reduced scale of 1:4.

5.1.1. PHASE 1 AND PHASE 2 – BENT PIER TESTS

The test setup assembled for this part of the work aimed to make the most use of the already existing infrastructures and equipment of the LESE laboratory. With that in mind, the main features associated with it were the following, also highlighted in Figure 5.1 for illustration purposes:

- 1 horizontal actuator (+/- 500 kN capacity; +/- 150mm stroke);
- 2 vertical jacks (500 kN capacity);

- 4 prestress threadbars (*Dywidag* 26WR);
- Mechanical hinged system;
- Reaction frame;
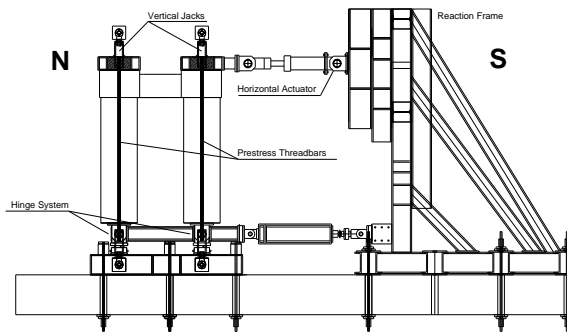
a) Construction drawings   b) Highlighted picture view
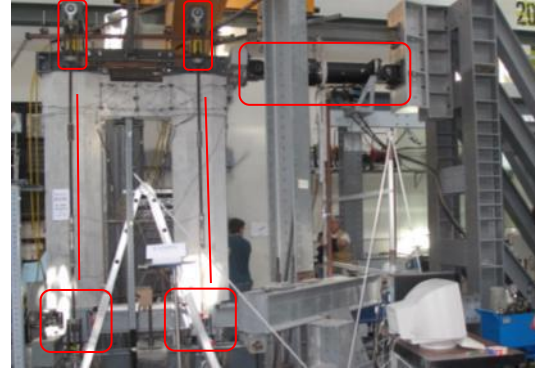
Figure 5.1 – Phase 1 and Phase 2 test setup

For the purpose of accuracy, the development of this experimental layout for assessing the cyclic performance of reduced scale bridge bent piers requires realistic simulation of the forces' transfer that occur during the seismic motion of an equivalent real scale structure. With that in mind, three main aspects were defined as the core guidelines for test setup design:

- Constant *axial loading* on the columns;
- *Free rotation* ability for simulation of curvature inflexion points due to moment symmetry simplification;
- Application of the *lateral loading* with respect to the expected interaction between bridge decks, bearings and the piers;

In order to address specific issues related to each of these topics, separate discussion is promoted in the following sections.

5.1.1.1.   Axial Loading

The applied type to a bridge pier is mostly caused by the dead weight of the bridge deck and associated permanent loads, which remain constant for the duration of any seismic event. With that in mind, keeping constant axial load in the test specimens is paramount, as it is well known that axial load variations affect the behavior of cyclically loaded columns. On single column structures, it is common to use vertically placed hydraulic actuators to compress the element body, possibly including some type of rotation or sliding enabling device designed to accommodate the pier head displacements (e.g. Delgado *et al.* (2009), Rodrigues *et al.* (2013)). More importantly, when that issue is accounted for, the vertical deformations on the columns are mainly due to the initial compression, while during lateral deflection the overall variation of

axial deformation is negligible. Therefore, significant axial load variations are also not expected.

On laterally loaded bent piers, the structural system may require different handling of that problem, since individual element deformations can be critical for keeping constant axial load. As seen in Chapter 2, the most common configuration associated with bent piers relates to girder bridges, or equivalent deck layouts that provide a wide support length for good transverse load distribution. The bent systems also usually represent a strong beam and weak column design, enabling nearly rigid beam behavior. In that case, many authors opt to study individual beam column joints (*"T"* or *"knee"* joints), as opposed to studying complete bents, since capacity design reinforced beams ensure similar behavior between all of the vertical elements. Nonetheless, when the complete pier is considered, dead-load application on test specimens can be performed in different ways, depending on the laboratory features, budget and purpose of the study:

- ▪ *Including deck masses in the test setup*: This approach can be adopted by including correctly placed and/or scaled external masses on top of the bent (Figure 5.2 – a)), or by constructing equivalent deck structures (Figure 5.2 – b)). It has the clear advantage of enabling the actual interaction between superstructure and substructure, with the column axial load variations determined by the geometric and material properties of the bent, as well as the loading pattern. It is the most accurate experimental simulation of axial loading conditions, especially suited for dynamic shaking table tests. On the other hand, the resources and budget required to establish this type of setup are considerable, and often impractical, for the purpose of most experimental studies.

a) Mostafa *et al.* (2004)   b) Pantelides and Gergely (2008)

Figure 5.2 – Test setup examples including deck masses

- ▪ *External prestress application*: This approach is generally more frequent in quasi-static cyclic loading tests. One option is to use hydraulic jacks in

conjunction with prestress rods to continually apply pressure on each column (Figure 5.3 – a)). Another one is to globally prestress the whole structure, using a large beam or similar structure on top of the bent frame to enable a wider distribution of the vertical load (Figure 5.3– b)). It is a testing layout that occupies a larger space, but generally requires fewer resources (such as jacks or prestress rods), while also being faster to install regarding multiple column structures.

a) Mclean *et al.* (1998)   b) Hose and Seible (1999)

Figure 5.3 – Test setup examples including vertical prestress for axial load application

The bent system studied in this work is constituted by strong columns, which are enhanced by the coupling action provided by the short beam. In this case (as discussed in Chapter 4) the shear forces transferred through the coupling beam lead to the occurrence of significant variations of the total axial load that is mobilized through the columns, which are dependent of the lateral displacement of the structure and, thus, should be taken into account.

Considering the resources available at the LESE laboratory and the scope of quasi-static cyclic loading tests, an external prestress solution was the most suited for this problem. Therefore, a system similar to that of Figure 5.3 – a) was designed. Two *Dywidag* 26WR threadbars and a 500 kN jack (*Enerpac* CLRG-502) enabled the individual application of targeted prestress loads of 300 kN per column (which is around the dead-weight per column of 4613 kN calculated earlier, scaled down to a 1:4 reduced value). Furthermore, to keep the overall external forces as constant as possible, while accounting for the beam shear induced axial load variations, the jacks were kept under force-controlled hydraulic pressure, involving real time adjustments for the purpose of maintaining the intended threadbar stress level.

In addition, a load distribution beam, made of reinforced UNP200 steel shapes was also adopted (Figure 5.4 – a)), including two hinged devices on each edge to enable the connection and simultaneous tensioning of both threadbars by the same jack, according to the red highlight in Figure 5.4 – b). A similar hinged device was also installed on the other end of the threadbars,

enabling them to follow the rotation of the columns to maintain the direction of their respective axial load forces.

a) Load distribution reinforced beam   b) Hinged device at the beam edge

Figure 5.4 – Axial loading system details

Finally, it must be acknowledged that the hydraulic flow capacity of the jacks and the corresponding power rig is naturally limited, which also limits the rate at which the strain increments due to shear can be compensated. Because of that, even though this system aims to provide real-time adjustments to the threadbars stress level, small variations can still occur if the rate at which those vary differs from the rate at which the system is capable of adjusting. With that in mind, strain gauges were installed on all prestress bars for monitoring purposes.

5.1.1.2. Free Rotation

According to the design concepts previously discussed on Chapter 4, a decision was made to only study half structures, taking advantage of the null moment point expected from the lateral loading of the bent pier. In order to fulfill that requirement, curvature inflexions should be simulated with free rotation constraints at the column bases, while also accommodating increasing intensity pier-head lateral displacements and the resulting high shear and axial load levels. For that purpose, column bases were bolted against free rotation steel plates, placed over mechanical hinges (Figure 5.5) designed for multi-directional (vertical and horizontal) shear stress states within the expected axial and shear loading variation thresholds.

a) Top view   b) Side view
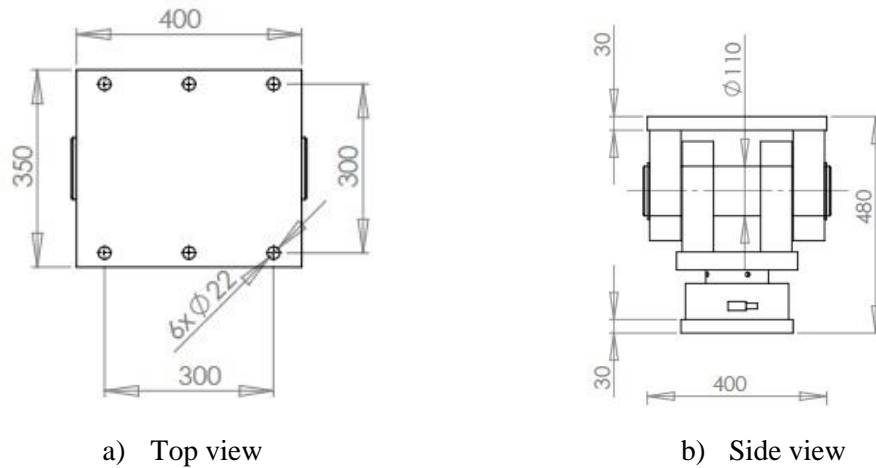
Figure 5.5 – Mechanical hinge and free rotation steel plates

This system provides free rotation ability to each of the columns, enabling the rotation of their vertical axes, which is also accounted for in the axial loading system. In that regard, aiming to prevent undesired eccentric moments and/or second order effects, the threadbar rotation centre should be the same as the column's, enabling equivalent movement and concentric axial loads. That was not possible to implement, however, since the mechanical hinge was not designed to include a connection for anchoring the threadbars. Therefore, a compromise solution was adopted, involving the attachment of the bottom hinged devices in the shortest possible vicinity, which was just below the mechanical hinges, as illustrated in Figure 5.6 – a). As a consequence, the column and threadbar axial loads become increasingly misaligned as pier-head displacements increase, as illustrated in Figure 5.6 – b). Nonetheless, for the horizontal displacement level associated with the actuator stroke (150mm), the misalignment would be around 2cm on the base of the columns, leading to a maximum eccentric moment of 6 kN.m. That value corresponds to less than 2% of the maximum expected moment, and therefore was considered negligible for the purpose of this study.
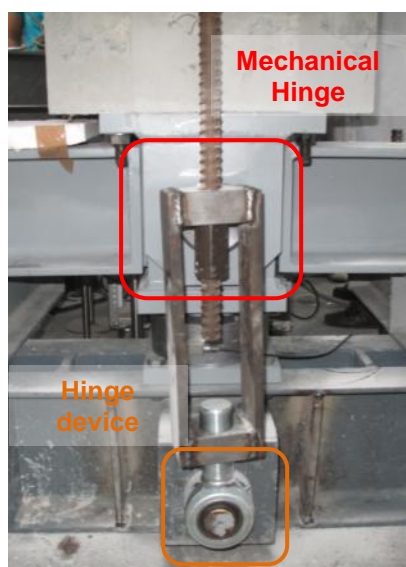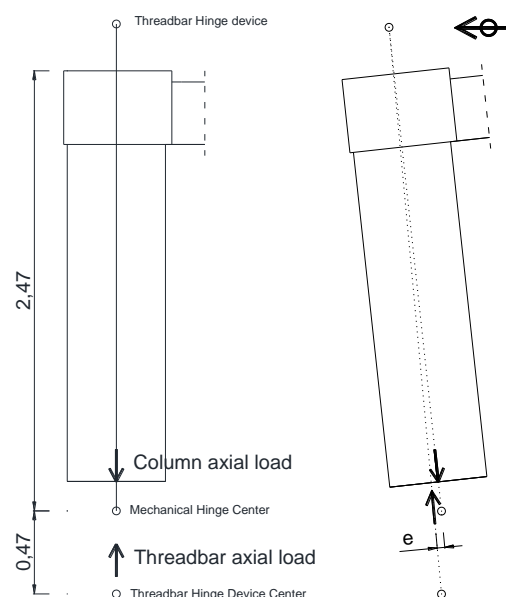
a) Setup detail   b) Eccentric moment from lateral loading

Figure 5.6 – Mechanical hinge and threadbar cap relative positions

5.1.1.3. Lateral Loading

The application of a lateral force aims to represent the action of the inertia forces developed during seismic events (namely from bridge deck masses), which are transmitted to the piers through the associated bearing devices. According to Marioni (2006), in HSRL structures elastomeric devices are generally not considered, with the adopted bearing schemes usually revolving around a combination of pot-bearing devices and shear keys in order to provide fixed connections between decks and piers. Therefore, since seismic forces are applied at the pier head level, aiming for accurate experimental simulation involves establishing a similar shear interaction between the hydraulic actuator and the test specimens.

In single column piers, the seismic force is fully transferred at the same location, and experimental simulations only require that actuator heads are firmly attached to the targeted loading point. Typical applications generally require the use of steel pieces bolted around the column for enabling the pier head movement, as highlighted in the examples of Figure 5.7.
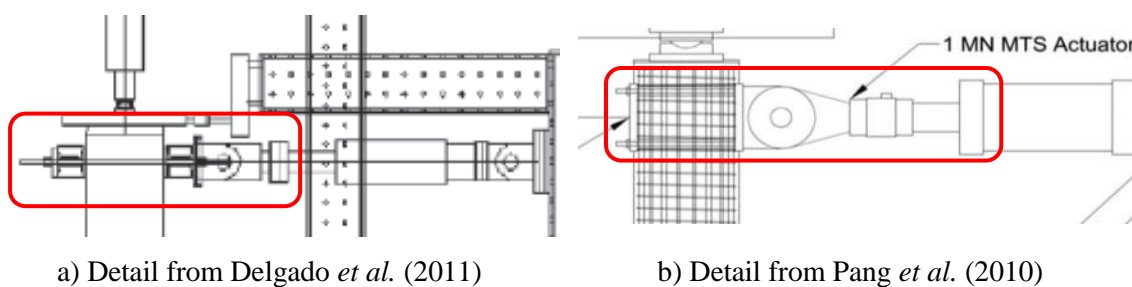
a) Detail from Delgado *et al.* (2011)   b) Detail from Pang *et al.* (2010)

Figure 5.7 – Lateral load application examples for single columns

Considering the geometry of this double column bent, however, replicating the previously described procedure is of increased difficulty, since the full seismic force developed at the deck level is transferred to two columns instead, meaning that the experimental setup should aim to provide simultaneous loading of both vertical elements. Using two *in sync* actuators (one for each column) under displacement control conditions could be possible if their respective loading rates were kept low enough, but that option was not eligible due to the availability of only one reaction frame for a single actuator. With that in mind, the only suitable solution considered application of the lateral load on a single column, while ensuring displacement compatibility over the column heads. For that purpose, the mechanical device presented in Figure 5.8 was designed for attachment to both columns, maintaining constant displacement between them for the expected load levels.

| a) 3D view | b) Overall placement in the setup |
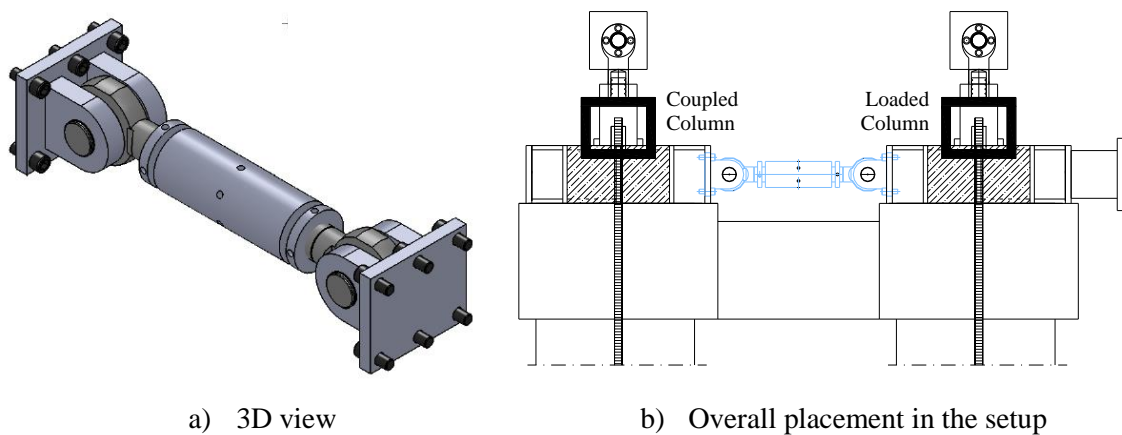
Figure 5.8 – Displacement compatibility device

Despite that, preliminary numerical simulations revealed that forcefully coupling the column heads actually increases the overall bent pier lateral stiffness, since the columns rotate around the base mechanical hinges, and the coupled points on the pier heads are vertically displaced while keeping constant (but not always horizontal) distance between them, as illustrated in Figure 5.9 - a). This means that a constant length device cannot actually ensure equal displacements between the two columns without being subjected to non-negligible axial strains, which may be a source of additional stiffness due to creating an artificial displacement constraint to the natural rotation of the column heads. This is further illustrated in Figure 5.9 -
 b), where reaction force results from a monotonic plane stress analysis (using the same modeling strategy that will be presented in Chapter 6) while accounting for constant distance between column heads are plotted against the imposed displacements at the loaded column. It can be observed the occurrence of a negative reaction force at the coupled column head, meaning that the constant width constraint was actually limiting the natural movement of the latter and, consequently, increasing the overall load applied at the other column. Eventually, on a real setting this issue might be less noticeable due to the unavoidable flexibility of mechanical

connections (gaps and slip between bolts and screws), contrasting with the rigid limitations imposed by a numerical constraint. Nonetheless, the possibility of affecting the experimental results and undermining the respective conclusions led to the decision of completely avoiding the use of the displacement compatibility device.

a) Movement during lateral displacements   b) Horizontal reaction forces
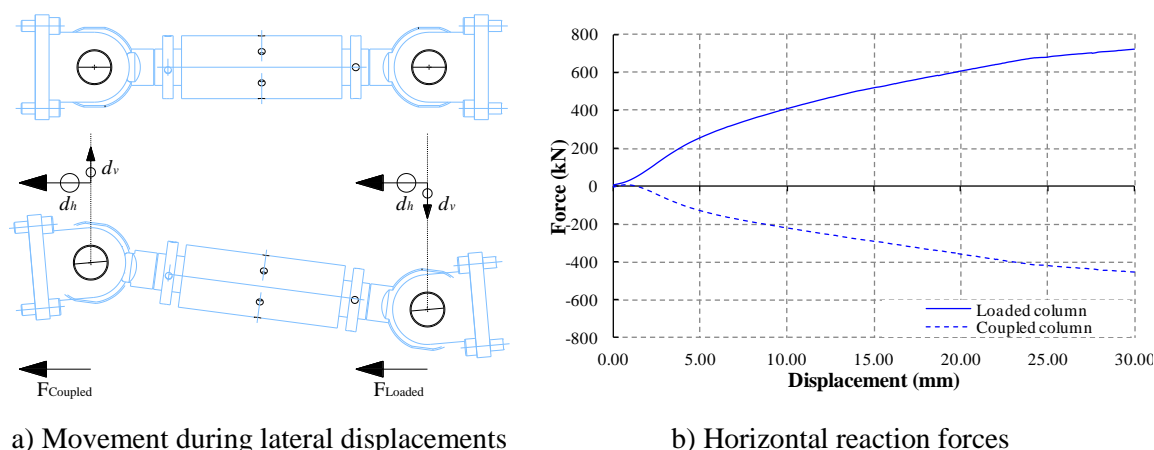
Figure 5.9 – Numerical simulation including constant displacement between coupled points

With that in mind, despite this seeming to be the most suitable solution to avoid disturbing the natural behavior of the bent piers, it inevitably leads to differences between the displacements recorded at each column. The magnitude of those differences is dependent of the damage accumulated in the beam, since that is the element through which the lateral load is transmitted from the loaded column to the coupled column, and also dependent of the load application point. Assuming a sideways loading procedure, two options were established:

- Application of the lateral load at the beam horizontal axis level;
- Application of the lateral load through shear interaction at the column head;

In a real bridge setting, horizontal forces are transferred through the bearings mainly by shear, at the pier head surface. If the beam-column nodes are small, it is generally safe to consider the load applied at the beam horizontal axis level because the distance between that point and the pier head surface is also small, therefore no significant changes in the overall force distribution are expected. This would be the preferable option for experimental implementation (similarly to single column procedures (Figure 5.7)), since it enables easier displacement monitoring and load application, by attaching the actuator head directly to the column.

However, that simplification may not be reasonable for the present case, considering the large dimensions of the test specimens and, particularly, of the beam-column nodes, since there is a non-negligible difference between the horizontal beam axis and the column head surfaces, which may result in considerably different distributions of internal force. Figure 5.10 illustrates a possible strut-and-tie representation of the force distributions inside the beam-column node for

positive (left) and negative (right) moments where it is clear that applying the load at beam axis level could disturb the internal force distribution and result in a different stress state. Considering the importance of the beam-column node behavior for the overall performance of these structures, a decision was made to establish shear induced loading, in order to represent the bridge pier seismic loading scenario as realistically as possible.
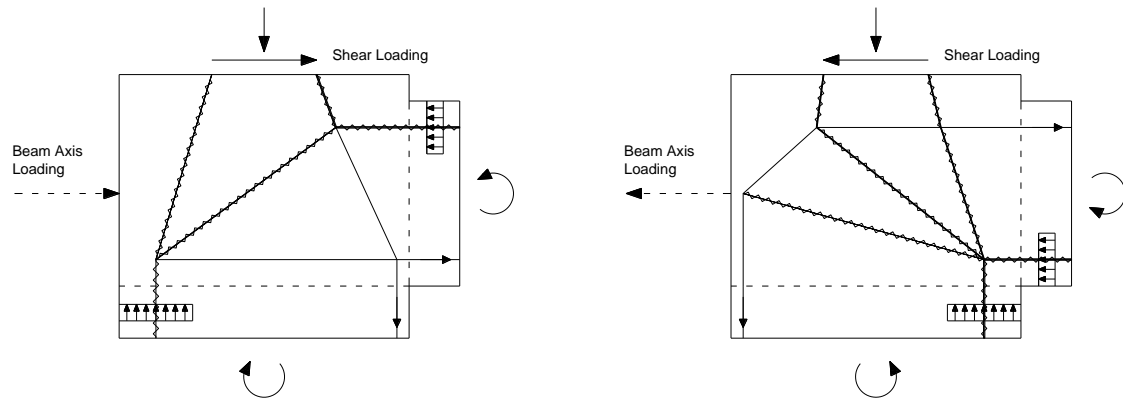
Figure 5.10 – Strut-and-tie representation of beam-column nodes under moment loading

With that in mind, a system had to be designed for appropriate shear loading of the specimens. The adopted solution was constituted by sets of two HEB200 steel shapes welded together and reinforced with additional ribbing plates, which were placed on the top of each column (Figure 5.11 – a)). That steel grid structure also included eight holes for the same number of M20 rods (designed for working at 50% of their design shear strength and considering an embedment length of 0.20m into the column) for fixation and shear loading purposes, according to the illustration presented in Figure 5.11 – b).
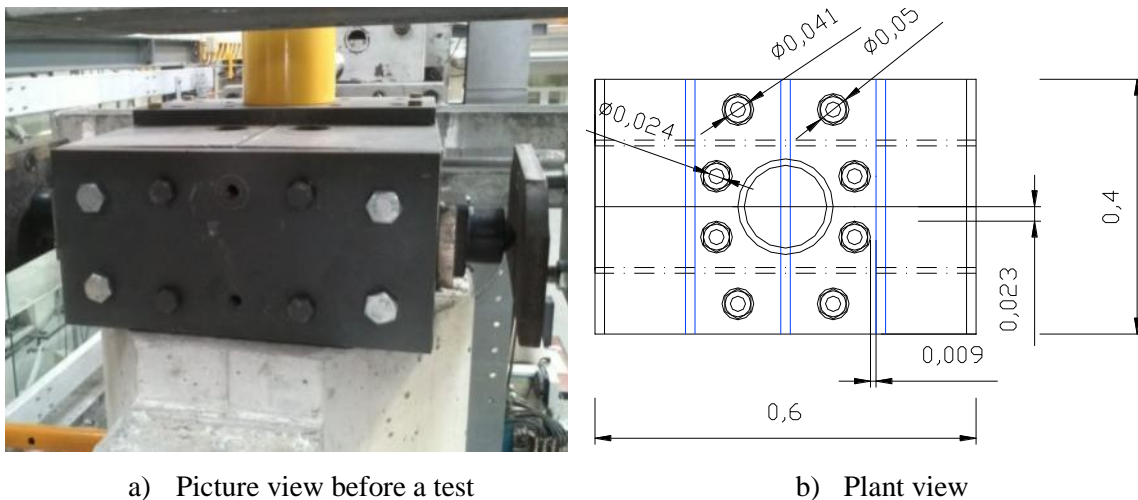
a) Picture view before a test   b) Plant view

Figure 5.11 – Lateral shear loading system

Finally, the lateral loading system required the establishment of two external connections for force transfer to the reaction frame: a fairly self-explanatory one for the actuator, and an

additional one for a force retention mechanism on the base of the experimental setup. In that regard, while the application of the lateral load on the test specimens has already been thoroughly discussed, appropriate anchoring for the whole structural system is also a concern. In particular, since free rotation in the column bases was expected by design, footings could not be considered to receive and transmit the loads to the strong slab of the laboratory.

Instead, a base supporting system for the bent pier specimens had to be developed to provide appropriate reaction against both vertical and horizontal loads, including connections to the vertical load cells and the prestressed threadbar connections, according to Figure 5.6 – a). Furthermore, accurate readings on the vertical load cells require that mostly axial displacements are recorded on their sensitive contact surfaces, but that is difficult to enforce when reaction forces are expected to rotate in correspondence with the pier drift. In order to address that issue, the force retention system installed on the base of the experimental setup (illustrated in Figure 5.12) consisted of an assembly of several steel beams connecting the column bases to the reaction frame just above the load cells. The purpose of this mechanism was to provide high stiffness to lateral movements, aiming to redirect the shear force from each column back to the reaction frame, avoiding significant rotations at the contact surface on the load cells underneath and, therefore, enabling more accurate readings.

a) Threadbar connections through the slab

b) Picture during assembly
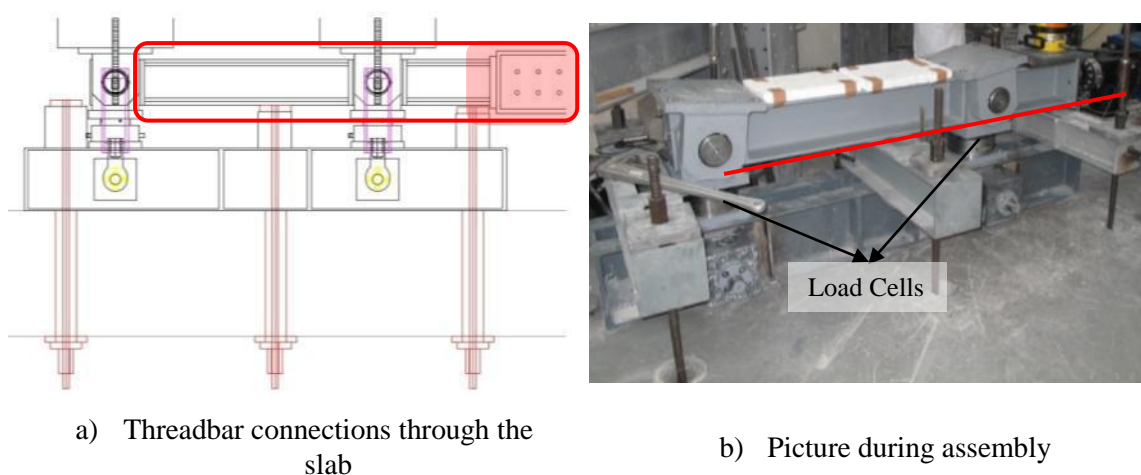
Figure 5.12 – Base supporting system with force retention beams

In addition, the first test (SP_M01) was performed using a rigid connection between the different steel beams along the force retention system (highlighted with the red shade within the red rectangle in Figure 5.12 – a)). That solution proved to be inefficient, causing the occurrence of shear/bending in addition to the expected axial load. In order to address that issue on the subsequent tests, the rigid connection was replaced by two mechanical hinge connections, illustrated in Figure 5.13 – a) and b). Preliminary laboratory tests showed that, with this improved setup version, no shear forces were transmitted through the force retention system to the reaction frame, and further data recorded during the actual tests showed that peak forces at

this level were always above 75% of the horizontal load applied at the top of the piers, evidencing the role of this force retention system as the main horizontal load reaction element.

a) Hinged connection to the supporting system during preliminary test

b) Hinged connection to the reaction wall

Figure 5.13 – Hinged force retention system

5.1.1.4. Out-of-Plane Bracing

As described, this experimental setup was developed to analyze the behavior of the bent pier under lateral seismic loading, representing the corresponding *"in-plane"* motion. The adoption of a testing layout especially suited to provide uniaxial demand was presented, but a bracing system was also prepared to accommodate eventual out-of-plane deformations. That possibility is a concern because it is impossible to achieve perfect symmetry in the test specimens along the loading plane. On that regard, not only the internal issues that may arise from a difficult concrete casting procedure (e.g. bad vibration, unequal concrete cover depths and/or rebar layouts) are worthy of mention, but the assembly of each test specimen on the experimental setup can also relate with slightly unsymmetrical loading (mainly due to unequal connection gaps) of both columns.

The impact of these issues on the overall behavior of a single pier testing system is generally perceived to be negligible and easily controlled by the testing setup. However, in the presented setup only the displacement of one of the bent pier columns is controlled by an external device, as the coupled column is dependent of the forces transferred through the beam. Within that context, it is understandable that with increasing progress of structural damage, an eventual small initial asymmetry can lead to larger differences along the loading plane and, therefore, increased possibility of out-of-plane deformations.

With that in mind, a bracing system was prepared around the column heads and coupling beam, aiming to provide increased stiffness against such movement. It was constituted by a set of several steel elements connected to a reaction wall, including a rolling system to enable

uniaxial longitudinal displacements while reacting against transverse out-of-plane displacements. This feature is further illustrated in Figure 5.14, highlighting the rolling system inside the red rectangle shape.

Figure 5.14 – Out-of-plane bracing system

5.1.1.5. Loading Protocol

The tests involved the application of uniaxial cyclic loading under displacement controlled conditions. Two loading displacement histories were considered: LH1 for the first test, SP_M01, while LH2 was applied for all the remaining tests, both characterized in Table 5.1 in terms of drift, and plotted in Figure 5.15 – a) and Figure 5.15 – b), respectively.

Table 5.1 – Loading displacement histories characterization – Phase 1 and 2

LH1				LH2			
Drift (%)	Actuator Displacement (mm)	Cycles	Load rate (mm/s)	Drift (%)	Actuator Displacement (mm)	Cycles	Load rate (mm/s)
0.05	1.15	1	0.2	0.05	1.20	1	0.2
0.10	2.30	3	0.2	0.10	2.40	1	0.2
0.19	4.37	1	0.5	0.20	4.80	3	0.5
0.29	6.67	3	0.5	0.30	7.20	1	0.5
0.38	8.74	1	0.5	0.40	9.60	3	0.5
0.48	11.04	3	0.5	0.50	12.00	1	0.5
0.72	16.56	3	1.0	0.75	18.00	3	1.0
0.96	22.08	3	1.0	1.00	24.00	3	1.0
1.44	33.12	3	1.0	1.50	36.00	3	1.0
1.92	44.16	3	1.0	2.00	48.00	3	1.0
2.40	55.20	3	1.0	2.50	60.00	3	1.0
2.88	66.24	3	1.0	3.00	72.00	3	1.0
3.35	77.05	3	2.0	3.50	84.00	3	1.0
3.83	88.09	3	2.0	4.00	96.00	3	1.0
4.31	99.19	3	2.0	4.50	108.00	3	1.0
4.79	110.21	3	2.0	5.00	120.00	3	1.0

a) LH1   b) LH2
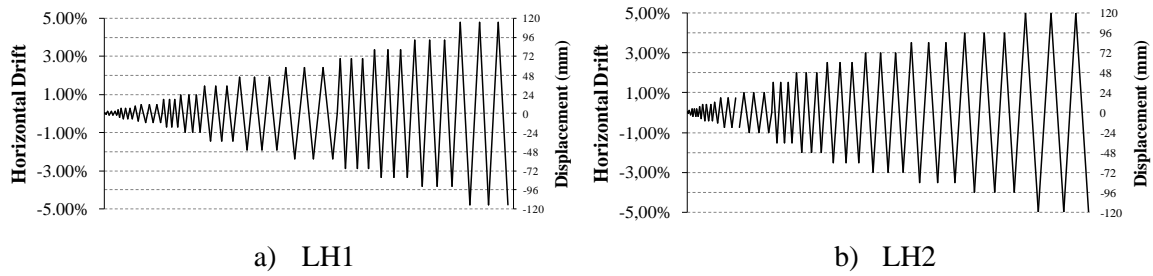
Figure 5.15 – Loading displacement histories

The differences between the two were not significant, and mainly relate to some minor adjustments performed in light of observations made during the first test (using LH1), namely:

- Reducing the loading rate on the larger displacement cycles;
- Adjusting the occurrence of repeated loading cycles only after cracking begins;
- Readjustment of the target drift values;

With respect to the first of the previous adjustments, it resulted from the observation of axial load variations of ±50 kN on the last few cycles, caused by insufficient jack hydraulic flow for real-time compensation of the axial strains caused by the cyclic displacement loading rate of 2.0 mm/s. The second adjustment, as mentioned, was aimed at enabling the occurrence of the repeated loading cycles to the 0.20% to 0.40% drift levels, since degradation is only expected to occur with the onset of cracking (which was observed to occur at that stage). The last adjustment mainly intended to adapt the target displacement levels for provision of drift values more suited for presentation.

Taking into account all of the latter, it must be acknowledged that a direct comparison between the SP_M01 test and all the other tests is innately hindered by the differences in their respective loading protocols and test setup. Despite that, a conscientious analysis and interpretation of experimental results should still enable comparison of the overall behavior and main parameters.

5.1.1.6. Monitoring Layout

A set of Linear Displacement Voltage Transducers (LVDTs), complemented with a few Draw Wire Transducers (DWT, potentiometer based) were used to monitor the displacements of several points in the structure, and two tiltmeters were placed on the top of the column heads to record beam-column node rotations. In addition, strain gauges were also installed on the threadbars, as previously discussed, as well as on the main beam of the force retention system, the latter aiming to evaluate bending or shear deformations. Furthermore, imposed loads and reaction forces were recorded by the following:

- Internal load cell (LC) of the horizontal actuator;
- Pressure transducer of the hydraulic jack lifting system;
- External Load Cell 1 (LC1) placed below the southside column;
- External Load Cell 2 (LC2) placed below the northside column;
- External Load Cell 3 (LC3) placed in the horizontal force retention system;

Figure 5.16 presents a full overview of the layout used in this work including all the previously mentioned features, where the digit based numbering scheme refers to LVDTs while LF## refers to DWTs:
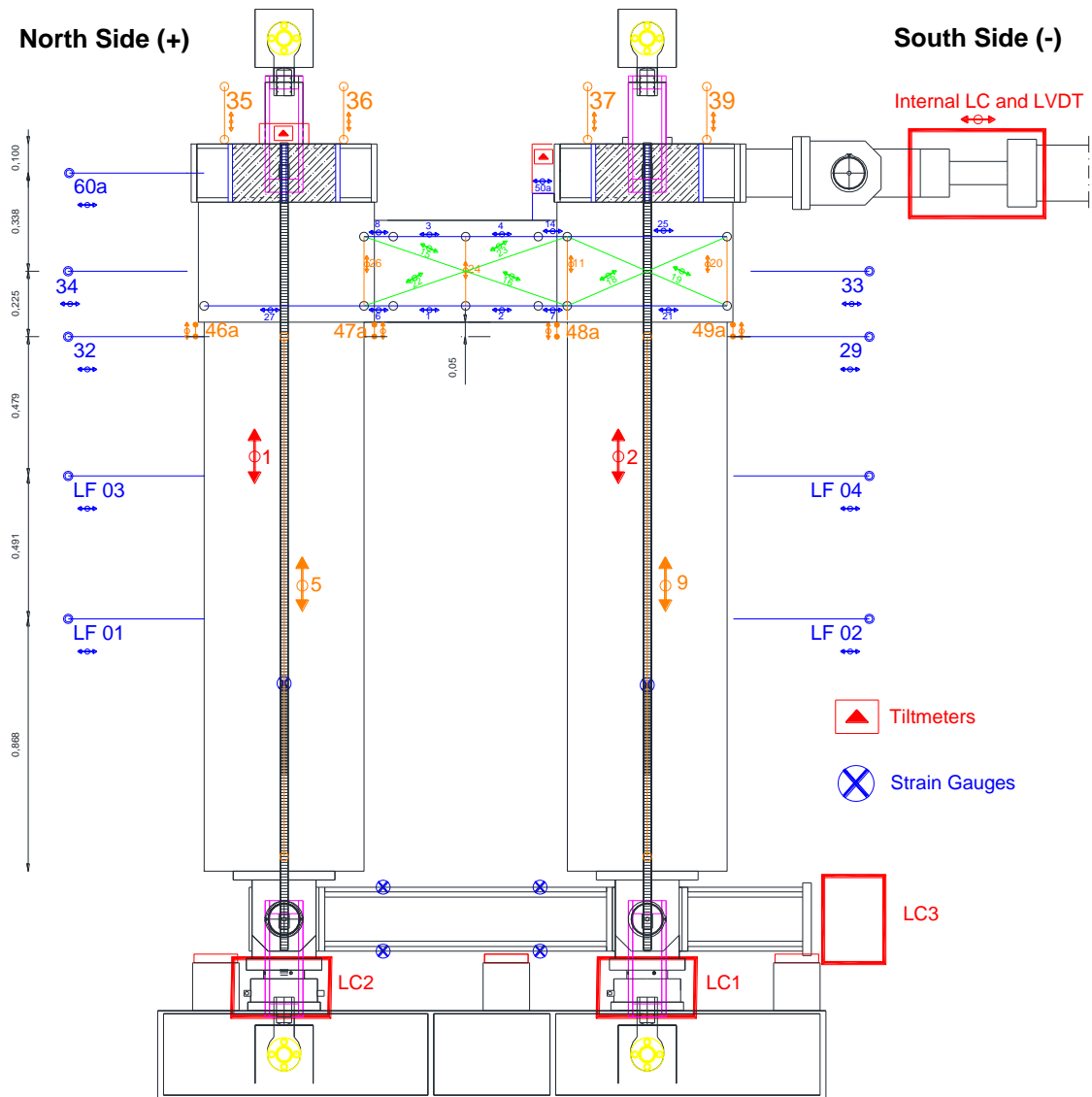
Figure 5.16 – Schematic overview of Phase 1 and 2 monitoring features

5.1.2. PHASE 3 - SINGLE COLUMN TESTS

The test setup assembled for the third phase of this work was adapted from other existing and proven layouts used on previous works at LESE, to the specific conditions of these columns. A general overview of the adopted system is presented in Figure 5.17, including the following:

- 1 horizontal actuator (+/- 500 kN capacity; +/- 150mm stroke);
- 1 vertical jack (500 kN capacity);
- 2 prestress threadbars (*Dywidag* 26WR);
- Reaction frame;
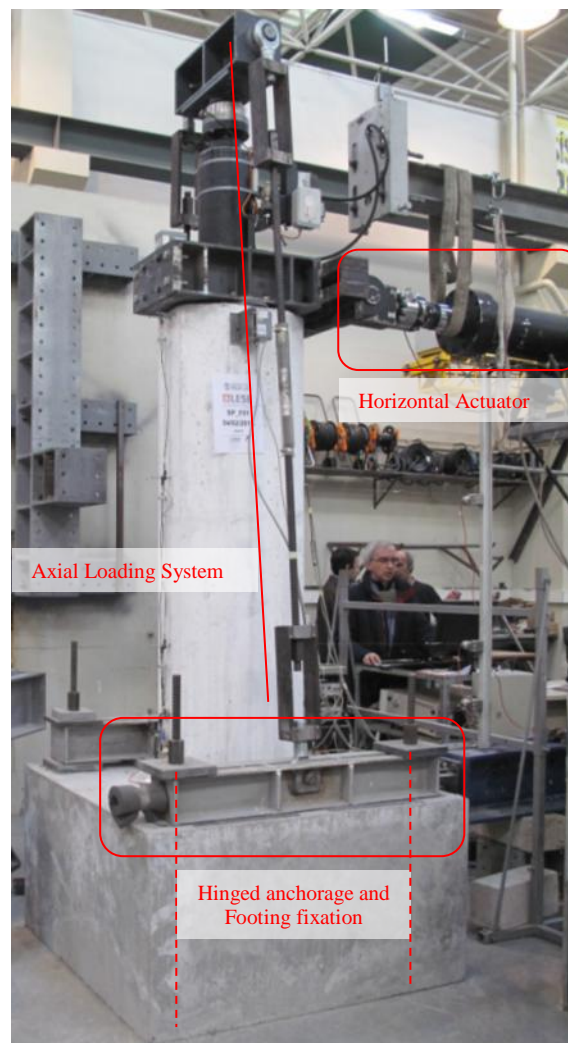
Figure 5.17 – Phase 3 test setup

The lateral loading system of phase 1 and 2, constituted by a horizontal 500 kN capacity actuator and the respective shear load transfer system (Figure 5.11) was installed for this application, as well as the previously used axial loading system (due to its capability to rotate and adjust to large displacements of the pier head) prepared for the target load of 300kN.

However, due to this testing phase focusing on the bottom part of the bent system in study, the elements of the corresponding threadbar hinge device had to be modified. As observed in Figure 5.17, the adopted solution took advantage of the prestress connection used to attach the footings against the laboratory slab, to also provide fixation for steel beams placed parallel to the column, where the hinged anchorages were attached.

5.1.2.1. Loading Protocol

Phase 3 tests were performed under displacement control conditions, involving the application of a displacement history with the same characteristics of LH2 (Table 5.1 and Figure 5.15 – b)), calculated for the displacement levels of the present horizontal actuator level, according to Table 5.2.

Table 5.2 – Loading time-history characterization – Phase 3

LH3			
Drift (%)	Actuator Displacement (mm)	Cycles	Load rate (mm/s)
0.05	0.98	1	0.2
0.10	1.97	1	0.2
0.20	3.93	3	0.5
0.30	5.90	1	0.5
0.40	7.86	3	0.5
0.50	9.83	1	0.5
0.75	14.74	3	1.0
1.00	19.65	3	1.0
1.50	29.48	3	1.0
2.00	39.30	3	1.0
2.50	49.13	3	1.0
3.00	58.95	3	1.0
3.50	68.78	3	1.0
4.00	78.60	3	1.0
4.50	88.43	3	1.0
5.00	98.25	3	1.0

5.1.2.2. Monitoring Layout

This testing stage was mostly focused on recording overall lateral displacement profiles for the single columns, and analyzing the behavior of their respective foundation-to-element connections. With that in mind, a simple layout of LVDTs was adopted along both sides of the whole column height, involving a concentration of recordings near the expected plastic hinge region for the two following specific output results:

- Lateral displacements – horizontal LVDTs and DWTs;
- Longitudinal deformations (crack openings) – vertical LVDTs;

Figure 5.18 illustrates the recording layout just for the North side of the columns, although the South side includes equivalent instrumentation.

a) Front view (horizontal displacement transducers)

b) Side view (vertical displacement transducers)
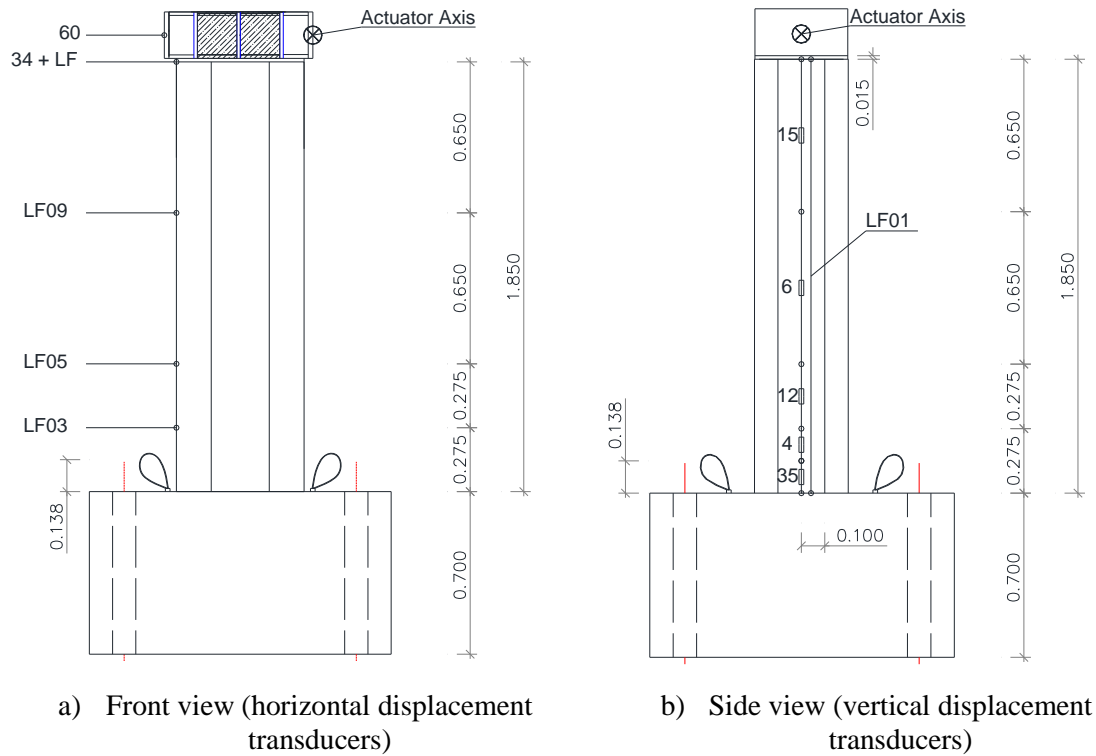
Figure 5.18 – Schematic overview of Phase 3 monitoring features and overall dimensions

5.2. EXPERIMENTAL RESULTS – BENT PIER TESTS

5.2.1. PHASE 1 OBSERVATIONS

The focus of this section regarding the results of Phase 1 is to present and discuss the experimental evidence related to the damage progression and failure of each specimen. The force – drift curves that are addressed were defined for the internal displacement of the actuator, according to Figure 5.16. Furthermore, a collapse threshold corresponding to a reduction of 20% of the peak force was also defined (Park and Ang (1985)) for the purpose of analysis and discussion, although tests continued until complete failure of the specimens, determined through visual inspection. In addition, the values recorded for lateral force and beam shear are also presented and compared with predictive estimates calculated using the real material properties presented in Chapter 4. For this purpose, the equilibrium model represented in Figure 5.19 can be used to determine the lateral peak force, assuming overall capacity governed by column bending or by beam shear. In the present case the latter was considered (critical beam shear), according to experimental observations, enabling the calculation of the lateral force for two scenarios:

- *Yielding*: Peak strength assumed at yielding of the main beam reinforcement;
- *Ultimate*: Peak strength assumed after hardening of the beam reinforcement;
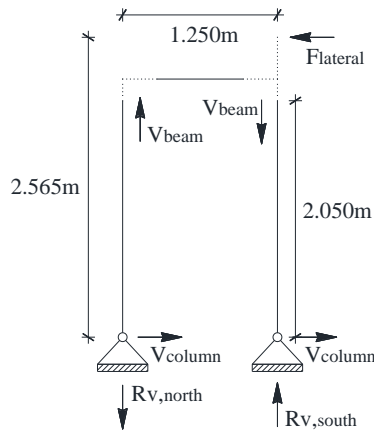
For critical beam shear:

$$F_{lateral} = \frac{V_{beam} \times 1.250}{2.565}$$

For critical column bending:

$$F_{lateral} = \frac{M_{column}}{2.050} \times 2$$

Figure 5.19 – Equilibrium model

Due to the way the lateral load is applied to the structure, some level of response asymmetry is expected. In fact, the axial load that is transmitted from the loaded column to the coupled column is approximately $\frac{F_{lateral}}{2}$. However, for the positive (pushing) loading direction it is carried through compression of the coupling beam, while for the negative (pulling) direction it is carried through tension. The effective loading of the structure is then dependent of the level of damage incurred in the beam, and it may impact the stiffness of the coupling action differently depending on whether the element is compressed or under tension. For that reason, predictive estimates according to the equilibrium model are performed only for the positive loading direction.

5.2.1.1. SP_M01 specimen results

The cyclic force-drift curve for this specimen is illustrated in Figure 5.20, where the collapse threshold is also identified, occurring at the 2.50% drift level on the positive loading direction. In addition, there is a clear distinction between positive and negative loading directions, which causes a difference in the peak force level recorded on both, of around 16%. Regarding this subject, the lateral force estimations are also illustrated in Figure 5.20:
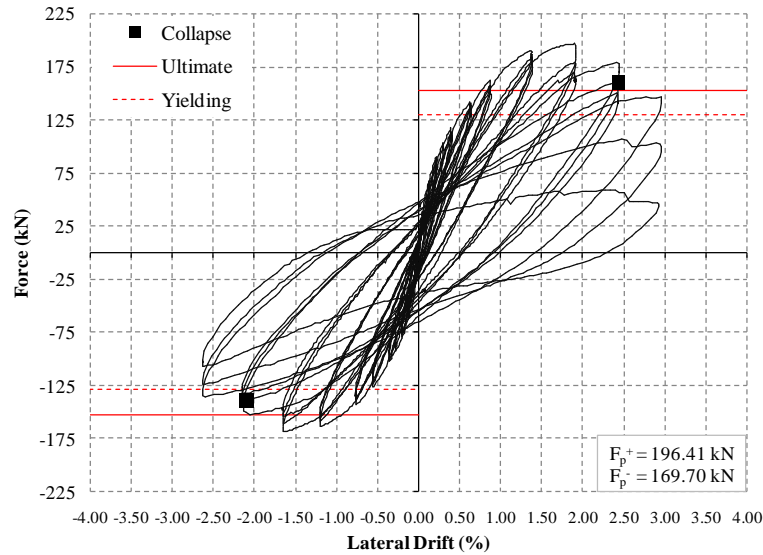
Figure 5.20 – SP_M01 force-drift results

As it is possible to observe, the experimental peak force overtakes the values calculated using the equilibrium model presented earlier by almost 30%, considering the shear capacity of the beam as defined by EC8 (equation 4.9). This can be further analyzed in Figure 5.21, which illustrates a comparison between the theoretical shear capacity of the beam calculated for the *Yielding* and *Ultimate* scenarios and the peak value recorded in the experimental test, determined by subtracting the axial load carried by the threadbars from the vertical reactions. Again, the values calculated using the bi-diagonal design model are both smaller than the experimental value, although with smaller difference, around 23% for the *Yielding* scenario and 4% for the *Ultimate* scenario.

In light of these results, there is the possibility that the additional vertical reinforcement provided for crack control is also contributing to the shear capacity of the beam, which is not accounted for in the coupling beam design model nor in these calculations, and could help explain the larger capacity of the experimental model. Furthermore, the shear capacity of the EC8 design model is governed by the tensile force on the steel rebars, and no additional strength provision is considered through concrete alone, which may be a conservative evaluation.

It should also be noted that the experimental capacity may, in fact, have also been artificially overestimated by non-monitored shear forces transferred through the retention system, since this test was performed with the rigid connection (Figure 5.12 – a)). Unfortunately, the first version of the test setup was not adequately prepared to deal with that issue, therefore it was not possible to understand how much did it influence the results.
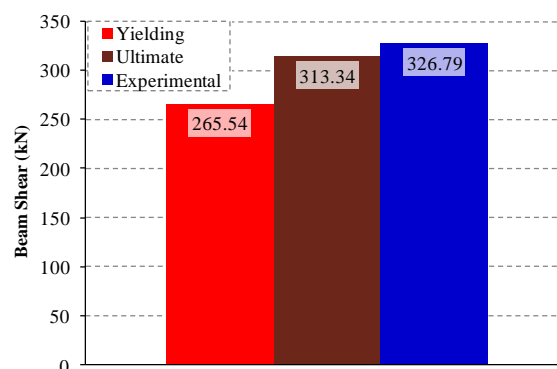
Figure 5.21 – SP_M01 Beam shear: comparison of experimental and theoretical estimates

The observed failure mode of the specimen can be attributed to the occurrence of "sliding shear" on the interface between the beam and the north side column, and a relatively undamaged structure can be observed on other locations, as illustrated in Figure 5.22.
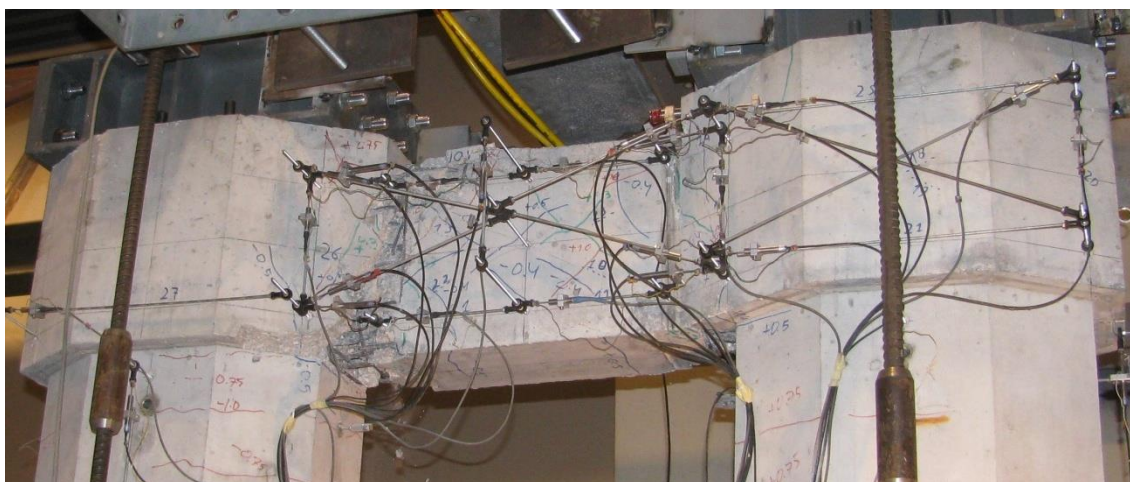
Figure 5.22 – SP_M01 after testing

The cracking pattern associated with this specimen also showed significant differences between the beam and the column. The first cracks appeared in the beam around 0.20% drift, with inclined orientation typical of shear, and new cracks continued to form up until 1.00% drift. Afterwards, that process stabilized and only crack width increases could be detected. This can be observed in Figure 5.23, for a sequence of 0.20%, 0.50%, 1.00% and 2.50% drift.
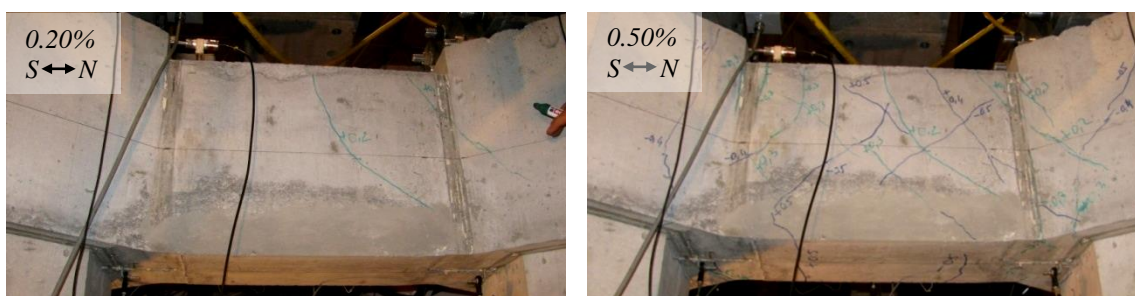
Figure 5.23 – SP_M01 Beam cracking pattern
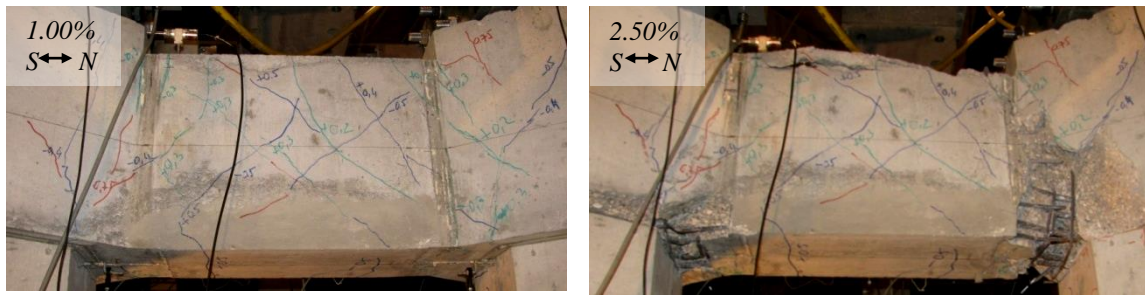
Figure 5.23 (cont.) – SP_M01 Beam cracking pattern

This contrasts with what was observed in the columns, which is illustrated in Figure 5.24, where cracks developed only after 0.75% drift and stabilized at 1.00% drift, displaying a regular distribution that seemed to closely follow the distance between transverse reinforcement stirrups (0.10m) until collapse.
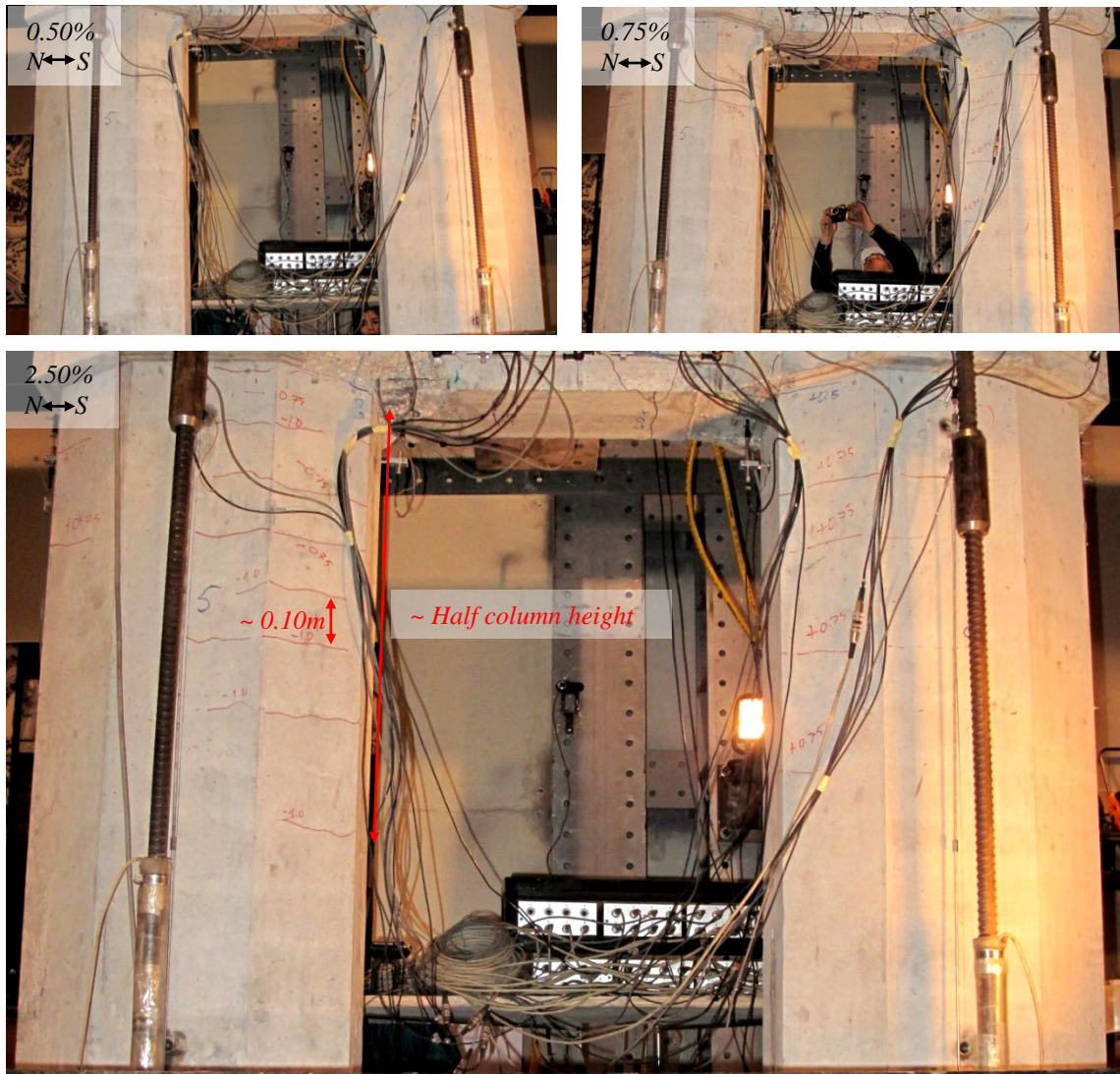
Figure 5.24 – SP_M01 Column cracking patterns

Furthermore, the damage taken by the structure was mostly localized in the beam and, more specifically, at the interface sections with the beam-column nodes. In fact, the first signs of spalling and concrete crushing occurred at those locations for 2.0% drift, on the enlargement cover cap of the nodes, while the rest of the mid-section of the beam still showed a relatively low damage progression. As far as it could be observed, the degradation of that interface caused a sudden localized loss of shear strength that ultimately led to failure by sliding of the beam over the column in the subsequent displacement cycles, as is illustrated in Figure 5.25.
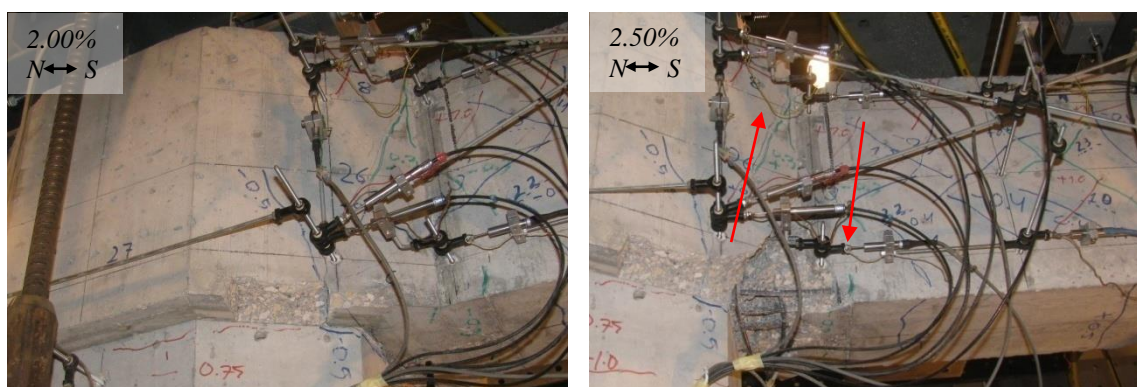
Figure 5.25 – SP_M01 Beam-Column node interface

This is also attributable to the low slope angle (~25º) of the diagonals, resulting in reduced efficiency of the axial force carried through the rebars, which increases the reliance of the structure in achieving stable compressive struts within the concrete. Since the development of a large crack (with opening widths of around 1.50 mm at 1.00% drift, 3.70mm at 2.00% and 9.95mm at 2.50% were recorded) at the interface sections removes that ability, failure took place thereafter.

5.2.1.2.   SP_M02 specimen results

The cyclic force-drift plot for this specimen is illustrated in Figure 5.26, exhibiting a slightly pinched response, as well as the collapse threshold, which occurs at the 3.00% drift level. In that regard, a large force asymmetry of nearly 25% was observed. Lateral peak force estimates are also included in Figure 5.26, calculated for the *Yielding* and *Ultimate* scenarios using the rhombic truss design model of equation 4.10 but disregarding the influence of the compressions parallelogram (*Vc* term on the same equation) since, for beam shear critical cases, the total compression carried through the concrete is influenced by the force applied by the actuator and, therefore, is not known beforehand. Thus, although both are lower than the experimental value, the *Ultimate* scenario provided a closer approximation, within 8% difference.
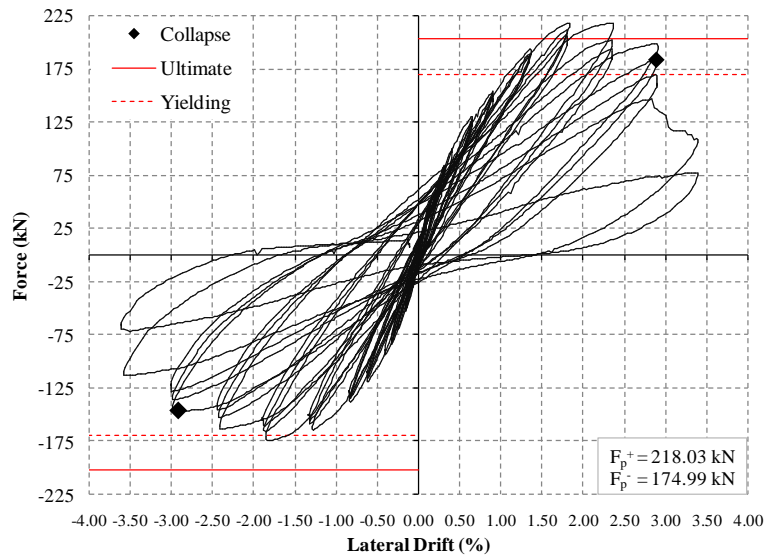
Figure 5.26 – SP_M02 force-drift results

Similar differences can be observed when theoretical shear capacity of the beam (dependent of reinforcement) is compared with the peak experimentally recorded shear value, as seen in Figure 5.27, where a relative difference of around 6% for the *Ultimate* scenario can be found. This seems to indicate that, just like in the SP_M01 case, the influence of the compressions (the previously mentioned *Vc* term) carried through the concrete is non-negligible.
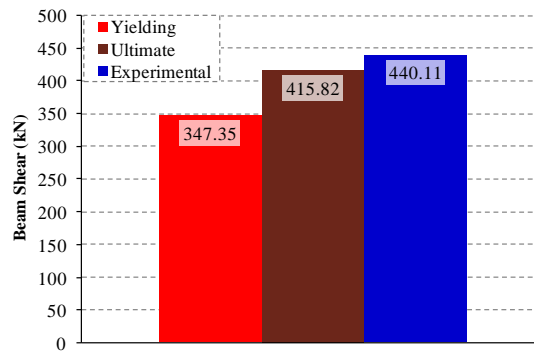
Figure 5.27 – SP_M02 Beam shear: comparison of experimental and theoretical estimates

Failure of this specimen can be attributed to the occurrence of "sliding shear" on the interface between the beam and the north side column, but with increased damage spread. A picture of the final stage of the test is included in Figure 5.28.
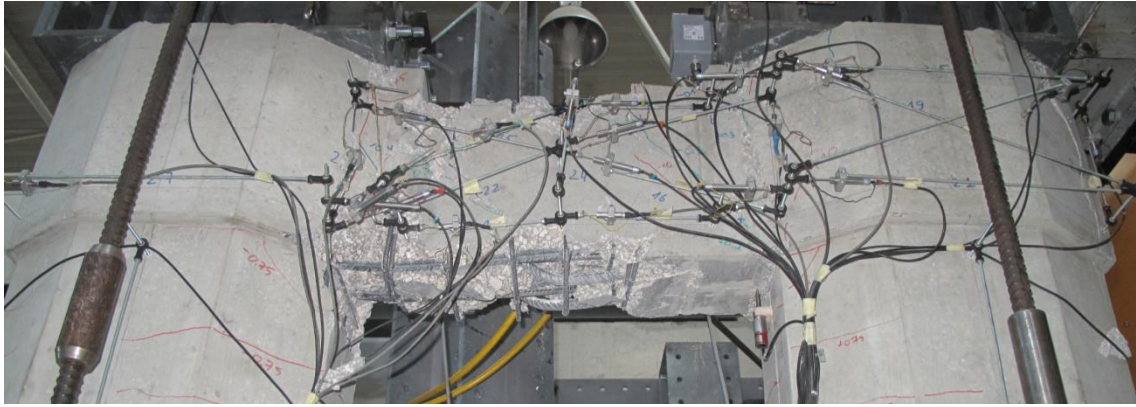
Figure 5.28 – SP_M02 after testing

The evolution of cracking observed during the test was similar to the previous specimen, as shear cracks appeared in the beam very early on, at around 0.20% drift. Formation of new cracks mostly stabilized after 1.00% drift, as it is possible to observe identical cracking patterns at 1.00% and 2.00% drift, in Figure 5.29 (color edited for visibility at the lower drifts).
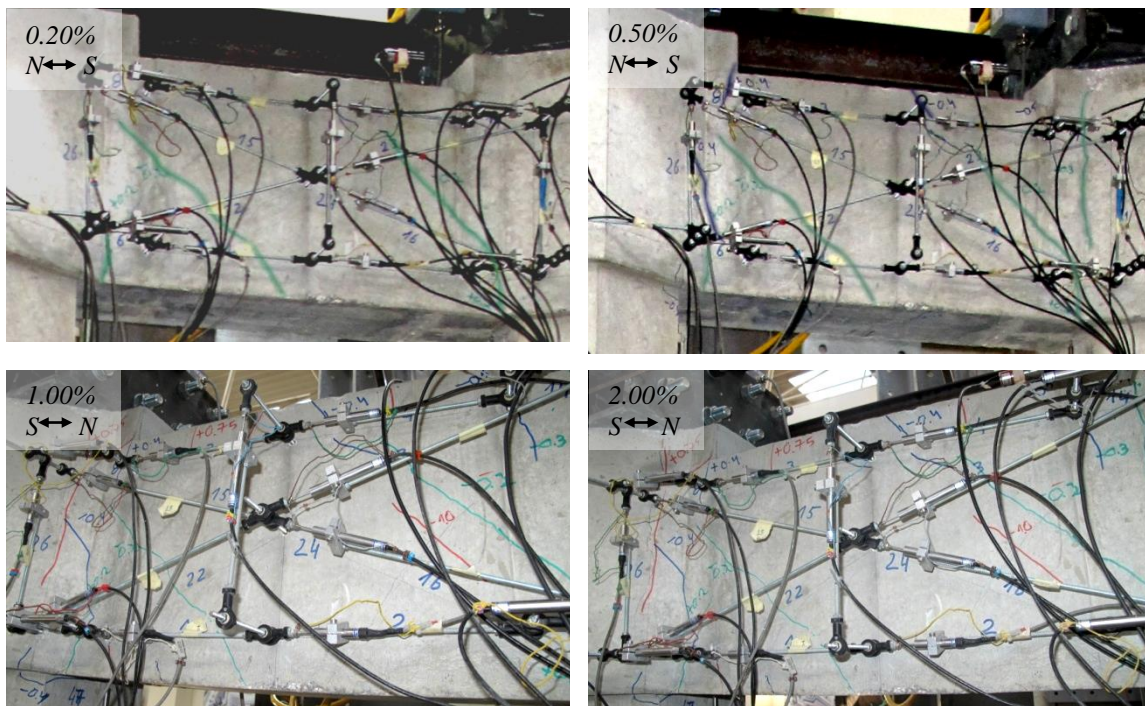
Figure 5.29 – SP_M02 Beam cracking pattern

The cracking pattern of the columns showed horizontal cracks, first forming at around 0.75% drift. Crack depth and width increased with the drift, and formation of new cracks progressed downwards to around half the column height, similarly to SP_M01. This is illustrated in Figure 5.30.
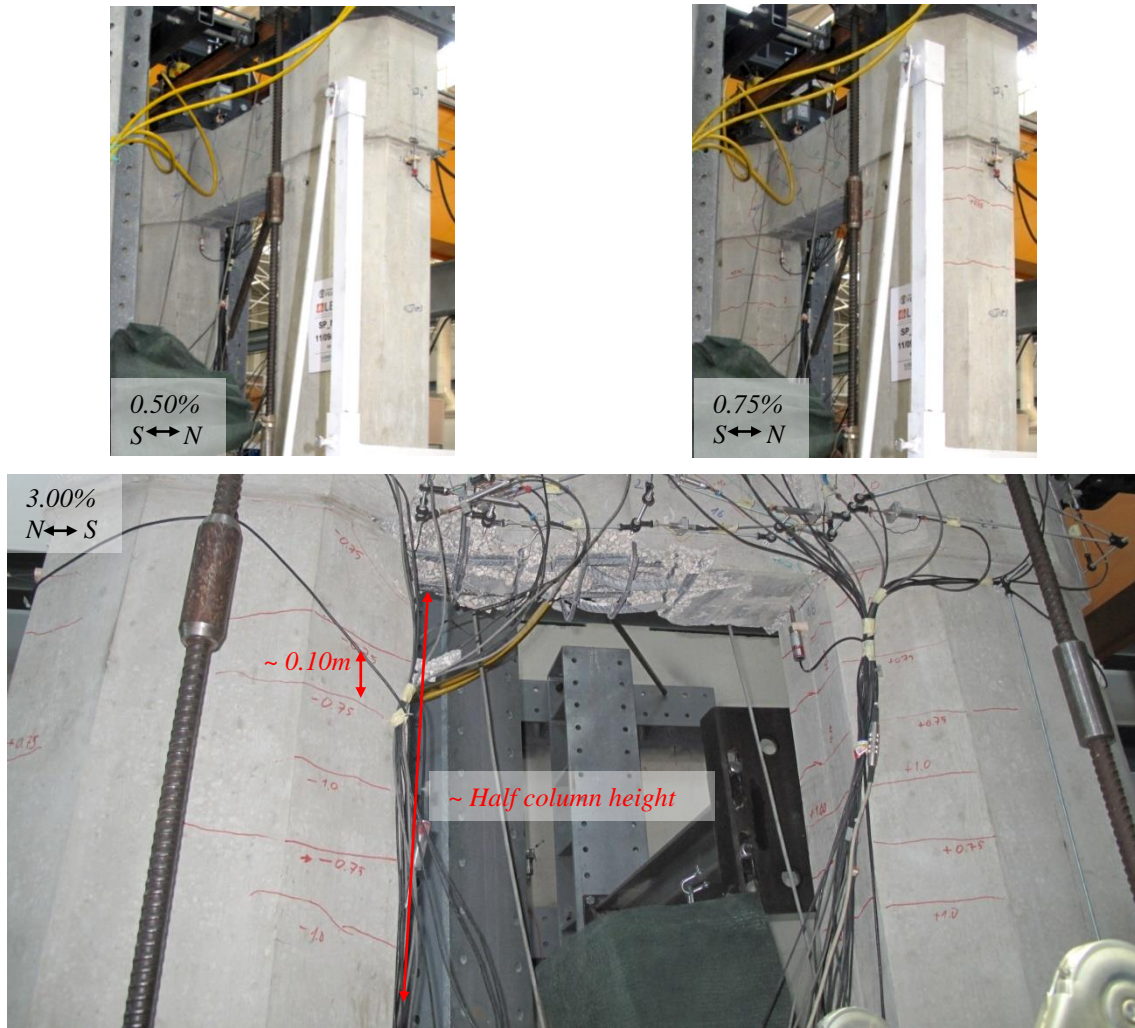
Figure 5.30 – SP_M02 Column cracking patterns

As it is possible to observe in Figure 5.28 and in the last panel of Figure 5.30, relevant damage was observed in the beam, occurring at the collapse level of 3.00% drift, while the columns displayed only mild cracking. Furthermore, spalling first occurred at the enlargement cover cap of the beam-column nodes at 2.00% drift, as a result of the progression of the vertical cracks in those sections, whose damage evolution is illustrated in Figure 5.31 for the north beam-column interface. The local crushing of concrete hinders the formation of a stable compression strut able to carry the shear load, causing the sliding movement to occur.
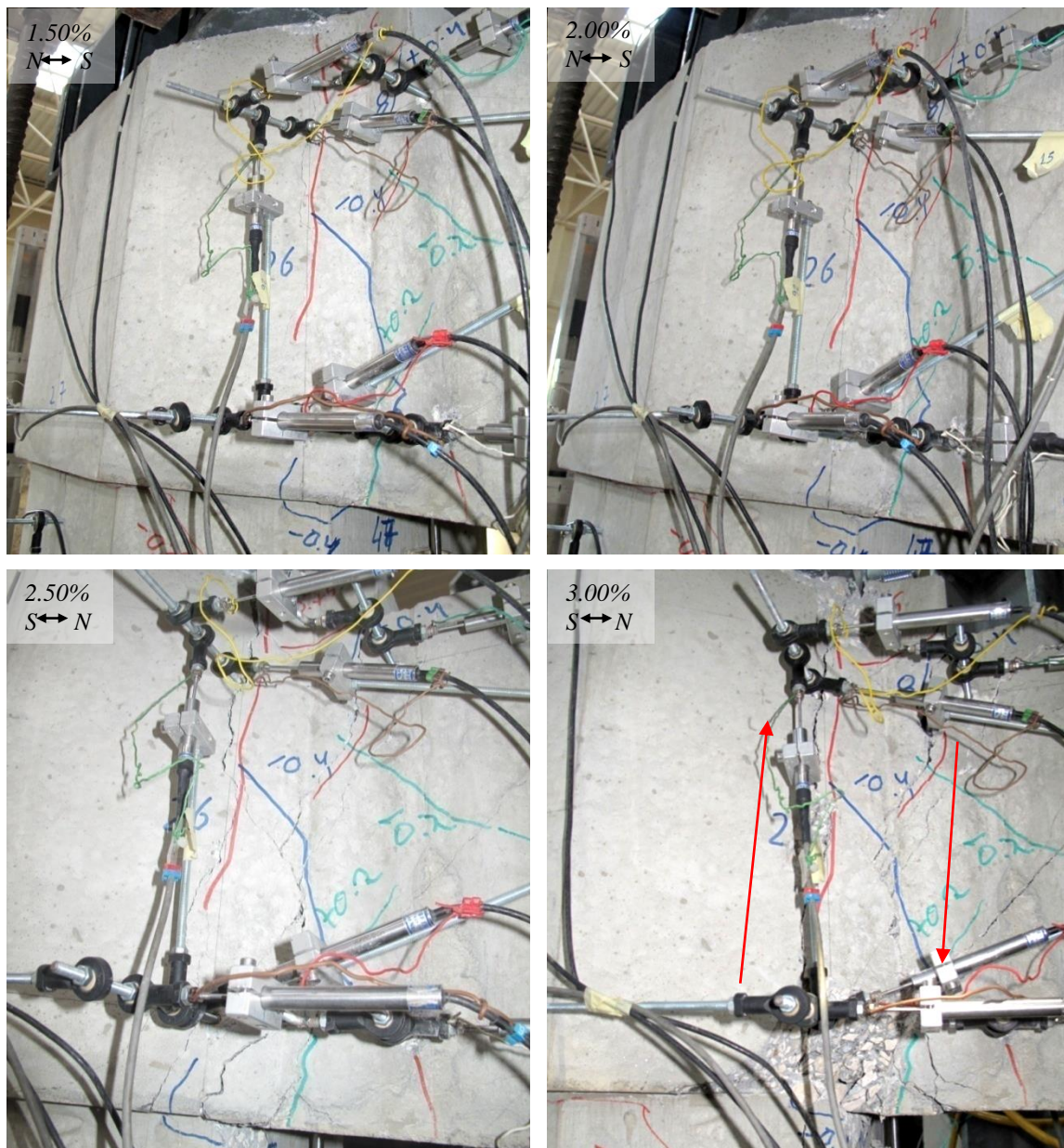
Figure 5.31 – SP_M02 Beam-column interface

5.2.1.3. SP_M03 specimen results

The cyclic force-drift curve for this specimen is illustrated in Figure 5.32, displaying very clear "pinching", with collapse determined at the 2.50% drift level. Peak force asymmetry was also observed, representing a difference of nearly 20%. In this case, predictive estimates for the lateral peak force using the shear capacity of the beam (equation 4.11) for the *Yielding* and *Ultimate* scenarios can lead to very different results depending on the value adopted for $\cot\theta$, according to the truss model for shear in beams. With that in mind, a single estimation is presented, which was found to provide the best prediction of the lateral peak force on the positive loading direction, and was calculated using rebar yielding properties and $\cot\theta = 1.80$

(corresponding to $\theta \approx 30°$, which is around the slope of the geometrical diagonals of the rectangular shape of the beam).
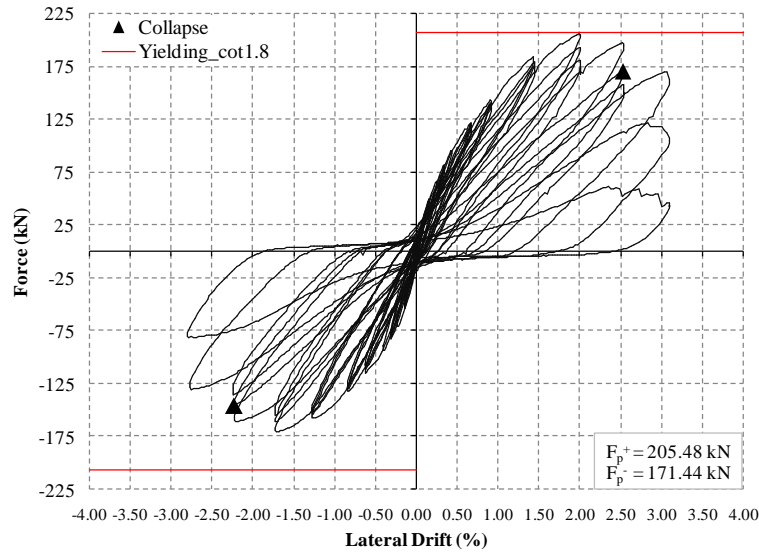
Figure 5.32 – SP_M03 force-drift results

The value $\cot \theta = 1.80$ also leads to a small difference under 4% between the theoretical shear capacity of the beam and the maximum value recorded in the experimental test, as illustrated in Figure 5.33.
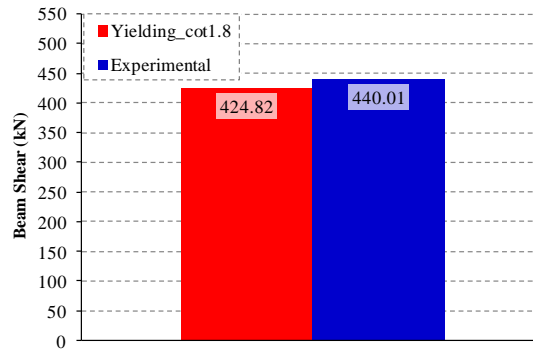
Figure 5.33 – SP_M03 Beam shear: comparison of experimental and theoretical estimates

Specimen SP_M03 exhibited a very clear case of "diagonal splitting" due to shear, which is illustrated in Figure 5.34, representative of the damage state of the beam at the end of the test. This occurred as a result of transverse reinforcement failure at the beam mid-section, immediately leading to the almost complete loss of overall structure strength. With respect to visual evidence alone, this specimen showed the most extensive damage from all the Phase 1 tests, but that can mostly be associated with the brittle occurrence at 2.50% drift.
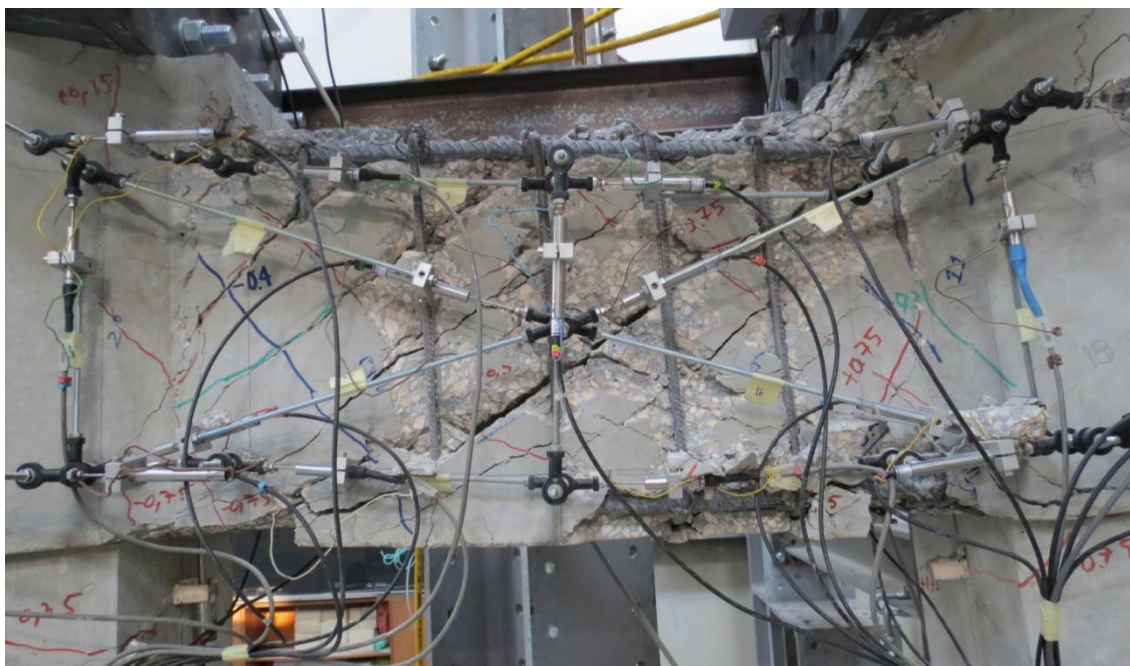
a) East Side

a) West side

Figure 5.34 – SP_M03 Beam after testing

A typical shear cracking pattern in the beam was again evident throughout the test, with its evolution starting at 0.20% drift, and the development of new cracks until 0.75% drift. Afterwards, crack width and depth progression was observed, and by 2.00% drift, spalling/detachment of the top surface of the beam was starting to occur, as highlighted in the last panel of Figure 5.35. Eventually, when that occurred, failure of the stirrups ensued, leading to global collapse.
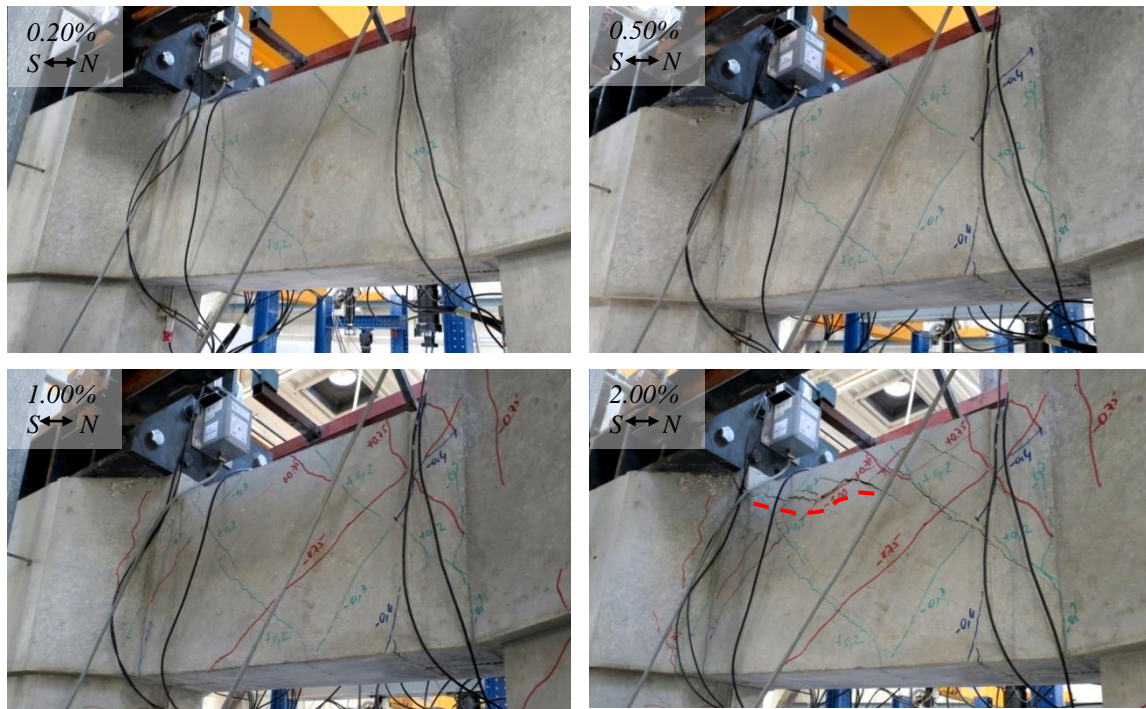
Figure 5.35 – SP_M03 Beam cracking pattern

Horizontal cracking in the columns developed essentially between 0.75% drift and 1.00% drift, but the overall cracking pattern was overall less pronounced than in the previous tests. The depth progression of the cracks was smaller, and shorter development into the column could also be observed, which did not reach half height, as represented in Figure 5.36.

Figure 5.36 – SP_M03 Column cracking patterns

Figure 5.36 (cont.) – SP_M03 Column cracking patterns

5.2.1.4.   SP_M04 specimen results

The cyclic force-drift curve for this specimen is illustrated in Figure 5.32, also exhibiting visible "pinching", with collapse determined at 3.00% drift for both loading directions, and a force asymmetry of nearly 18% was also observed. Peak force estimations calculated from the rhombic truss design model of equation 4.8 (disregarding the effect of the axial load) are also included in the same figure and, in this case, the maximum value calculated under the *Yielding* scenario compares better with the experimental force, with a relative difference of around 8%.
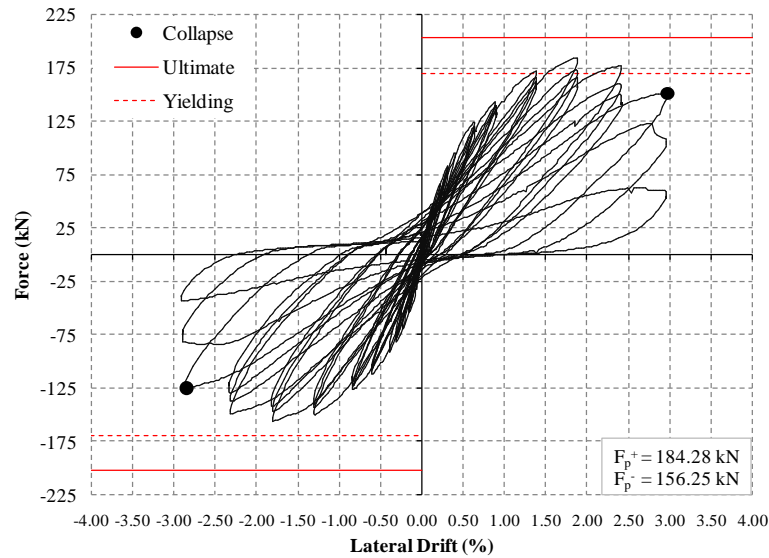
Figure 5.37 – SP_M04 force-drift results

That is also evidenced when comparing the experimental shear with its theoretical shear capacity (dependent of reinforcement) under the *Yielding* and *Ultimate* cases. As illustrated in Figure 5.38, the difference between *Yielding* and *Experimental* values is minimal, and this seems to indicate that the behavior of SP_M04 is more heavily associated with the capacity of the reinforcement than the compressions carried through the beam. In fact, this may be plausible since the original rhombic truss compressions parallelogram is disrupted with the shifted position of the diagonal rebars.
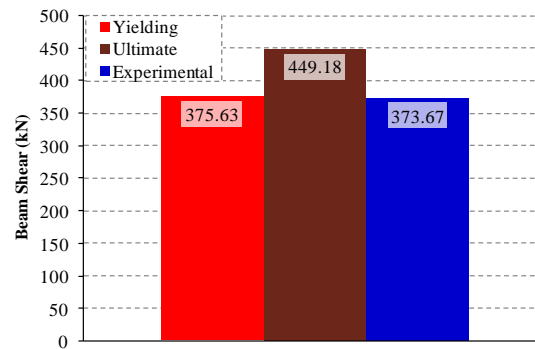
Figure 5.38 – SP_M04 Beam shear: comparison of experimental and theoretical estimates

Failure of SP_M04 occurred mainly due to the influence of shear, since the diagonal cracking under cyclic displacements deteriorated concrete integrity within the beam, causing progressive strength loss. This process was further increased when transverse reinforcement failure also occurred at the beam mid-section, leading to considerable degradation of the structural response and, eventually, failure. A picture of the final stage of the test is shown in Figure 5.39, illustrating the damage incurred by the beam.
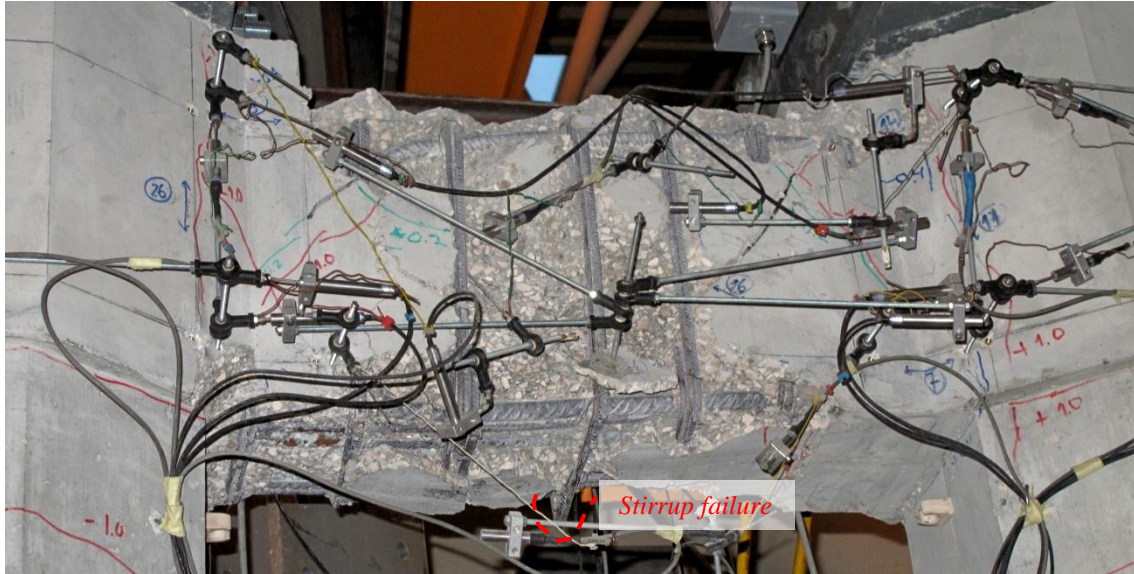
Figure 5.39 – SP_M04 after testing

The same shear cracking pattern observed in other cases also occurred in SP_M04, with crack formation between 0.20% drift and 1.00% drift. Afterwards, stable progression of crack depth and width could be observed and, at 2.00% drift, the concrete cover of the upper surface of the beam was spalling, as illustrated in Figure 5.40.
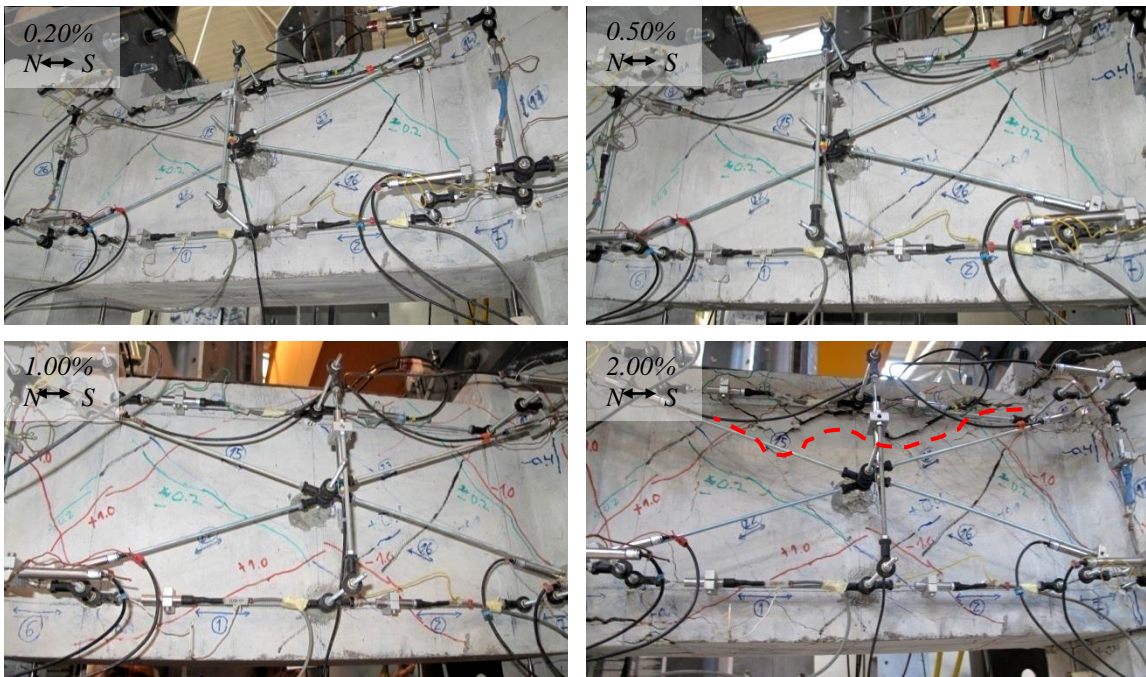
Figure 5.40 – SP_M04 Beam cracking pattern

As for the column cracking pattern, similar evidence to the other tests was observed in this case, with horizontal crack formation occurring between 0.75% drift and 1.00% drift, and progression through the column down to around half height. In general, the north column exhibited stronger cracking than the south one, as evidenced in Figure 5.41.
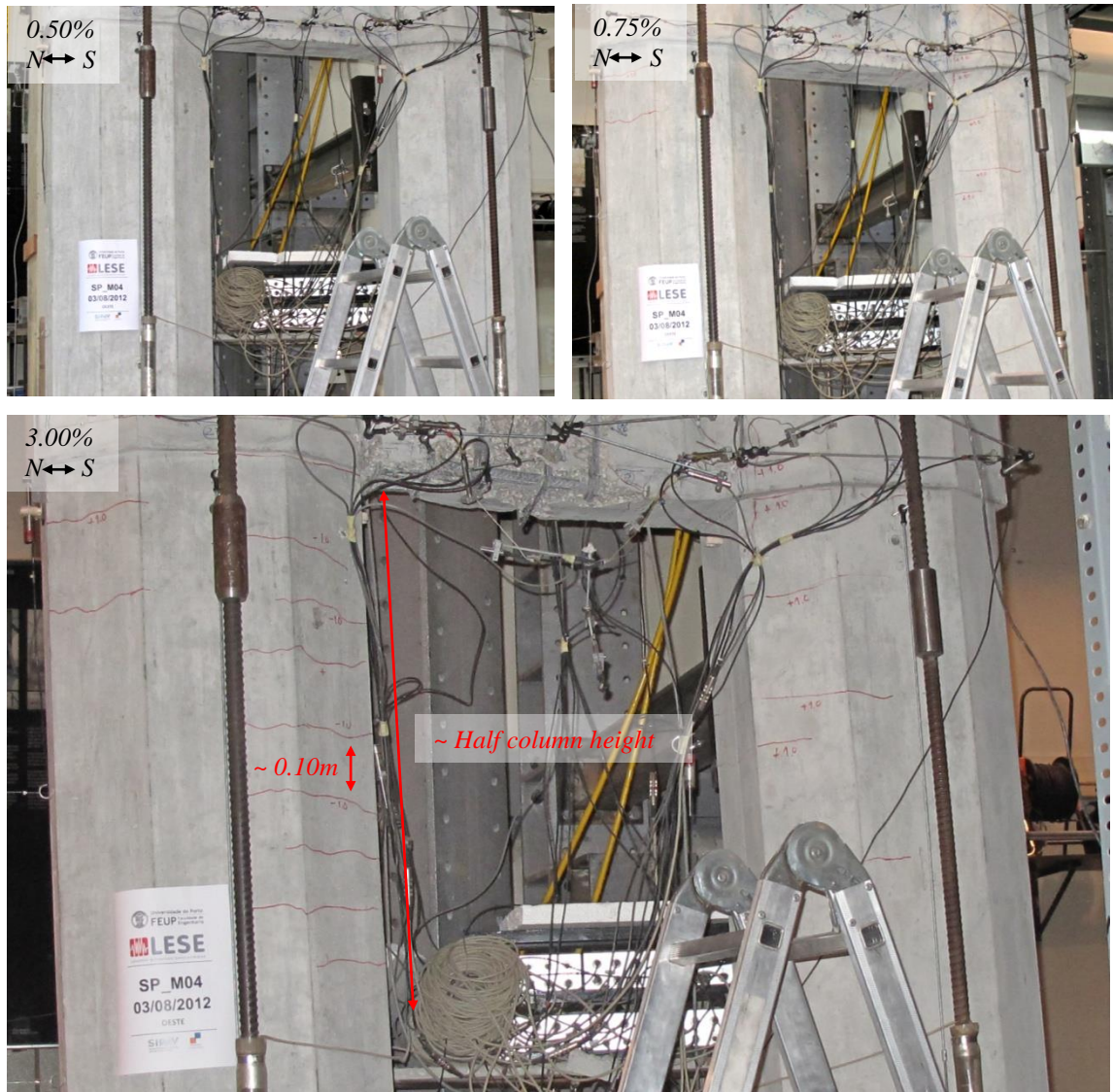
Figure 5.41 – SP_M04 Column cracking patterns

5.2.1.5. Summary of main results

The main observations taken from Phase 1 of the experimental campaign were the following:

- Beam shear dominated failure occurred in all the tests, typically involving considerable damage recorded in the beam, and only mild cracking in the columns;
- Crack formation occurred between 0.20% and 1.00% drift for the beams, and between 0.75% and 1.00% drift for the columns.
- The peak force asymmetry between loading directions ranged between 16% and 25%;
- The collapse threshold was calculated at 2.50% drift for SP_M01 and SP_M03, while the two rhombic truss variants SP_M02 and SP_M04 were able to achieve the 3.00% drift level;
- SP_M01 and SP_M02 experienced beam shear values greater than the calculated capacity for both *Yielding* and *Ultimate* scenarios, suggesting that those bent pier

structures have an increased shear capacity than that calculated using the design models, possibly due to larger influence of the interlock mechanism or the concrete compressions;

- SP_M03 and SP_M04 experienced beam shear values similar to the theoretical capacity for the *Yielding* scenario, and exhibited stronger "pinching" than the other specimens (particularly SP_M03);

- All the specimens were subjected to beam shear values larger than the axial load level previously installed on each column, leading to decompression on at least one of them;

5.2.2. PHASE 2 OBSERVATIONS

The experimental evidence regarding Phase 2 tests follows a similar presentation layout to that used for Phase 1. Force – drift curves will be presented according to the internal displacement recordings of the horizontal actuator (Figure 5.16), and the 20% peak force reduction will be used as the collapse threshold defining parameter. In this case, the predictive estimates of the peak lateral force were calculated using the real material properties using the equilibrium model of Figure 5.19 for the following two scenarios:

- *Beam_shear*: Assuming peak force occurs at shear yielding on the beam;
- *Joint_bending*: Assuming failure occurs at moment yielding of the longitudinal reinforcement crossing the joint section;

The beam shear capacity associated with the reinforcement layouts used in the Phase 2 specimens is the same of SP_M02, calculated according to the rhombic truss model. In order to determine the moment capacity of the joint section for the second case, a moment - curvature analysis was performed in Cast3m for each specimen of Phase 2, assuming that it can be represented by a regular concrete section with reduced reinforcement (this also assumes that compressions can be directly transferred between the precast beam and column elements through contact, and that full bond is achieved at both ends of the continuity rebars). The constitutive relationships considered for simulation of the uniaxial behavior of concrete and steel fibers were the previously mentioned models of Hognestad and Menegotto-Pinto, respectively, calibrated for the material properties presented in Table 4.12 (the corresponding modeling parameters are included in Annex A). Figure 5.42 - a) presents the results obtained for each specimen, calculated considering the application of the axial dead-load of 300 kN. In addition, Figure 5.42 - b) shows the peak force values calculated for all the specimens on both described scenarios.
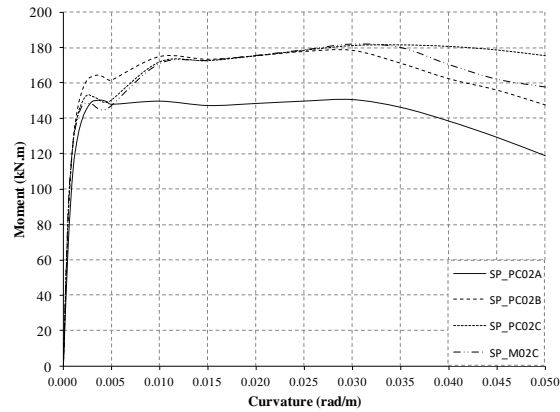
	Beam_Shear (kN)	Joint_Bending (kN)
SP_PC02A	169,27	146,93
SP_PC02B	169,27	173,96
SP_PC02C	169,27	177,25
SP_M02C	169,27	177,79

a)   Moment – curvature analyses   b)   Peak force estimates

Figure 5.42 – Strength results for Phase 2 specimens

5.2.2.1.   SP_PC02A specimen results

The cyclic force-drift curve for SP_PC02A is illustrated in Figure 5.43, where the collapse threshold is identified at the 3.50% drift level for the two loading directions. A peak force asymmetry of around 7% was observed between them. Furthermore, the relative difference between the lateral peak force recorded in the test and the values estimated under _Beam_shear_ and _Joint_bending_ scenarios is around the 8% for both.
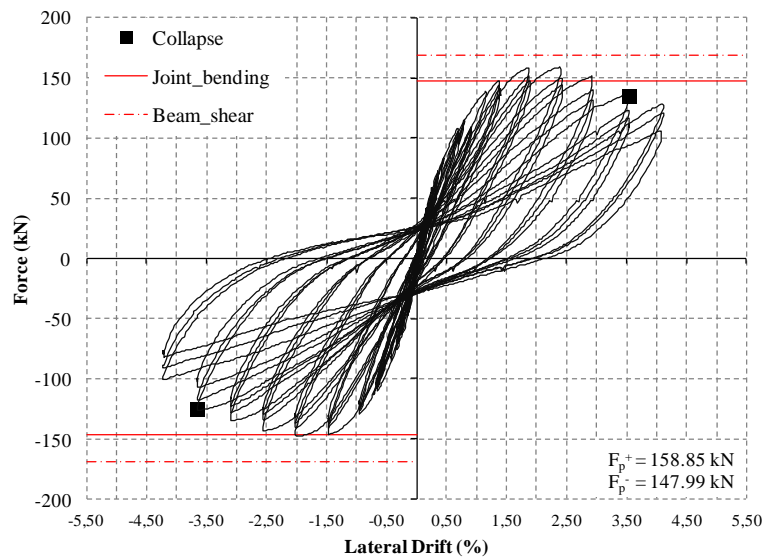
Figure 5.43 – SP_PC02A force-drift results

The experimentally recorded beam shear seems to be in line with these results, as illustrated in Figure 5.44, where the difference between the actual beam shear and the theoretically determined values is around 6% and 9% for the _Beam_shear_ and _Joint_bending_ scenarios, respectively.

5.36
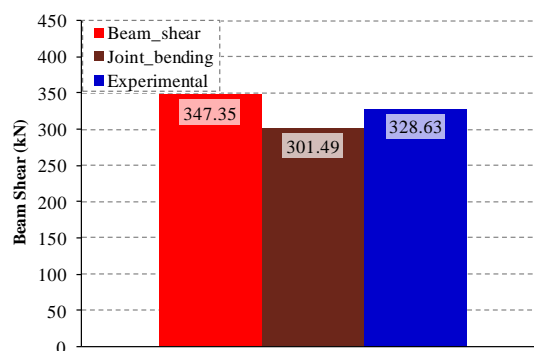
Figure 5.44 – SP_PC02A Beam shear: comparison of experimental and theoretical estimates

Failure of SP_PC02A was mainly due to the influence of shear in the beam, since a strong degradation of the beam-column interface led to sliding of the beam over the column element as a typical "sliding shear" occurrence. Figure 5.45 presents a picture illustrating the described mechanism during the final stage of the test (after the collapse threshold), corresponding to the 4.00% drift level.
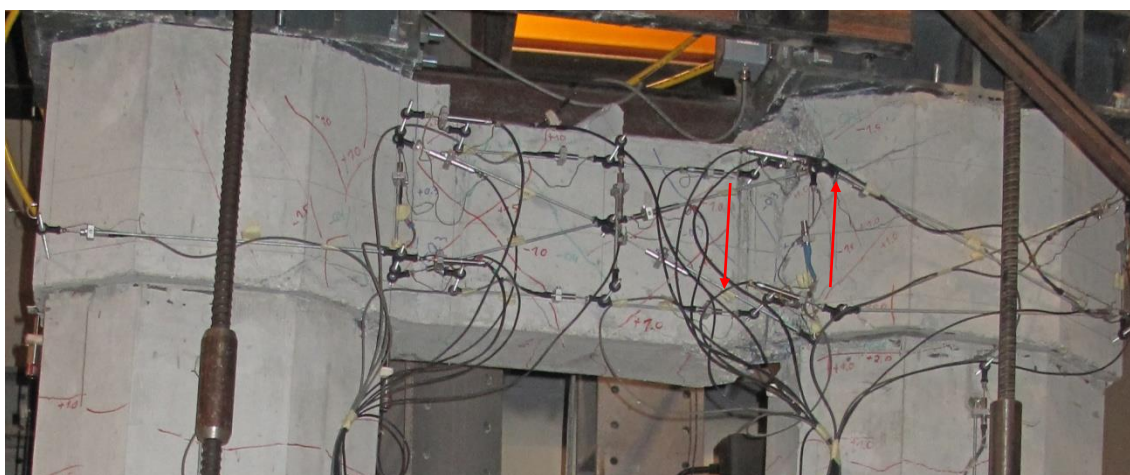
Figure 5.45 – SP_PC02A at the final stage of the test

Beam cracks first formed between 0.30% drift and 0.40% drift, having continued forming until 1.50% drift, where the bulk of cracking stabilized. In general the pattern was typical of shear, with diagonal orientation on both loading directions and concentration of vertical cracks near the beam-column interfaces. Figure 5.46 illustrates its evolution along four increasing drift levels.
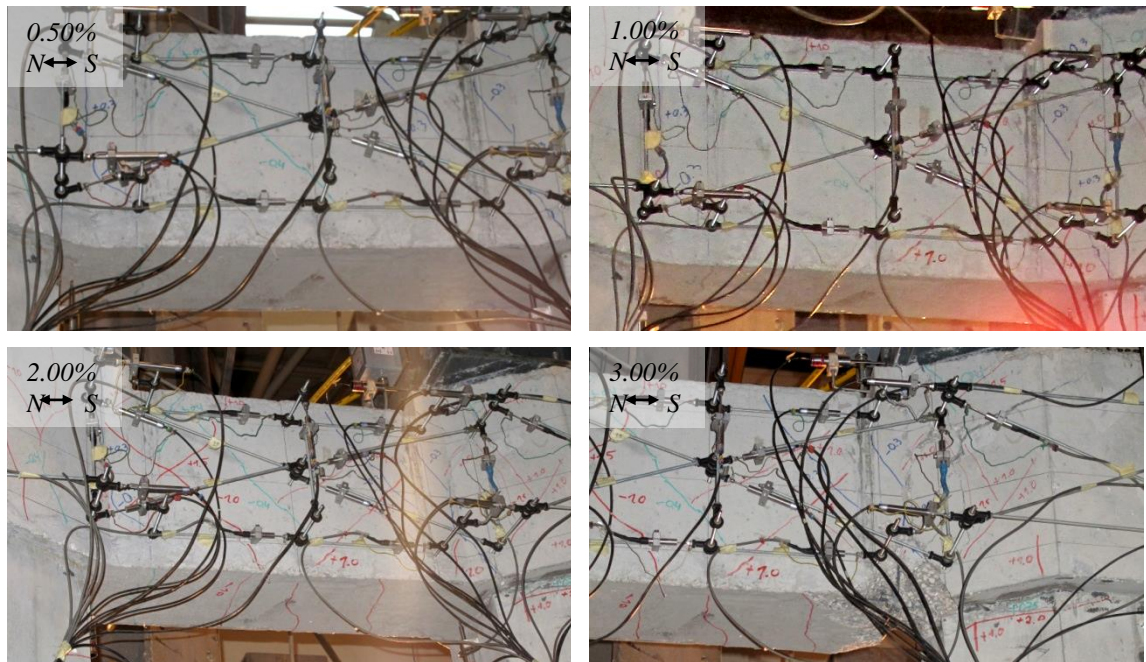
Figure 5.46 – SP_PC02A Beam cracking pattern

Column cracking is illustrated in Figure 5.47, and mainly developed between the 1.00% and 1.50% drift levels, displaying horizontal orientation and progressively increasing depth. At 1.50% drift, the cracking pattern was mostly stabilized.

Figure 5.47 – SP_PC02A Column cracking patterns
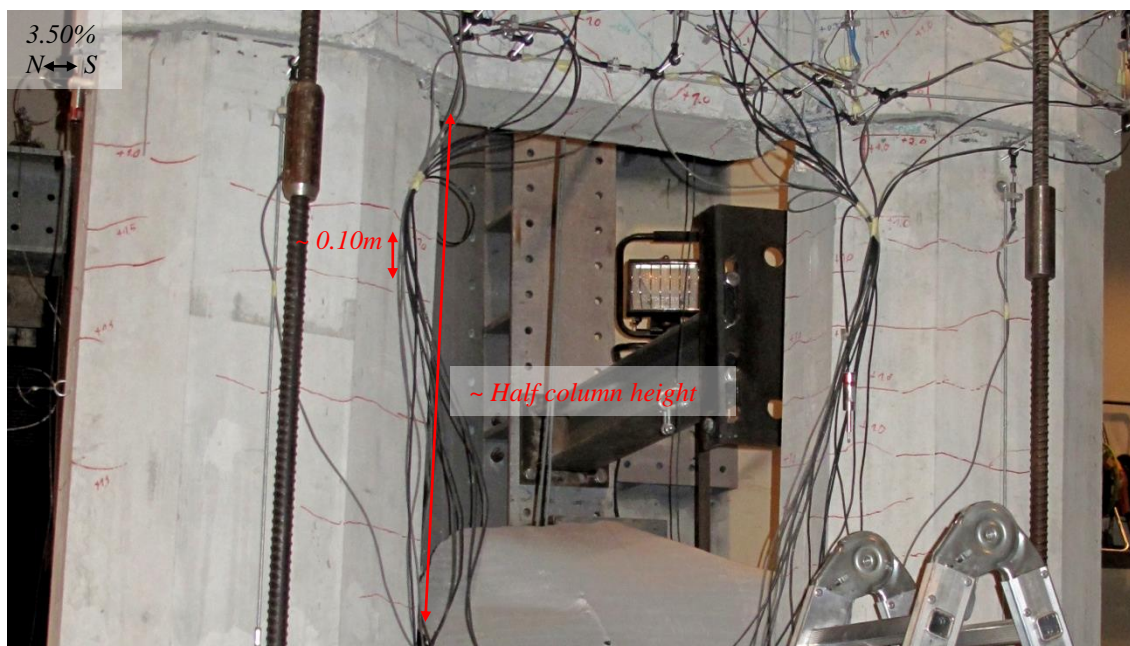
Figure 5.47 (cont.) – SP_PC02A Column cracking patterns

Despite that, most of the deformation observed in the column occurred at the joint sections, where visible signs of cracking were apparent from 0.75% drift, related to joint opening widths that had exceeded the maximum reading limit (5mm) of the associated LVDT when the 3.00% drift was reached (joint opening evolution illustrated in Figure 5.48).

Figure 5.48 – SP_PC02A North precast joint opening progression

In fact, that was the moment when spalling first occurred, and roughly also when the vertical cracks at the south beam-column interface started showing signs of sliding failure, related to local crushing of the concrete. This is further illustrated in Figure 5.49, where the magnitude of the damage incurred due to progression of that mechanism is presented until the end of the test (at 4.00% drift), and the contribution of the diagonal rebars in providing capacity to a heavy shear loaded interface is also understandable.
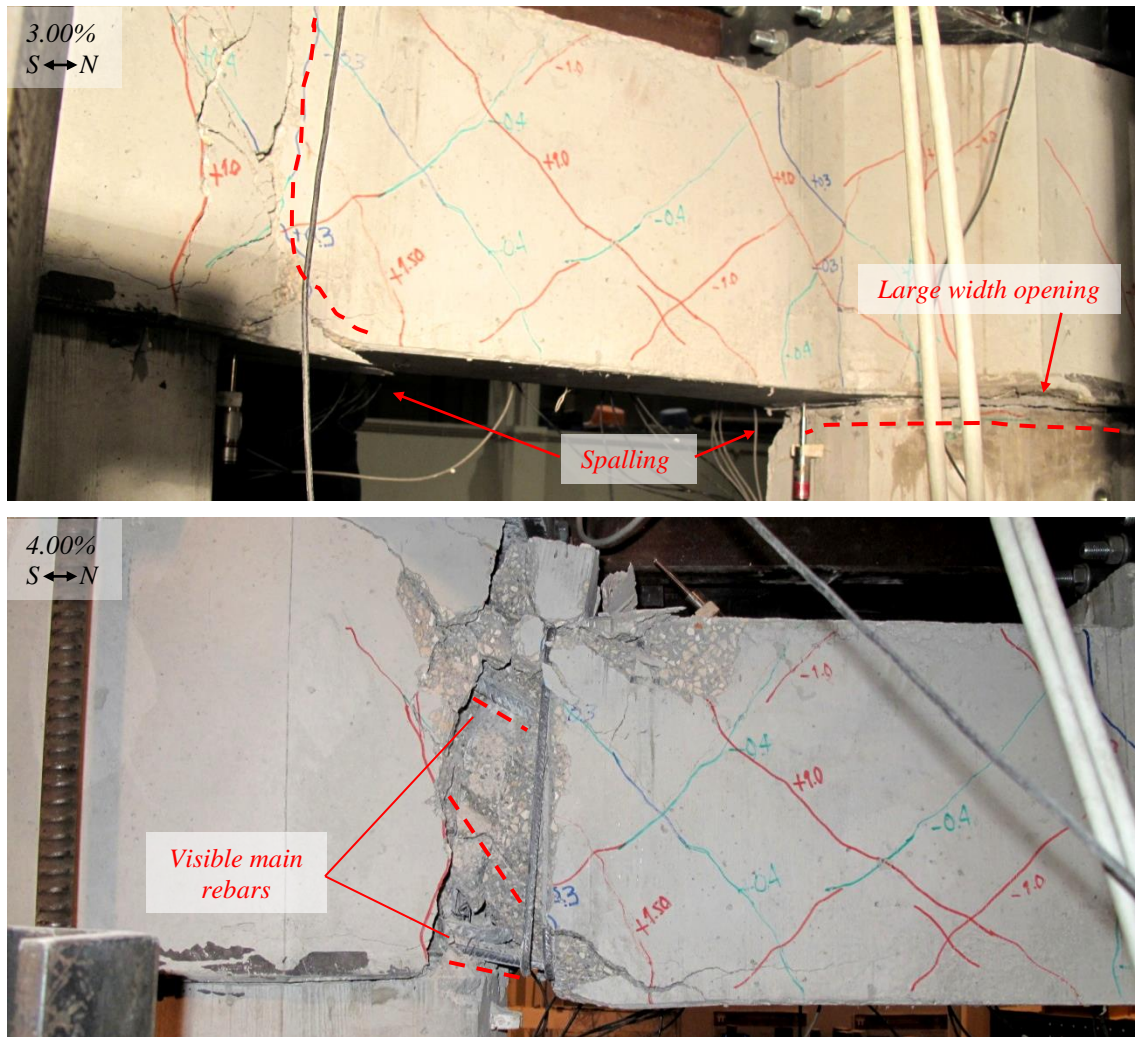
Figure 5.49 – SP_PC02A progression into failure

5.2.2.2. SP_PC02B specimen results

The cyclic force-drift curve for SP_PC02B is presented in Figure 5.50, illustrating a response to the full loading history (up to 5.00% drift). It is important to note that, for unexpected technical reasons, in the negative loading direction, the actuator went to the full extent of its stroke, which is why the last few cycles do not show displacement increase. Even so, the collapse threshold is identified at the loading step corresponding to the 4.00% and 3.50% drift level for positive and negative directions, respectively. The peak force asymmetry on this test was of around 28%, but the relative difference between the experimental value and those determined according to the *Beam_shear* and *Joint_bending* scenarios is negligible (less than 3%).
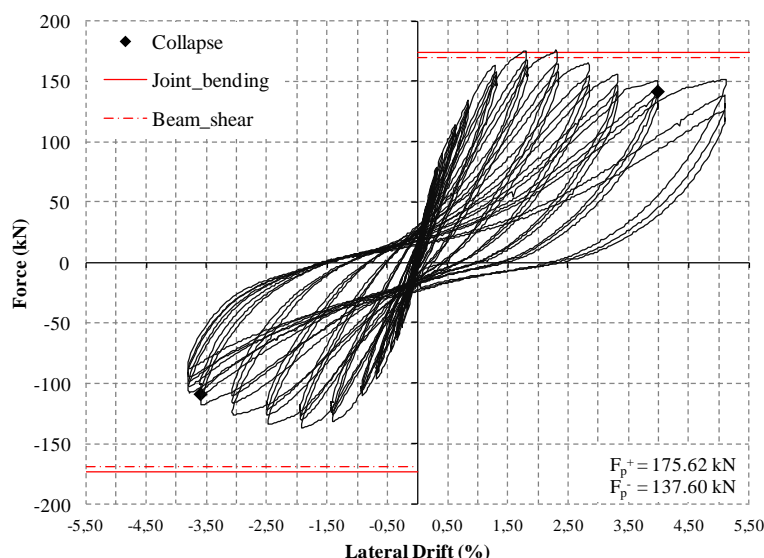
Figure 5.50 – SP_PC02B force-drift results

That difference slightly increases regarding the comparison between the experimentally recorded beam shear and the theoretical values. Specifically, both *Beam_shear* and *Joint_bending* scenarios indicate larger force than the experimental value, and the respective differences are around 6% and 9%.
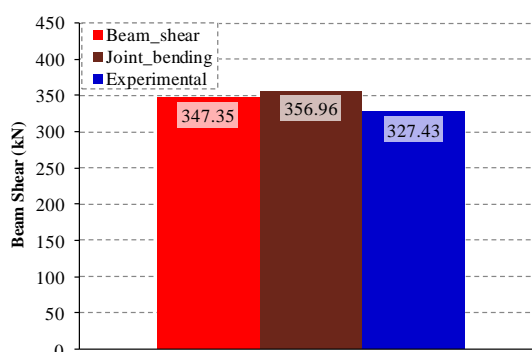
Figure 5.51 – SP_PC02B Beam shear: comparison of experimental and theoretical estimates

The failure mode of this specimen can be attributed to heavy degradation of both beam-column interfaces due to shear, although considerable sliding motions of the beam over the columns were not apparent like in the previous specimen. In addition, failure of transverse reinforcement due to spalling of the top surface of the beam (at 4.00% drift only), and continuity rebars' fracture could also be detected. Figure 5.52 shows the final state of the beam after loading at 5.00% drift, and is believed to provide a fairly good picture of the failure mechanism of SP_PC02B by itself.
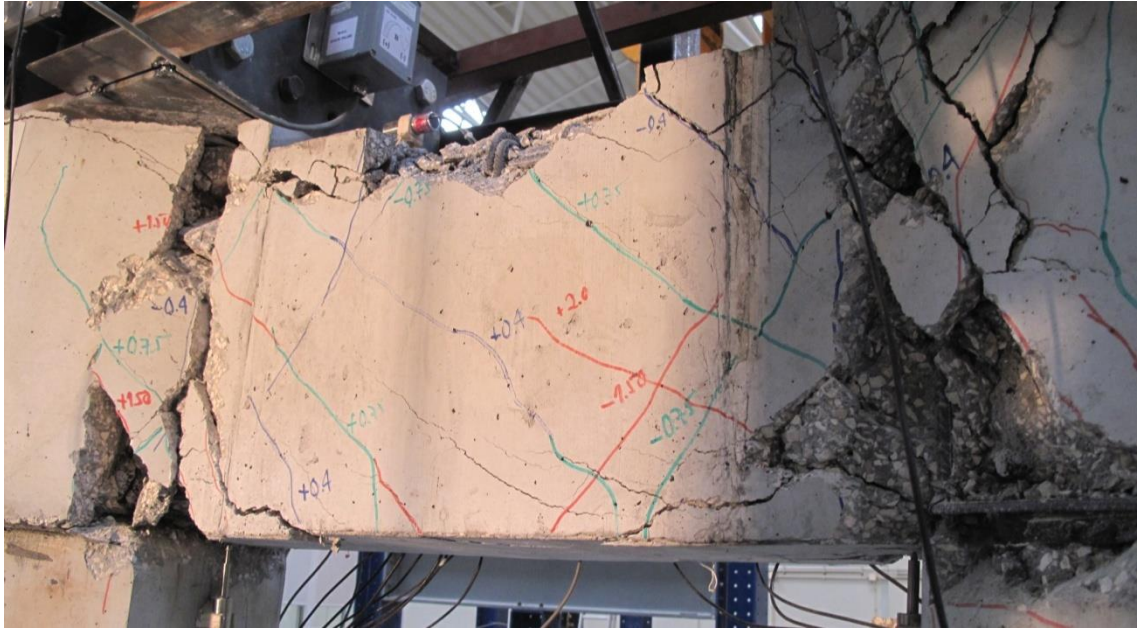
Figure 5.52 – SP_PC02B after testing

Beam cracks first formed at 0.40% drift, and that process stabilized after 1.50% drift. The same shear typical cracking pattern was also observed in this beam, with heavy concentration of cracks near the beam-column interfaces, as illustrated in Figure 5.53.
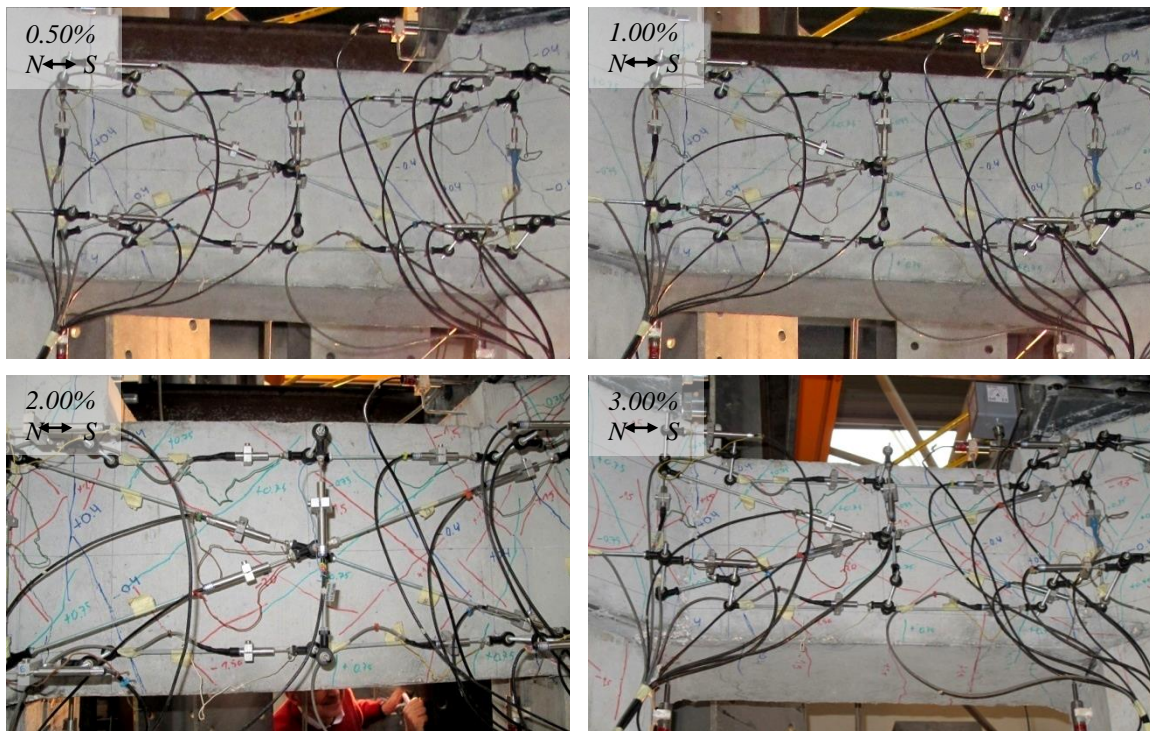
Figure 5.53 – SP_PC02B Beam cracking pattern

Column cracking in SP_PC02B only occurred between 1.00% drift and 1.50% drift, stabilizing after 2.00% drift, but the general appearance of the cracking pattern was the same of all the previously presented cases, with horizontal cracks until roughly half the column height,

as evidenced in Figure 5.54. However, the cracking on the first 0.30m below the precast joint was scarce, and marked by vertical cracks indicative of heavy straining of the longitudinal reinforcement and, possibly, of rebar slip.
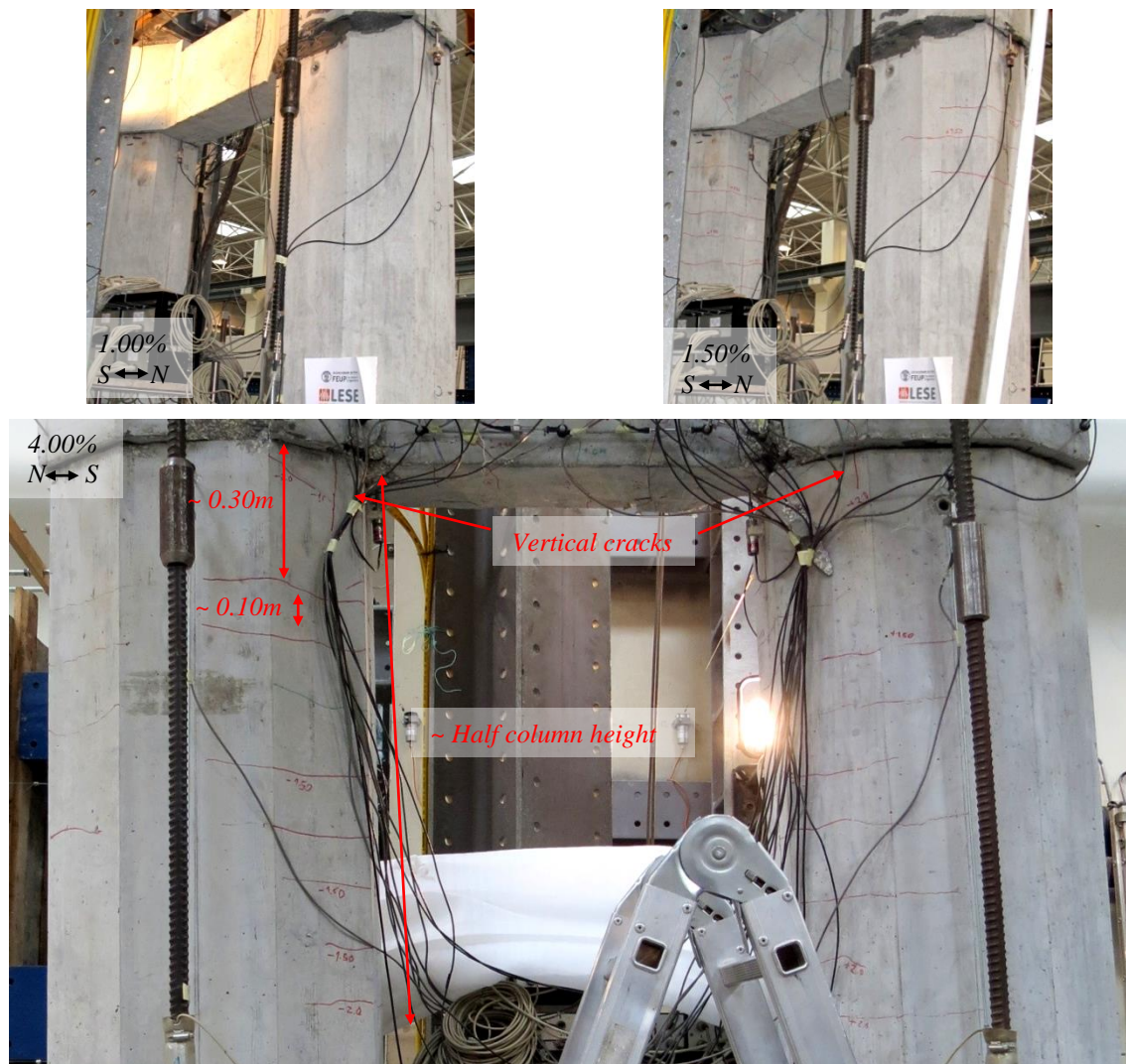
Figure 5.54 – SP_PC02B Column cracking patterns

The level of deformation recorded at the joint sections was also large, as the opening widths exceeded the maximum limit of the LVDT devices by the 2.50% drift level. In this case, however, the evolution of the joint opening led to fracture of one rebar of the longitudinal reinforcement that was providing continuity over the joint, as shown in Figure 5.55.
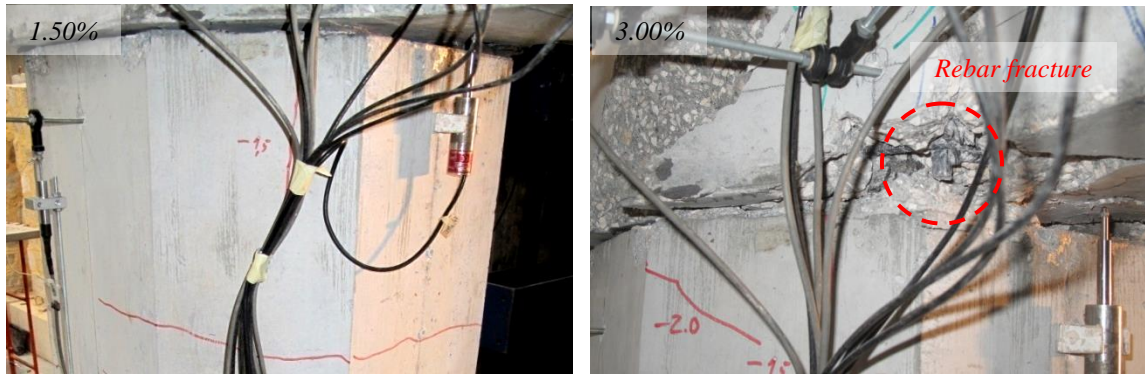
Figure 5.55 – SP_PC02B: Progression of north precast joint opening

5.2.2.3.   SP_PC02C specimen results

The cyclic force-drift curve for SP_PC02C is shown in Figure 5.56, where collapse is identified at the 4.00% drift level for the positive loading direction and near 3.00% for the negative loading direction. In addition, the peak force asymmetry was 23%, but the strength degradation is clearly more noticeable in the negative than in the positive loading direction. *Beam_shear* and *Joint_bending* predictive estimations are fairly on point, with minimal difference to the experimental peak force (again less than 3%).
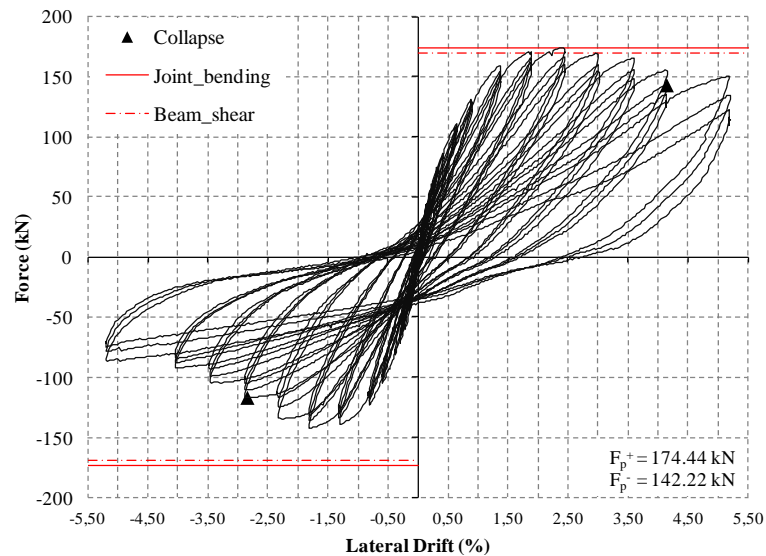
Figure 5.56 – SP_PC02C force-drift results

Similar maximum relative difference of 3% is observed when comparing the shear determined from experimental records with the theoretical shear values computed according to the two scenarios, as evidenced in Figure 5.57.
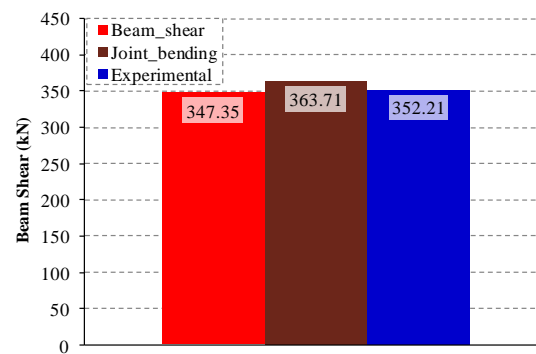
Figure 5.57 – SP_PC02C Beam shear: comparison of experimental and theoretical estimates

Failure of SP_PC02C was related to issues caused by both beam shear and joint bending. The degradation of the concrete due to crack propagation and concrete crushing was considerable at the beam-column interfaces. In addition, the deterioration and progressive increase of opening width at the precast joint sections also led to fracture of continuity rebars. Figure 5.58 presents the final state of the specimen, after loading up to 5.00% drift.

Figure 5.58 – SP_PC02C after testing

The first cracks in the beam formed at 0.30% drift, and progression of crack depth, width, and formation of new cracks stabilized after 1.50% drift. The cracking pattern of SP_PC02C (Figure 5.59) was also indicative of heavy shear loading, and the vertical cracks in this specimen had a strong development from 1.00% drift, having shown to be the dominant factor in beam deformation from an early stage of the test.
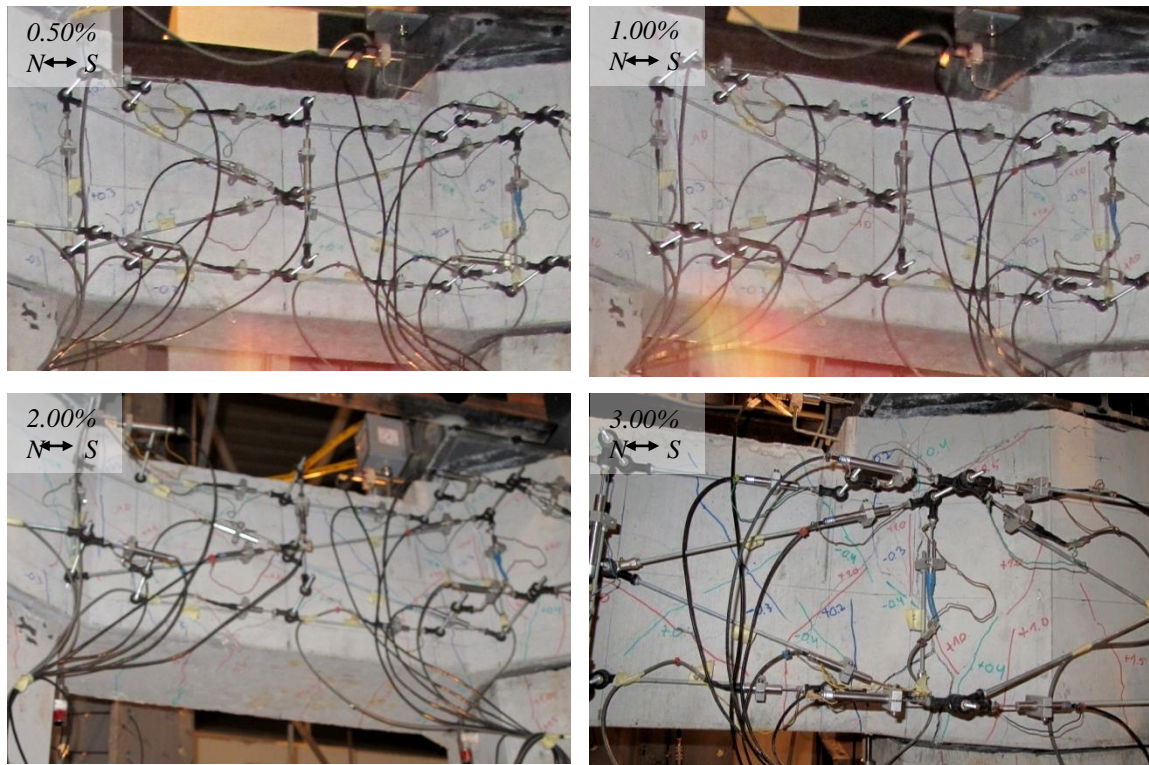
Figure 5.59 – SP_PC02C Beam cracking pattern

The outlook of the column cracking pattern of SP_PC02C was very similar to the previous specimen, with mainly horizontal cracks occurring at 1.00% drift and with a stable development from 1.50% drift, as presented in Figure 5.60. However, and just as in the previous specimen, in the zone below the precast joint, vertical cracks were observed instead of horizontal ones, aligned with the longitudinal reinforcement that crossed the precast joint.

Figure 5.60 – SP_PC02C Column cracking patterns
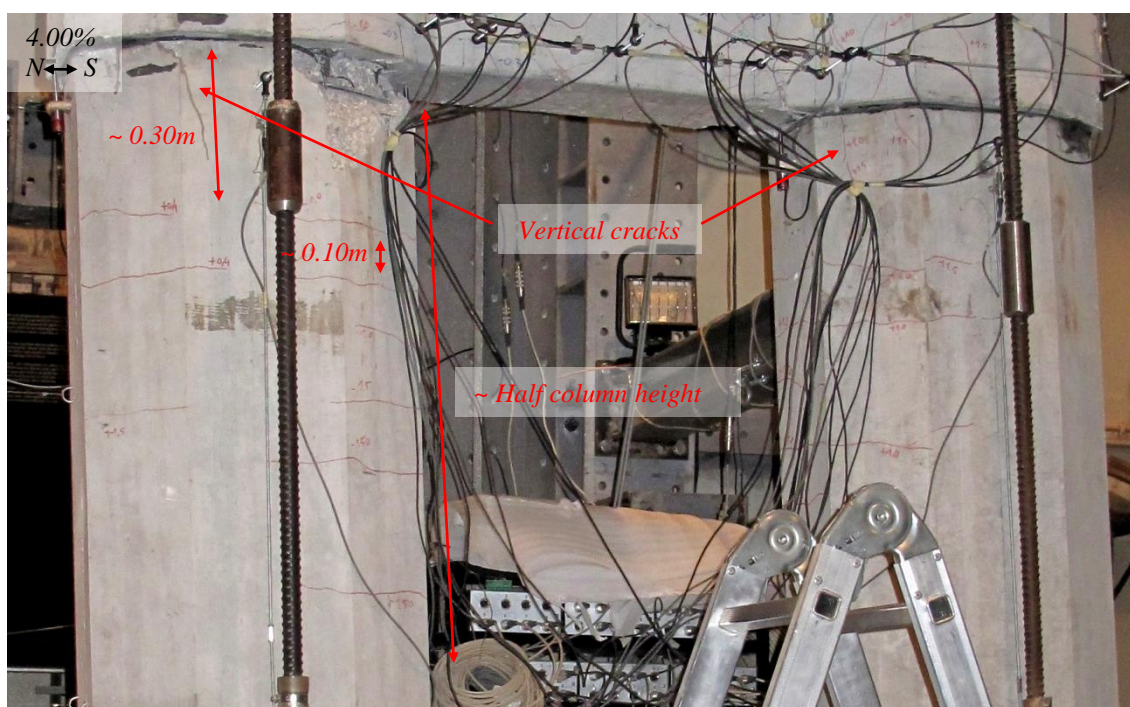
Figure 5.60 (cont.) – SP_PC02C Column cracking patterns

The joint deformations (Figure 5.61) were also significant in this specimen, as the opening widths exceeded the 5mm maximum by the 2.00% drift level. In addition, as the progression of the vertical cracks increased in the concrete below the precast joint, the deterioration of the vertical beam-column cracked interface (due to concrete crushing and spalling of the specimen) also occurred, exposing the reinforcement and, eventually, leading to rebar fracture in the south joint, as illustrated in Figure 5.61 – a).
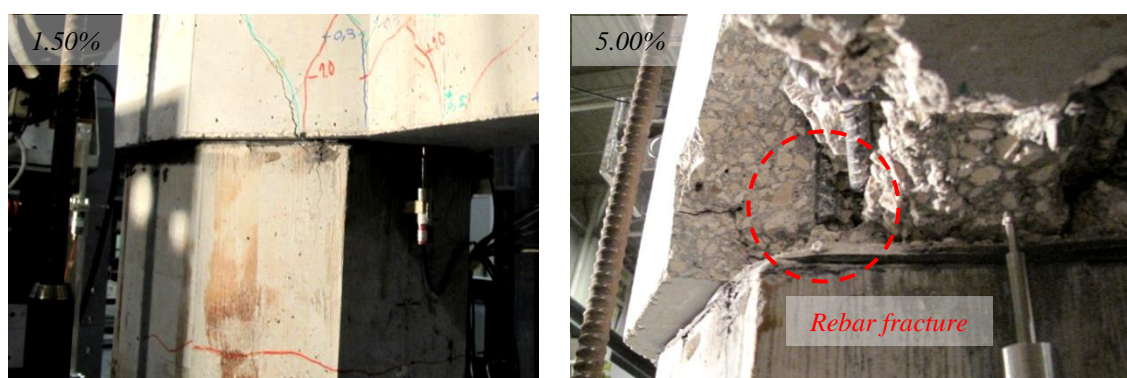
a) South joint (at 1.50% and 5.00% drifts)

Figure 5.61 – SP_PC02C precast joint opening progression

b) North joint

Figure 5.61 (cont.) – SP_PC02C precast joint opening progression

5.2.2.4. SP_M02C specimen results

The cyclic force-drift curve for SP_M02C (the monolithic replica of SP_PC02C) is presented in Figure 5.62, for which early collapse was determined at the 2.50% drift level for both loading directions. The peak force asymmetry between them was around 26%. Like in the previous cases, the values estimated using the theoretical scenarios *Beam_shear* and *Joint_bending* are very close to the experimental peak force for the positive loading direction (less than 3% difference).
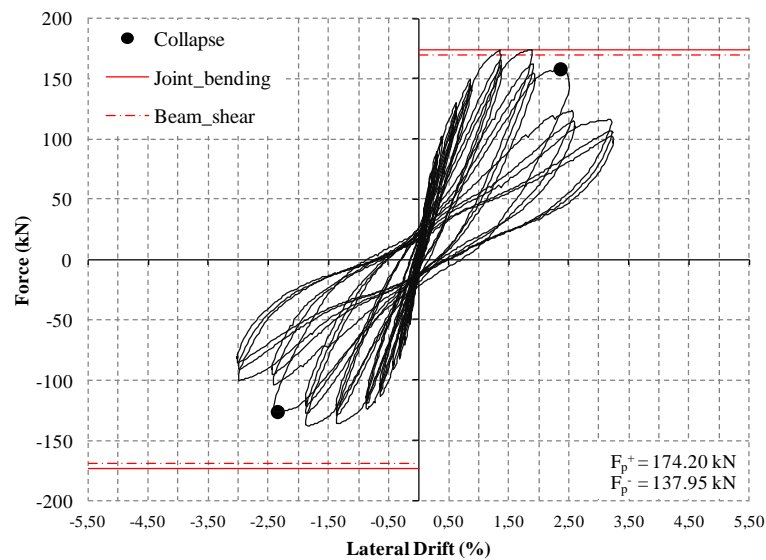
Figure 5.62 – SP_M02C force-drift results

Negligible relative difference is also observed when comparing the experimental beam shear with the theoretically determined values, as illustrated in Figure 5.63.
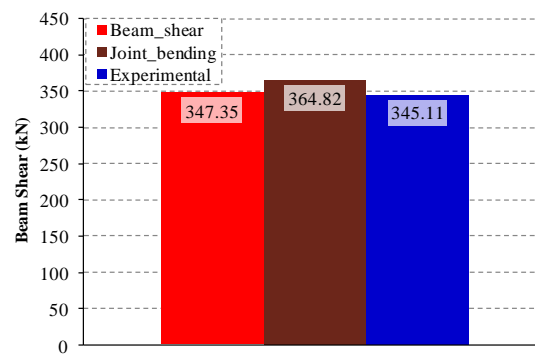
Figure 5.63 – SP_M02C Beam shear: comparison of experimental and theoretical estimates

The failure mode on SP_M02C occurred due to fracture of the longitudinal reinforcement on the beam-column node. The specimen, in general, experienced low damage. But early on, the cracking of the monolithic concrete in the zone corresponding to the precast joint on the SP_PC## cases led to very large opening widths and fracture of the crossing reinforcement, as well as subsequent sudden strength loss. Figure 5.64 presents a picture of the specimen after testing, where this is very noticeable by the large crack openings at the beam-column intersections, in contrast with the minimal damage on the rest of the structure.
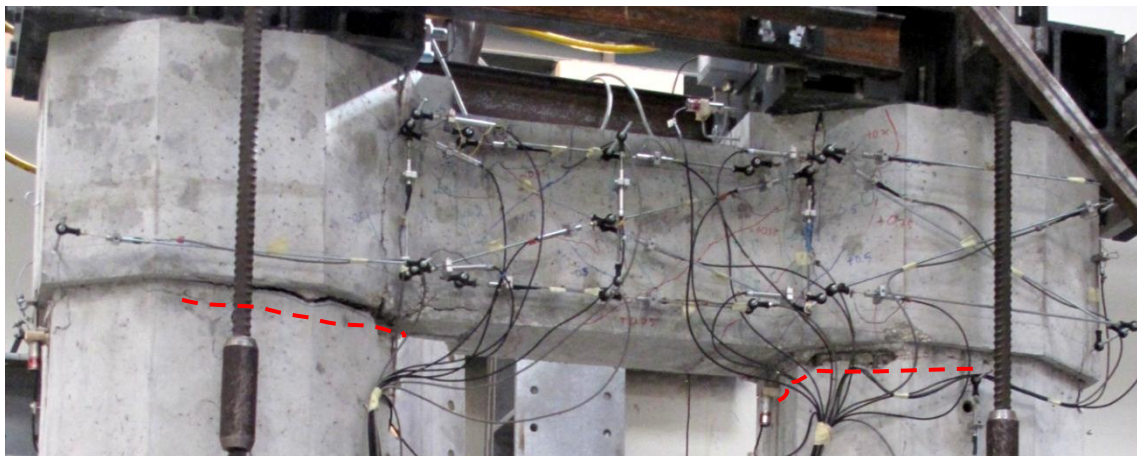
Figure 5.64 – SP_M02C after testing

The beam cracking pattern was typical of a shear dominated response, with diagonal oriented cracks and vertical cracks at the beam-column vertical interfaces that first formed around the 0.30% drift level (Figure 5.65). Formation of new cracks nearly stopped after 0.75% drift, when mostly crack depth and width were observed to be increasing. The influence of the strong shear mechanism that was apparent in the precast specimens could, nonetheless, also be identified in this case, and the vertical cracks saw a large development, as clearly illustrated by the last picture of Figure 5.65.
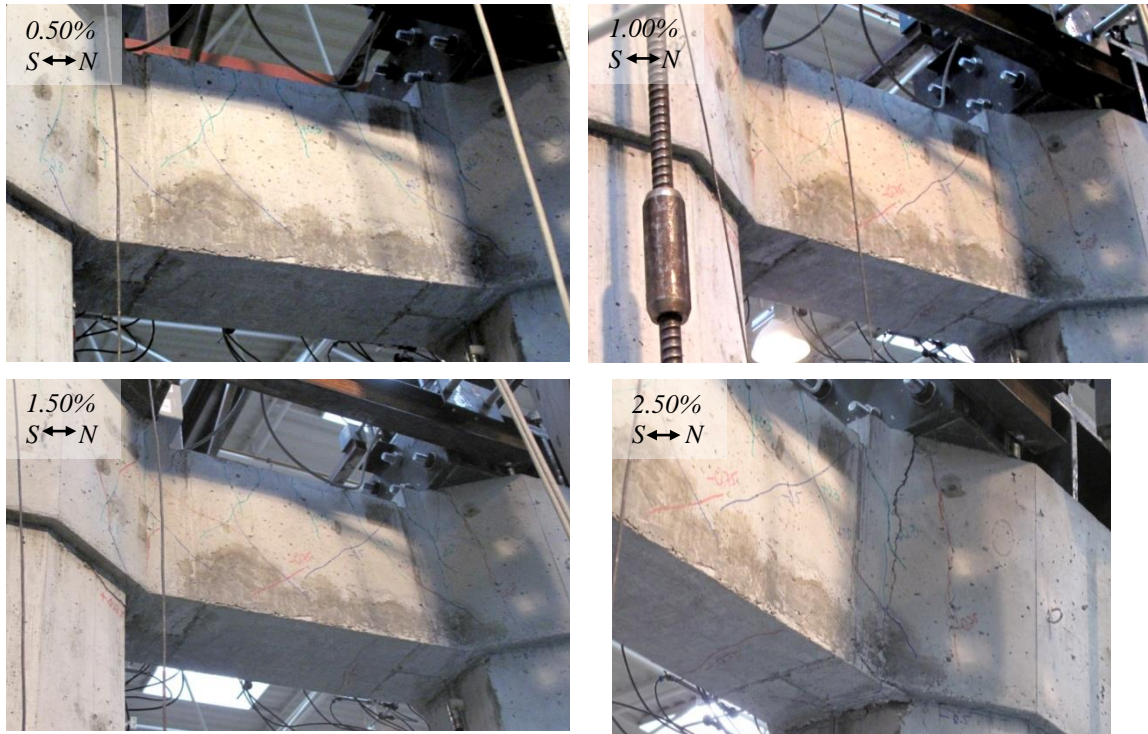
Figure 5.65 – SP_M02C Beam cracking pattern

The columns observed virtually no cracking outside of the previously identified zone. The formation of the main crack first occurred at 0.50% drift. Eventually, crack depth and width increased significantly, as shown in Figure 5.66, to the point where rebar fracture was detected.

Figure 5.66 – SP_M02C South beam-column joint crack width evolution

5.2.2.5. Summary of main results

The main observations taken from Phase 2 of the experimental campaign were the following:

- The failure mode of the precast specimens was related to shear failure at the vertical beam-column interfaces, involving large damage in the beam and low damage in the columns;
- Before failure, the precast specimens evidenced large deformations at the horizontal precast joint;

- By contrast, the reference monolithic specimen (SP_M02C) exhibited a brittle failure due to fracture of beam-column node reinforcement caused by concentration of column deformations on a single crack below the beam;

- Beam cracking started forming between 0.30% to 0.40% drift, and developed until between 0.75% and 1.50% drift;

- Column cracking generally developed between 1.00% drift and 1.50% drift, except on the monolithic specimen where it occurred earlier at 0.50% drift;

- The peak force asymmetry between loading directions ranged between 7% and 28%;

- The collapse threshold was determined at 2.50% drift in the monolithic SP_M02C specimen, while in the precast specimens it was between 3.50% drift and 4.00% drift;

- The predictive estimates of the peak force according to the *Beam_shear* and *Joint_bending* scenarios were in good agreement with the experimental values, showing differences smaller than 10% in every case.

- The experimental beam shear was in good agreement with the values determined according to the *Beam_shear* and *Joint_bending* scenarios, since the relative differences obtained were under 3%;

- All the specimens were subjected to beam shear values that exceeded the axial load level previously installed on each column, leading to decompression on at least one of them.

5.2.3. RESULTS DISCUSSION

Result analysis and discussion for the present work will mostly be provided in two segments, according to the different phases of experimental testing and their respective objectives. Nonetheless and for the purpose of global comparison, it is important that the analyses reflect the performance of each specimen over generalized demand parameters. With that in mind and taking into account that the collapse threshold and failure for all tests were determined at different drift levels, it seems appropriate to introduce the concept of cumulative ductility. Essentially, it enables characterization of the desired performance parameters over a standardized representation of inelastic incursion that inherently reflects the actual loading history and the mechanical properties of each structural system (e.g.: stiffness). By doing so, it also provides improved flexibility for comparing results of tests where different conditions were explored.

Within that context, in this work the concept is associated with displacement ductility, considered in cumulative terms for values recorded in the horizontal actuator's internal LVDT, calculated according to equation 5.1 where *i* represents each half-cycle on post yielding phase, aiming at evaluating the inelastic incursion of specimens under cyclic loading. For that purpose,

it is necessary to define the yielding displacement, which can be done by adopting an idealized equivalent bilinear response; in this work it is characterized by an elastic branch determined using the ¾ rule proposed in Park (1989) and a hardening branch established for the peak force. The yielding displacement and the hardening branch slope for the idealized system are calculated to display the same area under the curve up to the peak force displacement as the actual monotonic envelope of the cyclic tests. That procedure is further highlighted in Figure 5.67, in which the ductility of the first half-cycle after yielding occurrence is calculated according to equation 5.2, where d_y represents the yielding displacement. For each subsequent half-cycle the values of $\Delta\mu_i$ (calculated according to equation 5.3) are determined for the maximum absolute displacement $|d_i| > |d_y|$ with Δd_y defined by equation 5.4. This methodology was adapted from a similar proposal by Galano and Vignoli (2000) established for ductility values in rotation, in order to use displacement based recordings and to consider the possibility for a hardening branch. The described methodology has already been successfully used by the author for the purpose of experimental result analysis, according to the work published in Monteiro *et al.* (2017b) (and also in Monteiro *et al.* (2017a), currently under review).

$$\mu_i^{cum} = \mu_{i-1}^{cum} + \Delta\mu_i \qquad\qquad 5.1$$

$$\mu_1 = \frac{d_1}{d_y} \qquad\qquad 5.2$$

$$\Delta\mu_i = \frac{\Delta d_i}{d_y} \qquad\qquad 5.3$$

$$\Delta d_i = d_i - d_y \qquad\qquad 5.4$$
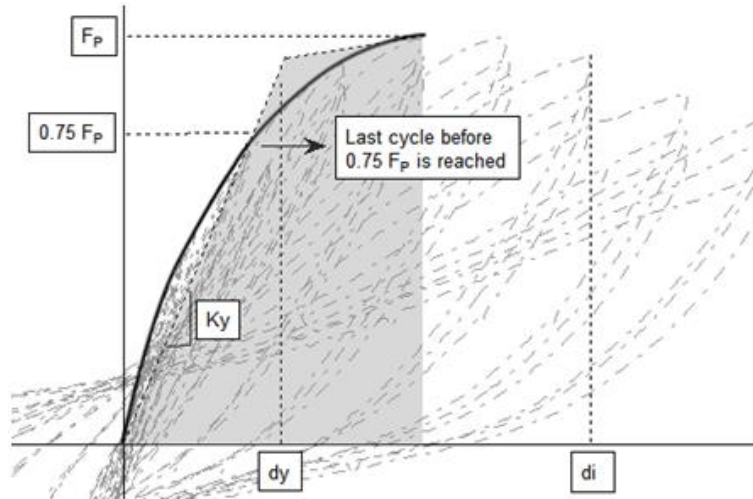
Figure 5.67 – Procedure for definition of equivalent bilinear systems

5.2.3.1.   Global Behavior and Damage Incursion

Comparison of the global behavior exhibited by each specimen is performed by analyzing the drift levels at which the experimental evidence shows increased damage. For that purpose, four performance levels were defined, according to the observations made during the tests:

- Performance Level 1 (PL1): Detection of beam cracking;
- Performance Level 2 (PL2): Detection of column cracking;
- Performance Level 3 (PL3): Detection of concrete crushing/spalling;
- Performance Level 4 (PL4): Collapse of the specimen;
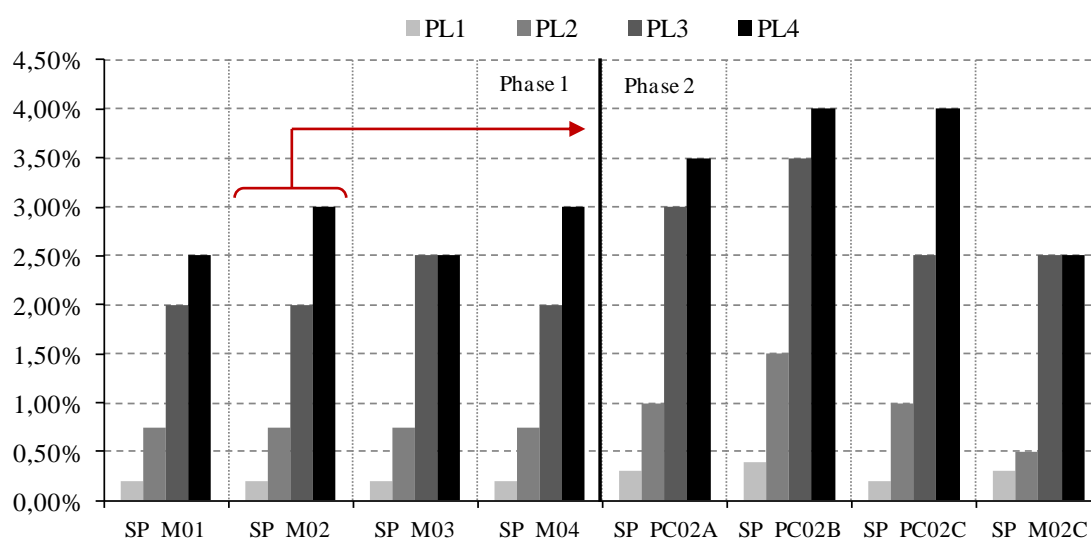
Figure 5.68 – Performance level comparison between Phase 1 and Phase 2 specimens

Figure 5.68 summarizes many of the points that were previously discussed, and presents them in a more intuitive and visual form, in which the red arrow serves as a reminder that all Phase 2 specimens were designed according to the same rhombic truss beam layout of SP_M02. In light of those results, it is clear that the precast specimens of Phase 2 displayed better performance than all of the monolithic specimens, even SP_M02C, since nearly all the performance levels occurred at higher drift levels. This is especially more relevant for the performance levels PL3 and PL4, which are the most revealing of considerable damage experienced by the specimens, and are generally delayed by around 1.00% drift in all the precast tests.

Regarding Phase 1 specimens, cumulative ductility and respective yielding drifts are illustrated in Figure 5.69. According to those results SP_M04 and SP_M01 achieved yielding significantly earlier than SP_M02 and SP_M03 (especially in the positive loading direction). This is particularly important because it also relates with the cumulative ductility experienced

by the specimens, since they were subjected to inelastic deformations from an earlier stage, potentially leading to overall increased energy dissipation. Despite that, only SP_M04 seemed to benefit from this, showing the highest cumulative ductility value of all the Phase 1 test specimens while SP_M01 mobilized around half that value, which may be explained by the earlier failure it also experienced. On the other hand, SP_M02 achieved yielding at a later stage, but also mobilized greater peak strength than both SP_M01 and SP_M04, and later failure than the former of the two, enabling the second largest cumulative ductility of all the test specimens, which are some of the reasons that supported the decision of designing Phase 2 specimens based on the reinforcement layout of SP_M02 (although results seem to indicate better overall performance on SP_M04). Finally, the conventionally reinforced specimen SP_M03 showed the overall lowest cumulative ductility values, which is not surprising considering its performance also showed a large "pinching" effect and the brittle failure that ensued.

	SP_M01	SP_M02	SP_M03	SP_M04
d_y^+ (%)	0,86	1,29	1,34	0,82
d_y^- (%)	0,74	0,84	0,94	0,81
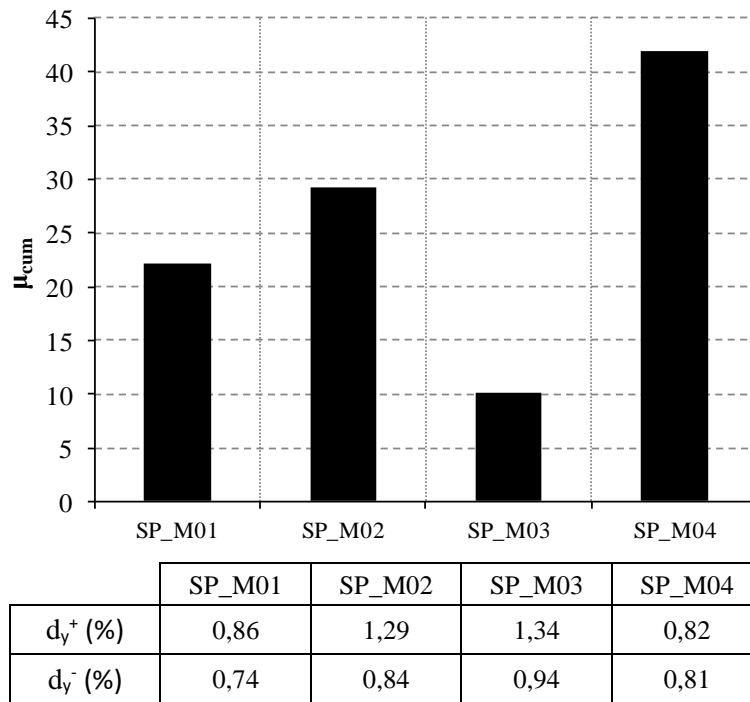
Figure 5.69 – Cumulative ductility at the collapse threshold (for the positive loading direction) and yielding drifts (for both directions) for Phase 1 specimens.

Regarding Phase 2 tests, the cumulative ductility was shown to be significantly larger in the precast than in the monolithic specimens, as observed in Figure 5.70, where results from the reference monolithic SP_M02 specimen (from Phase 1) were also included (in grey) for comparison. In that regard, SP_PC02A shows the lowest cumulative ductility value among the three precast models, but it still almost doubles the value of SP_M02C (highest of the monolithic specimens under analysis). That difference increases for the other two specimens, particularly for SP_PC02C, which, considering that similar yielding drifts were achieved in those three cases (SP_PC02B, SP_PC02C and SP_M02C), further evidences the difference in

performance between these precast and monolithic specimens. By contrast, yielding drifts are higher for SP_PC02A and SP_M02, which helps to explain the lower cumulative ductility values they exhibit, although, in the case of the precast specimen, the peak force was also lower than observed in the cases of SP_PC02B and SP_PC02C. Nonetheless, the overall performance of the precast specimens in comparison with the monolithic models seemed to show significant improvements.

	SP_PC02A	SP_PC02B	SP_PC02C	SP_M02C	SP_M02
d_y^+ (%)	1,07	0,88	0,88	0,89	1,29
d_y^- (%)	0,85	0,89	0,78	0,87	0,84
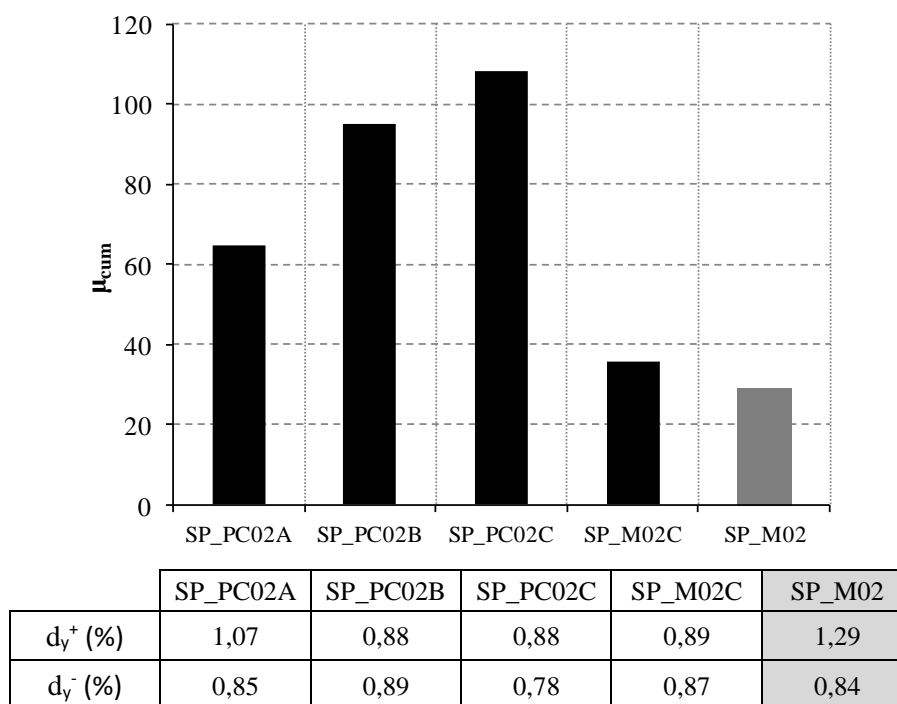
Figure 5.70 – Cumulative ductility at the collapse threshold (for the positive loading direction) and yielding drifts (for both directions) for Phase 2 specimens.

5.2.3.2. Beam Shear Degradation

As discussed before, shear forces mobilized in the beam are paramount for the cyclic response of this frame type because considerable lateral stiffness is added by the shear interaction between columns. The tests performed in this work allowed obtaining the actual internal forces involved in that structural mechanism, by relating the vertical reactions recorded in load cells at the columns' base sections with the axial loads imposed by the prestressed rods. Thus, regarding Phase 1 specimens the peak beam shear forces (V_p) obtained in the four tests are presented in Table 5.3 for both loading directions, while Figure 5.71 shows the plots for each half-cycle beam shear forces' ratios to their peak values (V/V_p) *versus* the cumulative ductility (μ^{cum}), which illustrates its influence on the inelastic incursion experienced by each specimen. Both positive and negative loading results are presented, where the former is uses a vivid blue color and the latter a light blue color. Furthermore, the drift levels recorded at 20% peak horizontal force reduction (which is equivalent to the base shear in these tests) are also

shown, where the beam shear values they represent correspond to the ultimate beam shear (V_u/V_p) recorded at the ultimate drift d_u.

Table 5.3 – Peak Beam Shear results for Phase 1 specimens

Specimen	V_p^+ (kN)	V_p^- (kN)
SP_M01	326.79	287.41
SP_M02	440.11	320.72
SP_M03	440.01	287.77
SP_M04	376.67	290.43
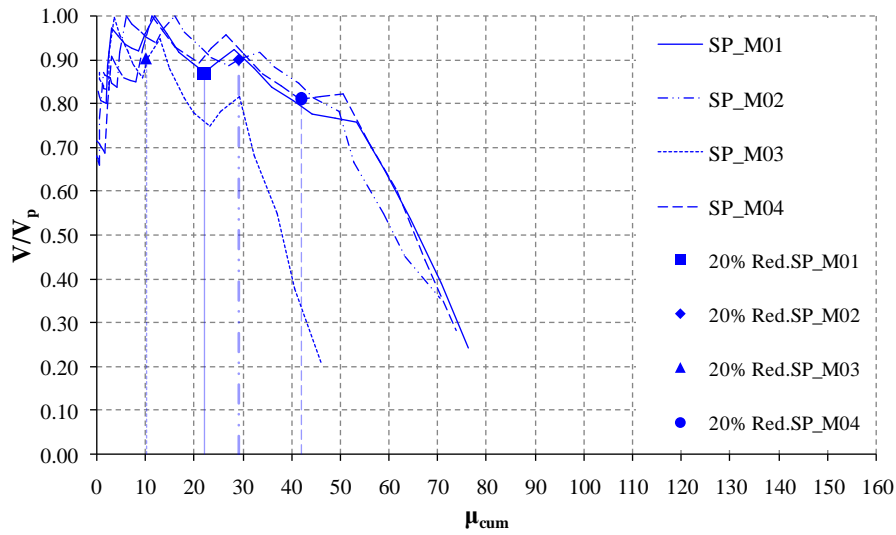
a) Positive loading direction
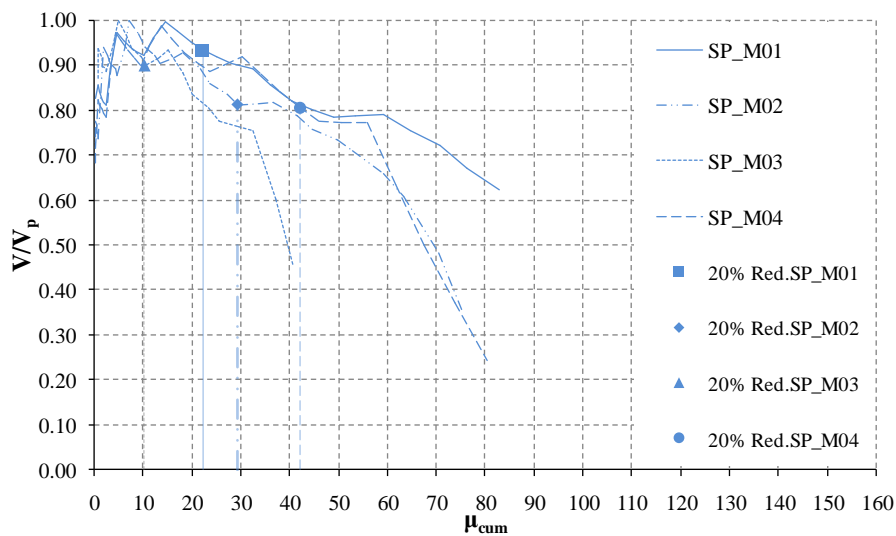
b) Negative loading direction

Figure 5.71 – Beam shear vs. Cumulative ductility for Phase 1 specimens

Despite significant differences in V_p values between specimens, particularly for the positive direction, it can be seen that the 20% reduction threshold was reached for beam shear forces V_u around 90% of their V_p values on all specimens except SP_M04, for which a bit lower ratio of 80% was found. Such findings agree well with experimental observations, which evidenced shear dominated brittle failure in SP_M01 and SP_M03, while in the "rhombic truss" variants (SP_M02 and SP_M04) it was observed after gradual strength degradation. In addition, 20% peak force reduction is achieved for beam shear reductions between 10% and 20%, thus indicating that the overall strength reduction is strongly related with the strength degradation in the beam. After the 20% peak force reduction threshold, it can be seen that the conventionally reinforced specimen SP_M03 was the least resilient one, keeping beam shear above $0.8V_u$ just up to cumulative ductility values about 20. All the other specimens performed similarly between them, being able to sustain the same shear load ($0.8V_u$) nearly until around twice the μ_{cum} value.

A relative difference around 35% is observed between overall peak beam shear values, with the smaller loads obtained again for SP_M01 and SP_M04, which is strongly related to the smaller base shear values also recorded in those tests, as opposed to SP_M02 and SP_M03. Nonetheless, the shear forces mobilized through the coupling beam in all the specimens are greater than the level of applied dead load (300 kN), highlighting the contribution of the coupling beam in this system.

Regarding Phase 2 specimens, Table 5.4 presents the maximum beam shear values recorded on the respective tests (including results from SP_M02 for comparison, in the grey shaded row), where, again, a considerable difference can be observed between loading directions. In these results, the important contribution of the coupling beam is again evidenced, since values for positive loading again exceeded the level of the applied dead load, although slightly smaller forces were observed for the negative loading direction.

Table 5.4 – Peak Beam Shear results for Phase 2 specimens

Precast	V_p^+ (kN)	V_p^- (kN)	Monolithic	V_p^+ (kN)	V_p^- (kN)
SP_PC02A	328,63	277,53	SP_M02C	345,11	263,40
SP_PC02B	327,43	275,13			
SP_PC02C	352,21	281,06	SP_M02	440,11	320,72

In addition, Figure 5.72 presents the plot of the normalized maximum beam shear (V/V_p) of each half-cycle against cumulative ductility for all the specimens, illustrating its evolution according to the inelastic incursion. Evolutions are again separated for positive and negative direction half-cycles' curves; the former are plotted in vivid red and the latter in light red, and in

both plots the values for the reference monolithic specimen SP_M02 are also presented in grey color for comparison. Within this context, it is possible to observe that a cumulative ductility value between 20 and 30 is the threshold upon which shear degradation starts to notably increase.
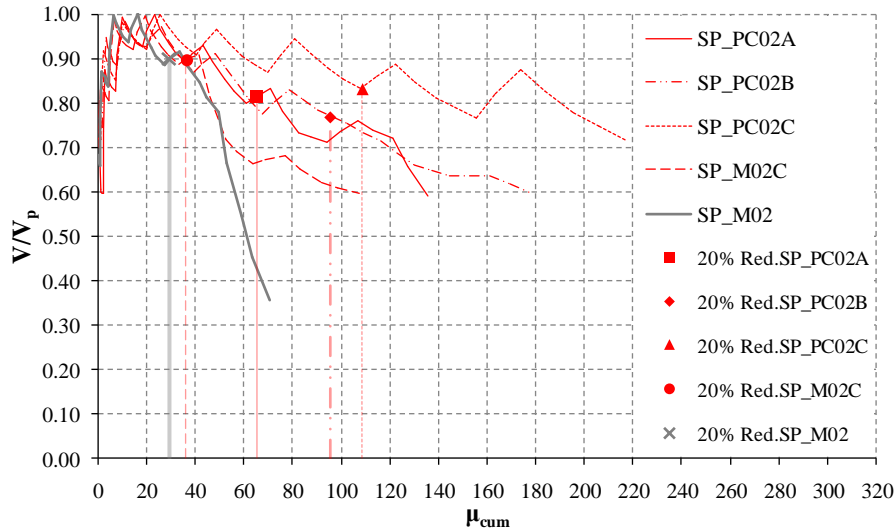
a) Positive loading direction
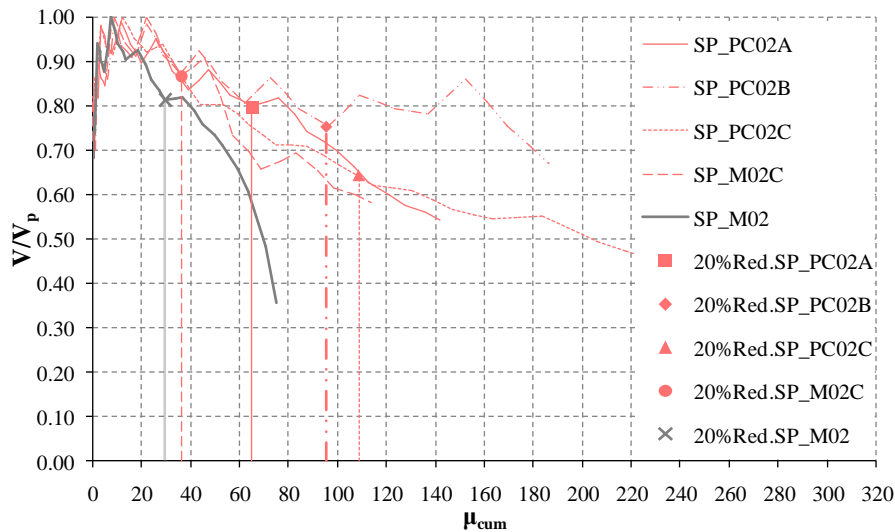
b) Negative loading direction

Figure 5.72 – Beam shear vs. Cumulative ductility for Phase 2 specimens

The results of the monolithic and the precast specimens present some noteworthy differences. Referring only to the positive direction, the former experienced beam shear drops to around 70% of the corresponding maximum at cumulative ductility values between 50 and 60, while the others were able to keep the same performance level up to nearly twice the cumulative ductility values (over 116). Additionally, the overall evolution of all precast specimens presents similar shear loss, although with slightly different decrease rates.

Regarding the previously defined collapse threshold of 20% reduction of the lateral peak force, it is possible to observe that specimens SP_PC02A and SP_PC02B reached that stage with beam shear loss around 20%, but in the SP_PC02C case, significant differences were recorded in both directions. For positive loading a value slightly above 80% can be observed, while for negative loading the shear loss was almost 40%. By contrast, the beam shear loss at the collapse threshold on the monolithic models was less than 20%, particularly for positive loading (around 90%). These findings support claiming that the precast specimens benefitted the most of exploring column capacity, since the 20% peak force reduction could be achieved with larger beam shear loss, in comparison with the other tests. Conversely, structural response in monolithic models shows more dependency of the beam, since force degradation is associated with smaller losses in beam shear.

5.2.3.3. Stiffness Degradation

Stiffness degradation can be an important aspect to take into account regarding the seismic performance of bridge piers. In fact, common design strategies require adequate structural ductility, which is often related with the secant stiffness for the last half-cycle before collapse is reached. Thus, lower stiffness degradation means that post-peak strength is kept at less reduced levels for larger deformation and, consequently, higher ductility is achieved.

Figure 5.73 shows stiffness degradation plotted against cumulative ductility for Phase 1 specimens, in terms of the ratio (K/K_y) of secant stiffness (K) to yielding stiffness (K_y), where the both loading directions are represented separately (vivid blue for positive loading and light blue for negative loading). The behavior was globally similar between all specimens, but around cumulative ductility values of 35 the conventionally reinforced model (SP_M03) showed increased rate of stiffness degradation, since the corresponding secant stiffness was found to be around 10% of the yielding stiffness at cumulative ductility of 45 on negative loading. On the other cases, cumulative ductility values around 70 could be achieved before similar degradation of the secant stiffness was achieved.

When looking at the 20% peak force reduction markers that are also illustrated in Figure 5.73, SP_M03 was found at more than 50% of the corresponding yielding stiffness, while the two rhombic truss variants SP_M04 and SP_M02 showed increased degradation up to nearly 30% of the yielding stiffness (for positive loading); SP_M01 ended up in between those two values.
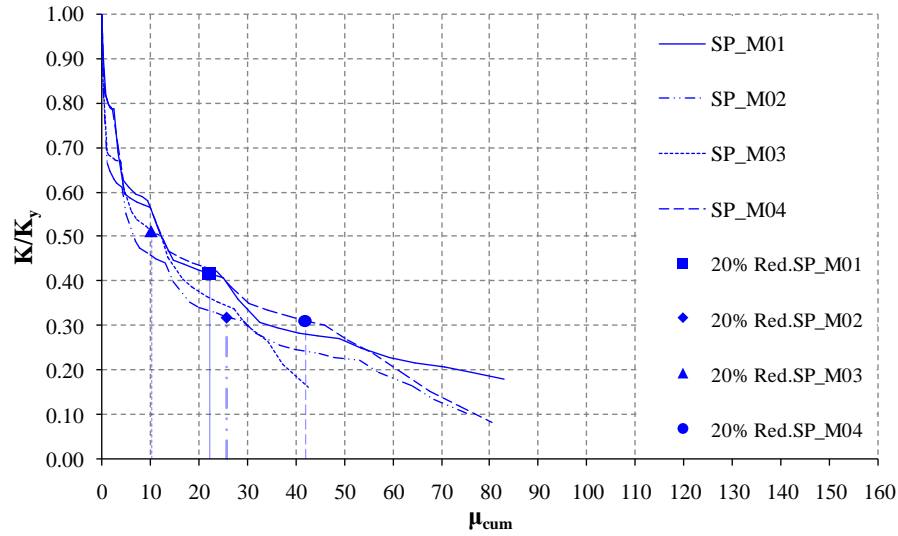
a) Positive loading direction
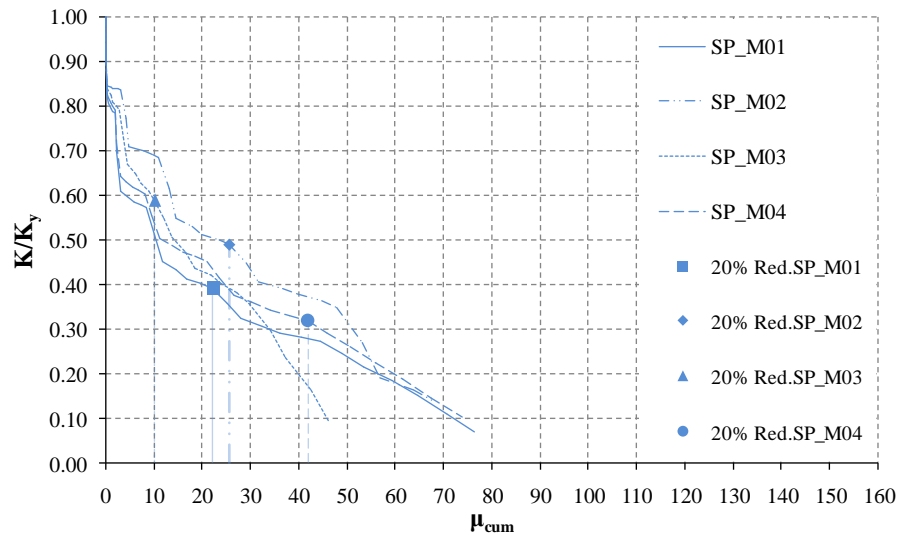
b) Negative loading direction

Figure 5.73 – Stiffness degradation vs. Cumulative ductility for Phase 1 specimens

Figure 5.74 illustrates the values of the secant stiffness (K) normalized by the yielding stiffness (K_y) calculated for the Phase 2 tests, which are plotted against the corresponding cumulative ductility. The values for positive loading are reported in vivid red, while negative loading values are shown in light red; the reference SP_M02 model results are also included in grey lines for comparison purposes.

It can be observed that the general performance of all the specimens was globally similar, according to the general development of the plotted curves. It can be observed that all the specimens reach 50% of the yielding stiffness very early on, for cumulative ductility values between 10 and 20. Regarding the 20% collapse threshold, in precast specimens it was achieved

with secant stiffness values between 15% and 30% of the yielding stiffness, while the monolithic specimens were found at upwards of 30% of the yielding stiffness. Furthermore, all the tests of Phase 2 showed relatively stabilized curves for values of K/K_y less than 20%.
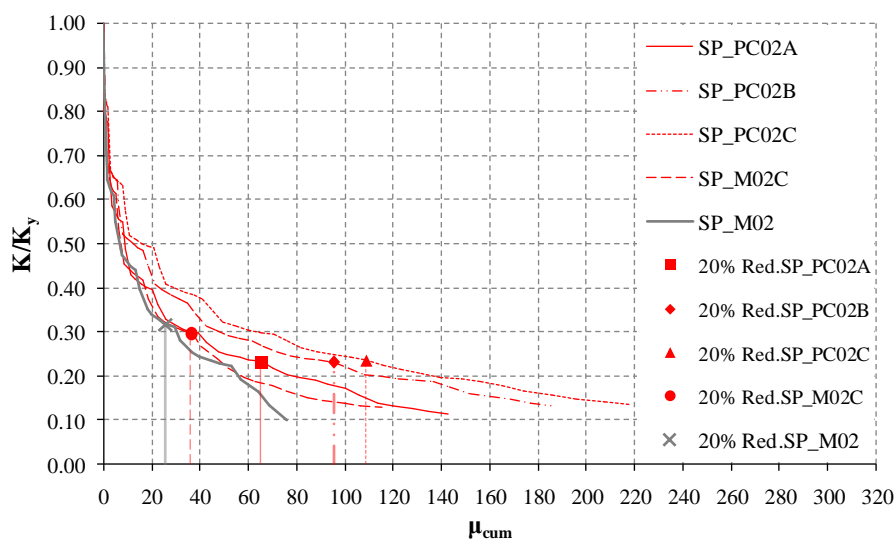
a) Positive loading direction
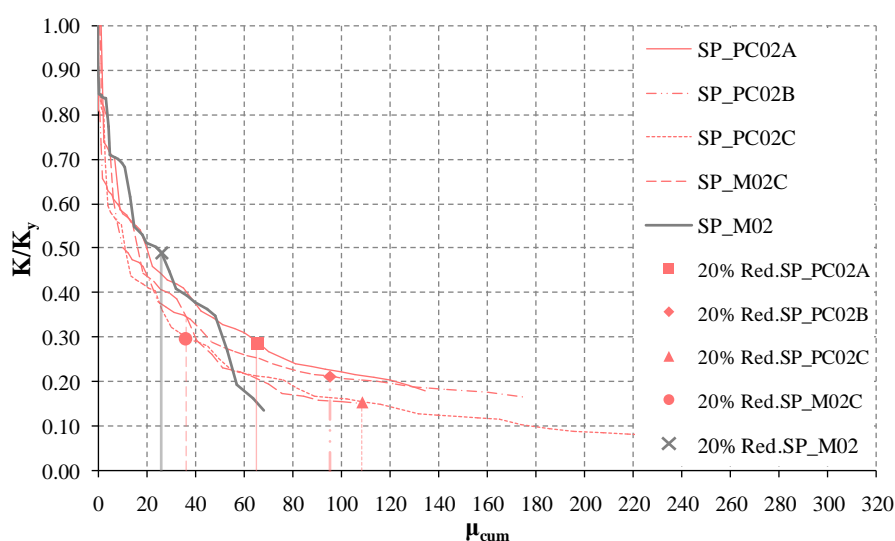
b) Negative loading direction

Figure 5.74 – Stiffness degradation vs. Cumulative ductility for Phase 2 specimens

5.2.3.4.   Energy Dissipation

Energy dissipation mechanisms in RC structures are mobilized mostly resorting to the inelastic capacity of steel to accommodate large deformations without significant force increase in the post-yielding range, which, for regular structures, occurs in the "plastic hinge" zones

usually associated with maximum bending moment locations such as column bases. In this structure, significant damage occurs in the beam region, but it is mostly originated by shear distortions and not flexural deformations of the reinforcement, which are mostly caused by the small span-to-depth geometric ratio. In this regard, although beam reinforcement is able to achieve yielding, it is believed that the same concept of plastic hinge should not be considered for interpretation of the energy dissipation of these structures, particularly because while concrete integrity holds, the load can be transferred between columns through a single compressive strut, which helps increase the total shear capacity above that which would be possible by reinforcement alone.

Regarding comparison of all Phase 1 specimens, Figure 5.75 shows the plot of cumulative energy dissipation against the number of loading half-cycles. The overall maximum dissipated energy recorded at the displacement corresponding to 20% peak force reduction was greatest on the SP_M02 specimen (about 58 kN.m), which was another reason supporting the adoption of that layout for Phase 2 tests. By contrast, SP_M03, with the conventional reinforcement layout, was notably the lowest dissipative specimen with 30 kN.m at that stage. Such results are not surprising, taking into account that the SP_M03 force vs. drift plot (Figure 5.32) exhibited severe *"pinching"* effect, considerably more pronounced than in SP_M01, SP_M02 or SP_M04 specimens. This is further confirmed by its Energy Dissipation curve, which shows considerably lower values than the other three specimens. Concerning the SP_M01 test, it showed similar energy dissipation evolution to the rhombic truss variants but lower value at 20% peak force reduction than SP_M02, suggesting that a potentially better performance was hindered by sudden occurrence of sliding shear failure, as previously discussed.
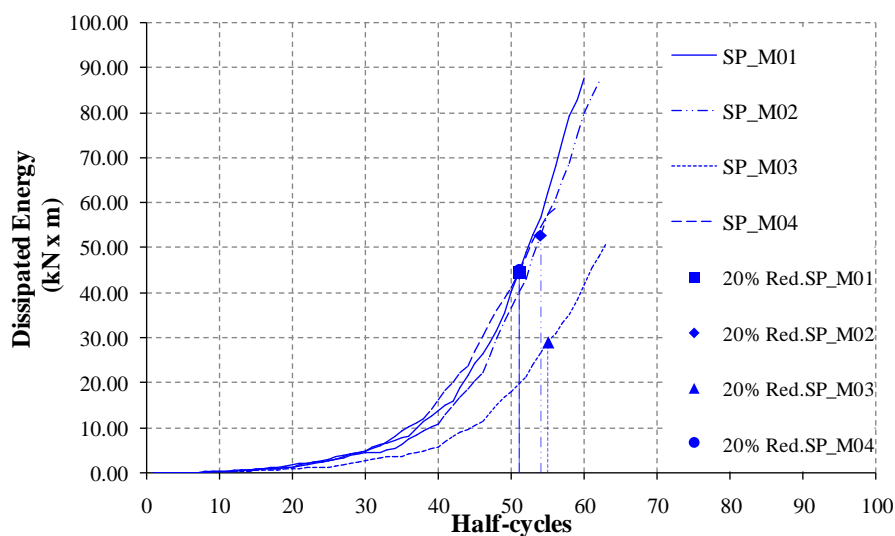
Figure 5.75 – Energy dissipation vs. Loading half-cycles for Phase 1 specimens

Results for cumulative dissipated energy for Phase 2 tests are presented in Figure 5.76, where related specimens' values are represented by the red lines and the grey lines link to results for the reference SP_M02 model, included for comparison purposes. As it is possible to observe, the rate of increase of energy dissipation is similar in all the specimens, since they generally follow the same outline. However, when taking into account the half-cycle at which the 20% force reduction threshold is achieved, it is possible to understand that the two monolithic models performed poorly relative to the precast specimens, since they provided considerably less energy dissipation until that stage. This is particularly relevant in the case of the SP_M02C specimen, confirming that the deformation mechanism provided by the opening/closing of the large crack formed at the beam-column intersection (Figure 5.66, which is naturally less ductile than the behavior evidenced by the precast specimens) had reasonable impact in the overall performance of that pier. Finally, the precast specimens SP_PC02B and SP_PC02C (where splicing φ12 rebars were used to provide moment continuity) enabled the best results in this regard, closely followed by SP_PC02A.
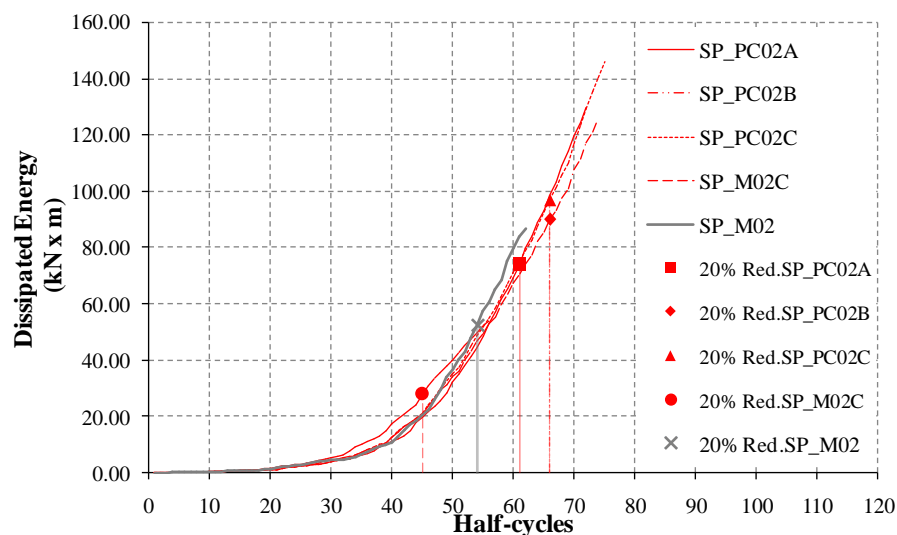
Figure 5.76 – Energy dissipation vs. Loading half-cycles for Phase 2 specimens

5.2.3.5.   Beam-column deformations

Two different ratios were considered for evaluating the relative deformations at the beam and column elements. The concepts indicated in Figure 5.77 were calculated according to the available data recorded during the tests, at the south column (S, see Figure 5.1 – a)), determined as follows:

1) $R_1 = \varphi_c/(\varphi_c + \varphi_b)$: ratio between the column and beam curvatures, calculated from mean rotations recorded on positive bending moments by local LVDTs, at the immediate vicinity of both interfaces of the beam-column node;

2) $R_2 = \alpha/\gamma$: ratio between the beam rotation (α), directly recorded by tiltmeters on the top of the column and the chord rotation (γ) of the column, obtained from horizontal LVDTs at its top section;

a) Ratio R₁   b) Ratio R₂
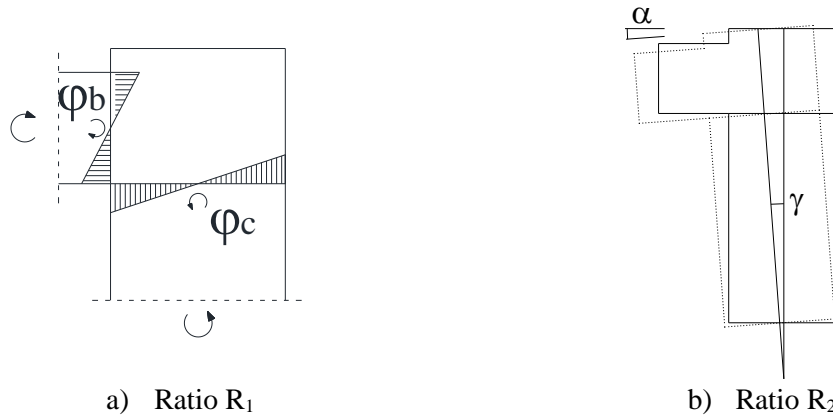
Figure 5.77 – Illustration of the parameters used for calculating the ratios used in this work for comparison of beam-column deformations

The above defined ratios were calculated only at the following four drift levels: 0.50%, 1.00%, 1.50% and 2.00%, since some LVDT recordings were not available for the full extent of the applied loading histories. Values of R₁ closer to 100% indicate that the local deformations recorded at the column side of the node are considerably more relevant than those at the beam, while the contrary is associated with values closer to 0%. Regarding ratio R₂, values of 100% can only be ensured if fully rigid motions of the column body are observed, since that would essentially be equivalent to have the same rotations of column axis and column head. Conversely, if the beam element exhibited fully rigid behavior, then the column head surface rotation would be negligible, and all deformations would occur at and below the beam-column intersections. For reference, the described methodology was also presented in Monteiro *et al.* (2017a).

Ratio R₁ values for Phase 1 (Figure 5.78) specimens were generally found between around 20% at 0.50% drift and 60% at 2.00% drift. In that regard, an evolution of R₁ values between the referred lower and upper bound could be observed for specimens SP_M01 and SP_M02, whereas less variation could be found in the case of SP_M03 and SP_M04. In general, these results tend to show that moment demands in the beam-column node mobilize greater curvatures in the beam than the column for a significant part of the applied loading history, which seems consistent with experimental observations of greater damage occurrences in the beams.
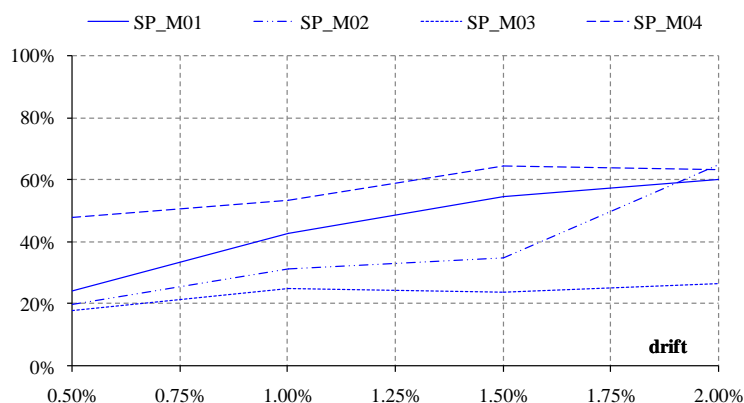
Figure 5.78 – R$_1$ deformation ratio vs. drift evolution for Phase 1 specimens

Figure 5.79 illustrates the values of R$_1$ values calculated for Phase 2 specimens (and the reference monolithic SP_M02 model), which can provide a good measurement of the local demand expected for this type of structure and, most importantly, of the contribution of the precast connection to the overall behavior and performance. This is particularly true because the LVDTs, from which column curvature data was calculated, were recording deformations within a short 0.05m distance from the joint, making it safe to assume that the calculated φ_c values were mostly due to joint opening/closing, rather than concrete strains.

Within that context, it is not surprising to see how R$_1$ values for the precast specimens are generally larger than for the monolithic models, almost achieving 100% in all three cases while the latter only achieve around 70% at 2.00% drift. Likewise, all precast specimens showed values greater than 60% from nearly 0.75% drift, while monolithic specimens only go above 60% well after 1.50% drift. It is also noteworthy that values for SP_PC02A and SP_02B show a significant decrease to the 70%-80% range at 2.00% drift, after having reached almost 100% a few cycles earlier; this is likely caused by the increase of beam deformations that occurs due to shear degradation of the vertical beam-column interfaces.
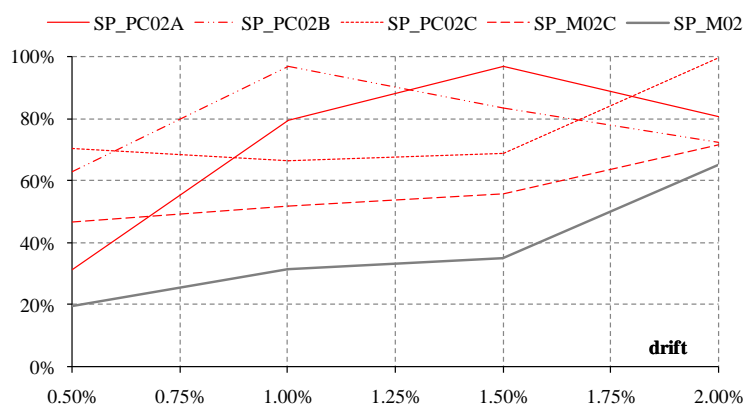
Figure 5.79 – R$_1$ deformation ratio vs. drift evolution for Phase 2 specimens

Figure 5.80 illustrates R_2 values for Phase 1 specimens, and nearly all of them show low variation throughout the test. In general, values between around 60% - 70% at 0.50% drift and 80% - 90% at 2.00% drift were recorded, showing that deformations along the column body have a relatively low impact on the overall rotation of the column head. The case of SP_M01 is the only one where significant variation occurs, since R_2 values go from 40% at 0.50% drift to nearly 90% at 2.00% drift, but this finding could also be related to gradual increases of the sliding motions observed during the test, since it accommodates most of the deformations.
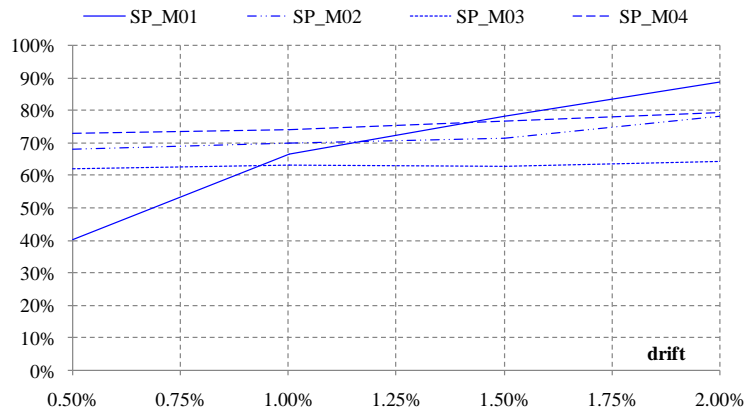
Figure 5.80 – R_2 deformation ratio vs. drift evolution for Phase 1 specimens

Regarding Phase 2 specimens, corresponding R_2 values are illustrated in Figure 5.81 (also including the reference monolithic SP_M02 model). Observed values show, in general, very different scenario from that observed in Phase 1 tests. In this case, all specimens exhibit a decrease of R_2 values throughout the tests, going from between 70% - 90% at 0.50% drift to 40% - 60% at 2.00% drift. A likely explanation is that the precast columns (and SP_M02C due to the formation of its large concrete crack at the joint location) accumulate large deformations at the joint section, leading to a shift in the beam-column stiffness ratio in favor of the beam. Although the decrease rate of R_2 seems to be similar on all the specimens, SP_PC02A (precast) and SP_M02C (monolithic) reach the 2.00% drift level with the smaller values of R_2, around and below 40%, respectively.
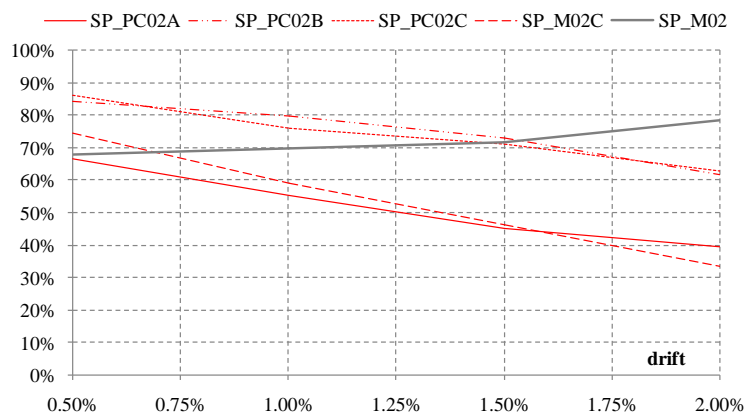
Figure 5.81 – R$_2$ deformation ratio vs. drift evolution for Phase 2 specimens

5.3. EXPERIMENTAL RESULTS – SINGLE COLUMN TESTS

5.3.1. PHASE 3 OBSERVATIONS

Experimental observations regarding Phase 3 tests are based on force – drift curves established for the internal displacement of the horizontal actuator (Figure 5.18), and the same strategy is also considered for defining the collapse threshold. In addition, a single predictive estimation scenario is presented for the peak lateral force, related to the bending capacity calculated in the base of the columns using the real material properties (Table 4.12) of each specimen, in order to calibrate the constitutive relationships for moment – curvature analyses in Cast3m (using the same constitutive models as before). For that purpose, the precast connections were assumed to enable similar performance to a monolithic cross-section under the same axial load (300 kN), leading to the results presented in Figure 5.82.
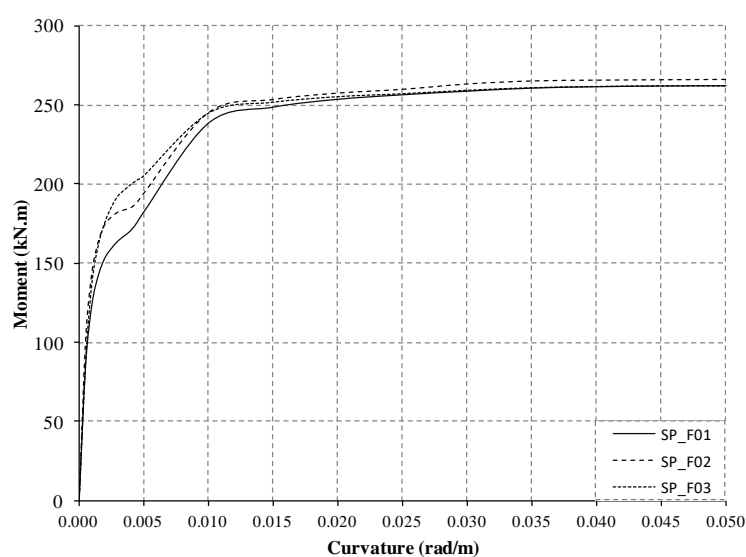
Figure 5.82 – Moment – curvature analysis results for Phase 3 specimens

5.3.1.1. SP_F01 specimen results

The cyclic force-drift curve for SP_F01 is illustrated in Figure 5.43, where the collapse threshold is identified at the 3.50% drift level for the positive loading direction only. A minimal peak force asymmetry of around 5% was observed between them, and the difference between the bending capacity determined from the results of Figure 5.82 (taking into account force application at 1.95m from the column base), and the experimental maximum values is also negligible. The failure mode on SP_F01 occurred due to buckling and consequent fracture of the longitudinal reinforcement.

$F_p^+ = 138.41$ kN
$F_p^- = 131.61$ kN
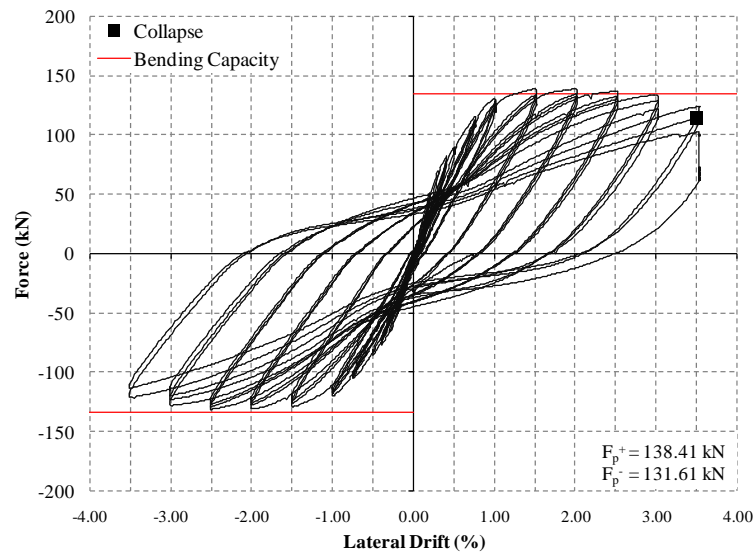
Figure 5.83 – SP_F01 force-drift results

Column cracking (Figure 5.83) was first detected at the 0.50% drift level, with a few thin cracks near the footing. That pattern developed between the 0.75% and 1.00% drift levels, where the crack width and depth increased and spread over a larger column height. In general, it could be observed that by the 1.00% drift level, the bottom crakcs from both the North and South side of the column transformed into a single crack spanning the whole cross-section depth. Furthermore, cracking was regularly distributed, since crack distance was similar to that of the transverse reinforcement.
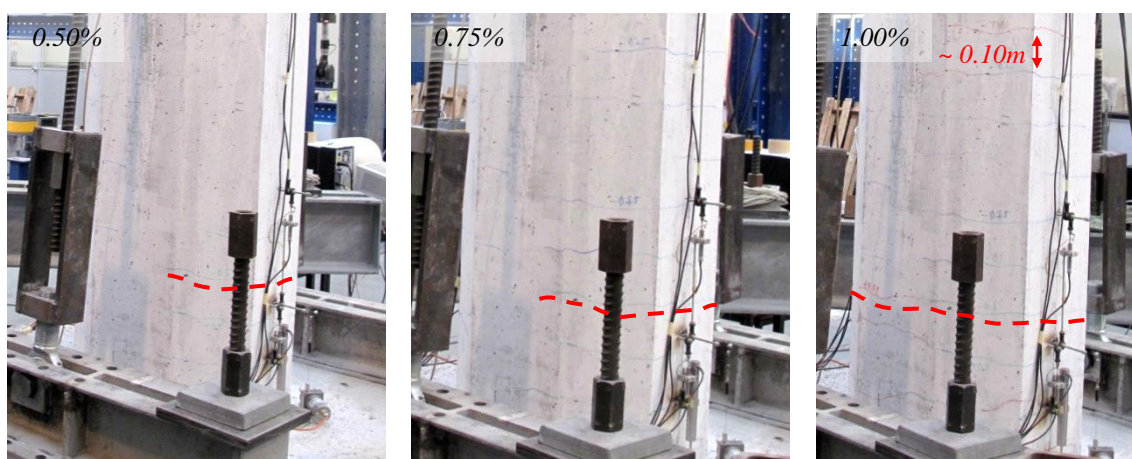
Figure 5.84 – SP_F01: Evolution of column cracking pattern

Afterwards, that process stabilized and only crack width increases could be observed. At the 2.50% drift level, mild spalling was detected, which evolved until full concrete cover detachment started occurring at 3.00% drift, as well as main rebar buckling that would eventually lead to rebar fracture at 3.50% drift, as illustrated in Figure 5.85. The main spread of concrete crushing and spalling damage was located in both sides of the column, and concentrated in roughly the first 0.20m near its base.

Figure 5.85 – SP_F01: South side onset of spalling, buckling and fracture

5.3.1.2.   SP_F02 specimen results

The cyclic force-drift curve for SP_F02 is illustrated in Figure 5.86, and the collapse threshold was found at the 3.00% drift level for both positive and negative loading directions. The peak force asymmetry was negligible, less than 3%. In addition, the bending capacity determined from the moment curvature analyses agrees well with the results obtained, since the difference between the numerical and experimental values is less than 4%. Failure of SP_F02 occurred through fracture of several longitudinal rebars, as a consequence of bending induced buckling.
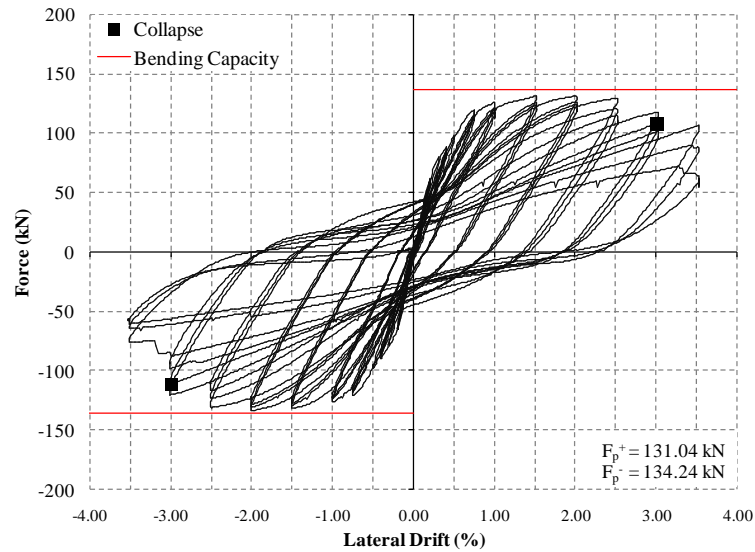
Figure 5.86 – SP_F02 force-drift results

Column cracking was first detected at the 0.30% drift level, on the north side of the column only. From 0.40% drift onwards, those cracks developed in the same way as SP_F01, with increases in crack width, depth, and progression over a larger column height. The observed cracks followed a horizontal orientation with regular distribution similar to the distance between stirrups (0.10m), as shown in Figure 5.87. Around 0.75% drift, the cracks formed at opposing sides of the columns nearest to the column base were sufficiently developed that they converged into a single crack.
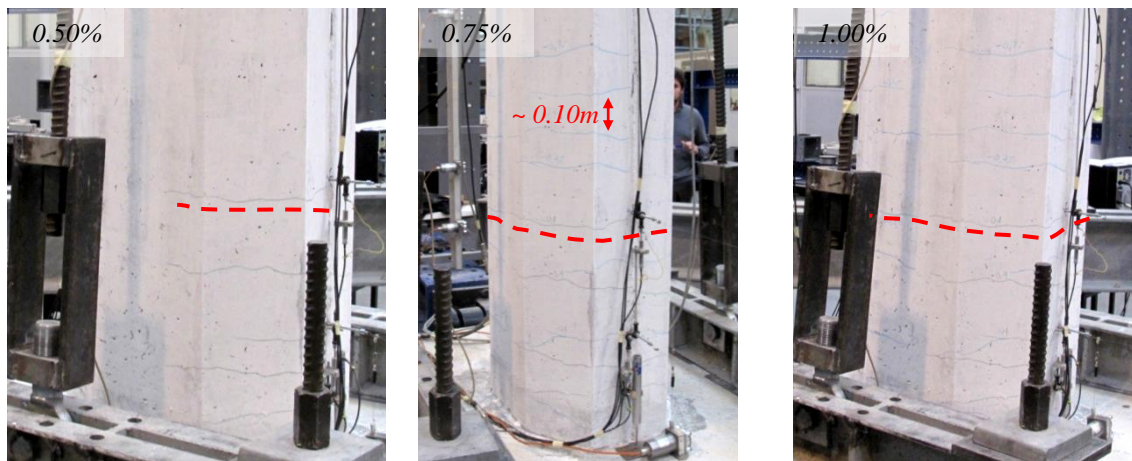
Figure 5.87 – SP_F02: Evolution of column cracking pattern

The bulk of cracking occurred until 1.00% drift, and a stabilized cracking pattern could be observed afterwards. Eventually, concrete crushing was detected at 2.00% drift, leading to spalling and buckling of the main reinforcement at 2.50% drift and subsequent fracture, first detected at 3.00% drift, according to the pictures shown in Figure 5.88. As it is possible to

observe, the main damage spread (particularly concrete crushing and spalling) was located quite near the footing, roughly in the first 0.10m to 0.15m length, on both sides of the column.

Figure 5.88 – SP_F02: North side onset of spalling, buckling and fracture

5.3.1.3.   SP_F03 specimen results

Figure 5.89 shows the force-drift results for SP_F03, where the collapse threshold can be found at the 2.50% drift level for both loading directions. However, the observed response shows unusual and unexpected behavior, where an effect similar to stiffening, rather than softening, can be observed for the post-peak displacement cycles (particularly for loading at the 2.50% and 3.00% drift levels). The reason for that is not clear, but one explanation may be the occurrence of sliding of the column along the precast joint section, leading to the progressive adjustment of the compressive struts, seeking stability after initial grout crushing and enabling further exploration of the reinforcement capacity. On the other hand, it may more likely be caused by a progressive failure of rebar anchorages, forcing the structure to find the required rebar strength at an increasingly lower depth, according to respective increases in drift demand, and gradually causing the degradation of surrounding grout. With the present monitoring layout it was not possible to assess this problem with certainty, however both explanations seem plausible.

The peak force asymmetry was around 6%, although the difference between experimental values and the theoretical bending capacity was of 35% and 26% for positive and negative loading directions, respectively. This relative difference is larger than that observed for either SP_F01 or SP_F02, but it can be explained by the general behavior observed in the specimen. In fact, despite the failure of SP_F03 having also occurred through rebar fracture at 3.00% drift, there are distinct characteristics of its performance pattern.
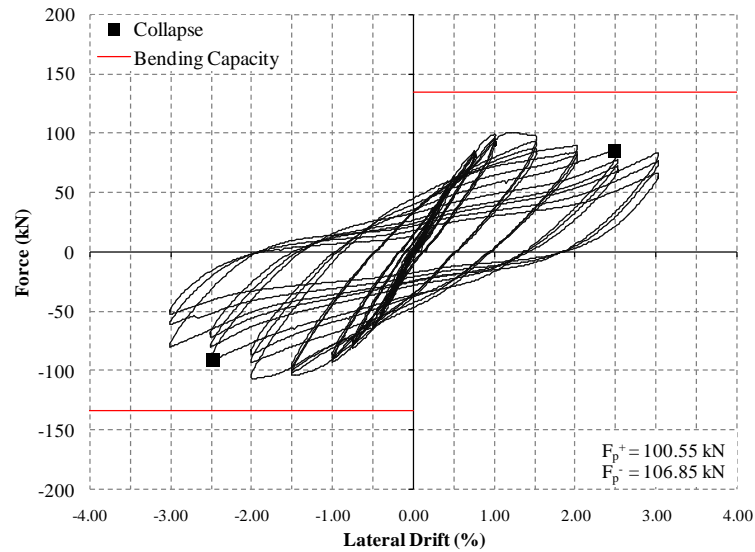
Figure 5.89 – SP_F03 force-drift results

Column cracking was first detected at the 0.40% drift level, as a clear crack formed exactly between the grout and concrete parts of the precast connection. That crack fully developed over the total cross-section depth and, while a few more cracks formed over the column height until 1.00% drift, the larger width of the first one was noticeable at naked eye. Nonetheless, horizontal cracks with a regular distribution could still be observed, as illustrated in Figure 5.90.
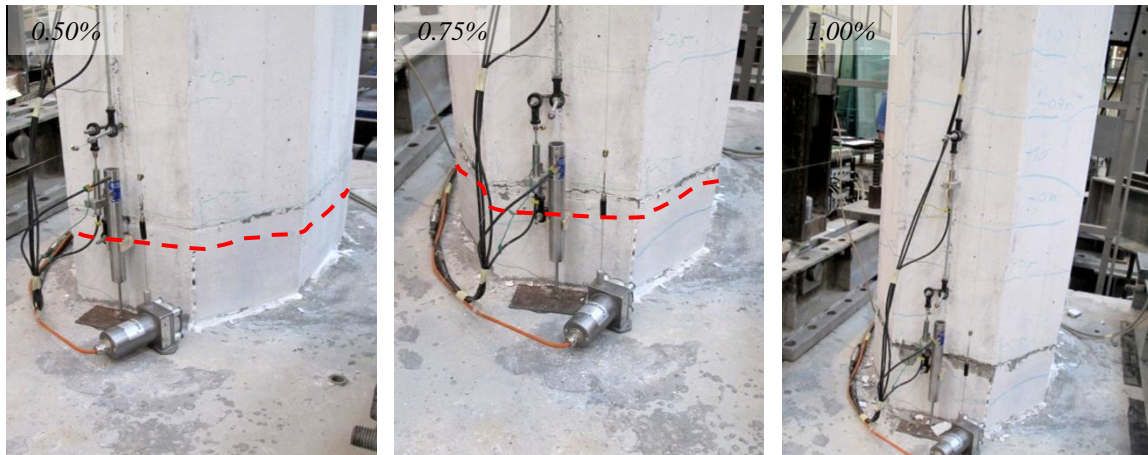
Figure 5.90 – SP_F03: Evolution column cracking pattern

After 1.00% drift, crushing and spalling of the grout below the main horizontal crack was increasingly more relevant and, at 2.00% drift, the longitudinal reinforcement was fully exposed and buckled. At this point, there was a clear gap between the grout and the column concrete, and, with the bulk of buckling occurring exactly at this section, it could be observed to be working similar to a hybrid rocking joint. Eventually, the large strains of the main reinforcement caused fracture of multiple rebars, as evidenced in Figure 5.91, and total collapse of the transition section constituting the first 0.20m of column length.
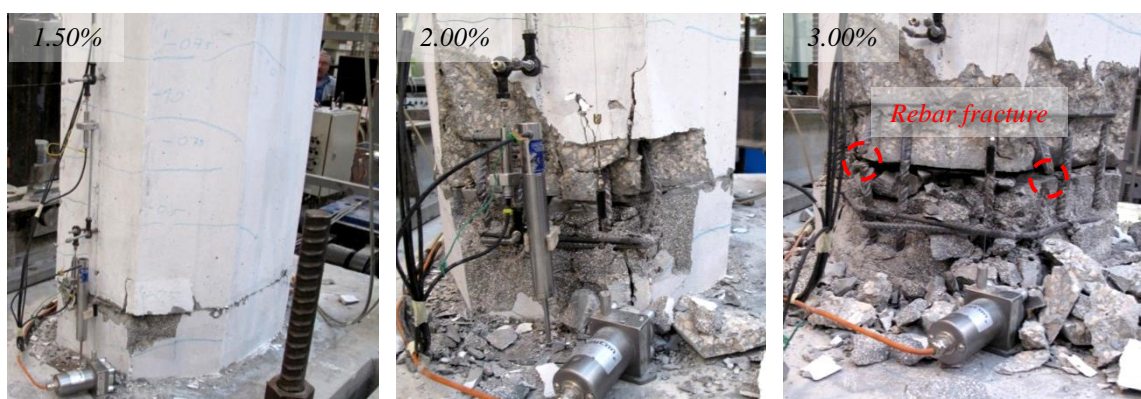
Figure 5.91 – SP_F03: North side spalling, buckling and fracture

5.3.1.4. Summary of results

The main observations taken from Phase 3 of the experimental campaign were the following:

- Cracking first occurred between 0.30% and 0.50% drift levels, and developed until 1.00% drift;

- Collapse was determined at 3.50% drift level for SP_F01 for the positive loading direction only, at 3.00% drift levels for both loading directions on SP_F02, and at the 2.50% drift level on SP_F03;

- All specimens' failure mode is associated with fracture of longitudinal reinforcement;

- Specimens SP_F01 and SP_F02 exhibited roughly equivalent behavior, with low peak force asymmetry between loading directions and similar peak forces in close agreement with the values estimated from moment-curvature analyses;

- Specimen SP_F03 exhibited considerably smaller peak force than the estimated value, related with early crushing of the grout part of the connection and overdevelopment of a gap between the grout and the column concrete;

- The large gap on SP_F03 could be observed to be performing similarly to a hybrid rocking joint;

- Specimen F03 exhibited a response in which the rebars were still able to mobilize greater strength for increasing displacement cycles, even after peak lateral force was recorded.

5.3.2. RESULT DISCUSSION

5.3.2.1. Global Behavior and Damage Incursion

Comparison of the global behavior exhibited by each specimen is performed by analyzing the drift levels corresponding to the occurrence of the following performance levels, defined according to experimental observations:

- ▪ Performance Level 1 (PL1): Detection of cracking;
- ▪ Performance Level 2 (PL2): Detection of concrete crushing/spalling;
- ▪ Performance Level 3 (PL3): Detection of longitudinal rebar buckling;
- ▪ Performance Level 4 (PL4): Fracture of longitudinal reinforcement;
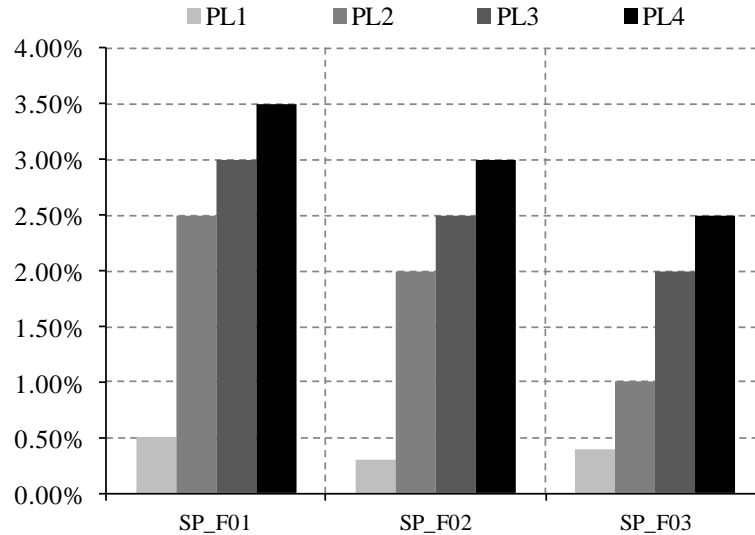
Figure 5.92 – Performance level comparison between Phase 3 specimens

Figure 5.92 presents the results associated with the performance of Phase 3 specimens regarding each of the previously defined levels. Taking into account that SP_F01 was a fully monolithic specimen, while SP_F02 and SP_F03 involved at least partial precast, it is clear that neither of the proposed footing-to-element connections could perform as good as intended. In that regard, both the precast models experienced the same performance as the monolithic specimen but at earlier drifts; considering that no significant material property or constructive detail, other than the precast mechanism, can be pointed out as a potential cause, it is firmly believed that the latter is the main reason for the worse performance of SP_F02 and SP_F03. Nonetheless, there are still considerable differences between the precast tests themselves, since SP_F03 incurred considerable damage earlier than SP_F02. In fact, the relative difference between the drift cycle when the performance levels are achieved in SP_F01 and SP_F02 is very similar to the difference between SP_F02 and SP_F03, which corresponds to a shift of around 0.50% drift.

The methodology for definition of an equivalent bilinear system previously presented in Figure 5.67 was also applied to these tests. In that regard, the obtained cumulative ductility values achieved by each specimen (until collapse is determined in the positive loading direction) are presented in Figure 5.93; relative diferences can be observed between the precast specimens, and both of them also exhibit smaller values than the monolithic model. The latter achieves a cumulative ductility of 97.4, which is around 30% larger than the value reached by SP_F02

(75.6), but almost three times larger than the value obtained in SP_F03 (35.1). The yielding drifts calculated for both loading directions according to the previously mentioned methodology are also given in Figure 5.93, showing similar values between them, with a slightly smaller one determined for SP_F02.

	SP_F01	SP_F02	SP_F03
d_y^+ (%)	0.73	0.66	0.71
d_y^- (%)	0.71	0.66	0.72
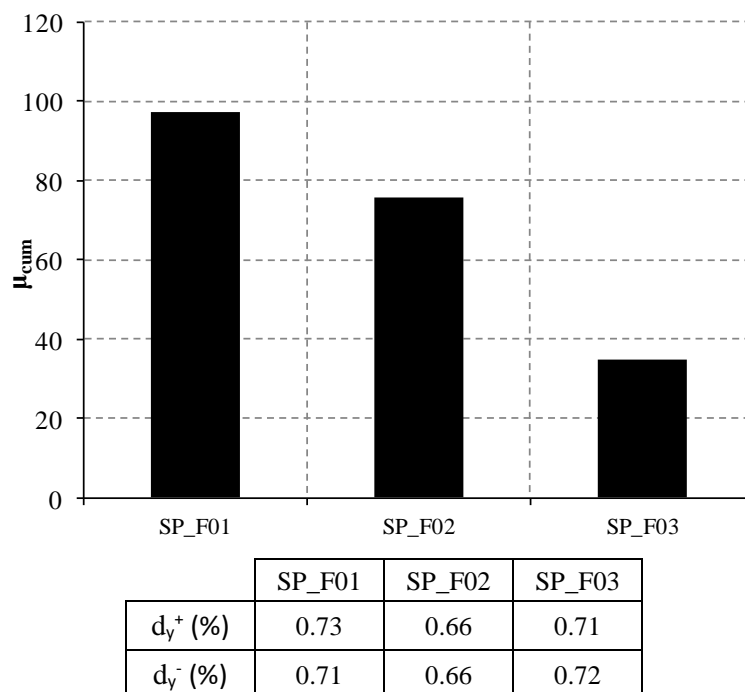
Figure 5.93 – Cumulative ductility at the collapse threshold for the positive loading direction

5.3.2.2. Stiffness Degradation

The stiffness degradation according to the cyclic loading of the Phase 3 columns was calculated for each post-yielding half-cycle and is plotted against cumulative ductility in Figure 5.94. For comparison purposes, the values for each specimen are normalized by the corresponding yielding stiffness K_y, and are represented by different line styles: solid, dash-dot and dashed, for SP_F01, SP_F02 and SP_F03 respectively. The cumulative ductility achieved as the columns reach the collapse threshold is also identified in the same figure by the different markers placed on the corresponding curves. In this regard, the general evolution of the secant stiffness is similar on all the tests, with degradation of around 50% of the yielding stiffness observed for cumulative ductility values about 10. Furthermore, while the collapse threshold is achieved within just above 30% of the yielding stiffness for SP_F03, both SP_F02 and SP_F01 are able to perform for longer, by reaching that mark within less than 25% of the yielding stiffness. The secant stiffness at the final stage (corresponding to a post-collapse threshold drift cycle) of the SP_F03 test (at about cumulative ductility of 110) was at nearly 15% of the corresponding yielding stiffness. By contrast, on the other two tests similar secant-to-yielding

stiffness ratio was achieved at cumulative ductility values of 135 and 140 (18%) for SP_F02 and SP_F01, respectively.
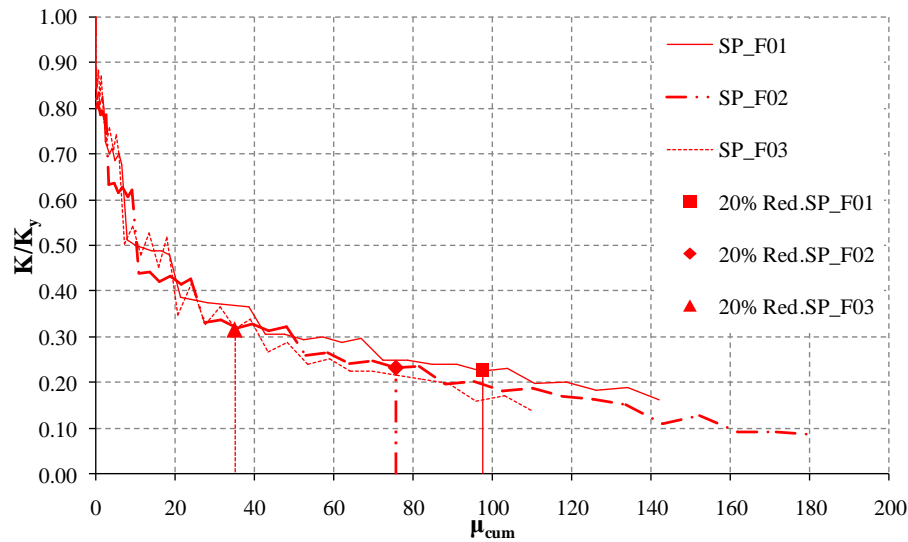
Figure 5.94 – Stiffness Degradation vs. Cumulative Ductility

5.3.2.3. Energy Dissipation

Cumulative energy dissipation is plotted against the number of loading half-cycles in Figure 5.95, and different specimens are again represented by distinct line styles: solid, dash-dot and dashed, for SP_F01, SP_F02 and SP_F03 respectively. Furthermore, the half-cycles, during which the collapse threshold was achieved, are also represented by different markers, placed over the corresponding curves.

According to experimental evidence, the most significant column damage due to increasing cyclic drifts was associated with concrete crushing/spalling, as well as rebar buckling and eventual fracture, which occurred in every test at comparable drift levels. Therefore, it is not surprising that the overall rate of energy dissipation is relatively similar between all the specimens, even if the shape of the force-drift response is not, since it is heavily dependent of the deformation incurred by the main longitudinal reinforcement, which is also similar in all of them.

Despite that, a closer look shows that, for the half-cycle (45) after the collapse threshold is achieved in SP_F03, the increase rate for that specimen slows down when compared with the other tests, which is arguably expected due to the more fragile behavior exhibited during the last drift stages. Furthermore, SP_F02 is the specimen that dissipates the most energy until the 57th half-cycle, which can be attributed to the fact that it also achieved yielding earlier (Figure 5.93). Still, the monolithic specimen SP_F01 shows the highest energy dissipation before collapse, which is also around 35% larger than for SP_F02, and almost three times as large as SP_F03.
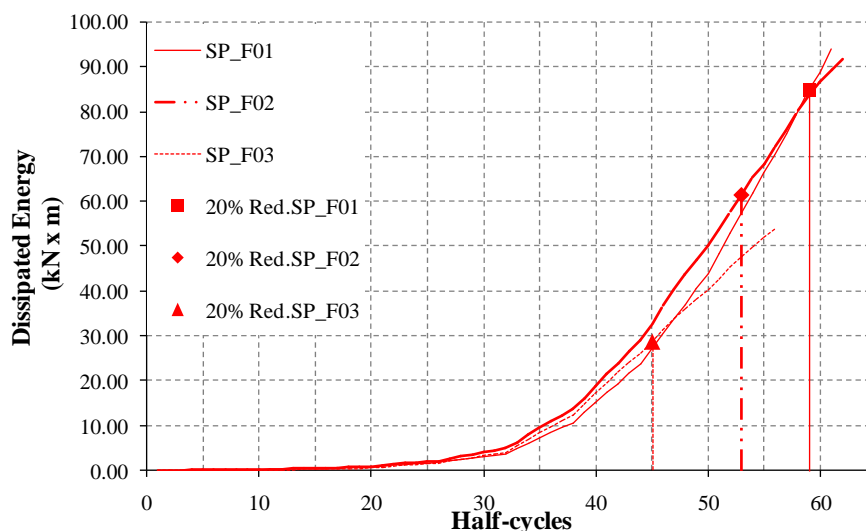
Figure 5.95 – Energy Dissipation vs. Loading Half-Cycles

5.3.2.4. Lateral Displacement and Curvature Profiles

The lateral displacement and vertical strains for the columns were recorded over several points along their height, according to the monitoring layout presented earlier in Figure 5.18. In order to characterize the relative differences between the deformation patterns for each of the columns, the following methodology was adopted:

- Comparison of the lateral displacement profile, defined for a mean of the horizontal displacement values obtained on both sides of the column, recorded at the height wise column levels of 0.275m, 0.550m, 1.200m and 1.950m;
- Comparison of the mean curvature profile calculated from the North and South side vertical deformation values, considering the mid cross-section between the application points of each vertical LVDT, corresponding to column height values of 0.069m, 0.206m, 0.413m, 0.875m and 1.525m;

For clarity, only three different drift levels were considered for calculations, namely: 0.50% drift (which corresponds to a pre-yield stage), 1.00% drift (corresponding to a post-yield stage) and 2.00% drift (which is a peak or post-peak stage, depending on the actual specimen).

Figure 5.96 illustrates the lateral displacement profiles obtained for the monolithic specimen SP_F01 for the three drift levels, represented by different colors and markers, according to the respective legend. It indicates a relatively linear shape, with slightly larger relative displacement increases occurring near the column head, as expected.
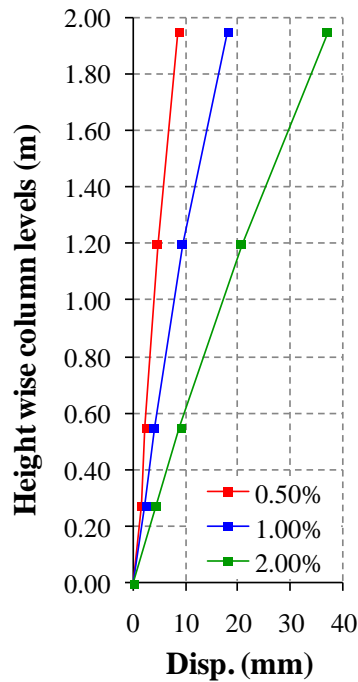
Figure 5.96 – SP_F01 lateral displacement profiles

Equivalent displacement profile shapes are obtained on the other specimens, with slight differences that are, however, difficult to evaluate at the scale of Figure 5.96. In order to provide better comparison, the ratio of the precast specimens' horizontal displacements to the equivalent displacement on SP_F01 is plotted in Figure 5.97 instead, and the respective results are represented as a percentage relative to the latter. In this regard, displacement profile differences between SP_F01 and both precast specimens at 2.00% drift were relatively small, as a maximum ratio of around 13% was found in the cross-section closest to the footing. However, a different scenario is observed at earlier drifts, where ratios above 20% could be found in several cases. Most of those differences are not relevant, because they result from relative variations of quite small absolute displacements. Still, at 1.00% drift ratios for SP_F02 were found all below 10%, but larger differences of up to 55% were observed in the case of SP_F03. Taking into account that this was also the same drift level where the precast connection section first showed signs of grout crushing, it may possibly indicate that some sliding might have occurred along the grout-concrete interface, which is located below the first reading point.

a) 0.50% drift   b) 1.00% drift   c) 2.00% drift
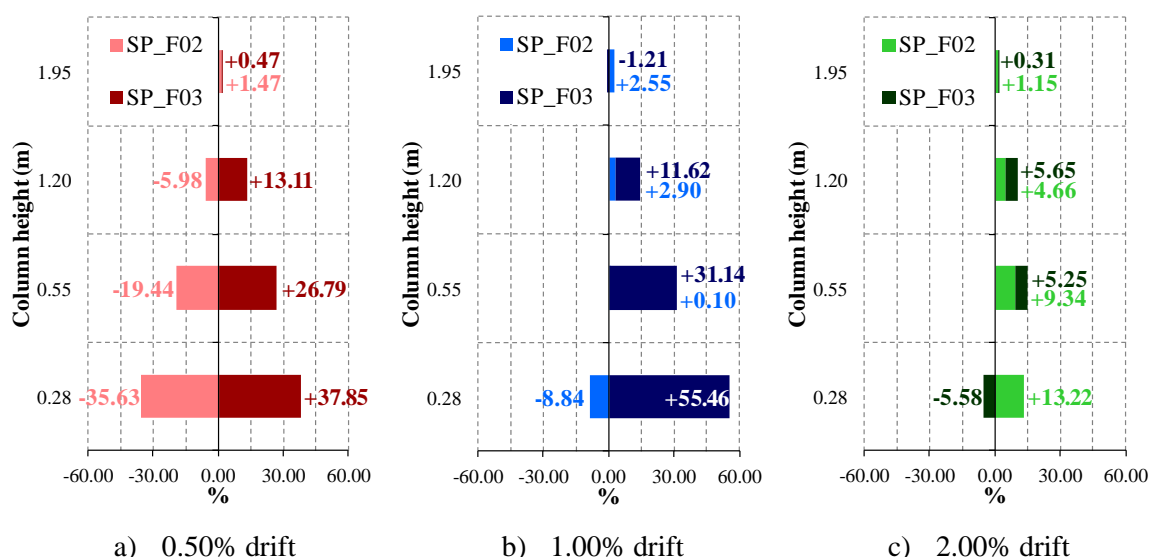
Figure 5.97 – SP_F01 to precast specimens lateral displacements ratio

The mean curvature profile obtained for each drift level is presented in Figure 5.98, where SP_F01, SP_F02 and SP_F03 are represented by the red, blue and green lines and markers, respectively, and an indicative yielding threshold is also included (Figure 5.82). Regarding these results, SP_F01 and SP_F02 display very similar progression for all the calculated drift levels, but SP_F03 presents an interesting detail. In fact, while the highest curvature on the former two specimens is always located at the cross-section closest to the footing, as expected on a bending-dominated reinforced concrete column response, the second closest cross-section always shows the largest value in the case of the SP_F03. However, despite the uncommon nature of that particular observation, it seems to be in line with the experimental evidence, since both rebar buckling and fracture occurred next to the grout-concrete interface, as illustrated in the last picture of Figure 5.91, and not closer to the footing as in the SP_F01 and SP_F02 specimens (Figure 5.85 and Figure 5.88, respectively).

The analysis of the curvature profiles shown in Figure 5.98 also seems to confirm the occurrence of yielding after the 0.50% drift cycle, because the largest curvatures are lower than the yielding threshold on all the tests. Furthermore, at 2.00% drift, the largest maximum curvature is recorded for SP_F03, followed by SP_F02 and SP_F01 as the second largest and the smallest maximum curvatures, respectively. This presents further evidence to understand the differences in the ultimate capacity of each specimen, which follows the same relative order.

a)   0.50% drift   b)   1.00% drift   c)   2.00% drift
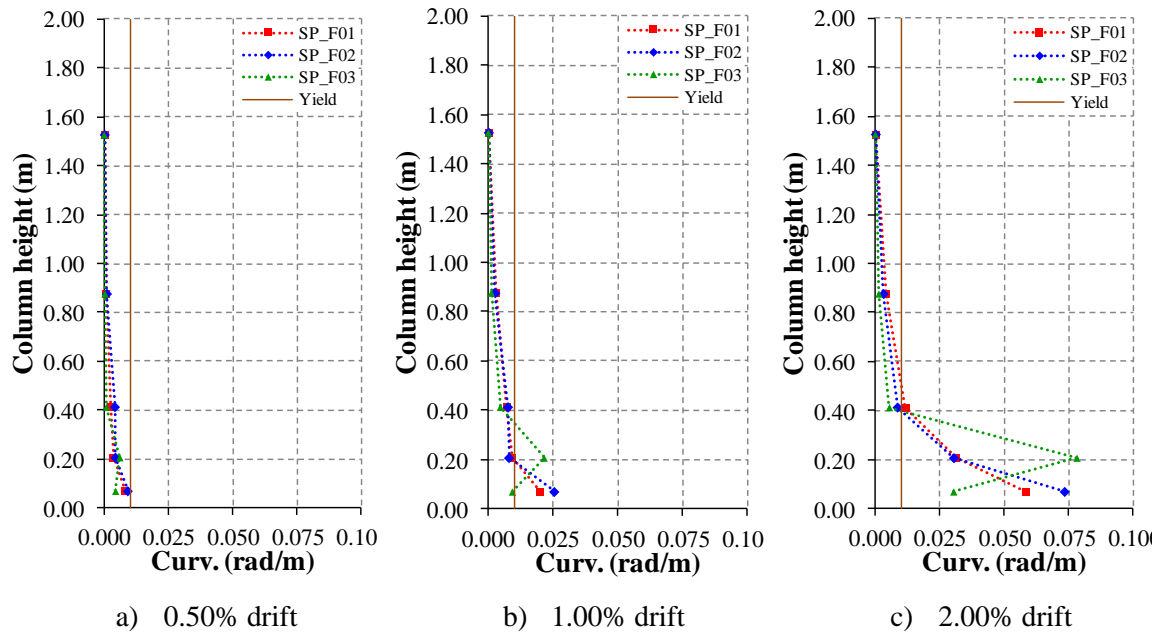
Figure 5.98 – Mean curvature profile

5.4.   FINAL REMARKS

The present chapter involved presenting the experimental campaign performed on the scope of the present work in full detail. According to the methodology adopted for the referred campaign, which was presented earlier in Chapter 4, a three phase approach was required. In that regard, two different experimental setups were developed for reduced scale (1:4) applications in order to adequately address the different challenges posed by each of them, where the same setup was used for Phase 1 and 2 and the second setup was used only on Phase 3. The first setup was aimed at handling the cyclical loading of the earlier defined monolithic (Phase 1) and precast (Phase 2) bent pier specimens, where some of the main challenges were the constant axial loading of the columns, free rotation at the column bases simulating null moment curvature inflexion points and lateral load application by shear at the expected interface between bearings and structure. The second experimental setup was a typical layout adequate to cyclical in-plane loading of single column structures.

The experimental tests performed on the Phase 1 specimens, which consisted of only monolithic models, showed structural responses largely dominated by shear at the coupling beam (exceeding the level of applied dead-load), wherein brittle failure modes could also be observed at relatively low drift levels (under 3.00%). In all cases, structural damage in the columns was moderate, and well distributed horizontal cracking patterns could be found. Analysis of experimental evidence and predictive peak force estimates suggested that the influence of shear could not be very well evaluated by the design models used in this work,

possibly due to the formation of a single strut-and-tie mechanism between columns, and increased reliance on the shear interlock mechanism at beam-column interfaces.

Regarding Phase 2 tests, performed on mostly precast specimens, significant improvements could be found. Although beam shear was still observed to be a highly relevant factor to the overall performance of the bent pier structures (the beam shear loads still exceeded the level of applied dead load), an increased reliance on rebar deformations at precast joint sections could also be observed. Due to that, all the precast specimens were able to show a more ductile response, where loading up to 4.00% drift could be performed within reductions of the peak force of 20%. Structural damage in the columns was also kept moderate, except on the SP_M02C case (monolithic structure with a reinforcement layout designed for a precast specimen) where a large horizontal crack could be found at the beam-column intersection.

Finally, Phase 3 specimens addressed foundation-to-element connection tests, but, in the tested cases, the structural performance of the precast specimens was always worse than the reference monolithic model. Nonetheless, precast specimen SP_F02 was able to show similar behavior patterns to those of the monolithic model, particularly regarding the occurrence of spalling, buckling and failure, suggesting that improvements on that regard may be easier to achieve than using the layout of SP_F03, which exhibited significantly worse performance.

6

NUMERICAL SIMULATIONS

6.1. INTRODUCTION

In order to extend conclusions from the experimental observations discussed in the previous chapter to the wider range of piers associated with the previously defined conceptual framework (double column piers with short span coupling beams with total height in between 5m to 20m for application in medium to long viaducts), those results should be independent of testing conditions and, namely, of the total height of the specimens. Within that context and due to the strong association of the structural response with the variable stiffness ratios, between the beam and the columns, that were previously shown to depend of the total height, doubts can be raised regarding the extrapolation of testing conclusions to other scenarios. Taking this into account and intending to evaluate the problem in further detail, a strategy was established for the work developed in this chapter, which was based on accomplishing two distinct objectives:

- Providing additional insight on the relative differences between monolithic and precast specimens aiming at improving the knowledge gathered by the previous experimental conclusions;
- Developing a modeling strategy capable of exploring different geometrical conditions and constraints than those tested at the laboratory, in order to assess the validity of extrapolating test results to a wider range of applications;

6.2. REFINED MODELING

In order to explore different applications of the bent pier systems presented in Chapter 4 within a purely numerical setting, a modeling strategy capable of addressing the main phenomena reported during the experimental tests is paramount. Additionally, considering the

availability of experimental data, a two-staged approach was adopted, first focused on providing a comparison of the numerical results obtained with the modeling approach presented in the current work, with those recorded during the experimental tests, for validation purposes. In this context, the following set of specimens was selected for numerical study:

- Monolithic specimens: SP_M02; SP_M03; SP_M04;
- Precast specimens: SP_PC02A; SP_PC02B;
- Single column specimens: SP_F01;

Afterwards, considering the experimentally validated numerical applications and the corresponding calibration parameters, the second stage focused on exploring other scenarios not experimentally tested; for the most part, this was based on introducing targeted structure changes, such as different total height, or support restraints.

For that purpose, the finite element method (FEM) was used with a refined approach, including thorough detailing of the inherent geometric and material properties of each specimen. Appropriate constitutive models were also chosen and calibrated against the available test data. Furthermore, since the numerical simulations in question generally require extensive and long analyses that are often very prone to numerical convergence problems, the modeling strategy was also developed with attention for computation time requirements and result precision. In this regard, all the analyses were performed with the structural analysis software Cast3m (http://www-cast3m.cea.fr/, Fichoux (2011)), considering the author's previous experience with the program, the support for both 3D and 2D applications, as well as the wide spectrum of different constitutive models that is available within its software environment.

6.2.1. MODELING STRATEGY

6.2.1.1.   Phase 1 and Phase 2 tests

Using a FEM based methodology for the numerical applications of this work requires a very early decision regarding the associated assumptions. In particular, it is important to decide beforehand between a three or two dimensional approach. Taking into account the scope of the experimental tests, focused on recording the cyclic behavior of the bent pier specimens under uniaxial loading, as well as the setup features installed to deal with out-of-plane displacements, it seems reasonable to assume that the structural problem in question can mostly be reduced to the loading plane. With that in mind, a valid strategy can consist on elaborating a 2D FEM mesh for analyses under the plane stress assumption.

Since the bent piers in question are essentially symmetric along the loading plane, reducing their full geometry to a two-dimensional representation can be done by adopting the mid-section

plane cut as the basis for mesh geometry, according to Figure 6.1. Therefore, the 2D model can be developed by adopting constant thickness in the beam elements and varying thickness on the column elements, aiming for an equivalent overall pier lateral stiffness. The solution adopted for this work involved the consideration of three different thickness zones, A, B and C.

a)   3D geometry: mid-section plane   b)   2D Plane stress mesh

c)   Column cross-section   d)   Beam section

e)   Column thickness layers   f)   Beam thickness layer
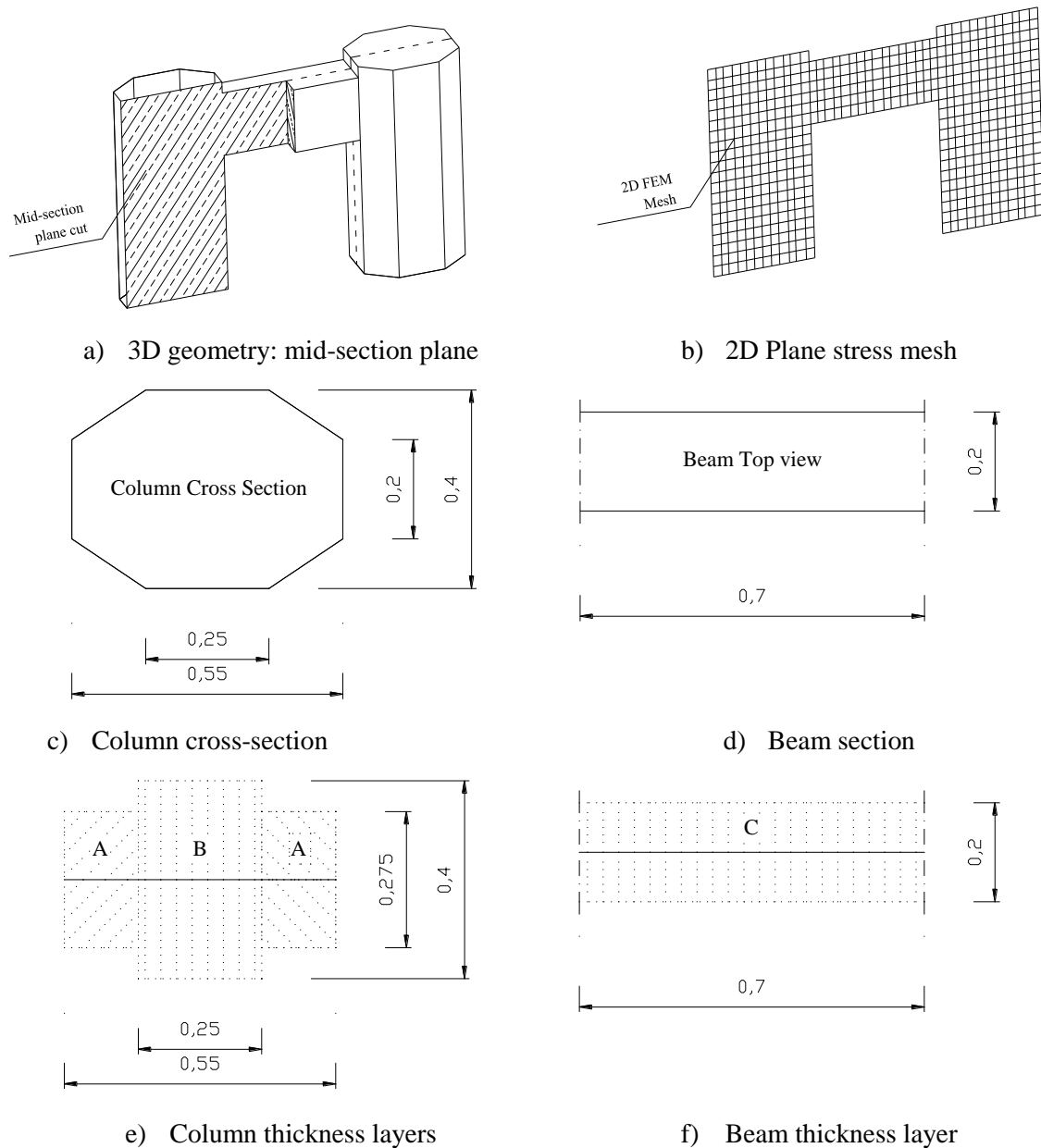
Figure 6.1 – Geometric definition for numerical modeling

In addition to the finite elements representative of the bent piers, the numerical model also considered the inclusion of 4 linear elastic element bands above and below the two columns (two per column) to enable lateral load application and column rotation occurring at the same relative positions (Figure 6.2) of the test setups.

All the analyses were performed considering at least two types of finite elements, defined for the representation of the concrete continuum (eight-node rectangular elements) and the steel reinforcement (two-node bar elements). Within that context, the adopted mesh density was the same for all the analyses, and considered 0.050m sized element divisions. The previous mesh density value was defined as the result of a parametric study regarding element size, which essentially intended to evaluate the computational efficiency associated with different meshes regarding calculation times (while taking into account result quality and detail), and is included in Annex B. An overview of the adopted FEM mesh layout is presented in Figure 6.2 as defined for the monolithic specimens of Phase 1, including an illustration of the associated support restraints and applied loading conditions, as well as the element thickness for the different zones.
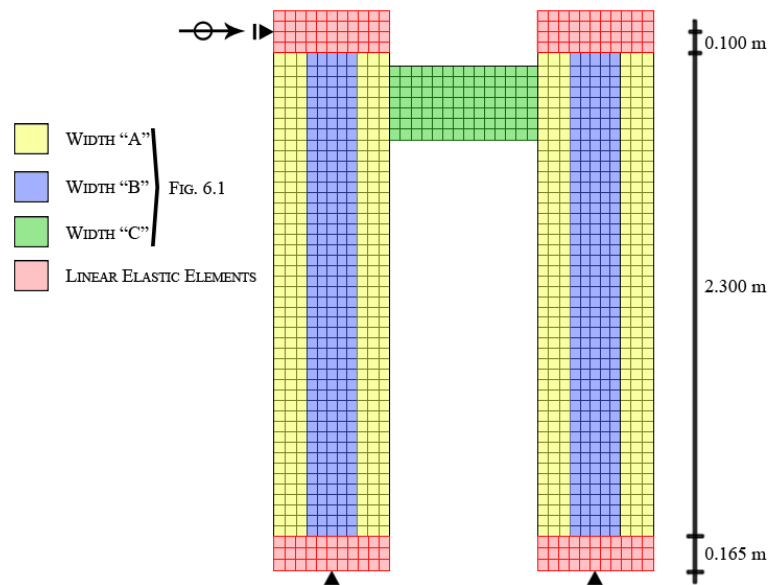
Figure 6.2 – Adopted generic layout for the FEM mesh

Accurate characterization of the concrete cover would be incompatible with the previously presented plane mesh due to its constant mesh size. Changing the mesh to accommodate that feature was possible but, ultimately, was not deemed a good option. The main reason supporting that decision was that due to the 2D modeling approach, only a part of the cover concrete can actually be represented, located in the external finite element layers according to the 2D representation. In addition, Figure 6.3 illustrates a hypothetical layer of finite elements for simulation of cover concrete, where the green and red colors represent elements with expected low and high ductility demand in compression (the color transitions represent the uncertainty associated with pinpointing the actual zones where that occurs). Elements in green (the majority) should have a low impact on the overall performance of the models; elements in red, however, are crucial for the development of the internal concrete struts that carry the load transferred through the beam and, therefore, are also critical to the accuracy and numerical

stability of the structural response. Within that context, it can be argued that the ductility capacity of those zones should be defined by careful assessment through calibration against experimental results, since it may be influenced by surrounding columns providing a local confinement effect, therefore making it less important to simulate the actual behavior of the cover concrete.
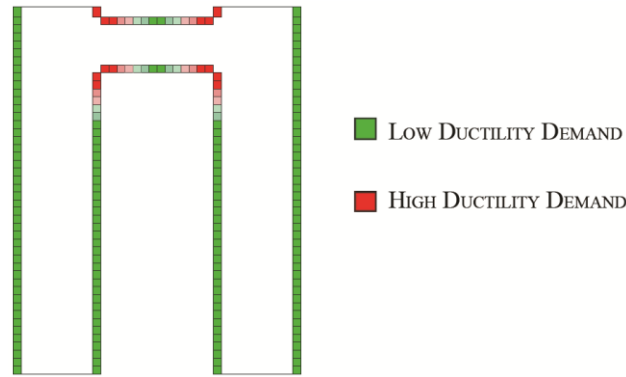
Figure 6.3 – Outer finite element layer and ductility demand

Regarding the simulation of the precast models of Phase 2, the finite element meshes need to include an additional feature, in order to enable the representation of the grouted joints. Within that framework, joint or interface elements are generally used to represent small/thin layers that incorporate considerably distinct constitutive characteristics over another continuum element (often with much larger dimensions), for example to model the thin mortar layer located between masonry blocks. In a way, that is believed to be similar to the current case, where the vertical columns are separated from the beam element by a passively reinforced grouted joint with negligible thickness. Therefore, the adoption of a joint element to simulate the force transfers occurring in that interface becomes a natural choice.

For that purpose, 6 node joint elements were used to establish a binding connection between the nodes on the beam segment and the vertical columns (by making use of the RACC operator available in Cast3m). Those joint elements follow the proposal of Bfer (1985), as implemented in Cast3m, and require the definition of adequate constitutive laws for the stress (normal σ_n, and tangential τ_s) – strain evolutions along their normal (δ_j) and tangential (γ_j) degrees of freedom, according to Figure 6.4. The structural analysis software includes several constitutive models developed for simulation of joint behavior, which will be discussed further ahead.
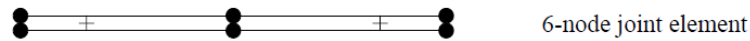
a) Joint element 2D representation
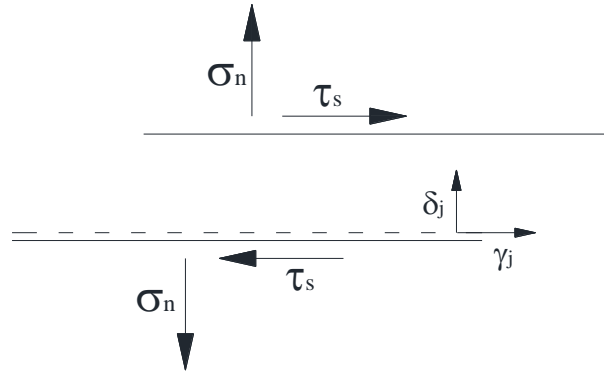
b) Joint degrees of freedom

Figure 6.4 – Joint element in Cast3m (Pegon), Costa (2009))

With this approach, the nodes of the rebar elements and the concrete continuum mesh cannot be connected directly, since the constant mesh size prevents coinciding points for both. In order to address that shortcoming, a linear kinematic constraint (resorting to the RELA 'ACCRO' operator in Cast3m) was established to bind together the displacements of concrete and steel finite element nodes.

The finite element layouts for the reinforcement were defined considering a similar approach to that presented in Figure 6.1 for the concrete continuum, by projecting all existing rebars onto the mid-plane section cut, involving the consideration of equivalent diameters for the various rebar elements of each structure. Figure 6.5 shows an overview of the upper part of the bar element meshes used for all the specimens of Phase 1 and 2, wherein the colored lines represent equivalent rebars with different diameters or mechanical properties tuned so as to match the set of original ones. It should be noted that according to the original specimen layouts, the same column mesh is used in all the analyses of Phase 1 specimens, since only the beams involve different detailing. By contrast, the beams respect the same mesh layout on Phase 2 specimens, and detailing differences are introduced on the vertical reinforcement around the precast joint section. Finally, the transverse reinforcement of the beam on SP_M03 was defined with shorter spacing than the other tests because calculation of this specimen presented particularly difficult numerical convergence issues due to high local distortions caused by shear. Shorter spacing on the stirrups enabled better handling of that difficulty, while accounting for reduced cross-sections for maintaining overall equivalent transverse reinforcement contents.

a) SP_M02   b) SP_M03

c) SP_M04

d) SP_PC02A   e) SP_PC02B
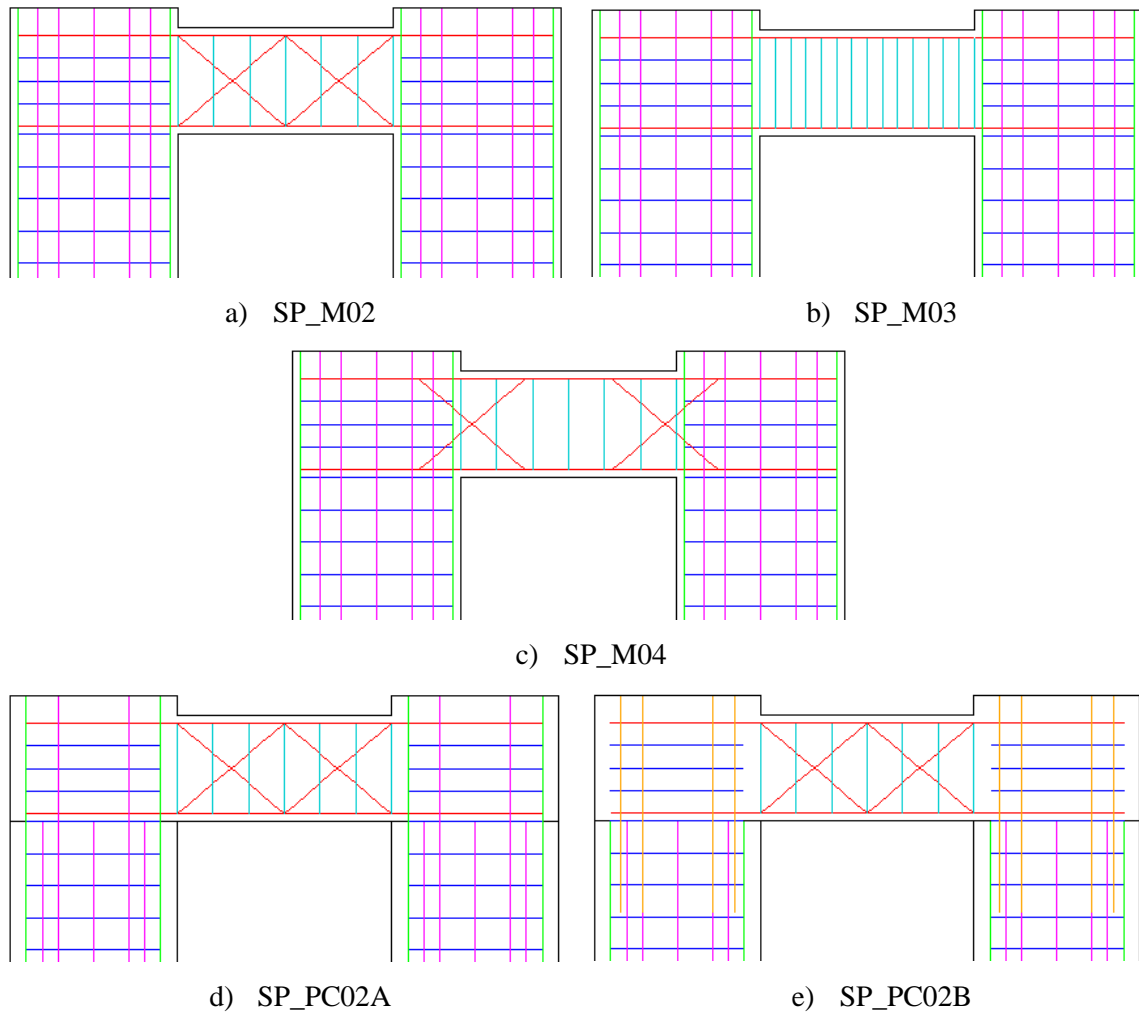
Figure 6.5 – FEM rebar meshes for Phase 1 and Phase 2 analyses

The interaction of the bar elements at the joint section on precast specimens required special attention, because, in addition to the disturbance of regular force transfers that it introduces, the discontinuity leads to weaker bond behavior between steel and concrete in the local vicinity. The implications of that can be related to the considerable differences of performance observed between specimens SP_PC02C and SP_M02C, which can be attributed to that specific issue, since both included the same reinforcement layouts whereas the only significant difference was the existence of the precast joint. In the present application, this was addressed with a careful selection of the nodes and elements to be bound with the previously mentioned kinematic constraint, since binding all the rebar nodes in the precast joint vicinity can easily lead to an artificially increased stiffness because this creates an indirect connection between superposed nodes at the joint (which then become linked through the kinematic relation in addition to the intended joint stiffness). Therefore, the binding strategy adopted for continuity rebars skipped the joint nodes, while the rebars that were cut at that level were bound only to the column part, as illustrated in Figure 6.6 for one of the beam-column joints.
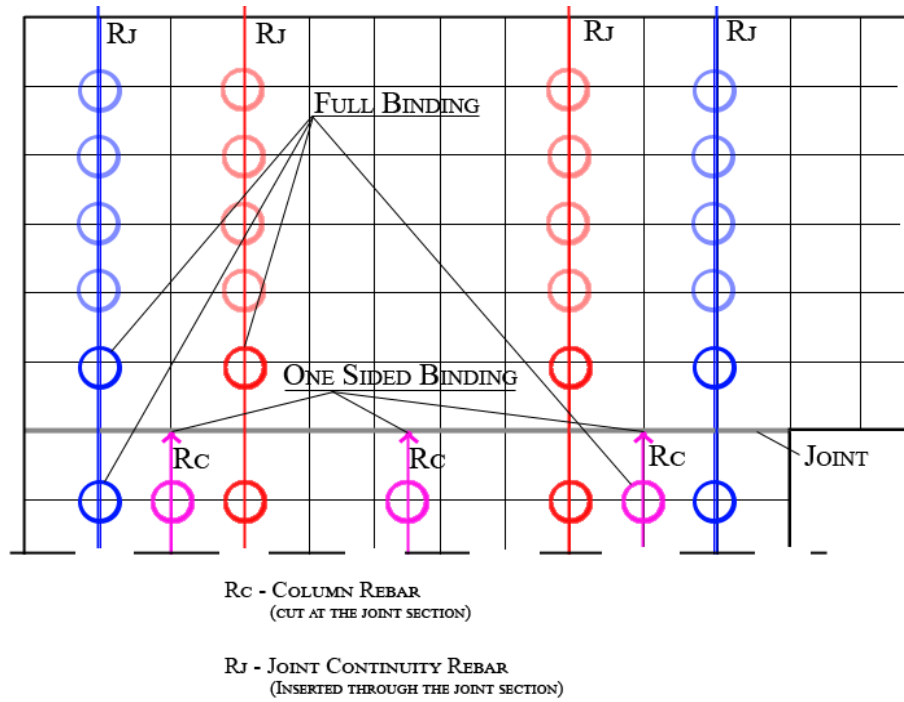
Figure 6.6 – Binding strategy at the precast joints

6.2.1.2. Phase 3 tests

Modeling single columns under bending dominant loading is generally a more straightforward task than what is required for simulation of phase 1 and 2 tests, and good results can be obtained by involving experimental calibration and using accurate mesh geometry with adequately assessed constitutive relationships. Within that context, and owing to the reduced complexity of that numerical application, 3D modeling was considered, aiming to improve the overall accuracy of the results in relation to comparable 2D tests (for example, by fully modeling the cover concrete). It is important to note, however, that this is a reasonable approach because the same constitutive models and general behavior relationships used for the 2D tests can also be applied to a 3D application.

Within this context, taking advantage of the essentially symmetric nature of the column structure, only half of its body continuum was considered, and the volumetric envelope for the FEM mesh was defined according to the representation of Figure 6.7.

a) Total specimen   b) Half specimen
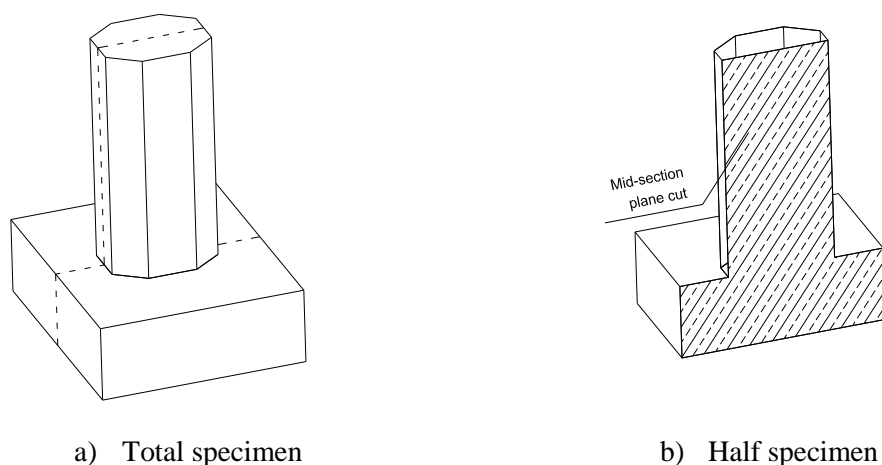
Figure 6.7 – Geometric 3D envelope definition for columns.

The FEM mesh elaborated for this purpose focused on the use of eight-node cubic elements for representation of the concrete continuum and two-node bar elements for the steel reinforcement. Different mesh densities were used in the column elements (0.025m and 0.050m), to provide a more refined mesh on the column base region (defined for roughly half cross-section height), where the concentrated inelastic phenomena occurrences are mostly expected. Linear elastic behavior was adopted for the footing elements, as well as the upper finite element band (red elements) included for load application, supporting the use of a more coarse mesh. Figure 6.8 illustrates an overview of the described mesh.

Mesh density: 0.050m

Mesh density: 0.025m

a)   3D view

b)   Mid-section cut view

(with boundary conditions)
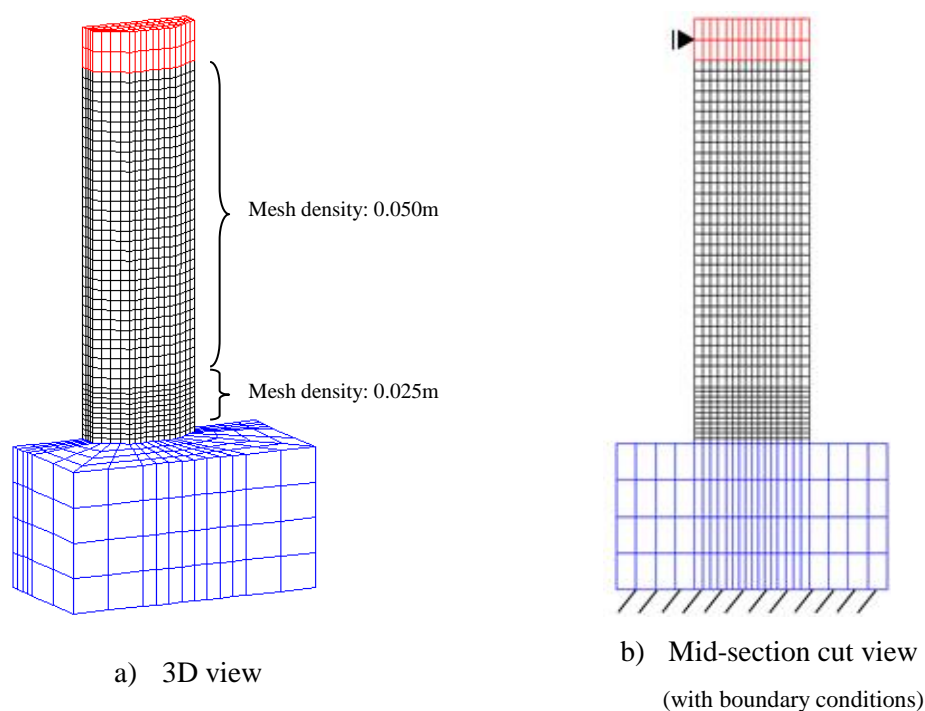
Figure 6.8 – Phase 3 FEM mesh

Concerning steel reinforcement (Figure 6.9), longitudinal (blue elements) and transverse reinforcement (red elements) were also defined individually, accounting for every rebar placed on its accurate position inside the column. A similar strategy to that presented for the bent pier specimens was also adopted to bind the displacements of steel reinforcement nodes to the concrete mesh.
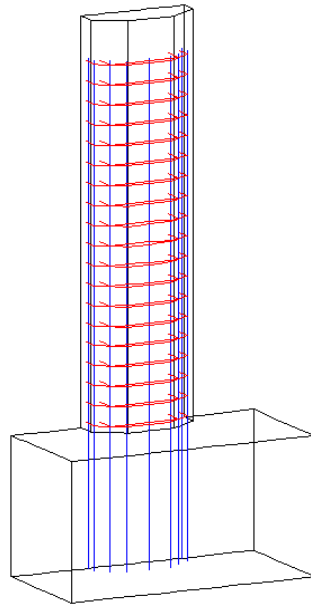
Figure 6.9 – Steel reinforcement finite element mesh

6.2.2. CONSTITUTIVE MODELS

Selection of adequate constitutive relations for simulation of concrete and steel is of the utmost importance on the context of non-linear modeling of reinforced concrete structures. Moreover, increasing the quality and detail of the numerical responses given by those constitutive models has always been a relevant research topic, with ever more robust and efficient models being developed continuously. In that regard, one of the main advantages of using the Cast3m software for the current exercise is the amount of non-linear models available for use, for which several different formulations can be considered, from plasticity based models to others associated with continuum damage mechanics. A choice between different alternatives should, then, inevitably be related to each model's ability to reproduce (efficiently and accurately) the required local phenomena. Regarding this work, that choice is evaluated by promoting separate discussion over concrete, steel and joint constitutive models. All the adopted model parameters are included in Annex A.

6.2.2.1.   Concrete Model

There are several models available in Cast3m for simulation of concrete, from which the following were selected for consideration, because they are more suitable for plane stress cyclic applications:

- BETON_INSA: This model was developed at INSA (*Institute national des sciences aplicquées de Lyon*) within the framework of plasticity theory for uncracked concrete in plane stress, following the Ottosen criterion Ottosen (1977) for compression and tension.
  A smeared fixed crack approach is also considered, and when the ultimate failure surface is reached in tension, the model considers the opening of a crack, leading to the uncoupling of compressive and tensile behaviors, which are afterwards modeled by an orthotropic law (Ile and Reynouard (2000)).

- DAMAGE_TC: A constitutive model developed on the framework of continuum damage mechanics (Faria and Oliver (1993), Faria (1994)), using the concept of effective stresses defined on the principal directions space, to characterize the non-linearity according to the energy dissipation produced by the accumulation of damage. Two independent and scalar damage variables are introduced to describe the strength degradation under tensile and compressive stresses separately, according to individually calibrated evolution laws. Furthermore, fracture mechanics is taken into account, as a smeared crack approach is adopted for the tensile behavior. In addition, plastic deformations in compression are also considered in the implemented version in Cast3m (but not in tension).

- DRUCKER_PRAGER_2: A full plasticity based model (Jason and Durand (2007)) developed with two yield surfaces, following different criteria according to the loading state. In compression, a Drucker-Prager criterion is adopted, including a hardening-softening law calibrated to enable an equivalent response to experimental uniaxial tests. By contrast, a Rankine type surface governs the tensile behavior, considering an exponential softening law defined in accordance with fracture mechanics. The parameters required to calibrate this model are straightforward and easy to obtain from standard material tests.

  RICRAG: This model was developed in the framework of thermodynamics of irreversible processes (Richard *et al.* (2010)), intended to address inelastic phenomena by introducing an isotropic variable that is linked to the

thermodynamic state of the material volume under consideration. The loading state is then characterized by a single damage variable (whether compression or tension occurs) and a single flow rule. It also aims to accurately reproduce reinforced concrete monotonic and cyclic behavior by decoupling the elastic free energy in order to address inelastic effects separately (e.g. crack opening/closure and frictional sliding).

Understanding the options and the differences between is deemed a quite valuable help to choose an adequate model for use in the subsequent numerical analyses. Nonetheless, seeking a deep and attentive review of all of these models is out of the scope for this work. With that in mind, a very simple analysis was performed instead, focusing on modeling a single $1m^2$ element with all the four concrete constitutive model alternatives, considering monotonic (in tension and compression, Figure 6.10 – b)) and cyclic (Figure 6.11) loading conditions. Its main purpose was to obtain the numerical responses at the Gauss point level, and to analyze potential outcomes of application in the full model. The characterizing parameters of each model were calibrated for reasonable fit of a class C25/30 concrete, defined for the corresponding mean values of f_{cm} and E_{cm} according to Eurocode 2, and considering similar tension-stiffening effect for the tensile behavior in all the models.

The loading was made as imposed displacements, with appropriate boundary conditions as shown in Figure 6.10 - a). Figure 6.10 – b) highlights the differences exhibited between the four models for the same monotonic loading. As observed, there are some clear differences on the softening behavior of the curves, although the overall envelope shapes stays relatively unchanged in both compression and tension. It is only when cyclic loading results are observed that larger differences become apparent.

a) Single element model   b) Compression and tension envelopes
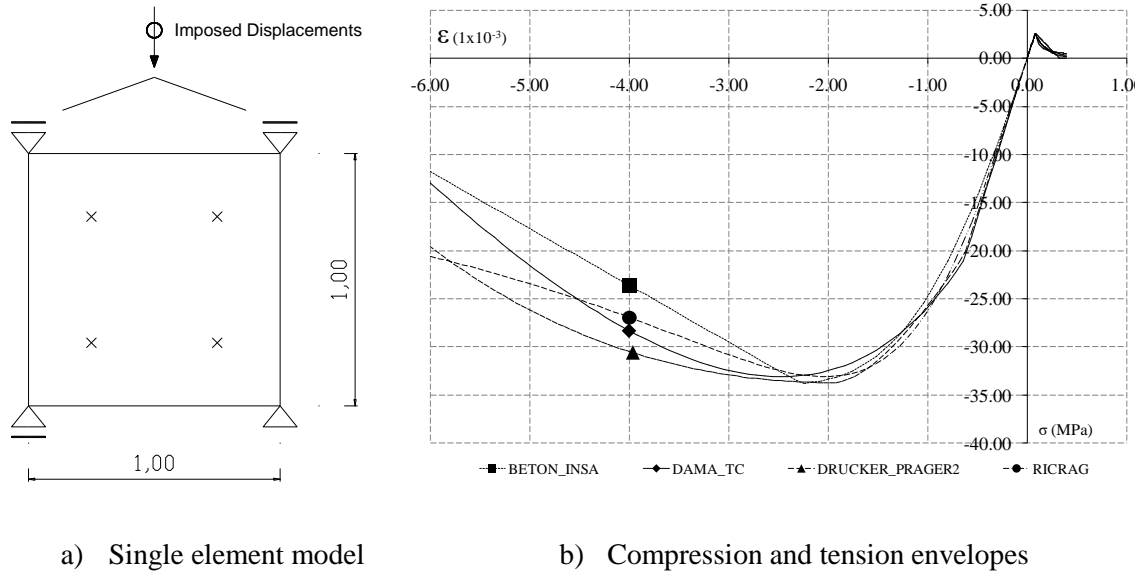
Figure 6.10 – Concrete models Gauss point monotonic response

Figure 6.11 displays the cyclic response obtained with all the tested models. There are striking differences between them, especially in the RICRAG and DRUCKER_PRAGER2 results, in light of key aspects inherent to the respective formulations. For example, the RICRAG model takes into account a single damage variable to characterize the concrete degradation, for both tension and compression. When cyclic loading is applied, a part of the damage accumulated in compression or tension goes through for the other loading direction, since the model just includes a partial unilateral effect. When large strains are expected for both loading directions, this effect is more prevalent, affecting the overall structure stiffness and energy dissipation substantially. On that regard, Cast3m also includes an upgraded version of this model, called RICBET (Richard and Ragueneau (2013)), which accounts for a full unilateral effect but, unfortunately, is only implemented for 3D elements. As for the DRUCKER_PRAGER2 model, it does not include any unloading/reloading stiffness degradation, thus always adopting elastic values instead. That results in larger permanent deformations than expected and, potentially, higher energy dissipation as well.

a)   BETON_INSA model

b)   DAMAGE_TC model

c)   DRUCKER_PRAGER2 model

d)   RICRAG model
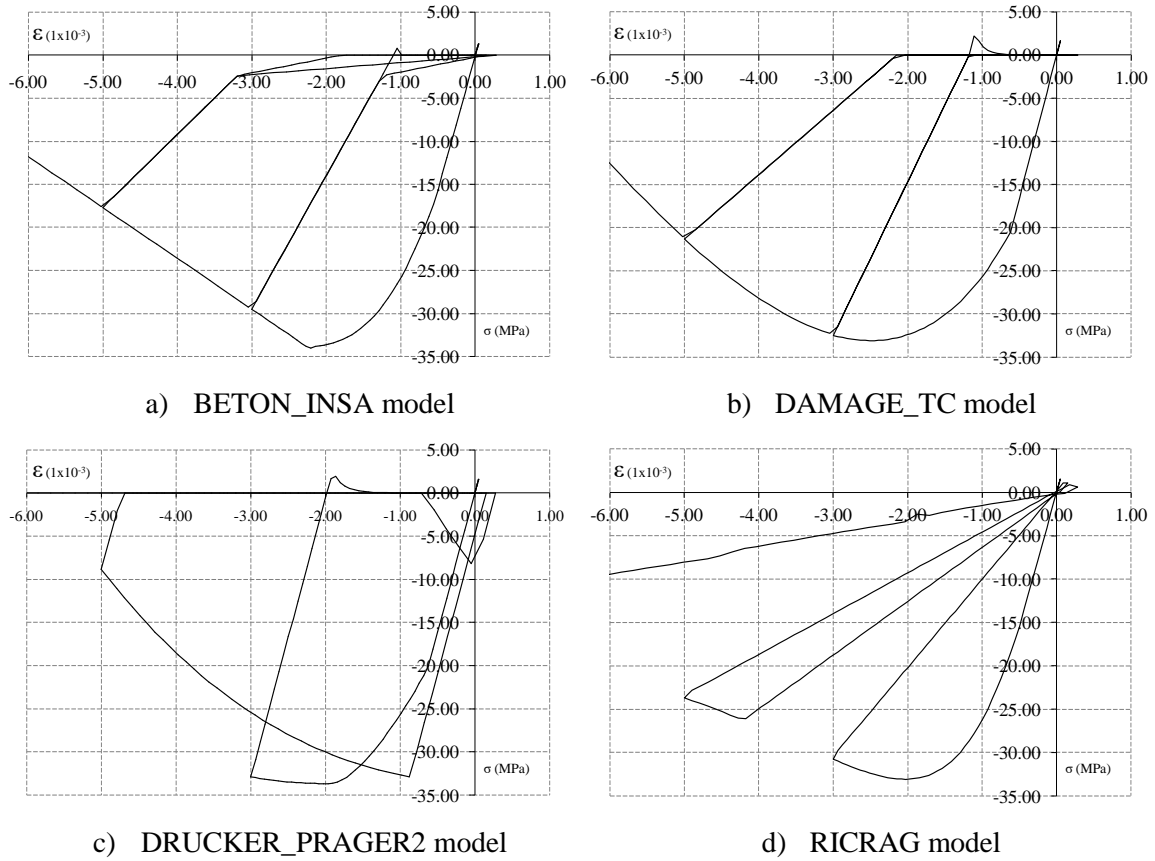
Figure 6.11 – Concrete models Gauss point cyclic response

With that in mind, the results obtained from the BETON_INSA and DAMAGE_TC models can be expected to provide more accurate cyclic behavior simulation than the other two, as both include stiffness degradation, full unilateral effect, permanent deformations and display comparable envelope shapes. Their main difference (which isn't apparent in Figure 6.11) is that the BETON_INSA model takes into account permanent deformations for both compression and tension, while the DAMAGE_TC version implemented in Cast3m only accounts for permanent deformations in compression. Despite that, the former revealed to be harder to calibrate, since testing different combinations of characterizing parameters led to substantially more numerical problems than the latter. In addition, DAMAGE_TC can provide a very valuable result assessment tool for post-processing, due to its two independent damage variables.

Within this context, an argument could be made for the viability of using the BETON_INSA model, as permanent deformations in tension are important for accurate simulation of unloading/reloading stiffness and overall energy dissipation, especially in shear dominant situations where the tensile behavior of concrete is likely more relevant. Nonetheless, DAMAGE_TC has already been used for applications similar to those in the current work with considerable success by Vila Pouca (2001), Monteiro (2009) or Delgado *et al.* (2011) even without plasticity in tension, and the advantage of enabling straightforward result interpretation

due to the damage variables should not be underestimated. These reasons and the author's previous experience with it supported a choice for the DAMAGE_TC model, which was used to simulate the concrete continuum for all the numerical analyses of this work. A more detailed overview of the uniaxial cyclic behavior computed by this model is presented in Figure 6.12, including a numbered path (from 1 to 7) related to the associated loading variations.
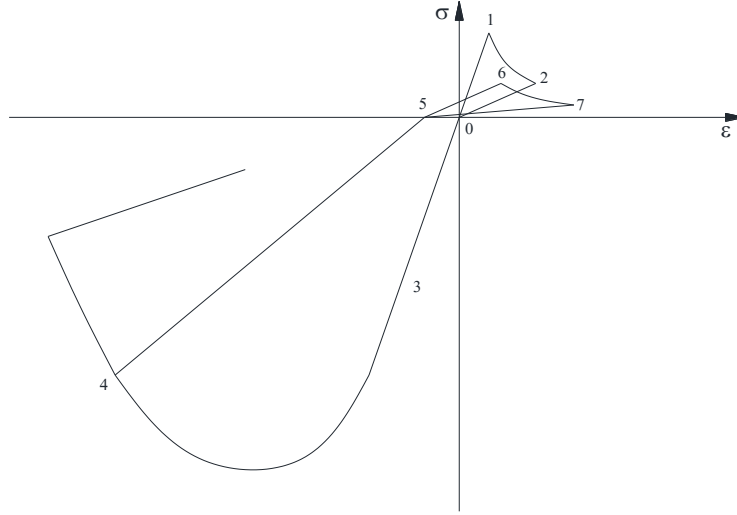
Figure 6.12 – Example of DAMAGE_TC uniaxial cyclic behavior

According to Faria (1994), the complete characterization of this model requires the definition of the independent evolution laws of damage variables for compressive and tensile behavior (equations 6.1 and 6.2, respectively). With that in mind, the parameters required for that purpose, like the elastic or cracking thresholds, can mostly be obtained from uniaxial sample tests. Additionally, one evolution law is adopted for compressive behavior and another for tensile behavior (although two are available in the current Cast3m implementation). In compression, two fitting points must be provided to compute the evolution of the d^- damage variable (related to the A^- and B^- parameters of equation 6.1). Those points can readily be obtained from experimental uniaxial stress-strain curves, if available. Otherwise, the DAMAGE_TC model can be calibrated against theoretical concrete curves, such as Mander *et al.* (1988) or Kent and Park (1971), among others available in the literature.

$$d^- = 1 - \frac{r_0^-}{\bar{\tau}^-} \times (1 - A^-) - A^- \times e^{B^- \times \left(1 - \frac{\bar{\tau}^-}{r_0^-}\right)}$$

6.1

Where:

$\bar{\tau}^-$: Effective stress; A^-: Fitting point related parameter;

r_0^-: Elastic threshold; B^-: Fitting point related parameter;

$$d^+ = \begin{cases} 1 - \dfrac{r_0^+}{r_u^+ - r_0^+} \times \left(\dfrac{r_u^+}{\bar{\tau}^+} - 1 \right) & , \quad if \ r_0^+ \leq \bar{\tau}^+ \leq r_u^+ \\ 1 & , \quad if \qquad \bar{\tau}^+ > r_u^+ \end{cases} \qquad 6.2$$

where:

$\bar{\tau}^+$: Effective stress;

r_0^+: Cracking threshold;

$\boldsymbol{r_u^+}$: Effective stress corresponding to the ultimate strain in tension;

In tension, two evolution laws are available for the d^+ damage variable, one with exponential softening decay, and another with linear decay, which was used in this work. With this approach, the r_u^+ effective stress is related with depletion of the tensile capacity on the concrete fracture width, considering a smeared crack based formulation. In reinforced concrete problems, fully depleted tensile capacity is usually considered to occur close to reinforcement yielding, due to steel-concrete bonding. The overall G_f fracture energy involved in the formation of a discrete crack (Figure 6.13 – a)), is equivalent to the total fracture energy involved in the smeared crack approach (Figure 6.13 – b)), which can then be determined from equation 6.3, taking into account the l_1 characteristic length of the FEM mesh. This was the approach followed in the current applications, as linear tension softening was considered, as described in Figure 6.13.

a) Discrete crack   b) Equivalent smeared crack
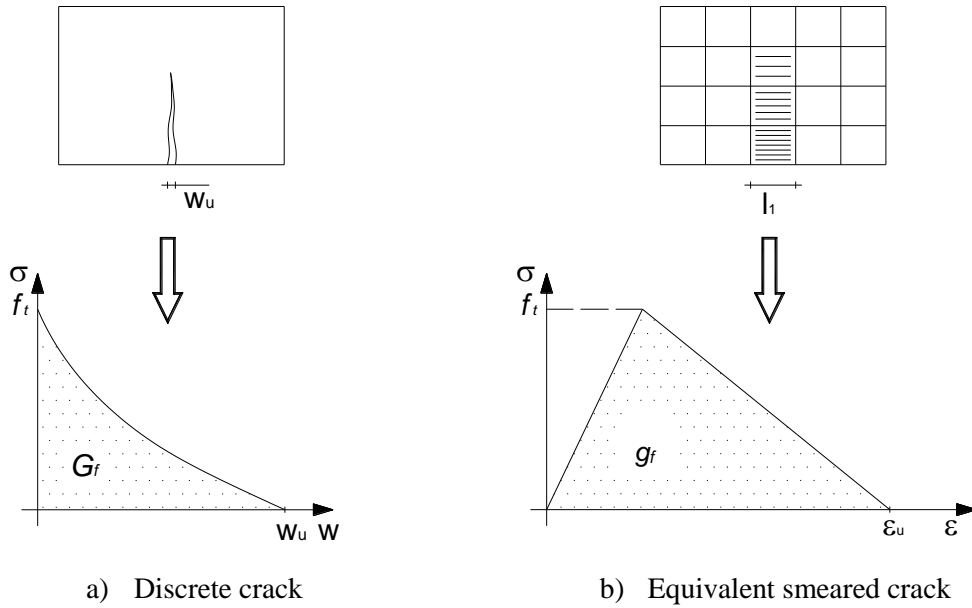
Figure 6.13 – Fracture energy in smeared crack based models

$$G_f = \frac{\varepsilon_u \times f_{ct} \times l_1}{2} = g_f \times l_1 \qquad 6.3$$

where:

g_f, G_f: Fracture energy;

f_{ct}: Cracking stress;

l_1: Characteristic mesh length;

$\boldsymbol{\varepsilon_u}$: Ultimate tensile strain (yielding strain of the main reinforcement);

For 2D and 3D applications, the definition of l_1 requires taking into consideration different possibilities for the cracking direction, thus it is usual to adopt simplified relations based on the square root of the Gauss Point represented area or volume, respectively, as indicated by equations 6.4 and 6.5.

$$l_1 = \begin{cases} \sqrt{A_{Gauss}} & , \quad for\ 2D\ problems \\ \sqrt[3]{V_{Gauss}} & , \quad for\ 3D\ problems \end{cases}$$

$$\begin{matrix} 6.4 \\ 6.5 \end{matrix}$$

Regarding the numerical simulations, each analysis was performed using two domains for concrete characterization, wherein distinct behavior curves were used. On Phase 1 and Phase 2 tests, a high ductility concrete was defined in addition to the regular concrete, aiming to provide increased ductility on beam edges (as previously discussed, and based on Figure 6.3), as illustrated in Figure 6.14 – a). For Phase 3 analyses, unconfined cover concrete and core concrete domains were defined, according to the representation shown in Figure 6.14 – b).

a)   Phase 1 and Phase 2 analyses   b)   Phase 3 analyses
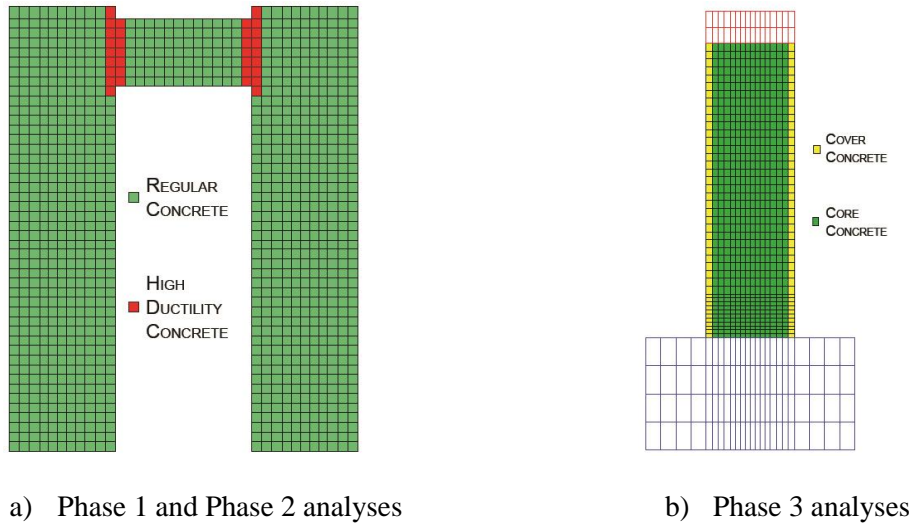
Figure 6.14 – Different domains for concrete behavior laws

Within that context, model parameters were determined individually for each model by aiming to reproduce the material properties identified in Table 4.12, by considering an amplification of peak strength and ultimate strain based on Mander's stress-strain theoretical model for confined concrete (except for the SP_F01's cover concrete, which has no confinement). The main results obtained for the corresponding confined-to-unconfined ratios are presented in Table 6.1, which were calculated considering confinement enabled by not only the vertical stirrups, but also the diagonal parts of the main rebars crossing the beam web. In fact, in the rhombic truss model, for each pair of compressed rebars there is another set of rebars in tension. Due to their position and the fact that they fully cross the web length, it can be argued that they may apply a similar effect as the inwards confining pressure of enveloping

stirrup corners, although likely not as efficiently. Still, assuming that the effectively confined concrete area may be larger than the area calculated accounting only for stirrups' contribution (e.g. the area represented in the right side of Figure 6.15 versus the area on its left side), then the contribution of the diagonal parts of the main beam rebars were also required, which is why it was included in the calculations, although at 50% reduced effectiveness.

Table 6.1 – Confinement factors

f_{cc}/f_{uc}		
Specimen	Beam	Column
SP_M02	1.13	1.17
SP_M03	1.05	1.21
SP_M04	1.13	1.17
SP_PC02A	1.15	1.22
SP_PC02B	1.14	1.19
SP_F01	N/A	1.25
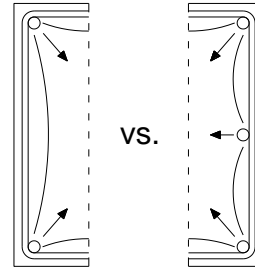
Figure 6.15 – Effectively confined concrete assumption

In addition, trial and error calibration of the ultimate strain of the high ductility concrete was made, aiming to have the numerical tests indicating similar concrete compressive damage and failure as reported on the experimental results, particularly because it is heavily associated with most of the phenomena reported for collapse characterization (concrete crushing onto sliding failure, or onto spalling and subsequent tensile failure, like diagonal splitting).

6.2.2.2. Steel and steel-concrete bond models

Simulating the behavior of steel rebars is often performed with simple bilinear models, depending on the purpose of the application. Generally, only the elastic stiffness and hardening stiffness are required in addition to yielding and ultimate strengths for full characterization of the envelope for a given cyclic loading. This is a well-known pattern, for which several models have been developed over the years. On that regard, the Menegotto-Pinto model (Menegotto and Pinto (1973)) has been one of the most widely accepted proposals, including the addition of the softening aspect of the curves related to the *Bauschinger* effect, and is also implemented in Cast3m (designated by the ACIER_UNI alias). An overview of the corresponding uniaxial cyclic behavior enabled by this model is presented in Figure 6.16.
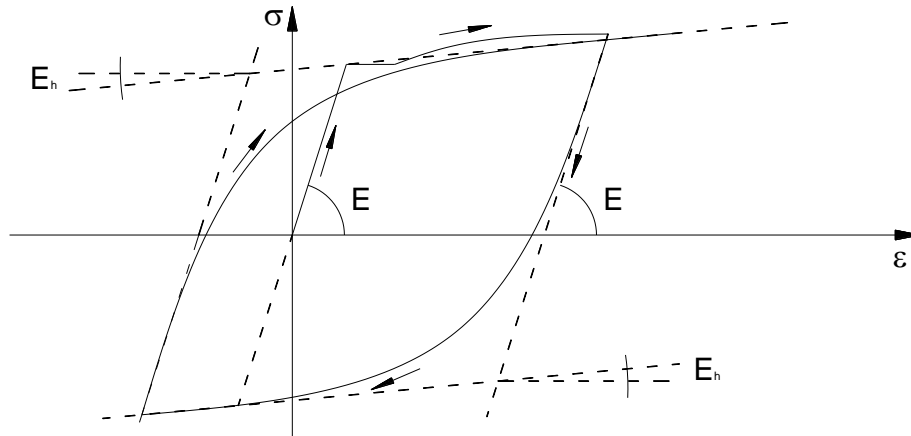
Figure 6.16 – Menegotto-Pinto uniaxial cyclic behavior

In addition to the steel rebar constitutive model, it is important to discuss the steel-concrete bond behavior. A rebar embedded in concrete and subjected to tensile forces accumulates strains over the embedment length that cause an extension of the bar, which can be related with the overall crack opening width for tensile strained concrete. However, rebar slip relative to the embedment concrete can also occur, causing increased displacements/rotations for no increase of force. This issue is also very relevant to the present bent pier system due to the large cracks observed at the beam-column interfaces, and also due to the large opening width experienced at the precast joints, as identified in Chapter 5, wherein some vertical cracks were actually observed, and suggesting rebar slip.

The steel-concrete bond behavior is generally described by bond stress (τ_b) defined as a function of the displacement of rebars, relative to the surrounding concrete and along the anchorage length (L_{anch}, in Figure 6.17), which is commonly referred to as slip (s). The overall relation between them depends on the actual stage of the bond connection, with a total of three different stages usually referred as the most relevant:

- The first stage, controlled by chemical adherence, occurs up to very small slip values and depends of the molecular connections established between the steel and the cement paste.
- The second stage, governed by mechanical adherence, initiates when the chemical adherence is broken and friction forces start developing (up to s_1 in Figure 6.17), causing internal micro cracks to form as well. This mechanism gradually increases, in proportion with the friction and mechanical interlock, especially in the presence of rugged indentations of deformed bars (with peak bond force developed between the s_1 and s_2 slip thresholds).
- The third and last stage, ruled by residual adherence (up to and after the s_3 threshold), occurs after the peak bond stress ($\tau_{b,peak}$) is achieved and degradation

occurs, since a small residual strength ($\tau_{b,res}$) can generally be maintained through friction.
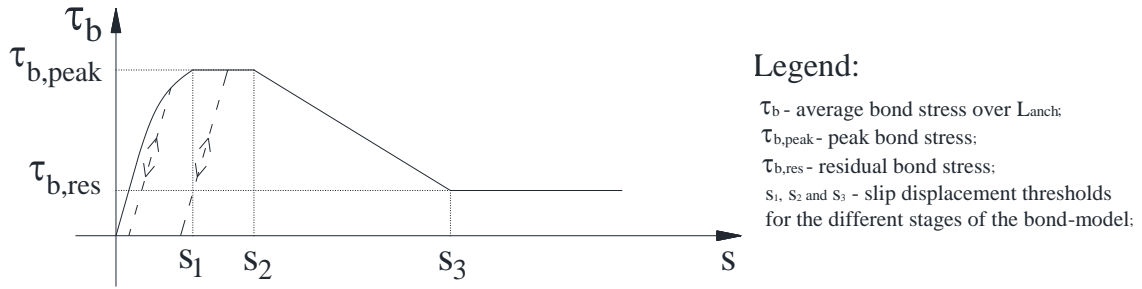
Figure 6.17 – Eligehausen bond model as implemented with ACIER_ANCRAGE in Cast3m

Within this context, several theoretical models were proposed to enable taking into account the effects of slip between concrete and rebars. Works presented by Tassios (1979), Eligehausen *et al.* (1982), Harajli *et al.* (1995) or Huang and Engstrom (1996), for example, were well-received by the community and some were incorporated in design codes. In Cast3m, the consideration of a constitutive behavior for the bond simulation can be performed by explicitly modeling the steel-concrete interface using specific finite elements for that purpose, or by adopting a constitutive model for the steel bar finite elements that implicitly takes into account the occurrence of both slip and rebar deformations. The latter approach was adopted in this work, using the constitutive model labeled ACIER_ANCRAGE, which considers the previously described Menegotto-Pinto constitutive behavior for the rebars as well as the model proposed by Eligehausen (Eligehausen *et al.* (1982)) for the bond-slip behavior. Its formulation requires the calculation of the effective rebar strain and slip from the total strain ε_{total} established at the bar finite element level, according to Equation 6.6:

$$\varepsilon_{total} = \varepsilon_s + \frac{s}{L_{anch}}$$
6.6

where:

ε_{total}: is the total strain calculated at the finite element level;

ε_s: is the strain associated with rebar deformations;

s: is the mean slip displacement value over the L_{anch} length;

L_{anch} : is the embedment length of the anchored rebar;

The overall behavior enabled by this model relies on the separation of slip and rebar strains in order to, simultaneously, develop both bond and rebar stresses, according to the corresponding constitutive laws. During cyclic loading, the unload and reload stages of bond-slip behavior are managed with the corresponding elastic stiffness, while the rebars' behavior is subjected to the hysteresis rules of the aforementioned Menegotto-Pinto model. The

main parameters required for calibration of the bond-slip model are those represented in Figure 6.17, where s_1, s_2 and s_3 are the slip values corresponding to the start and end of peak mechanical adherence stage and start of residual adherence stage, respectively, while $\tau_{b,peak}$ and $\tau_{b,res}$ represent the peak and residual bond stresses.

Calibration of the Menegotto-Pinto model for use in each test was performed by considering the material properties identified on Table 4.12 and adopting the default values for the cyclic behavior controlling parameters. Regarding the bond model, it was considered for simulation of all the heavily strained rebar elements located at the beam and precast joints, whereas it was disregarded for general modeling of the columns. Therefore, it was used on all but the single column test SP_F01, and the corresponding values were evaluated according to literature references (CEB (1993), Santos (2012)) while taking into account adjustment for the concrete strength values relative to each test. In this regard, the s_3 value, which is usually taken as the distance between rebar ribbings, was evaluated for the highest diameter bar of each test, considering A500 NR steel.

6.2.2.3. Joint Model

There are several constitutive models available in Cast3m for joint modeling. The most relevant selected for this application are the following:

- JOINT_DILATANT: This model follows the proposal of Snyman *et al.* (1991), using a Mohr-Coulomb criterion characterized by cohesion (c_0, corresponding to null normal joint stress) and friction angle (ϕ_j) (See Figure 6.18 – a)). Normal displacements in the joint (δ_j – see Figure 6.4 – b)) are managed by the elastic stiffness K_n, originating normal stresses σ_n which are limited in tension (σ_{n0}^+ - Figure 6.18 – b)). Shear forces are managed by an elasto-plastic model according to the elastic stiffness K_s, originating from shear displacements along the joint transverse direction Figure 6.18 – c)).

- JOINT_SOFT: This model also relates to a Mohr-Coulomb criterion. There are several implementations available, according to the actual Cast3m version, since some variants were developed from the original version of the model. However, all of them essentially aimed to improve the accuracy of results by enabling the consideration of hardening/softening rules for both normal and tangential joint behaviors, and improving the associated hysteresis rules. Further details can be reviewed in Costa (2009).

ϕ_j

$\tau_s = c_0 + \sigma_n \cdot \tan \phi_j$ c_0 τ_s σ_n

$\sigma_{n_0}^+$ σ_n

σ_n

$\sigma_{n_0}^+$ K_n

δ_j

τ_s K_s

γ_j

a) Yielding surface   b) Normal behavior   c) Shear behavior
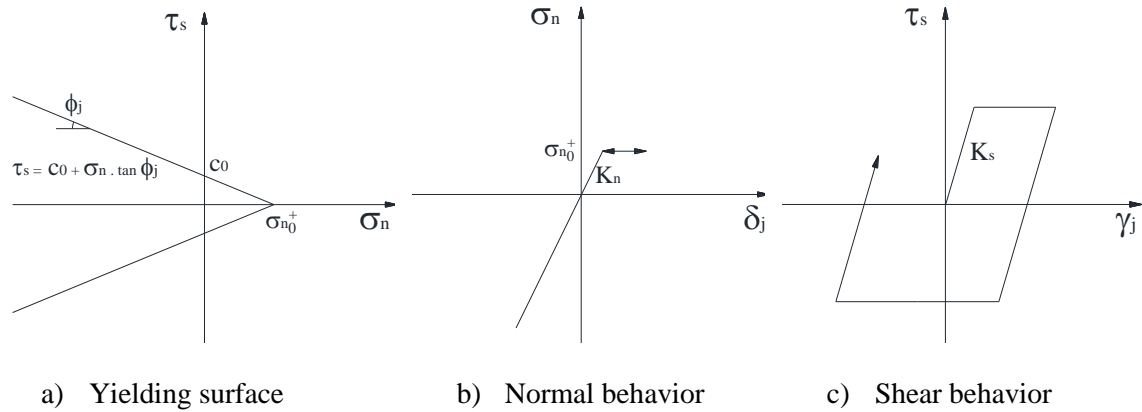
Figure 6.18 – JOINT_DILATANT model in Cast3m (Costa (2009))

Within this context, the adoption of the more complex formulations can broaden the scope of structural aspects to take into account, although generally at the cost of added computational effort and, potentially, of undesirable increased numerical problems. Considering that the present work FEM tests involve large and concentrated inelastic strains at the joint sections, it was considered important to keep with simple approaches, aiming to reduce the difficulty of achieving numerical convergence.

In that regard, the importance of the shear behavior in the joint elements can be argued. In fact, in addition to usual friction forces (under the prestress axial load), an important dowel action should be expected from the many rebars that cross the connection interfaces, leading to a high shear stiffness and low displacements. Furthermore, since considerable sliding is not expected, then softening and capacity depletion in shear should also not be relevant features for these applications. Therefore, only the normal degree of freedom seems to be critical for accurate simulations, as it is directly associated with the opening and closure of the joint during cyclic lateral motions, thus regulating the contact forces that are transferred between beam and columns.

Taking that into account, the choice between JOINT_SOFT or JOINT_DILATANT should be related to the importance of softening in the normal tensile behavior of the models, since it is considered on the former but not in the latter. In this regard, considering post-yielding loading levels, where the joint motions were observed to lead to large opening widths that can be related with full depletion of joint tensile capacity, its contribution to the overall energy dissipation should be negligible. Therefore, considering the modeling tools presented above, while the JOINT_SOFT model could be an option, it does not seem like it would provide considerable benefits for this specific application. The alternative of using the simpler JOINT_DILATANT model also addresses the main concerns regarding accurate simulation of the joint opening/closure motions with less calibration effort and less subject to numerical convergence

problems. Nonetheless, it also requires that the cracking threshold is defined as a low or null value, otherwise the elasto-plastic behavior in tension would lead to unrealistic energy dissipation in the joints at large openings. With this approach, the early behavior of the numerical models can exhibit slightly less stiffness than the experimental counterparts before joint cracking occurs, but accurate joint performance is expected to be better addressed for the later stages, namely for the onset of yielding and collapse. With that in mind, the option was made to use JOINT_DILATANT as the constitutive model for precast joints. For that purpose, the shear and normal stiffnesses K_s and K_n, respectively, are required for full characterization of the elastic behavior of this model, while the friction angle and cracking threshold σ_{n0} define the yielding surface. When applicable, a dilatancy angle can also be defined to enable plastic flow.

The values for the K_s and K_n parameters were estimated from actual test data, due to the unavailability of adequate sampling results to evaluate from. Furthermore, the monitoring layout used in the experimental campaign was not developed accounting for this requirement, leading to considerable difficulty in obtaining adequate values. Nonetheless, a methodology was developed with that purpose which, for the normal stiffness K_n, involved the following assumptions and procedure, also illustrated in Figure 6.19:

- Evaluation of the peak displacement instant for one of the first few cycles of each test (until a maximum of 0.40% drift), gathering data for analysis from those load-steps only;
- Assuming a linear strain distribution over the connection section, for determination of the neutral axis and the compressive strain ε_n^- from the recorded displacements, δ_j^- and δ_j^+;
- Calculation of σ_n^- by equilibrium, in order to balance the total vertical reaction R_v^- recorded at the load cell underneath the corresponding columns; at the local joint section, all the compressive force is transferred through the zone under compression, which is assumed to be adequately represented by the strain diagram from Figure 6.19;
- Determination of an adequate value for K_n from the experimental σ_n^- - ε_n^- relationship;

6.23
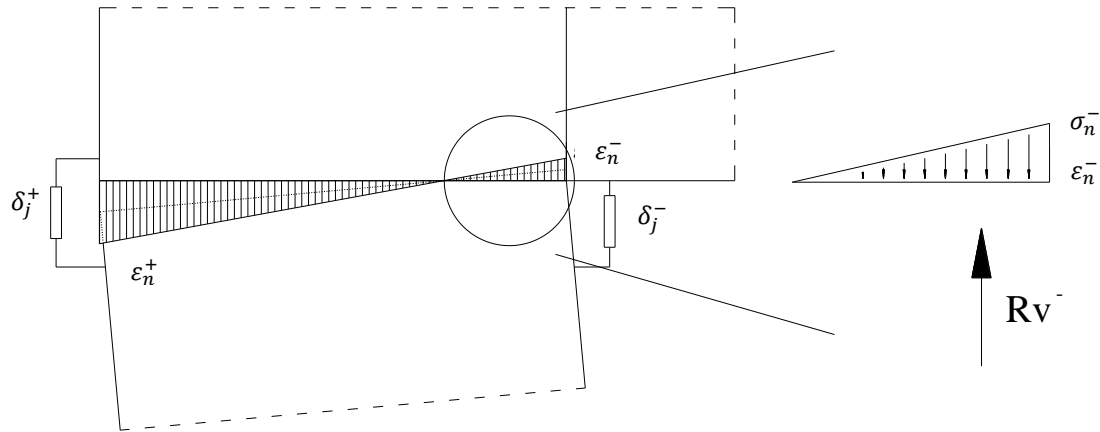
Figure 6.19 – Methodology for determination of K_n

The calibration of shear stiffness K_s was performed against experimental data, by adopting a procedure based on comparison of the plots between the experimental σ_n - τ_s relationship, and a calculated version of σ_n - τ_s using the previously obtained K_n and assumed values for K_s instead:

- Evaluation of the peak displacement instant for one of the first few cycles of each test (until a maximum of 0.40% drift), gathering data for analysis from those load-steps only;

- Assuming equal distribution of the applied horizontal force between the two precast joints (as shear) for calculating the experimental shear stress τ_s;

- Using the experimental values for σ_n and the previous shear stress τ_s, determination of the experimental σ_n - τ_s relationship;

- Calculation of a numerical σ_n - τ_s relationship assuming σ_n governed by the previously defined normal stiffness K_n, and τ_s by an initial K_s shear stiffness;

- Iterative adjustment of the initial K_s parameter until both σ_n - τ_s relationships are characterized by similar evolution. In this procedure, the experimental σ_n - τ_s curves and the normal stiffness K_n are kept constant, and only K_s is a variable input;

A friction angle ϕ of 60º and a residual cracking threshold (σ_{n0}^{+}) of 25 KPa were also considered for full definition of the joint model.

6.3. EXPERIMENTAL RESULTS VS. NUMERICAL SIMULATIONS

The results presented in this section were obtained from numerical simulations with the models elaborated according to the methodology described in 6.1. The loading conditions considered for the analyses respected a constant axial loading of 300 kN per column and aimed to reproduce the same displacements recorded for each tested specimen. However, considering

the modeling strategy presented earlier and the characteristics of the constitutive models, strong degradation is not expected between the repeating cycles for each individual drift level. Therefore, the horizontal drift loading history applied in the numerical analyses only included one full cycle per drift level.

6.3.1. MONOLITHIC SPECIMENS: SP_M02, SP_M03 AND SP_M04

Figure 6.20 presents a comparison of the applied force results obtained in both the numerical and experimental tests, plotted against the actual displacements recorded on top of the piers in terms of drift percentage, only the first full cycle for each drift.

a) SP_M02

b) SP_M03

c) SP_M04
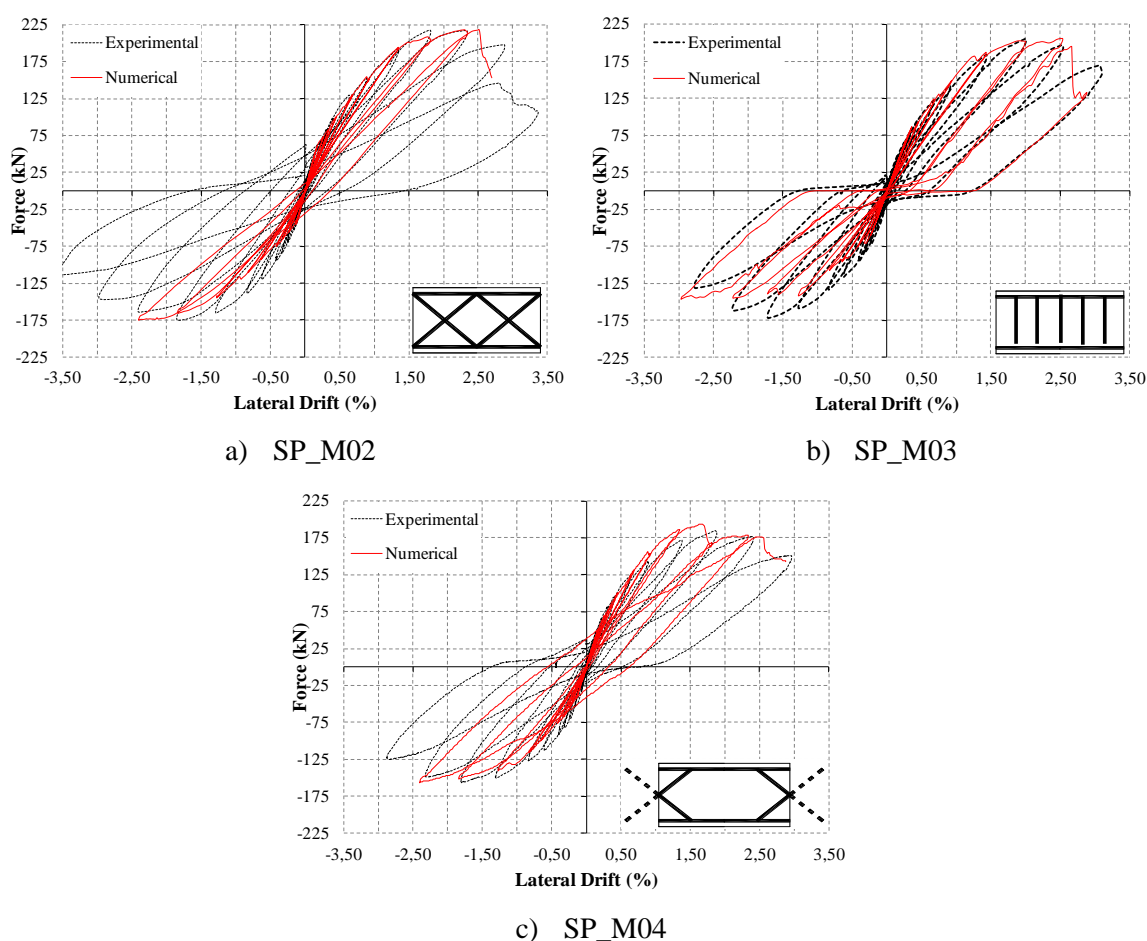
Figure 6.20 – Numerical vs. Experimental Force – Drift results for monolithic specimens

As it is possible to observe, the numerical and experimental results are in good agreement, presenting similar peak forces (between 1.50% and 2.00% drifts for SP_M04 and around 2.50% drift for both SP_M02 and SP_M03) and general envelope; the numerical models were also able to characterize the force asymmetry between the two loading directions. In fact, the asymmetry for the negative loading direction was generally even slightly larger in the numerical simulation than in the experimental test, particularly on the negative unloading stiffness on SP_M02 and SP_M03. The lack of numerical simulation of plasticity in tension comes to mind as a possible

explanation of these results. Nonetheless, this result may also be explained by a larger demand applied to the shear interlocking mechanism on that direction, which would help increase the corresponding beam stiffness, although that feature is not accounted for by the adopted modeling strategy. Recalling what was previously discussed about the coupling action at the beam (section 5.2.1), on the negative loading direction it is mobilized with a tensile pulling force, leading to overall reduced beam stiffness due to less efficient crack closing. However, the interlocking mechanism mostly depends on the differential shear displacements occurring at existing cracks, rather than the overall lateral movement, and therefore it should be relatively the same for both loading directions (except when the crack widths are too large to enable efficient shear transfers). Taking that into account, it is possible that for pushing coupling action (positive direction) the numerical model is able to mobilize the beam shear force transfer mainly through concrete compression struts, without significant contribution of interlocking, but for pulling coupling action (negative direction) the lack of interlocking leads to smaller forces. With this in mind, results will be further presented addressing the positive loading direction only, as for instance, the maps of compressive damage variable d^-, shown in Figure 6.21 for the monolithic specimens.

a) SP_M02 at peak force b) SP_M02 at failure

c) SP_M03 at peak force d) SP_M03 at failure

(scale)

e) SP_M04 at peak force f) SP_M04 at failure
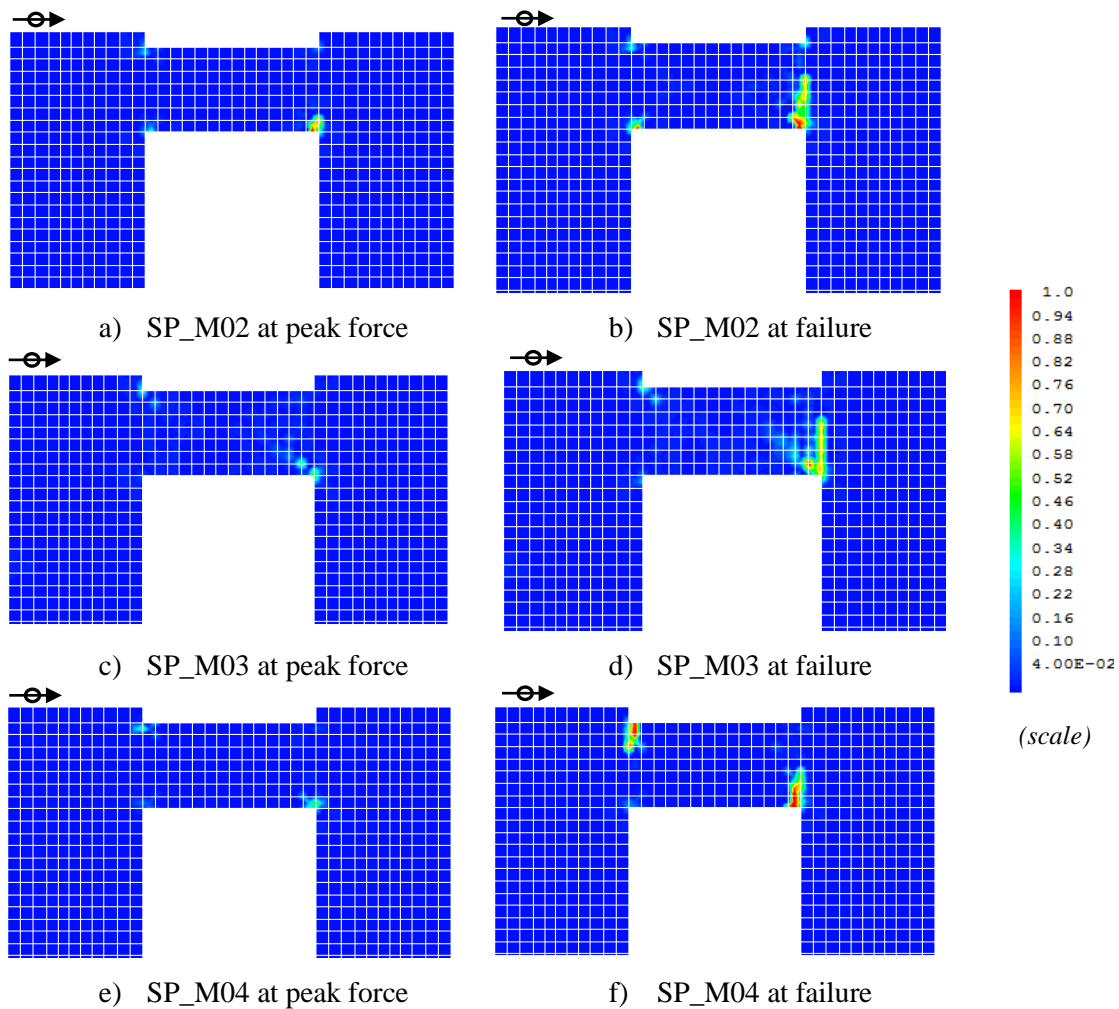
Figure 6.21 – Maps of compressive damage variable $\boldsymbol{d^-}$ maps on monolithic specimens

At the 3.00% drift loading level, the numerical models experienced a strength loss on all the specimens, leading to the occurrence of severe numerical convergence difficulties that caused the simulation to stop on all but SP_M03. An in depth analysis of the problem showed that it was mostly caused by failure of the beam in compression, because the respective damage variable d^- developed values around 1.0 (which is representative of fully damaged section with no further capacity) near the edges close to the columns. Figure 6.21 evidences the previous description, where it is possible to observe the incursion of damage in compression at the loading levels corresponding to peak and failure, showing that increasing damage progresses upwards along the beam-column interface.

The failure of the concrete in compression at the beam-column interface goes in line with experimental observations, where some level of concrete crushing and/or spalling was detected in those locations for the largest drifts (a clear example is Figure 5.25, for SP_M02). In this regard, the importance of the shear force transfer between columns is also noted, considering the strength drops recorded in accordance with disruption of the compression struts mobilized through the beam. In fact, based on the plots of principal compressions σ_{22} shown in Figure 6.22 for the monolithic specimens, the main shear transfer mechanism until reaching the peak force drift level (Figure 6.22 – a), c) and e)) is related with the formation of a single compression strut; it is only after the concrete failure that multiple struts are formed (Figure 6.22 – b), d) and f)).

a) SP_M02 at peak force

b) SP_M02 at failure

c) SP_M03 at peak force

d) SP_M03 at failure
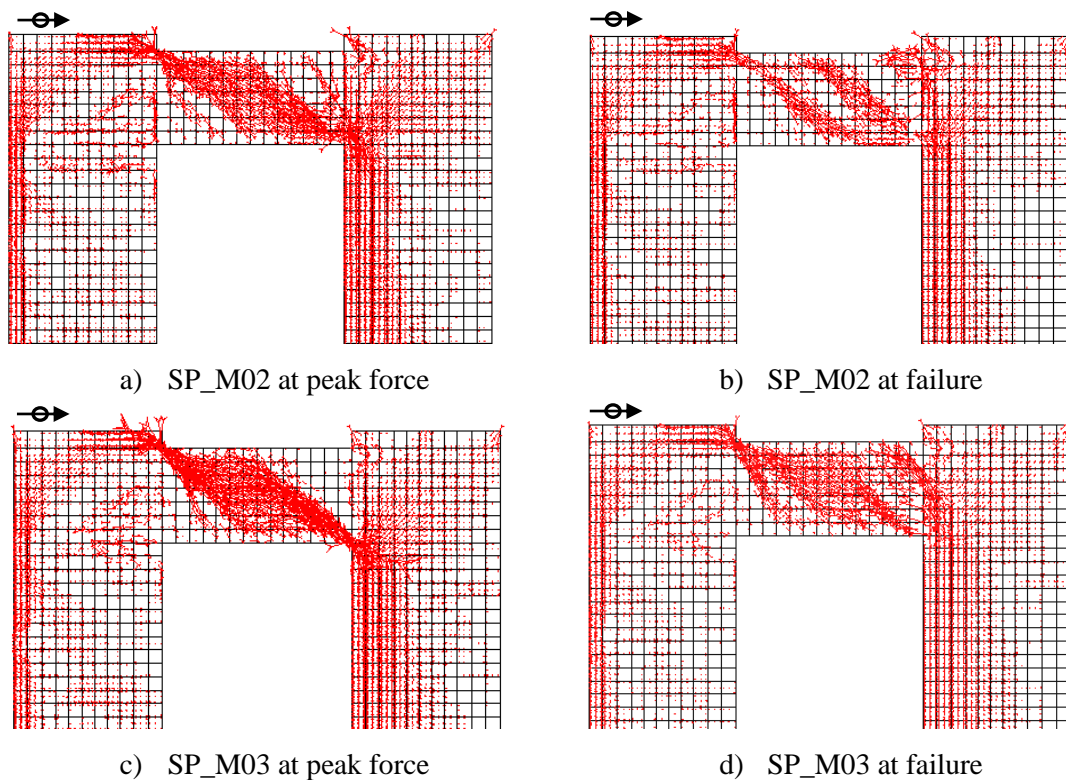
Figure 6.22 – Principal compressions σ_{22} on monolithic specimens

e) SP_M04 at peak force   f) SP_M04 at failure
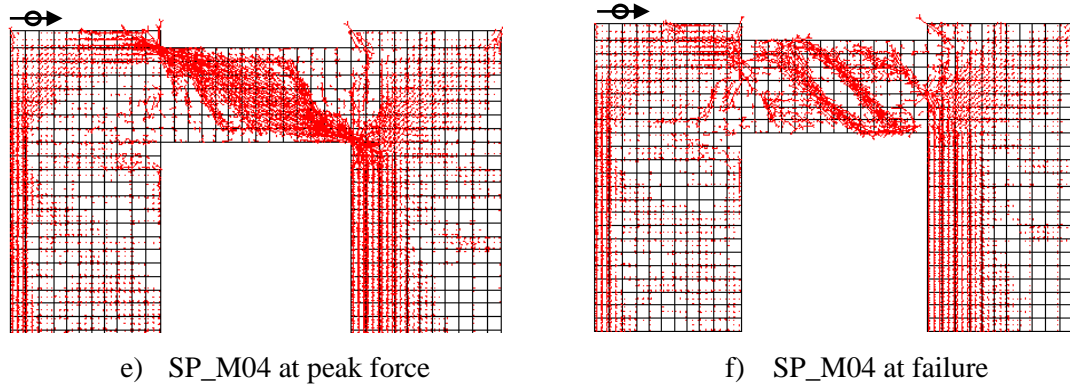
Figure 6.22 (cont.) – Principal compressions σ₂₂ on monolithic specimens

Regarding the level of shear that is transferred through the beams, the numerical models were able to simulate with reasonable accuracy the values recorded during the experimental tests. Figure 6.23 illustrates a comparison of maximum beam shear values from the numerical analyses (red bars) with the respective experimental results (blue bars), where the presented values were evaluated from the amplitude variation of the vertical reactions at the base of each column. Furthermore, numerical and experimental result values are also indicated within their respective columns, showing minor differences as highlighted by the colored labels above the numerical one.
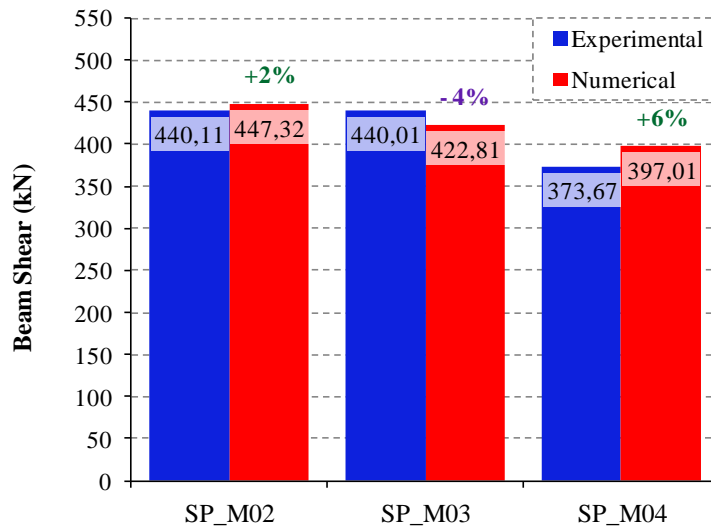
Figure 6.23 – Beam shear results for monolithic specimens: numerical vs. experimental

The damage pattern observed in the pier system throughout the tests indicated early cracks in the beam at the first few drift levels, progressing to considerable beam damaged close to the collapse level. However, the cracking pattern was generally observed to be mostly stabilized after 1.00% drift, with just mild cracking on the columns recorded around 0.75% drift. Figure 6.24 presents the results for the tensile damage variable d^+ for 0.20% drift, 0.50% drift and

1.00% drift, where a similar progression can also be observed. The regular distribution of tensile damage on the columns is also noted.

a) SP_M02 - 0.20% drift   b) SP_M02 - 0.50% drift   c) SP_M02 - 1.00% drift

d) SP_M03 - 0.20% drift   e) SP_M03 - 0.50% drift   f) SP_M03 - 1.00% drift

(scale)

g) SP_M04 - 0.20% drift   h) SP_M04 - 0.50% drift   i) SP_M04 - 1.00% drift
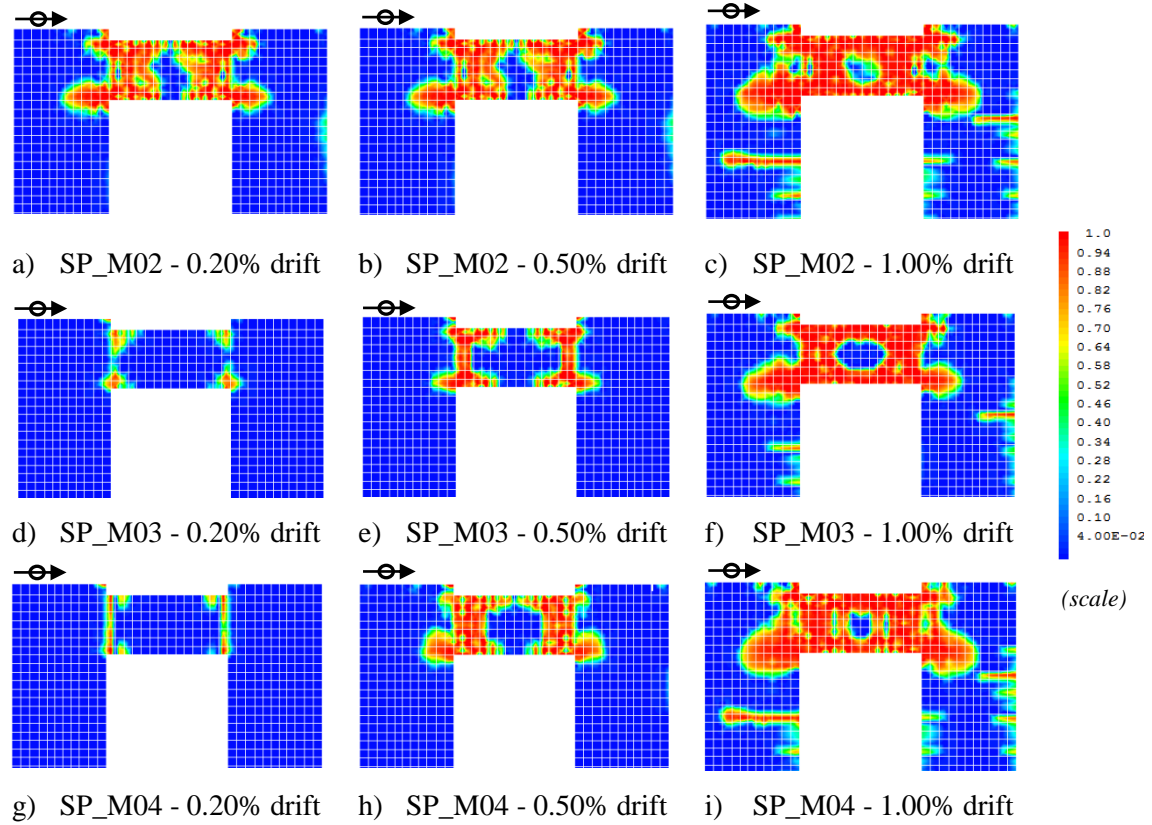
Figure 6.24 – Maps of tensile damage variable d^+ maps on monolithic specimens

The previous results show that the demand is large at the beams, where damage is mostly found near the nodes, similarly to experimental evidence. In addition, the virtual loss of concrete tensile capacity indicative of generalized cracking that is observed in the previous figure for the 1.00% drift level, suggests that crack width increases are likely to occur along with progression of main reinforcement yielding. This is confirmed by Figure 6.25, which provides illustrations of the principal positive (tensile) strains ε_{11}over the deformed shapes (with 5.0 amplification factor) for loading levels corresponding to the first yielding of the main reinforcement and to failure, thus clearly reflecting what was previously described.

a) SP_M02 at first yielding   b) SP_M02 at failure
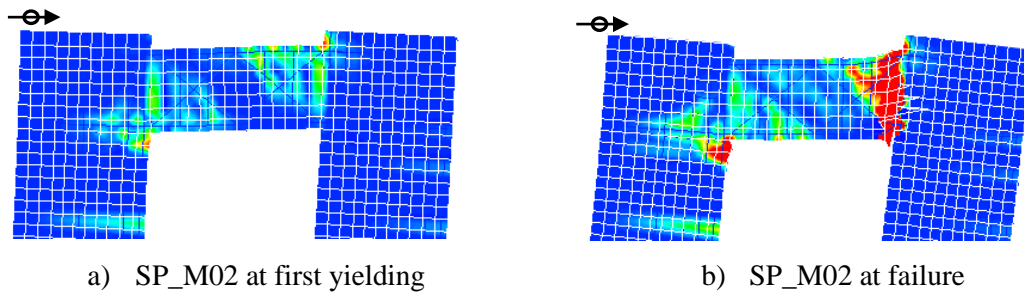
Figure 6.25 - Principal strain ε_{11} maps over the deformed shape on monolithic specimens

c) SP_M03 at first yielding   d) SP_M03 at failure

e) SP_M04 at first yielding   f) SP_M04 at failure
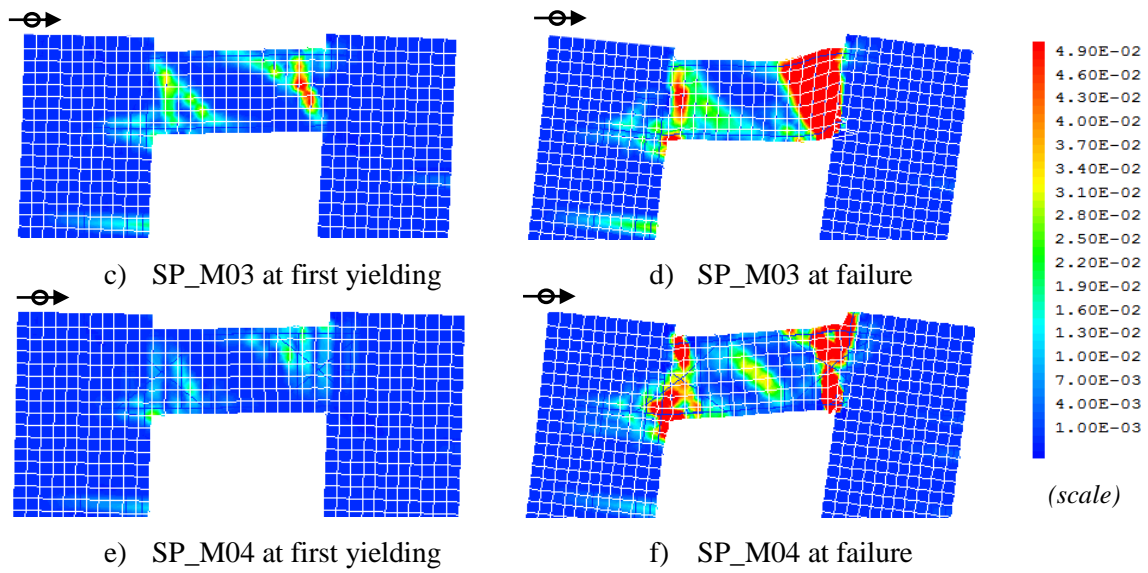
Figure 6.25 (cont.) – Principal strain ε_{11} maps over the deformed shape on monolithic specimens

Concerning the main reinforcement yielding, it was observed to always occur firstly at the beam reinforcement, according to the axial stress maps shown in Figure 6.26, determined for the first yielding of the main column or beam reinforcement. Despite that, column reinforcement also develops high stresses and, at peak force, several of its rebars have achieved yielding. For ease of analysis, results are presented in normalized terms, with main rebar stresses σ_{sl} divided by the corresponding individual yielding stress σ_{sly}.

a) SP_M02 at first yielding   b) SP_M02 at peak force

c) SP_M03 at first yielding   d) SP_M03 at peak force
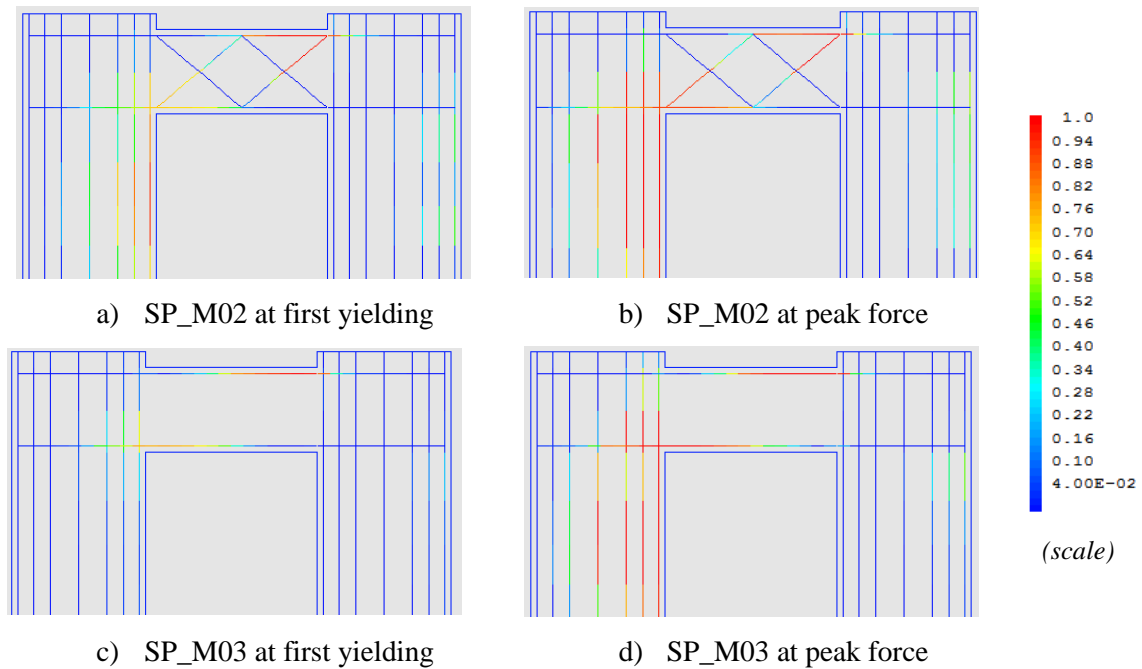
Figure 6.26 - Maps of rebar stress ratios (σ_{sl}/σ_{sly}) on monolithic specimens

| e) SP_M04 at first yielding | SP_M04 at peak force |
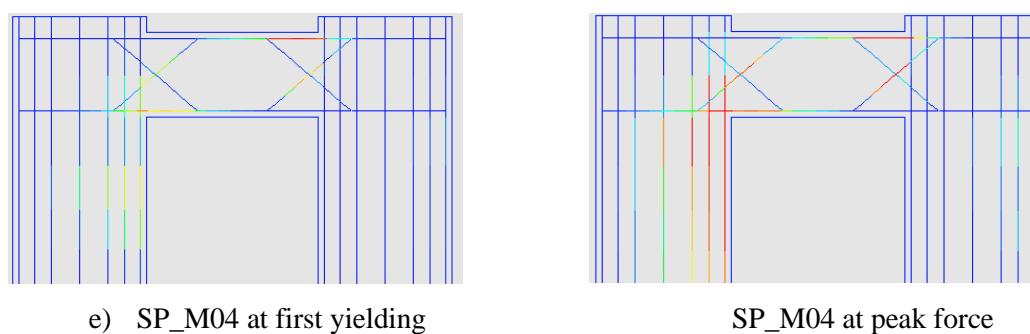
Figure 6.26 (cont.) – Maps of longitudinal reinforcement stress ratios (σ_{sl}/σ_{sly}) on monolithic specimens

The drift values corresponding to the first occurrence of yielding represented in the previous figures can also be compared with the values determined through the bilinear equivalent system procedure adopted in Chapter 5 (Figure 5.67). Figure 6.27 illustrates that comparison, where relatively small differences under 15% are observed between numerical and experimental results of SP_M02 and SP_M04.
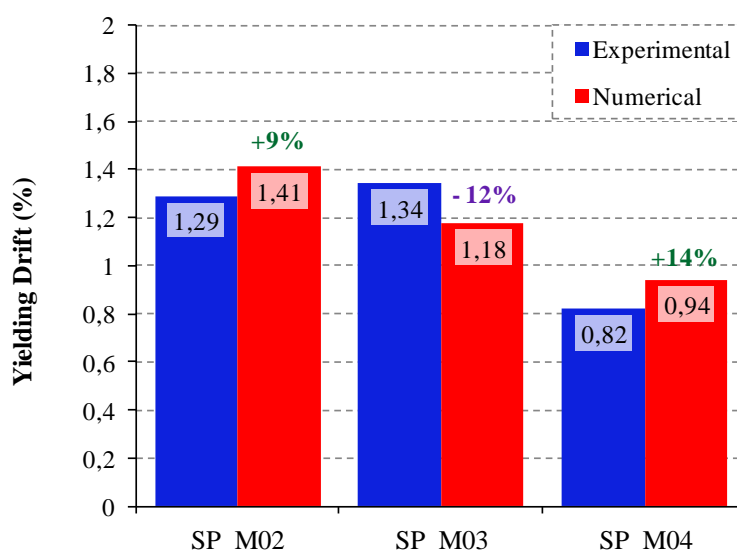
Figure 6.27 – Yielding drift for monolithic specimens: numerical vs. experimental

Lastly, for the drift range simulated in the analyses, the numerical models did not show significant demand on the transverse reinforcement on either the columns or, more importantly, the beam, particularly for the peak force level. Considering the level of shear that is transferred through that element, as previously discussed, those results are interesting to note. Figure 6.28 illustrates the axial stress σ_{st} map of beam transverse reinforcement bars for each specimen, normalized by their respective yielding stress σ_{sty}, for loading drifts corresponding to the peak force level and failure.

This means that most of the vertical component of the shear load is handled by the concrete struts and the diagonal parts of the reinforcement (when applicable), instead of the

vertical stirrups, actually as intended by design of all specimens except SP_M03. Moreover, it is believed to be also a consequence of the modeling strategy not being able to adequately explore the post-peak stage, since the compressive failure and the occurrence of numerical convergence problems prevented longer simulations. This is particularly relevant because, as seen in Chapter 5, experimental evidence showed that significant tensile degradation or failure (e.g: Figure 5.34, Figure 5.39) were detected after compression driven occurrences.

In light of these results, it is believed that the demand for transverse reinforcement capacity is mostly relevant at the larger drifts, as the result of the concrete degradation associated with the shear load transfer on the beam. In fact, the stirrups tend to prevent loss of integrity of the damaged core concrete, thus it is only upon failure of the compressive strut mechanism that originally enables shear loading through the beam, that their role as the main shear resisting element becomes apparent. This is the reason why these results do not show that effect, because they refer to the behavior mostly before failure of the compressive strut.

a) SP_M02 at peak force   b) SP_M02 at failure

c) SP_M03 at peak force   d) SP_M03 at failure

e) SP_M04 at peak force   f) SP_M04 at failure

(scale)
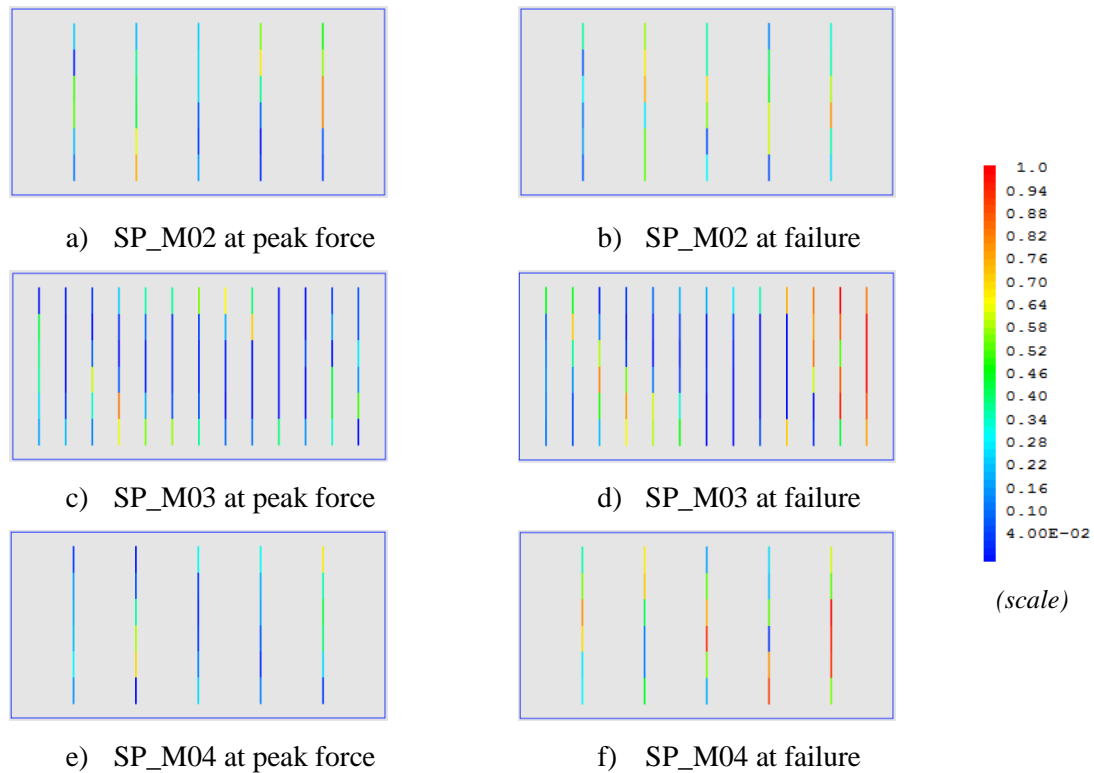
Figure 6.28 – Maps of transverse reinforcement stress ratios (σ_{st}/σ_{sty}) on monolithic specimens

6.3.2. PRECAST SPECIMENS: SP_PC02A AND SP_PC02B

Results obtained for the precast specimens subjected to numerical simulation are presented in Figure 6.29, where a comparison of the applied force plotted against the percentage of drift

(associated with the displacements at the top of the piers) is shown for both the simulations and experimental tests. Regarding the latter, only results for the first full loading cycle at each drift level are included, similarly to the strategy adopted for presenting the monolithic simulations.

In the precast specimen analyses, calculations were only performed until the 3.50% drift loading level, since evaluation of those results for larger drifts was deemed unnecessary, and because it is believed the obtained responses already characterize performance for an adequate demand range capable of detailing the most important phenomena. In addition, it is also noted that due to the small loading increment used for all the analysis (for the purpose of numerical convergence), the output file size for the later cycles becomes quite large, leading to impractical post-processing.

In general, the responses obtained with the numerical analyses provide satisfactory results, showing similar peak forces (at near the 2.50% and 3.00% drift loading levels for SP_PC02A and SP_PC02B, respectively) and unloading behavior. Despite that, some differences can be observed between the numerical and experimental output on both specimens. In SP_PC02A and roughly between drifts 0.50% to 1.50% (corresponding to the yielding range) the lateral force is greater than the experimentally obtained, although for larger drifts the difference reduces to a negligible margin. In addition, both specimens show higher stiffness in the reloading stages (wider force-drift loops, particularly in the positive loading direction) that lead to increased energy dissipation relative to the experimental tests. Although this was not evaluated in depth, it is believed that it can be related with differences between the numerical and experimental bond-slip behavior, enabling stronger bond on the former (which could also help explain the earlier yielding range observed on SP_PC02A), or with the joint stiffness parameters. Regardless, this was not further adjusted because, by contrast with the reloading stiffness, the unloading stiffness is believed to be closely captured on both cases and, despite the energy dissipation may be slightly higher than intended, the overall performance is deemed to be adequately similar to experimental results. The loading direction asymmetry was also well captured, particularly for SP_PC0B, where peak values for both the positive and negative directions are quite close to the experimental records.

d) SP_PC02A   e) SP_PC02B
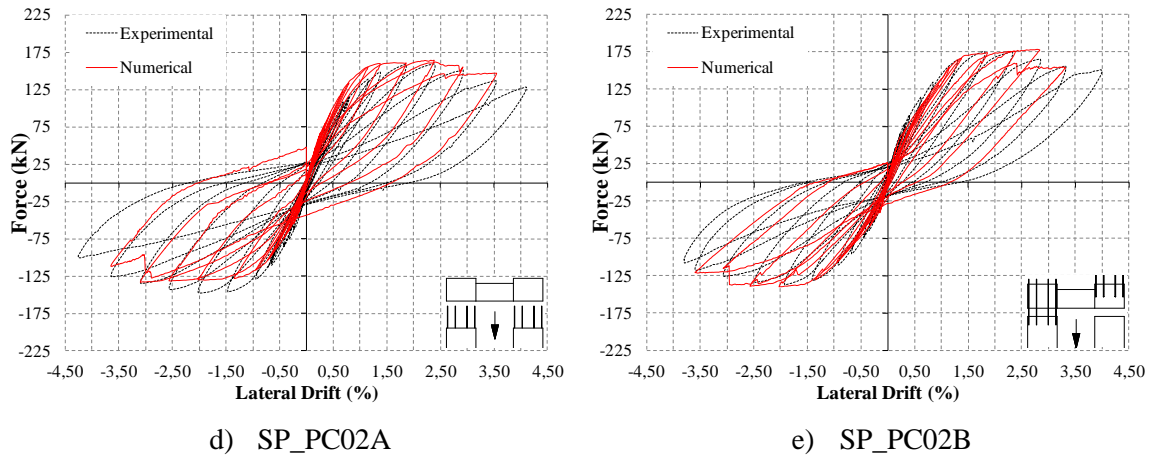
Figure 6.29 – Numerical vs. Experimental Force – Drift results for precast specimens

In general, the performance in both cases was dependent on both the joint and beam behavior, contrasting with the monolithic tests where clear prevalence of beam failure was observed. This can be seen in Figure 6.30, which illustrates the values recorded for the compressive damage variable d^- at the loading displacement associated with peak force for the positive direction, and the 3.50% drift cycle. As it is possible to observe, accumulation of concrete damage in compression near the beam edges still occurs. However, crushing of the beam-column node concrete along the precast joints is also evident around 3.50% drift in both of the precast specimens, which indicates the importance of the balance between the compressive forces transferred from the beam to the column. Nonetheless, full degradation of the associated concrete capacity in compression along the precast joint was not evidenced by the experimental tests as much, in the outer edges of the beam-column nodes, although the inner edge experienced significant crushing (e.g. Figure 5.49 and Figure 5.55). In light of this, it is possible that the concrete compressive ductility calibrated for these numerical applications was too low for those particular zones. Additionally, incorrectly calibrated joint model stiffness could also lead to increased local stresses (which may be another reason supporting the evidence above described).

a) SP_PC02A at peak force   b) SP_PC02A at 3.50% drift

c) SP_PC02B at peak force   d) SP_PC02B at 3.50% drift
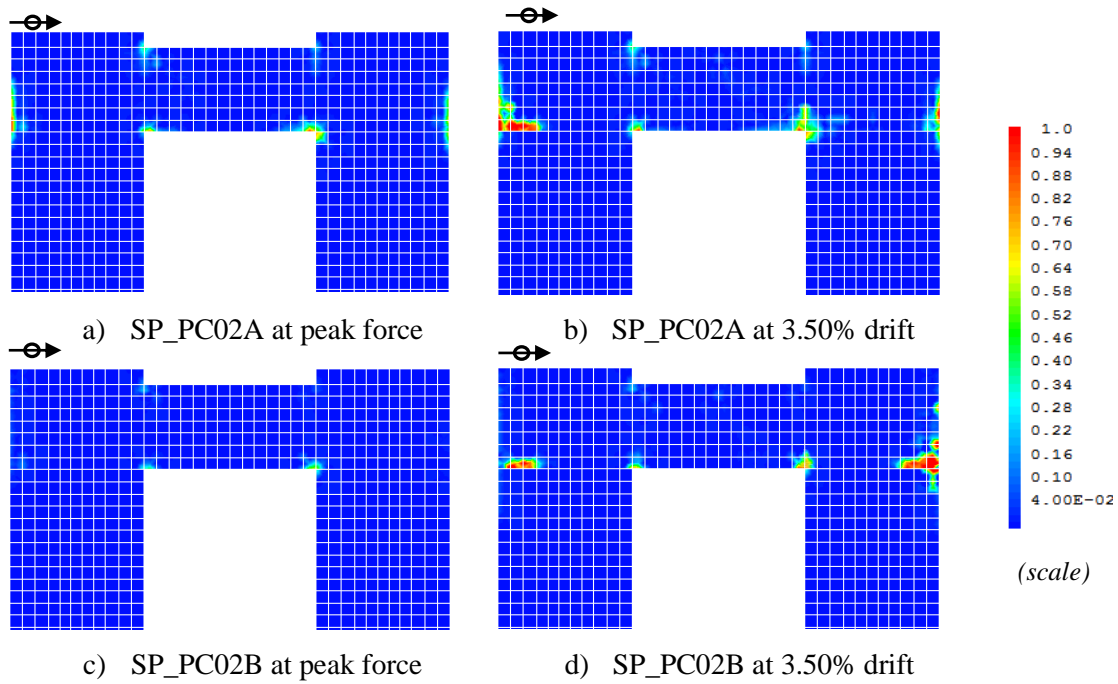
Figure 6.30 – Maps of compressive damage variable d^- maps on precast specimens

Despite the concrete failure in compression (at the largest drifts) that is detected in the numerical analyses, the general distributions of compressive forces is very similar to those of the monolithic specimens, as illustrated by the σ_{22} principal compressions' maps shown in Figure 6.31. In fact, at the peak force level, a single compression strut in the beam is responsible for shear transfer between columns in both SP_PC02A and SP_PC02B. Furthermore, increasing damage causes modifications on the principal stresses, leading to the formation of multiple struts from the original one, when approaching the ultimate drift stages.

a)   SP_PC02A at peak force   b)   SP_PC02A at 3.50% drift
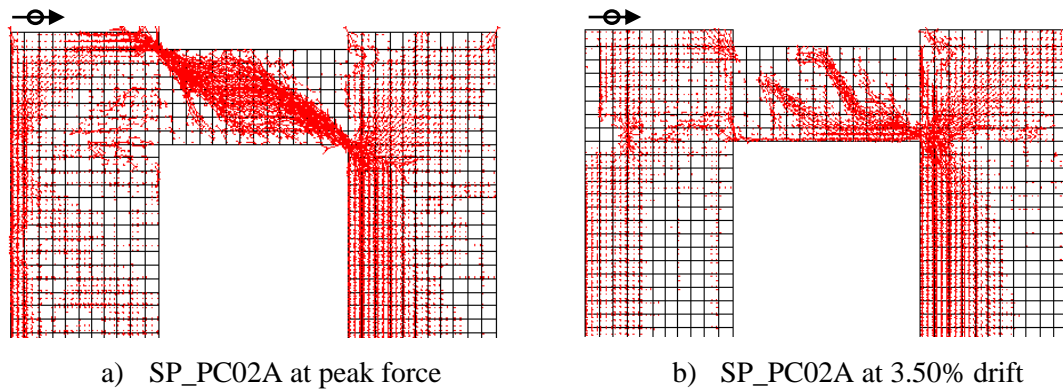
Figure 6.31- Principal compressions σ_{22} on precast specimens

6.35

c) SP_PC02B at peak force   d) SP_PC02B at 3.50% drift
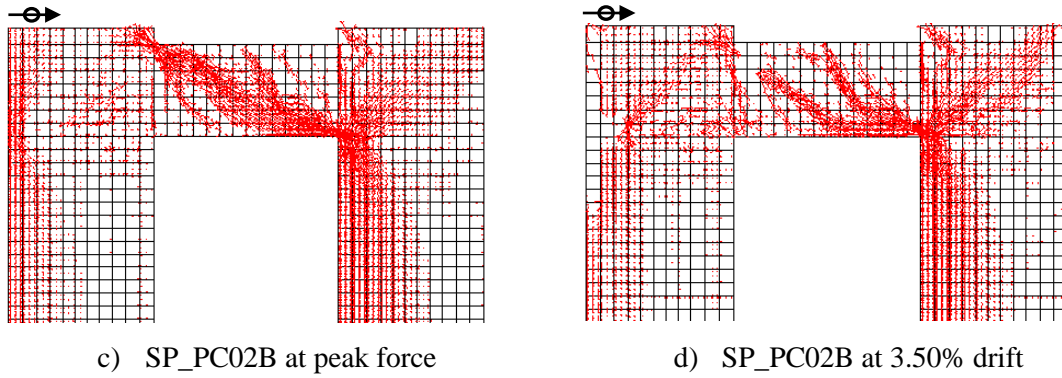
Figure 6.31 (cont.) – Principal compressions σ_{22} on precast specimens

The difference between the maximum beam shear evaluated from experimental tests and the corresponding value determined from numerical analyses was small in both cases. Figure 6.32 illustrates the comparison of those values, where experimental and numerical data are represented by the blue and red columns, respectively. The accuracy of the numerical simulations is confirmed by the relative minor differences observed and expressed in percentage over the numerical columns.
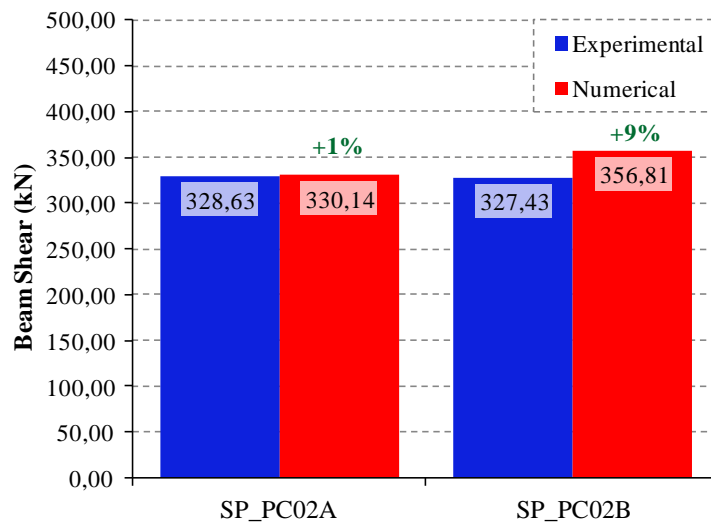
Figure 6.32 – Beam shear results for precast specimens: numerical vs. experimental

Concerning the tensile damage on the precast specimens, it was found concentrated on the coupling beam, first observed around the 0.20% drift level near the beam-column node vertical interfaces, progressing to complete tensile capacity degradation over the total length of the element and also into the node. Column cracking occurred after the 0.75% drift level, but not to the same extent as in the beam.

a) SP_PC02A   b) SP_PC02A   c) SP_PC02A

0.20% drift   0.50% drift   1.00% drift

d) SP_ PC02B   e) SP_ PC02B   f) SP_ PC02B

0.20% drift   0.50% drift   1.00% drift
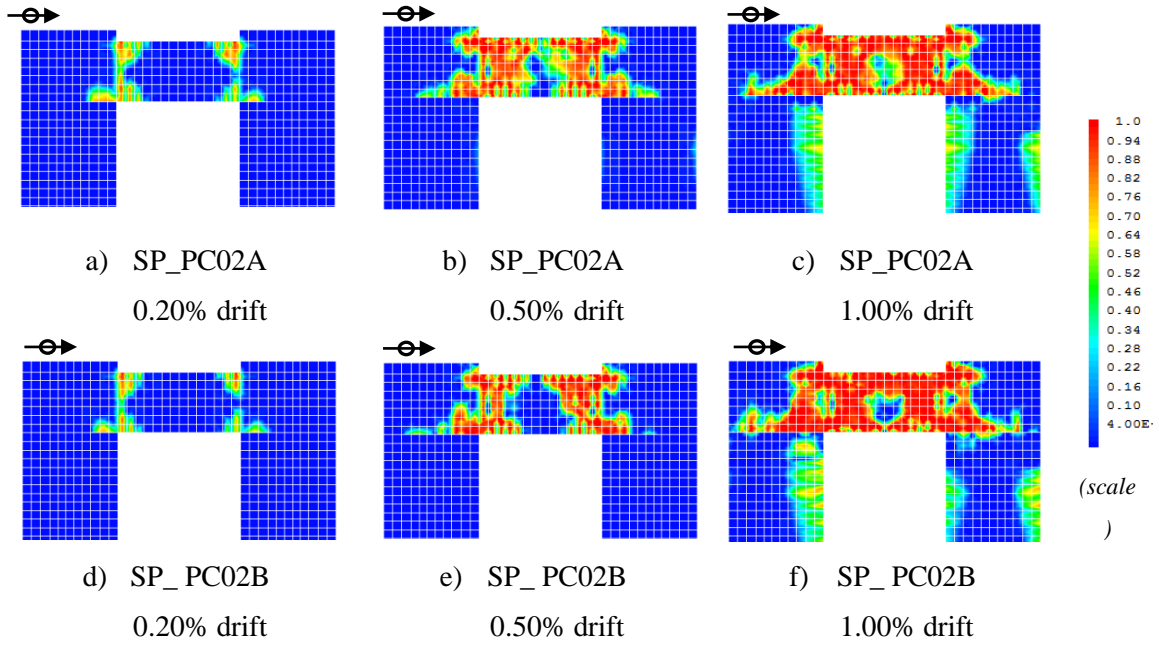
Figure 6.33 – Maps of tensile damage variable d^+ maps on precast specimens

The previous results suggest that the performance of both precast specimens shows similar demand on the beam but reduced demand on the columns, when compared with the previous monolithic cases (Figure 6.24). In that regard, concentrated rotations do occur at the interface connection section, enabling reduced strains in the beam comparatively with the monolithic specimens, especially on SP_PC02A, as evidenced by the principal tensile strains ε_{11} maps plotted over the deformed shapes (with amplification factor of 5.0) represented in Figure 6.34. Nonetheless, the deformations that take place in the beam are still large enough so that considerable damage cannot be prevented, as reported on the experimental tests and adequately simulated by the numerical models. Furthermore, as it can be observed in Figure 6.34, at 3.50% drift, concrete crushing in the edges of the precast joints is apparent, as well as the large strains in the beams.

a) SP_PC02A at first yielding   b) SP_PC02A at 3.50% drift

c) SP_PC02B at first yielding   d) SP_PC02B at 3.50% drift
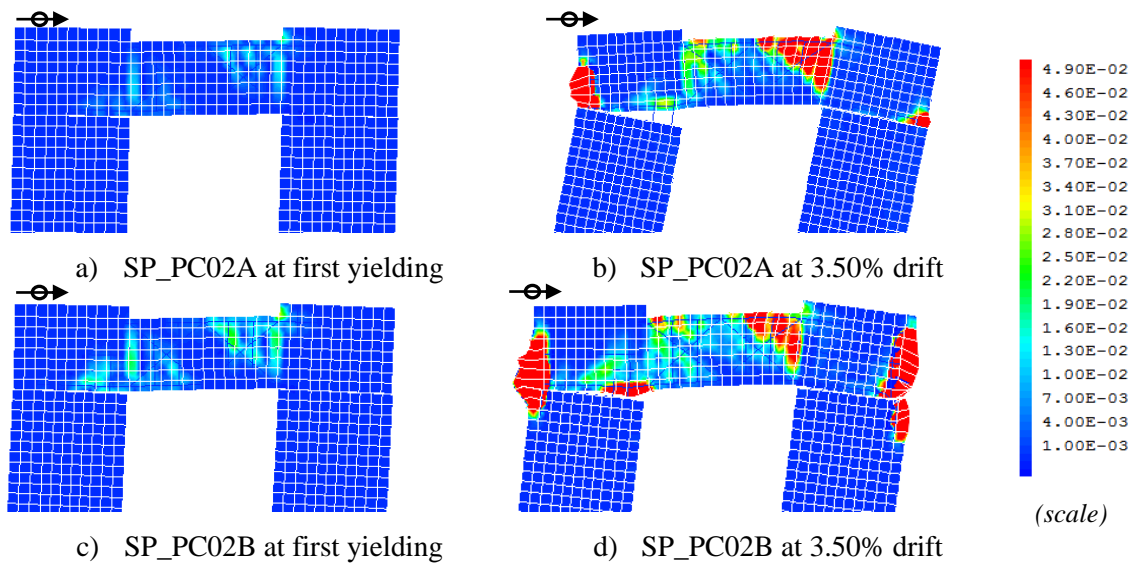
Figure 6.34 – Principal strain ε_{11} maps over the deformed shape on precast specimens

It is interesting to note that SP_PC02B seems to develop larger strains in the beam at an earlier stage relative to SP_PC02A, and that, at larger drifts, it also shows increased column damage. As presented in Chapter 5, the moment capacity of SP_PC02B at the joint section is slightly larger than SP_PC02A's, leading to increased connection stiffness and larger deformations on the beams and columns, at the expense of more reduced joint motions. In this regard, Figure 6.35 illustrates a comparison of the maximum precast joint opening widths recorded in the experimental tests and those determined from the numerical analysis, for the 0.50% drift, 1.00% drift and 1.50% drift levels on both specimens. Values for SP_PC02A and SP_PC02B are not very different, especially regarding the experimental data. Nonetheless, numerical results seem in line with the previous, even though lower values are generally reported by the numerical models (particularly on SP_PC02B), which could also help explain the larger reloading stiffness on the numerical force-drift curves, relative to the experimental values.
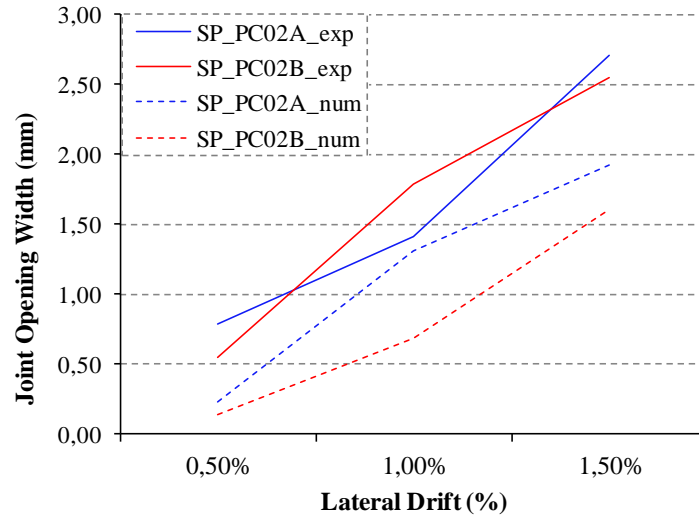
Figure 6.35 – Precast joint maximum opening width results: numerical vs. experimental

A major difference between numerical results for monolithic and precast specimens is that while first yielding was always detected in the beam reinforcement in the former, joint reinforcement yielding occurs first in the precast specimens. Figure 6.36 illustrates the axial stress σ_{sl} maps for main reinforcement bars, normalized by the corresponding yielding stresses σ_{sly}, where this can be observed in further detail. Moreover, despite the occurrence of rebar yielding first at the joint section, as intended by design, the beam reinforcement still shows relevant stresses, particularly at the peak force stage for each specimen, thus again confirming that the behavior pattern of the precast models is associated with complex interactions between the beams and columns.

a) SP_PC02A at first yielding   b) SP_PC02A at peak force

c) SP_PC02B at first yielding   d) SP_PC02B at peak force
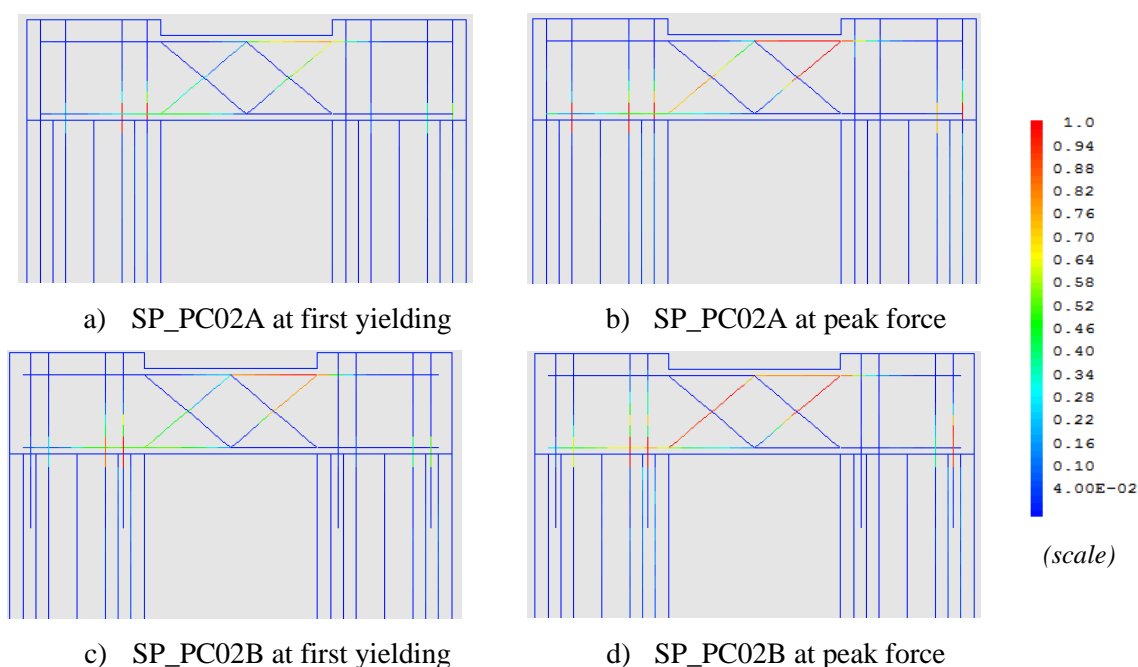
Figure 6.36 – Maps of longitudinal reinforcement stress ratios (σ_{sl}/σ_{sly}) on precast specimens

    Still concerning reinforcement yielding, the comparison of values determined for the yielding drift from experimental and numerical results shows larger differences than those observed in the monolithic cases. Specifically, the yielding drift determined from the bilinear equivalent system for experimental results on SP_PC02A is around 26% lower than the lateral drift at which first yielding was detected in the numerical analysis. By contrast, an even larger difference of around 38% in favor of the numerical value was identified regarding SP_PC02B. These results can be observed in Figure 6.37, and are relatively unsurprising, considering all that was already discussed regarding the calibration of joint stiffness and bond behavior.
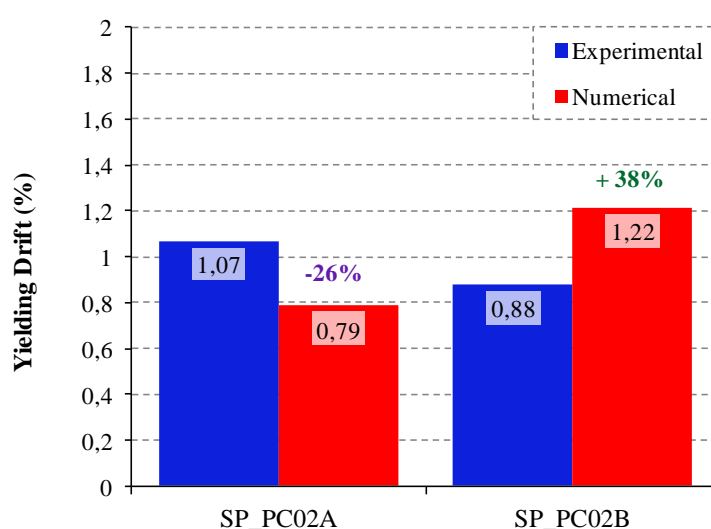
Figure 6.37 – Yielding drift for precast specimens: numerical vs. experimental

Figure 6.38 illustrates the axial stress σ_{st} map of beam transverse reinforcement bars for each specimen, normalized by their respective yielding stress σ_{sty}, for lateral drifts correspondent to the peak force level and 3.50% drift. As observed for the monolithic tests, the numerical analyses for the precast specimens also do not show significant demand on the transverse reinforcement for the drift range applied in the simulations, which is likely related to the same reasons already mentioned before.

a) SP_PC02A at peak force   b) SP_PC02A at 3.50% drift

c) SP_PC02B at peak force   d) SP_PC02B at 3.50% drift
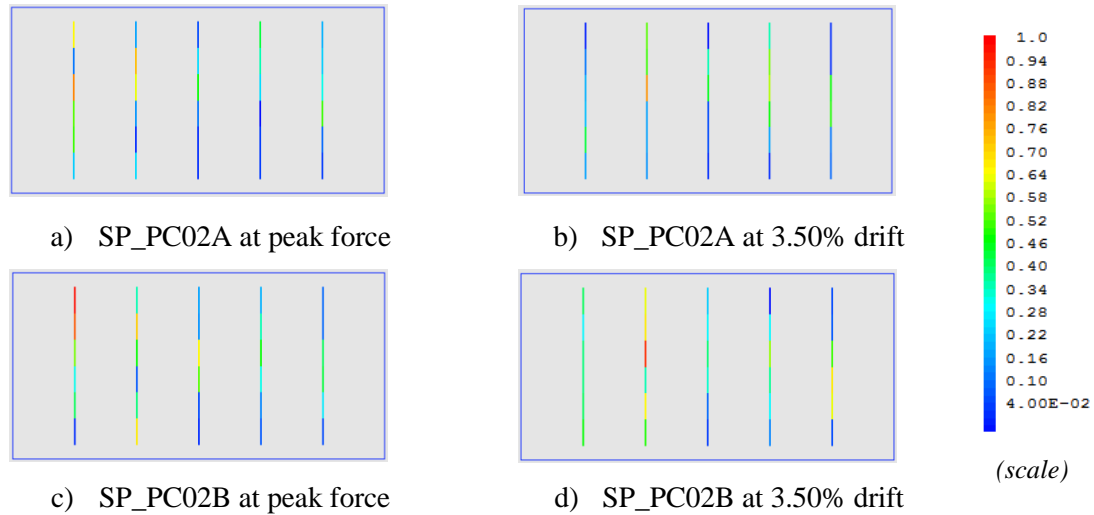
Figure 6.38 – Maps of transverse reinforcement stress ratios ($\boldsymbol{\sigma_{st}/\sigma_{sty}}$) on precast specimens

6.3.3. SINGLE COLUMN SPECIMENS

Numerical simulation of single columns was only performed for the SP_F01 specimen. Nonetheless, the corresponding analysis provided results that compare quite well against the experimental data. Figure 6.39 illustrates the results for lateral force plotted against the displacements recorded at the top of the column in terms of drift percentage. As it is possible to observe, the numerical and experimental curves are in good agreement, displaying similar peak force and general envelope. The unloading and reloading behavior is also well captured, showing a similar slight "pinching" effect between both responses. Despite that, however, the numerical results show increased reloading stiffness relative to the experimental findings, particularly for the positive loading direction. This can be explained by the fact that no bond-slip relationship was used to model the interaction between the rebars and the concrete, resulting in increased energy dissipation in the numerical case. In addition, the experimental results exhibit slight strength degradation between subsequent cycles due to the damage accumulated in the column, but although the global force envelope is well simulated by the numerical model, this effect is not as apparent in its results.
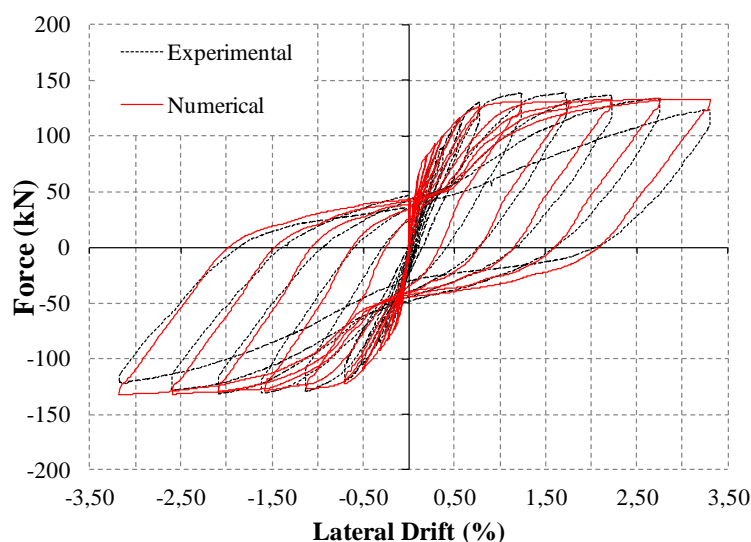
Figure 6.39 – Numerical vs. Experimental Force – Drift results for SP_F01

The general behavior pattern exhibited by the specimen in the numerical analysis was typical of a standard reinforced column test subjected to bending, with the response limited by yielding of the longitudinal reinforcement at its base, and corresponding increase of compressive damage around the edges of the cover concrete. Furthermore, the displacement at which yielding is first identified in the numerical analysis corresponds to 0.56% drift, compared to the value of 0.73% reported from the experimental tests, resulting in a difference of around 22%, which could likely also be better simulated if bond-slip had been considered.

Results for normalized rebar stresses and the compressive damage in concrete are presented on a front-view of the symmetry plane in Figure 6.40 for the last displacement cycle, corresponding to the 3.50% drift level. Although both illustrations that are included represent different measurements, the same scale applies to both of them, where the blue color indicates values close to or less than zero, and the red color shows values equal or greater than 1.0.

a) Map of longitudinal rebar stress ratios (σ_{sl}/σ_{sly})

b) Map of compressive damage variable d^-

(scale)
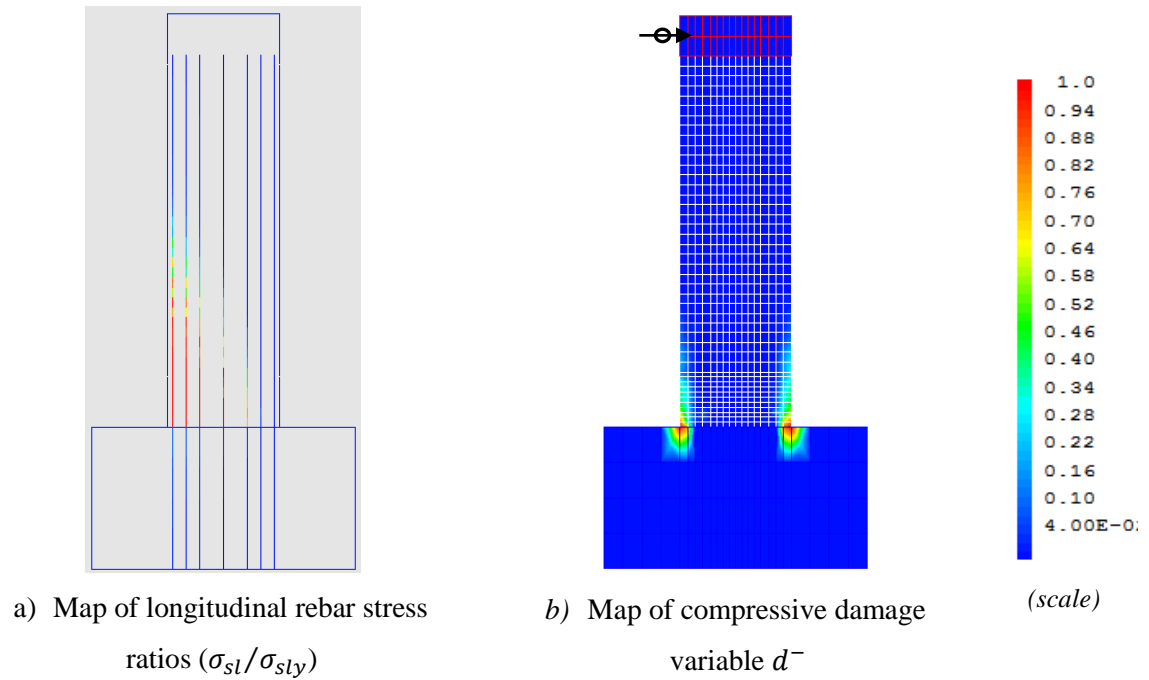
Figure 6.40 – Numerical results representing typical column bending behavior at 3.50% drift

Moreover, most of the deformations occur on the base of the column, as expected, specifically in the first 0.275m layer of smaller elements, according to Figure 6.41 - a) (deformed shape with an amplification factor of 5.0), comparing reasonably well to the value of 0.20m reported in Chapter 5 for the main damage location. Despite that, cracking extends further along the column, as it can be observed from Figure 6.41 - b).

a) Principal strain ε_{11} map over the deformed shape

b) Map of tensile damage variable d^+

(scale)   *(scale)*
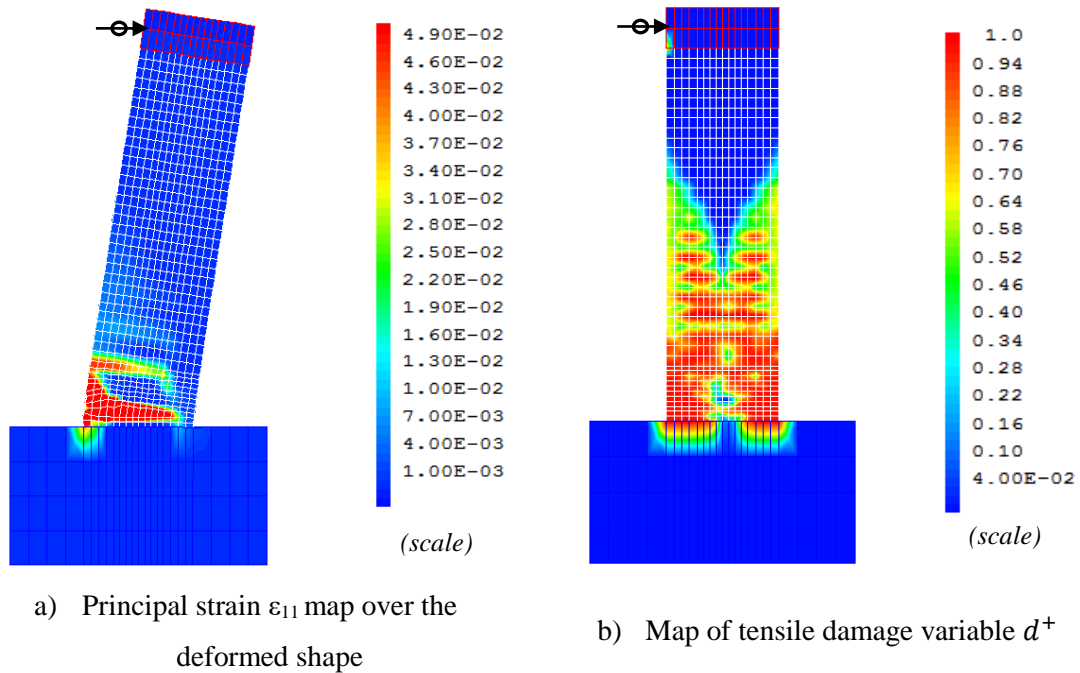
Figure 6.41 – Numerical results for the tensile behavior of concrete at 3.50% drift

6.4. NUMERICAL SIMULATIONS OF UNTESTED PIER SYSTEMS

The main objective for this section is to provide application context to the results obtained during the experimental campaign, and to evaluate the possibility of using them for the calibration of global bridge modeling tools for seismic performance assessment, which will be addressed in Chapter 7. For that purpose, as previously discussed in the introductory section of the present chapter, two main scenarios were established:

- Comparison of results obtained from the experimental setup based on half-pier structures, with those determined by using full height columns;
- Assessment of possible behavior pattern differences evidenced in shorter piers, taking into account that the tested structures are already close to the maximum value of the height range proposed for study in Chapter 4 (5.00m to 20.00m);

Within this context, the previous modeling assumptions and strategy were kept mostly unchanged; only very specific modifications were introduced to create the required differences for simulation of these untested pier scenarios.

6.4.1. SIMULATIONS WITH FULL HEIGHT PIERS

The test setup used throughout the experimental campaign was developed taking advantage of the expected null moment point in the distribution of moments of the pier structure for lateral loading. Taking that into consideration, numerical simulation of full height piers essentially involves extending the column length to account for the full structure, and adjustment of supporting constraints to characterize a fully fixed footing. With this in mind, the original finite element mesh used for the pier tests (Figure 6.2) was modified according to Figure 6.42. The full height of the modified piers then becomes 4.693m, which is determined from doubling the height of the previous mesh up to the horizontal axis of the beam (including the 0.165m length of the linear elastic elements connecting the pier elements to the rotation points, for coherence relative to curvature inflexions).
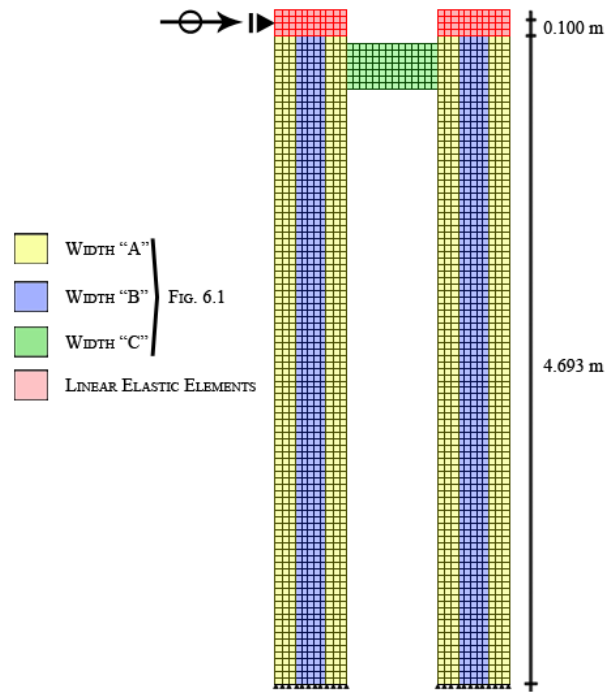
Figure 6.42 – Finite element mesh layout for full height pier numerical simulations.

Within this framework, two simulations were performed, aiming to numerically describe the behavior for the full structure in representation of one monolithic case and one precast case as follows:

- SP_M02_full – Full height pier simulation of the SP_M02 test, using the same model calibration parameters;
- SP_PC02A_full – Full height pier simulation of the SP_PC02A test, using the same model calibration parameters;

Figure 6.43 presents a comparison of the applied force results obtained in both tests, plotted against lateral displacements in terms of drift percentage. The figures also include the original results obtained with the half pier simulation, as well as the corresponding experimental records. As it is possible to observe, results for the full pier simulations are in good agreement with both the experimental records and the previous half pier analyses. For positive loading, similar peak forces and unloading stiffness are recorded on both the numerical analyses. The increased reloading stiffness issue that was previously discussed for precast specimens is also apparent. In the case of SP_M02_full, numerical difficulties were observed near 3.00% drift due to concrete failure, similarly to what was reported on the original half pier analysis.

a) SP_M02_full   b) SP_PC02A_full
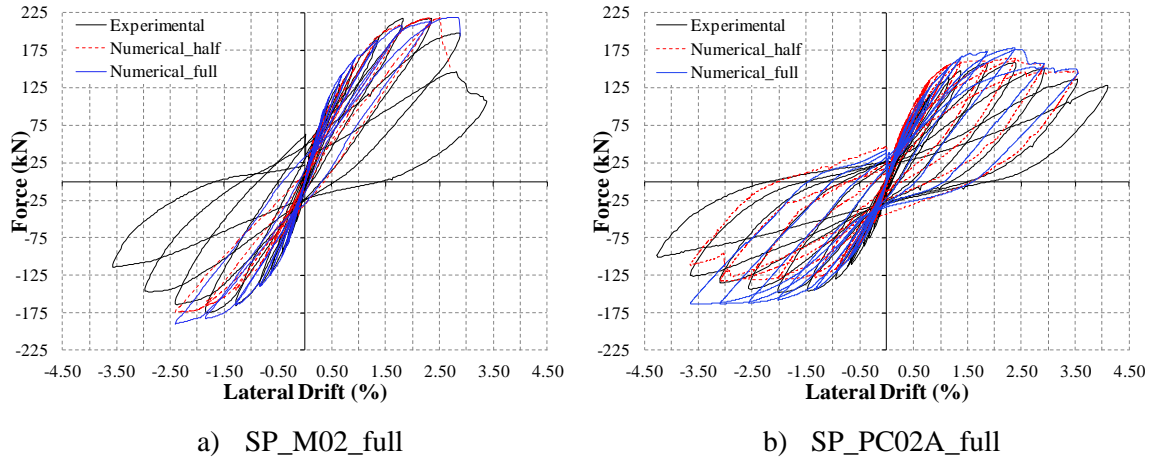
Figure 6.43 – Force – drift results for full pier tests

Regardless, the responses for the full pier analyses seem to display less loading direction asymmetry than the corresponding half pier simulations, and that is particularly evident on the precast specimen SP_PC02A. As far as it was possible to assess, this might be related with the fact that the test setup used for the half pier analyses essentially forces the inflexion point of column curvature to be at the same column section (base rotation hinges), while the curvatures develop freely in the full structure. Therefore, the inflexion point in the latter can change between loading directions, leading to unsymmetrical bending moments between the two columns, which can cause the longitudinal reinforcement that exists therein to perform according to different demands.

A characterization of what was described is presented on Figure 6.44, with a rough illustration (according to the green color bands) of curvature inflexion zones for positive and negative loading at 2.50% drift on SP_PC02A_full, established by visually determining the column locations where the compression forces are equally oriented (essentially vertical) along the cross-section (indicative of approximately null moment). Despite resulting from approximate strategy, Figure 6.44 does seem to suggest that the inflexion zones change between loading directions, thus agreeing with the previous argument.

This is particularly relevant because, while on the tested half pier structures the demand is mostly directed to the beam and beam-column nodes (where structural damage was found hard to prevent or mitigate), on full piers the column bases are also expected to develop strong moments. Therefore, full structures have the ability to adapt to the unsymmetrical nature of damage and loading, without the limitations that the present half pier testing conditions impose in that regard.

a) at +2.50% drift   b) at -2.50% drift
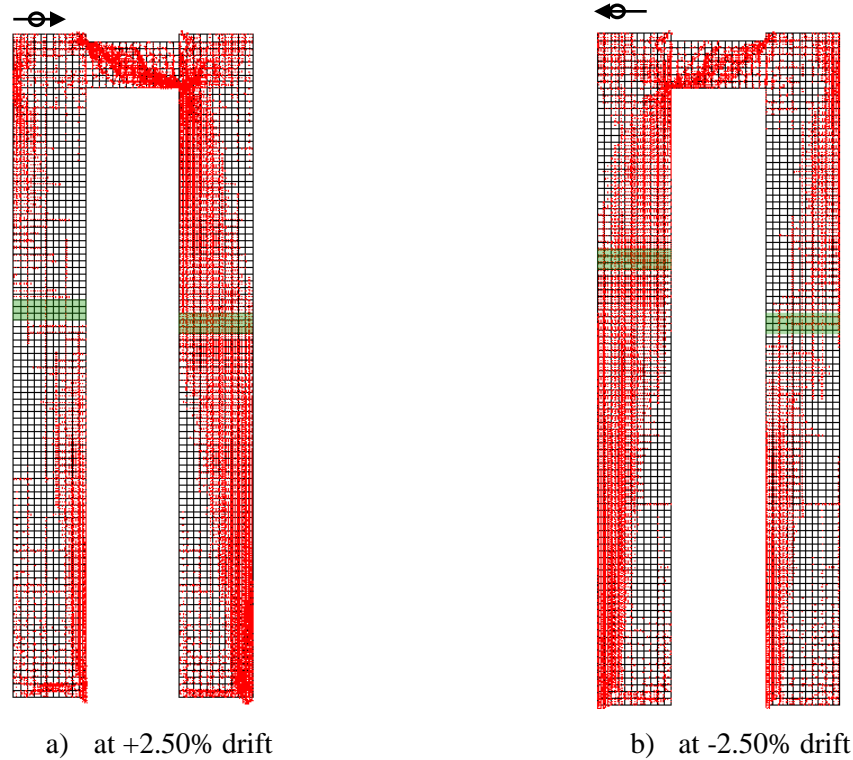
Figure 6.44 – σ_{22} compressions on SP_PC02A_full

Both structures showed shear transfer mechanisms similar to their half-pier counterparts, where the force is transferred mostly through a single compressive strut (which can also be observed in Figure 6.44), later degrading into several struts on larger drifts. For comparison purposes, the data from Figure 6.23 and Figure 6.32 was reworked to include results from SP_M02_full and SP_PC02A_full into Figure 6.45, where quite close values can be readily identified for the different scenarios of both cases.
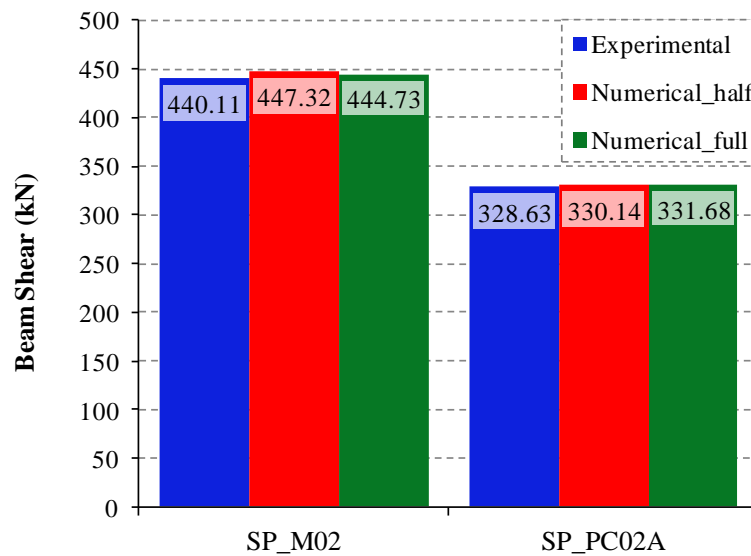
Figure 6.45 – Maximum beam shear value comparisons for full structure analyses

Accumulation of damage in compression is also observed on beam edges in both cases, as a result of the high compressions caused by the transferred shear forces, as well as generalized depletion of the tensile capacity of the concrete on the beam element. Moreover, according to the maps represented in Figure 6.46, determined for failure in the case of SP_M02_full or 3.50% drift in the case of SP_PC02_full, it is possible to observe the corresponding damage incurred in the bottom sections of the columns, indicating generalized cracking of concrete and some crushing.

a) SP_M02_full   b) SP_M02_full   c) SP_PC02A_full   d) SP_PC02A_full

d^- map d^+ map d^- map d^+ map
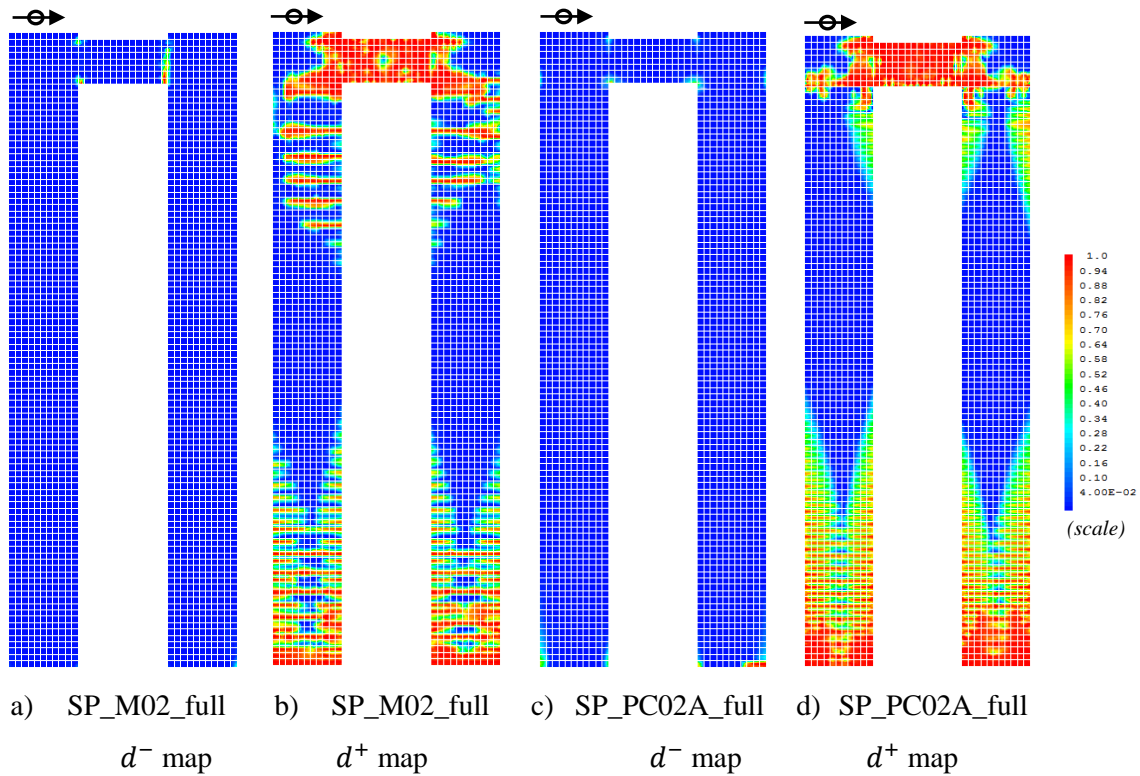
Figure 6.46 – Maps of damage variables for full structure analyses (at failure for SP_M02_full and at 3.50% drift for SP_PC02A_full)

The two models showed some differences regarding reinforcement yielding, as illustrated in Figure 6.47, where normalized values for rebar stresses are provided for the displacements corresponding to first reinforcement yielding and peak lateral force. While on SP_PC02A_full it was first detected at the precast joint reinforcement just like in the half pier simulation, on SP_M02_full that occurred first on column bases. Nonetheless, progression of each pier's behavior into the peak force level eventually led to the same patterns observed before, including generalized yielding in the beam and beam-column node on the monolithic model SP_M02_full, and localized yielding at the precast joint of the SP_PC02_full simulation, with complementary beam contribution.

a)   SP_M02_full   b)   SP_M02_full   c)   SP_PC02A_full   d)   SP_PC02A_full

first yielding   peak force   first yielding   peak force
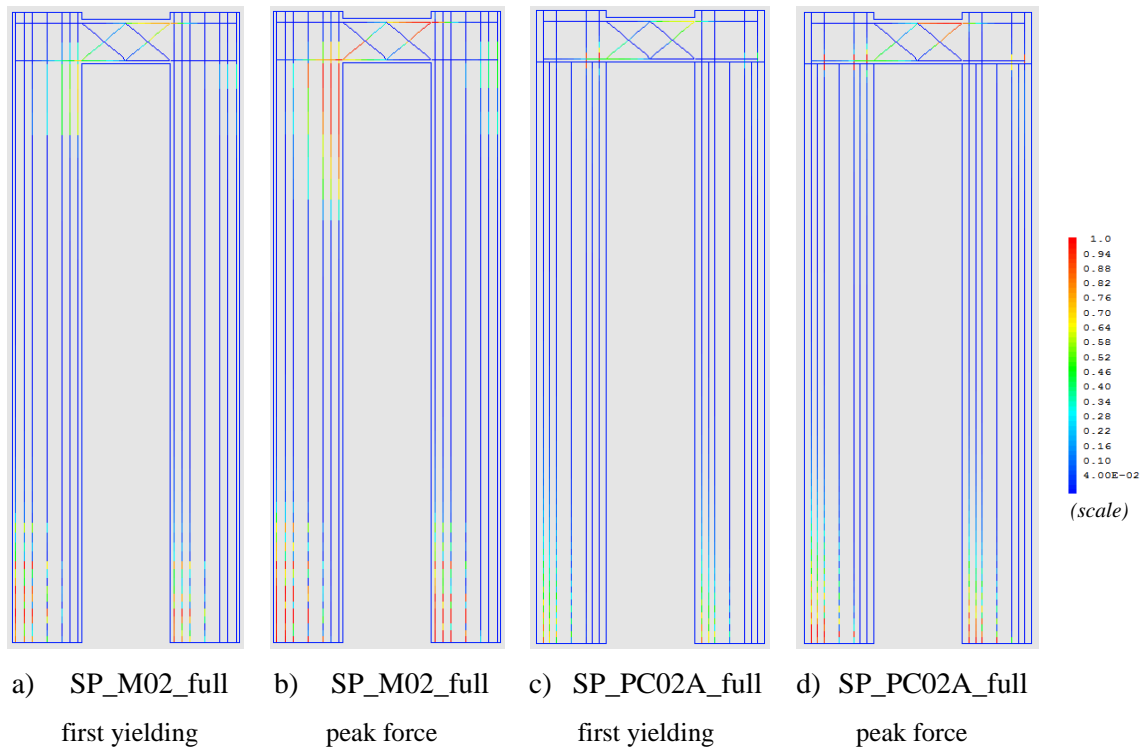
Figure 6.47 – Map of longitudinal rebar stress ratios (σ_{sl}/σ_{sly}) from full height pier

analyses

6.4.2. SHORTER PIER SCENARIOS

The full scale height of the prototypes corresponding to the tested piers is around 18.80m (four times 4.693m, according to the originally reduced scale of 1:4 and the pier height of Figure 6.42). In that regard, considering the height range established for study in Chapter 4, which focused on structures between 5.00 to 20.00m, and also taking into account already addressed findings concerning the complex height-dependent relationship between column and beam stiffness ratios, it is in the interest of this work to evaluate whether or not the observations made for the tested structures are representative of the complete pier range. Within this context, the tested pier represents nearly its maximum value, so shorter piers should be studied instead. However, reducing pier height naturally shifts the stiffness ratio between beams and columns in favor of the latter, which become increasingly more rigid in shorter structures, causing increased beam strains relative to columns'. Taking that into account, the usefulness of studying shorter monolithic piers can be argued, as they already revealed to be quite limited by the performance of the beam, both on the experimental as well as the numerical case studies. On the other hand, the precast specimens revealed larger concentrated column deformations at the precast joint section, caused by the localized yielding. In that framework, it may be useful to evaluate the impact of reducing column height only on precast specimens on the global pier performance.

For that purpose, the full height mesh for SP_PC02A_full was modified according to the two following scenarios:

- SP_PC02A_50: Reduction of the column length to account for a shorter pier with 50% of the original height (4.693m to 2.347m);
- SP_PC02A_75: Reduction of the column length to account for a shorter pier with 75% of the original height (4.693m to 3.520m);

Furthermore, the same modeling assumptions and calibration parameters were used for these simulations as for SP_PC02A_full, and the loading history applied therein was scaled to target the same drift values in each simulation. For comparison purposes, the lateral peak forces from SP_PC02A_full were also scaled to the reduced heights, according to the representation of Figure 6.48 and equation 6.7. Essentially, the scaled results of SP_PC02A_full represent a scenario where the interaction between beam, columns, and precast joint of that particular analysis is kept unchanged for different height piers. It also assumes no relevant influence of stiffness ratio shifts and, therefore, characterizes a global behavior that is influenced by yielding of the column reinforcement at the column base and precast joint, as well as by the beam degradation due to shear. Furthermore, this strategy also assumes that the peak moment from the lateral load (determined from the peak lateral force) is the same despite the column height reductions, which can only occur if the available capacity is explored to a considerable extent on both the beam and the columns, since yielding was achieved on both elements in the original SP_PC02A_full simulation.

$$F_{scaled} = F_{original} \times \frac{H_{original}}{H_{scaled}}$$
6.7
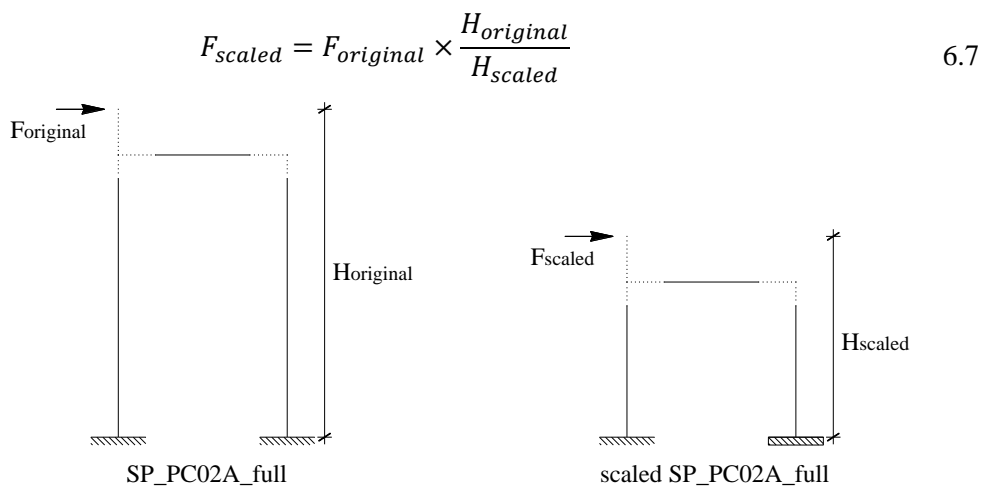
Figure 6.48 – Illustration of the procedure for obtaining scaled results from SP_PC02A

Lateral force results obtained with the described approach are presented in Figure 6.49, plotted against displacement in terms of drifts, for both the simulations, including the

corresponding peak force scaling. It is possible to observe that both the positive and negative loading direction responses compare well against the scaled peak forces, since a maximum absolute difference of 5.50% was recorded amongst all results. According to what was assumed earlier, that seems to indicate that despite a reduction in column length and overall pier height, demand at local level is still quite close to the available capacity in all the relevant locations (column bases, precast joint and beam).

a) SP_PC02A_50   b) SP_PC02A_75
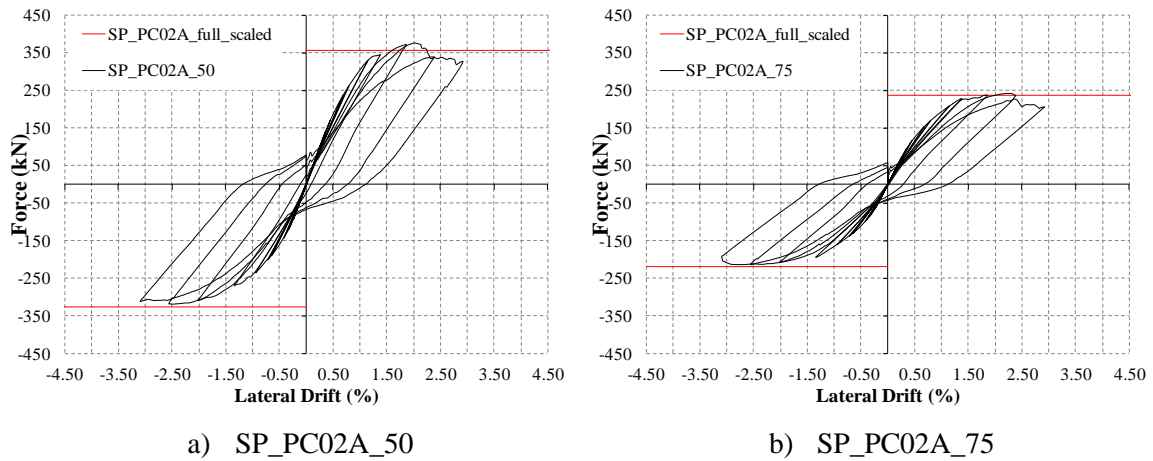
Figure 6.49 – Force – drift results for reduced height pier scenarios

Rebar stress results for first yielding and peak force levels agree with the previous conclusion, because generalized yielding is identified on column bases, at the precast joint and at the beam. This can be observed in Figure 6.50, where rebar axial stresses σ_{sl} are normalized by the respective yielding stresses σ_{sly}. Reinforcement yielding is first detected at the column bases in both cases, being achieved in the precast joint and beam at a later stage.

a) SP_PC02A_50   b) SP_PC02A_50   c) SP_PC02A_75   d) SP_PC02A_75

　　first yielding　　　　　　peak force　　　　　　first yielding　　　　　　peak force
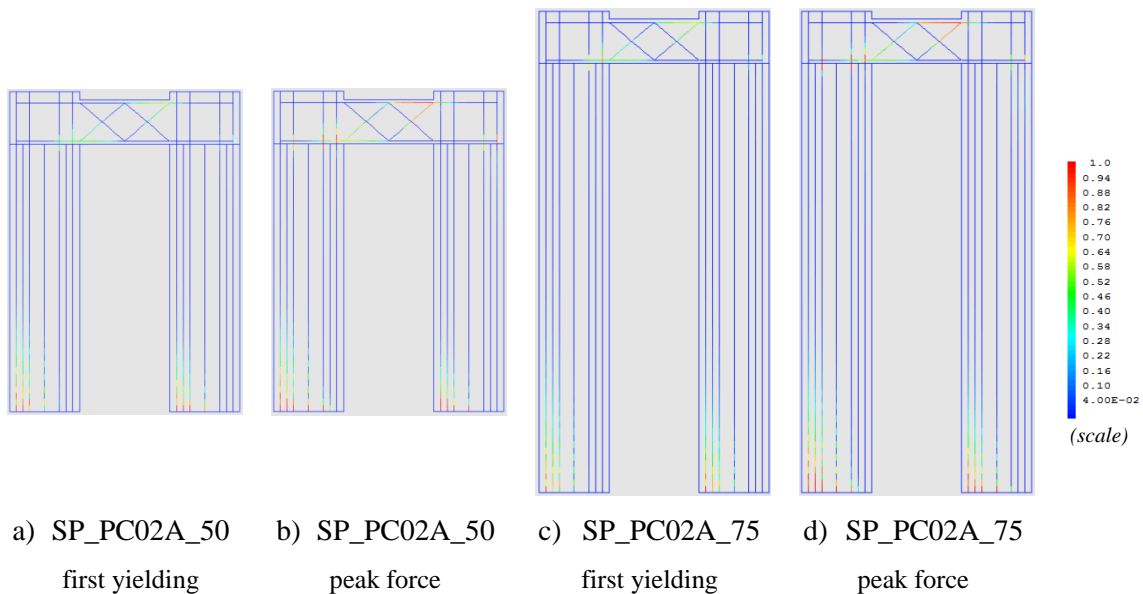
Figure 6.50 – Map of longitudinal rebar stress ratios (σ_{sl}/σ_{sly}) from reduced height

pier analyses

Accordingly, results for the two concrete damage variables indicate similar damage progression to that calculated for SP_PC02A_full (Figure 6.46 – c) and d)) on both cases. Particularly, full degradation of the tensile capacity in the beam and at column bases, as well as accumulation of compressive damage at the beam edges and column bases can be identified in Figure 6.51, which is indicative of the large local demands and in agreement with what was observed previously.

a) SP_PC02A_50
d^- map

b) SP_PC02A_50
d^+ map

c) SP_PC02A_75
d^- map

d) SP_PC02A_75
d^+ map
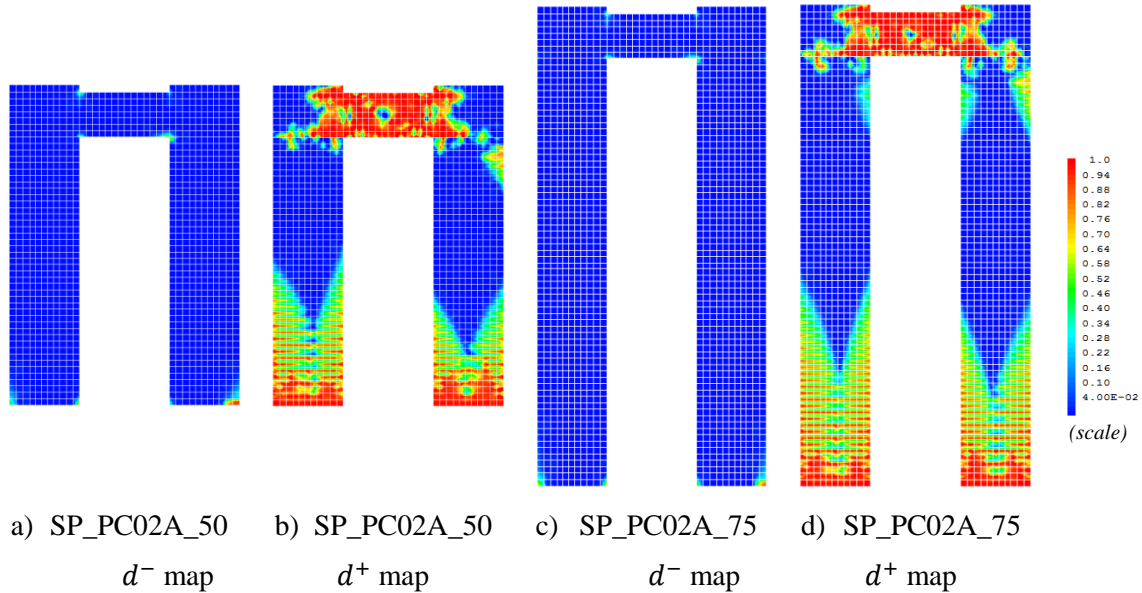
Figure 6.51 – Maps of damage variables for reduced height pier analyses

Considering these results, it seems reasonable to assume that: the experimental observations reported on Chapter 5 can represent a wider range of different pier applications, namely for different pier heights; and direct scaling of total lateral moment according to pier height provides a fairly good estimation of the overall capacity.

6.5. FINAL REMARKS

The work developed on this chapter aimed to address two specific issues with the present work: a strong dependency between the conclusions extracted from the experimental work and the specific testing conditions of the adopted setup; the fixed height of the test specimens, which raised doubts over the accuracy of the experimental results for representing the range of structures set for study (piers between 5.00m to 20.00m tall). Therefore, the strategy adopted for dealing with these issues was supported by the numerical simulation of structural scenarios different than those subjected to experimental testing, using a finite element based methodology with individual constitutive characterization of concrete, steel reinforcement, bond-slip behavior and joint behavior, when applicable.

The first set of numerical applications performed under this strategy targeted the simulation of some of the experimental tests presented in Chapter 5, focusing on evaluating the quality and precision of the obtained results in comparison with experimental evidence. In that regard, the numerical simulations provided results which were generally in good agreement with the experimentally observed values, particularly concerning the evaluation of peak forces, overall force-displacement envelopes and damage spread. Furthermore, they enabled confirmation that beam shear was a critical factor for the behavior and failure of the pier structures (whether through concrete crushing or sliding shear), and that the precast mechanism devised for Phase 2 specimens helped improve the overall ductility of the specimens, by mobilizing increased deformations on the rebars crossing the respective precast joints.

Within that context, the adopted modeling strategy and associated parameters were assumed to provide fairly good results, enabling further testing of other structural scenarios for which experimental calibration was not available. The first of those was focused on evaluating significant result differences when considering equivalent cyclic loading of a full height pier, with clamped support column base connections, instead of half-pier structures with free rotation base connections. These analyses showed that full structures are able to adapt better to the occurrence of damage or unsymmetrical loading, by developing different force patterns within the columns under those conditions. Nonetheless, no significant differences were observed between half and full piers regarding the main response defining parameters, such as peak force, which further emphasizes the precision of the experimental results on a global sense.

Finally, the last simulations presented in this chapter focused on evaluating the validity of the general conclusions, extracted from the work presented in both Chapter 5 and 6, for addressing pier structures of different heights. In that regard, only shorter piers were analyzed, since the tested structures already represent close to the upper bound of the height range set for the present study (5.00m to 20.00m), and the obtained results were generally in good agreement with most of the previous observations. Therefore, it was considered reasonable to assume that, for that pier height range, the critical factor for pier behavior and failure is still the shear load transferred through the coupling beam, and that the possibility of scaling the experimental results according to the moment mobilized through lateral loading at variable height is a valid strategy.

7
SEISMIC PERFORMANCE ASSESSMENT

7.1. OBJECTIVES AND MAIN METHODOLOGY

The current chapter presents the last part of this work, which focuses on considering the application of the pier systems studied in previous chapters in real railway bridge structures, for the purpose of evaluating the resulting seismic performance. With that in mind, full structure models respecting the structural layout defined for study (Chapter 4) are calibrated against the results of precast and monolithic specimens (Chapter 5), which are scaled for generalized application using a pier height dependent strategy that was validated earlier (Chapter 6). Furthermore, the viaducts presented in Table 4.4 were selected for this case study.

Within that context, it was explicitly assumed that the main focus of the present chapter should essentially target a comparison between the two types of pier system - monolithic and precast - rather than a full and comprehensive performance assessment report. The main reason for that decision is that doing so would require extensive study, which would be out of scope for the present work to address thoroughly, because performance based engineering is a wide and complex framework, for which other sources can also provide more in depth discussion (Vision2000 (1995), Moehle (2003)). This also means that the main scope of this work is the application of well-established methodologies to the case studies, rather than further developments. With that in mind, the PEER's Performance-Based Earthquake Engineering proposal (Krawinkler and Miranda (2004)) was considered as the present study reference, which is supported on a probability based approach. Essentially, that proposal addresses the characterization of system performance involving four different stages (Günav and Mosalam (2012)), taking into account the variability and uncertainties related with each of them:

- Hazard analysis: Characterization of the earthquake hazard, considering the existence of nearby faults, magnitude recurrence rates, fault mechanisms, source-site distance, site conditions, etc... It mostly targets the adequate selection of a number of compatible ground motions for representation of the variability of the earthquake action, enabling the definition of the Intensity Measure (IM) for seismic assessment of the intended structure;

- Structural analysis: Prediction of structure behavior while accounting for the seismic loading with variable characteristics, which generally requires elaboration of a suitable computational model to perform adequately under dynamic loading conditions and reasonable modeling assumptions. It aims to determine the values of a given selection of Engineering Demand Parameters (EDPs), which are deemed capable of characterizing the response of the structure for the intended performance levels;

- Damage analysis: Definition of the Damage Measures (DM) used for evaluation of the required performance levels, which are generally related with the occurrence of physical damage or loss of functionality at element or system levels. The probability of the EDPs exceeding the corresponding DMs is then calculated for the varying range of IM, and is often characterized through the adoption of Fragility curves;

- Loss analysis: Evaluation of the probability of exceedence for the Decision making Variables (DV) regarding losses on each of the pre-defined damageable groups. Loss analysis often involves the determination of loss curves;

In the present work, the adopted methodology essentially aims to determine the probability of exceedence of certain DMs for both monolithic and precast structures, to be expressed in the form of fragility curves. Within that context, the work presented herein mostly focuses on the structure analysis and damage analysis parts of the PBEE methodology. For further discussion on probabilistic seismic assessment methods, Romão (2012), Monteiro (2011), and Marques (2011), among other works, can provide more in depth information.

7.2. GROUND MOTION CHARACTERIZATION

One of the main requirements of seismic performance assessment is having ground motion records capable of adequately representing code compatible mean seismic demand. In that regard, it is widely known how the characteristics of different earthquake events may have distinct effects on the response of structures, as for instance the type of record (artificial, real or simulated (Iervolino and Manfredi (2008), Katsanos *et al.* (2010))), the scaling methods used

for providing correspondence with a given target spectrum (Cantagallo *et al.* (2014), Grant and Diaferia (2013)), the number of records required for assurance of acceptable representativeness (Monteiro (2011)), etc…

Admittedly, the framework of ground motion input addresses one of the most complex issues of seismic engineering, due to the large number of variables capable of influencing the outcome of seismic demand characterization. Additionally, some of them are also difficult to evaluate thoroughly, thus it is not of interest for the present work to tackle this subject in depth. Within that context, ground motion record scaling and selection was instead performed using the SelEQ program (Macedo *et al.* (2013), Macedo and Castro (2016)), a tool developed at FEUP, which searches known earthquake record databases and incorporates several meta-heuristic algorithms and filtering criteria, enabling users to find compatible record sets for any type of target response spectrum.

For the current application, Type 1 EQ was previously observed to be the most relevant within the test specimen design stage (Chapter 4). Following those results, the ground motion spectra represented in Figure 4.13 – a) was considered as the target spectrum for record selection using the SelEQ tool. In that regard, the program was configured to find a suitable set of ground motions within the range defined by $0.20T_1$ and $2.00T_1$, according to EC8 guidelines, where T_1 represents the fundamental period of the structure under analysis. However, since this study aims to compare the seismic performance on four different structures, it was deemed necessary to have the same records used for all the analyses, which essentially limits the search to a single period range that should, ideally, be representative for all of them. Therefore, the largest fundamental period T_1 of all the structures was considered, corresponding to that of Viaduct over Ribeira da Laje, as will be presented in further ahead.

Twenty ground motion records were then obtained from the Harmony Search algorithm incorporated in SelEQ, involving the optimization of the differences between the mean spectrum of the record set and the target spectrum, within a given tolerance and the pre-established period range. Results of that procedure are illustrated in Figure 7.1, for the ground motion records listed in Table 7.1 and further characterized in Annex C. Regarding the scaling of these records for the purpose of determining fragility curves, the adopted IM characterization parameter was the spectral acceleration Sa_1 (corresponding to the first vibration mode of each structure), whose values are also listed in Table 7.1.
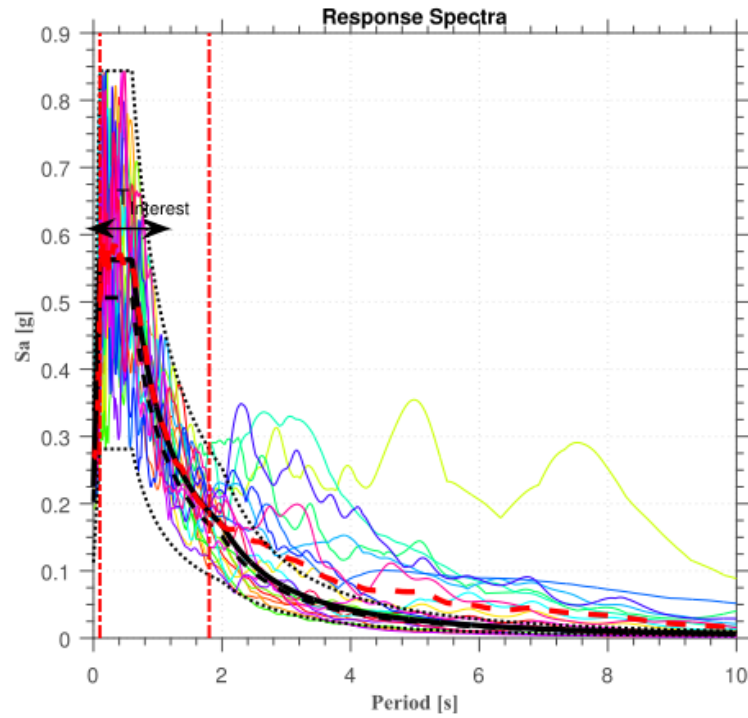
Figure 7.1 – SelEQ ground motion selection output

Table 7.1 – Scaling factors for the Ground Motion records for all viaducts

Earthquakes	1-ImperialValley-06	2-ChalfantValley-02	3-TaiwanSMART1(40)	4-LomaPrieta	5-Chi-ChiTaiwan	6-Northridge-01	7-TaiwanSMART1(40)	8-Chi-ChiTaiwan-05	9-ImperialValley-06	10-Chi-ChiTaiwan	11-SuperstitionHills-02	12-Chi-ChiTaiwan-04	13-Chi-ChiTaiwan	14-Chi-ChiTaiwan-06	15-LomaPrieta	16-BigBear-01	17-Northridge-01	18-Northridge-01	19-ImperialValley-06	20-VictoriaMexico
SelEQ scaling parameter	0,60	3,40	1,84	0,79	3,61	0,33	1,13	2,90	3,17	0,89	2,50	3,56	1,10	3,70	3,77	2,70	2,69	2,86	1,21	3,44
Sa_1 (g) - A	0,65	0,42	0,76	0,76	0,56	0,55	0,53	0,45	0,69	0,50	0,49	0,57	0,34	0,34	0,57	0,45	0,56	0,59	0,62	0,54
Sa_1 (g) - B	0,67	0,49	0,68	0,59	0,62	0,49	0,35	0,49	0,74	0,41	0,61	0,45	0,49	0,41	0,79	0,40	0,46	0,76	0,83	0,40
Sa_1 (g) - C	0,76	0,39	0,64	0,64	0,69	0,37	0,38	0,61	0,68	0,43	0,75	0,38	0,51	0,45	0,69	0,34	0,56	0,79	0,75	0,60
Sa_1 (g) - D	0,28	0,24	0,41	0,35	0,26	0,40	0,37	0,29	0,28	0,37	0,37	0,33	0,35	0,34	0,45	0,31	0,27	0,35	0,24	0,27

A - Macheda Viaduct

B - Palheta Viaduct

C - Viaduct over Degebe River

D - Viaduct over Ribeira da Laje

7.4

7.3. STRUCTURE CHARACTERIZATION

A computational model for seismic response evaluation was elaborated in OpenSees (McKenna *et al.* (2010)) for the four viaducts under analysis. For the sake of simplicity and faster dynamic analyses, a 2D approach was adopted, following the same strategy presented in Delgado (2009), which is illustrated on Figure 7.2 – a) for a generic viaduct case. Essentially, this methodology focuses on characterizing the transverse response of the piers, which are constrained to the lateral behavior of the deck by means of axially rigid bars (to impose coupling of u_x displacements). This approach disregards deck torsion and longitudinal effects, which is an acceptable assumption for the present chapter scope.

Therefore, for consistency in calibrating the lateral stiffness of each viaduct while having piers with different heights (H_{pier}), the values for H_{pier} take into account the total length between the fixed restraint at the base of the piers and the deck's centroid, where inertia forces are considered. The double column bent pier system is modeled by a single vertical element with linear elastic properties, adjacent to a zero-length plastic hinge at the base, according to Figure 7.2 – b). Deck masses were lumped at several locations along the total length of the structure, separated by 5 segments per span, while roughly half the total mass of the piers (including the beam segment) was lumped at the beams' centroid level.

For the characterization of the dynamic properties of each viaduct, a Rayleigh-type damping approach proportional to the mass and initial stiffness was adopted, assuming 5% of the critical damping at the first and second transverse vibration modes of each structure.

a) 2D representation   b) Pier model
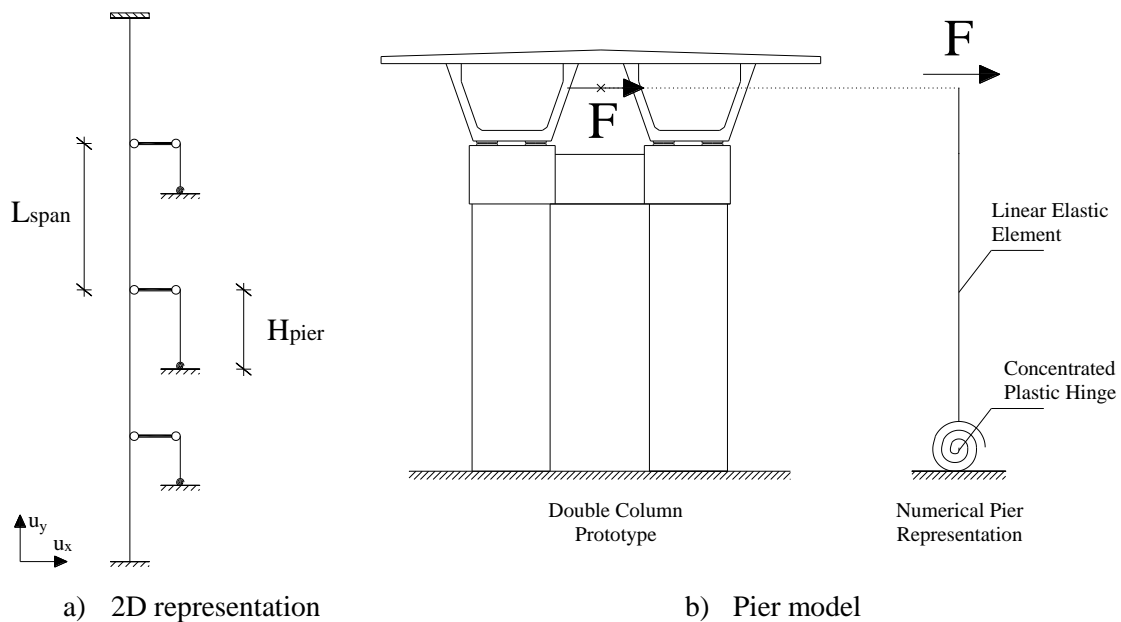
Figure 7.2 – Structural modeling scheme for a generic viaduct

With this methodology, the inelastic behavior is globally considered only at the plastic hinge level, which is calibrated for performing in the degree of freedom corresponding to rotations and according to a uniaxial material model in OpenSees. For that purpose, the software includes a large variety of user selection models, from which the Modified Ibarra-Medina-Krawinkler (IMK, Ibarra *et al.* (2005)) deterioration model with "pinched" hysteretic response was adopted, having already been successfully used in other performance based earthquake engineering studies (e.g. Lignos (2008), Lignos and Krawinkler (2012)). Calibrating this model assumes definition of a backbone curve, from which cyclic degradation is determined according to several stiffness and strength related parameters.

7.3.1. PIER BEHAVIOR CALIBRATION

Realistic assessment of the seismic performance on the present case studies, involves ensuring that the computational models are capable of returning dynamic responses compatible with the experimental evidence gathered during the cyclic tests. For that purpose, the numerical model chosen for characterization of the inelastic behavior of the modeled viaducts should incorporate similar damage incursion patterns and collapse features as those observed in the experimental tests. In other words, it should be characterized by equivalent (but necessarily scaled) force-displacement or moment-rotation results to those presented in Chapter 5. With that in mind, the following two scenarios were considered:

- *Monolithic*: Plastic hinge uniaxial model parameters calibrated to simulate the monolithic specimen SP_M02;
- *Precast*: Plastic hinge uniaxial model parameters calibrated to simulate the precast specimen SP_PC02C;

The selection of SP_M02 and SP_PC02C as the calibration sources is related to their performance, which, as presented in Chapter 5, is among the best in each respective category (monolithic and precast). Furthermore, only the positive loading direction was taken into account in this process, since it is believed that the observed loading direction asymmetry would not be so evident during a real earthquake event, considering that seismic loading is simultaneously applied to both columns, instead of the one-sided loading as adopted on the experimental tests.

The actual calibration procedure was based on the uniaxial cyclic loading of a fixed base sample pier, aiming to reproduce the same behavior of the corresponding experimental models (monolithic or precast, as mentioned above), and by taking into account the applicable scale factors to peak force (due to both the reduced scale of the test models and the half-pier testing constraint), which is illustrated in Figure 7.3. Furthermore, IMK model parameters related with

unloading/reloading stiffness, energy dissipation and cyclic degradation were adjusted within the set of recommended values through trial and error, aiming to minimize differences to the experimental values as much as possible.
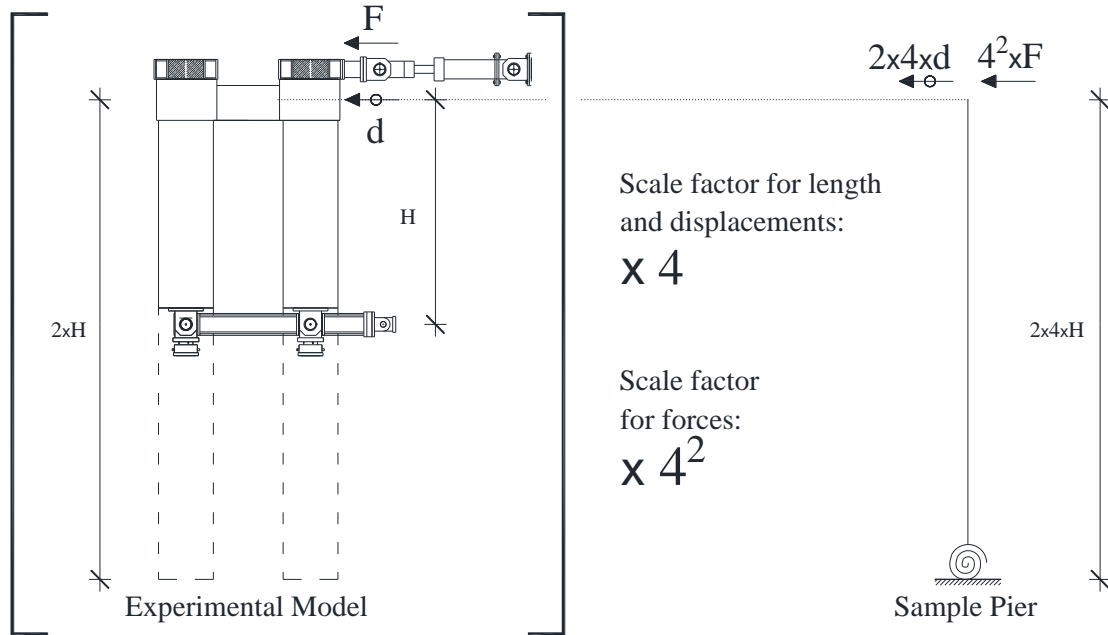
Figure 7.3 – Sample pier calibration against experimental model results

The stiffness of the linear elastic element is also an important part of the calibration procedure, since it directly influences both static and dynamic results, considering that the moment mobilized at the base plastic hinge depends on the rotation conveyed through the vertical element. In turn, this depends on the stiffness relationship between both elements of the pier assembly (with global stiffness denoted by $K_{assembly}$), namely the plastic hinge and vertical element (whose stiffnesses are designated by K_{hinge} and $K_{elastic}$, respectively), which is unknown beforehand. Furthermore, considering the adoption of stiffness proportional Rayleigh-type damping for dynamic analysis purposes, this issue extends to the overall energy dissipation that is obtained for a given displacement history, particularly because the inelastic behavior is concentrated only in the plastic hinge.

In order to address this, the approach presented by Zareian and Medina (2010) was adopted, where a set relationship between the hinge and vertical element stiffness components is enforced for the sample pier, governed by the parameter n, as described in equations 7.1 and 7.2. In this application, according to the conclusions of that same work where a large value of n is recommended, it was assumed $n = 20$. Within this context, the value of $K_{assembly}$ represents the global lateral stiffness of the pier system (governed by equation 7.3), which should be equivalent to the experimental values of the applicable scenarios. Therefore, for a pre-yielding stage, the $K_{assembly}$ stiffness can be determined from the yielding displacements of Figure 5.69

and Figure 5.70 (and the corresponding yielding forces), taking also into account the force and displacement scaling procedure presented in Figure 7.3. After calculation of $K_{assembly}$, the values of K_{hinge} and $K_{elastic}$ can be determined using the *n* parameter and equations 7.1 and 7.2, respectively. Furthermore, this strategy considers initial stiffness based Rayleigh damping applied only to the elastic elements, since the IMK uniaxial model controls the overall value of K_{hinge}, where energy dissipation due to inelastic deformations is expected to be dominant.

$$K_{hinge} = (n + 1) \times K_{assembly} \qquad\qquad 7.1$$

$$K_{elastic} = \left(\frac{n + 1}{n}\right) \times K_{assembly} \qquad\qquad 7.2$$

$$\frac{1}{K_{assembly}} = \frac{1}{K_{elastic}} + \frac{1}{K_{hinge}} \qquad\qquad 7.3$$

The remaining part of the calibration process is related to the estimation of the backbone curve, from which cyclic degradation is established. Ideally, the backbone curve characteristics are determined from monotonic loading results, which were, unfortunately, unavailable. As an alternative, a trial and error estimation of the backbone curves was attempted, by taking into account in-cycle and cyclic strength and stiffness degradation according to recommendations by Haselton *et al.* (2009), in order to adapt the model parameters that control those effects to the present case studies. The resulting moment – drift relationships obtained with this procedure are presented in Figure 7.4 for both Monolithic and Precast cases (whose corresponding model parameters are provided in Annex A). As it is possible to observe, there is a good fit between the experimental and numerical curves, particularly regarding moment values for the positive loading direction and regarding the cyclic degradation for the repeating cycles. A residual strength ratio of 20% of the peak value was adopted in both models (which, however, is not apparent for the drift values shown in the plots).

a) Monolithic   b) Precast
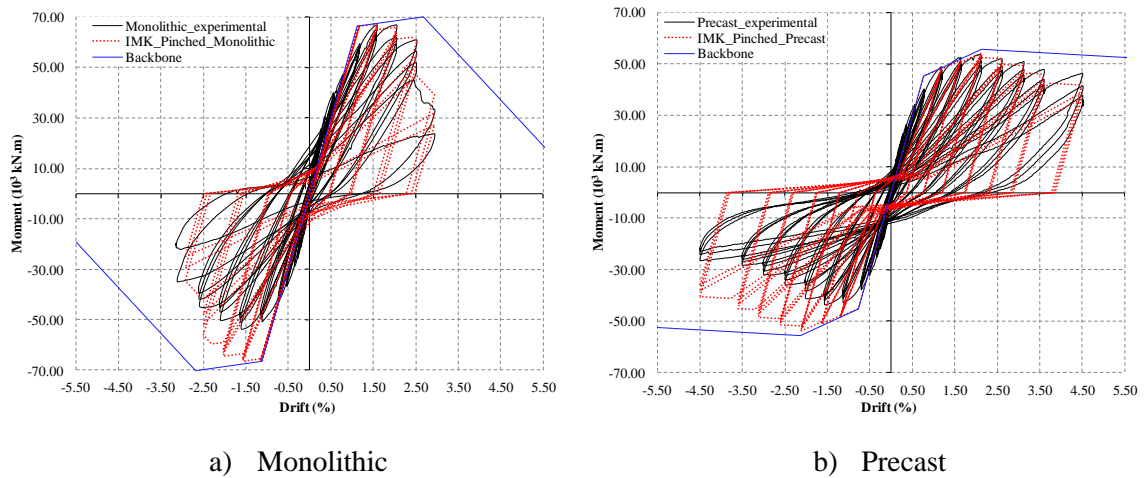
Figure 7.4 – Comparison of the moment – drift relationship calibration results

Despite providing satisfactory moment-drift comparisons against the scaled experimental records, the IMK model's precision is less noticeable for simulating of the energy dissipation per half-cycle, tending to lead to higher values relative to the experimental results, mostly due to the larger unloading stiffness branch. It is noteworthy that, the above presented moment – drift relationships already reflect the best result of several parameter adjustment attempts, performed to address that particular issue, but the energy dissipation difference between the experimental results and those produced by the IMK models is still noticeable. This can be identified in Figure 7.5, where post-yielding energy dissipation per positive loading half-cycle is presented for both Monolithic and Precast cases, considering representation on normalized terms, obtained by dividing each dissipated energy value by the energy dissipation of the first experimental cycle after yielding, according to equation 7.4:

$$E_{norm} = \frac{E_i}{E_{1,exp}} \hspace{4cm} 7.4$$

<div align="center">

a) Monolithic   b) Precast
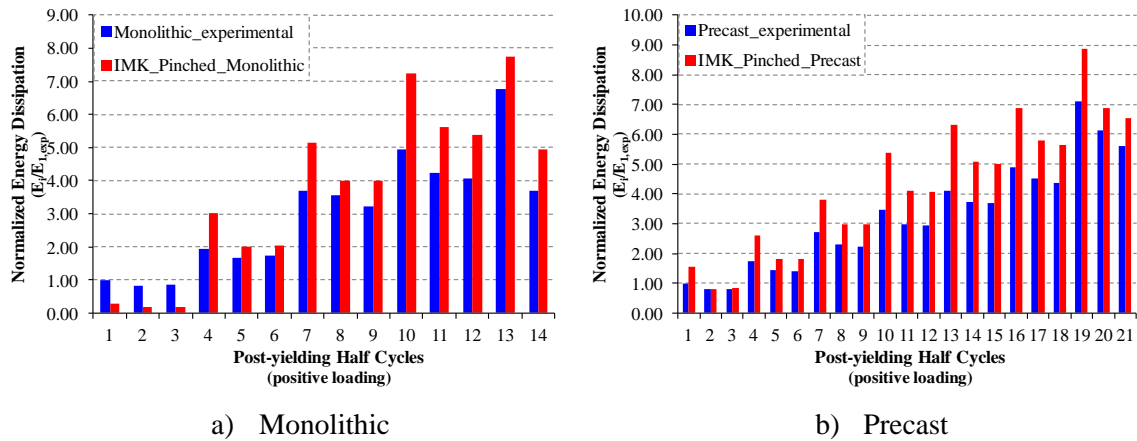
Figure 7.5 – Comparison of the Energy dissipation per cycle results

</div>

Nonetheless, while energy dissipation is larger on the numerical models than observed on the test specimens, they still exhibit similar increase rate. In addition, it may be reasonable to say that this strategy can provide sufficiently adequate simulation, considering that it mainly targeted the comparison between the global behavior of monolithic and precast structures.

General application of a methodology where the behavior of all the piers is determined from a single sample pier calibration can be arguable, when considering the accuracy of stiffness scaling for different pier heights. In that regard, the adopted strategy involved the same hinge component on all the piers, and the elastic component is derived from an equivalent inertia calculated for the sample pier stiffness, hereby labeled method A, which means that stiffness scaling according to different pier heights is managed by the elastic component alone. This also means that the relative contribution of hinge and stiffness components determined for

the sample pier actually changes according to pier height. A preferable solution would be to enforce the same $n = 20$ relationship on all the piers, hereby labeled method B, but that would involve significant work, requiring individual calibration of different hinge models for all the different pier heights. Regardless, the actual difference between these two approaches is not that large, as seen in Figure 7.6, where the ratio between the total lateral pier stiffness calculated with the two approaches (method B values divided by method A values) is illustrated for the pier height range under analysis. The overall difference between the two approaches is never greater than 15%, and only for pier structures shorter than 9.50m it is greater than 5%. In light of that, it is believed that method A still provides reasonable accuracy while being significantly easier to perform, which is why it was adopted for the current work.
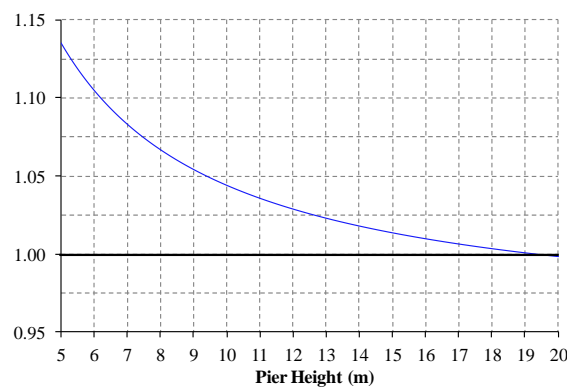
Figure 7.6 – Lateral stiffness ratio between method B and A

7.3.2. NON-LINEAR STATIC PUSHOVER ANALYSES

In order to develop an understanding of the demand distribution over all the piers of the selected viaducts, in order to help with defining the control piers for further dynamic evaluation, non-linear static pushover analyses were performed. For that purpose, force-based conventional pushover with first-mode proportional load pattern was considered (EN1998-1 (2004)). In that regard, the first vibration mode of each viaduct is represented for the corresponding deck nodes in Figure 7.7, considering normalized modal displacements for unitary maximum value. Comparing the associated periods (which are essentially the same within the Monolithic or Precast models) with the values previously evaluated in SAP2000 earlier in Chapter 4, small differences are found, which can be attributable not only to the fact that the current structure models were developed in a 2D framework, but also to the calibration that was made herein against actual experimental data.
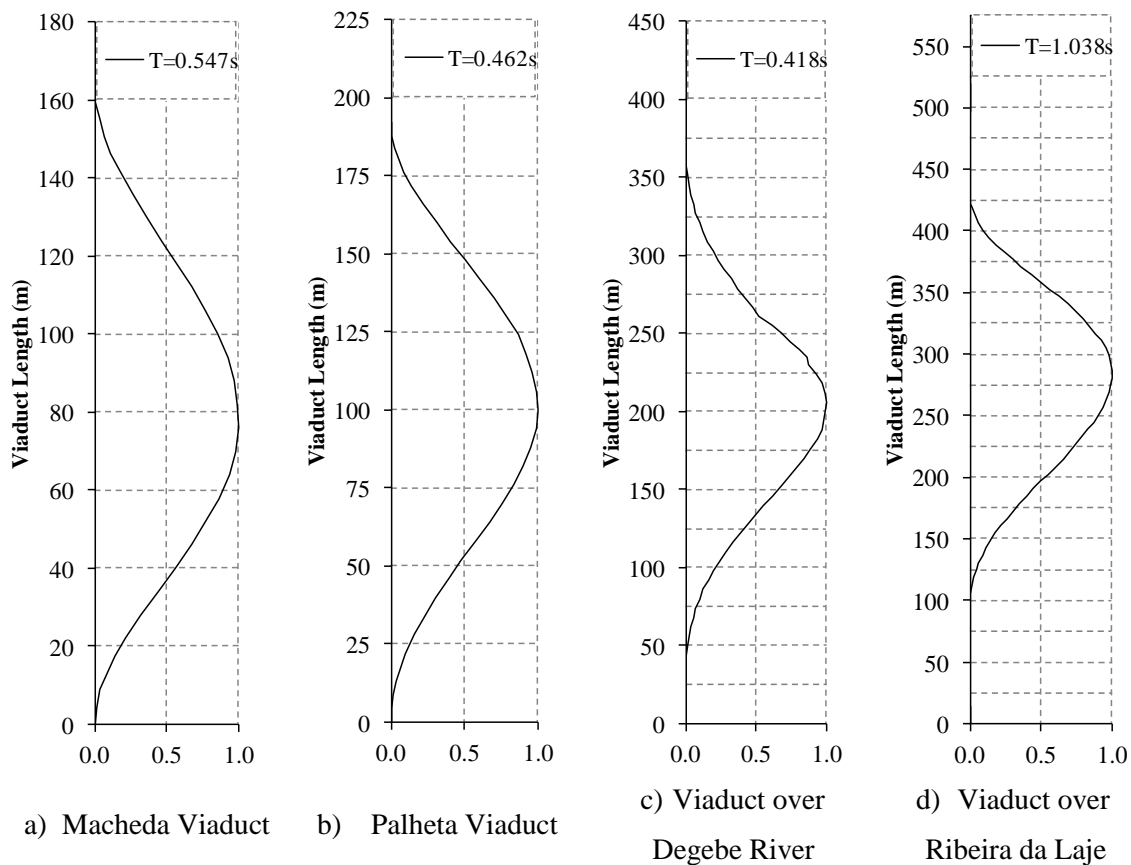
Figure 7.7 – First lateral vibration mode for the case study viaducts

The pushover analyses were performed for a target drift of 10% on the pier closest to the mid section of the viaducts, at 82.00m, 100.00m, 200.00m and 256.70m for Figure 7.7 - a) to Figure 7.7 – d) viaducts, respectively. Results for ductility demands were normalized by the ductility demand of those piers and are presented in Figure 7.8 for monolithic and precast behavior models. Unsurprisingly, the ductility demand is largest on the piers close to the mid section of the viaducts, considering that first-mode proportional load pattern was adopted and the fact that all the viaducts are quite regular, with low spread between the median pier height and the corresponding minimum and maximum values (Table 4.4). Taking into account these results, the following piers were chosen for control sections regarding dynamic performance evaluation:

- Macheda Viaduct: P3 at 82.00m of total length;
- Palheta Viaduct: P4 at 112.00m of total length;
- Viaduct over Degebe River: P7 at 200.00m of total length;
- Viaduct over Ribeira da Laje: P10 at 286.70m of total length;

a)   Macheda Viaduct

b)   Palheta Viaduct

c)   Viaduct over Degebe River

d)   Viaduct over Ribeira da Laje
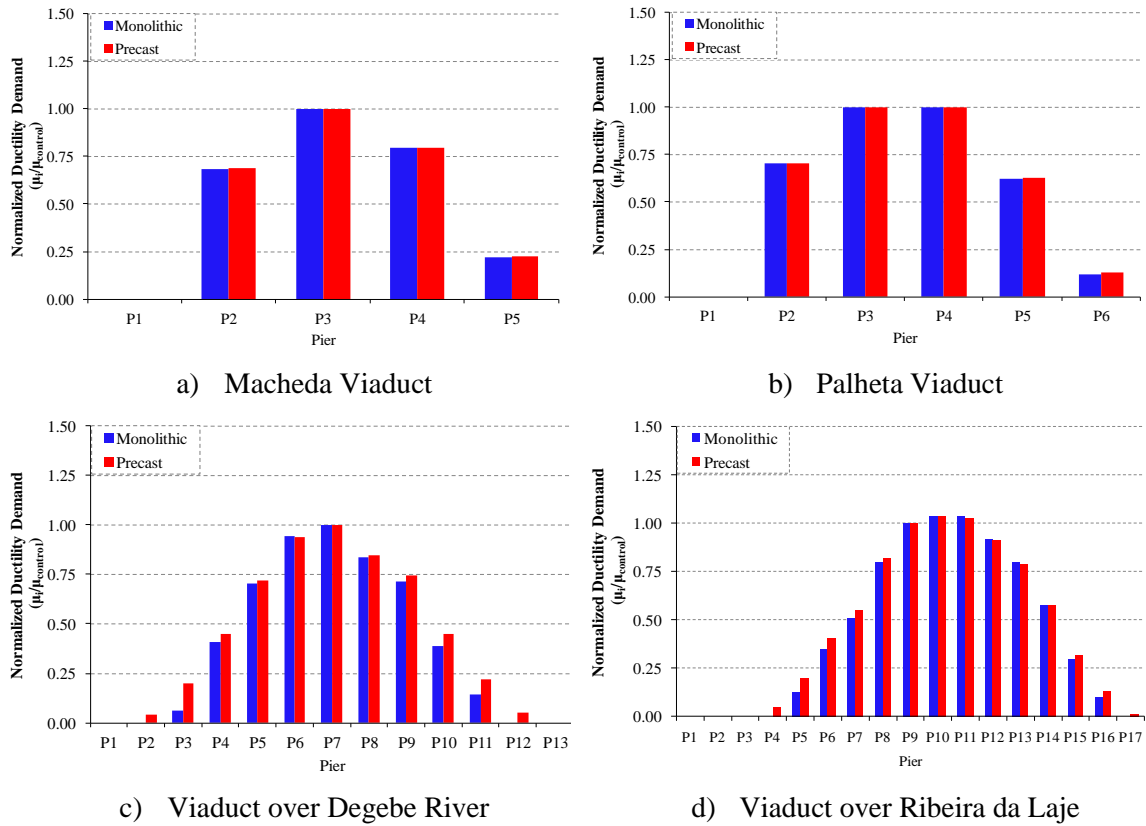
Figure 7.8 – Ductility demand on the piers of the case study viaducts

7.4.   DAMAGE CHARACTERIZATION

This stage of performance based earthquake engineering ultimately aims to be able to establish relations between the intensity of earthquakes (IM) and the damage caused by them. For that purpose, structural response is numerically characterized by estimates of EDPs, and their values are compared against the established performance targets (DMs). In that regard, the three following DMs were chosen for this study:

- *DM #1: Structural performance* (sp)

  DMsp1 – Yielding of the main pier reinforcement;

  DMsp2 – Conventional collapse of the pier structure due to strength loss;

- *DM #2: Lateral deflection* (ld)

  DMld1 – Maximum angular rotation of the deck for running safety of trains;

  DMld2 – Maximum angular rotation of the deck for restorability of the track;

- *DM #3: Derailment conditions* (dr)

  DMdr1 – Maximum lateral vibration of the deck for running safety of trains;

7.4.1. DM #1 STRUCTURAL PERFORMANCE

In performance based earthquake engineering studies, structural performance is usually evaluated from a selection of common damage states involving yielding, spalling, buckling, rebar fracture and collapse (Kunnath *et al.* (2006), Mander *et al.* (2007)). In the present study, yielding and collapse were adopted as the performance targets, and the corresponding EDP associated with DM #1 was the rotation recorded at the simplified plastic hinge model on the control pier for each viaduct. The associated performance limits (included in Table 7.2 for reference) were calculated as the rotation values (at the hinge level) that characterize the same load state of the equivalent experimental results. In the case of yielding, for example, (which is characterized by the displacements from Figures 5.69 and 5.70), the value of 0.88% found in the experimental results from SP_PC02C addresses the same load state (yielding) as 0.80% on Figure 7.4 – b). Accordingly, at the local plastic hinge level the same yielding stage is associated with a rotation of 0.037×10^{-2} rad, which can then be defined as the corresponding EDP limit.

Table 7.2 – EDP limits for DM#1

EDP - Hinge Rotation (10^{-2} rad)		
DM#1 targets	Monolithic	Precast
DMsp1 - Yielding	0.054	0.037
DMsp2 - Collapse	1.587	2.859

It is important to discuss, however, that the strategy for collapse definition adopted in the present work may not be reasonable for every such application. For example, Vamvatsikos and Cornell (2002) state that *"If the model is realistic enough it ought to explicitly contain such information, i.e. show a collapse by non-convergence instead of by a definite DM output"*, leading to the adoption of so-called flatlines, in correspondence with the IM values for which the capacity points occur.

Additionally, Haselton *et al.* (2009) recommend that non-convergence should only be identified as collapse when it occurs for large demands, representative of structural failure. This is, in fact, because non-convergence should ideally be caused by dynamic instability at the onset of structure collapse, and not just due to failure of the solution algorithm. However, this requires that the model is adequately prepared for representing the structure behavior up to that moment when dynamic instability occurs, which may not be the case with the present modeling strategy, particularly because the plastic hinge models are only experimentally validated up to the drift threshold of the test specimens that served as calibration source. Within this context, the adoption of a plastic hinge rotation limit for definition of the capacity point may just represent a conservative check of the no collapse limit state, but nonetheless, that is believed to be the most reasonable approach considering the present application.

On another note, is should also be said that, under normal circumstances, EDP characterization for performance based earthquake engineering involves the evaluation of uncertainties related with identification of the material properties and/or the modeling strategy employed for structural behavior assessment. For example, on Monso and Miranda (2013) fragility functions developed by Berry and Eberhard (2003) accounting for a statistical distribution of column strength parameters are used to assess the mean DM limits and the corresponding dispersion, while in Delgado (2009), Latin Hypercube simulations are performed to obtain the probability distribution that characterizes structural strength. In the present work, the small number of experimental tests for each scenario prevents application of common statistical procedures to determine the dispersion of the adopted EDP limits. Likewise, since the previously presented modeling strategy focuses on the local reproduction of the recorded moment-drift histories and not constitutive characterization based on material properties, extensive numerical simulations using statistical sampling methods would require the calibration of other computational models more suited for such task. In this regard, it is worth mentioning that, while the refined 2D FEM models presented in Chapter 6 are constitutive based and provided generally good results, the amount of time required for a single full analysis is quite large, rendering them very inefficient for this particular purpose.

Even so, it may be argued that the comparison between the two established scenarios is still well served by assessing the probability of exceedence of the limit states in consideration while disregarding the uncertainties related with DM#1 performance limits, because it can be assumed that they affect both scenarios equally. Consequently, this acknowledges the values indicated in Table 7.2 as deterministic measurements of those structural systems, leading to performance assessment representing only the response variability that is introduced by considering different ground-motions, which seems to be a reasonable compromise.

7.4.2. DM #2 LATERAL DEFLECTION

The lateral deflection of the viaducts was evaluated according to the maximum angular rotation observed between subsequent deck spans (which is mostly relevant to simply supported span structures), notwithstanding the fact that the present modeling strategy reflects the displacements recorded at the deck centroid level, and not at the upper deck surface, as would be preferable. However, this difference is deemed not to be relevant so as to compromise the conclusions of the present study. The corresponding value for angular rotation, calculated at the end of each span, is graphically illustrated in Figure 7.9.
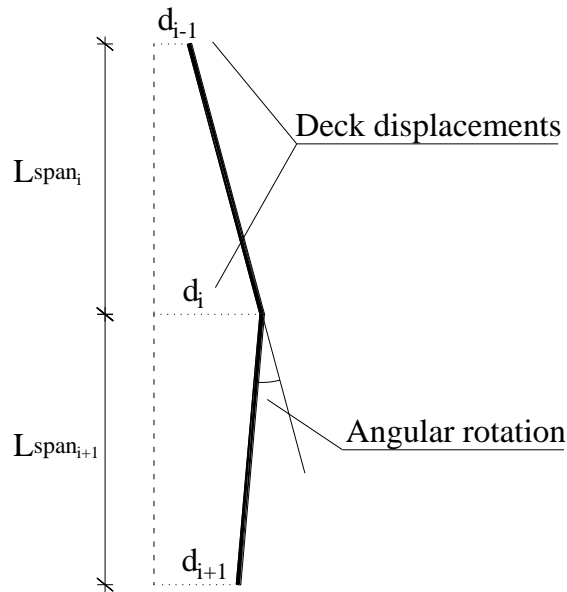
Figure 7.9 – Lateral deflection evaluation procedure.

EDP limits for the two selected damage states on this subject are presented in Table 7.3, corresponding to the values proposed by the RTRI guidelines (Table 2.2). The choice to adopt RTRI values instead of European Eurocode angular limits was made because the former explicitly considers differences between performance under ordinary travel conditions and during a seismic event, according to previous discussion on Chapter 2. Furthermore, it also provides more consistent methodology since it relies on a performance based approach. In that regard, this work focused on the performance objectives related with running safety of high speed trains and the assurance of restorability conditions when significant track damage occurs, for DMld1 and DMld2, respectively. Additionally, for the DMld2 damage state, the most severe track type conditions were considered, which in this case refer to a slab track. It is worth mentioning that Table 7.3 shows identical limits for monolithic and precast specimens, since this DM focuses on a global track related assessment.

Table 7.3 – EDP limits for DM#2 (according to RTRI (2007))

EDP – Angular Rotation (rad)		
DM#2 targets	Monolithic	Precast
DMld1 – Running Safety	0.002	0.002
DMld2 – Track Damage	0.006	0.006

7.4.3. DM #3 DERAILMENT CONDITIONS

European codes do not provide clear guidance regarding the evaluation of derailment during earthquake, and designers are often required to perform track-structure interaction studies to address that in further detail, such as in Montenegro (2015), for example, which proposes a methodology for the assessment of running safety of trains on HSRL, based on

wheel-track contact criteria. Other authors like Luo (2005), Luo and Miyamoto (2008), proposed an approach based on the concept of Spectral Intensity (SI, equation 7.5, where $S_v(\xi, T)$ is the pseudo-velocity spectrum).

$$SI = \int_{0.10}^{2.50} S_v(\xi, T)\, dT \qquad\qquad 7.5$$

This concept is contemplated in the RTRI guidelines, essentially aiming to reflect the relationship between the energy content of the seismic input and the structural response, which is simpler to account for with the present modeling strategy. Within this context, SI has been selected as the EDP for assessment of derailment, and the corresponding limits for safety can be identified in Figure 2.6. It should be noted that, while the values presented therein were determined for a wide variety of soil conditions and derailment mechanisms still, they reflect the dynamic properties of Japanese rather European trains. However, owing to the lack of a better alternative for the European case and taking into account the structural vibration periods for the case study viaducts, the limit value of 4100mm included in Figure 2.6 was adopted for SI, according to Table 7.4. Similarly to DM#2, these damage measure limits are equal for both scenarios, since they also report to a global track assessment.

Table 7.4 – EDP limits for DM#3

EDP – Spectral Intensity (mm)		
DM#3 targets	Monolithic	Precast
DMdr1 – Running Safety	4100	4100

The original procedure for SI assessment involves the characterization of the full structure as a SDOF model with equivalent properties, and computation of the corresponding displacements at the track level when subjected to seismic loading. Afterwards, the velocity response spectrum of the response may be determined, from which the SI is calculated. This methodology is illustrated in Figure 7.10. However, in this study, the full length of all the viaducts was explicitly considered instead of using equivalent SDOF structures, since the response data at all the deck nodes was already available from the full set of dynamic analyses ran for the other DMs. For that purpose, calculation of the velocity spectrum of the response was made at the control pier for each viaduct, using only the corresponding first vibration mode periods, which may constitute a conservative approach for the evaluation of SI.
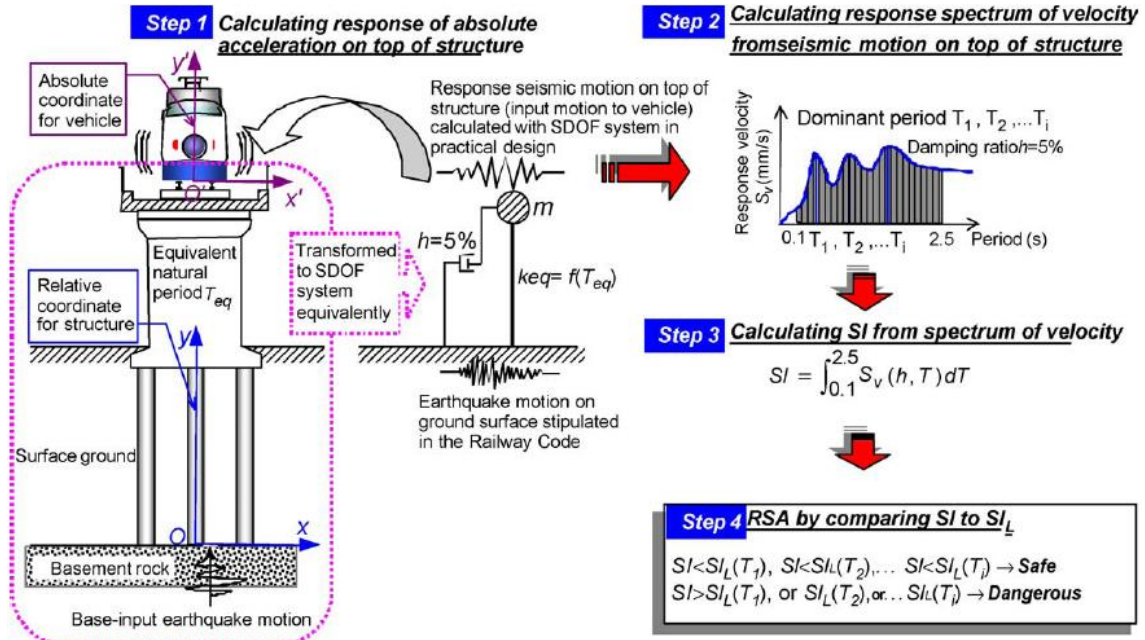
Figure 7.10 – Procedure for running safety assessment using SI (Luo (2005)).

7.5. SEISMIC PERFORMANCE OUTPUT

For the purpose of seismic performance assessment, non-linear dynamic analyses were performed on all the four case study viaducts according to an Incremental Dynamic Analysis (IDA) procedure (Vamvatsikos and Cornell (2002)), for which the earthquake intensity scaling of the previously presented records was considered. For that purpose, the Newmark integration method (Newmark (1959)) was used (with typical parameters $\gamma = 0.50$ and $\beta = 0.25$) and an IM scaling factor $\lambda_{scaling}$ was individually defined for each ground motion, in proportion to the spectral acceleration Sa_1 corresponding to the first vibration mode of each structure. Furthermore, this means that, for IDA purposes, a different scaling factor was determined for each structure and ground motion *i*, according to equation 7.6, where Δ_{IDA} and n_{IDA} represent the scaling increment and the increment number, respectively. In that regard, a Δ_{IDA} of 0.20g was used for the full analysis range of [0.0 ; 6.0] *g*.

$$\lambda_{scaling} = \frac{1}{Sa_{1,i}} \times (\Delta_{IDA} \times n_{IDA})$$

7.6

The output of the IDA analyses can be organized in the form of IDA curves, representing the distribution of the maximum EDP values, determined individually at each IM level (Figure 7.11 – a)) for all the analyzed ground motions. An example of such a curve is illustrated in Figure 7.11 – b), relating to data obtained for the Macheda Viaduct with precast behavior and DM#1, where the 16th, 50th and 84th fractiles of the data distribution are also represented. Due to

the large amount of data produced by the IDA methodology, all the IDA curves are not presented in the main body of this document, but were instead included in Annex C.

| a) EDP response at $Sa_1 = 1.0g$ and 5th GM | b) IDA curve for DM#1 |
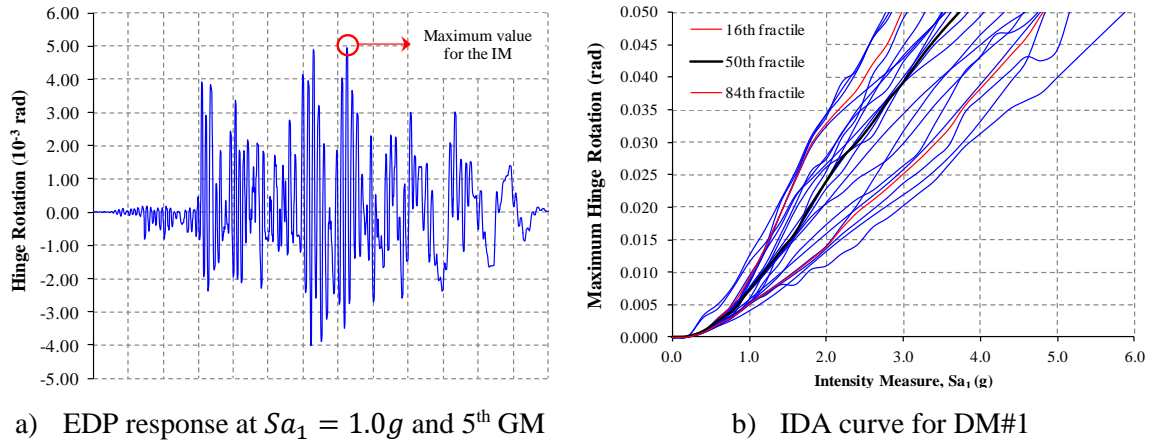
Figure 7.11 – Example results obtained for the Macheda Viaduct with Precast behavior.

On account of the IDA output, fragility curves were determined for each performance level of the three selected DMs. For this purpose, the probability of exceedence of the corresponding damage states *i* was determined for each IM level, by selecting the performance points from EDP *j* values regarding the lowest IM occurrence (DM based approach). Furthermore, this information was gathered in the form of a cumulative distribution function (CDF) according to equation 7.7, to which lognormal curves were fitted using procedures developed by Baker (2015).

$$CDF(DM_i|IM) = \int_0^{+\infty} P[EDP_j > DM_i|IM = x]\, dx \qquad 7.7$$

7.5.1. DM#1: STRUCTURAL PERFORMANCE RESULTS

The fragility curves obtained for the structural performance DMs are presented in Figure 7.12 for all the viaducts, including the comparison between monolithic and precast systems' results. In addition, the first mode spectral acceleration values were evaluated from the elastic ground motion acceleration response spectra and for each structure, considering the reference PGA defined for the damage limitation and no collapse requirements. Those values are also indicated by the green and purple vertical lines (for damage limitation and no collapse, respectively).

a) Macheda Viaduct   b) Palheta Viaduct

c) Viaduct over Degebe River   d) Viaduct over Ribeira da Laje
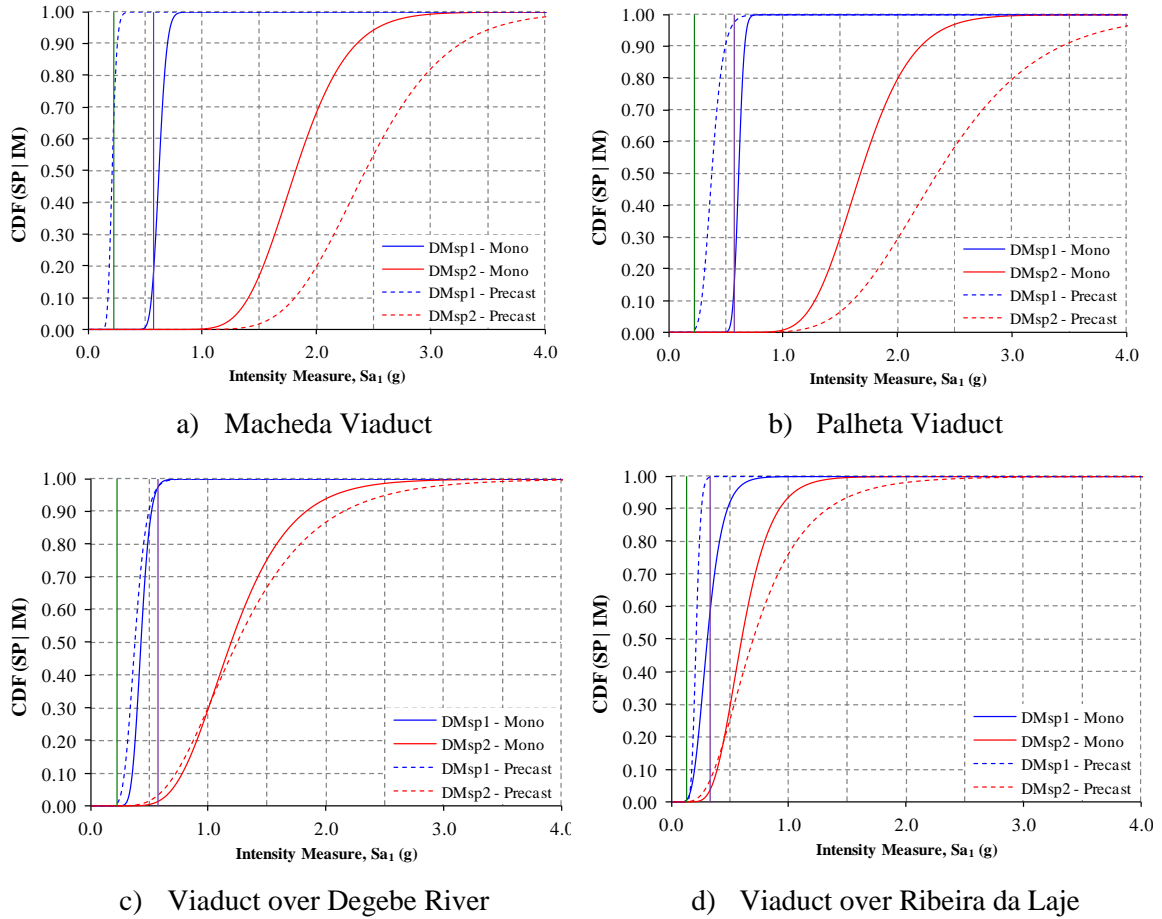
Figure 7.12 – Fragility curves for DM#1 – Structural Performance results

The structural performance inherent to these results shows that the precast model is able to maintain stable behavior up to larger ground motion intensities, as the respective DMsp2 fragility curves generally exhibit lower probability of exceedence than those relative to monolithic behavior. The contrary is observed regarding yielding, where precast DMsp1 occur earlier than for the monolithic model. That is an expected result, and can be understood as the natural outcome of the precast piers having lower yielding threshold, whereas the monolithic cases lead to slightly larger yielding displacements. Regardless, this agrees with the conclusions obtained through reduced scale testing, where the precast model was able to carry larger ductility capacity than the monolithic counterpart.

With respect to the performance observed on different structures, a general trend for earlier collapse can be observed on the longer viaducts (Viaduct over Degebe River and Viaduct over Ribeira da Laje, Figure 7.12 – c) and d), respectively). That can be attributed to the fact that longer structures have less overall contribution of their abutments to the transverse load carrying capacity, leading to significant demand to be observed on a relatively larger part of the piers. In these cases, the difference between monolithic and precast systems is less pronounced, and both

exhibit very similar exceedence probability values, particularly within the CDF range between 0.00 and 0.30.

Representation of the first mode spectral acceleration provides an indication of the performance that is expected relative to EC8 requirements. In that regard, the damage limitation requirement could be at risk on the Macheda viaduct with precast behavior, since the corresponding probability of exceedence for yielding is significant. In addition, a low probability of exceedence is observed on every other relevant scenario, although further detailed analyses should be performed, particularly for Viaduct over Degebe River and Viaduct over Ribeira da Laje, if increased precision is required.

7.5.2. DM#2: LATERAL DEFLECTION RESULTS

Lateral deflection DM#2 fragility curves are illustrated in Figure 7.13 for all the viaducts and both behavior models.

a) Macheda Viaduct   b) Palheta Viaduct

c) Viaduct over Degebe River   d) Viaduct over Ribeira da Laje
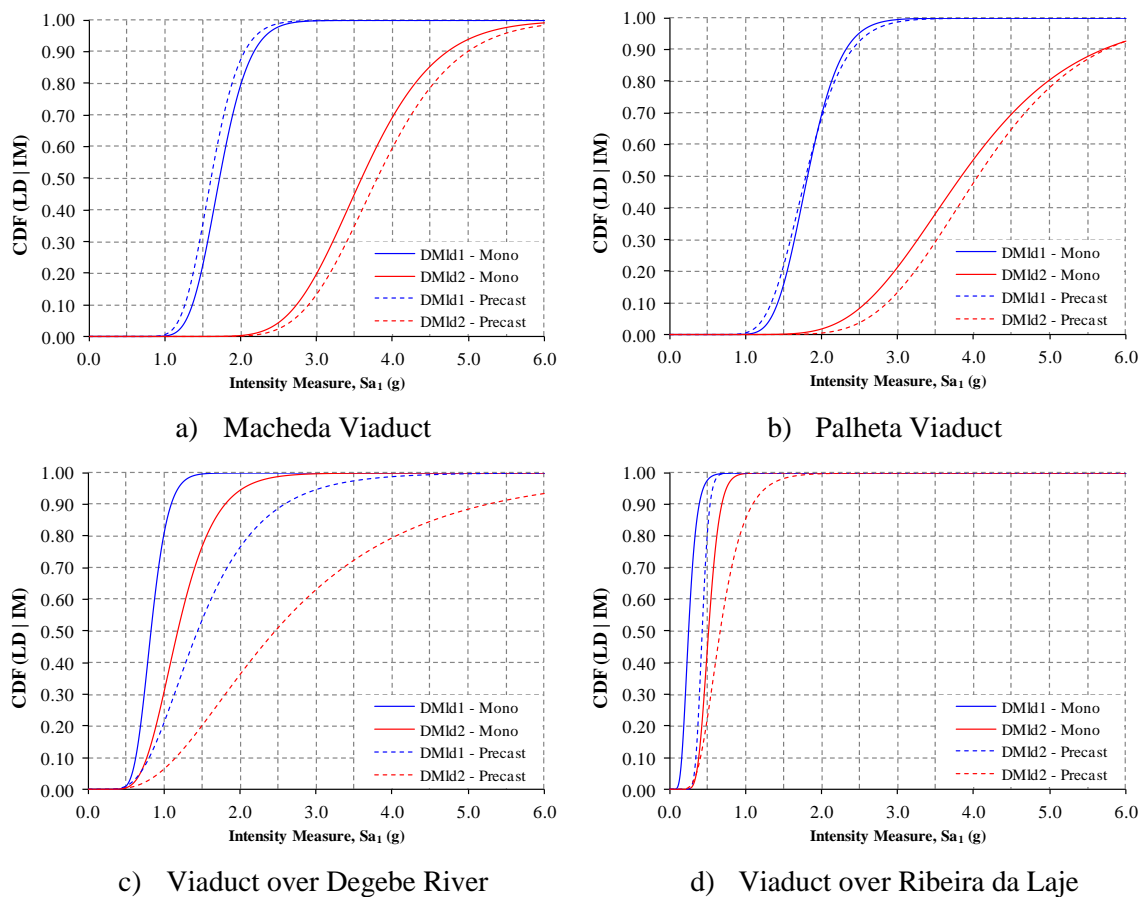
Figure 7.13 – Fragility curves for DM#2 – Lateral Deflection results

In general, these results illustrate two different trends regarding differences between the monolithic and precast scenarios. On the shorter viaducts (Macheda Viaduct and Palheta Viaduct) those scenarios show quite close fragility curves, suggesting that the transverse

stiffness of the deck is more relevant to the control of corresponding displacements than pier stiffness, which seems reasonable. On the longer viaducts that is no longer the case, and a clear distinction between precast and monolithic fragility curves can be identified, particularly on Viaduct over Degebe River. As far as it was possible to assess, that occurs because that is a long structure (395.00m of length) with relatively short piers (mean pier height of 7.56m), which benefits from the earlier yielding of precast behavior to see a larger ductility demand on a greater number of piers, in comparison with the monolithic model, and therefore less overall angular variation between subsequent deck spans. It is also worth mentioning that running safety and track damage related fragility curves (DMld1 and DMld2, respectively) are closer together in the longest viaducts than in the shortest viaducts.

7.5.3. DM#3: DERAILMENT CONDITIONS RESULTS

Figure 7.14 illustrates the fragility curves relative to derailment conditions, evaluated through DM#3 for all the viaducts and behavior models.

| e) Macheda Viaduct | f) Palheta Viaduct |

| g) Viaduct over Degebe River | h) Viaduct over Ribeira da Laje |

Figure 7.14 – Fragility curves for DM#3 – Derailment Conditions results

Small differences can generally be observed between the precast and monolithic results for all the viaducts. Considering that Spectral Intensity values are determined from pseudo-velocity

which, in correspondence, can be related with the dynamic lateral displacement records at the control pier, this evidences that the differences between the precast and monolithic models deck displacements are mostly negligible. Unsurprisingly, this is particularly true for the shortest length viaducts (Macheda Viaduct and Palheta Viaduct), whereas slightly larger differences can be identified on the other two study cases.

7.6. FINAL REMARKS

The present chapter encloses the seismic performance assessment study that was developed as the final part of this thesis. Its main objective was to provide a 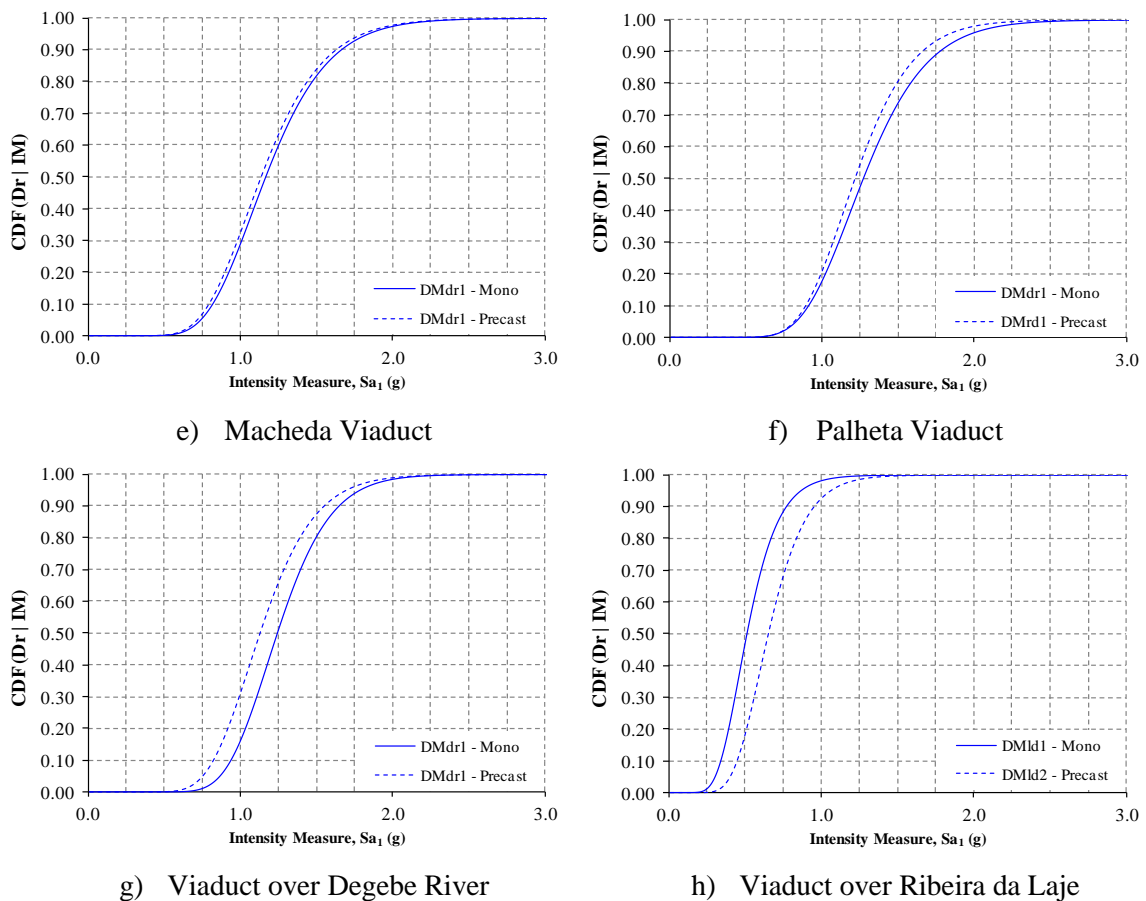comparative overview of performance differences that can be expected from using the proposed precast systems (which were previously tested and analyzed on earlier chapters) regarding more common monolithic applications.

For that purpose, a methodology based on the calculation of fragility curves for different damage measures was adopted, wherein ground motion characterization was made using twenty seismic records obtained from the SelEQ tool for the applicable EC8 target spectrum, and structural characterization was evaluated within a computational model elaborated in OpenSees. In that regard, 2D models were defined, in which modeling the transverse behavior of the structure was the main focus. Inelastic behavior was governed by a uniaxial model mobilized at the piers, which was calibrated according to a force-displacement scaling procedure and experimental results corresponding to two scenarios: one monolithic and one precast.

Within that context, incremental dynamic analysis were performed on four different viaducts for a seismic intensity range of [0.0 ; 6.0] *g*, and the corresponding results were evaluated regarding three damage measures, where the first was related with structural performance damage state, while the other two consisted of track related assessments. Interestingly, results generally showed small differences between the precast and monolithic scenarios on these track related DMs, suggesting that they are more sensitive to deck stiffness variations than pier behavior. Nonetheless, in the cases where larger differences were observed, the precast scenario tended to show lower probability of exceedence than the monolithic case for the most severe damage state under evaluation (Non-Collapse for structural performance and Track Damage for lateral deflection). Even though the present study was developed from a simplified approach, those observations arguably support an improved seismic performance of the precast solutions relative to monolithic specimens.

8
CONCLUSIONS

8.1. MAIN REMARKS

The main purpose of the work presented in the current document was to provide additional insight into the framework of the seismic behavior of bridge piers designed for HSRL viaducts, therefore involving work under two wide and important research fields: the seismic performance of bridge structures and the strict requirements of HSRL transportation. Furthermore, it also encloses several activities that were carried out on account of the SIPAV project, which is a previous research program carried out at the Faculty of Engineering of the University of Porto, from which the aim to study precast applications was originally derived. In that regard, while widespread application of the precast technology can be observed for the construction of bridge deck structures, the same cannot be said regarding the construction of bridge piers, where cast-in-place construction is most often considered.

Within that context, the underlying concept of precast bridge piers for HSRL is believed to be innovative, in nature, since it is inherent to structure designs that are not only uncommon, but also virtually nonexistent in the context of HSRL. This was also the reason why most of the work was focused on assessing the different features and outcomes of a precast application in contrast with a monolithic CIP construction, since that has been the historically preferred option. Additionally, according to research performed during this study, widespread application of precast for bridge piers is limited by several factors, not only manufacture and operational issues that influence the cost-effectiveness comparison against typical monolithic solutions, but also critical technical aspects that lead to weaker or unreliable designs. And while on this topic, seismic loading related weaknesses are undeniably some of the most difficult to address, since

they stem from having to account for ductile deformations whilst HSRL SLS criteria demand high stiffness and low displacements.

This may lead to the design of limited ductility structures, such as wall-pier solutions where shear yielding tends to be avoided, or generally more ductile single column structures, where large deformations are more easily accounted for. In that case, if the Portuguese venture project into HSRL can serve as good representation of the general outlook for HSRL viaducts, the vast majority of structures face long lengths and short/medium pier heights. Therefore, according to previous discussion, both of the aforementioned designs were deemed not particularly well suited for large scale precast applications. As an alternative, the double column bent pier structure designed for the same project can represent an acceptable solution, providing considerable stiffness on the bridges' transverse direction, while being easier to accommodate for a precast application due to the inherent division between columns and beam, which can be tackled using relatively common construction industry techniques, such as the top-down cap beam assembly methodology.

Nonetheless, the seismic performance of the double column structure can still be a concern, since it is able to provide high lateral stiffness, in a large part, due to the robust cross-section of the columns, resulting in a short free span length on the coupling beam. This raises some doubts regarding the efficiency of the usual seismic design methodologies for bridge bents in the current structure, since cap beams are often targeted for rigid behavior, aiming to mostly serve as elements capable of enforcing similar displacement demand on all columns, and general deformation compatibility between them. According to what was possible to assess, the provision of the large column stiffness comes at the cost of not being able to design the beam for that rigid behavior, since its geometrical limitations cannot be easily compensated by reinforcement alone. As a consequence, some level of damage in the beam can be expected, related with a significant shear demand that is difficult to address within an acceptable level of ductility. Moreover, a very similar problem is also experienced by coupling beams of shear walls with low shear span-to-depth ratios, having been a strong research field in the past few decades, from which alternative design strategies can be evaluated for the current application.

Therefore, the complex interactions between beam and columns that could be understood from the preliminary study of the double column bent pier structure constituted a design challenge of particularly difficult nature, which was deemed better addressed by experimental studies. For that purpose, a first stage 1:4 reduced scale testing was performed at LESE on four distinct monolithic pier models, which had the same reinforcement in the columns, but different in the beams. In that regard, all the specimens revealed shear critical behavior on the beams, where the conventional design layout based on horizontal reinforcement and vertical stirrups

showed particularly brittle failure. As far as it was possible to assess, that is a consequence of the large strains that occur at the beam, and of the cyclic degradation of the cracked concrete surfaces. In addition, the beam-column interfaces were observed to concentrate most of the deformations, and the reported collapse modes could be linked with concrete failure in those same locations. In fact, the high level of damage experienced by all specimens was largely tied to those occurrences, because once the compression failure threshold is achieved, damage progression is significantly more pronounced. Likewise, it can be argued that up until that point, the level of damage experienced by the piers could be repaired easily, but it would require a significantly bigger effort if further loading was considered, particularly for the specimens that showed the most sudden failures. Furthermore, the rhombic truss based reinforcement layouts were those that provided arguably the best results. However, it should also be stated that, in order to deal with the large demand in the coupling beam, all the resulting reinforcement layouts are required to be quite strong, particularly those that were inspired by EC8 or ACI318, which can lead to significant difficulties considering real-scale construction. In fact, this issue would most likely cause any precast application based on such a design to not be economically competitive.

A conclusion that could be assessed from the previous results was that the large deformation demand at the beam level is related to the general inability of forming stable energy dissipating mechanisms located on the columns rather than the beams (since significant damage occurs earlier on the latter), therefore preventing solid mobilization of the flexural capacity of the columns. In light of those results, the precast specimens were designed aiming to forcefully induce earlier column yielding, by reducing moment continuity reinforcement on the beam-column section by nearly 50%, seeking a reduction of the overall beam deformations by providing a more desirable alternative energy dissipation mechanism. This was performed along with the adoption of a precast system based on a top-down assembly of an integral beam element similar to a cap beam, descending onto two previously placed columns. Thus, a second stage of experimental assessment was devised, focused on evaluating the effects of three different connection detailing layouts, designed for the purpose of decreasing construction complexity.

All the precast double column pier specimens performed reasonably well, reaching higher drifts, with larger energy dissipation, and the intended design goal of promoting increased deformations at the precast joint for earlier column yielding was clearly achieved. In fact, comparison of two equivalent and identically reinforced specimens, where the only variation was the adoption of precast construction on one of them (requiring the respective joints), showed noticeable differences and, in particular, considerably improved behavior with the

precast specimen. Nonetheless, even if that strategy enabled larger ductility capacity, the collapse mode of all the specimens was still related to shear deformations occurring at the beam, particularly at the beam-column vertical interfaces, where most of the structural damage was observed. Taking that into consideration and, if similar performance can be ensured with any of the tested systems, then the one that is associated with less operational constraints or increased flexibility in the construction procedures can be sustained as the preferred alternative. Regardless, despite the precast specimens having showed globally improved cyclic behavior, the level of damage observed at the last few drift cycles was still significant and, as mentioned before, related with the shear demands on the beam.

The experimental study also included a third testing stage, focused on evaluating precast mechanisms for the foundation-to-column connections that are required for column bases. This part of the study was not developed to the same extent as for the upper part of the frame but, nonetheless, two precast connection systems were designed and tested. One of those was based on a precast construction of the column element with protruding rebars and second phase casting of the footing while holding the column above it. The other was also based on constructing the column with protruding rebars, but considering their introduction into existing foundations through duct holes. In this regard, the former was able to exhibit acceptable performance, even if slightly worse in nearly every way (ductility, energy dissipation and failure mode), when compared to a monolithic specimen. By contrast, the latter showed significant weaknesses and undesirable failure modes that could be linked to the precast design itself, particularly the grout crushing that resulted in early rebar buckling and fracture. As far as it was possible to assess, that was mostly due to a design misconception, since grout was observed to be inadequate for the intended purpose. Unfortunately, it was not possible to repeat this test due to the project constraints, but it is believed that better performance was achievable if an adequate micro-concrete mix was used instead.

The information obtained during the experimental campaign is undoubtedly one of the strongest features of the present work, and it is the author's belief that it provides an interesting perspective on the framework of HSRL bridge piers subjected to seismic loading. In that regard, in order to further understand the experimental observations and to extend conclusions of that initiative to a wider range of similar applications, several numerical simulations were made, based on 2D FEM applications. A two stage approach was considered, wherein a first set of numerical analyses were performed for the purpose of experimental validating the modeling strategy, and a second set of analyses for evaluating other scenarios not experimentally studied, namely full length columns with clamped base supports, and shorter piers. In that regard, the modeling strategy was successful in simulating several of the experimental tests, enabling

confirmation of several assumptions regarding experimental observations, such as the overall importance of beam deformations on the global behavior of the double column pier structure or the role of the precast joint in the overall ductility increase of the structural system. Furthermore, it enabled validation of the test setup by providing similar results between the half pier and full pier analyses. Likewise, it was also possible to confirm that most of the phenomena observed on the experimental campaign (e.g. large beam deformations, mild cracking at the columns) are also as relevant on other untested scenarios, since similar response features can be identified therein for equivalent capacity, from which it was possible to conclude that the overall double column behavior can be scaled according to the associated lateral seismic moment.

The final part of the work aimed at using the previously analyzed test data to calibrate numerical applications, for evaluation of the global behavior of idealized HSRL viaducts involving some of the tested pier systems. Essentially, this required characterizing the moment capacity of piers within a numerical viaduct simulation through use of lumped plasticity 2D models, where the inelastic behavior was defined according to the experimental lateral forces, scaled for different application heights, and set only at the base of each pier. In this regard, only two scenarios were considered: one for a monolithic construction and one for a precast construction, calibrated from the two assumed best test results for each category. The methodology used for the assessment of the viaducts' performance was based on well established performance based methodologies, but due to the inherent limitations of the present study, only the response variability was taken into account by considering different ground motion records. Furthermore, three Damage Measures were evaluated, one related with the structural performance of the viaducts and the other two with service criteria relative to performance on the framework of HSRL bridges, namely lateral deflection and derailment conditions. In this regard, the results were evaluated by means of IDA analyses, from which fragility curves were determined, which essentially showed that within this scope there is a large probability of the required safety and service conditions to be met for the analyzed structures. Nonetheless, it is acknowledged that the adopted methodology is not sufficiently refined to extract those conclusions in a more definitive manner, namely due to lack of, for example, soil-structure interaction or DM limits dispersion data, although that was also never its main purpose.

On the scope of all that was presented, it is a firm belief of the author that the main objectives of this work were fairly accomplished, and that some of the results achieved present an interesting alternative for precast applications on these structures, with respect to the rapid construction of bridges.

8.2. FUTURE DEVELOPMENTS

Concerning future developments, it is not possible to address this subject without first reinforcing the importance of the SIPAV research project in the development of the present work. In fact, that project aimed to study new opportunities for precast solutions while envisioning application on the first part of the foreseen Portuguese HSRL network: the Poceirão-Caia project; the political and economical junctures at that time were highly favorable to the establishment of HSRL in Portugal, which naturally provided a demand for improved knowledge that the engineering community sought to address. That mindset has changed, unfortunately, throughout the time period between the beginning and conclusion of this work, since the deep economic crisis that the country had been facing in the past few years radically modified public and institutional perceptions of the relative worth of HSRL on the global context of the national economy.

Despite the above described, the data that was obtained during this work certainly still holds valuable scientific information that is relevant on its own, particularly since the seismic behavior of HSRL bridges is not a very frequently addressed topic by the community. Furthermore, while a Portuguese HSRL network may be out of consideration for the foreseeable future, the discussion on precast design and overall performance of these structures may be applicable for other endeavors.

Therefore, some ideas that could further improve the work presented in this document are enlisted as follows:

- Economic assessment of the viability of the tested systems would be a very valuable feature, enabling the extraction of matured conclusions regarding the practical outcome of seeking precast applications in comparison with the common CIP construction alternatives;
- For budget reasons and time constraints, the third stage of the experimental campaign was quite limited in both its scope and number of tested precast systems. An extension of this stage to involve additional design options and construction methods would likely help refining the knowledge on that particular subject and, possibly, improving the outlook over the foundation-to-element connections. At the very least, considering the weaknesses that were identified on the model most suited for pre-fabrication, repeating that test using a different precast connection material would be desirable;
- Considering the high level of damage experienced by all the double column tested specimens, it would be fairly important to evaluate alternative construction features

aiming to improve this condition, such as, for example, using fiber reinforced concrete; Additionally, definition of adequate performance thresholds for repairable and non-repairable damage levels could help with evaluating the effectiveness of repair measures;

- The global behavior of the double column structures was observed to be highly commanded by either the shear level in the beam or the bending moments in the columns/precast joint. Due to that, the capacity prediction models used throughout this work were somewhat simple, and in some cases have not been able to provide satisfactory results. A stronger understanding of the relative importance of beam shear and column bending on the overall pier capacity could certainly help on improving capacity prediction and, ultimately, providing better informed design decisions;

- The performance assessment numerical study that is included in Chapter 7 of the current work was mainly developed aiming for the comparison between the two monolithic and precast scenarios, which is why the conclusions extracted from that section may hold valuable information despite the simplicity of the approach. Nonetheless, considering further applications and an eventual need to develop more in depth knowledge on that subject, there are several aspects of the adopted methodology that could be improved. For example, future works could seek to include soil-structure interaction, or at least different scenarios for soil flexibility due to how it may affect both the forces and the displacements recorded during an earthquake event. Additionally, if a refined performance assessment study is sought, then the performance levels for the selected damage measures would likely need to be better reviewed, including their EDP limits and the associated dispersion data.

REFERENCES

A

ACI 318 (2014). *"Building Code Requirements for Structural Concrete (ACI 318-14)"* Farmington Hills, MI 48331,American Concrete Institute (ACI)

Alinaitwe, H. M., Mwakali, J. A. and Hansson, B. (2006). *"Assessing the degree of industrialisation in construction."* Journal of Civil Engineering and Management 12(3): 221-229

Altavia (2009). *"BAFO "*. Concessão RAV Poceirão - Caia. Linha Ferroviária de Alta Velocidade. Eixo Lisboa - Madrid. Troço Poceirão - Caia

ANSR (2013). *"Código da Estrada"*. Autoridade Nacional de Segurança Rodoviária. Decreto-Lei nº 72/2013

AREMA (2003). *"Railway Track Design"*

B

Baker, J. W. (2015). *"Efficient Analytical Fragility Function Fitting Using Dynamic Structural Analysis."* Earthquake Spectra 31(1): 579-599

Berry, M. P. and Eberhard, M. (2003). *"Performance Models for Flexural Damage in Reinforced Concrete Columns"*. Pacific Earthquake Engineering Research Center Report.Pacific Earthquake Engineering Research Center

Bfer, G. (1985). *"An isoparametric joint/interface element for finite element analysis."* International Journal for Numerical Methods in Engineering 21(4): 585-600

Billington, S. L., Barnes, R. W. and Breen, J. E. (1999a). *"A precast segmental substructure system for standard bridges."* PCI Journal 44(4): 56-73.

Billington, S. L., Barnes, R. W. and Breen, J. E. (1999b). *"A precast substructure design for standard bridge systems"*. Research Report 1410-2.Center for Transportation Research. Austin, Texas.

Billington, S. L., Barnes, R. W. and Breen, J. E. (2001). *"Alternate substructure systems for standard highway bridges."* Journal of Bridge Engineering 6(2): 87-94.

Billington, S. L. and Yoon, J. K. (2004). *"Cyclic response of unbonded posttensioned precast columns with ductile fiber-reinforced concrete."* Journal of Bridge Engineering 9(4): 353-363.

Biskinis, D. and Fardis, M. N. (2010). *"Deformations at flexural yielding of members with continuous or lap-spliced bars."* Structural concrete 11(3): 127-138.

Boqueho, G. (2002). *"SNCF's TGV Safety System"*. International Railway Safety Council, Tokyo.

C

California Department of Transportation (2000). *"Bridge Design Specifications Manual:7 - Substructures"*

Calçada, R., Delgado, P. and Matos, A. C. (2008). *"Bridges for High-Speed Railways"*. Revised Papers from the Workshop, Porto, Portugal, 3 - 4 June 2004. R. Calçada, P. Delgado and A. C. Matos, CRC Press.

Canbolat, B. A., Parra-Montesinos, G. J. and Wight, J. K. (2005). *"Experimental study on seismic behavior of high-performance fiber-reinforced cement composite coupling beams."* ACI Structural Journal 102(1): 159-166

Cantagallo, C., Camata, G. and Spacone, E. (2014). *"Seismic Demand Sensitivity of Reinforced Concrete Structures to Ground Motion Selection and Modification Methods."* Earthquake Spectra **30**(4): 1449-1465

Carmichael, A. and Desrosiers, N. (2008). *"Comparative Highway Bridge Design"*.Faculty of the Worcester Polytechnic Institute.

Castilho, V. C. and Lima, M. C. V. (2012). *"Comparative Costs of the Production, Transport and Assembly Stages of Prestressed Precast Slabs using Genetic Algorithms."* International Journal of Optimization in Civil Engineering 2(3): 407-422.

CEB (1993). *"CEB Bulletin 217"*. Selected Justification Notes - Bond and Detailing CEB. Lausanne, Switzerland

Couchard, I. and Detandt, H. (2003). *"Viaducts for high-speed trains consisting of a series of skew portal frames and intermediate simply supported girders"*. IABSE Symposium, Antwerp

Costa, C. (2009). *"Análise Numérica e Experimental do Comportamento Estrutural de Pontes em Arco de Alvenaria de Pedra"*. Porto, Tese de Doutoramento, Faculdade de Engenharia da Universidade do Porto

Cruz Lesbros, L. F., Carranza Aubry, R. and Reinoso Angulo, E. (2003). *"Design and construction of the Ayuntamiento 2000 Bridge, Cuernavaca, Mexico."* PCI Journal 48(4): 58-65.

Cutillas, A. (2007). "Track-bridge interaction problems in bridge design". Track-bridge interaction on High-Speed railways. FEUP. Porto, Portugal.

D

Davis, P., Janes, T., Eberhard, M. and Stanton, J. (2012). *"Unbonded Pre-Tensioned Columns for Bridges in Seismic Regions"*. PEER Report.Pacific Earthquake Engineering Research Center.Department of Civil and Environmental Engineering of University of Washington

Delgado, P. (2009). *"Avaliação da Segurança Sísmica de Pontes"*. Porto, Tese de Doutoramento, Faculdade de Engenharia da Universidade do Porto

Delgado, P., Monteiro, A., Arêde, A., Vila Pouca, N., Delgado, R. and Costa, A. (2011). *"Numerical simulations of RC hollow piers under horizontal cyclic loading."* Journal of Earthquake Engineering 15(6): 833-849

Delgado, P., Monteiro, A., Arêde, A., Vila Pouca, N., Delgado, R. and Costa, A. (2011). *"Numerical simulations of RC hollow piers under horizontal cyclic loading."* Journal of Earthquake Engineering 15(6): 833-849

Delgado, R., Delgado, P., Vila Pouca, N., Arêde, A., Rocha, P. and Costa, A. (2009). *"Shear effects on hollow section piers under seismic actions: Experimental and numerical analysis."* Bulletin of Earthquake Engineering 7(2): 377-389

Design Standards for Railway Structures and Commentary (2007a). "Seismic Design" Railway Bureau of the Ministry of Land, Infrastructure and Transport Government of Japan

Design Standards for Railway Structures and Commentary (2007b). "Displacement Limits" Railway Bureau of the Ministry of Land, Infrastructure and Transport Government of Japan

DGF. (2007). *"Instrucción de acciones a considerar en puentes de ferrocarril (IAPF)"*. Gobierno de España Ministerio de Fomento, Secretaria General Técnica Ministerio de Fomento

Dutoit, D., Wouts, I. and Martin, D. (2004). *"Seismic Design of Structures in the French Mediterranean and Asian High Speed Railway Lines"*. Bridges for High-Speed Railways, Porto, Portugal.

Dutoit, D. (2007). *"New Evolutions for High Speed Rail Line Bridge Design Criteria and Corresponding Design Procedures"*. Track-bridge interaction on High-Speed railways. FEUP. Porto, Portugal

E

Elgawady, M. and Sha'lan, A. (2011). *"Seismic Behavior of Self-Centering Precast Segmental Bridge Bents."* Journal of Bridge Engineering 16(3): 328–339.

Eligehausen, R., Popov, E. and Bertero, V. (1982). *"Local bond stress-slip relationships of deformed bars under generalized excitations"*.Universitätsbibliothek der Universität Stuttgart. Stuttgart

EN1990 (2002). *"Eurocode 0: Basis of structural design"* Brussels,European Committee for Standardization (CEN)

EN1990-1, +A1:2005 (2002). *"Eurocode - Basis of structural design"* Brussels,European Committee for Standardization (CEN)

EN1991-2 (2003). *"Eurocode 1: Actions on Structures - Part 2: Traffic Loads on Bridges"* Brussels,European Committee for Standardization (CEN)

EN1998-1 (2004) *"Eurocode 8: Design of structures for earthquake resistance. Part 1: General rules, seismic actions and rules for buildings"* Brussels,European Committee for Standardization (CEN)

EN1998-2 (2005). *"Eurocode 8: Design of structures for earthquake resistance. Part 2: Bridges"* Brussels,European Committee for Standardization (CEN)

F

Fardis, M. N., Kolias, V., Panagiotakos, T. B., Katsaras, C. and Psychogios, T. (2012). *"Guide for bridge design with emphasis on seismic aspects"*

Faria, R. (1994). *"Avaliação do Comportamento Sísmico de Barragens de Betão Através de um Modelo de Dano Contínuo"*. Porto, Tese de Doutoramento. Faculdade de Engenharia da Universidade do Porto

Faria, R. and Oliver, J. (1993). *"A rate dependent plastic-damage constitutive model for large scale computations in concrete structures."*. CIMNE Monograph, Barcelona

fib (2008). *"fib Bulletin 43 Structural connections for precast concrete buildings".fib* (fédération international du béton). Switzerland

Fichoux, E. (2011). "*Présentation et Utilisation de Cast3M*." from http://www-cast3m.cea.fr/html/Documentation_Cast3M/Presentation_Cast3M.pdf

Figueiredo, H., Calçada, R. and Delgado, R. (2009a). *"Aspectos Regulamentares no Cálculo de Pontes Ferroviárias em Linhas de Alta Velocidade"*

Figueiredo, H., Calçada, R. and Delgado, R. (2009b). *"Soluções Estruturais para Pontes Ferroviárias em Linhas de Alta Velocidade"*

Fouad, F. H., Rizk, T. and Stafford, E. L. (2006). *"A Prefabricated Precast Concrete Bridge System for the State of Alabama"*. UTCA Report 05215.University Transportation Center for Alabama (UTAC)

Freeby, G., Medlock, R. and Slage, S. (2003). *"Prefabricated Bridge Innovations"*. Second New York City Bridge Conference, New York

G

Galano, L. and Vignoli, A. (2000). *"Seismic behavior of short coupling beams with different reinforcement layouts."* ACI Structural Journal 97(6): 876-885

Gibbens, B. and Smith, P. S. (2004). *"Design-Construction of Sorell Causeway Channel Bridge, Hobart, Tasmania."* PCI Journal 10(4): 56-66

Goicolea, J. M. (2007). *"Service Limit States for Railway Bridges in New Design Codes IAPF and Eurocodes"*. Track-Bridge Interaction on High-Speed Railways

Grant, D. N. and Diaferia, R. (2013). *"Assessing adequacy of spectrum-matched ground motions for response history analysis."* Earthquake Engineering & Structural Dynamics 42(9): 1265-1280

Günav, M. and Mosalam, K. (2012). *"PEER Performance Based Earthquake Engineering Methodology, Revisited"*. 15th World Conference on Earthquake Engineering, Lisboa

H

Haber, Z. B., Saiidi, M. S. and Sanders, D. H. (2013). *"Precast Column-Footing Connections for Accelerated Bridge Construction in Seismic Zones"*.Reno University of Nevada.Center for Civil Engineering Earthquake Research

Haraldsson, O., Janes, T., Eberhard, M. and Stanton, J. (2013). *"Seismic Resistance of Socket Connection between Footing and Precast Column."* Journal of Bridge Engineering 18(9): 910-919

Harajli, M., Hamad, B. and Rteil, A. (1995). *"Effect of Confinement on Bond Strength between Steel Bars and Concrete."* Structural Journal 101(5)

Haselton, C. B., Liel, A. B. and Deierlein, G. G. (2009). *"Simulating structural collapse due to earthquakes: Model idealization, model calibration and numerical solution algorithms"*. COMPDYN - Computational Methods in Structural Dynamics and Earthquake Engineering, Rhodes, Greece

Hewes, J. T. and Priestley, M. J. N. (2002). *"Seismic Design and Performance of Precast Concrete Segmental Bridge Columns"*. Technical Report UCSD/SSRP-2001/25.State of California Department of Transportation

Hieber, D. G., Wacker, J. M., Eberhard, M. O. and Stanton, J. F. (2005). *"Precast Concrete Pier Systems for Rapid Construction of Bridges in Seismic Regions"*.Washington State Transportation Center (TRAC).Washington State Transportation Commission

Hognestad, E., University of, I., Engineering Experiment, S., Reinforced Concrete Research, C. and Engineering, F. (1951). *"A study of combined bending and axial load in reinforced concrete members"*. Urbana, University of Illinois

Hose, Y. and Seible, F. (1999). *"Performance Evaluation Database for Concrete Bridge Components and Systems under Simulated Seismic Loads"*. PEER Report.Pacific Earthquake Engineering Research Center.Department of Structural Engineering of University of California, San Diego

Hoshikuma, J.-i., Unjoh, S. and Sakai, J. (2009). *"Seismic Performance and Structural Details of Precast Segmental Concrete Bridge Columns"*. 25th US - Japan Bridge Engineering Workshop, Tsukuba, Japan

Huang, Z. and Engstrom, B. (1996). *"Experimental and analytical studies of the bond behaviour of deformed bars in high strength concrete."*. 4th international symposium on utilization of high-strength/high-performance concrete, Paris, France

I

Ibarra, L. F., Medina, R. A. and Krawinkler, H. (2005). *"Hysteretic models that incorporate strength and stiffness deterioration."* Earthquake Engineering and Structural Dynamics **34**(12): 1489-1511

Iervolino, I. and Manfredi, G. (2008). *"A Review of Ground Motion Record Selection Strategies for Dynamic Structural Analysis"*. Modern Testing Techniques for Structural Systems: Dynamics and Control. Oreste S. Bursi and David Wagg. Vienna, Springer Vienna**:** 131-163

Ile, N. and Reynouard, J. (2000). *"Nonlinear analysis of reinforced concrete shear wall under earthquake loading."* Journal of Earthquake Engineering 4(2): 183-213

International Building Code (2009). *"International Building Code"* .U.S.A., International Code Council

J

Jason, L. and Durand, S. (2007). *"A two-surface plastic model for concrete behaviour."* Revue Européenne de Génie Civil 11(5): 579-602

K

Kent, D. C. and Park, R. (1971). *"Flexural members with confined concrete."* Journal of the Structural Division 97(7): 1969-1990

Khaleghi, B. (2005). *"Use of precast concrete members for accelerated bridge construction in Washington State"*. 6th International Bridge Engineering Conference: Reliability, Security, and Sustainability in Bridge Engineering, Boston, MA

Konishi, J. (2012). *"Breakthrough in Japanese Railways 10 - Railways and Bridges 2."* Japan Railway and Transport Review(59): 48 - 55

Koyama, Y. (1997). *"Railway Technology Today 1: Railway Construction in Japan."* Japan Railway & Transport Review(14): 36-41

Kumar Subedi, N. (1991a). *"RC-coupled shear wall structures. I. Analysis of coupling beams."* Journal of structural engineering New York, N.Y. 117(3): 667-680

Kumar Subedi, N. (1991b). *"RC coupled shear wall structures. II. Ultimate strength calculations."* Journal of structural engineering New York, N.Y. 117(3): 681-698

Kunnath, S. K., Larson, L. and Miranda, E. (2006). *"Modelling considerations in probabilistic performance-based seismic evaluation: case study of the I-880 viaduct."* Earthquake Engineering & Structural Dynamics 35(1): 57-75

L

Lignos, D. G. (2008). *"Sidesway Collapse of Deteriorating Structural Systems Under Seismic Excitations"*. Department of Civil and Environmental Engineering, Stanford University

Lignos, D. G. and Krawinkler, H. (2012). *"Development and Utilization of Structural Component Databases for Performance-Based Earthquake Engineering."* Journal of Structural Engineering: 1382-1394

Luo, X. (2005). *"Study on methodology for running safety assessment of trains in seismic design of railway structures."* Soil Dynamics and Earthquake Engineering(25): 79-91

Luo, X. and Miyamoto, T. (2008). *"Examining the Adequacy of the Spectral Intensity Index for Running Safety Assessment of Railway Vehicles during Earthquakes"*. 14th World Conference on Earthquake Engineering, Beijing, China

M

Macedo, L., Araújo, M. and Castro, J. M. (2013). *"Assessment and calibration of the harmony search algorithm for earthquake record selection"*. Vienna Congress on Recent Advances in Earthquake Engineering and Structural Dynamics, Vienna, Austria

Macedo, L. and Castro, J. M. (2016). *"SelEQ: An advanced ground motion selection and scaling tool."* Computer-Aided Civil and Infrastructure Engineering (under submission)

Mander, J. B., Priestley, M. J. N. and Park, R. (1988). *"Theoretical Stress-Strain Model for Confined Concrete."* Journal of Structural Engineering 114(8): 1804-1826

Mander, J. B., Dhakal, R. P., Mashiko, N. and Solberg, K. M. (2007). *"Incremental dynamic analysis applied to seismic financial risk assessment of bridges."* Engineering Structures 29(10): 2662-2672

Manrique, J. D., Hussein, M. A., Telyas, A. and Funston, G. (2007). *"Case Study-Based Challenges of Quality Concrete Finishing for Architecturally Complex Structures."* Journal of Construction Engineering and Management 133(3): 208-216

Manterola, J. and Cutillas, A. M. (2004). *"Prestressed Concrete Railway Bridges"*. Bridges for High Speed Railways, Porto

Marioni, A. (2006). *"Bearing Systems for High Speed Railway Bridges"*. 6th Joints, Bearings and Seismic Systems for Concrete Structures, Halifax (Canada)

Marques, M. (2011). *"Avaliação Probabilística da Segurança Sísmica de Edifícios"*. Porto, Tese de Doutoramento, Faculdade de Engenharia da Universidade do Porto

Marsh, L. (2011). *"Application of Accelerated Bridge Construction Connections in Moderate-to-High Seismic Regions"*, Transportation Research Board

Marsh, M., Stanton, J. and Eberhard, M. (2010). *"A precast bridge bent system for seismic regions"*. Fully Precast Bridge Bents for Use in Seismic Regions. FHWA

Matsumoto, E. E., Waggoner, M. C., Kreger, M. E., Vogel, J. and Wolf, L. (2008). *"Development of a precast concrete bent-cap system."* PCI Journal 53(3): 74-99

Mclean, D., Kuebler, S. and Mealy, T. (1998). *"Seismic Performance and Retrofit of Multi-Column Bridge Bents"*. Research Project T9902 - Multi-Column Retrofit - Experiments. Washington State Department of Transportation

McKenna, F., Fenves, G. and Fillipou, F. (2010). "*OpenSees*." from http://www-cast3m.cea.fr/html/Pegon/elemjoint.pdf

Menegotto, M. and Pinto, P. (1973). *"Method of analysis for cyclically loaded reinforced concrete plane frames including changes in geometry and non-elastic behaviour of elements under combined normal force and bending."*. Resist. Ultimate Deform. of Struct. Acted on by Well-Defined Repeated Loads, Final Report.IABSE Symposium. Lisbon

Millanes Mato, F. (2004). *"Composite and Prestressed Concrete Solutions for Very Long Viaducts: Analysis of Different Structural Designs for the Spanish High Speed Lines"*. Bridges for High Speed Railways, Porto

Millanes Mato, F. and Ortega Cornejo, M. (2007). *"Track-Structure Interaction and Seismic Design of the Bearings System for Some Viaducts of Ankara-Istanbul HSRL Project"*. Track-Bridge Interaction on High-Speed Railways, FEUP, Porto

Moehle, J. P. (2003). *"A framework for performance-based earthquake engineering"*. ATC-15-9 Workshop on the Improvement of Building Structural Design and Construction Practices, Maui, HI

Moehle, J. P., Ghodsi, T., Hooper, J. D., Fields, D. C. and Gedhada, R. (2012). *"Seismic Design of Cast-in-Place Concrete Special Structural Walls and Coupling Beams: A guide for Practicing Engineers"*. NEHRP Seismic Design Technical Brief No. 6.NEHRP Consultants Joint Venture.U.S. Department of Commerce

Monso, G. M. and Miranda, E. (2013). *"Performance-Based Seismic Assessment of a Recently Built High-Speed Rail Viaduct in Spain. The Archidona Viaduct"*. 7th National Seismic Conference on Bridges and Highways, Oakland, CA

Monteiro, A., Arêde, A. and Vila Pouca, N. (2017a). *"Comparative Analysis of Monolithic vs. Precast Solutions for Bent-Type Reinforced Concrete Bridge Piers Under Cyclic Loading: Experimental Assessment (Under review)."* Bulletin of Earthquake Engineering.

Monteiro, A., Arêde, A. and Vila Pouca, N. (2017b). *"Seismic behavior of coupled column bridge RC piers: Experimental campaign."* Engineering Structures 132: 399-412

Monteiro, A. (2009). *"Simulação Numérica e Validação Experimental do Comportamento Cíclico de Pilares Ocos de Pontes de Betão Armado"*. Porto, Tese de Mestrado, Faculdade de Engenharia da Universidade do Porto

Monteiro, R. (2011). *"Probabilistic Seismic Assessment of Bridges"*. Porto, Tese de Doutoramento, Faculdade de Engenharia da Universidade do Porto.

Montenegro, P. (2015). *"A Methodology for the Assessment of the Train Running Safety on Bridges"*, Tese de Doutoramento, Faculdade de Engenharia da Universidade do Porto.

Mostafa, K., Sanders, D. H. and Saiidi, M. S. (2004). *"Impact of Aspect Ratio on Two-Column Bent Seismic Performance"*.California Department of Transportation.Center for Earthquake Engineering Research, Department of Civil and Environmental Engineering, University of Nevada

N

Newmark, N. (1959). *"A Method of Computation for Structural Dynamics."* ASCE Journal of Engineering Mechanics Division 85(EM3)

NP EN1992-1-1 (2010). *"Eurocódigo 2: Projecto de estruturas de betão Parte 1-1: Regras gerais e regras para edifícios."* Bruxelas,Comité Europeu de Normalização (CEN)

NP EN1998-1 (2010). *"Eurocódigo 8: Projecto para estruturas para resistência aos sismos Parte 1: Regras gerais, acções sísmicas e regras para edifícios."* Bruxelas, Comité Europeu de Normalização (CEN)

NCHRP (2003). *"Prefabricated Bridge Elements and Systems to Limit Traffic Disruption During Construction - A Synthesis of Highway Practice"*. NCHRP Synthesis 324.Transportation Research Board.National Cooperative Highway Research Program. Washington, D.C

O

Ou, Y., Lee, G. C., Wang, P., Tsai, M. and Chang, K. (2008). *"Large scale cyclic tests of precast segmental concrete bridge columns with unbonded post-tensioning tendons"*. Bridge Maintenance, Safety Management, Health Monitoring and Informatics. H.M. Koh and D. M. Frangopol, Taylor & Francis

Ou, Y., Tsai, M., Chang, K. and Lee, G. C. (2010). *"Cyclic behavior of precast segmental concrete bridge columns with high performance or conventional steel reinforcing bars as energy dissipation bars."* Earthquake Engineering and Structural Dynamics 39(11): 1181-1198

Ottosen, N. (1977). *"A Failure Criterion for Concrete"*

P

Palermo, A., Pampanin, S. and Calvi, G. M. (2005). *"Concept and development of hybrid solutions for seismic resistant bridge systems."* Journal of Earthquake Engineering 9(6): 899-921

Palermo, A., Pampanin, S. and Marriott, D. (2007). *"Design, modeling, and experimental response of seismic resistant bridge piers with posttensioned dissipating connections."* Journal of Structural Engineering 133(11): 1648-1661

Pampanin, S. (2003). *"Alternative design philosophies and seismic response of precast concrete buildings."* Structural Concrete 4(4): 203-211

Pang, J. B. K., Eberhard, M. O. and Stanton, J. F. (2010). *"Large-bar connection for precast bridge bents in seismic regions."* Journal of Bridge Engineering 15(3): 231-239

Pantelides, C. P. and Gergely, J. (2008). *"Seismic Retrofit of Reinforced Concrete Beam-Column T-Joints in Bridge Piers with FRP Composite Jackets"*. SP-258: Seismic Strengthening of Concrete Buildings

Park, Y.-J. and Ang, A. H. S. (1985). *"Mechanistic Seismic Damage Model for Reinforced Concrete."* Journal of Structural Engineering 111(4): 722-739.

Parra-Montesinos, G. J., Wight, J. K. and Setkit, M. (2010). *"Earthquake-Resistant Coupling Beams Without Diagonal Reinforcement."* Concrete International 32(12): 36-40

Paulay, T. (1971). *"Coupling beams of reinforced concrete shear walls."* Journal of Structural Engineering 97(3): 843-862

Paulay, T. and Binney, J. R. (1974). *"Diagonally reinforced coupling beams of shear walls"*. Shear in Reinforced Concrete. Detroit, Michigan, American Concrete Institute**:** 579-598

Pegon, P. "*Présentation des joints dilatants*." from http://www-cast3m.cea.fr/html/Pegon/elemjoint.pdf

PCI Bridge Design Manual (1997). *"Fabrication and Construction"*

Priestley, M., Calvi, G. and Kowalsky, M. (2007). *"Displacement-Based Seismic Design of Structures"*, IUSS Press.

Priestley, M. J. N. (1991). *"Overview of PRESSS research program."* PCI Journal 36(4): 50-57.

Proença, J., Romba, J., Barros Viegas, J. and Vieira, A. (2002). *"Experimental Development Stages of an Innovative Earthquake-Resistant Precast Frame System"*. 12nd European Conference on Earthquake Engineering (12ECEE), London, UK

R

Richard, B. and Ragueneau, F. (2013). *"Continuum damage mechanics based model for quasi brittle materials subjected to cyclic loadings: Formulation, numerical implementation and applications."* Engineering Fracture Mechanics 98(0): 383-406

Richard, B., Ragueneau, F., Cremona, C. and Adelaide, L. (2010). *"Isotropic continuum damage mechanics for concrete under cyclic loading: Stiffness recovery, inelastic strains and frictional sliding."* Engineering Fracture Mechanics 77(8): 1203-1223

Rodrigues, H., Arêde, A., Varum, H. and Costa, A. (2013). *"Experimental evaluation of rectangular reinforced concrete column behaviour under biaxial cyclic loading."* Earthquake Engineering & Structural Dynamics 42(2): 239-259

Romão, X. (2012). *"Deterministic and Probabilistic Methods for Structural Seismic Safety Assessment"*. Porto, Faculdade de Engenharia da Universidade do Porto

S

Santos, R. (2012). *"Avaliação da aderência aço-betão em elementos estruturais de B.A."*. Departamento de Engenharia Civil. Aveiro, Tese de Mestrado, Universidade de Aveiro.

Schlaich, M. (2012). *"Die neuen Brücken der deutschen Bahn (english translation) "*. 22 Dresdener Brückenbausymposium. Dresden, Germany

Schokker, A. J., West, J. S., Breen, J. E. and Kreger, M. E. (1999). *"Interim Conclusions, Recommendations and Design Guidelines for Durability of Post-Tensioned Bridge Substructures"*.Center for Transportation Research.The University of Texas at Austin

Snyman, M. F., Bird, W. W. and Martin, J. B. (1991). *"A Simple Formulation of a Dilatant Joint Element Governed by Coulomb Friction."* Engineering Computations 8(3): 215-229

Sobrino, J. A. and Murcia, J. (2007). *"Structural Analisys of High Speed Rail Bridge Substructures. Application to Three Spanish Case Studies"*. Track-Bridge Interaction on High-Speed Railways, Porto, Portugal

Stanton, J., Eberhard, M. and Steuck, K. (2006). *"Rapid construction details for bridges in seismic zones"*. 22th US-Japan Bridge Engineering Workshop

T

Tamai, S. (2014). *"Landscape Bridges - A Technique for a stable roadbed"*. Kunskapsseminarium, Stockholm, Sweden

Tassios, T. P. (1979). *"Properties of bond between concrete and steel under load cycles idealizing seismic actions."* Bulletin d'information du CEB,(131): 65-122

Tassios, T. P., Moretti, M. and Bezas, A. (1996). *"On the behavior and ductility of reinforced concrete coupling beams of shear walls."* ACI Structural Journal 93(6): 711-720

Taylor, D. P. "*Fluid Lock-Up Devices - A Robust Means to Control Multiple Mass Structural Systems Subjected to Seismic or Wind Inputs"*. Inc. Taylor Devices. North Tonawanda, NY, Taylor Devices, Inc.

Tegos, I. A. and Penelis, G. G. (1988). *"Seismic Resistance of Short Columns and Coupling Beams Reinforced with Inclined Bars."* ACI Structural Journal 85(1): 82-88

Tran, V. (2012). *"Drilled Shaft Socket Connections for Precast Columns in Seismic Regions"*, University of Washington

U

UIC (2010). *"High speed rail - Fast track to sustainable mobility"*

V

Vamvatsikos, D. and Cornell, C. A. (2002). *"Incremental dynamic analysis."* Earthquake Engineering & Structural Dynamics(31): 491-514

VanGeem, M. (2006). *"Achieving Sustainability with Precast Concrete."* PCI Journal 51(1): 42-61

Vavel, A. (2004). *"Une innovation pour les ouvrages ferroviaires"*. Construction Moderne/Annuel Ouvrages d'art: 33-36

Vila Pouca, N. (2001). *"Simulação Numérica da Resposta Sísmica de Elementos Laminares em Betão Armado"*. Porto, Tese de Doutoramento, Faculdade de Engenharia da Universidade do Porto

Vision2000 (1995). *"Performance-based seismic engineering"*.SEAOC. Sacramento, CA

W

Wang, J., Ou, Y., Chang, K. and Lee, G. C. (2008). *"Large-scale seismic tests of tall concrete bridge columns with precast segmental construction."* Earthquake Engineering and Structural Dynamics 37(12): 1449–1465

Y

Yee, A. A. (1991). *"Design considerations for precast prestressed concrete building structures in seismic areas."* PCI Journal 36(3): 40-55

Yee, A. A. P. (2001). *"Social and environmental benefits of precast concrete technology."* PCI Journal 46(3): 14-19

Yee, A. A. P. and Eng, H. D. (2001). *"Structural and economic benefits of precast/prestressed concrete construction."* PCI Journal 46(4): 34-43

Z

Zacher, M. and Baeßler, M. (2005). *"Dynamic behavior of ballast on railway bridges"*. Advance Course Dynamics of high speed railway bridges, Porto

Zareian, F. and Medina, R. A. (2010). *"A practical method for proper modeling of structural damping in inelastic plane structural systems."* Computers & Structures 88(1–2): 45-53

WEB LINKS

1. http://www.railtemperature.com/   (Last visit on Jun 2015)
2. http://en.structurae.de/   (Last visit on Jun 2015)
3. http://www.lusas.com/   (Last visit on Jun 2015)
4. http://www.rff.fr/   (Last visit on Jun 2015)
5. http://www.nishimatsu.co.jp/   (Last visit on Jun 2015)
6. http://cms.asce.org/   (Last visit on Jun 2015)
7. http://www.ioa.fr/   (Last visit on Jun 2015)
8. http://horsost.blogs.upv.es/   (Last visit on Jun 2015)
9. http://www.vde8.de/   (Last visit on Jul 2015)
10. http://www.tucrail.be/   (Last visit on Jul 2015)
11. https://www.flickr.com   (Last visit on Jul 2015)
12. http://www.pedelta.es/   (Last visit on Jul 2015)
13. http://www.lgvrhinrhone.com   (Last visit on Sep 2015)
14. http://www.peikko.ca/   (Last visit on Mar 2016)
15. http://www.pfeifer.de/   (Last visit on Mar 2016)
16. https://www.smcon.co.jp/en/   (Last visit on Mar 2016)
17. http://www.uic.org/   (Last visit on Mar 2016)

18. http://www-cast3m.cea.fr/   (Last visit on Jan 2017)
19. http://www.csiamerica.com/products/sap2000   (Last visit on Jan 2017)
20. http://www.liebherr.com/   (Last visit on Feb 2017)
21. http://www.mageba.ch/   (Last visit on Feb 2017)
22. www.sika.pt   (Last visit on Feb 2017)

ANNEXES

A
MODELING PARAMETERS

A.1. MOMENT - CURVATURE ANALYSES (CHAPTER 4 AND CHAPTER 5)

Table A.1 – Concrete modeling parameters for Moment – Curvature analyses

Beton_uni	Chapter 4	Chapter 5						
		SP_PC02A	SP_PC02B	SP_PC02C	SP_M02C	SP_F01	SP_F02	SP_F03
$YOUN\ (x10^9)$	33.00	36.00	37.00	36.00	41.00	40.00	45.00	37.00
NU	0.20	0.20	0.20	0.20	0.20	0.20	0.20	0.20
$STFC\ (x10^6)$	38.00	37.00	45.00	49.00	51.00	47.00	57.00	47.00
$EZER$	0.0022	0.0022	0.0022	0.0022	0.0022	0.0022	0.0022	0.0022
$STFT\ (x10^6)$	2.90	3.00	3.40	3.10	3.00	2.80	3.50	3.70
$ALF1$	0	0	0	0	0	0	0	0
$OME1$	0	0	0	0	0	0	0	0
$ZETA$	200.00	200.00	200.00	200.00	200.00	200.00	200.00	200.00
$ST85$	0	0	0	0	0	0	0	0
$TRAF$	20.00	20.00	20.00	20.00	20.00	20.00	20.00	20.00
$FACL$	0.75	0.75	0.75	0.75	0.75	0.75	0.75	0.75
$FAMX$	20.00	20.00	20.00	20.00	20.00	20.00	20.00	20.00
$STPT$	0	0	0	0	0	0	0	0
RHO	2400	2400	2400	2400	2400	2400	2400	2400
$FAM1$	2.00	2.00	2.00	2.00	2.00	2.00	2.00	2.00
$FAM2$	20.00	20.00	20.00	20.00	20.00	20.00	20.00	20.00

Table A.2 – Steel modeling parameters for Moment – Curvature analyses

Acier_uni	Chapter 4	Chapter 5						
		SP_PC02A	SP_PC02B	SP_PC02C	SP_M02C	SP_F01	SP_F02	SP_F03
YOUN (x10⁹)	200.00	200.00	200.00	200.00	200.00	200.00	200.00	200.00
NU	0.30	0.30	0.30	0.30	0.30	0.30	0.30	0.30
STSY (x10⁶)	500.00	504.00	504.00	504.00	504.00	504.00	504.00	504.00
EPSU	0.2500	0.2500	0.2500	0.2500	0.2500	0.2500	0.2500	0.2500
STSU (x10⁶)	580.00	590.00	590.00	590.00	590.00	590.00	590.00	590.00
ESPH	0.001	0.001	0.001	0.001	0.001	0.001	0.001	0.001
RHO	2400	7850	7850	7850	7850	7850	7850	7850
FALD	4.00	4.00	4.00	4.00	4.00	4.00	4.00	4.00
A6FA	620	620	620	620	620	620	620	620
CFAC	0.50	0.50	0.50	0.50	0.50	0.50	0.50	0.50
AFAC	0.006	0.006	0.006	0.006	0.006	0.006	0.006	0.006
ROFA	20.00	20.00	20.00	20.00	20.00	20.00	20.00	20.00
BFAC (x10⁻³)	6.15	6.15	6.15	6.15	6.15	6.15	6.15	6.15
A1FA	18.50	18.50	18.50	18.50	18.50	18.50	18.50	18.50
A2FA	0.15	0.15	0.15	0.15	0.15	0.15	0.15	0.15

A.2

A.2. REFINED 2D FEM ANALYSES (CHAPTER 6)

Table A.3 – Concrete Modeling Parameters for 2D FEM analyses – Regular Concrete

Damage_tc	Chapter 6					
	SP_M02	SP_M03	SP_M04	SP_PC02A	SP_PC02B	SP_F01
$YOUN\ (x10^9)$	36.00	36.00	40.00	36.00	37.00	40.00
NU	0.20	0.20	0.20	0.20	0.20	0.20
RHO	2400.00	2400.00	2400.00	2400.00	2400.00	2400.00
$GVAL$	250.00	290.00	240.00	200.00	220.00	180.00
$FTUL\ (x10^6)$	3.80	4.40	3.60	3.00	3.40	2.80
$REDC$	0	0	0	0	0	0
$FC01\ (x10^6)$	-20.50	-17.00	-21.50	-17.00	-20.00	-23.50
$RT45$	1.20	1.20	1.20	1.20	1.20	1.20
$FCU1\ (x10^6)$	-51.00	-43.00	-54.00	-42.50	-51.50	-58.50
$STRU\ (x10^{-3})$	-15.00	-15.00	-15.00	-15.00	-15.00	-15.00
$EXTP\ (x10^{-3})$	-5.00	-5.00	-5.00	-5.00	-5.00	-5.00
$STRP\ (x10^6)$	-43.00	-38.00	-45.00	-38.00	-46.00	-52.00
$EXT1\ (x10^{-3})$	-2.30	-2.30	-2.30	-2.20	-2.30	-2.40
$STR1\ (x10^6)$	-48.00	-40.00	-50.00	-40.00	-49.00	-55.00
$EXT2\ (x10^{-3})$	-4.50	-4.50	-4.80	-4.50	-4.50	-4.80
$STR2\ (x10^6)$	-48.00	-40.00	-50.00	-40.00	-49.00	-55.00
$NCRI$	2	2	2	2	2	2

Table A.4 – Concrete Modeling Parameters for 2D FEM analyses – High Ductility Concrete

Damage_tc	Chapter 6					
	SP_M02	SP_M03	SP_M04	SP_PC02A	SP_PC02B	SP_F01
$YOUN$ $(x10^9)$	36.00	36.00	40.00	36.00	37.00	40.00
NU	0.20	0.20	0.20	0.20	0.20	0.20
RHO	2400.00	2400.00	2400.00	2400.00	2400.00	2400.00
$GVAL$	250.00	290.00	240.00	200.00	220.00	180.00
$FTUL$ $(x10^6)$	3.80	4.40	3.60	3.00	3.40	2.80
$REDC$	0	0	0	0	0	0
$FC01$ $(x10^6)$	-20.50	-17.00	-21.50	-17.00	-20.00	-23.50
$RT45$	1.20	1.20	1.20	1.20	1.20	1.20
$FCU1$ $(x10^6)$	-51.00	-43.00	-54.00	-42.50	-51.50	-58.50
$STRU$ $(x10^{-3})$	-25.00	-25.00	-25.00	-25.00	-25.00	-25.00
$EXTP$ $(x10^{-3})$	-8.00	-8.00	-8.00	-8.00	-8.00	-8.00
$STRP$ $(x10^6)$	-43.00	-38.00	-45.00	-38.00	-46.00	-52.00
$EXT1$ $(x10^{-3})$	-2.30	-2.30	-2.30	-2.20	-2.40	-2.40
$STR1$ $(x10^6)$	-45.00	-37.00	-46.50	-37.00	-45.50	-52.00
$EXT2$ $(x10^{-3})$	-7.30	-7.30	-7.30	-7.20	-7.30	-7.30
$STR2$ $(x10^6)$	-45.00	-37.00	-46.50	-37.00	-45.50	-52.00
$NCRI$	2	2	2	2	2	2

A.4

Table A.5 – Steel Modeling Parameters for 2D FEM analyses

Acier_uni Acier_ancrage	Chapter 6 - All specimens		
	Column reinforcement	Stirrups	Beam Reinforcement
$YOUN\ (x10^9)$	190.00	190.00	180.00
NU	0.30	0.30	0.30
$STSY\ (x10^6)$	504.00	504.00	601.00
$EPSU$	0.2500	0.2500	0.2500
$STSU\ (x10^6)$	590.00	590.00	702.00
$ESPH$	0.001	0.001	0.003
RHO	7850	7850	7850
$FALD$	4.00	4.00	4.00
$A6FA$	620	620	620
$CFAC$	0.50	0.50	0.50
$AFAC$	0.006	0.006	0.006
$ROFA$	20.00	20.00	20.00
$BFAC\ (x10^{-3})$	6.15	6.15	6.15
$A1FA$	18.50	18.50	18.50
$A2FA$	0.15	0.15	0.15

Table A.6 – Bond - Slip Modeling Parameters for 2D FEM analyses

Acier_ancrage	Chapter 6				
	SP_M02	SP_M03	SP_M04	SP_PC02A	SP_PC02B
$s_1\ (mm)$	0.79	0.86	0.79	0.90	0.82
$s_2\ (mm)$	2.37	2.57	2.37	2.70	2.45
$s_3\ (mm)$	7.59	8.21	7.59	8.64	7.84
$\tau_{peak}\ (MPa)$	16.77	16.01	17.32	15.21	16.77
$\tau_{res}\ (MPa)$	6.71	6.40	6.93	6.08	6.71

Table A.7 – Joint Modeling Parameters for 2D FEM analyses

Joint_Dilatant	SP_PC02A	SP_PC02B
$K_n\ (MPa/mm)$	65.30	47.60
$K_s\ (MPa/mm)$	18.00	19.10

A.3. GLOBAL 2D BRIDGE IDA ANALYSES (CHAPTER 7)

Table A.8 – Modified Ibarra-Medina-Krawinkler modeling parameters

Backbone			Hysteretic behavior and degradation		
Parameters	Monolithic	Precast	Parameters	Monolithic	Precast
K0	124487653	123677379	*FprPos*	0.35	0.25
as_Plus	0.002	0.007	*FprNeg*	0.35	0.25
as_Neg	0.002	0.007	*A_pinch*	0.00	0.20
My_Plus	66567	42000	*Lamda_S*	0.32	1.00
My_Neg	-66567	-42000	*Lamda_C*	0.32	1.00
theta_p_Plus	0.015	0.012	*Lamda_A*	0.32	1.00
theta_p_Neg	0.015	0.012	*Lamda_K*	0.32	1.00
theta_pc_Plus	0.050	0.600	*c_S*	1.00	1.00
theta_pc_Neg	0.050	0.600	*c_C*	1.00	1.00
Res_Pos	0.200	0.200	*c_A*	1.00	1.00
Res_Neg	0.200	0.200	*c_K*	1.00	1.00
theta_u_Plus	0.180	0.900	*D_Plus*	1.00	1.00
theta_u_Neg	0.180	0.900	*D_Neg*	1.00	1.00

B
MESH DENSITY

Following the modeling strategy presented in Chapter 6, focused on using 2D finite elements under a plane stress assumption for simulation of the double column pier tests, a mesh efficiency study was developed, aiming to define an adequate mesh density for balanced result quality and calculation times. The adopted methodology firstly considered characterization of the main 2D pier dimensions using around 10 eight-node rectangular finite elements, which would lead to targeted mesh densities of 0.035m and 0.055m, regarding beam height and column width, respectively. Those values served as guidance for the establishment of a wider range of mesh density values, enabling the definition of the following four different models, wherein constant mesh density is considered:

- Model A: Maximum element size of the mesh of 1.00cm;
- Model B: Maximum element size of the mesh of 2.50cm;
- Model C: Maximum element size of the mesh of 5.00cm;
- Model D: Maximum element size of the mesh of 10.00cm;

In addition, two plane stress analyses were performed with every mesh, regarding evaluation under both monotonic and cyclic loading conditions, using the same constitutive models that were presented for the main applications in Chapter 6. Considering that high finite element strains are expected for reasonable lateral displacements (due to, for example, low concrete tensile capacity), the loading increments and element size should ideally be calibrated in order to guarantee that the non-linear response calculated at the gauss point level is described by a sufficient number of values. Furthermore, accurate numerical simulations should also take element size into account in the definition of the constitutive properties, in order to reduce mesh dependency. Correspondingly, fine and coarse meshes should be analyzed under different loading conditions, in order to guarantee adequate result quality and reliability. However, if that

were the case in this study, then direct comparison would not be possible, since every model would require a different loading history and constitutive parameters. Within this context, it was decided that accounting for constant loading step and modeling parameters was the best approach, which can lead to varying degrees of convergence difficulty on different models. Nonetheless, it also enables comparison in a straightforward manner, which was deemed suitable for this task.

With that in mind, the current study focused on the following premises:

- Base FEM meshes representing the same specimen (SP_M02);
- The same loading histories were adopted for the four models, using a displacement increment of 0.2mm;
- A maximum displacement limit of 50 mm was considered for both the monotonic and cyclic analyses (roughly corresponding to a 2.00% drift level) in order to prevent the occurrence of large non-linear incursion and near-collapse effects, aiming to avoid the resulting convergence problems;

The previously described strategy guarantees that all the models were subjected to the same exact number of loading steps, which enables direct comparison of calculation times. The respective results are summarized in Table B.1.

Table B.1 – Mesh refinement calculation times

Parameters	Monotonic (250 loading increments)				Cyclic (2272 loading increments)			
Model	1	2	3	4	1	2	3	4
Mesh density *(cm)*	1.0	2.5	5.0	10.0	1.0	2.5	5.0	10.0
Mesh size *(Number of 2D elements)*	31620	4958	1264	368	31620	4958	1264	368
Total calculation time *(min)*	N/A	96	21	20	N/A	443	94	64
Avg. time per element *(sec)*	N/A	1.16	1.00	3.26	N/A	5.36	4.46	10.43
Avg. time per increment *(sec)*	N/A	23.04	5.04	4.80	N/A	11.70	2.48	1.69

The first thing that comes to mind by analyzing Table B.1 is that no results were available for Model A. That is because its model size was too large due to the fine mesh density, leading to the inability to complete the analyses under the wall clock time of 20 hours, as set on the computer cluster. In addition, average calculation time per element and average calculation time per loading increment can serve as an efficiency measurement of the analyses. In that regard, considering that all the analyses used the same loading histories, it is not surprising that Model

D exhibited the smallest average time per loading increment (4.80 and 1.69 seconds for monotonic and cyclic analyses, respectively), as it was also the smallest model. Despite that, the relative increase in calculation time regarding Model C is less than 50% for cyclic analyses, and only 5% for monotonic analyses, which is important to note since Model C is around 250% larger than Model D. The same efficiency cannot be observed with Model B, however, as the decrease in the mesh density parameter leads to an exponentially larger increase in mesh size, which slows down the overall analysis time by a considerable amount (380% and 600% for monotonic and cyclic loading conditions, respectively), when compared to Model D times. On another note, Model D actually shows the lowest values regarding calculation time per element, with an average value that is between two to three times larger than the equivalent value in Models B and C. That means that although the model is considerably small (since it is built using the larger 0.10m 2D elements), its mesh is not refined enough to capture the local deformations of this structure, requiring more iterations per load increment to reach a balanced state than the more refined alternatives. As it stands, Model C displayed the fastest calculation times per element, followed closely by Model B.

It is also interesting to note that the average calculation time parameters indicate higher efficiency for cyclic analyses, which is curious since they typically involve more complex behavior, leading to more lengthy iterations for each loading increment. In reality, that observation could be related to the target displacement limit set for the analyses, which corresponds to a demand level equivalent to a loading stage between yielding and peak response. In that case, it also means that elastic loading and unloading constitute a considerable part of the overall analyses, where the computation of FEM relevant quantities is easier.

Figure B-1 illustrates the Force – Displacement plots obtained from the monotonic and cyclic results of the analyses. As expected, numerical results between the three models are generally equivalent until the onset of cracking and, particularly, yielding. When that occurs, the finer mesh models (B and C) exhibit a slight force reduction when in comparison the coarse mesh model (D). Nonetheless, the overall differences between all the models are small, and even smaller between Models B and C.

a) Monotonic loading   b) Cyclic loading
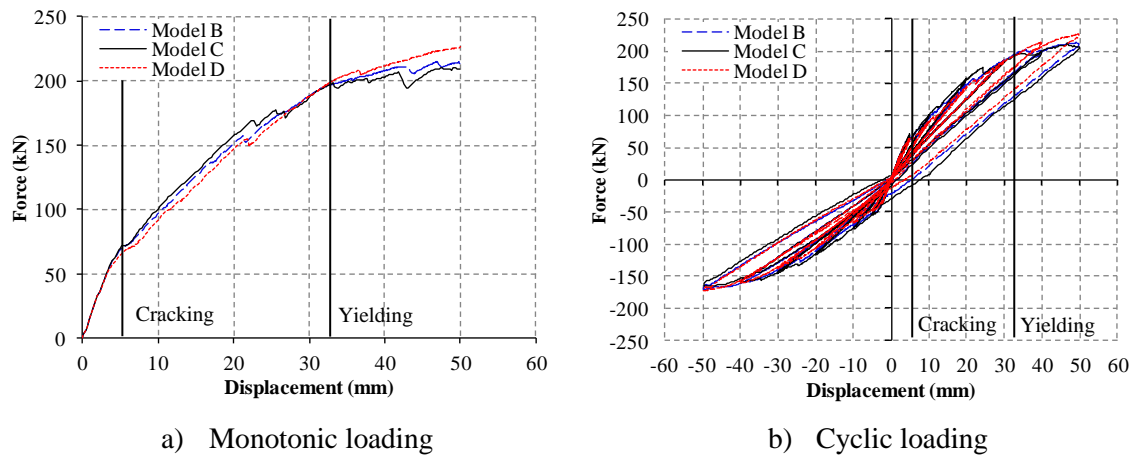
Figure B-1 – Force-Displacement relations for the mesh refinement analyses

With that in mind, Mesh C was considered to enable the best compromise between result quality and computational effort and was, therefore, adopted as the basis for the analyses whose results are presented in Chapter 6.

C
INCREMENTAL DYNAMIC ANALYSES

C.1. GROUND MOTIONS

Name	Year	Magnitude (Mw)	PHA (g)	Duration (s)	SelEQ scaling parameter	Sa_1 (g) - A	Sa_1 (g) - B	Sa_1 (g) - C	Sa_1 (g) - D
1-ImperialValley-06.dat	1979	6.5	0.29	38.96	0.60	0.65	0.67	0.76	0.28
2-ChalfantValley-02.dat	1986	6.2	0.28	21.98	3.40	0.42	0.49	0.39	0.24
3-TaiwanSMART1(40).dat	1986	6.3	0.34	29.00	1.84	0.76	0.68	0.64	0.41
4-LomaPrieta.dat	1989	6.9	0.22	39.64	0.79	0.76	0.59	0.64	0.35
5-Chi-ChiTaiwan.dat	1999	7.6	0.23	90.00	3.61	0.56	0.62	0.69	0.26
6-Northridge-01.dat	1999	7.6	0.19	40.00	0.33	0.55	0.49	0.37	0.40
7-TaiwanSMART1(40).dat	1986	6.3	0.29	29.13	1.13	0.53	0.35	0.38	0.37
8-Chi-ChiTaiwan-05.dat	1999	7.6	0.26	86.00	2.90	0.45	0.49	0.61	0.29
9-ImperialValley-06.dat	1979	6.5	0.35	39.99	3.17	0.69	0.74	0.68	0.28
10-Chi-ChiTaiwan.dat	1999	7.6	0.30	59.00	0.89	0.50	0.41	0.43	0.37
11-SuperstitionHills-02.dat	1987	6.5	0.39	22.12	2.50	0.49	0.61	0.75	0.37
12-Chi-ChiTaiwan-04.dat	1999	6.2	0.23	79.00	3.56	0.57	0.45	0.38	0.33
13-Chi-ChiTaiwan.dat	1999	7.6	0.20	90.00	1.10	0.34	0.49	0.51	0.35
14-Chi-ChiTaiwan-06.dat	1999	6.3	0.20	101.00	3.70	0.34	0.41	0.45	0.34
15-LomaPrieta.dat	1989	6.9	0.34	39.95	3.77	0.57	0.79	0.69	0.45
16-BigBear-01.dat	1992	6.5	0.24	60.01	2.70	0.45	0.40	0.34	0.31
17-Northridge-01.dat	1999	7.6	0.23	40.00	2.69	0.56	0.46	0.56	0.27
18-Northridge-01.dat	1994	6.7	0.25	40.00	2.86	0.59	0.76	0.79	0.35
19-ImperialValley-06.dat	1979	6.5	0.29	99.92	1.21	0.62	0.83	0.75	0.24
20-VictoriaMexico.dat	1980	6.3	0.24	15.58	3.44	0.54	0.40	0.60	0.27

A - Macheda Viaduct
B - Palheta Viaduct
C - Viaduct over Degebe River
D - Viaduct over Ribeira da Laje

1-ImperialValley-06
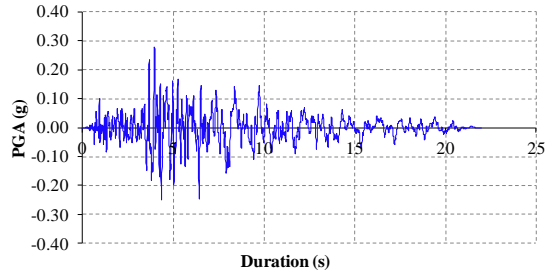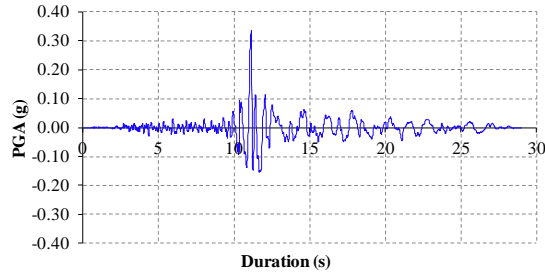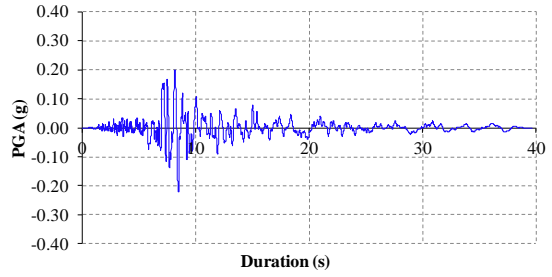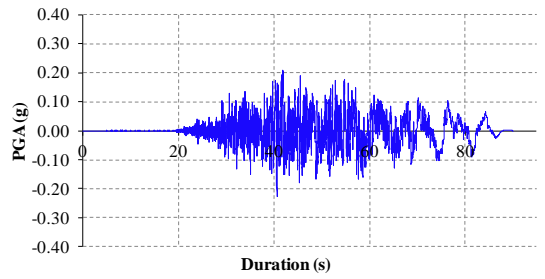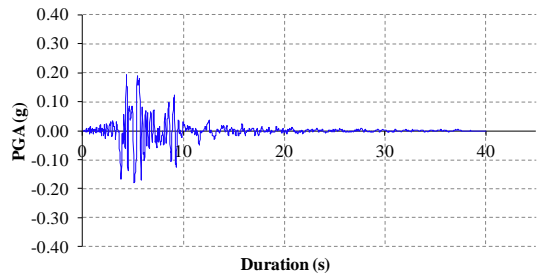
2-ChalfantValley-02

3-TaiwanSMART1(40)

4-LomaPrieta

5-Chi-ChiTaiwan

6-Northridge-01

7-TaiwanSMART1(40)

8-Chi-ChiTaiwan-05

9-ImperialValley-06

10-Chi-ChiTaiwan

C.2
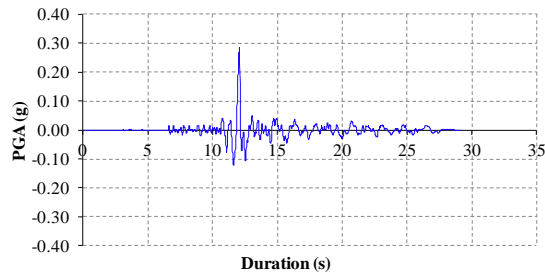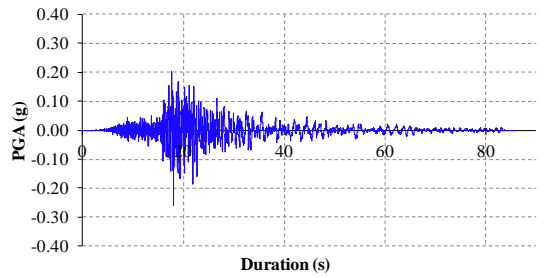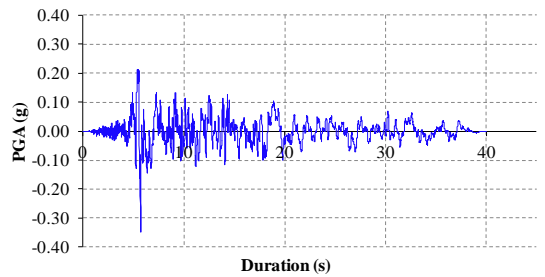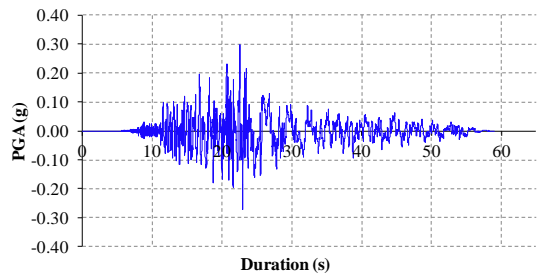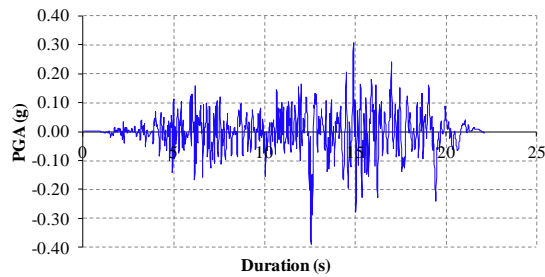
11-SuperstitionHills-02
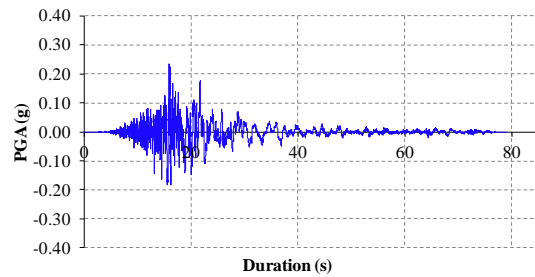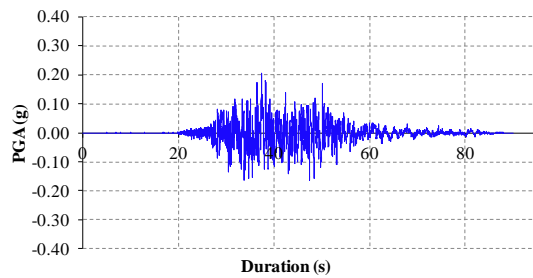
12-Chi-ChiTaiwan-04

13-Chi-ChiTaiwan.dat
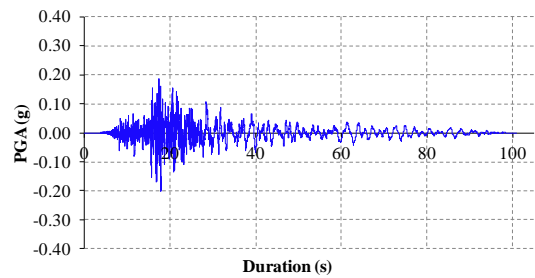
14-Chi-ChiTaiwan-06
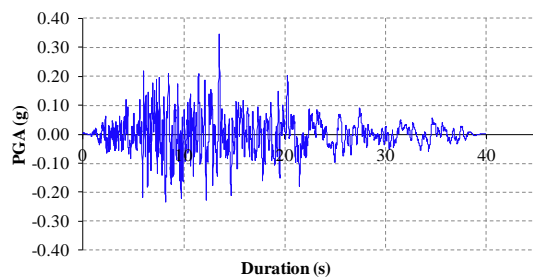
15-LomaPrieta
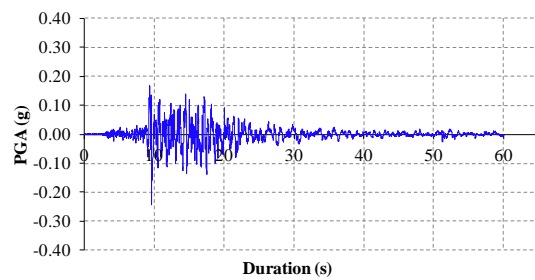
16-BigBear-01
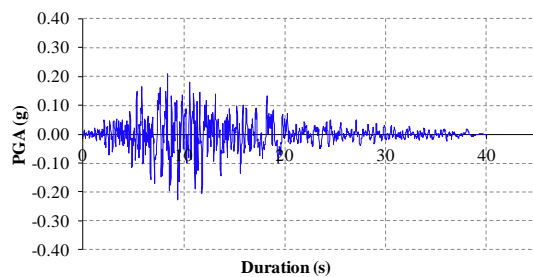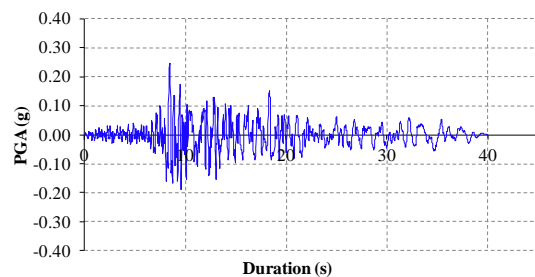
17-Northridge-01

18-Northridge-01
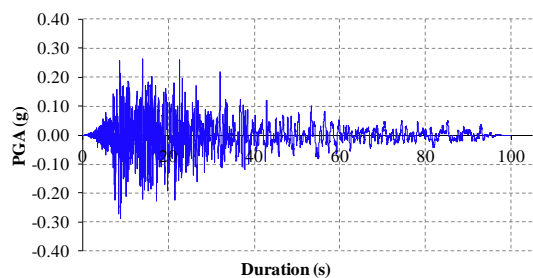
19-ImperialValley-06
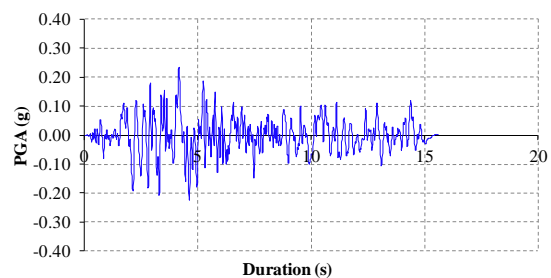
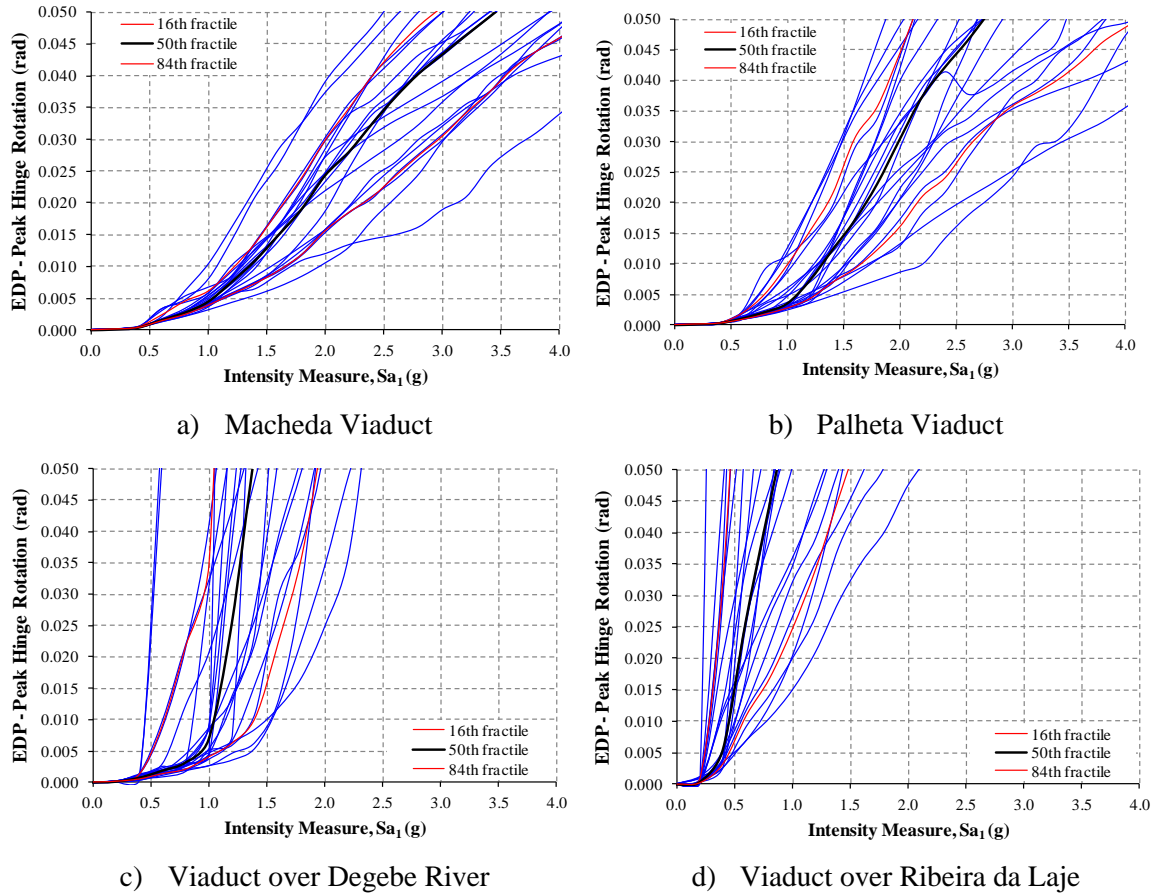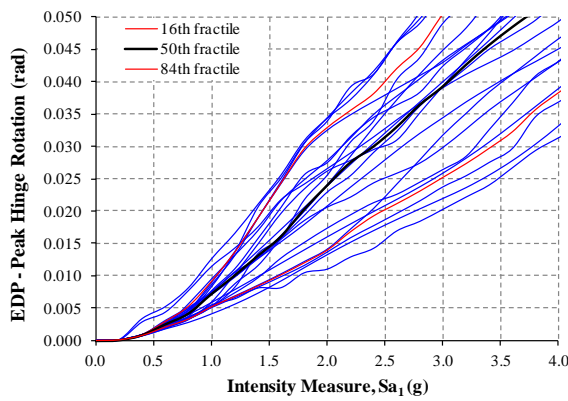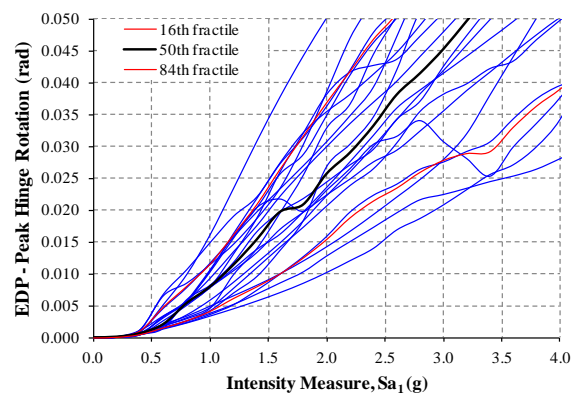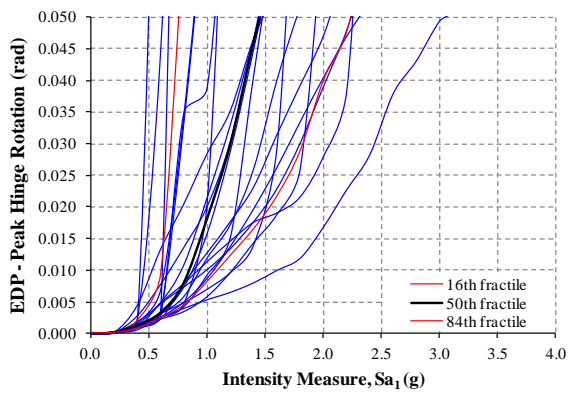20-VictoriaMexico

C.2. DAMAGE MEASURE 1: STRUCTURAL PERFORMANCE

a) Macheda Viaduct

b) Palheta Viaduct

c) Viaduct over Degebe River

d) Viaduct over Ribeira da Laje

Figure C.1 – Hinge Rotation IDA curves – Monolithic Model

a)   Macheda Viaduct

b)   Palheta Viaduct

c)   Viaduct over Degebe River
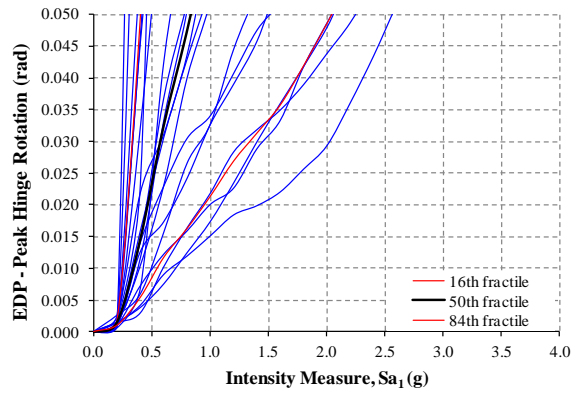
d)   Viaduct over Ribeira da Laje

Figure C.2 – Hinge Rotation IDA curves – Precast Model
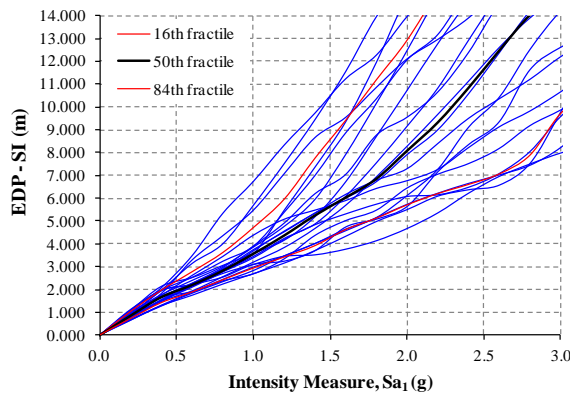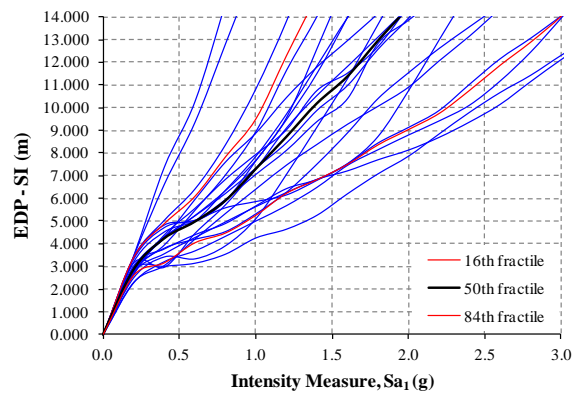
C.3. DAMAGE MEASURE 2: LATERAL DEFLECTION

a)   Macheda Viaduct

b)   Palheta Viaduct

c)   Viaduct over Degebe River

d)   Viaduct over Ribeira da Laje
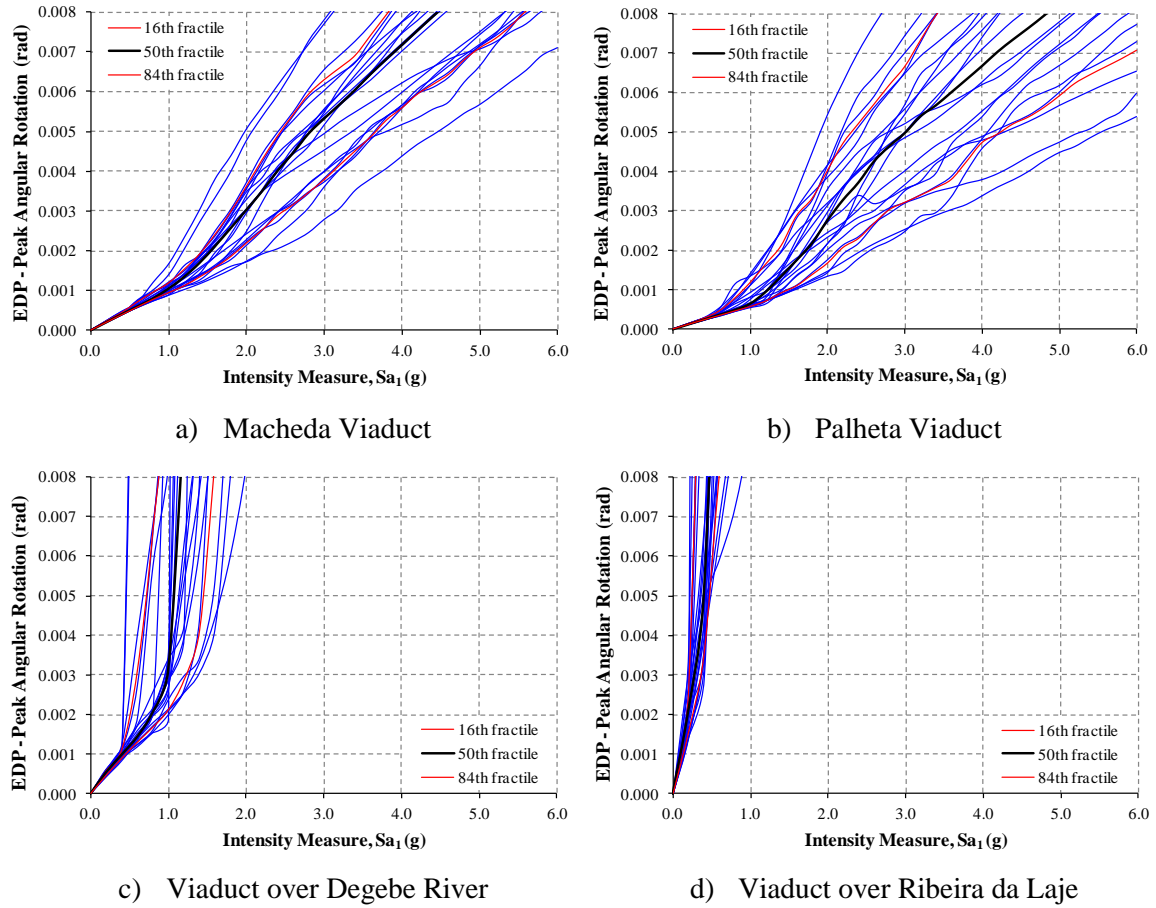
Figure C.3 – Angular Rotation IDA curves – Monolithic Model
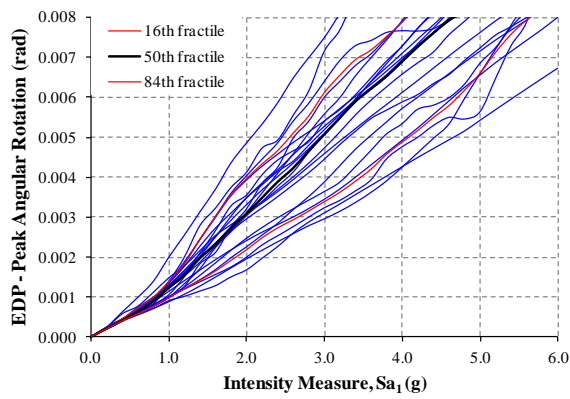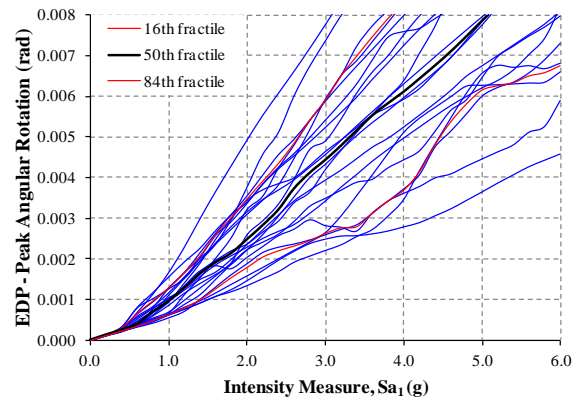
a) Macheda Viaduct
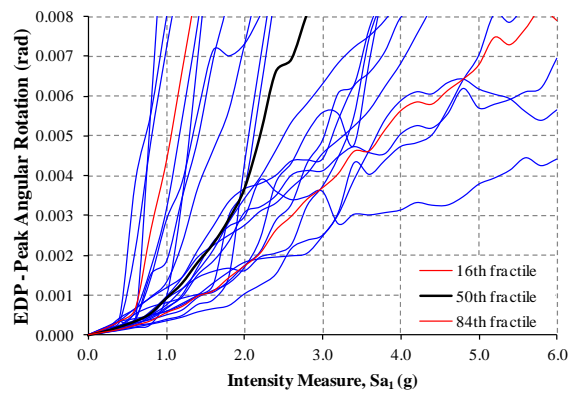
b) Palheta Viaduct

c) Viaduct over Degebe River
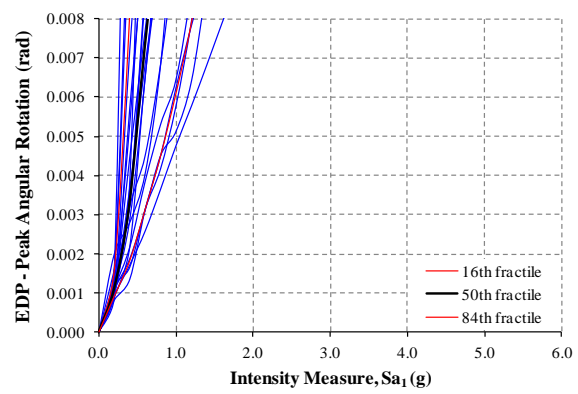
d) Viaduct over Ribeira da Laje

Figure C.4 – Angular Rotation IDA curves – Precast Model

C.4. DAMAGE MEASURE 3: DERAILMENT CONDITIONS
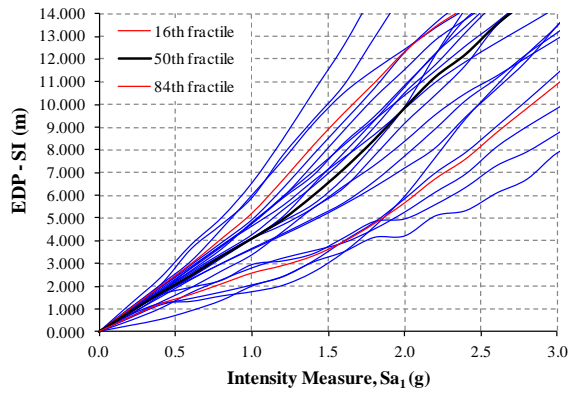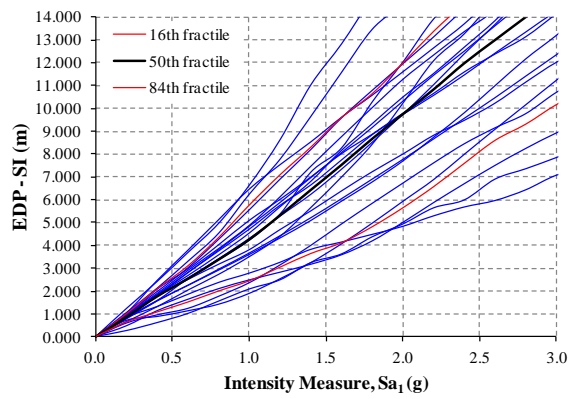

a) Macheda Viaduct
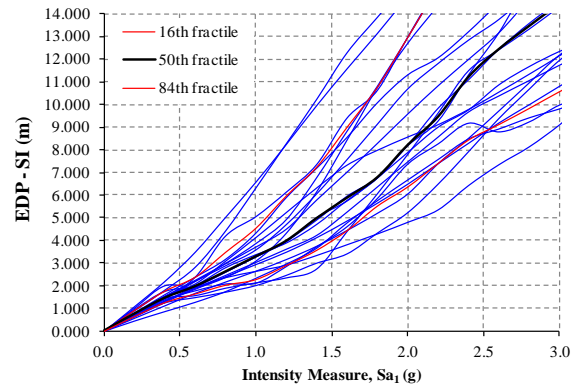
b) Palheta Viaduct
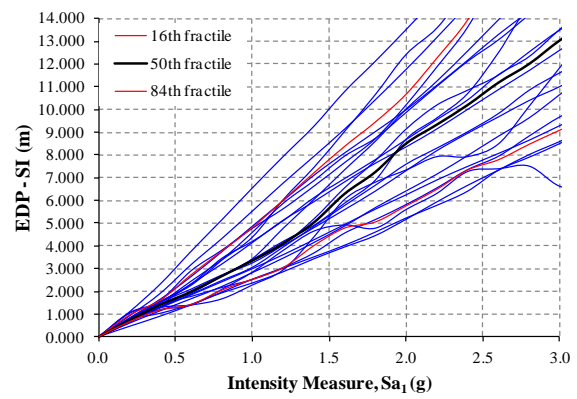
c) Viaduct over Degebe River

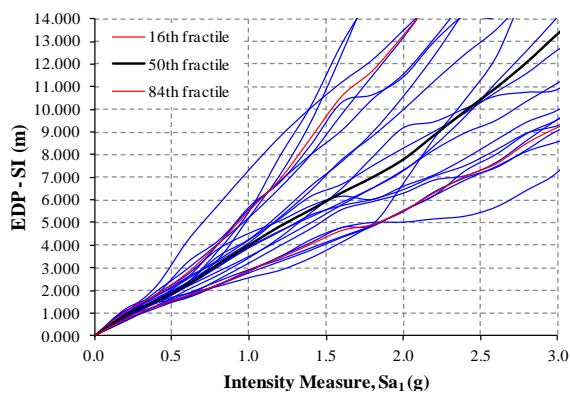d) Viaduct over Ribeira da Laje

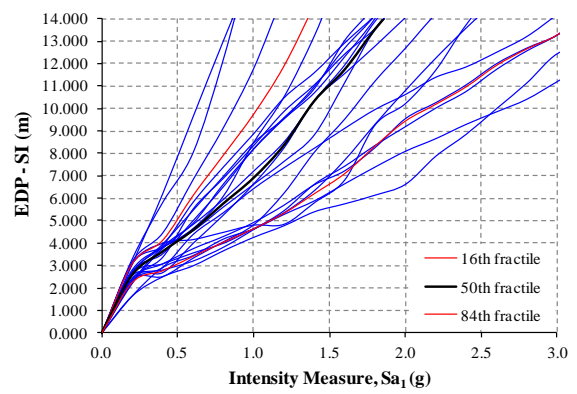Figure C.5 – Spectral Intensity IDA curves – Monolithic Model

a)   Macheda Viaduct

b)   Palheta Viaduct

c)   Viaduct over Degebe River

d)   Viaduct over Ribeira da Laje

Figure C.6 – Spectral Intensity IDA curves – Precast Model